1-1-2010

Experimental And Theoretical Analysis Of The Electronic Behavior In Five-Coordinate Iron(iii) And Six-Coordinate Cobalt(iii) Complexes With Electroactive Phenol-Rich Ligands

Marco Mathieu Allard
Wayne State University

Recommended Citation

EXPERIMENTAL AND THEORETICAL ANALYSIS OF THE ELECTRONIC BEHAVIOR IN FIVE-COORDINATE IRON(III) AND SIX-COORDINATE COBALT(III) COMPLEXES WITH ELECTROACTIVE PHENOL-RICH LIGANDS

by

MARCO MATHIEU ALLARD

DISSERTATION

Submitted to the Graduate School

of Wayne State University,

Detroit, Michigan

in partial fulfillment of the requirements

for the degree of

DOCTOR OF PHILOSOPHY

2010

MAJOR: CHEMISTRY (Inorganic)

_____

Advisor   Date

_____

_____

DEDICATION

This dissertation is dedicated to my dearest wife Tina, and my sons Tristan and Maxence for their patience, understanding, and affection towards me while I completed this Ph. D.

ACKNOWLEDGEMENTS

TABLE OF CONTENTS

LIST OF TABLES

LIST OF FIGURES

LIST OF SCHEMES

Chapter 1

Introduction

Chapter 1

1.1. Introduction

New materials figure among the major driving factors in technological advancements that result in an improved standard of living and an overall benefit to mankind.[1] Historically, scientific advancements have never occurred at such a fast pace since the industrial revolution.[1] One of these major advancements was the invention of the transistor at Bell laboratories[2] in 1947, where even since its first inception, its usefulness seems to have made its way into our everyday lives. The first transistor was centimeters in size, and now commercially available transistors in Central Processing Units (CPU) have reached 32 nanometers in size.[3] Gordon E. Moore, a cofounder of Intel Inc. in 1965, famously made the statement that is better known as "Moore's law" which states that "the complexity for minimum component costs has increased [and will be increased] at a rate of roughly a factor of two per year...." [4] This "law" has been debated and evoked on numerous occasions ever since it was first enunciated, resulting in the consensus that commercial manufacturers will *someday* face the daunting challenge of having to deal with molecular sized components.[5] As can be shown in **Figure 1.1** this limit is imminent, and practical approaches to molecular sized computing have been of great interest.[5] The Nobel laureate Richard Feynman[5], as far back as 1959, had predicted that the practical use of nanometer molecular components would be utterly challenging and accurately stated the enormous challenge "of controlling things on the small scale." The original idea of "moletronics" [6] has been debated and further discussion can be found in numerous books and scientific publications.[5, 7] In this dissertation, we will restrict our discourse to

the well accepted idea that molecular sized components will be a reality within the next couple decades, as one can readily argue that 32 nm sized transistors are *already* the size of some very large molecules, such as proteins.
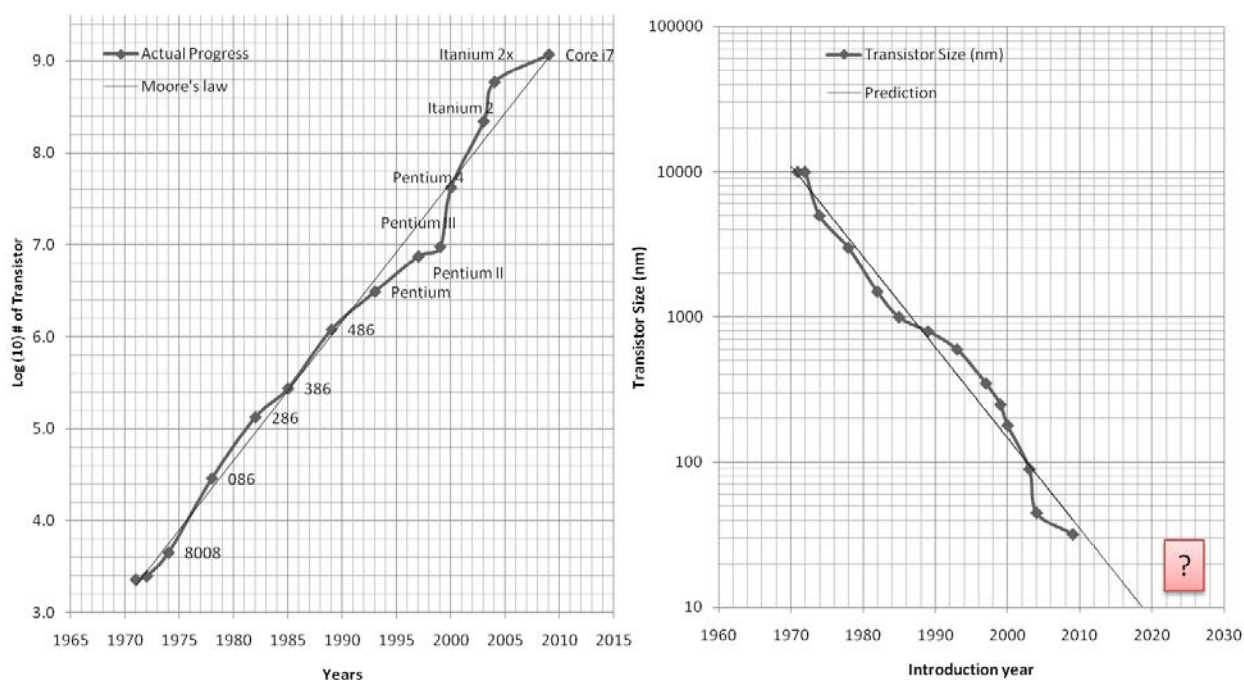
Figure 1.1. Transistor size over the years.[4]

1.2. Thin Films

Arguably, thin films are a part of all commercial processes in the manufacture of electronic components,[8] and are an integral part of the remaining issues which need to be addressed in order to be compatible with widely used processes. Our research group is actively involved in the understanding of how metal containing surfactants behave at the air-water interface, and how to control their physical properties.[9] We are actively studying self-assembled monolayers and Langmuir-Blodgett thin film deposition techniques[9d, 10] to study how metal-containing surfactants behave on a solid substrate.

However, it has become apparent[9b, c, 10e] that fundamental studies to investigate the metal and ligand interactions are crucial for this approach to be successful.

1.3. Molecular Requirements

There are many complex requirements for molecular electronics, as previously summarized by Lindsey and Bocian[11] such as (but not limited to): the ability to (i) be self-assembled, (ii) be addressed electrically, (iii) operate at ambient conditions, (iv) be cycled multiple times, (v) require no moving parts for writing/reading, (vi) be scalable to small dimensions, and (vii) have small footprints required for high charge density. All of these requirements are crucial for finding a successful route to further miniaturization. Numerous approaches have been devised[12] using a panoply of molecules in combination with different modes of action, ranging from interlocked molecules[13] to organic semi-conductors.[14] However, molecules are not without limitations, since they have properties that can be challenging to control, such as (i) electron quantum tunneling, (ii) dimer formation, (iii) excited states, and (iv) impurities. All of these problems could yield devices with thermal stability issues as well as resulting in erroneous calculations or corruption of stored data. There are also numerous signal amplification[5] issues to overcome for molecular compatibility with the "macroscopic" world. Nonetheless, molecular and nanometer sized components and products will inevitably be part of some logic functions in one form or another. There are numerous companies[15] involved in bringing to market memory-type devices, and this is where molecular electronics are making their first "main-stream" appearances.

1.4. Bistability

It is well known that digital data is based on a binary system of "1's" and "0's", and it is therefore crucial that molecular electronics be compatible with this "two states" mode of operation. Molecules that exhibit two reversible stable states are a logical starting point (see **Figure 1.2**) for molecular switching. Electrochemically-driven bistability is therefore a very attractive proposition, since electrons are involved, and could eventually be compatible with modern electronic circuitry, provided that signal amplification issues can be addressed. Many strides have been made regarding signal amplifications, and various techniques have been described in the scientific literature,[16] that are outside the scope of this dissertation.
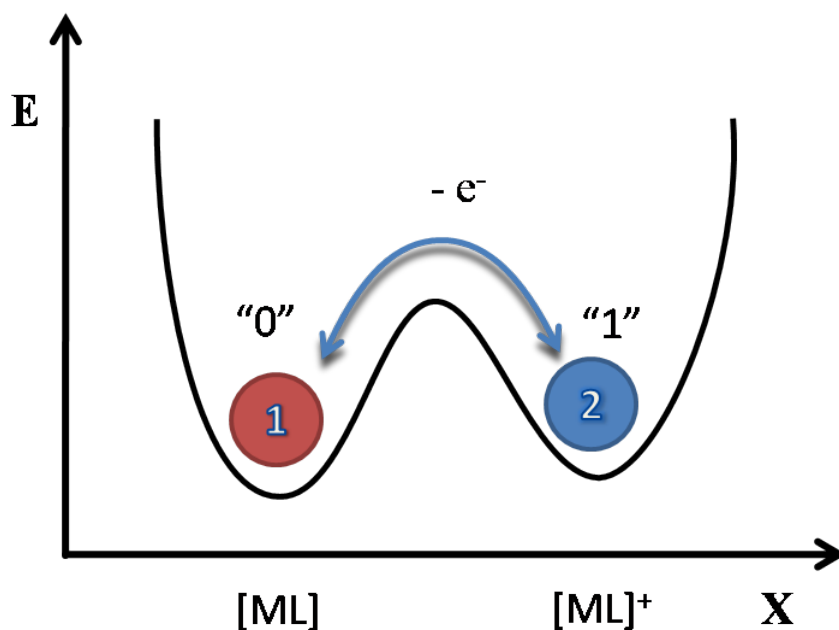
Figure 1.2. Bistability.

1.5. Metal-Radical Approach

Our research group is actively involved in the fundamental understanding of how metal-organic radical complexes behave.[9, 17] We hypothesize that metal-radical complexes exhibit bistability and therefore fulfill some of the requirements necessary for molecular switches. This bistability is based on two states: (i) a resting metal-ligand state, and (ii) a metal-organic radical state. This approach involves the design and synthesis of transition metal complexes with electroactive or non-innocent ligands capable of stabilizing relatively long-lived organic radicals.[9] The built-in ability of these complexes to generate and stabilize radicals fulfills two of the basic requirement for molecular switching, namely: (i) responding to an external stimulus, and (ii) displaying effective bistability.[12b] Their study is by no means trivial, since organic radicals tend to be extremely reactive and/or air unstable.[18] Metal complexes containing organic radicals have complicated electronic behaviors and are challenging to study due to the difficulty in assigning proper physical oxidation states.[19] Generating these radicals by electrochemical[20] methods with readily available bench top electrochemical equipment is therefore our method of choice.

Within this approach it is therefore preferable, as a starting point, to have only one metal center with multiple nearby redox moieties rather than multiple metal centers with one redox bridging ligand. There is an added prospect of multiple states if more than one radical can be stabilized in combination with more than one stable oxidation state of the metal ion, potentially increasing local charge density equivalence in resulting films.

Substituted phenols have been shown to coordinate to nearly all first row transition metal ions and possess the ability to generate extremely stable phenoxyl radicals.[19b, 21] In some rare cases, crystal structures of phenoxyl radical-containing metal complexes were even isolated.[22] Metal complexes capable of generating phenoxyl radical intermediates are commercially used as catalysts[23] for a wide variety of oxidative processes, and we therefore settle our choice on them as a starting point. We hypothesize that because they can be used as efficient catalysts with high turnover rates, they should be chemically robust enough to withstand extensive redox cycling. This robustness is one of the other requirements for a molecular switch.

1.6. Background on Phenoxyl Radicals

The stability of phenoxyl radicals has been shown to be extremely dependent on the nature and position of substituents of the phenol ring.[24] Electron-donating groups, such as methyl, methoxy, and *t*-butyl, are excellent at stabilizing phenoxyl radicals through electron-donation into the aromatic ring. The *–ortho* and *–para* positions of the ring are important due to resonance structure stabilization of these radicals, as shown in **Scheme 1.1**. The same trend can be observed from **Table 1.1** which shows that the electron-donating groups can better stabilize the radical than electron-withdrawing groups. This stabilization is achieved by lowering the enthalpy of formation.[25]
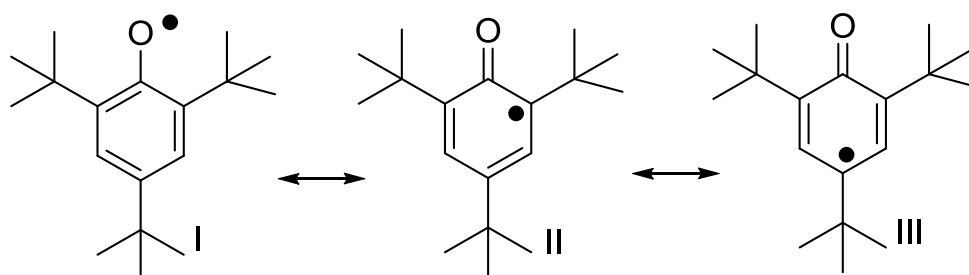
Scheme 1.1. Phenoxyl radical resonance forms.

Table 1.1. Calculated relative enthalpies of oxidation (B3LYP, 6-311+G(d))

R =	Relative Energy Difference for Oxidation
	(ΔH, kcal/mol)
-OCH$_3$	-14.2
-CH$_3$	-8
-C$_4$H$_9$	-5.3
-H	0
-F	9.7
-Cl	17.8
-Br	20.2
-NO$_2$	60.7
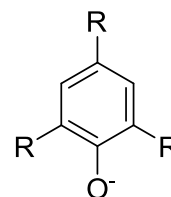
When the data from **Table 1.1** is arranged in terms of increasing enthalpy of oxidation, the following order is obtained: -OCH$_3$ > -CH$_3$ > -C$_4$H$_9$ > -H > -F > -Cl > -Br > -NO$_2$. This trend relates the ease of formation of the phenoxyl radical to readily available substituents. Unfortunately this does not give any immediate useful information about the kinetic stability of the radicals or possible solvation effects which can be important

driving factors for radical stability.[26] As **Scheme 1.2** shows, phenoxyl radicals are extremely reactive and if they are not adequately protected will easily dimerize when the radical is generated.[27] A more resilient approach is to have good electron-donating groups at both the –*ortho* and -*para* positions, such as *t*-butyl, groups which are bulky enough to act as kinetic protectors. As a testament to their stability and dimer formation resistance, Mayer *et al.*[28] recently published a crystal structure of a radical-containing monomer (**Figure 1.3**).
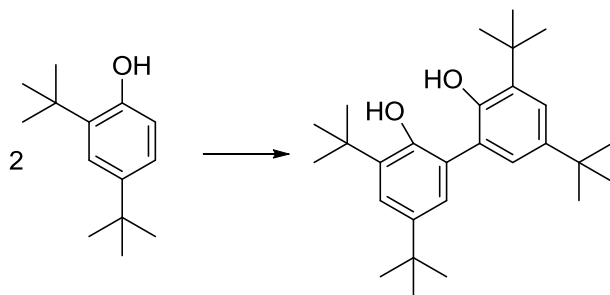
Scheme 1.2. Phenoxyl radical dimer formation.
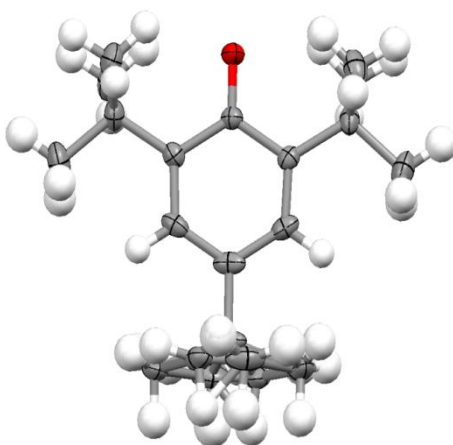
Figure 1.3. Crystal structure of a phenoxyl radical.[28]

hydrogen, carbon, and oxygen atoms in white, gray, and red, respectively

Though the study of multiple redox centers is not without challenges, we have explored two series of such complexes and the results are described in Chapters 4 and 5 of this dissertation. We discuss in detail their structures, electrochemistry, spectroscopy, and electronic structures.

1.7. References

1.   Beck B., R., *World History: Patterns of Interaction.* McDougal Littell: Evanston, Illinois, 1999.

2.   Arns, R. G., The other transistor: early history of the metal-oxide semiconductor field-effect transistor. *Engineering Science and Education Journal* **1998,** *7* (5), 233-240.

3.   http://www.intel.com/products.

4.   http://en.wikipedia.org/wiki/Moores_law.

5.   Tour, J. M., *Molecular Electronics: Commercial Insights, Chemistry, Devices, Architecture and Programming* World Scientific Publishing Company, Incorporated: 2003.

6.   http://en.wikipedia.org/wiki/Moletronics.

7.   (a) Garzon, A.; Granadino-Roldan, J. M.; Moral, M.; Garcia, G.; Fernandez-Liencres, M. P.; Navarro, A.; Pena-Ruiz, T.; Fernandez-Gomez, M., Density functional theory study of the optical and electronic properties of oligomers based on phenyl-ethynyl units linked to triazole, thiadiazole, and oxadiazole rings to be used in molecular electronics. *J. Chem. Phys.* **2010,** *132* (6), 064901; (b) Astruc, D.; Boisselier, E.; Ornelas, C., Dendrimers designed for functions: from physical, photophysical, and supramolecular

properties to applications in sensing, catalysis, molecular electronics, photonics, and nanomedicine. *Chem. Rev.* **2010,** *110* (4), 1857-1959; (c) Yaffe, O.; Scheres, L.; Puniredd, S. R.; Stein, N.; Biller, A.; Lavan, R. H.; Shpaisman, H.; Zuilhof, H.; Haick, H.; Cahen, D.; Vilan, A., Molecular electronics at metal/semiconductor junctions. Si inversion by sub-nanometer molecular films. *Nano Lett.* **2009,** *9* (6), 2390-4; (d) Akkerman, H. B.; Blom, P. W.; de Leeuw, D. M.; de Boer, B., Towards molecular electronics with large-area molecular junctions. *Nature* **2006,** *441* (7089), 69-72; (e) Martin, C. R.; Baker, L. A., Materials science. Expanding the molecular electronics toolbox. *Science* **2005,** *309* (5731), 67-8; (f) *Introducing Molecular Electronics*. Springer: New York, 2005; (g) Elke, S.; Peter, R., Focus on molecular electronics. *New J. Phys.* **2008,** *10* (6), 065004.

8.   Wetzig, K.; Schneider, C. M., *Metal Based Thin Films for Electronics*. Wiley-VCH Verlag & Co.: 2005.

9.   (a) Imbert, C.; Hratchian, H. P.; Lanznaster, M.; Heeg, M. J.; Hryhorczuk, L. M.; McGarvey, B. R.; Schlegel, H. B.; Verani, C. N., Influence of Ligand Rigidity and Ring Substitution on the Structural and Electronic Behavior of Trivalent Iron and Gallium Complexes with Asymmetric Tridentate Ligands. *Inorg. Chem.* **2005,** *44* (21), 7414-7422; (b) Lanznaster, M.; Heeg, M. J.; Yee, G. T.; McGarvey, B. R.; Verani, C. N., Design of Molecular Scaffolds Based on Unusual Geometries for Magnetic Modulation of Spin-Diverse Complexes with Selective Redox Response. *Inorg. Chem.* **2007,** *46* (1), 72-78; (c) Lanznaster, M.; Hratchian, H. P.; Heeg, M. J.; Hryhorczuk, L. M.; McGarvey, B. R.; Schlegel, H. B.; Verani, C. N., Structural and Electronic Behavior of

Unprecedented Five-Coordinate Iron(III) and Gallium(III) Complexes with a New Phenol-Rich Electroactive Ligand. *Inorg. Chem.* **2006,** *45* (3), 955-957; (d) Lesh, F. D.; Hindo, S. S.; Heeg, M. J.; Allard, M. M.; Jain, P.; Peng, B.; Hryhorczuk, L.; Verani, C. N., On the effect of coordination and protonation preferences in the amphiphilic behavior of metallosurfactants with asymmetric headgroups. *Eur. J. Inorg. Chem.* **2009,** (3), 345-356; (e) Shakya, R.; Hindo, S. S.; Wu, L.; Allard, M. M.; Heeg, M. J.; Hratchian, H. P.; McGarvey, B. R.; Da Rocha, S. R. P.; Verani, C. N., Archetypical Modeling and Amphiphilic Behavior of Cobalt(II)-Containing Soft-Materials with Asymmetric Tridentate Ligands. *Inorg. Chem.* **2007,** *46* (23), 9808-9818; (f) Shakya, R.; Imbert, C.; Hratchian, H. P.; Lanznaster, M.; Heeg, M. J.; McGarvey, B. R.; Allard, M.; Schlegel, H. B.; Verani, C. N., Structural, spectroscopic, and electrochemical behavior of trans-phenolato cobalt(III) complexes of asymmetric NN'O ligands as archetypes for metallomesogens. *Dalton Trans.* **2006,** (21), 2517-2525.

10.	(a) Driscoll, J. A.; Allard, M. M.; Wu, L.; Heeg, M. J.; da Rocha, S. R. P.; Verani, C. N., Interfacial behavior and film patterning of redox-active cationic copper(II)-containing surfactants. *Chem.--Eur. J.* **2008,** *14* (31), 9665-9674; (b) Hindo, S. S.; Shakya, R.; Rannulu, N. S.; Allard, M. M.; Heeg, M. J.; Rodgers, M. T.; da Rocha, S. R. P.; Verani, C. N., Synthesis, Redox, and Amphiphilic Properties of Responsive Salycilaldimine-Copper(II) Soft Materials. *Inorg. Chem.* **2008,** *47* (8), 3119-3127; (c) Hindo, S. S.; Shakya, R.; Shanmugam, R.; Heeg, M. J.; Verani, C. N., Metalloamphiphiles with [Cu2] and [Cu4] Headgroups: Syntheses, Structures, Langmuir Films, and Effect of Subphase Changes. *Eur. J. Inorg. Chem.* **2009,** (31), 4686-4694; (d)

Jayathilake, H. D.; Driscoll, J. A.; Bordenyuk, A. N.; Wu, L.; da Rocha, S. R. P.; Verani, C. N.; Benderskii, A. V., Molecular Order in Langmuir-Blodgett Monolayers of Metal-Ligand Surfactants Probed by Sum Frequency Generation. *Langmuir* **2009,** *25* (12), 6880-6886; (e) Lesh, F. D.; Shanmugam, R.; Allard, M. M.; Lanznaster, M.; Heeg, M. J.; Rodgers, M. T.; Shearer, J. M.; Verani, C. N., A Modular Approach to Redox-Active Multimetallic Hydrophobes of Discoid Topology. *Inorg. Chem.* **2010,** *49* (16), 7226-7228; (f) Shakya, R.; Hindo, S. S.; Wu, L.; Allard, M. M.; Heeg, M. J.; Hratchian, H. P.; McGarvey, B. R.; Da Rocha, S. R. P.; Verani, C. N., Archetypical Modeling and Amphiphilic Behavior of Cobalt(II)-Containing Soft-Materials with Asymmetric Tridentate Ligands. *Inorg. Chem.* **2007,** *46* (23), 9808-9818; (g) Shakya, R.; Hindo, S. S.; Wu, L.; Ni, S.; Allard, M.; Heeg, M. J.; da Rocha, S. R. P.; Yee, G. T.; Hratchian, H. P.; Verani, C. N., Amphiphilic and magnetic properties of a new class of cluster-bearing [L2Cu4(micro 4-O)(micro 2-carboxylato)4] soft materials. *Chem.--Eur. J.* **2007,** *13* (35), 9948-9956; (h) Verani, C. N., Efforts toward mono and multimetallic redox-active amphiphiles. *Polym. Prepr.* **2009,** *50* (2), 271-272.

11.   (a) Liu, Z.; Yasseri, A. A.; Lindsey, J. S.; Bocian, D. F., Molecular Memories That Survive Silicon Device Processing and Real-World Operation. *Science* **2003,** *302* (5650), 1543-1545; (b) Roth, K. M.; Lindsey, J. S.; Bocian, D. F.; Kuhr, W. G., Characterization of Charge Storage in Redox-Active Self-Assembled Monolayers. *Langmuir* **2002,** *18* (10), 4030-4040.

12.   (a) Aviram, A.; Ratner, M. A., Molecular rectifiers. *Chem. Phys. Lett.* **1974,** *29* (2), 277-283; (b) Marchivie, M.; Guionneau, P.; Howard, J. A. K.; Chastanet, G.; Letard,

J. F.; Goeta, A. E.; Chasseau, D., Structural Characterization of a Photoinduced Molecular Switch. *J. Am. Chem. Soc.* **2002,** *124* (2), 194-195; (c) Chisholm, M. H.; Feil, F.; Hadad, C. M.; Patmore, N. J., Electronically Coupled MM Quadruply-Bonded Complexes (M = Mo or W) Employing Functionalized Terephthalate Bridges: Toward Molecular Rheostats and Switches. *J. Am. Chem. Soc.* **2005,** *127* (51), 18150-18158; (d) Uchiyama, S.; McClean, G. D.; Iwai, K.; Prasanna de Silva, A., Membrane Media Create Small Nanospaces for Molecular Computation. *J. Am. Chem. Soc.* **2005,** *127* (25), 8920-8921; (e) Holten, D.; Bocian, D. F.; Lindsey, J. S., Probing Electronic Communication in Covalently Linked Multiporphyrin Arrays. A Guide to the Rational Design of Molecular Photonic Devices. *Acc. Chem. Res.* **2002,** *35* (1), 57-69; (f) Wassel, R. A.; Fuierer, R. R.; Kim, N.; Gorman, C. B., Stochastic variation in conductance on the nanometer scale: a general phenomenon. *Nano Lett.* **2003,** *3* (11), 1617-1620.

13.　　Pease, A. R.; Jeppesen, J. O.; Stoddart, J. F.; Luo, Y.; Collier, C. P.; Heath, J. R., Switching Devices Based on Interlocked Molecules. *Acc. Chem. Res.* **2001,** *34* (6), 433-444.

14.　　Mathijssen, S. G. J.; Smits, E. C. P.; van Hal, P. A.; Wondergem, H. J.; Ponomarenko, S. A.; Moser, A.; Resel, R.; Bobbert, P. A.; Kemerink, M.; Janssen, R. A. J.; de Leeuw, D. M., Monolayer coverage and channel length set the mobility in self-assembled monolayer field-effect transistors. *Nat. Nanotechnol.* **2009,** *4* (10), 674-680.

15.　　(a) http://www.calmec.com/; (b) http://www.zettacore.com/.

16.　　(a) Abruna, H. D.; Kiya, Y.; Henderson, J. C., Batteries and electrochemical capacitors. *Physics Today* **2008,** *61* (12), 43-47; (b) Takada, K.; Goldsmith, J. I.;

Bernhard, S.; Abruna, H. D., Redox-active dendrimers in solution and as films on surfaces. *Encyclopedia of Electrochemistry* **2007,** *11*, 729-753; (c) Ulgut, B.; Abruna, H. D., Electron Transfer through Molecules and Assemblies at Electrode Surfaces. *Chem. Rev.* **2008,** *108* (7), 2721-2736.

17.   Shetty, S.; Kar, R.; Kanhere, D. G.; Pal, S., Intercluster reactivity of metalloaromatic and antiaromatic compounds and their applications in molecular electronics: a theoretical investigation. *J. Phys. Chem. A* **2006,** *110* (1), 252-6.

18.   Carter, S. M.; Sia, A.; Shaw, M. J.; Heyduk, A. F., Isolation and Characterization of a Neutral Imino-semiquinone Radical. *J. Am. Chem. Soc.* **2008,** *130* (18), 5838-5839.

19.   (a) Chaudhuri, P.; Verani, C. N.; Bill, E.; Bothe, E.; Weyhermueller, T.; Wieghardt, K., Electronic Structure of Bis(o-iminobenzosemiquinonato)metal Complexes (Cu, Ni, Pd). The Art of Establishing Physical Oxidation States in Transition-Metal Complexes Containing Radical Ligands. *J. Am. Chem. Soc.* **2001,** *123* (10), 2213-2223; (b) Chaudhuri, P.; Wieghardt, K., Phenoxyl radical complexes. *Prog. Inorg. Chem.* **2001,** *50*, 151-216; (c) Pierpont, C. G., Unique properties of transition metal quinone complexes of the MQ3 series. *Coord. Chem. Rev.* **2001,** *219-221*, 415-433; (d) Verani, C. N.; Gallert, S.; Bill, E.; Weyhermuller, T.; Wieghardt, K.; Chaudhuri, P., [Tris(o-iminosemiquinone)cobalt(III)] - a radical complex with an St = 3/2 ground state. *Chem. Commun.* **1999,** (17), 1747-1748.

20.   Chang, B.-Y.; Crooks, J. A.; Chow, K.-F.; Mavré, F. o.; Crooks, R. M., Design and Operation of Microelectrochemical Gates and Integrated Circuits. *J. Am. Chem. Soc.* **2010**, ASAP.

21.   Lahti, P. M., *Magnetic properties of organic materials.* New York: Marcel Dekker. : 1999.

22.   (a) Orio, M.; Jarjayes, O.; Kanso, H.; Philouze, C.; Neese, F.; Thomas, F., X-Ray Structures of Copper(II) and Nickel(II) Radical Salen Complexes: The Preference of Galactose Oxidase for Copper(II). *Angew. Chem.* **2010,** *49* (29), 4989-4992; (b) Sokolowski, A.; Bothe, E.; Bill, E.; Weyhermueller, T.; Wieghardt, K., Phenoxyl radical complexes of chromium(III). *Science* **1996,** (14), 1671-1672; (c) Benisvy, L.; Blake, A. J.; Collison, D.; Davies, E. S.; Garner, C. D.; McInnes, E. J. L.; McMaster, J.; Whittaker, G.; Wilson, C., A phenoxyl radical complex of copper(II). *Chem. Commun.* **2001,** (18), 1824-1825; (d) Shimazaki, Y.; Stack, T. D. P.; Storr, T., Detailed Evaluation of the Geometric and Electronic Structures of One-Electron Oxidized Group 10 (Ni, Pd, and Pt) Metal(II)-(Disalicylidene)diamine Complexes. *Inorg. Chem.* **2009,** *48* (17), 8383-8392; (e) Storr, T.; Wasinger, E. C.; Pratt, R. C.; Stack, T. D. P., The geometric and electronic structure of a one-electron-oxidized nickel(II) bis(salicylidene)diamine complex. *Angew. Chem.* **2007,** *46* (27), 5198-5201.

23.   (a) Gupta, K. C.; Sutar, A. K., Catalytic activities of Schiff base transition metal complexes. *Coord. Chem. Rev.* **2008,** *252* (12-14), 1420-1450; (b) Jones, C. W., On the Stability and Recyclability of Supported Metal-Ligand Complex Catalysts: Myths, Misconceptions and Critical Research Needs. *Topics in Catalysis* **2010,** *53* (13-14), 942-952; (c) Kleij, A. W., Nonsymmetrical salen ligands and their complexes: synthesis and applications. *Eur. J. Inorg. Chem.* **2009,** (2), 193-205.

24.   Adam, B.; Bill, E.; Bothe, E.; Goerdt, B.; Haselhorst, G.; Hildenbrand, K.; Sokolowski, A.; Steenken, S.; Weyhermueller, T.; Wieghardt, K., Phenoxyl radical complexes of gallium, scandium, iron and manganese. *Chem.--Eur. J.* **1997,** *3* (2), 308-319.

25.   Allard, M. M., Computational Study on Phenoxyl radicals Substituent effects. *unpublished* **2010**.

26.   (a) Shimazaki, Y.; Huth, S.; Karasawa, S.; Hirota, S.; Naruta, Y.; Yamauchi, O., Nickel(II)−Phenoxyl Radical Complexes: Structure−Radical Stability Relationship. *Inorg. Chem.* **2004,** *43* (24), 7816-7822; (b) Bordwell, F. G.; Cheng, J., Substituent effects on the stabilities of phenoxyl radicals and the acidities of phenoxyl radical cations. *J. Am. Chem. Soc.* **1991,** *113* (5), 1736-1743.

27.   Taki, M.; Kumei, H.; Itoh, S.; Fukuzumi, S., Hydrogen atom abstraction by Cu(II)- and Zn(II)-phenoxyl radical complexes, models for the active form of galactose oxidase. *J. Inorg. Biochem.* **2000,** *78* (1), 1-5.

28.   Manner, V. W.; Markle, T. F.; Freudenthal, J. H.; Roth, J. P.; Mayer, J. M., The first crystal structure of a monomeric phenoxyl radical: 2,4,6-tri-tert-butylphenoxyl radical. *Chem. Commun.* **2008,** (2), 256-258.

Chapter 2

Objectives

The main focus of my research can be summarized in the following two statements:

2.1. Research Statement #1

Our main goal in this research project is concerned with the design and synthesis of novel metal complexes using asymmetric redox-active ligands capable of generating phenoxyl radicals. The limitations of this asymmetrical approach will be identified through the synthesis of discrete independent "modules" (see **Figure 2.1**) that can later be assembled onto surface substrates. This modular approach which necessitates a complete understanding of each module separately in order to optimize and fine tune the desired properties before assembling the modules together. Being able to accurately describe the chemical behavior of each molecule is a necessity in order to make accurate predictions, especially in the redox part of the molecule, since it is the bistable component of our approach.
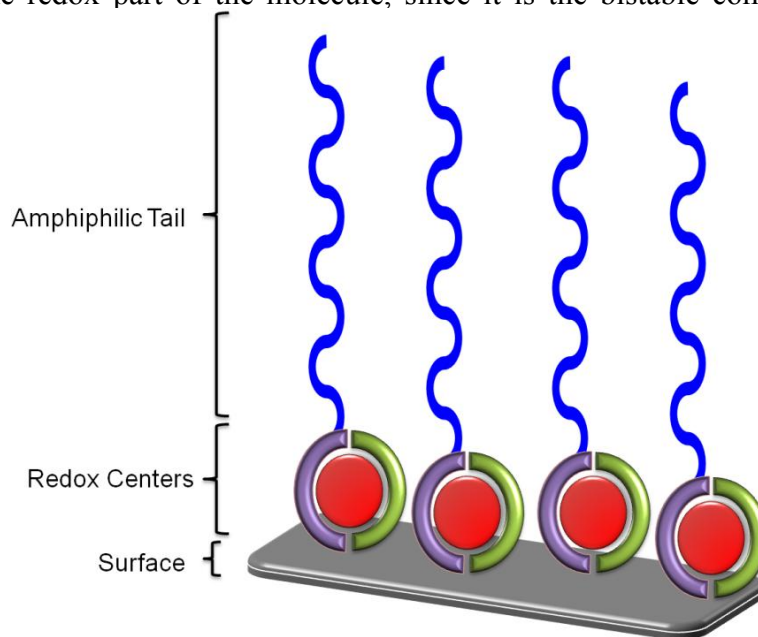
Figure 2.1. Modular approach

This work involves synthetic, electrochemical, spectrometric, and spectroscopic techniques. Selected structures were analyzed with computational methods, with special emphasis on geometry optimization (of the neutral and oxidized complexes), Mulliken population, dipole moment directionality, and geometric isomer preferences, as well as molecular orbital analysis, and used to explain molecular behaviors. A detailed section concerning the electrochemical behavior observed through redox cycling is also presented.

2.1.1. General Ligand Design

To achieve these objectives, we use an [N$_2$O$_3$]-type ligand containing two amines and three phenolates (**Scheme 2.1**). The introduction of various substituents (in our case mainly the *tertiary*-butyl group) in the 4th- and 6th-positions of the phenol ring, leads to steric and electronic effects. Upon deprotonation, the phenolato rings decrease the overall positive charge; in the case of trivalent ions the overall charge is zero, thereby eliminating couterions completely. The pentadentate nature of our ligand allows for the synthesis of asymmetric five coordinate complexes.
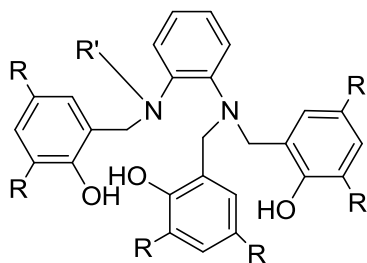
Scheme 2.1. Generic ligand design.

2.1.2. Metal Preference

In our research, we studied iron and cobalt quite extensively. We are using the trivalent form of iron, a d^5 metal ion with spin of $S = 5/2$, which prefers to be high-spin with our donor type. On the other hand, the cobalt(III) cation is a d^6 metal ion that prefers to be in a low-spin state with a spin of $S = 0$ with our donor set. We are using both of the metals with the knowledge that they have similar affinity for our ligands, but that they will have markedly different magnetic coupling behaviors upon generating radicals due to their diamagnetic/paramagnetic natures.

2.2. Research Statement #2

It is a crucial requirement to control and tune desired properties of these new materials within highly ordered surface assemblies. The long-term group objectives are towards making metalo-organic films that can store information, using amphiphilic behavior to deposit and organize these "soft materials". The understanding to predict binding modes of metal-containing soft materials is crucial in order to build-up organized supramolecular architectures based on transition metal complex scaffolds that will allow for surface deposition. This knowledge is especially critical since the nature of these metallosurfactants precludes full elucidation of molecular structures through X-ray diffraction. Accordingly the later part of this dissertation contains mainly physical-inorganic assessments as well as Density Functional Theory (DFT) calculations. We focused extensively on geometrical isomeric preferences, oxidized/reduced states, Mulliken population, dipole moments, and frontier orbitals. We seek to gain insight for

the understanding how these metalosurfactants behave when compared to our archetypical complex systems.

2.3. Research Goals

Goal #1: To develop, synthesize and characterize molecules that can act as molecular switches through the use of multiple redox states.

The results of Goal #1 are presented in Chapters 4-5, in which we address some Iron and Cobalt complexes.

Goal #2: To use computational chemistry methods as a tool for a better understanding of the underlying discrete redox processes and electronic behaviors of metal-containing complexes.

The results of Goal #2 and described in Objective #2 are presented in Chapter 4-5 and in the Appendix.

Chapter 3

Review of Selected Techniques and Methods

The work contained within this dissertation was achieved by means of synthetic development and redox/structural physical property investigations. All precursors, ligands, and metal complexes were characterized using standard techniques. These include: Infrared (IR), Nuclear Magnetic Resonance (NMR), Ultraviolet-visible (UV-vis) Spectroscopy, Mass Spectrometry (MS), Electron Paramagnetic Resonance (EPR), and Cyclic Voltammetry (CV). Single crystal X-ray Diffraction crystallography (XRD) studies were undertaken when suitable crystals could be grown. This section will elaborate on some of these techniques, but the reader is referred to other more authoritative references[1] for further details and to previously published work from our group.[2]

3.1. Materials

Standard protocols[1a, 3] were followed in the preparation and syntheses of organic ligands and metal complexations. Key intermediates and precursors were either synthesized according to literature procedures or directly purchased from commercial sources. Solvents and chemicals were used as received from commercial sources unless otherwise specified. For air or water sensitive reactions, methanol and dichloromethane were distilled over calcium hydride and Schlenk techniques[3] using an argon blanketing were followed. The ligands were obtained from multistep syntheses, with characterization of each intermediate. Stringent safety precautions were undertaken whenever potentially

dangerous materials was present. Waste materials were disposed of in accordance with Wayne State University guidelines.

3.2. Infrared Spectroscopy (IR)

Infrared spectroscopy is a widely used technique for identifying major functional groups present in target molecules. An infrared spectrum consists of plotting transmission (%) versus the inverse of the wavenumber (cm^{-1}). The identification of functional groups is done by comparison with well established literature data.[1b, 1e-h, 4] This can be achieved because each functional group absorbs infrared radiation at a unique wavelength. Multiple modes of vibration can be present within a molecule which can help differentiate closely related functional groups.

In this work solid samples are prepared as pellets in a transparent hydraulically pressed potassium bromide solid suspension. Infrared spectra were measured from 4000 to 400 cm^{-1} using KBr pellets on a Tensor 27 FTIR-Spectrophotometer from Bruker. Data collection, manipulation, and background corrections were made using Optics User Software (OPUS) version 5.0 supplied by the manufacturer.

3.3. Nuclear Magnetic Resonance Spectroscopy (NMR)

NMR spectroscopy is by far one of the most widely used techniques for chemical structure determinations. An NMR spectrum consists of a plot of signal intensity as a function of chemical shifts in ppm. A signal is obtained from the relaxation of the magnetic nuclei within the magnetic field of the instrument to a brief radio frequency pulse, recorded as the free induction decay (FID) and is converted to the equivalent chemical shift using a Fourier transform function. There are a wide variety of nuclei can

be observed by NMR. The main two NMR techniques used in this dissertation are ^{1}H-NMR and ^{13}C-NMR. Both give valuable information concerning the structural backbone of a given molecule through the chemical shift, and J-coupling between nuclear spins, which contains information regarding dihedral angles between centers. Both ^{1}H-NMR and ^{13}C-NMR can identify different functional groups according to their chemical shifts through comparison with well established literature data.[1b]

In this work, NMR spectra of the compounds were obtained by dissolving in deuterated solvents and measuring using the Varian 300 and/or 400 MHz instrument in the Wayne State University Central Instrument Facility (CIF).

3.4 Mass Spectrometry (MS)

Mass spectrometry is a routine technique used for the determination of exact molecular weight by means of the parent ion mass to charge ratio. A mass spectrometer records relative intensities as a function of *m/z* ratios. Compounds are charged/ionized by means of different ionization techniques, which will result in different fragmentation patterns of the initial parent ions.[1b] These charged ions are accelerated and passed through a series of electric and/or magnetic sectors which separates them according to their *m/z* ratio. Standard calibration techniques are followed to ensure the accuracy of the results obtained.

In this dissertation, mainly electron ionization using electrospray ionization (ESI) in the positive mode was used. All experimental assignments were simulated based on peak positions and isotopic distributions. All compounds were dissolved in protic solvents, usually methanol, and resulted in positively charged ions. All spectra were

measured in a Micromass Quattro LC triple quadrupole mass spectrometer with an electrospray/APCI source and Waters Alliance 2695 LC autosampler and photodiode array UV detector.

3.5. X-ray Single Crystal Analysis

X-ray crystallography is one of the most powerful tools available to scientists for elucidating complex molecular structures. For inorganic chemists it provides invaluable insights into bond lengths, angles, coordination modes of ligands, chirality, and intermolecular interactions. These structural elucidations are based on Bragg's Law of diffraction (**Eq. 3.1**).

$$n\lambda = 2d \sin \theta \quad \textbf{(Eq. 3.1)}$$

in which 'd' is defined as the spacing of the parallel planes in the atomic lattice, 'θ' is the scattering angle, and 'λ' is the wavelength.[5] In single crystal X-ray diffraction, a high quality crystal has to be collected and mounted on a goniometer head,[6] and it is then subjected to an X-ray beam which will scatter according to **Eq. 3.1**. The diffraction patterns are recorded and the crystal is rotated until a complete diffraction pattern is obtained. This pattern is analyzed and fitted by an algorithm to an electron density map to finally obtain a three dimensional model of a unit cell.

In this dissertation, Dr. Mary Jane Heeg from the Wayne State Central Instrumentation Facility performed all structural elucidations. All diffraction data were measured on a Bruker *X8* APEX-II kappa geometry diffractometer with Mo radiation and a graphite monochromator. APEX-II[7] and SHELX-97[8] software were used in the collection and refinement of the models.

3.6. Ultraviolet and Visible Spectroscopy (UV-vis.)

The technique of UV-visible spectroscopy is based on the absorption of light by the compound of interest. The resulting electronic spectrum is an invaluable tool for inorganic chemists, because it provides insight into the electronic structure of a given molecule. An UV-visible spectrum consists of recording absorbance as a function of wavelength in nanometers (nm). All absorptions observed are the result of the electronic transitions from a ground state to an excited state, as shown in **Figure 3.1**.
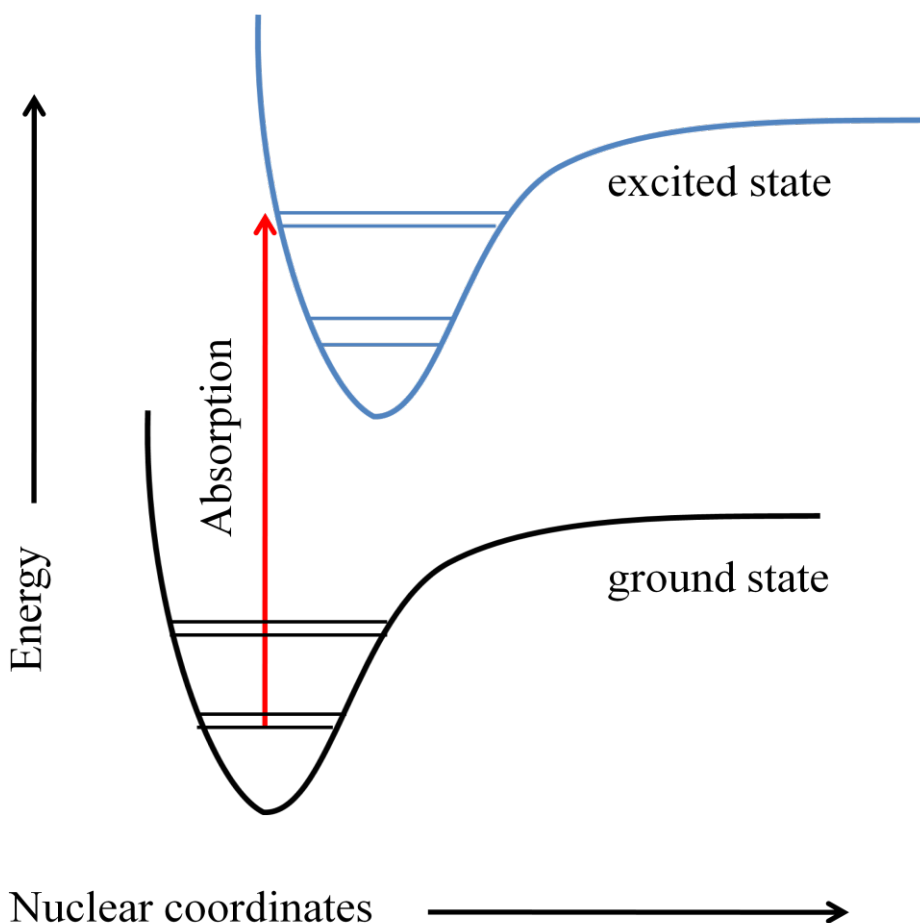
Figure 3.1. Potential energy surface for absorption to an excited state (adapted from reference[1i]).

Absorption of light by molecular compounds can be described by the Beer-Lambert[1i] law **(Eq. 3.2)**

$$A = \varepsilon bc = \log I_o/I \quad \textbf{(Eq. 3.2)}$$

where 'A' is the absorbance, 'b' is the path length through the sample, 'c' is the concentration of the absorbing species, and 'ε' is the molar absorptivity constant, 'I_o' is the intensity of the reference beam, and 'I' is the intensity of the sample beam. The Beer-Lambert law states that the absorption of a compound is directly proportional to its concentration.

There are many important types of transitions[1i] that can occur in the UV-visible region:

(i)   transition of π, σ, and n electrons

(ii)   transition of charge transfer electrons

(iii)   transition of d-d and f-f electrons.

Some of the possible allowed electronic transitions of π, σ, and n electrons include but not limited to: $\sigma \rightarrow \sigma^*$, $n \rightarrow \sigma^*$, $n \rightarrow \pi^*$, and $\pi \rightarrow \pi^*$ transitions[9]. Of critical importance to inorganic chemists are the charge transfer bands that occur between electron-donating and electron-accepting groups, since they can provide valuable insight into the interactions between the metal and the ligand. Transitions of d→d and f→f electrons take place within their corresponding d and f orbitals of the metal center.

There are two main selection rules that govern an electronic spectrum[10]:

(i) $\Delta l = +/- 1$, known as Laporte's rule, implies that transitions such as s→s, p→p, d→d and f→f are forbidden in centrosymmetric compounds.

(ii) $\Delta S = 0$, implies that no change in spin multiplicity is allowed.

These rules apply to all of our systems, though rule (i) is usually relaxed due to lowering of symmetry of the molecule and/or Jahn-Teller distortions, which are well known phenomena.[10] The number of absorption bands, and their individual observable separation in a spectrum corresponds, to a first approximation, to the different chromophores present in the molecule. It is important to note that for charge transfer spectra, both the donors and the acceptors are important in determining the wavelength and the intensity of the transitions.[11]

In this dissertation UV-visible spectra of sample solutions of known concentration, in a 1 x 1 cm quartz cuvette were obtained using a Cary 50 spectrometer in the range of 250–1000 nm.[12] λ_{max} (lambda maxima) are reported.

3.7. Electron Paramagnetic Resonance Spectroscopy (EPR)

Electron Paramagnetic Resonance (EPR), also known as Electron Spin Resonance (ESR), is a technique used to detect paramagnetic species.[1j] An EPR spectrum is acquired by irradiating a sample in the microwave region and recording the signal as a function of the external magnetic field (G). Signal processing and electronics are all computer controlled. The data plotted is the first derivative of the absorbance due to the relatively broad absorbances.. The external magnetic field splits the energy of spin states, namely $m_s = -1/2$ (lower in energy) and $m_s = +1/2$ (higher in energy). This is known as the Zeemann effect.[13] When subjected to microwave radiation, which behaves as an alternating magnetic field, transitions between those two states are observed.[1j]

In this dissertation first derivative X-Band EPR spectra of selected compounds were acquired with a Bruker ESP 300 spectrometer at temperatures ranging between 115-125 K, using a liquid nitrogen cryostat. The result analysis and fitting of the data were performed in collaboration with Prof. Bruce R. McGarvey from the Department of Chemistry and Biochemistry at the University of Windsor, Canada.

3.8. Cyclic Voltammetry (CV)

Cyclic voltammetry (CV) or potential sweep chronoamperometry is a technique used to study the reduction/oxidation (redox) properties of compounds.[14] This technique is used to study the transfer of electrons between electrode surfaces and molecules in the solution nearby. The typical CV experimental configuration consists of three electrodes: (i) a working electrode, (ii) an auxiliary or counter electrode, and (iii) a reference electrode.[1c] The electrodes are arranged within a closed vessel equipped with ports to allow purging of both the solution and the space above the solution with argon gas. A known concentration of the sample to be analyzed and an electrolyte salt such as $TBAPF_6$ or $TBAClO_4$ are added. The electrolytes are present to increase the conductivity, which is especially important in organic solvents. A cyclic voltammogram consists of plotting current as a function of potential, as illustrated in **Figure 3.2**.
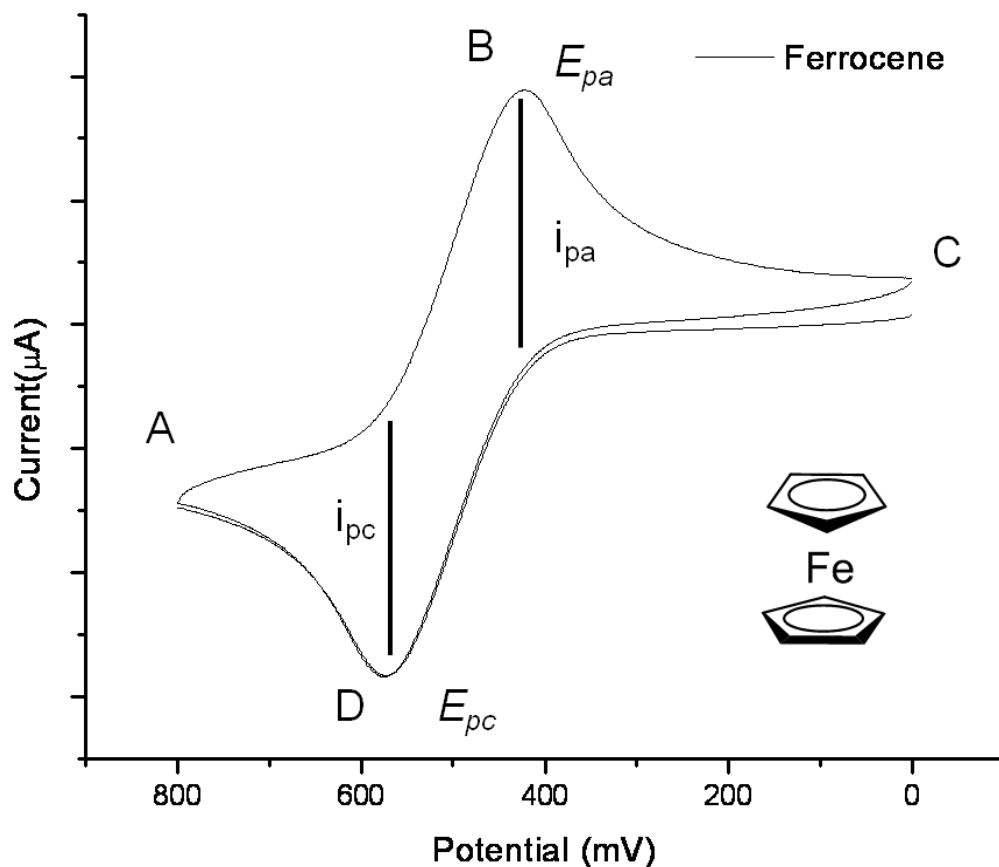
Figure 3.2. Cyclic voltammogram of ferrocene (in dichloromethane, 150 mV/s vs. Ag/AgCl, TBAPF$_6$).

The current-voltage curve of an electrochemically reversible process is shown in **Eq. 3.3**,

$$O \; + \; ne \underset{k_b}{\overset{k_f}{\rightleftharpoons}} \; R \quad \textbf{(Eq. 3.3)}$$
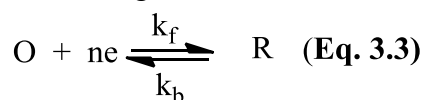
in which the transfer of 'n' electrons from the oxidized species 'O' to the reduced form 'R' has occured. A reversible process can be described with the Butler-Volmer and Cottrell equations[15] combined in **Eq. 3.4**,

$$\left| E_{pc} - E_{pa} \right| = \frac{57 \, mV}{n} \quad \textbf{(Eq.3.4)}$$

where 'E$_{pc}$' and 'E$_{pa}$' are the reduction and oxidation potential, respectively; 'n' is the number of electrons involved from **Eq. 3.3**.

The potential at which a reversible process is observed depends on the Nernst equation **(Eq. 3.5)**,

$$E = E^{o'} + \frac{RT}{nF} \ln \frac{[O]}{[R]} \quad \textbf{(Eq. 3.5)}$$

where 'E' is the electrode potential, 'E$^{o'}$' is the standard electrode potential, 'R' is the universal gas constant, 'T' is the absolute temperature, 'n' is the number of electrons involved, 'F' is Faraday's constant, and '[O]' and '[R]' refer to surface concentrations of the oxidized and reduced species, respectively, related to **Eq. 3.3**.

The characteristics used to define a process as reversible include the following: (i) the cathodic and anodic peak potential separation; ΔE (E$_{pc}$ - E$_{pa}$) = 0.057 V at all scan rates at 25 ^{o}C, (ii) the peak current ratio; i$_{pa}$/i$_{pc}$ = 1.0 at all scan rates, (iii) the polarographic half-wave potential, E$_{1/2}$ calculated as (E$_{pc}$ + E$_{pa}$)/2 which also gives the peak width of 0.029 V for all scan rates.[16]

Solvation effects and poor conductivity of the organic solvents used can result in real systems deviating from theoretical parameters. To address this issue, it is usually strongly advised to run an internal standard and report experimental values against that standard, in our case we use the ferrocene/ferrocenium^{+} (Fc/Fc^{+}) couple as reference.[17]

In order to determine the overall number of electrons involved in **Eq. 3.4**, one can use a related technique known as controlled potential bulk coulometry. The basic set up is similar to CV, with the main notable difference being the use of a very large surface area

working electrode to allow more contact between the electrode and the solution. The electrode potential is fixed at a previously established value obtained by a CV experiment. Our typical set up is shown in **Figure 3.3**, for which the reference electrode is a standard Ag/AgCl electrode, the auxiliary electrode (a coiled platinum wire) is usually separated by a glass frit from the rest of the solution, and the working electrode is a very large porous electrode made of either platinum or glassy carbon. The potentiostat displays the amount of charge delivered to the cell, from which one can deduce the number of moles of electrons passing through the cell. This technique is also useful for preparing a limited amount of the oxidized or reduced species for further investigation. Carefully isolated aliquots can be characterized as required by using EPR and electronic spectroscopy to identify the newly formed species.

In this dissertation, all electrochemical experiments were performed using a BAS 50W potentiometer. A standard three-electrode cell was employed with a glassy-carbon working electrode, a Pt-wire auxiliary electrode, and a freshly prepared Ag/AgCl reference electrode, all under an inert atmosphere at ambient conditions. Potentials are all reported versus Fc/Fc^+ [17] as an internal standard. Bulk electrolysis experiments were carried out at -77 $^{\circ}$C in a dry ice/acetone bath.
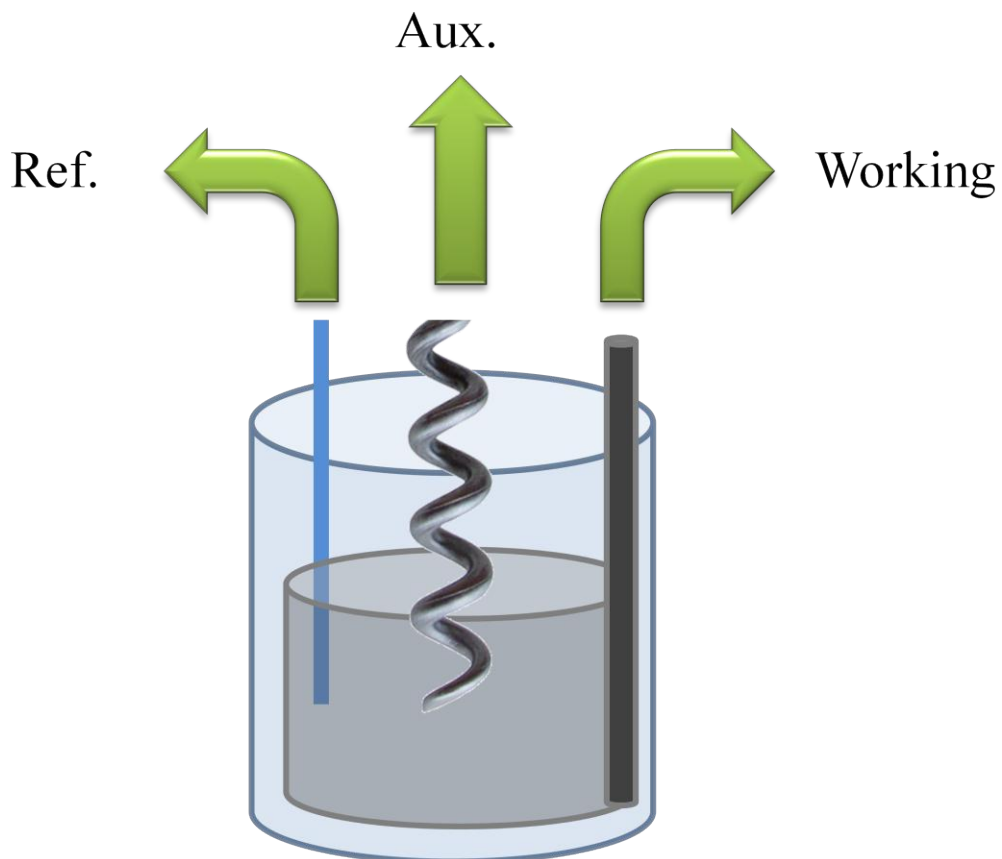
Figure 3.3. Bulk electrolysis cell arrangement.

3.9. Density Functional Theory (DFT) Calculations

Density Functional Theory (DFT) is an accurate and cost effective method for calculating electronic structures.[18] It is one of the dominant methods used in inorganic chemistry,[19] and it is especially useful to study ground state electronic structures of metal complexes. It provides invaluable insight into experimentally observable properties, and is particularly adept for the study of bonding interactions within a molecule,[18] without having to rely on extensive experimental evidence. Density Functional Theory seeks to replace the many-body wave functions by an electronic density as the basic quantity. The many-body wave function is dependent upon '3N' variables since each of the 'N'

electrons has three associated spatial variables.[18] The one electron density is only a function of three variables making it both conceptually and practically simpler to compute. Density Functional Theory has been implemented in most software packages through the use of the Kohn-Sham method. [18]

Although there have been numerous improvements and refinements to DFT functionals, there are still some difficulties as predicting accurate intermolecular interactions and calculating band gaps in semiconductors.[18] There are also problems associated with charge transfer excitations and transition states, but ground state electronic structures have been found to be reliable and very useful,[18] especially to inorganic chemists, where higher level of theories are prohibitive due to their high computational costs.

In the following work, DFT calculations were performed with the GAUSSIAN[20] series of programs in order to explain experimental observations for a wide variety of compounds synthesized by the Verani Group. The calculations were performed by the author with guidance from both Prof. H. Bernhard Schlegel at Wayne State University, Dr. Jason Sonnenberg, a past post-doctoral fellow in Prof. Schlegel's lab, and Dr. Hrant Hratchian, a research scientist at Gaussian, Inc. The B3LYP/6-31G(d) level of theory[21] was employed throughout this work unless otherwise specified. Geometries were fully minimized, without symmetry constraints, using standard methods.[2a, 22] Located stationary points were characterized by computing analytic vibrational frequencies. Reported energies always include zeropoint corrections unless otherwise specified. The Cartesian coordinates of the optimized structures are provided in the Appendix. Some

variations of these methods were explored and are discussed in more detail in the appropriate corresponding sections.

3.10. References.

1.   (a) Bell, C. E.; Taber, D. F.; Clark, A. K., *Organic Chemistry Laboratory*. third ed.; Brooks/Cole Thomson: Pacific Grove, CA, 2001; (b) Silverstein, R. M.; Webster, F. X., *Spectrometric Identification of Organic Compounds*. Sixth ed.; John Wiley & Sons, Inc.: New York; (c) Harris, D. C., *Qualitative Chemical Analysis*. W.H. Freeman and Company: New York, 2000; (d) Drago, R. S., *Physical Methods in Inorganic Chemistry*. Reinhold Publishing Corp.: New York, 1965; (e) Nakamoto, K., *Theory of Normal Vibrations*. John Wiley & Sons, Inc.: 2008; p 1-147; (f) Nakamoto, K., *Applications in Inorganic Chemistry*. John Wiley & Sons, Inc.: 2008; p 149-354; (g) Nakamoto, K., *Appendixes*. John Wiley & Sons, Inc.: 2008; p 355-413; (h) Nakamoto, K., *Index*. John Wiley & Sons, Inc.: 2008; p 415-419; (i) Atkins, P.; Paula, J. d., *Physical Chemistry*. 9th ed.; W. H. Freeman: New York, 2009; (j) Squires, T. L., *An introduction to electron spin resonance*. Academic Press: New-York, 1964.

2.   (a) Imbert, C.; Hratchian, H. P.; Lanznaster, M.; Heeg, M. J.; Hryhorczuk, L. M.; McGarvey, B. R.; Schlegel, H. B.; Verani, C. N., Influence of Ligand Rigidity and Ring Substitution on the Structural and Electronic Behavior of Trivalent Iron and Gallium Complexes with Asymmetric Tridentate Ligands. *Inorg. Chem.* **2005,** *44* (21), 7414-7422; (b) Lanznaster, M.; Heeg, M. J.; Yee, G. T.; McGarvey, B. R.; Verani, C. N., Design of Molecular Scaffolds Based on Unusual Geometries for Magnetic Modulation of Spin-Diverse Complexes with Selective Redox Response. *Inorg. Chem.* **2007,** *46* (1),

72-78; (c) Lanznaster, M.; Hratchian, H. P.; Heeg, M. J.; Hryhorczuk, L. M.; McGarvey, B. R.; Schlegel, H. B.; Verani, C. N., Structural and Electronic Behavior of Unprecedented Five-Coordinate Iron(III) and Gallium(III) Complexes with a New Phenol-Rich Electroactive Ligand. *Inorg. Chem.* **2006,** *45* (3), 955-957; (d) Lesh, F. D.; Hindo, S. S.; Heeg, M. J.; Allard, M. M.; Jain, P.; Peng, B.; Hryhorczuk, L.; Verani, C. N., On the effect of coordination and protonation preferences in the amphiphilic behavior of metallosurfactants with asymmetric headgroups. *Eur. J. Inorg. Chem.* **2009,** (3), 345-356; (e) Lesh, F. D.; Shanmugam, R.; Allard, M. M.; Lanznaster, M.; Heeg, M. J.; Rodgers, M. T.; Shearer, J. M.; Verani, C. N., A Modular Approach to Redox-Active Multimetallic Hydrophobes of Discoid Topology. *Inorg. Chem.* **2010,** *49* (16), 7226-7228; (f) Shakya, R.; Hindo, S. S.; Wu, L.; Allard, M. M.; Heeg, M. J.; Hratchian, H. P.; McGarvey, B. R.; Da Rocha, S. R. P.; Verani, C. N., Archetypical Modeling and Amphiphilic Behavior of Cobalt(II)-Containing Soft-Materials with Asymmetric Tridentate Ligands. *Inorg. Chem.* **2007,** *46* (23), 9808-9818; (g) Shakya, R.; Hindo, S. S.; Wu, L.; Ni, S.; Allard, M.; Heeg, M. J.; da Rocha, S. R. P.; Yee, G. T.; Hratchian, H. P.; Verani, C. N., Amphiphilic and magnetic properties of a new class of cluster-bearing [L2Cu4(micro 4-O)(micro 2-carboxylato)4] soft materials. *Chem.--Eur. J.* **2007,** *13* (35), 9948-9956; (h) Shakya, R.; Imbert, C.; Hratchian, H. P.; Lanznaster, M.; Heeg, M. J.; McGarvey, B. R.; Allard, M.; Schlegel, H. B.; Verani, C. N., Structural, spectroscopic, and electrochemical behavior of trans-phenolato cobalt(III) complexes of asymmetric NN'O ligands as archetypes for metallomesogens. *Dalton Trans.* **2006,** (21), 2517-2525.

3. Szafran, Z.; Pike, R. M.; Singh, M. M., *Microscale Inorganic Chemistry: A Comprehensive Laboratory Experience* Wiley: 2008.

4. Nakamoto, K., *Frontmatter*. John Wiley & Sons, Inc.: 2008; p i-xi.

5. West, A. R., *Basic Solid State Chemistry, 1st ed*. John Wiley and Sons, Inc; New York 1988.

6. Clegg, W., *Crystal Structure Determination*. Oxford science publication.

7. Bruker *APEX II collection and processing programs are distributed by the manufacturer*, APEX II, AXS Inc., Madison WI, USA.

8. Sheldrick, G. SHELX-97, University of Gottingen, Germany, : 1997.

9. Lever, A. B. P., *J. Chem. Educ.* **1974,** *51*, 612.

10. Miessler, G. L.; Tarr, D. A., *Inorganic Chemistry*. 4th ed.; Prentice Hall: 2009.

11. (a) Allard, M. M.; Odongo, O. S.; Lee, M. M.; Chen, Y.-J.; Endicott, J. F.; Schlegel, H. B., Effects of Electronic Mixing in Ruthenium(II) Complexes with Two Equivalent Acceptor Ligands. Spectroscopic, Electrochemical, and Computational Studies. *Inorg. Chem.* **2010,** *49* (15), 6840-6852; (b) Odongo, O. S.; Allard, M. M.; Schlegel, H. B.; Endicott, J. F., Observations on the Low-Energy Limits for Metal-to-Ligand Charge-Transfer Excited-State Energies of Ruthenium(II) Polypyridyl Complexes. *Inorg. Chem.* **2010,** *49* (20), 9095-9097.

12. Clarck, B. J.; T.Forst; Russell, M. A., *UV Spectroscopy: Technique, Instrumentation, Data Handeling/ UV Spectrometry Group.* Chapman and Hall: London 1993.

13. Wertz, J. E.; Bolton, J. R., *Electron Spin Resonance, Elementary Theory and Practical Applications*. Chapman and Hall: New York, 1986.

14. Christinsen, P. A.; Hamnett, A., *Techniques and Mechanisms in Electrochemmistry*. Chapmann and Hall.

15. Nicholson, R. S.; Shain, I., Theory of Stationary Electrode Polarography. Single Scan and Cyclic Methods Applied to Reversible, Irreversible, and Kinetic Systems. *Anal. Chem.* **1964,** *36* (4), 706-723.

16. Wang, J., *Analytical electrochemistry; Chapter 2*. Wiley, and Sons Inc.: New York.

17. Gagne, R.; Koval, C.; Licenski, G., Ferrocene as an internal standard for electrochemical measurements. *Inorg. Chem.* **1980,** *19*, 2854-2855.

18. Cramer, C. J., *Essential of Computational Chemistry*. Second ed.; Wiley, and Sons Inc.: New-York.

19. Li, J.; Noodleman, L.; Case, D. A., Electronic structure calculations: density functional methods with applications to transition metal complexes. *Inorg. Electron. Struct. Spectrosc.* **1999,** *1*, 661-724.

20. (a) Frisch, M. J.; Trucks, G. W.; Schlegel, H. B.; Scuseria, G. E.; Robb, M. A.; Cheeseman, J. R.; Montgomery, J. A.; Jr., T. V.; Kudin, K. N.; Burant, J. C.; Millam, J. M.; Iyengar, S. S.; Tomasi, J.; Barone, V.; Mennucci, B.; Cossi, M.; Scalmani, G.; Rega, N.; Petersson, G. A.; Nakatsuji, H.; Hada, M.; Ehara, M.; Toyota, K.; Fukuda, R.; Hasegawa, J.; Ishida, M.; Nakajima, T.; Honda, Y.; Kitao, O.; Nakai, H.; Klene, M.; Li, X.; Knox, J. E.; Hratchian, H. P.; Cross, J. B.; Bakken, V.; Adamo, C.; Jaramillo, J.;

Gomperts, R.; Stratmann, R. E.; Yazyev, O.; Ayala, P. Y.; Morokuma, K.; Voth, G. A.; Salvador, P.; Dannenberg, J. J.; Zakrzewski, V. G.; Dapprich, S.; Daniels, A. D.; Strain, M. C.; Farkas, O.; Malick, D. K.; Rabuck, A. D.; Raghavachari, K.; Foresman, J. B.; Ortiz, J. V.; Cui, Q.; Baboul, A. G.; Clifford, S.; Cioslowski, J.; Stefanov, B. B.; Liu, G.; Liashenko, A.; Piskorz, P.; Komaromi, I.; Martin, R. L.; Fox, D. J.; Keith, T.; Al-Laham, M. A.; Peng, C. Y.; Nanayakkara, A.; Challacombe, M.; Gill, P. M. W.; Johnson, B.; Chen, W.; Wong, M. W.; Gonzalez, C.; J. A. Pople; , *Gaussian 03, Revision D.01 Gaussian, Inc., Wallingford CT, 2004*; (b) Frisch, M. J.; Trucks, G. W.; Schlegel, H. B.; Scuseria, G. E.; Robb, M. A.; Cheeseman, J. R.; Scalmani, G.; Barone, V.; Mennucci, B.; Petersson, G. A.; Nakatsuji, H.; Caricato, M.; Li, X.; Hratchian, H. P.; Izmaylov, A. F.; Bloino, J.; Zheng, G.; Sonnenberg, J. L.; Hada, M.; Ehara, M.; Toyota, K.; Fukuda, R.; Hasegawa, J.; Ishida, M.; Nakajima, T.; Honda, Y.; Kitao, O.; Nakai, H.; Vreven, T.; Montgomery, J. A., Jr.; Peralta, J. E.; Ogliaro, F.; Bearpark, M.; Heyd, J. J.; Brothers, E.; Kudin, K. N.; Staroverov, V.; Kobayashi, R.; Normand, J.; Raghavachari, K.; Rendell, A.; Burant, J. C.; Iyengar, S. S.; Tomasi, J.; Cossi, M.; Rega, N.; Millam, J. M.; Klene, M.; Knox, J. E.; Cross, J. B.; Bakken, V.; Adamo, C.; Jaramillo, J.; Gomperts, R.; Stratmann, R. E.; Yazyev, O.; Austin, A. J.; Cammi, R.; Pomelli, C.; Ochterski, J. W.; Martin, R. L.; Morokuma, K.; Zakrzewski, V. G.; Voth, G. A.; Salvador, P.; Dannenberg, J. J.; Dapprich, S.; Parandekar, P. V.; Mayhall, N. J.; Daniels, A. D.; Farkas, O.; Foresman, J. B.; Ortiz, J. V.; Cioslowski, J.; Fox, D. J. *Gaussian DV*, Revision H.04; Gaussian, Inc.: Wallingford, CT, 2009; (c) Frisch, M. J.; Trucks, G. W.; Schlegel, H. B.; Scuseria, G. E.; Robb, M. A.; Cheeseman, J. R.; Scalmani, G.; Barone, V.; Mennucci, B.;

Petersson, G. A.; Nakatsuji, H.; Caricato, M.; Li, X.; Hratchian, H. P.; Izmaylov, A. F.; Bloino, J.; Zheng, G.; Sonnenberg, J. L.; Hada, M.; Ehara, M.; Toyota, K.; Fukuda, R.; Hasegawa, J.; Ishida, M.; Nakajima, T.; Honda, Y.; Kitao, O.; Nakai, H.; Vreven, T.; Montgomery, J. A.; Peralta, J. E.; Ogliaro, F.; Bearpark, M.; Heyd, J.; Brothers, J. E.; Kudin, K. N.; Staroverov, V. N.; Kobayashi, R.; Normand, J.; Raghavachari, K.; Rendell, A.; Burant, J. C.; Iyengar, S. S.; Tomasi, J.; Cossi, M.; Rega, N.; Millam, J. M.; Klene, M.; Knox, J. E.; Cross, J. B.; Bakken, V.; Adamo, C.; Jaramillo, J.; Gomperts, R.; Stratmann, R. E.; Yazyev, O.; Austin, A. J.; Cammi, R.; Pomelli, C.; Ochterski, J. W.; Martin, R. L.; Morokuma, K.; Zakrzewski, V. G.; Voth, G. A.; Salvador, P.; Dannenberg, J. J.; Dapprich, S.; Parandekar, P. V.; Mayhall, N. J.; Daniels, A. D.; Farkas, O.; Foresman, J. B.; Ortiz, J. V.; Cioslowski, J.; Fox, D. J., *Gaussian G09* Wallingford CT, 2009; (d) Frisch, M. J. T., G. W.; Schlegel, H. B.; Scuseria, G. E.; Robb, M. A.; Cheeseman, ; J.R.; Montgomery, J. A. V., T.; Kudin, K. N.; Burant, J. C.; Millam, J. M.; Iyengar, S. S.;Tomasi, J.; Barone, V.; Mennucci, B.; Cossi, M.; Scalmani, G.; Rega, N.; Petersson, G. A.; Nakatsuji, H.; Hada, M.; Ehara, M.; Toyota, K.; Fukuda, R.; Hasegawa, J.; Ishida, M.; Nakajima,T.; Honda, Y.; Kitao, O.; Nakai, H.; Klene, M.; Li, X.; Knox, J. E.; Hratchian, H. P.; Cross, J. B.; Bakken, V.; Adamo, C.; Jaramillo, J.; Gomperts, R.; Stratmann, R. E.; Yazyev, O.; Austin, A. J.; Cammi, R.; Pomelli, C.; Ochterski, J. W.; Ayala, P. Y.; Morokuma, K.; Voth, G. A.; Salvador, P.; Dannenberg, J. J.; Zakrzewski, V. G.; Dapprich, S.; Daniels, A. D.; Strain, M. C.; Farkas, O.; Malick, D. K.; Rabuck, A. D.; Raghavachari, K.; Foresman, J. B.; Ortiz, J. V.; Cui, Q.; Baboul, A.G.; Clifford, S.; Cioslowski, J.; Stefanov, B. B.; Liu, G.; Liashenko, A.; Piskorz, P.; Komaromi, I.;

Martin, R. L.; Fox, D. J.; Keith, T.; Al-Laham, M. A.; Peng, C. Y.; Nanayakkara, A.; Challacombe, M.; Gill, P. M. W.; Johnson, B.; Chen, W.; Wong, M. W.; Gonzalez, C.; Pople, J. A. , *GAUSSIAN 03; Gaussian, Inc.: Wallingford, CT, 2003.*

21.   (a) Becke, A. D., *Phys. Rev. A* **1988**; (b) Becke, A. D., *J. Chem. Phys.* **1993,** (98), 5648; (c) Ditchfield, R. H., W. R.; Pople, J. A. , Self-Consistent Molecular Orbital Methods. Extended Gaussian-type basis for molecular-orbital studies of organic molecules. *J. Chem. Phys.* **1971,** (54), 724; (d) Gordon, M. S., *Chem. Phys. Lett.* **1980,** *76*, 163; (e) Hariharan, P. C.; Pople, J. A., *Theo. Chim. Acta.* **1973,** (28), 213; (f) Hariharan, P. C.; Pople, J. A., *Mol. Phys.* **1974,** (27), 209; (g) Hehre, W. J. D., R.; Pople, J. A. , *J. Chem. Phys.* **1972,** *56*, 2257; (h) Lee, C. T.; Yang, W. T.; Parr, R. G., *Phys. Rev. B* **1988,** *37*, 785; (i) Stephens, P. J.; Devlin, F. J.; Chabalowski, C. F.; Frisch, M. J., *J. Phys. Chem.* **1994,** *98*, 11623.

22.   Schlegel, H. B., *J. Comput. Chem.* **1982,** *3*, 214.

Chapter 4.

Electronic and Redox Behavior of Low-Symmetry Iron(III)

Complexes with [N₂O₃] Electroactive Ligands
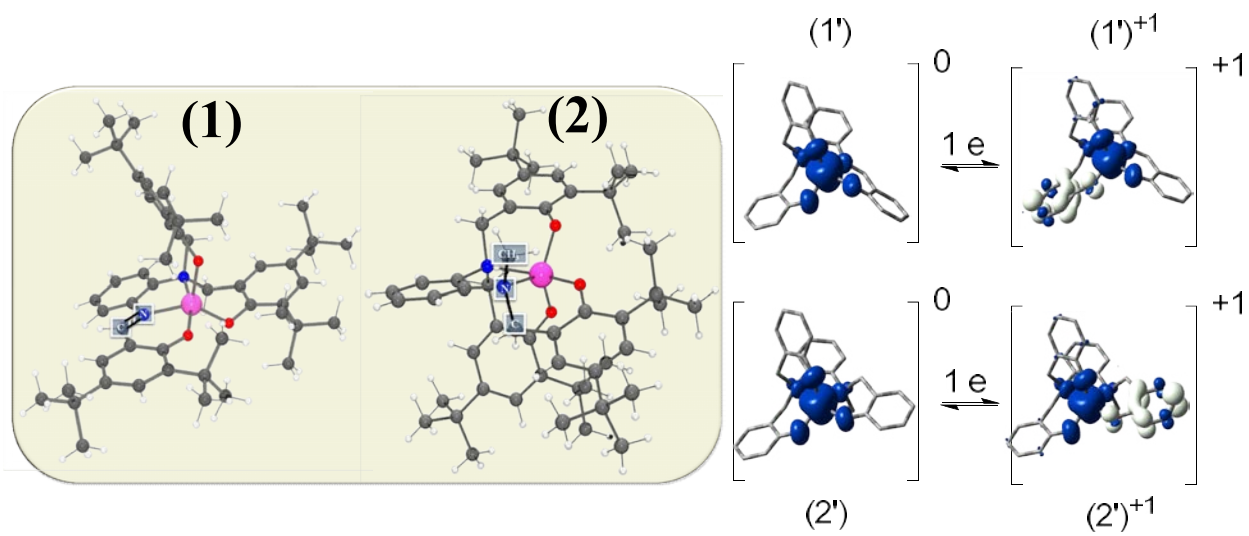
4.1. Introduction

Considerable effort has been directed toward the incorporation of bioinspired structure elements into developing responsive molecular materials with customized and controllable properties. Particularly, within the realm of molecular switching[1] the response of a given molecule to external stimuli, such as redox potential or temperature variations, can lead to observable structural and electronic changes between two equally stable ground states. Thus, transition metal complexes containing electroactive ligands capable of supporting the generation and stabilization of organic radicals are of special interest.[2] Such redox-responsive molecules that can act as bistable switches have received increasing attention due to their significant potential toward high-end applications such as information technology.[3] Among well-characterized electroactive ligands, those containing phenolate moieties are particularly relevant due to their synthetic versatility. However, complexes exhibiting octahedral or pseudo-octahedral[4] geometries fail to support multiple redox cycles required for molecular switching, implying that the bistability of the phenolate/phenoxyl couple needs to be improved in order to take advantage of this versatile group for switching purposes.

Our group has been investigating the behavior of iron complexes confined to low-symmetry five-coordinate $[N_2O_3]$ environments. This design mimics the basic geometrical needs observed in tyrosine-rich enzymes such as the non-heme tyrosine hydroxylase[5] and intradiol dioxygenase[6], which rely on radical-based mechanisms to form L-DOPA and cleave catechol-type rings, respectively. These five-coordinate environments result in molecular orbitals with low degeneracy and several distinct energies, as compared to those in octahedral fields. We hypothesize that orbital

rearrangement will take place when phenoxyl radicals are formed via phenolate oxidation. Although advances have been made in understanding the electronic and redox behavior of these low-symmetry complexes, complications arise when multiple redox-active sites are present within the same molecule. The proper assignment of classical physical oxidation states[7] becomes rather challenging due to numerous contributions of ligand- and/or metal-centered orbitals toward the same redox process.

In this dissertation we investigate the behavior of **[Fe^{III}L^1] (1)** and **[Fe^{III}L^2] (2)** (**Figure 4**.**1**), in which the ligands purposefully force asymmetry and contain three phenolato moieties denoted as A, A', and B. Two of the phenolates (A and A') are chemically equivalent, whereas B is dissimilar. Each of these moieties coordinates to the metal center and can undergo oxidation[8] to produce four different ground states associated with **[Fe$^{III/II}$L]**, **[Fe^{III}L$^{\uparrow}$]**, **[Fe^{III}L$^{\uparrow\uparrow}$]**, and **[Fe^{III}L$^{\uparrow\uparrow\uparrow}$]**. Therefore, we aim to (i) determine the sequence by which the metal and the ligand are oxidized by probing experimentally the redox dependence on supporting electrolytes and the organic linker, (ii) describe the electronic differences between the parent and each of the oxidized forms by spectroscopic methods, and (iii) corroborate the observed redox and electronic properties by means of computational methods. This study constitutes the first comprehensive experimental and theoretical effort for describing such electronic changes associated with redox phenomena in low-symmetry five-coordinate iron species. This fundamental understanding will contribute significant insight into the step-wise, well-defined multi-electron redox reactions.
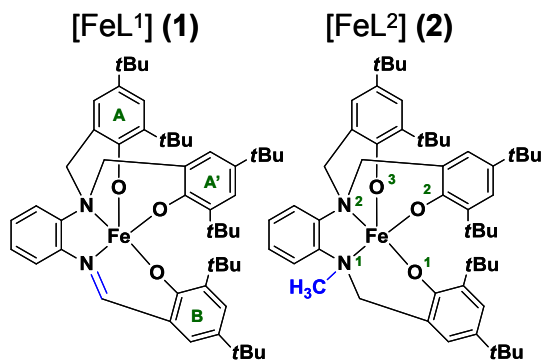
Figure 4.1. Complexes with targeted variations.

Experimental section

4.2. Materials and methods

Reagents and solvents were used as received from commercial sources, unless otherwise noted. Dichloromethane and methanol were distilled over CaH_2. Infrared spectra were measured from 4000 to 400 cm^{-1} as KBr pellets on a Tensor 27 FTIR-Spectrophotometer. ^{1}H-NMR spectra were measured using Varian 300 and 400 MHz instruments. ESI (positive mode) spectra were measured in either a triple-quadrupole Micromass QuattroLC or in a single-quadrupole Waters ZQ2000 mass spectrometer with an electrospray/APCI or ESCi source. Experimental assignments were based on simulations of peak position and isotopic distributions. Elemental analyses were performed by Midwest Microlab, Indianapolis, IN. Cyclic voltammetry experiments were performed using a BAS 50W voltammetric analyzer. A standard three-electrode cell was employed with a reference Ag/AgCl electrode which was freshly prepared and calibrated internally versus ferrocene.[9] A platinum wire was used as an auxiliary electrode and a vitreous carbon disk was used as a working electrode for the cyclic voltammetric experiments. The bulk electrolysis experiment was carried out using a vitreous carbon basket. Concentrations of the analytes were 1.0×10^{-3} M, and all supporting electrolytes

were 0.1 M, except where stated otherwise. The Fc/Fc$^+$ couple in CH_2Cl_2 was found to be

0.45 V (ΔE_p 0.14). [8a, 9b] First derivative X-band EPR spectra of 1.0×10^{-3} M in

dichloromethane solutions were performed with a Bruker ESP 300 spectrometer at 125 K

using liquid nitrogen as the coolant. Manipulations of EPR spectra were performed using

the WINEPR suite from Bruker, and are shown in the Appendix.

4.3. Electronic calculation methods

Spin unrestricted density functional theory (DFT) calculations were carried out

with the B3LYP[10] functional and the 6-31G(d)[11] basis set in the development version of

Gaussian.[12] Solvation in dichloromethane was modeled with the integral equation

formalism polarizable continuum model (IEF-PCM).[13] Geometries were fully optimized

without symmetry constraints, and stationary points were verified via frequency analysis.

Molecular orbital analysis was facilitated by using the biorthogonal or corresponding

orbital approach[14]; energies for these orbitals were obtained by a unitary transform of the

unrestricted Fock matrices into the biorthogonal basis. The averages of the energies of

the alpha and beta biorthogonalized orbitals were used to approximate the energies of the

restricted MO energies and these energies were used to build a classical restricted MO

ladder diagram. Cartesian coordinates of all optimized structures are provided as

Supporting Information in SI.

4.4. X-ray structural determinations

Diffraction data was collected for the ligands $H_3L^{1'}$, H_3L^2 and complexes **1, 2**. The structure for $H_3L^{1'}$ was collected on a Bruker *P4/CCD* diffractometer equipped with Mo radiation ($\lambda = 0.71069$ Å) and a graphite monochromator at 210 K. A sphere of data was measured at 10 sec/frames and 0.2 degree between frames. The remaining structures for H_3L^2, **1**, **2**, and **3** were measured on a Bruker *APEX-II* kappa geometry diffractometer with Mo radiation and a graphite monochromator at 100 K. Frames were collected as a series of sweeps with the detector at 40 mm and 0.2-0.3 degrees between each frame and 10-60 sec/frames. The frame data was indexed and integrated with the manufacturer's *SMART*, *SAINT* and *SADABS* software.[1] All structures were refined using Sheldrick's *SHELX-97* software. A summary of the crystal structure parameters for all structures is contained in **Table 4.1**.

The precursor ligand H_3L^1 [$C_{51}H_{74}N_2O_3$]·CH_3CN crystallized as colorless irregular fragments. A total of 26,665 reflections were measured, of which 11,153 were independent. The neutral ligand crystallized with one equivalent of acetonitrile solvent. On the ligand, the *tert*-butyl groups show typical disorder; some were modeled with partial occupancy positions. One of the pendant rings, labelled C15-C20, displays an approximate 2-fold disorder, with the hydroxyl substituent occupying alternate *ortho* positions in an 80/20 distribution. All non-hydrogen atoms, even those assigned with partial occupancies, were refined anisotropically. The more interesting disorder occurs around the protonated nitrogen N1. The single methylene linkage on N1 occupies two alternate positions in the model which refined to a 70/30 distribution and are labelled C7 and C7'. This disorder propagates into the C1-C6 ring and could be a product of the *ortho*

hydroxyl group lying on either side of the methylene linkage. These kinds of disorders are difficult to model and refine because the equivalent alternative positions are very close. As a result there could be unreliable bond lengths and angles involving the partial atoms of the disordered region. The new ligand **H₃L²** [$C_{52}H_{76}N_2O_3$] crystallized as colorless irregular fragments. A total of 16,651 data were integrated resulting in 11,361 unique reflections. One of the *tert*-butyl groups (C45-C47) was disordered and described with partial alternate atomic sites and kept isotropic. All hydrogen atoms were placed in calculated and observed positions.

[FeL¹] (1) [$Fe(C_{51}H_{69}N_2O_3)$] crystallized as dark plates. A total of 29,085 reflections were collected, of which 10,851 were independent. The asymmetric unit contains one neutral complex with no associated solvates. One of the *tert*-butyl groups was highly disordered requiring the methyl positions around C32 to be assigned partial occupancies and held isotropic. **Complex [FeL²] (2)** [$Fe(C_{52}H_{73}N_2O_3)$] appeared as minute red needles. A total of 49,239 data were harvested, of which 11,772 were unique. However, even at 60 s/frames, these small crystals diffracted poorly; out of 11,772 reflections, only 4089 had $I > 2\sigma(I)$.

Table 4.1. Crystal Data[a] [1]

	H_3L^1	H_3L^2	$[FeL^1]$ (1)	$FeL^2]$ (2)
Formula	$C_{53}H_{77}N_3O_3$	$C_{52}H_{76}N_2O_3$	$C_{52}H_{73}FeN_2O_3$	$C_{51}H_{69}FeN_2O_3$
M	804.18	777.15	815.95	813.93
Space group	P2(1)/n	P(-1)	P2(1)/c	P(-1)
a / Å	19.8422(18)	9.4303(14)	13.412(2)	12.9054(7)
b/ Å	15.3453(16)	14.583(20	26.256(3)	13.7840(8)
c/ Å	18.5425(15)	18.455(3)	14.9306(17)	14.5719(8)
α/ °		99.770(6)		88.317(4)
β/ °	114.391(3)	102.597(5)	115.293(7)	65.626(3)
γ/ °		96.323(6)		88.499(4)
V/ Å^3	5142.0(8)	2412.2(6)	4753.6(1.1)	2359.8(2)
Z	4	2	4	2
T/ K	211(2)	100(2)	100(2)	100(2)
λ/ Å	0.71073	0.71073	0.71073	0.71073
D_{calc}/ g cm^{-3}	1.039	1.070	1.160	1.145
μ/ mm^{-1}	0.063	0.065	0.359	0.361
$R(F)$ (%)	6.36	6.83	9.46	6.67
$Rw(F)$ (%)	17.44	14.33	10.52	14.90

[a] $R(F) = \sum \|F_o| - |F_c\| / \sum |F_o|$ for $I > 2\sigma(I)$; $Rw(F) = [\sum w(F_o^2 - F_c^2)^2 / \sum w(F_o^2)^2]^{1/2}$ for $I > 2\sigma(I)$.

4.5. Syntheses

The ligands **H₃L¹** and **H₃L²** (**Scheme 4.1**) were synthesized by modifications of our previously reported[8b, 15] route,[8b, 15] in which 10 mmol of the appropriate aromatic diamine (**Scheme 4.2**) (*i.e.* benzene-1,2-diamine for **1,** *N*-methylbenzene-1,2-diamine for **2**,) were refluxed for 48 h in dichloromethane in the presence of 30 mmol 2,4-di-*tert*-butyl-6-(chloromethyl)phenol and 30 mmol of triethylamine. The reaction solution was washed 3 times with water in a separatory funnel and dried over Na₂SO₄/activated charcoal. The solvent was then removed by rotary evaporation yielding yellowish viscous oils that were dissolved in acetonitrile and kept at 0 °C for 24 hours. Colorless crystalline precipitates were then recovered.
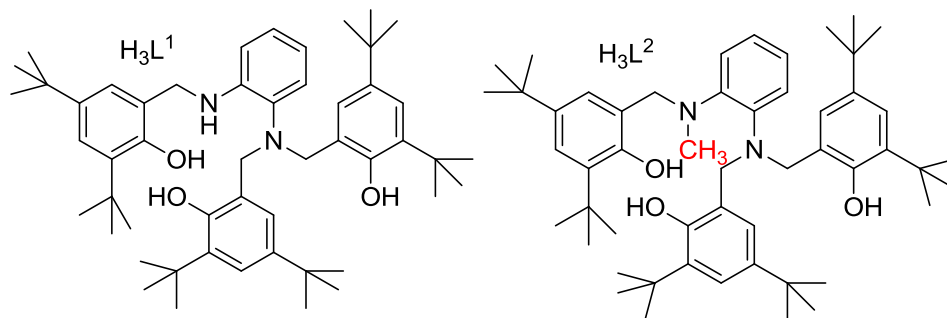
Scheme 4.1. Ligand.
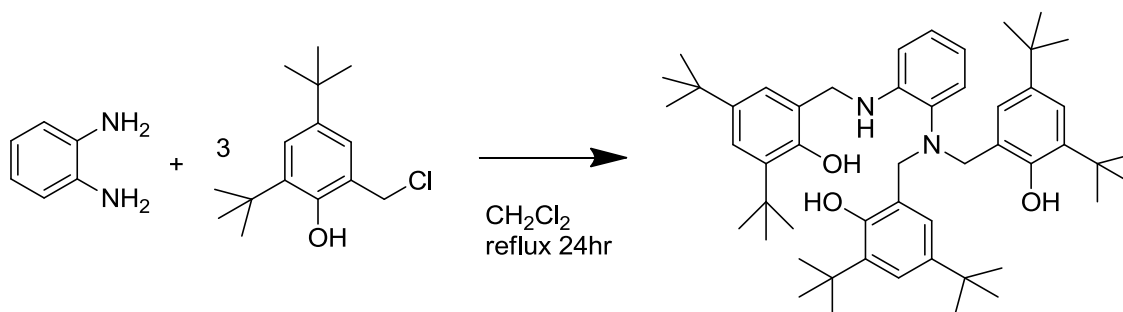
Scheme 4.2. Ligand synthesis.

H₃L¹: (Yield: 85%). ESI (m/z⁺) = 763.41, 100% for [C₅₁H₇₄N₂O₃ + H⁺]⁺. IR data (KBr, cm⁻¹): 3330(b) (O-H); 2958(s), 2897(s), 2863(s), (C-H, alkane); 1601(s), (C=C aryl); 1289(s), (C-N); 1229(s), (C-O); 879(b), (C-H, phen). Mp = 133-136 °C. ¹H-NMR [400 MHz, CDCl₃] data δ (ppm): 1.17 – 1.43 [m, 54H (multiple *t*-butyl)]; 3.92 [s, 4H (CH₂)]; 4.25 [s, 2H (CH₂-N')]; 6.80 – 7.34 [m, 10H (aryl)].

H₃L² (N,N,N'-tris-(3,5-di-tert-butyl-2-hydroxybenzyl)-N'-methyl-benzene-1,2-diamine) (Yield: 85%). ESI (m/z⁺) = 778.2, 100%, for [C₅₂H₇₆N₂O₃ + H⁺]⁺. IR data (KBr, cm⁻¹): 3370(s), (O-H); 2910(s), 2856(s), (C-H, alkane); 1594(s), (C=C aryl); 1289(s), (C-N); 1224(s), (C-O); 876(b), (C-H, phen). Mp = 185-189 °C. ¹H-NMR [400 MHz, CDCl₃] data δ (ppm): 1.24 – 1.35 [m, 54H (multiple *t*-butyl)]; 2.80 [s, 3H (CH₃)]; 3.69 [s, 4H (CH₂)]; 4.22 [s, 2H (CH₂-N')]; 6.64 – 7.26 [m, 10H (aryl)].

Compounds **[FeL¹] (1)** and **[FeL²] (2)** were synthesized following a general procedure that involved dissolution of 1 equivalent of the appropriate ligand in dry dichloromethane and treatment with 1 equivalent of iron(III) chloride dissolved in warm anhydrous methanol in the presence of 3 equivalents of NaOCH₃. The mixture was heated at 50 °C and stirred for 30 min. under an inert atmosphere then the solvent was removed by rotatory evaporation (**Scheme 4.3**). The resulting dark reddish-brown crude powders were recrystallized from MeOH/CH₂Cl₂ (1:2), yielding X-ray suitable single crystals.

[FeL¹] (1): H₃L¹ (0.38g, 0.5 mmol); FeCl₃·6H₂O (0.135g, 0.5 mmol); NaOCH₃ (0.081g, 1.5 mmol). (Yield: 0.25, 60 %). ESI (*m/z⁺*) = 814.4, (100%) for [C₅₁H₆₉N₂O₃Fe + H⁺]⁺. Anal. Calcd for [C₅₇H₇₁N₄O₃Fe]: C, 75.07; H, 8.77; N, 3.43%. Found: C, 75.34;

H, 8.91; N, 3.45%. IR data (KBr, cm^{-1}): 2956(s), 2870(s), (C-H, alkane); 1611(s), (C=N); 1470(s), 1445(s), (C=C aryl); 1199(s), (C-O); 873(s), (C-H, phen).

[FeL^2] (2): H$_3$L^2 (0.10g, 0.13 mmol); FeCl$_3$ (0.20g, 0.13 mmol); NaOCH$_3$ (0.20g, 40 mmol) (Yield: 0.1g 65 %). ESI (m/z^+) (in MeOH) = 830.9 (100%) for [C$_{52}$H$_{73}$N$_2$O$_3$Fe + H$^+$]$^+$. Anal. Calcd: C, 75.23; H, 8.87; N, 3.38%. Found: C, 74.97; H, 8.80; N, 3.28%. IR data (KBr, cm^{-1}): 2955(s), 2909(s), 2872(s), (C-H, alkane); 1274(s), (C-N); 1481(s), 1445(s), 851(s), (C-H, phen).
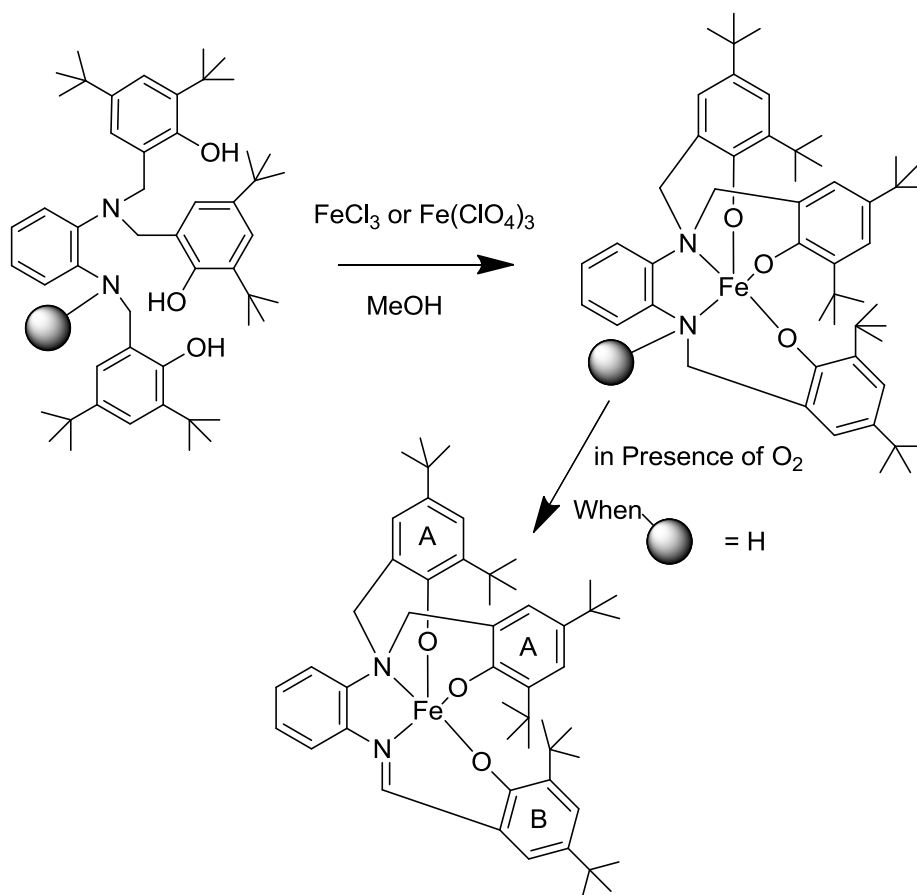
Scheme 4.3. Metal complex synthesis.

Results and discussion.

4.6. Ligand design

The use of [N$_2$O$_3$] pentadentate ligands allows for the development of five-coordinate complexes with selected trivalent metal centers. The design of the ligand takes advantage of our recent observation[8b, 15] that five-coordinate trivalent ions appear to enhance the formation and reversibility of phenolate/phenoxyl processes on the cyclic voltammetric timescale. Similar motifs are observed in certain non-heme iron enzymes[5], responsible for the synthesis and high turnover rates of radical-containing substrates. Understanding the properties of these redox-active species may lead to knowledge on experimental and computational relationships that explain the electronic behavior associated with multiple spin carriers in the same molecule. We have previously published on the chemistry of the precursor ligand **H$_3$L^1**, where a phenylenediamine moiety bridges three methylene-phenol groups. Two of these groups are attached to a tertiary amine, whereas the third group is attached to a vicinal secondary amine. Ligand **H$_3$L^1** can yield a complex **[FeL^{1amine}]** when isolated anaerobically and was discussed previously.[15] In this work we focus on the related imine version of **H$_3$L^1** that upon coordination exhibits a C=N bond associated with the secondary nitrogen atom when crystallized under aerobic conditions. On the other hand, the new ligand **H$_3$L^2** displays a methyl group appended to the mono-phenolated nitrogen atom that prevents such imine formation. Both ligands gave yields ranging between 50 and 90 % and were characterized by ^{1}H-NMR, electron spray ionization (ESI), and infrared spectroscopy.

4.7. Synthesis and characterization of the complexes

The compounds **(1)** and **(2)** were obtained as dark reddish-brown powders upon treatment of their respective deprotonated ligands, dissolved in a minimum amount of dichloromethane, with iron(III) chloride in methanol. All complexes were recrystallized in air with (1:2) MeOH:CH$_2$Cl$_2$ to yield X-ray quality crystals. Upon complexation the ligand H$_3$L^1 was converted into the imine, as observed by the appearance of a new band in the IR around 1602-1611 cm^{-1} attributed to C=N. Similarly, the absence of this peak for **(2)** indicates that imine formation does not occur for the methylated ligand. The tertiary-butyl groups present in all ligands are seen as intense stretches between 2870 and 2956 cm^{-1}. The peak for the methyl group in **(2)** is observed in this same range at 2909 cm^{-1}. These attributions have been confirmed by DFT frequency calculations of the optimized structures. Electrospray ionization in the positive mode (ESI$^+$) in methanol gave well defined peaks corresponding to m/z = [M + H$^+$]$^+$ at 814.4 (calc. 814.47) and m/z = [M + K$^+$]$^+$ at 852.4 (calc. 852.43) for **(1)** and m/z = [M + H$^+$]$^+$ at 830.9 (calc. 830.50) for **(2)**.

4.8. Molecular structures

Crystals suitable for X-Ray diffraction were obtained for the ligands H$_3$L^1, H$_3$L^2, and complexes **(1)** and **(2)**. The structures of the ligands are available in the Appendix A4. The ligand H$_3$L^1 shows clearly its initial amine nature with C22-N2 = 1.45 Å. Other pertinent bond lengths and angles will be discussed in conjunction with the complexes. All three complexes crystallize with five-coordinate iron(III) centers surrounded by fully deprotonated and pentadentate ligands and yield neutral, high-spin species. The observed bond lengths and angles are consistent with other examples in the literature.[8b, 15-16] The

ORTEP plots for **(1)** and **(2)** are given in **Figure 4.2** and selected bond lengths and angles are shown in **Table 4**.**2**. The structure for **(1)** shows a short bond (1.322(4) Å) between the mono-substituted nitrogen atom N1 and the methyl of the 2,4-di-*tert*-butyl-6-methylphenol moiety C7. This is consistent with the formation of a C=N imine bond, as suggested by the IR results, and associated with ligand oxidation. Complex **(2)** is similar to **(1)** except for the fact that N1 displays a –CH$_3$ group appended, thus forming a tertiary amine structure impervious to imine formation. This is indicated by the significantly longer C7-N1 bond of 1.512 Å. For both complexes, the iron(III) centers are penta-coordinated to the nitrogen atoms N1 and N2 of the phenylene group and to the oxygen atoms O1, O2, and O3 of the phenolato groups. The Fe-N1 distances of ~ 2.07 Å and Fe-O1 ≈ 1.91 Å in **(1)** indicate shorter Fe-N and longer Fe-O bonds associated with the mono-substituted phenolate arm. The Fe-N and Fe-O bonds for the tertiary amine and its associated phenolate groups reach, respectively, ~ 2.25 Å (Δ_{Fe-N} = 0.18 Å) and ~ 1.87 Å (Δ_{Fe-O} = 0.04 Å). The methyl-substituted amine complex **2** displays Fe-N1 ≈ 2.18, Fe-N2 ≈ 2.23, Fe-O1 ≈ 1.89, Fe-O2 ≈ 1.86, and Fe-O2 ≈ 1.87 Å, respectively.

A convenient way to analyze five-coordinate complexes is to report a τ value,[17] given by $\tau = (\beta - \alpha)/60$, ($\alpha$ and β are the two largest angles in the coordination sphere) where $\tau = 0$ indicates square pyramidal and $\tau = 1$ indicates trigonal bipyramidal geometries. Hence, **1** and **2**, have τ = 0.54, 0.66, respectively, suggesting distorted trigonal bipyramidal environments as for previously reported species.[8b] Finally, we observe a dihedral angle between C9-C8-N1-C7 is 13.4° for **(1)** and 65.4° for **(2)**.
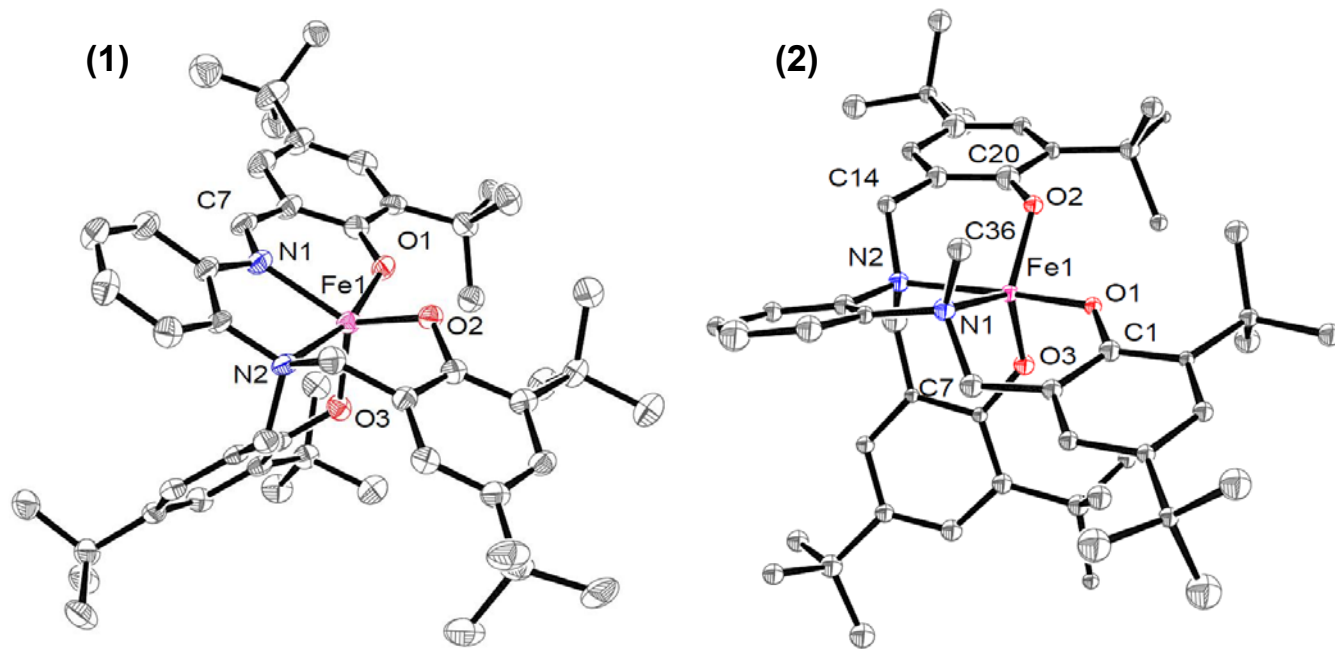
Figure 4.2. ORTEP of **(1)** (left)**:** Fe-O ≈ 1.89 Å, Fe-N1 = 2.072(2) Å, Fe-N2 = 2.24(2) Å,

C7-N1 = 1.32(3) Å. ORTEP of **(2)** (right): Fe-O ≈ 1.87 Å, Fe-N1 = 2.177(2) Å, Fe-N2 =

2.234(2) Å, C7-N1= 1.512(3) Å. Hydrogens omitted for clarity.

Table 4.2. Selected bond distances (Å) and angles ($^{\circ}$) for **(1)** and **(2)**.

(1)		(2)	
Fe-O1	1.918(2)	Fe-O1	1.885(3)
Fe-O2	1.868(2)	Fe-O2	1.863(3)
Fe-O3	1. 869 (2)	Fe-O3	1.873(3)
Fe-N1	2.072(3)	Fe-N1	2.177(4)
Fe-N2	2.248(3)	Fe-N2	2.234(4)
N1-C7	1.322 (4)	N1-C7	1.512(5)
N2-C21	1.494(4)	N1-C36	1.496(5)
N2-C14	1.514(4)	N2-C21	1.501(5)
		N2-C14	1.514(5)
O1-Fe-O2	95.81(10)	O1-Fe-O2	97.92(13)
O1-Fe-O3	101.71(9)	O1-Fe-O3	100.89(13)
O2-Fe-O3	112.92(10)	O2-Fe-O3	111.89(13)
O1-Fe-N2	163.97(10)	O1-Fe-N2	163.16(13)
O3-Fe-N2	89.56(9)	O3-Fe-N2	89.02(13)
O2-Fe-N2	90.12(10)	O2-Fe-N2	90.84(13)
O1-Fe-N1	87.23(11)	O1-Fe-N1	85.55(14)
O3-Fe-N1	113.59(10)	O3-Fe-N1	122.44(14)
O2-Fe-N1	131.64(10)	O2-Fe-N1	123.85(13)
N2-Fe-N1	77.75(11)	N2-Fe-N1	77.63(14)

4.9. Redox properties

It is established[8, 15] that iron phenolate species display complex electrochemical behavior attributed both to metal- and ligand-centered processes. The cyclic voltammograms (CV) of **[FeL^1] (1)** and **[FeL^2] (2)** were measured in dichloromethane using TBAPF$_6$ and TBAClO$_4$ (TBA = tetrabutylammonium) electrolytes. We aimed to evaluate the redox potentials for the metal- and ligand-centered processes, as well as to assess the intraligand oxidation sequence and the ability of the compound to withstand extensive redox cycling. Species **(1)** and **(2)** exhibit a wide range of processes that include the formation of the iron(II)/iron(III) couple and the successive formation of up to three phenolate/phenoxyl couples. The ligand-centered processes seem particularly dependent on the electrolyte choice and its associated anion. This phenomenon has been observed and explored by Geiger *et al*[18] and is related to ion-pairing effects. However, to the best of our knowledge, this phenomenon has not been studied for electrogenerated cationic phenoxyl radical species of metal complexes.

Ion-pairing effects occur when the anion of the electrolyte forms an ionic adduct with the cationic species, affecting the potential for the formation of consecutive cationic processes. Yet, one can select the appropriate electrolyte to modulate the potential of the anodic processes, either separating overlapped waves or merging separated ones. As a general rule the bulkier the electrolyte anion, the larger the gap between the oxidative peaks $E_{1/2}^{ox1}$ and $E_{1/2}^{ox2}$ ($\Delta E_{1/2}^{ox}$). One can therefore, suggest that the presence of a larger counterion such as PF$_6^-$ from the supporting electrode would lead to the formation of a more geometrically distorted **[1']**$^+$-PF$_6$ ion pair leading to two individual 1e$^-$ processes,

whereas a slightly smaller perchlorate ion would lead to less extensive distortion, enabling the two rings (A and A') to be oxidized at near identical potentials.

All the Fe(III)/Fe(II) couples are observed near -1.5 V *vs.* Fc$^+$/Fc and are similar for complexes **(1)** and **(2)** (**Table 4.3**). This is expected considering that the three complexes have iron centers in similar ligand environments with N_2O_3 pentadentate donors. Furthermore, we consistently observe a small shift of potentials of ~ 0.06-0.1 V when TBAClO$_4$ is used in place of TBAPF$_6$. Species **(1)** shows the most pronounced effect while **(2)** has the most negative potential for the Fe(III)/Fe(II) couple, indicating resistance towards reduction. These values are consistent with our previously published results of -1.44 V.[8b]

Table 4.3. Cyclic voltammetry values for **(1)** and **(2)** (*vs.* ferrocene in DCM)

Compound	Electrolyte	a) E1/2 (red.)	b) (1st ox.)	c) (2nd ox.)	c) (3rd ox.)
(1)	TBAPF$_6$	-1.48V (ΔE 0.10V)	0.55V (ΔE 0.15V)	0.73V (ΔE 0.16V)	NA
(1)	TBAClO$_4$	-1.37V (ΔE 0.13V)	0.63V (ΔE 0.16V)	NA	NA
(2)	TBAPF$_6$	-1.55V (ΔE 0.23V)	0.48V (ΔE 0.12V)	0.75V (ΔE 0.12V)	1.01V (ΔE 0.08V)
(2)	TBAClO$_4$	-1.49V (ΔE 0.23V)	0.52V (ΔE 0.13V)	NA	NA

At first glance the anodic side of the voltammograms are similar to their previously published gallium counterparts,[15] which can support phenoxyl radical generation, and for iron(III) complexes which have overlapping processes.[8b, 19] For complex **(1)**, it is evident that the identity of the electrolyte anion plays a more significant role in comparison to complex **(2)**. We observe only one anodic wave for **(1)** centered at 0.63 V (ΔE_p = 0.16 V) when TBAClO$_4$ is used. The amplitude of this wave suggests the

oxidation of two phenolates when compared internally to the Fe(III)/Fe(II) couple. On the other hand, 0.1 M TBAPF$_6$ electrolyte fosters some degree of separation with the appearance of two closely separated anodic waves at 0.55 V (ΔE_p = 0.15 V) and 0.73 V (ΔE_p = 0.16 V) suggestive of sequential one-electron processes. Lower concentrations (0.05 M) of electrolyte led to higher peak separation, but dramatically affected the reversibility of the Fe(III)/Fe(II) couple.

Bistability between reduced and oxidized forms must be achieved to withstand extensive redox cycling. Thirty CV cycles of **(1)** resulted in minimal decomposition at the surface of the electrode, as indicated by a nearly perfect superposition of the waves for cycling through both the first ligand-centered oxidation and the metal-centered reduction.

For **(2)** we observed three one-electron anodic waves centered at 0.48 V (ΔE_p 0.12 V), 0.75 V (ΔE_p = 0.12), and 1.01 V (ΔE_p = 0.08) when TBAPF$_6$ was used as the supporting electrolyte (**Figure 4.3**). These processes are consistent with all three of the phenolate groups being oxidized to phenoxyl radicals. A small process can be observed near 0.45 V, when the third oxidative process is carried out--possibly due to some decomposition. When TBAClO$_4$ is used, only two oxidation processes at 0.6 V and 0.7 V were observed for **(2).** Interestingly, these oxidations correlate to a single reduction at 0.5 V, rendering these processes irreversible. Redox cycling revealed a consistent behavior for the first ligand-centered process, while the metal-based process showed some minor decomposition. In general, most processes appear to be reversible/quasi-reversible, with values of ΔE ranging from ~ 0.10 to 0.23 V, when compared to the standard Fc$^+$/Fc couple (ΔE_p = 0.14 V). All the anodic oxidation waves reported here are believed to be associated with phenoxyl radical formation.
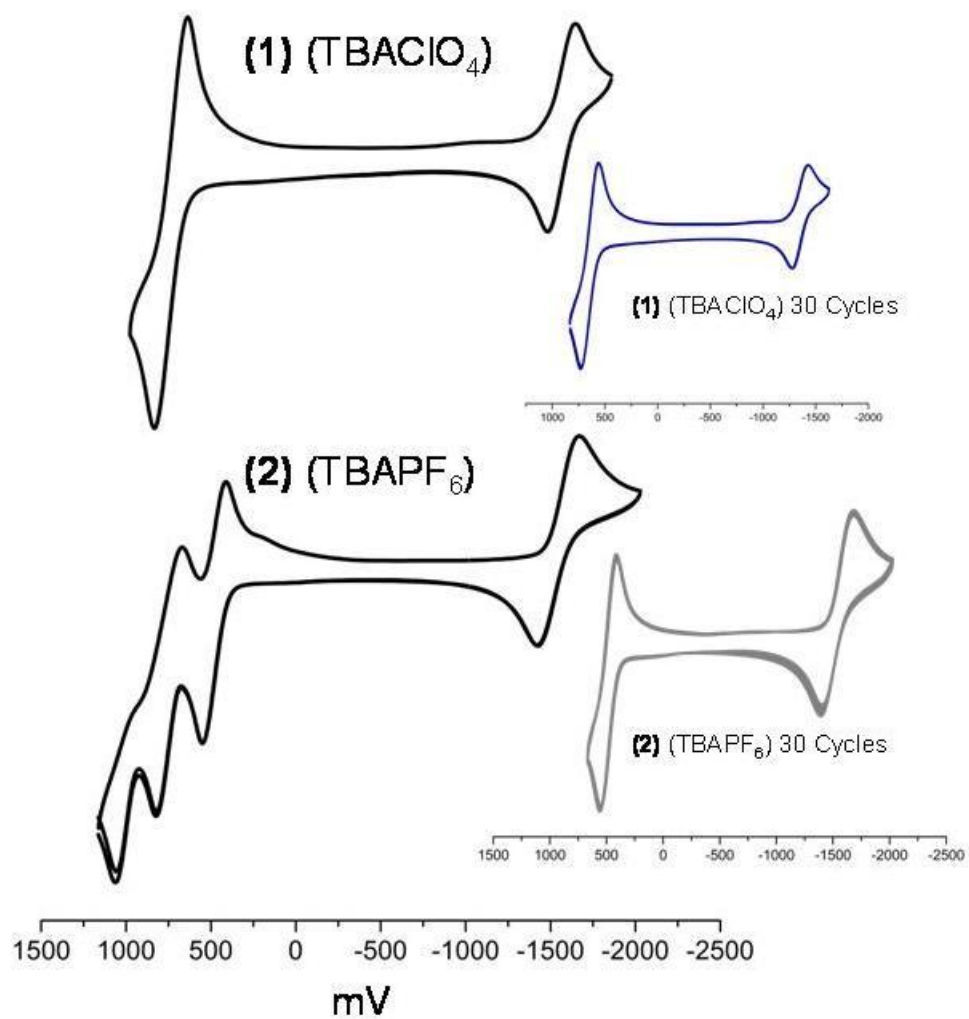
Figure 4.3. Cyclic voltammograms for **(1)** (top) and **(2)** (bottom) (in

dichloromethane *vs*. ferrocene).

4.10. Electronic properties

The electronic properties of complexes **(1)** and **(2)** and their oxidized forms **(1)**$^+$ and **(2)**$^+$, were studied by UV-visible and EPR spectroscopies (**Figure 4.4**). The UV-visible spectra in dichloromethane show several bands associated with multiple electronic processes, as expected for such low-symmetry environments. The transitions attributed to $\pi^* \leftarrow \pi$ appear at about 285 nm with $\varepsilon \sim$ 30,000 to 40,000 $M^{-1}cm^{-1}$ for **(1)**, and somewhat less intense for the methyl-substituted **(2)** with 17,000 $M^{-1}cm^{-1}$. A weaker transition is observed between 310-340 nm ($\varepsilon \sim$ 20,000 for **(1)** and 8,000 $M^{-1}cm^{-1}$ for **(2)** and was attributed to a (Fe$\leftarrow$N) LMCT band. Finally, **(1)** shows the (Fe$_{d\sigma^*}\leftarrow$O$_{p\pi}$) LMCT processes at $\sim$ 400 nm ($\varepsilon \sim$ 11,000 $M^{-1}cm^{-1}$), whereas the complimentary (Fe$_{d\pi^*}\leftarrow$O$_{p\pi}$) LMCT processes appear as slightly less prominent shoulders at 503 nm (6,600 $M^{-1}cm^{-1}$) for **(1)** and 440 nm (10,200 $M^{-1}cm^{-1}$) for **(2)**. The methylated **(2)** shows the first (Fe$_{d\sigma^*}\leftarrow$O$_{p\pi}$) LMCT process at 479 nm (6,200 $M^{-1}cm^{-1}$) in a band with obvious non-gaussian shape, as indicative of a prominent Fe$_{d\pi^*}\leftarrow$O$_{p\pi}$ component, but no maximum can be inferred. Also noteworthy is the fact that the transitions attributed to the (Fe$\leftarrow$O) LMCT processes contain, in fact, multiple components associated with the distinctiveness of the three phenolates oriented in a low symmetry space.
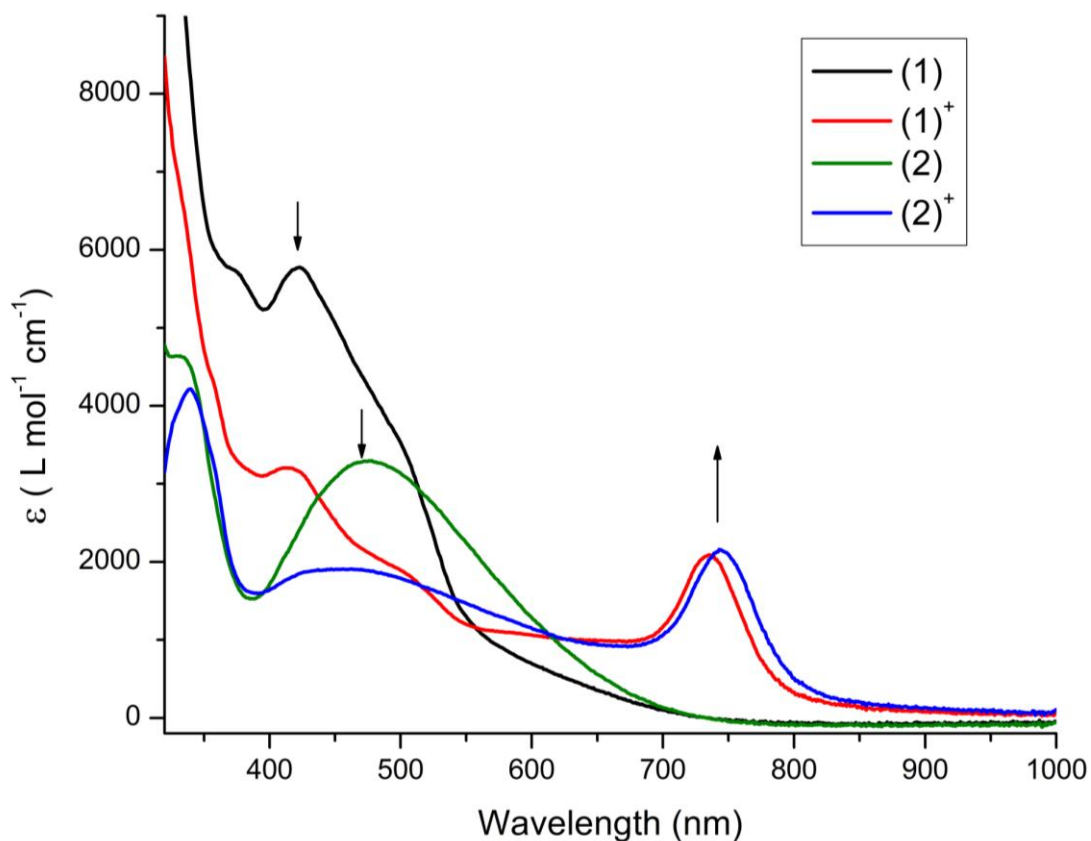
Figure 4.4. UV-vis absorption of (1), (1)[+], (2), and (2)[+]. **(1)** (black) 286 (13000); 308 (12000); 378 (6000); 422 (6600); 503sh (4000); **(1)**[+] (red) 335 (4300); 415 (3200); 505sh (1800); 735 (2100); **(2)** (green) 285 (8000); 335 (4000); 479 (3800); **(2)**[+] (blue) 338 (4200); 470 (1900); 745 (2100).

Exhaustive bulk electrolysis was carried out at -78 °C under a constant stream of solvent saturated inert nitrogen gas[8b] and were followed by cyclic voltammetry to ensure the completeness of the reaction. After single-electron oxidation of the solutions an aliquot was collected for each species and revealed considerable decreases in the intensities of the (Fe←O) LMCT processes. This phenomenon was expected and can be explained by the conversion of one phenolate arm to a phenoxyl radical. Due to the close proximity of the several oxidation potentials, it is also possible that, to some degree, either a second oxidation or complex disproportionation may also occur.[20] A new band (≈ 750 nm) appears for **(1)**[+] and **(2)**[+] which is associated with a phenoxyl/phenolate inter-

ligand charge transfer (ILCT) band[21] and is consistent with the decreasing intensities of the remaining phenolate (Fe←O) LMCT processes.

EPR spectra were taken for **(1)** and **(2)** and for the electrolysis-generated monocationic species **(1)$^+$** and **(2)$^+$** allowing for the assessment of magnetic properties of the oxidized species and their relative stabilities. All monocationic species were also obtained by treatment with tetrabutyl-ammonium cerium(IV) salt,[22] to reproduce and verify the results from the bulk electrolysis experiment. **Figure A.4.1** shows that before oxidation, three inflections were present for complexes **(1)** and **(2)** , with *g*-values near 8.2, 5.4, and 4.3 associated with an anisotropic iron(III) S = 5/2 center. The association with a high-spin ferric ion in low-symmetry has been previously reported.[8b, 15, 23] Upon oxidation, an approximate 90 % decrease in signal intensity was observed. The signal at *g* = 4.3 remains visible, whereas the signals at 8.2 and 5.4 are greatly diminished. Additionally, a new sharp signal of small magnitude appears at *g* = 2.0 (~3300 gauss) associated with phenoxyl radical formation. An antiferromagnetic coupling[16b, 24] between a high-spin iron(III) and a phenoxyl radical should lead to a silent S = 5/2 − 1/2 = 4/2 EPR signal, as previously reported.[8b] The fact that such a signal is visible suggests an uncoupled total S = 5/2 + 1/2 spin system consisting of the S = 5/2 from the iron(III) center and an S = 1/2 attributed to a phenoxyl radical. These observed signals suggest that (i) the phenoxyl ring becomes a poor donor due to the rearrangement with localization of bonds into a quinoid-like ring, (ii) that the Fe-O$_{phenoxyl}$ bond may break, and (iii) that the metal center may associate with adventitious solvents or electrolytes increasing its coordination number to a pseudo-octahedral geometry. Interestingly, our results for a similar phenanthroline-containing system[8b] have shown almost complete phenoxyl

radical magnetic coupling to the iron center. Several of the proposed arguments in this and the previous sections are discussed further in the following section.

4.11. Electronic structure calculations

Electronic structure calculations were carried out on two series of two different models comparable to **(1)** and **(2)**, and named respectively **(1')** and **(2')** (**Figure 4.5**). The six *tert*-butyl groups appended to the phenolate rings were replaced by hydrogen atoms (-H) to make the calculations more practical.
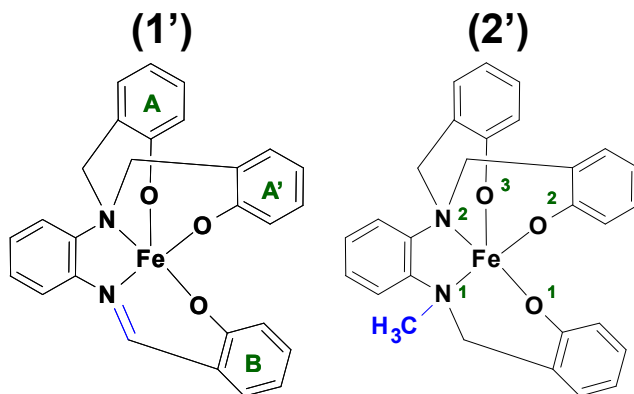
Figure 4.5. Computational models for **(1)** and **(2)**.

4.12. Calculated structural properties

We were interested in the comparison of the structural and electronic properties between the initial complexes **(1)** and **(2)** and the changes imposed by single and double oxidations, both in the gas phase and using a PCM solvation model. Throughout the discussion, the two phenolate rings appended to the same nitrogen atom will be referred to as A and A', whereas the third phenolate is referred to as B. Upon inspection, the geometries of the optimized complexes are generally in good agreement with the X-ray structures. As can be seen in **Table 4.4** for **(1)**, the calculated bond lengths are usually

around 2% shorter than the X-ray diffraction data. The PCM solvation model used to study the electrochemistry and electronic absorption spectroscopy did not affect the geometries significantly. The calculations show that replacing the *tert*-butyl groups on the phenolates by hydrogen has very little effect on the Fe-O bond lengths. This is an important point, since it is well known[8a, 25] that these substituents can have substantial effects on the phenolato/phenoxyl couple redox potential and can also affect radical stability/reversibility in solution. Models **(1')** and **(2')** show the same trends as the crystal structures, as indicated in **Table 4.4.** For **(1)** and **(1')** the Fe-O1 and Fe-O2 bond lengths associated with the "A" rings are shorter, while for the "B" ring Fe-O3 is a ~0.08 Å longer bond, suggesting that our models are accurate enough to allow for meaningful comparisons in bond lengths.

Table 4.4. Selected comparison between experimental and calculated bond lengths (Å) (refer to **Figure 4.2** for numbering)

	Fe-O1	Fe-O2	Fe-O3	Fe-N1	FeN2	C-O1	C-O2	C-O3	Method
(-*t*-butyl) **(1)**	1.869(2)	1.868(2)	1.918(2)	2.072(3)	2.248(3)	1.352(4)	1.353(4)	1.319(4)	Exp.
(-*t*-butyl) **(1)**	1.86	1.84	1.92	2.09	2.30	1.34	1.34	1.31	Calc. (gas)[a]
(-H) **(1')**	1.86	1.84	1.92	2.10	2.32	1.33	1.34	1.30	Calc. (gas)[a]
(-H) **(1')**	1.86	1.87	1.93	2.10	2.30	1.34	1.34	1.31	Calc. (PCM)[a]

[a]Calculated with B3LYP/6-31G(d)

4.13. Calculated electronic redox behavior

The identification of the sequential order in which the phenolate rings are oxidized into phenoxyl radicals is of pivotal interest in this work**.** The cyclic voltammetry data discussed earlier showed considerable differences between **(1)** and **(2)**. Complex **(2)** exhibits three independent 1e⁻ oxidative processes, whereas **(1)** shows a multi-electronic process. In our previous work[8] it was demonstrated that the nature of the electronic

coupling between a five-coordinate iron(III) (S = 5/2) and the phenoxyl radical (S = 1/2) in an [N_2O_3] environment is predominantly antiferromagnetic, yielding a S = 4/2 ground state. The same spin-coupling was adopted here for **(1)** and **(2)**, and used in the investigation of the electronic states for **(1')** (S = 5/2), **(1')**$^+$ (S = 4/2), and **(1')**$^{2+}$ (assumed to be S = 3/2) in which a phenoxyl radical is magnetically-coupled with one of the unpaired electrons from the iron(III) center. Similarly, the series **(2')**, **(2')**$^+$, and **(2')**$^{2+}$ was also investigated with similar spins states. As pointed out by Wieghardt *et al.*[24a, 26] the study of spin-coupled metal/organic radical systems is far from trivial. It is even more difficult to understand this behavior in low-symmetry environments, where the molecular orbital (MO) scheme deviates considerably from the ones usually invoked for the highly degenerate octahedral case. In unrestricted calculations, the canonical molecular orbitals for the α space can have different shapes and energies than for the β space. The orbital analysis can be simplified by using corresponding biorthogonal orbitals. These are obtained by a unitary transformation of the canonical α and β orbitals so that each α occupied orbital has maximum overlap with the corresponding β occupied orbital and vice versa. The average of the α and β orbital energies of the corresponding orbitals can be used to construct a classical MO ladder diagram.[27] Some caution is needed to ensure that the calculations yield the correct coupling schemes in these metal/radical compounds. When the members of each series are compared, **(1')**→**(1')**$^+$→**(1')**$^{2+}$ and **(2')**→**(2')**$^+$→**(2')**$^{2+}$, respectively, the metal centers have similar Mulliken spin densities of ~ 4.18 and charges of ~1.37, consistent with a high-spin Fe(III) ion (see **Table 4.5**). Thus, the oxidations are properly assigned as phenolate/phenoxyl radical-based rather than Fe(III)/Fe(IV) species, which is in agreement with literature.[24a, 25, 28]

Table 4.5. Mulliken charge and spin density analysis and selected bond lengths (Å) for (**1'**), (**1'**)$^+$, (**1'**)$^{2+}$, (**2'**), (**2'**)$^+$, and (**2'**)$^{2+}$.

	Mulliken Spin Density	Mulliken Charge	Fe-O	C(ring)-O
(**1'**) (S = 5/2)				
Fe (III)	4.19	1.34		
Ring A	0.24	-0.42	1.86	1.34
Ring A'	0.23	-0.43	1.87	1.34
Ring B (C=N)	0.17	-0.30	1.93	1.31
(**1'**)$^+$ (S = 4/2)				
Fe (III)	4.17	1.39		
Ring A	0.28	-0.30	1.83	1.34
Ring A' (R$^\uparrow$)	-0.88	0.20	1.98	1.28
Ring B	0.23	-0.40	1.88	1.31
(**1'**)$^{2+}$ (S = 3/2)				
Fe (III)	4.18	1.34		
Ring A (R$^\uparrow$)	-0.87	0.33	1.93	1.28
Ring A' (R$^\uparrow$)	-0.90	0.29	1.97	1.28
Ring B	0.34	-0.44	1.85	1.32
(**2'**) (S = 5/2)				
Fe (III)	4.18	1.30		
Ring A	0.21	-0.35	1.88	1.34
Ring A'	0.22	-0.35	1.88	1.34
Ring B	0.22	0.23	1.88	1.33
(**2'**)$^+$ (S = 4/2)				
Fe (III)	4.16	1.34		
Ring A	0.28	-0.25	1.84	1.35
Ring A'	0.27	-0.20	1.85	1.34
Ring B (R$^\uparrow$)	-0.92	0.13	2.01	1.28
(**2'**)$^{2+}$ (S = 3/2)				
Fe (III)	4.12	1.39		
Ring A	0.45	-0.19	1.83	1.34
Ring A' (R$^\uparrow$)	-0.90	0.27	1.96	1.28
Ring B (R$^\uparrow$)	-0.91	0.27	1.97	1.28

[a]B3LYP/6-31G(d) with IEF-PCM solvation in dichloromethane. R$^\uparrow$ denotes the phenoxyl location.

The spin density plot demonstrates consistency, with (**1'**) conserving its excess α-density predominantly localized on the high-spin iron(III) center (**Figure 4.6**). A very small amount of α-density can be found on the donors, but none is observed on the rings. This spin density does not change upon formation of (**1'**)$^+$, nor (**1'**)$^{2+}$. However, excess β-density becomes apparent upon oxidation to (**1'**)$^+$, which has a localized phenoxyl character on the A' ring. Upon closer inspection, we can quantify the amount of spin density and charges that are related to each phenolate/phenoxyl ring by summing the contributions of the ring atoms (**Table 4.5**). For (**1'**) the A, A', and B rings display similar Mulliken spin densities, between 0.17 and 0.24. The oxidized (**1'**)$^+$ was found to have a spin of -0.88 on A', thus clearly indicating the location of the radical. Consistently, the Mulliken charges also support an oxidized ring A' going from -0.43 to 0.20. Close examination of the Fe-O bond length, indicates that A' had an elongation of ~ 0.11 Å. It is also clearly shown that this ring becomes quinoid-like in nature, with a 0.06 Å shorter C=O bond length. Hence, the quinoid-like ring A' becomes a less effective electron donor forcing the remaining phenolate rings to shorten their respective Fe-O bonds. The rest of the geometry of (**1'**)$^+$ is fairly similar to that of (**1'**), as seen by the superimposition of structures (**Figure 4.6**, top left). The absence of major geometric rearrangements fosters an overall bistability for fast redox cycling between these species. A very similar observation can be made for (**1'**)$^{2+}$, in which a second phenolate-to-phenoxyl conversion takes place on ring A, allowing for the identification of the second oxidative process from the cyclic voltammetric experiment. As suggested in the electrochemical section, smaller electrolyte anions such as ClO_4^- lead to a potentially less

distorted ion pair, enabling the two rings (A and A') to be oxidized at nearly identical potentials.

Compound $(2')^+$ behaves in quite a different mode than its counterpart $(1')^+$. Upon oxidation, radical formation is observed (**Figure 4.6**, bottom) on the B ring as opposed to rings A or A', as noted previously for **(1')**. Ring B relates to the N-appended CH_3 group and shows Mulliken spin density and charge of -0.92 and 0.13, respectively. The Fe-O bond is elongated by 0.13 Å and the C=O bond is shortened to 1.28 Å, thus comparable to $(1')^+$ and consistent with a quinoid-like structure. The remaining parts of the geometries of **(2')**, $(2')^+$, and $(2')^{2+}$ are very similar. Generally speaking, the results for **(1')** and **(2')** agree to previously published[15] electronic structures for a similar amine-containing complex. A word of caution is nonetheless needed for direct comparison, because a vertical oxidation was used in that study without further structural minimization of the oxidized species. Calculation in the gas phase instead of PCM solvation, results in the phenoxyl radical partially delocalized over both rings A and A', where ring A' has close to 50% more β spin density than ring A. This delocalization is not unusual, since rings A and A' are chemically equivalent.[21, 23, 29]
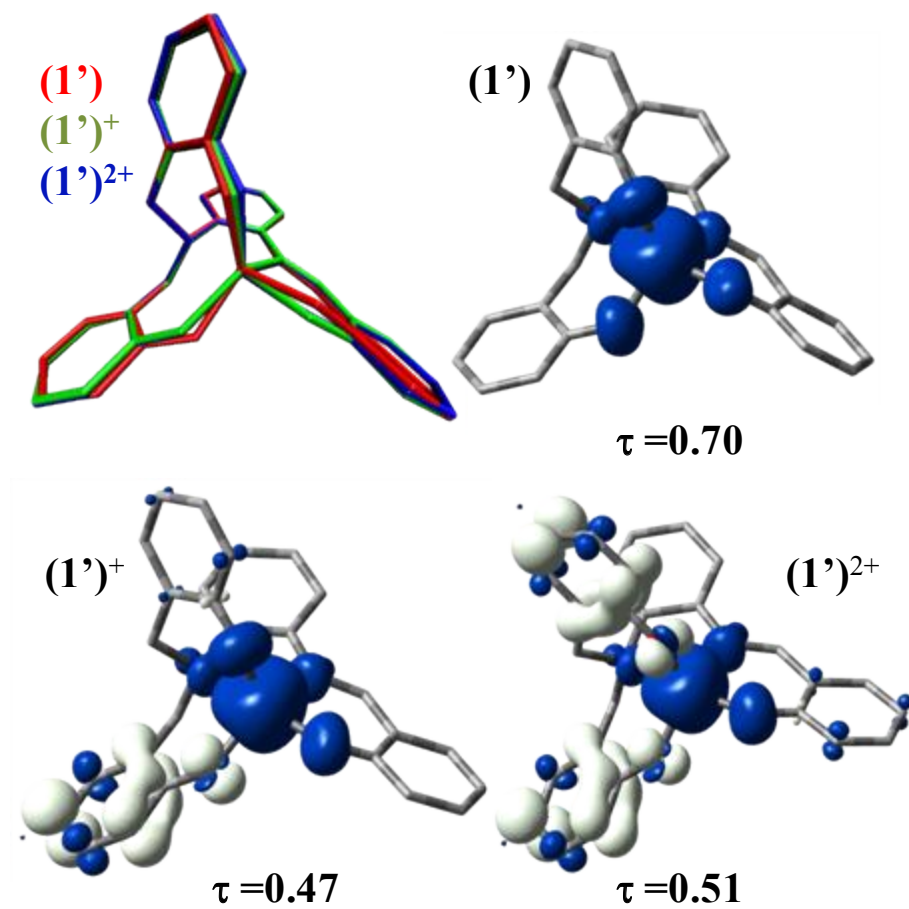
Figure 4.6. Spin density plots of optimized geometries of **(1')**, **(1')**[+], and **(1')**[2+]. The white and blue shades correspond to excess β and α electron spin densities, respectively. Superimposition of **(1')**, **(1')**[+], and **(1')**[2+] (top left).
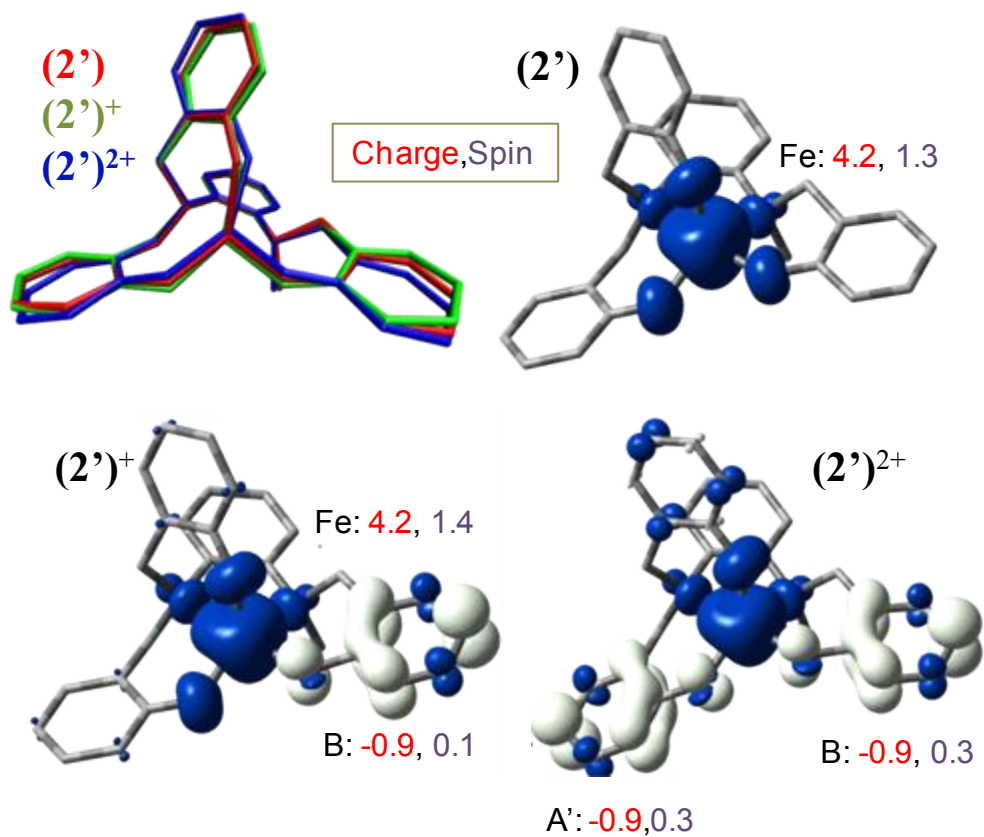
Figure 4.7. Spin density plots of optimized **(2')**, **(2')**[+], and **(2')**[2+] The white and blue shades correspond to excess β and α electron spin densities, respectively. Superimposition of **(2')**, **(2')**[+] and **(2')**[2+] (top left).

4.14. Comparison of ligand fragments

In compounds **1-2**, two equivalent rings A and A' are appended to the same nitrogen atom, whereas the dissimilar ring B is appended to the C=N or $(CH_3)C-N$ nitrogen atom. The phenolate B is significantly different in terms of π-bonding delocalization than the other two, and likely points to the dramatically different redox behavior experimentally observed. Partial models (or fragments) of the ligands in (**1**) and (**2**) were used to evaluate this effect. This approach has been used previously by our group.[2]
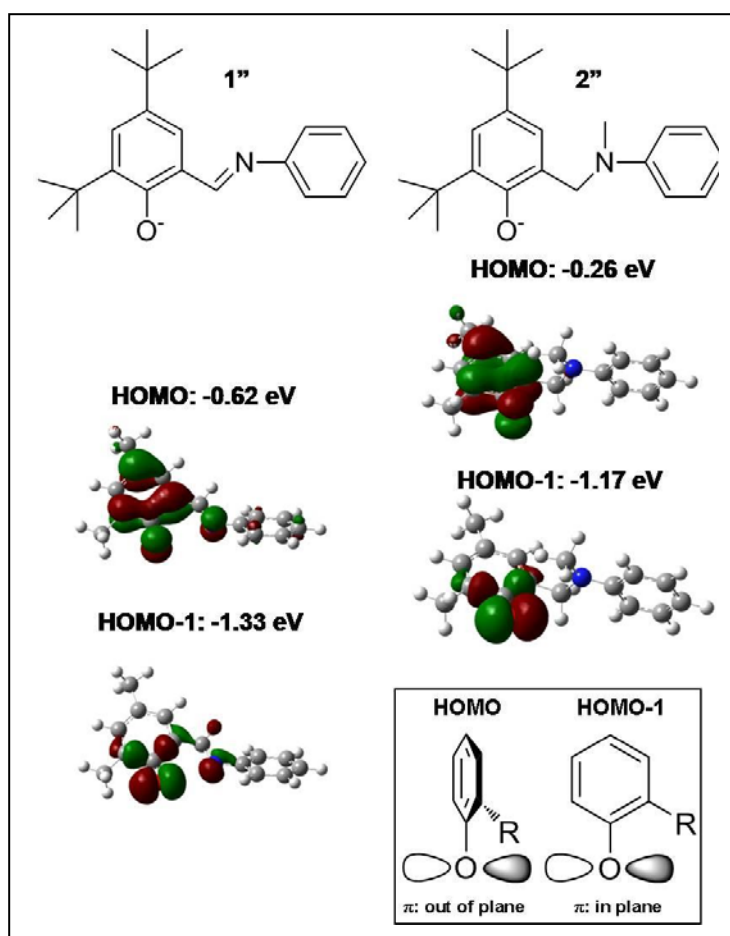
Figure 4.8. Computational models for ligand fragments.

It is clear that **(1")** is harder to oxidize than **(2")** by ~3 kcal/mol. This trend is also consistent with the energy of the HOMOs, which according to Koopman's theorem[30] should relate to the first ionization energy (the HOMO of 1" is about 0.4 eV (9 kcal/mol) lower than **(2")**. Upon inspection of the MOs, it is clear that **(1")** has a larger electronic delocalization than **(2")**, thus affecting the outcome of the redox properties. The inset in **Figure 4.8** shows that there are two different π-orbitals that can interact with the metal center, namely an "out-of-plane" and an "in-plane", as previously described by Solomon *et al.* [31] The "out-of-plane" orbital is always higher in energy than the "in-plane" orbital.

4.15. MO variations between parent and oxidized species

After considering in detail the structural and electronic properties of complexes **(1')** and **(2')**, we now compare the variations in the MO energies between these species and their singly- and doubly-oxidized counterparts. This analysis takes into account subtle changes in geometries, along with total charge and local spin variation, reflected by MO rearrangements associated with each oxidative step. Unlike high-symmetry pseudo-octahedral species, or low-symmetry low-spin species, the present analysis requires the use of corresponding orbitals[26-27] in order to gain some information about radical generation and stabilization. The discussion is restricted here to singly occupied orbitals and spin-coupled pairs (corresponding orbital pairs with α/β overlap between 0.12-0.30). **Figures 4.9** and **4.10** show MO ladder diagrams (left) and the frontier orbitals (right) arranged vertically by the average energy of the matched α and β pairs. The five-coordinate **(1')** and **(2')** are heavily distorted trigonal bipyramids that can be viewed as lying partway along a Berry pseudo-rotation pathway between idealized trigonal bipyramidal and square planar structures. As a consequence, the choice of a common

Cartesian axis system for both species becomes a more intricate task. The issue is further complicated by the presence of multiple σ– and π–interactions. **Figure 4.9** displays a comparative energy ladder diagram along with tentative labeling assignments for the d orbitals in (**1'**) and (**2'**). It becomes evident that even though the [N_2O_3] donor sets for both species are similar, they have a significant effect on the energies of the metal-based orbitals.

The presence of a C=N fosters some delocalization between N1 and the phenolate B in (**1'**) leading to shorter N1-Fe and longer O1-Fe bonds. The most affected iron-based SOMO coincides with the N1-Fe-O1 plane and shows increased energy due to π anti-bonding interactions.
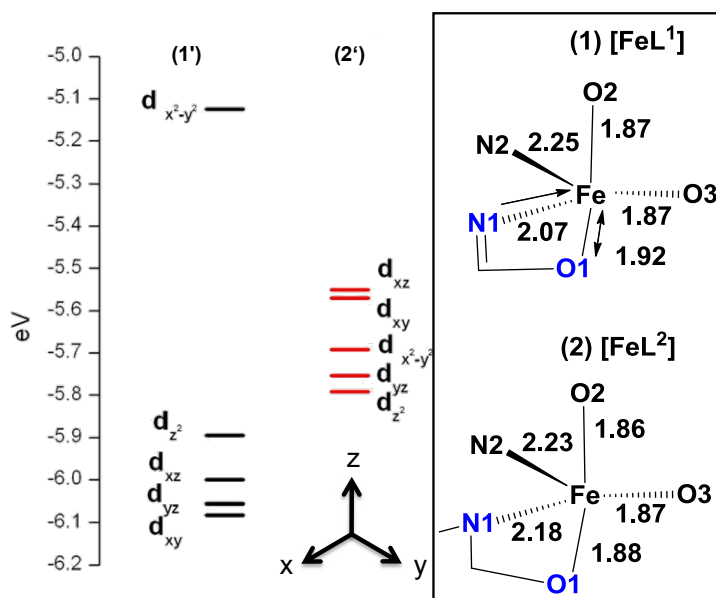
Figure 4.9. Averaged d orbital splitting for (**1'**) and (**2'**) and selected bond lengths for (**1**) and (**2**) (right).

The elongation of this Fe-O1 bond prompts the lowering of the remaining four d orbitals. These SOMOs display predominant metal character (78 to 85 %) and are tentatively labeled as $d_{x2-y2} >> d_{z2} > d_{xz} > d_{yz} > d_{xy}$. On the other hand, the doubly-occupied

HOMO-5 to HOMO-7 display, respectively, 79, 87, and 81 % ligand character, and are phenolate π-bonding MOs built on various combinations of the three phenolate groups.

Figure 4.10 and **4.11** present a detailed description of the changes that accompany multiple oxidation processes in **(1')** and **(2')**, along with the plot of the relevant singly- and doubly-occupied MOs (black and blue, respectively) and spin-coupled pairs (red). Starting with **(1')**, generation of **(1')**$^+$ and **(1')**$^{2+}$ leads to a typical decrease of the relative energies of all frontier orbitals, indicating an increased ionization potential related to a larger positive charge. The order of these orbitals does not appear to change and the lowest energy uncoupled d_{xy} electron (α-orbital, 85 % iron) spin-pairs with the 89% phenoxyl-based β-orbital localized on ring A'. Both α and β orbitals have similar energies, with their respective orbital energies lying below the out-of-plane doubly-occupied combination of phenolate orbitals.

Upon the second oxidation, another spin-coupled orbital combination is formed between the d_{yz} orbital (α, Fe-based) and the phenoxyl radical (β, ring A). These resulting sets of spin-coupled orbitals are relatively close in energy.

Compound **(2')** is depicted in **Figure 4.10** and presents a different d orbital splitting pattern in the order: $d_{xz} \geq d_{xy} > d_{x2-y2} > d_{yz} > d_{z2}$. All SOMOs are closely packed in energy and the spin-coupled orbitals generated upon oxidation for both **(2')**$^+$ and **(2')**$^{2+}$ differ from those in **(1')**$^+$. These spin-coupled orbitals involve the out-of-plane phenoxyl β orbital on ring B (rather than A or A') coupled with the d_{yz} iron-centered orbital. Species **(2')**$^{2+}$ displays an additional spin-coupled orbital based on the iron d_{z2} /phenoxyl from ring A'. Based on logical assumptions, it is possible to infer that a third

oxidation that leads to **(1')**$^{3+}$ and **(2')**$^{3+}$ will be based, respectively, on phenoxyl formation of rings B and A, but may lead to the decomposition of the resulting species.
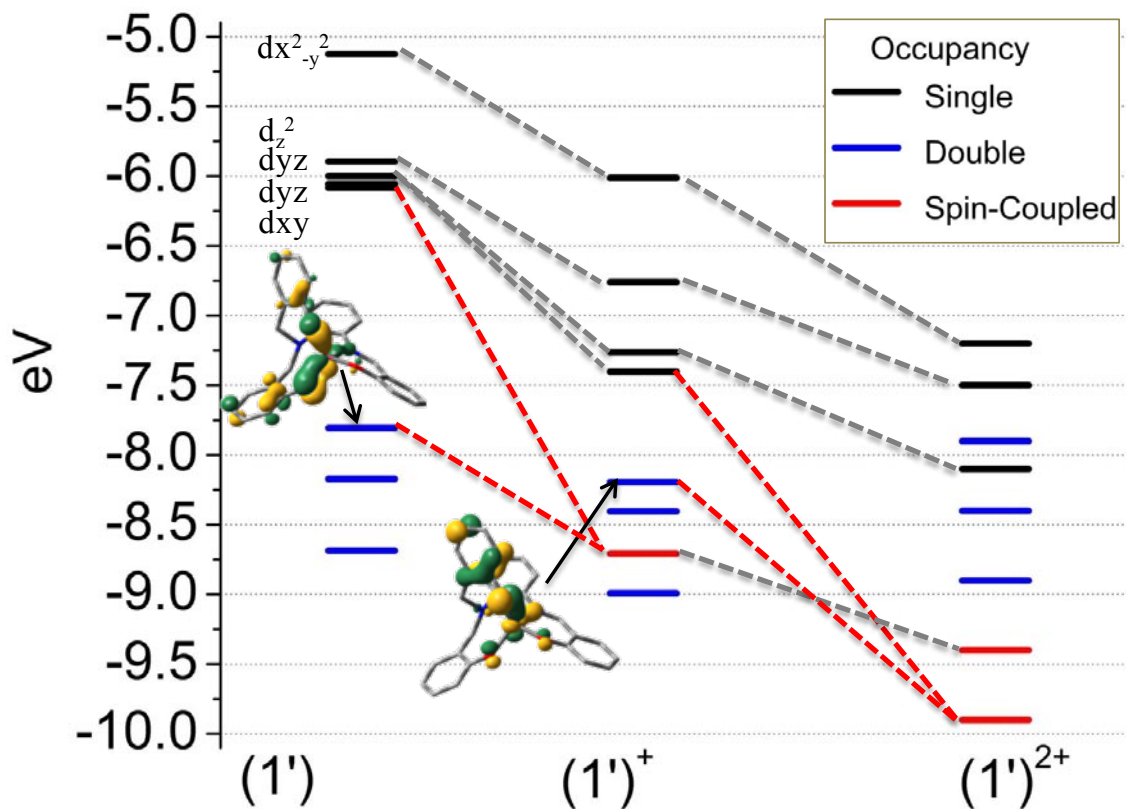
Figure 4.10. Average orbital energy ladder (left) and selected frontier orbitals (right, α-SOMOs and spin coupled pairs with hydrogen atoms omitted for clarity) for **(1')**, **(1')**$^{+}$, and **(1')**$^{2+}$ (B3LYP/6-31G(d) IEF-PCM dichloromethane).
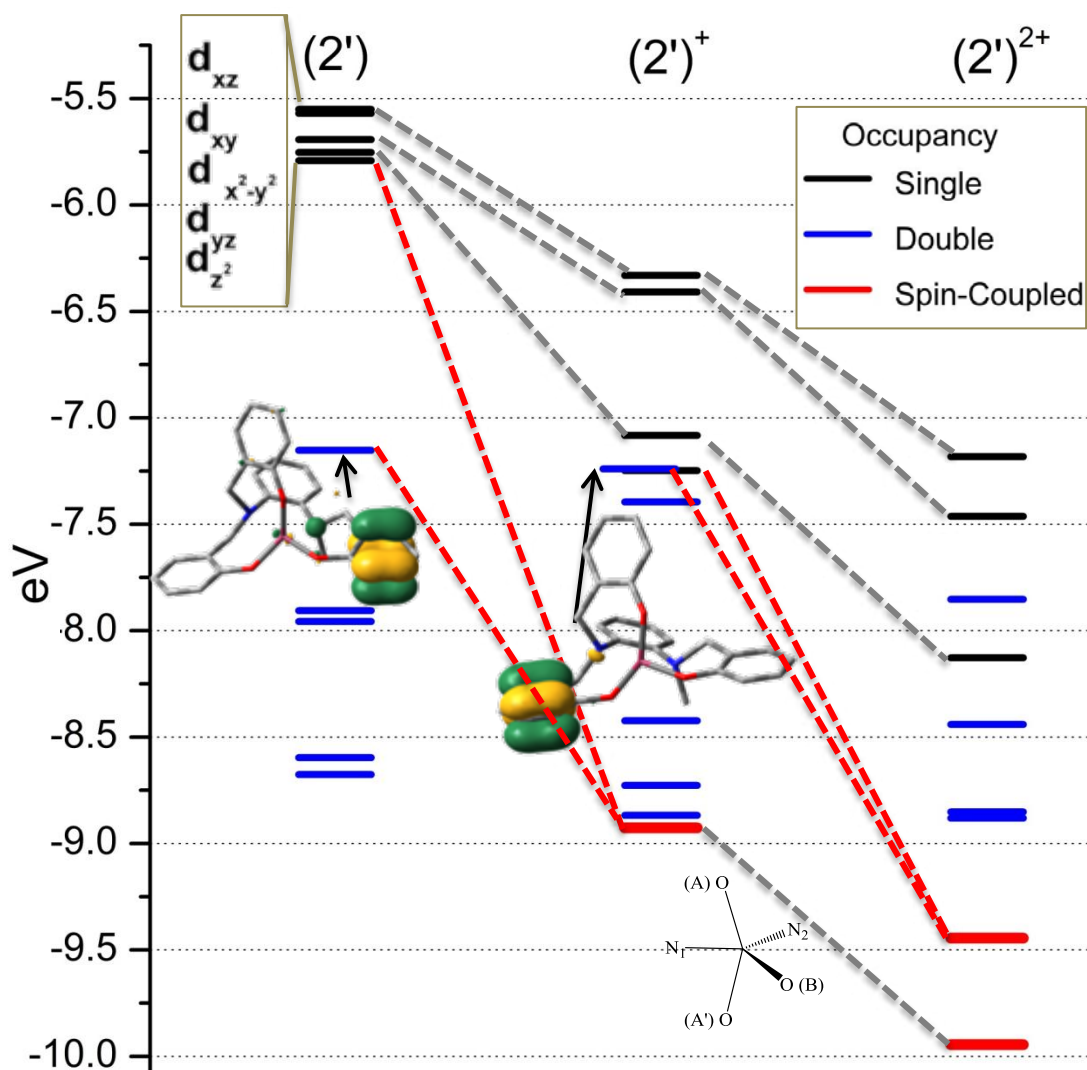
Figure 4.11. Average orbital energy ladder (left) and selected frontier orbitals (right, α-SOMOs and spin coupled pairs with hydrogen atoms omitted for clarity) for **(2')**, **(2')**[+],and **(2')**[2+] (B3LYP/6-31G(d) IEF-PCM dichloromethane).
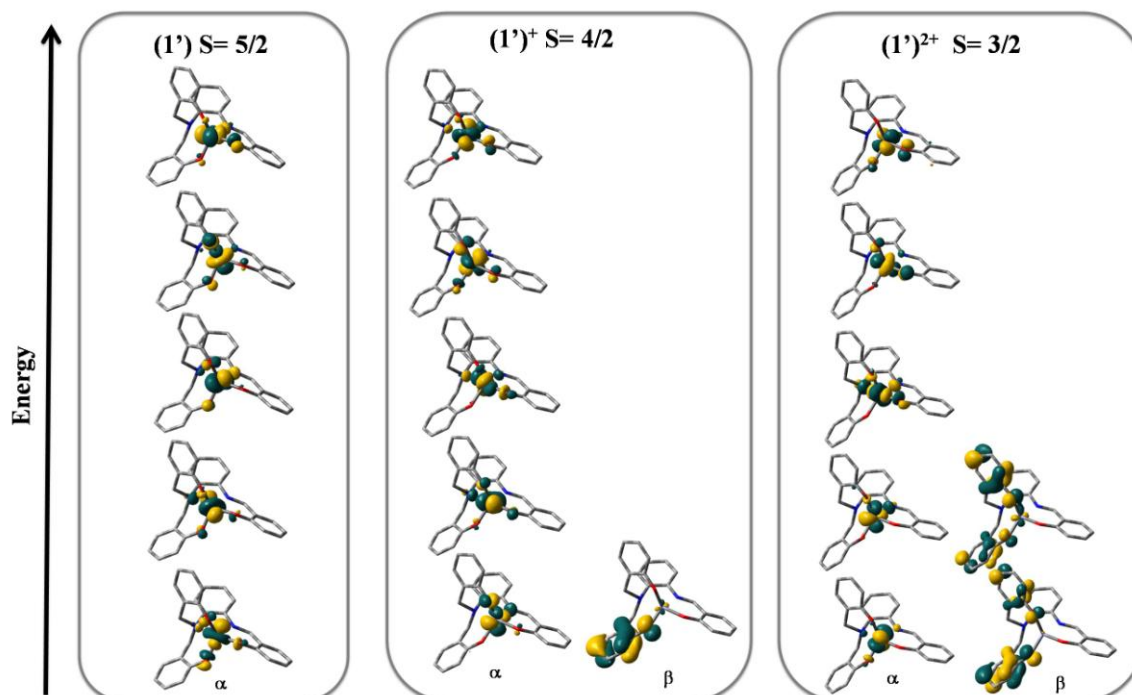
Figure 4.12. Frontier orbitals (right, α-SOMOs and spin coupled Pairs with hydrogen atoms omitted for clarity) for **(1')**, **(1')**[+], and **(1')**[2+] (B3LYP/6-31G(d) IEF-PCM dichloromethane).
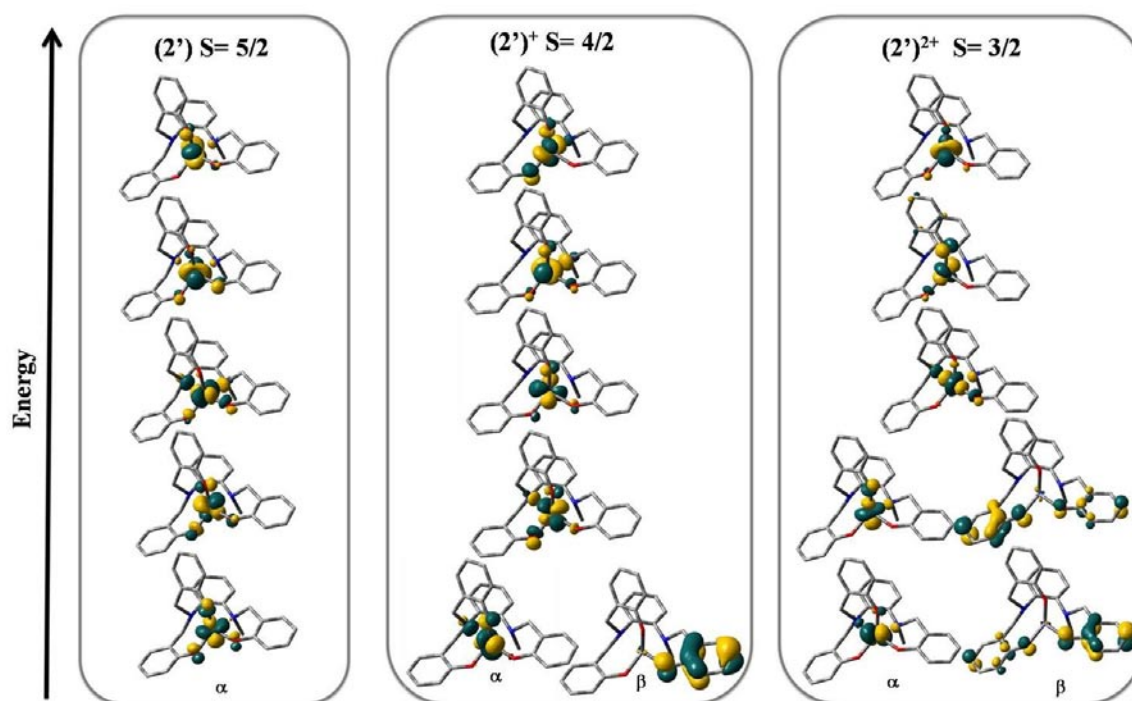
Figure 4.13. Frontier orbitals (right, α-SOMOs and spin coupled pairs with hydrogen atoms omitted for clarity) for **(1')**, **(1')**[+], and **(1')**[2+] (B3LYP/6-31G(d) IEF-PCM dichloromethane).

4.16. Overview and conclusions

In this dissertation we have investigated two newly synthesized iron complexes **(1)** and **(2)** with pentadentate [N_2O_3] ligands, aiming at a deeper understanding of how low symmetries influence orbital distribution and consequently their resulting electrochemical properties. We have also pinpointed the origin of the spectroscopic changes associated with sequential oxidations and corroborated such observations with high-level computational calculations. These results allowed us to assign the individual molecular loci within each of these compounds and their associated oxidized species.

The nature of the organic linker and the anion of the supporting electrolyte can lead to closely-spaced oxidative electrochemical potentials being used to stabilize multi-electron redox processes. It was shown that these compounds are redox-cyclable with minimal decomposition over thirty cycles. We also demonstrated that the introduction of a methyl group to one of the nitrogen atoms of the organic linker leads to an improved reversible character of the oxidative processes. This enhanced behavior allows for the removal of up to three electrons on the timescale of the cyclic voltammetric experiment and prevents further imine formation by adventitious oxygen. Finally, DFT calculations were used to elucidate the mechanism of oxidation, suggesting that slightly different topologies lead to preferred sequences and *loci* within each of the phenolate arms present. Therefore, the first phenoxyl radical to be generated in **(1)** coincides with phenolate A', whereas for **(2)** this radical coincides with phenolate B. **Figure 4.14** depicts these findings.
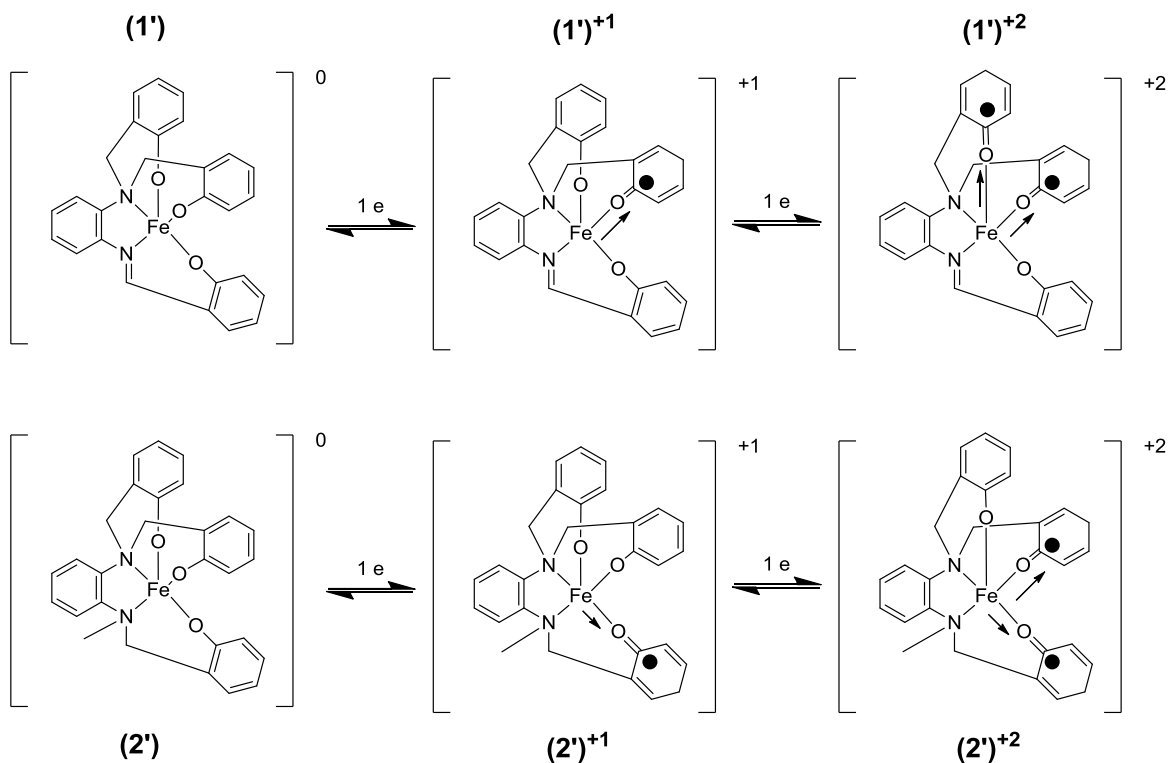
Figure 4.14. Proposed mechanism of oxidations.

These results suggest that species (**1**) and (**2**) and their mono-cationic and di-cationic counterparts, are good candidates for bistable switching systems needed for applications as diverse as films for information storage and catalysis. Ongoing studies in our labs involve the incorporation of this design into Langmuir-Blodgett and self-assembled films.

4.18. References.

1.   (a) Fabbrizzi, L.; Licchelli, M.; Pallavicini, P., Transition Metals as Switches. *Acc. Chem. Res.* **1999,** *32* (10), 846-853; (b) Marchivie, M.; Guionneau, P.; Howard, J. A. K.; Chastanet, G.; Létard, J.-F.; Goeta, A. E.; Chasseau, D., Structural Characterization of a Photoinduced Molecular Switch. *J. Am. Chem. Soc.* **2001,** *124* (2), 194-195; (c) Pease, A. R.; Jeppesen, J. O.; Stoddart, J. F.; Luo, Y.; Collier, C. P.; Heath, J. R., Switching Devices Based on Interlocked Molecules. *Acc. Chem. Res.* **2001,** *34* (6), 433-444.

2.   (a) Aukauloo, A.; Ottenwaelder, X.; Ruiz, R.; Poussereau, S.; Pei, Y.; Journaux, Y.; Fleurat, P.; Volatron, F.; Cervera, B.; Munoz, M. C., A square-planar dinickel(II) complex with a noninnocent dinucleating oxamate ligand. Evidence for a ligand radical species. *Eur. J. Inorg. Chem.* **1999,** (7), 1067-1071; (b) Hicks, R. G.; Lemaire, M. T.; Thompson, L. K.; Barclay, T. M., Strong Ferromagnetic and Antiferromagnetic Exchange Coupling between Transition Metals and Coordinated Verdazyl Radicals. *J. Am. Chem. Soc.* **2000,** *122* (33), 8077-8078; (c) Kahn, O., Chemistry and Physics of Supramolecular Magnetic Materials. *Acc. Chem. Res.* **2000,** *33* (10), 647-657; (d) Miller, J. S., Organometallic- and Organic-Based Magnets: New Chemistry and New Materials for the New Millennium. *Inorg. Chem.* **2000,** *39* (20), 4392-4408.

3.   (a) Dei, A.; Gatteschi, D.; Sangregorio, C.; Sorace, L., Quinonoid Metal Complexes: Toward Molecular Switches. *Acc. Chem. Res.* **2004,** *37* (11), 827-835; (b) Flores-Torres, S.; Hutchison, G. R.; Soltzberg, L. J.; Abruña, H. D., Ruthenium Molecular Wires with Conjugated Bridging Ligands: Onset of Band Formation in Linear Inorganic Conjugated Oligomers. *J. Am. Chem. Soc.* **2006,** *128* (5), 1513-1522; (c)

Holten, D.; Bocian, D. F.; Lindsey, J. S., Probing Electronic Communication in Covalently Linked Multiporphyrin Arrays. A Guide to the Rational Design of Molecular Photonic Devices. *Acc. Chem. Res.* **2001,** *35* (1), 57-69; (d) Joachim, C.; Gimzewski, J. K.; Aviram, A., Electronics using hybrid-molecular and mono-molecular devices. *Nature* **2000,** *408* (6812), 541-548; (e) Park, J.; Pasupathy, A. N.; Goldsmith, J. I.; Chang, C.; Yaish, Y.; Petta, J. R.; Rinkoski, M.; Sethna, J. P.; Abruna, H. D.; McEuen, P. L.; Ralph, D. C., Coulomb blockade and the Kondo effect in single-atom transistors. *Nature* **2002,** *417* (6890), 722-725; (f) Wassel, R. A.; Gorman, C. B., Establishing the Molecular Basis for Molecular Electronics. *Angewandte Chemie International Edition* **2004,** *43* (39), 5120-5123; (g) Kahn, O.; Martinez, C. J., Spin-Transition Polymers: From Molecular Materials Toward Memory Devices. *Science* **1998,** *279* (5347), 44-48.

4.   (a) Chaudhuri, P.; Wieghardt, K., *Phenoxyl Radical Complexes*. John Wiley & Sons, Inc.: 2002; p 151-216; (b) Jazdzewski, B. A.; Tolman, W. B., Understanding the copper-phenoxyl radical array in galactose oxidase: contributions from synthetic modeling studies. *Coord. Chem. Rev.* **2000,** *200-202*, 633-685; (c) Pratt, R. C.; Mirica, L. M.; Stack, T. D. P., Snapshots of a Metamorphosing Cu(II) Ground State in a Galactose Oxidase-Inspired Complex. *Inorg. Chem.* **2004,** *43* (25), 8030-8039.

5.   (a) Solomon, E. I.; Decker, A.; Lehnert, N., Non-heme iron enzymes: Contrasts to heme catalysis. *Proc. Natl. Acad. Sci. U. S. A.* **2003,** *100* (7), 3589-3594; (b) Koehntop, K. D.; Emerson, J. P.; Que, L., The 2-His-1-carboxylate facial triad: a versatile platform for dioxygen activation by mononuclear non-heme iron(II) enzymes. *J. Biol. Inorg. Chem.* **2005,** *10* (2), 87-93; (c) Ramsey, A. J.; Hillas, P. J.; Fitzpatrick, P. F.,

Characterization of the Active Site Iron in Tyrosine Hydroxylase. *J. Biol. Chem.* **1996,** *271* (40), 24395-24400.

6.   (a) Borowski, T.; Siegbahn, P. E. M., Mechanism for Catechol Ring Cleavage by Non-Heme Iron Intradiol Dioxygenases: A Hybrid DFT Study. *J. Am. Chem. Soc.* **2006,** *128* (39), 12941-12953; (b) Ferraroni, M.; Seifert, J.; Travkin, V. M.; Thiel, M.; Kaschabek, S.; Scozzafava, A.; Golovleva, L.; Schloemann, M.; Briganti, F., Crystal Structure of the Hydroxyquinol 1,2-Dioxygenase from Nocardioides simplex 3E, a Key Enzyme Involved in Polychlorinated Aromatics Biodegradation. *J. Biol. Chem.* **2005,** *280* (22), 21144-21154; (c) Pau, M. Y. M.; Davis, M. I.; Orville, A. M.; Lipscomb, J. D.; Solomon, E. I., Spectroscopic and Electronic Structure Study of the Enzyme-Substrate Complex of Intradiol Dioxygenases: Substrate Activation by a High-Spin Ferric Non-heme Iron Site. *J. Am. Chem. Soc.* **2007,** *129* (7), 1944-1958; (d) Wasinger, E. C.; Davis, M. I.; Pau, M. Y. M.; Orville, A. M.; Zaleski, J. M.; Hedman, B.; Lipscomb, J. D.; Hodgson, K. O.; Solomon, E. I., Spectroscopic Studies of the Effect of Ligand Donor Strength on the Fe-NO Bond in Intradiol Dioxygenases. *Inorg. Chem.* **2003,** *42* (2), 365-376.

7.   (a) Chirik, P. J.; Wieghardt, K., Radical Ligands Confer Nobility on Base-Metal Catalysts. *Science* **2010,** *327* (5967), 794-795; (b) Bowman, A. C.; Milsmann, C.; Bill, E.; Lobkovsky, E.; Weyhermüller, T.; Wieghardt, K.; Chirik, P. J., Reduced N-Alkyl Substituted Bis(imino)pyridine Cobalt Complexes: Molecular and Electronic Structures for Compounds Varying by Three Oxidation States. *Inorg. Chem.* **2010,** *49* (13), 6110-6123; (c) Hess, C. R.; Weyhermüller, T.; Bill, E.; Wieghardt, K., Influence of the Redox

Active Ligand on the Reactivity and Electronic Structure of a Series of Fe(TIM) Complexes. *Inorg. Chem.* **2010,** *49* (12), 5686-5700.

8.   (a) Imbert, C.; Hratchian, H. P.; Lanznaster, M.; Heeg, M. J.; Hryhorczuk, L. M.; McGarvey, B. R.; Schlegel, H. B.; Verani, C. N., Influence of Ligand Rigidity and Ring Substitution on the Structural and Electronic Behavior of Trivalent Iron and Gallium Complexes with Asymmetric Tridentate Ligands. *Inorg. Chem.* **2005,** *44* (21), 7414-7422; (b) Lanznaster, M.; Heeg, M. J.; Yee, G. T.; McGarvey, B. R.; Verani, C. N., Design of Molecular Scaffolds Based on Unusual Geometries for Magnetic Modulation of Spin-Diverse Complexes with Selective Redox Response. *Inorg. Chem.* **2007,** *46* (1), 72-78.

9.   (a) Connelly, N. G.; Geiger, W. E., Chemical Redox Agents for Organometallic Chemistry. *Chem. Rev.* **1996,** *96* (2), 877-910; (b) Gagne, R. R.; Koval, C. A.; Lisensky, G. C., Ferrocene as an internal standard for electrochemical measurements. *Inorg. Chem.* **1980,** *19* (9), 2854-2855.

10.   (a) Becke, A. D., Density-functional thermochemistry. III. The role of exact exchange. *J. Chem. Phys.* **1993,** *98* (7), 5648-5652; (b) Lee, C.; Yang, W.; Parr, R. G., Development of the Colle-Salvetti correlation-energy formula into a functional of the electron density. *Phys. Rev. B* **1988,** *37*, 785; (c) Miehlich, B.; Savin, A.; Stoll, H.; Preuss, H., Results obtained with the correlation energy density functionals of becke and Lee, Yang and Parr. *Chem. Phys. Lett.* **1989,** *157* (3), 200-206.

11.   (a) Binning Jr., R. C.; Curtiss, L. A., Compact contracted basis-sets for 3rd-row atoms - GA-KR. *J. Comp. Chem.* **1990,** *11* (10), 1206-1216; (b) Blaudeau, J.-P.; McGrath, M. P.; Curtiss, L. A.; Radom, L., Extension of Gaussian-2 (G2) theory to

molecules containing third-row atoms K and Ca. *J. Chem. Phys.* **1997,** *107* (13), 5016-5021; (c) Ditchfield, R.; Hehre, W. J.; Pople, J. A., Self-Consistent Molecular Orbital Methods. Extended Gaussian-type basis for molecular-orbital studies of organic molecules. *J. Chem. Phys.* **1971,** *54* (2), 724; (d) Francl, M. M.; Pietro, W. J.; Hehre, W. J.; Binkley, J. S.; DeFrees, D. J.; Pople, J. A.; Gordon, M. S., Self-Consistent Molecular Orbital Methods. 23. A polarization-type basis set for 2nd-row elements. *J. Chem. Phys.* **1982,** *77* (7), 3654-3665; (e) Gordon, M. S., The isomers of silacyclopropane. *Chem. Phys. Lett.* **1980,** *76* (1), 163-168; (f) Hariharan, P. C.; Pople, J. A., Influence of polarization functions on molecular-orbital hydrogenation energies. *Theor. Chem. Acc.* **1973,** *28* (3), 213-222; (g) Hariharan, P. C.; Pople, J. A., Accuracy of AH equilibrium geometries by single determinant molecular-orbital theory. *Mol. Phys.* **1974,** *27* (1), 209-214; (h) Hehre, W. J.; Ditchfield, R.; Pople, J. A., Self-Consistent Molecular Orbital Methods. 12. Further extensions of Gaussian-type basis sets for use in molecular-orbital studies of organic-molecules. *J. Chem. Phys.* **1972,** *56* (5), 2257; (i) Rassolov, V. A.; Pople, J. A.; Ratner, M. A.; Windus, T. L., 6-31G* basis set for atoms K through Zn. *J. Chem. Phys.* **1998,** *109* (4), 1223-1229; (j) Rassolov, V. A.; Ratner, M. A.; Pople, J. A.; Redfern, P. C.; Curtiss, L. A., 6-31G* Basis Set for Third-Row Atoms. *J. Comp. Chem.* **2001,** *22* (9), 976-984.

12.   Frisch, M. J.; Trucks, G. W.; Schlegel, H. B.; Scuseria, G. E.; Robb, M. A.; Cheeseman, J. R.; Scalmani, G.; Barone, V.; Mennucci, B.; Petersson, G. A.; Nakatsuji, H.; Caricato, M.; Li, X.; Hratchian, H. P.; Izmaylov, A. F.; Bloino, J.; Zheng, G.; Sonnenberg, J. L.; Hada, M.; Ehara, M.; Toyota, K.; Fukuda, R.; Hasegawa, J.; Ishida, M.; Nakajima, T.; Honda, Y.; Kitao, O.; Nakai, H.; Vreven, T.; Montgomery, J. A., Jr.;

Peralta, J. E.; Ogliaro, F.; Bearpark, M.; Heyd, J. J.; Brothers, E.; Kudin, K. N.; Staroverov, V.; Kobayashi, R.; Normand, J.; Raghavachari, K.; Rendell, A.; Burant, J. C.; Iyengar, S. S.; Tomasi, J.; Cossi, M.; Rega, N.; Millam, J. M.; Klene, M.; Knox, J. E.; Cross, J. B.; Bakken, V.; Adamo, C.; Jaramillo, J.; Gomperts, R.; Stratmann, R. E.; Yazyev, O.; Austin, A. J.; Cammi, R.; Pomelli, C.; Ochterski, J. W.; Martin, R. L.; Morokuma, K.; Zakrzewski, V. G.; Voth, G. A.; Salvador, P.; Dannenberg, J. J.; Dapprich, S.; Parandekar, P. V.; Mayhall, N. J.; Daniels, A. D.; Farkas, O.; Foresman, J. B.; Ortiz, J. V.; Cioslowski, J.; Fox, D. J. *Gaussian DV*, Revision H.04; Gaussian, Inc.: Wallingford, CT, 2009.

13.   (a) Miertus, S.; Scrocco, E.; Tomasi, J., Electrostatic interaction of a solute with a continuum - a direct utilization of abinitio molecular potentials for the prevision of solvent effects. *Chem. Phys.* **1981,** *55* (1), 117-129; (b) Miertus, S.; Tomasi, J., Approximate evaluations of the electrostatic free-energy and internal energy changes in solution processes. *Chem. Phys.* **1982,** *65* (2), 239-245; (c) Tomasi, J.; Mennucci, B.; Cammi, R., Quantum Mechanical Continuum Solvation Models. *Chem. Rev.* **2005,** *105* (8), 2999-3094.

14.   Neese, F., Definition of corresponding orbitals and the diradical character in broken symmetry DFT calculations on spin coupled systems. *J. Phys. Chem. Solids* **2004,** *65* (4), 781-785.

15.   Lanznaster, M.; Hratchian, H. P.; Heeg, M. J.; Hryhorczuk, L. M.; McGarvey, B. R.; Schlegel, H. B.; Verani, C. N., Structural and Electronic Behavior of Unprecedented Five-Coordinate Iron(III) and Gallium(III) Complexes with a New Phenol-Rich Electroactive Ligand. *Inorg. Chem.* **2006,** *45* (3), 955-957.

16.   (a) Tong, L. H.; Wong, Y.-L.; Pascu, S. I.; Dilworth, J. R., Synthesis, structures and catalytic properties of iron(III) complexes with asymmetric N-capped tripodal NO3 ligands and a pentadentate N2O3 ligand. *Dalton Trans.* **2008,** (35), 4784-4791; (b) Snodin, M. D.; Ould-Moussa, L.; Wallmann, U.; Lecomte, S.; Bachler, V.; Bill, E.; Hummel, H.; Weyhermüller, T.; Hildebrandt, P.; Wieghardt, K., The Molecular and Electronic Structure of Octahedral Tris(phenolato)iron Complexes and Their Phenoxyl Radical Analogues: A Mössbauer and Resonance Raman Spectroscopic Study. *Chemistry - A European Journal* **1999,** *5* (9), 2554-2565.

17.   Addison, A. W.; Rao, T. N.; Reedijk, J.; Van Rijn, J.; Verschoor, G. C., Synthesis, structure, and spectroscopic properties of copper(II) compounds containing nitrogen-sulfur donor ligands: the crystal and molecular structure of aqua[1,7-bis(N-methylbenzimidazol-2'-yl)-2,6-dithiaheptane]copper(II) perchlorate. *Dalton Trans.* **1984,** (7), 1349-1356.

18.   (a) Barriere, F.; Geiger, W. E., Use of Weakly Coordinating Anions to Develop an Integrated Approach to the Tuning of Delta E1/2 Values by Medium Effects. *J. Am. Chem. Soc.* **2006,** *128* (12), 3980-3989; (b) Nafady, A.; Chin, T. T.; Geiger, W. E., Manipulating the electrolyte medium to favor either one-electron or two-electron oxidation pathways for (fulvalenediyl)dirhodium complexes. *Organometallics* **2006,** *25* (7), 1654-1663; (c) Geiger, W. E.; Barrière, F. d. r., Organometallic Electrochemistry Based on Electrolytes Containing Weakly-Coordinating Fluoroarylborate Anions. *Acc. Chem. Res.* **2010,** *43* (7), 1030-1039.

19.   Kurahashi, T.; Kobayashi, Y.; Nagatomo, S.; Tosha, T.; Kitagawa, T.; Fujii, H., Oxidizing Intermediates from the Sterically Hindered Iron Salen Complexes Related to

the Oxygen Activation by Nonheme Iron Enzymes. *Inorg. Chem.* **2005,** *44* (22), 8156-8166.

20.   Rachlewicz, K.; Latos-Grażynski, L., Disproportionation of Iron(III) Porphyrin π-Cation Radicals in the Presence of Sterically Hindered Pyridines. Spectroscopic Detection of Asymmetric Highly Oxidized Intermediates. *Inorg. Chem.* **1996,** *35* (5), 1136-1147.

21.   (a) Storr, T.; Verma, P.; Pratt, R. C.; Wasinger, E. C.; Shimazaki, Y.; Stack, T. D. P., Defining the Electronic and Geometric Structure of One-Electron Oxidized Copper-Bis-phenoxide Complexes. *J. Am. Chem. Soc.* **2008,** *130* (46), 15448-15459; (b) Storr, T.; Wasinger, E. C.; Pratt, R. C.; Stack, T. D. P., The geometric and electronic structure of a one-electron-oxidized nickel(II) bis(salicylidene)diamine complex. *Angew. Chem.* **2007,** *46* (27), 5198-5201.

22.   Muathen, H. A., Tetrabutylammoniumcerium(IV) nitrate: a mild oxidizing agent. *Indian J. Chem., Sect. B: Org. Chem. Incl. Med. Chem.* **1991,** *30B* (5), 522-4.

23.   Strautmann, J. B. H.; DeBeer George, S.; Bothe, E.; Bill, E.; Weyhermueller, T.; Stammler, A.; Boegge, H.; Glaser, T., Molecular and electronic structures of mononuclear iron complexes using strongly electron-donating ligands and their oxidized forms. *Inorg. Chem.* **2008,** *47* (15), 6804-6824.

24.   (a) Adam, B.; Bill, E.; Bothe, E.; Goerdt, B.; Haselhorst, G.; Hildenbrand, K.; Sokolowski, A.; Steenken, S.; Weyhermueller, T.; Wieghardt, K., Phenoxyl radical complexes of gallium, scandium, iron and manganese. *Chem.--Eur. J.* **1997,** *3* (2), 308-319; (b) Kimura, S.; Bill, E.; Bothe, E.; Weyhermueller, T.; Wieghardt, K., Phenylthiyl

Radical Complexes of Gallium(III), Iron(III), and Cobalt(III) and Comparison with Their Phenoxyl Analogues. *J. Am. Chem. Soc.* **2001,** *123* (25), 6025-6039.

25.   Verani, C. N.; Bothe, E.; Burdinski, D.; Weyhermuller, T.; Florke, U.; Chaudhuri, P., Synthesis, structure, electrochemistry, and magnetism of [MnIIIMnIII], [MnIIIFeIII] and [FeIIIFeIII] cores: generation of phenoxyl radical containing [FeIIIFeIII] species. *Eur. J. Inorg. Chem.* **2001,** (8), 2161-2169.

26.   Chlopek, K.; Muresan, N.; Neese, F.; Wieghardt, K., Electronic structures of five-coordinate complexes of iron containing zero, one, or two pi-radical ligands: a broken-symmetry density functional theoretical study. *Chem.--Eur. J.* **2007,** *13* (30), 8390-8403.

27.   (a) Khusniyarov, M. M.; Weyhermueller, T.; Bill, E.; Wieghardt, K., Tuning the Oxidation Level, the Spin State, and the Degree of Electron Delocalization in Homo- and Heteroleptic Bis(alpha -diimine)iron Complexes. *J. Am. Chem. Soc.* **2009,** *131* (3), 1208-1221; (b) Roy, N.; Sproules, S.; Bill, E.; Weyhermuller, T.; Wieghardt, K., Molecular and Electronic Structure of the Square Planar Bis(o-amidobenzenethiolato)iron(III) Anion and Its Bis(o-quinoxalinedithiolato)iron(III) Analogue. *Inorg. Chem.* **2008,** *47* (23), 10911-10920.

28.   Lauffer, R. B.; Heistand, R. H.; Que, L., Dioxygenase models. Crystal structures of the 2,4-pentanedionato, phenanthrenesemiquinone, and catecholato complexes of N,N'-ethylenebis(salicylideneaminato)iron(III). *Inorg. Chem.* **1983,** *22* (1), 50-55.

29.   Pratt, R. C.; Stack, T. D. P., Intramolecular Charge Transfer and Biomimetic Reaction Kinetics in Galactose Oxidase Model Complexes. *J. Am. Chem. Soc.* **2003,** *125* (29), 8716-8717.

30.   Koopmans, T., Über die Zuordnung von Wellenfunktionen und Eigenwerten zu den Einzelnen Elektronen Eines Atoms. *Physica* **1934,** *1* (1-6), 104-113.

31.   Davis, M. I.; Orville, A. M.; Neese, F.; Zaleski, J. M.; Lipscomb, J. D.; Solomon, E. I., Spectroscopic and Electronic Structure Studies of Protocatechuate 3,4-Dioxygenase: Nature of Tyrosinate, Fe(III) Bonds and Their Contribution to Reactivity. *J. Am. Chem. Soc.* **2002,** *124* (4), 602-614.

Chapter 5

Redox Chemistry Of Selected 6 Coordinates Cobalt And Iron Complexes Using Pentadentate-N₂O₃ Electroactive.

(1) [CoL¹]

(1'), S = 0   (1')⁺¹, S = 1/2   (1')⁺², S = 2/2   (1')⁺³, S = 3/2
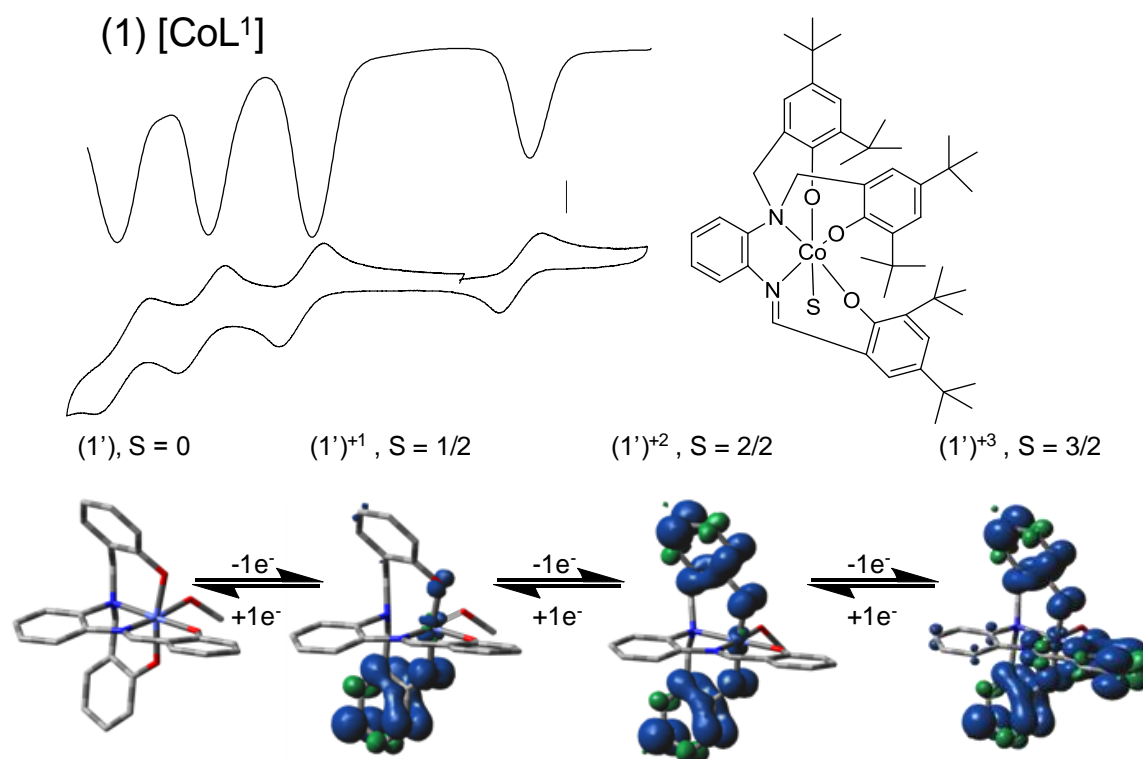
5.1. Introduction

Our group recently published[1] a five-coordinate iron(III) complex that exhibited properties similar to those expected from molecular switches. We propose the use of an electrochemical potential trigger as a switching mechanism, in which radical/metal spin pairing results in bistable systems that can be relevant for computer random access memory (RAM) elements. In this chapter, we discuss similar complex[1b] systems which contain six-coordinate iron(III) and cobalt(III) metal centers, in which we have an N_2O_3-type of ligand and where the sixth coordination position is occupied by a labile solvent molecule. The following ligands were chosen to investigate variations in the resulting complexes; such as in their (i) structural geometry, (ii) radical formation stability and (iii) redox reversibility (see **Figure 5.1**).
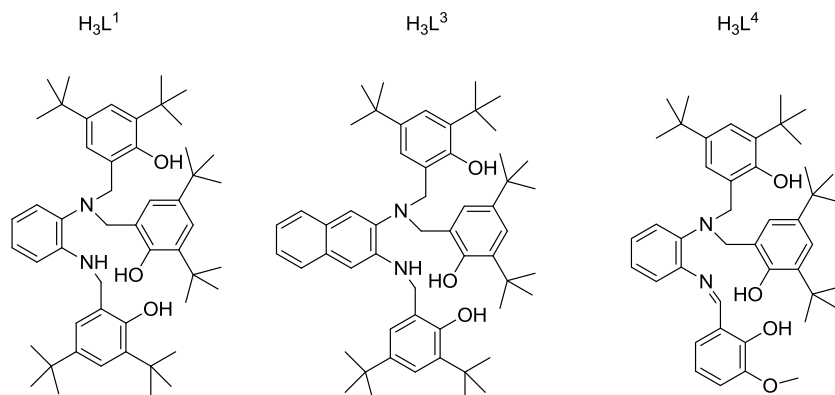
Figure 5.1. Ligand identity.

We demonstrated redox chemical reversibility for pentadentate complexes including an iron(III) restricted to a five coordinates[1b] environment in Chapter 4 and here we survey the analogous behavior for magnetically inert low-spin cobalt(III) systems. The purposely built-in asymmetry within the ligands system is shown to have some effects on the central metal coordination mode, depending on both the ligand variations

and metal centers. In this chapter we are comparing three cobalt(III) six-coordinate complex **(1)**, **(2)** and **(3)** with a related six-coordinate iron(III) complex **(4)**, shown in **Figure 5.2**. The previous chapter demonstrated the challenges of using a high-spin iron(III) complex system , when combined with the fact that iron(III) is a relatively labile metal ion, studies with a more inert metal is therefore critical. Investigating an inert low-spin cobalt(III) ions, which do not contain unpaired electrons capable of antiferromagnetic coupling to phenoxyl radicals, can provide insight in the ligand centered processes.

S = CH_3OH, H_2O
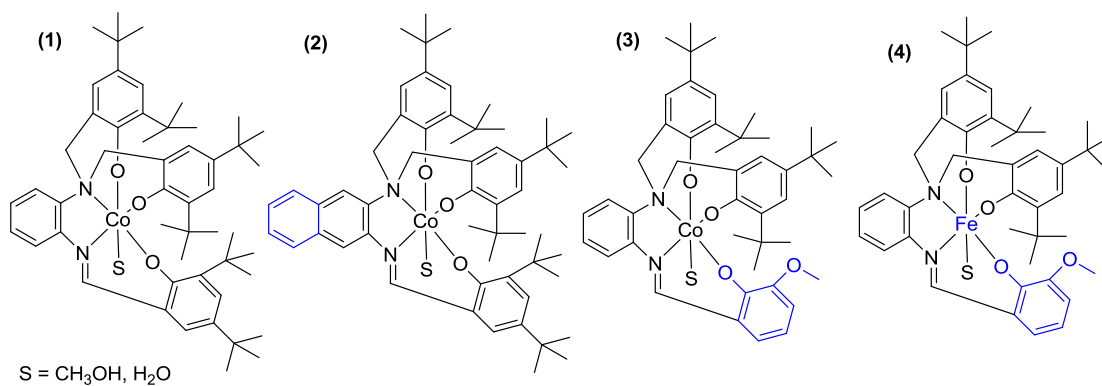
Figure 5.2. Complex **(1)** $[CoL^1]$, **(2)** $[CoL^2]$, **(3)** $[CoL^4]$ and **(4)** $[FeL^4]$.

Experimental section

5.2. Materials and methods

Reagents and solvents were used as received from commercial sources, unless otherwise noted. Dichloromethane and methanol were distilled over CaH_2. Infrared spectra were measured from 4000 to 400 cm^{-1} as KBr pellets on a Tensor 27 FTIR-Spectrophotometer. ^{1}H-NMR spectra were measured using Varian 300 and 400 MHz instruments. ESI (positive mode) spectra were measured in either a triple-quadrupole

Micromass QuattroLC or in a single-quadrupole Waters ZQ2000 mass spectrometer with an electrospray/APCI or ESCi source. Experimental assignments were simulated on the basis of peak position and isotopic distributions. Elemental analyses were performed by Midwest Microlab, Indianapolis, IN. Cyclic voltammetric experiments were performed using a BAS 50W voltammetric analyzer. A standard three electrode cell was employed with the reference Ag/AgCl electrode freshly prepared and calibrated versus ferrocene.[2] A platinum wire was used as an auxiliary electrode and a vitreous carbon disk was used as a working electrode for the cyclic voltammetry experiments. For the bulk electrolysis experiment a vitreous carbon basket was used. Concentrations of the analytes were 1.0 x 10^{-3} M, and all supporting electrolytes were 0.1 M, except where otherwise stated. The Fc/Fc^+ couple in CH_2Cl_2 was found to be 0.45 V (ΔE 0.14), which is in good agreement with literature.[3]

5.3. X-ray structural determinations for complexes (1), (2), (3), and (4)

Diffraction data were measured on a Bruker *X8 APEX-II* kappa geometry diffractometer with Mo radiation and a graphite monochromator. Frames were collected as a series of sweeps with the detector at 40 mm and 0.3 degrees between each frame. Frames were recorded for 10 s. *APEX-II* and *SHELX-97* software were used in the collection and refinement.

Crystals of **(1)** [$C_{52}H_{73}N_2O_4Co_1$] appeared as dark rhomboids, and a sample approximately 0.25 x 0.20 x 0.20 mm^3 was used for data collection. A total of 3162 frames were collected at 100 K, yielding 44204 reflections, of which 11752 were independent. Hydrogen positions were placed in observed positions. The asymmetric unit

consists of one neutral complex including one equivalent of coordinated methanol. Crystals of **(2)** $[C_{57}H_{79}N_2O_5Co_1]$ appeared as dark rods and the fragment used was approximately 0.14 x 0.14 x 0.12 mm^3. A total of 117784 reflections were recorded, of which 13041 were unique. Hydrogen atoms were placed in observed positions. The asymmetric unit contains one cobalt complex with one coordinated methanol and one methanol solvate.

Crystals of **(3)** $[C_{57}H_{79}N_2O_5Co_1]$ appeared as dark rods and the fragment used was approximately 0.14 x 0.14 x 0.12 mm^3. A total of 117784 reflections were recorded, of which 13041 were unique. Hydrogen atoms were placed in observed positions. The asymmetric unit contains one cobalt complex with coordinated methanol and one methanol solvate. Crystals of **(4)** $[C_{55}H_{71}N_2O_3Fe_1]$ appeared as dark rods and the crystal selected was 0.32 x 0.16 x 0.06 mm^3. A total of 92860 reflections were recorded, of which 24321 were unique. Hydrogen atoms were placed in observed or calculated positions. One of the *t*-butyl groups was disordered over 3 positions and was therefore kept isotropic.

5.4. Electronic structure methods

Electronic structure calculations were carried out with the Gaussian 09 suite of programs[4] using Density Functional Theory (DFT). The B3PW91/6-31G(d) level of theory[5] was employed throughout. Geometries were fully optimized without symmetry constraints, and stationary points were verified via frequency analysis. Solvent effects in dichloromethane were estimated using the IEF-PCM polarizable continuum model.[6]

Molecular orbitals were plotted using GaussView.[1b] Cartesian coordinates of all optimized structures are provided as Supporting Information (SI) in the appendix.

Table 5.1. Crystal Data[a][7]

	(1)	(2)	(3)	(4)
Formula	$[C_{52}H_{73}N_2O_4Co_1]$	$[C_{57}H_{79}N_2O_5Co_1]$	$[C_{57}H_{79}N_2O_5Co_1]$	$[C_{55}H_{71}N_2O_3Fe_1]$
M	849.05	931.15	809.34	793.82
Space group	P(-1)	$P2_1/c$	P(-1)	P(-1)
a / Å	12.5503(3)	13.4355(8)	15.4747(3)	10.8371(3
b/ Å	14.0106(3)	20.8538(13)	15.7986(3)	14.0880(3)
c/ Å	14.4339(4)	19.0011(12)	18.8968(4)	15.6499(4)
α/ °	88.9690(10)		106.3500(10)	113.5840(10)
β/ °	86.1680(10)	99.932(2)	90.7000(10)	90.7660(10)
γ/ °	71.0990(10)		106.0900(10	101.5830(10)
V/ Å^3	2395.78(10)	5244.0(6)	4238.93(15)	2133.44(9
Z	2	4	4	2
T/ K	100(2)	100(2)	100(2)	100(2)
λ/ Å	0.71073	0.71073	0.71073	0.71073
D_{calc}/ g cm^{-3}	1.177	1.179	1.268	1.236
μ/ mm^{-1}	0.403	0.375	0.514	0.402
$R(F)$ (%)	3.98	4.73	5.10	6.14
$Rw(F)$ (%)	9.75	9.37	14.20	15.77

[a] $R(F) = \sum \|F_o| - |F_c\| / \sum |F_o|$ for $I > 2\sigma(I)$; $Rw(F) = [\sum w(F_o^2 - F_c^2)^2 / \sum w(F_o^2)^2]^{1/2}$ for $I > 2\sigma(I)$.

5.5. Syntheses

Preparation of the ligand H$_3$L^1

The ligand H$_3$L^1 was synthesized as previously reported.[1b]

Preparation of the ligand H$_3$L^3

N,N,N'-tris-(3,5-di-tert-butyl-2-hydroxybenzyl)-naphtalene-1,2-diamine (H$_3$L^3) 2,3-diaminonaphthalene (0.25 g, 1.6 mmol), 2,4-di-*tert*-butyl-6-(chloromethyl)phenol (1.2 g, 4.7 mmol) and triethylamine (0.50 g, 4.7 mmol) in dichloromethane (80 mL) were refluxed at 40 °C for 48 hours. After confirmation of reaction via TLC, the solution was extracted 3 times with 50 mL of 5% Na$_2$CO$_3$ solution. The solution was dried over MgSO$_4$, filtered, and solvent was removed by rotatory evaporation to obtain the crude ligand. The ligand was recrystallized in acetonitrile to obtain a light brown crystalline powder. Yield = 0.66 g (51.4%). ESI (in CH$_2$Cl$_2$) (*m/z$^+$*) = 813.8 for [C$_{55}$H$_{76}$N$_2$O$_3$ + H]$^+$. IR data (KBr, cm^{-1}): 3638(b), (O-H); 3477(s), (N-H); 2960(s), (C-H, alkane); 1595(s), (C=C aryl); 1286(s), (C-N); 1200(s), (C-O); 879(b), (C-H, phen). Mp = 178-181 °C. ^{1}H-NMR [400 MHz, CDCl$_3$] data δ (ppm): 1.24 – 1.35 [m, 54H (multiple *t*-butyl)]; 3.94 – 4.47 [m, 6H (CH$_2$)]; 7.03 – 7.65 [m, 12H (aryl)].

Preparation of the ligand H$_3$L^4

(**N,N-di-(3,5-di-tert-butyl-2-hydroxybenzyl)-N'-(3-methoxy-2-hydroxybenzyl)-benzene-1-amine-2-imine**) (E)-2-((2-aminophenylimino)methyl)-6-methoxyphenol (2.7 g, 8 mmol) was added to 2,4-di-*tert*-butyl-6-(chloromethyl)phenol (2.2 g, 9 mmol) and triethylamine (2.4 g, 24 mmol) were refluxed for 48 hours in dichloromethane. The reaction solution was extracted three times with water using a separatory funnel, dried

over Na_2SO_4 and the solvent removed by rotatory evaporation. The purple residue was recrystallized with acetonitrile and kept at 0 ^{o}C for 24 hours, forming an orange crystalline precipitate. MS data (ESI+ in MeOH): m/z = 677.5 [$C_{44}H_{58}N_2O_4$ + H+]. IR data (KBr, cm^{-1}): 3600 (b) (O-H), 2958 (s) (C-H, alkane), 1615 (s) (C=N imine). NMR: ^{1}H-NMR [400 MHz, CDCl$_3$] data δ (ppm): 1.21 – 1.42 [m, 36H (multiple t-butyl)]; 4.25 [s, 4H (CH$_2$)]; 4.68 [s, 3H (O-CH$_3$)]; 6.89– 7.29 [m, 11H (aryl)]. 8.87 [s, 1H (H-C=N)]. Mp: 87-90 ^{o}C.

Preparation [Co^{III}L^1(MeOH)] (1).

H$_3$L^1 (1.0 g, 1.3 mmol) was dissolved in anhydrous methanol and treated with NaOCH$_3$ (0.2 g, 3.93 mmol) under argon. To the resulting solution was added Co(ClO$_4$)$_2$ (0.47 g, 1.31 mmol) and the mixture was heated at 50 ^{o}C and stirred for 30 min. The solvent was removed by rotatory evaporation and the product was crystallized in a MeOH/CH$_2$Cl$_2$ 1:2 solvent, forming X-ray suitable single crystals. Yield: m = 0.66 g (60 %). Other suitable X-ray crystals were obtained by crashing the complex with water instead of evaporating it. The powder was then recrystallized in a mixture of MeOH/ether. Yield = 75%. MS data (ESI in MeOH): m/z = 817.6 ([$C_{51}H_{69}N_2O_3Co$ + H$^+$]. IR data (KBr, cm^{-1}): 2949-2865 (C-H tert-butyl); 1599-1475 (C=C ring stretch); 1270 (C-O stretch); 880-749 (C-H bend out of plane). Elemental analysis data: found = 73.61% C, 8.71% H, 3.28 %N; calculated = 73.56% C, 8.67% H, 3.30% N.

Preparation of [Co^{III}(L^3)(MeOH)] (2).

A Schlenk flask was flushed with nitrogen gas for five minutes, then H$_3$L^3 (0.20 g, 0.25 mmol) and sodium methoxide (0.040 g, 0.74 mmol) were dissolved in dry CH$_2$Cl$_2$

(80 mL). Dry MeOH (30 mL) was added via a cannulation. $[Co^{II}(ClO_4)_2]6(H_2O)$ (0.073 g, 0.20 mmol) was added to a small round-bottom flask, and purged with nitrogen. Approximately 10 mL amount of dry MeOH was added to dissolve the metal salt, and the solution was purged again. The methanolic cobalt perchlorate solution was transferred slowly with a cannula to the ligand solution. The ligand solution turned from a milky color to a deep brown color as the cobalt perchlorate solution was added. The mixture was stirred under nitrogen for two hours, then under oxygen for 24 h. The reddish solution was concentrated into a brown solid by rotatory evaporation. The crude complex was washed with water, and recrystallized via slow evaporation in a 1:1 mixture of methanol:ether at room temperature to give small crystals. Yield = 0.21 g (99%). MS data: (ESI+ in MeOH): m/z = 867.7 for $[Co^{III}L^1 H]^+$. Elemental analysis data: found = 73.05% C, 8.66% H, 3.12% N; calculated = 73.42% C, 8.36% H, 3.06% N. IR data (KBr, cm^{-1}): 2955 (s) (C-H, alkane); 1604 (s) (C=N); 1586 (s) (C=C, aryl); 1262 (s) (C-N); 1202 (s) (C-O); 865 (b) (C-H, phen).

Preparation of $[Co^{III}L^4(MeOH)]$ (3).

H_3L^4 (1.30 g, 1.9 mmol) was dissolved in methanol (300 mL) in a 500 mL round bottom flask and $Co(ClO_4)_2 \cdot 6H_2O$ (0.80 g, 1.7 mmol) was in the presence of triethylamine. A brown solution immediately formed and was refluxed for 60 minutes. The solution was then cooled in an ice bath and methanol was removed by rotary evaporation. After drying, the product was recrystallized in methanol: dichloromethane (1:1) and yielded X-ray suitable crystals. Yield: 70% MS data (ESI in MeOH): m/z = 735.5 ($C_{44}H_{55}CoN_2O_4 + H^+$). IR data (KBr, cm^{-1}): 2957-2866 (C-H tert-butyl); 1611-1470

(C=C ring stretch); 1246 (C-O stretch); 890-739 (C-H bend out of plane) Mp: 282-286
°C. % Elemental analysis data: Found = 67.37% C, 7.42% H, 3.44% N; Calculated =
70.48% C, 7.75% H, 3.65% N.

Preparation of [Fe^{III}L^4(MeOH)] (4).

H$_3$L^4 (1.7 g, 2.5 mmol) was dissolved in methanol (300 mL) in a 500 mL round
bottom flask. Sodium methoxide (0.32 g, 7.5 mmol) was added and the solution was
purged with argon gas. In a separate flask Fe(ClO$_4$)$_3$·6H$_2$O (1.2 grams, 2.5 mmol) was
dissolved in dry methanol and purged with argon gas. The iron containing solution was
then transferred via a cannula into the first flask and the mixture was stirred for 1 hour.
The solvent was removed using rotary evaporation and the solid product was washed
three times with water using a separatory funnel. After drying, the product was
recrystallized in methanol:dichloromethane (1:1) and yielded X-ray suitable crystals.
MS data (ESI in MeOH): m/z = 732.4 C$_{44}$H$_{55}$FeN$_2$O$_4$. IR data (KBr, cm^{-1}): 2946 (m)
(CH$_3$, alkane), 1606 (s) (N=C, imine), 1388 (b) (C(CH$_3$)$_3$, tert-butyl), 1191 (b) (C(CH$_3$)$_3$,
tert-butyl). Mp: 168-173°C. %Yield: 75%. Elemental analysis data: Found = 69.66% C,
7.73% H, 3.70% N; Calculated = 70.67% C, 7.91% H, 3.66% N.

5.6. Results and discussion.

Synthetic approach.

The ligands H$_3$L^1 and H$_3$L^3 were synthesized by treatment of their respective
diamino precursors with 2,4-di-tert-butyl-6-(chloro-methyl)phenol under basic conditions
as previously reported.[1] The ligands were obtained, and characterized by ^{1}H NMR,
electrospray ionization (ESI) mass spectrometry (MS), and infrared (IR), with an overall

yield of 40-50%. It is worth mentioning that the ligand moiety gets oxidized upon complexation with the metal center, thus resulting in a C=N bond on the mono-substituted amine for **(1)** and **(2)**. Compounds **(3)** and **(4)** incorporated the Schiff base C=N bond in the ligand by design. The ligand H_3L^4 was synthesized in two steps to allow for the introduction of different substituted phenolate groups, according to **Figure 5.3.**
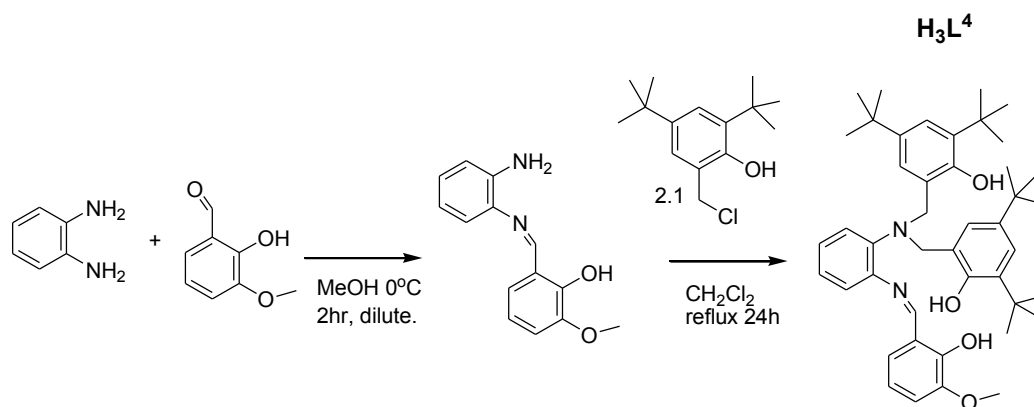
Figure 5.3. H^3L^4 synthesis.

All complexes were obtained as a dark brown powder upon treatment of the ligand H_3L^2 with hexahydrated cobalt(II) perchlorate dissolved in dry dichloromethane and dry methanol respectively. The complexes were characterized by elemental analysis, IR, CV, UV-vis, and ESI-MS. The iron (III) complex **(4)** was obtained by a similar method. There were no perchlorate anions present in the Infrared spectra, and a clear C=N ($\approx 1600 cm^{-1}$) bond for all complexes. The synthesis of compound **(1)** is shown in **Figure 5.4.**
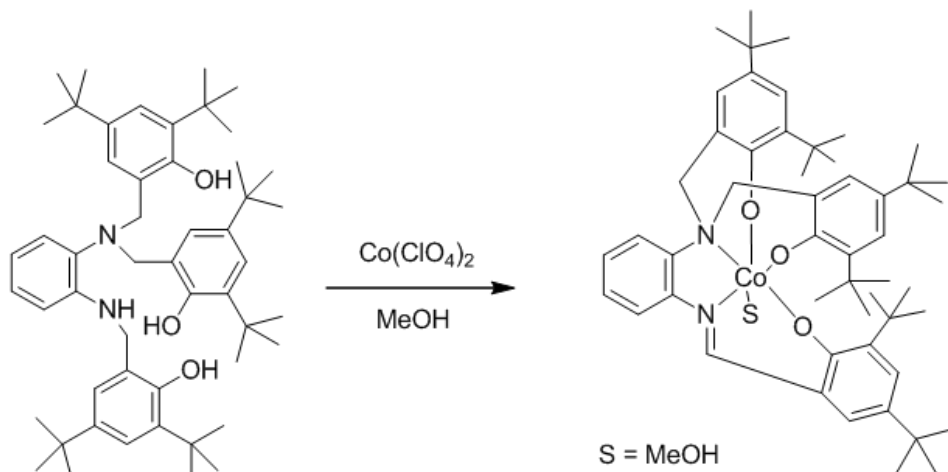
Figure 5.4. Synthesis of **[Co^{III}L^1(MeOH)] (1)**.

5.7. Molecular Structure.

All four complexes **(1)**, **(2)**, **(3)** and **(4)** were crystallized as six-coordinate metal complexes, each with a -N$_2$O$_3$ tri-anionic-pentadentate ligand and a solvent molecule at the sixth position. ORTEP diagrams showing a perspective view of the complex along with the selected atom numbering are shown in **Figures 5.5, 5.6, 5.7** and **5.8** for **(1)**, **(2)**, **(3)**, and **(4)** respectively. Selected bond lengths and bond angles are listed in **Table 5.2.** All four compounds consist of discrete mononuclear neutral units.
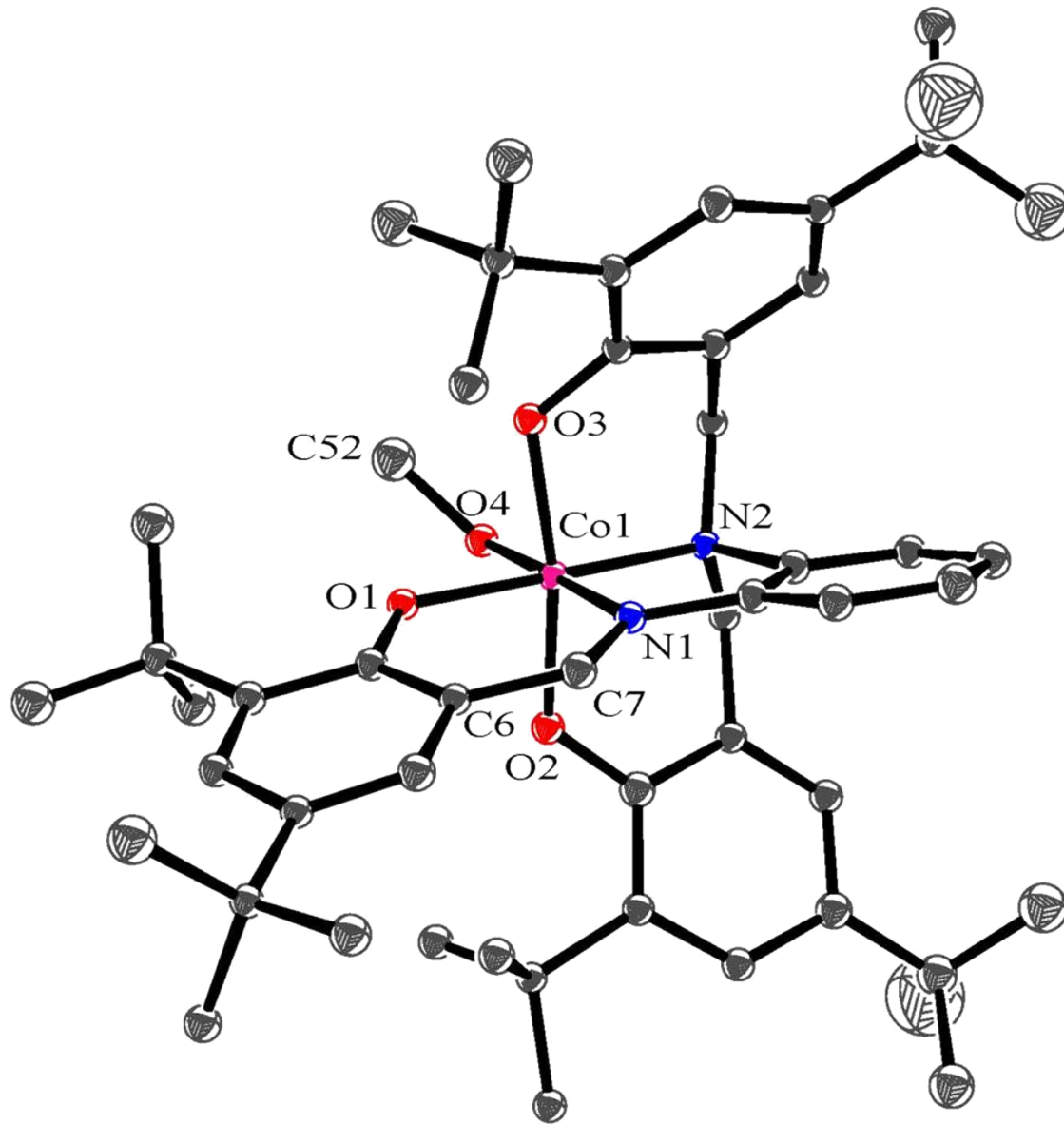
Figure 5.5. ORTEP diagram of **(1) [Co^{III}L^1(MeOH)]**.
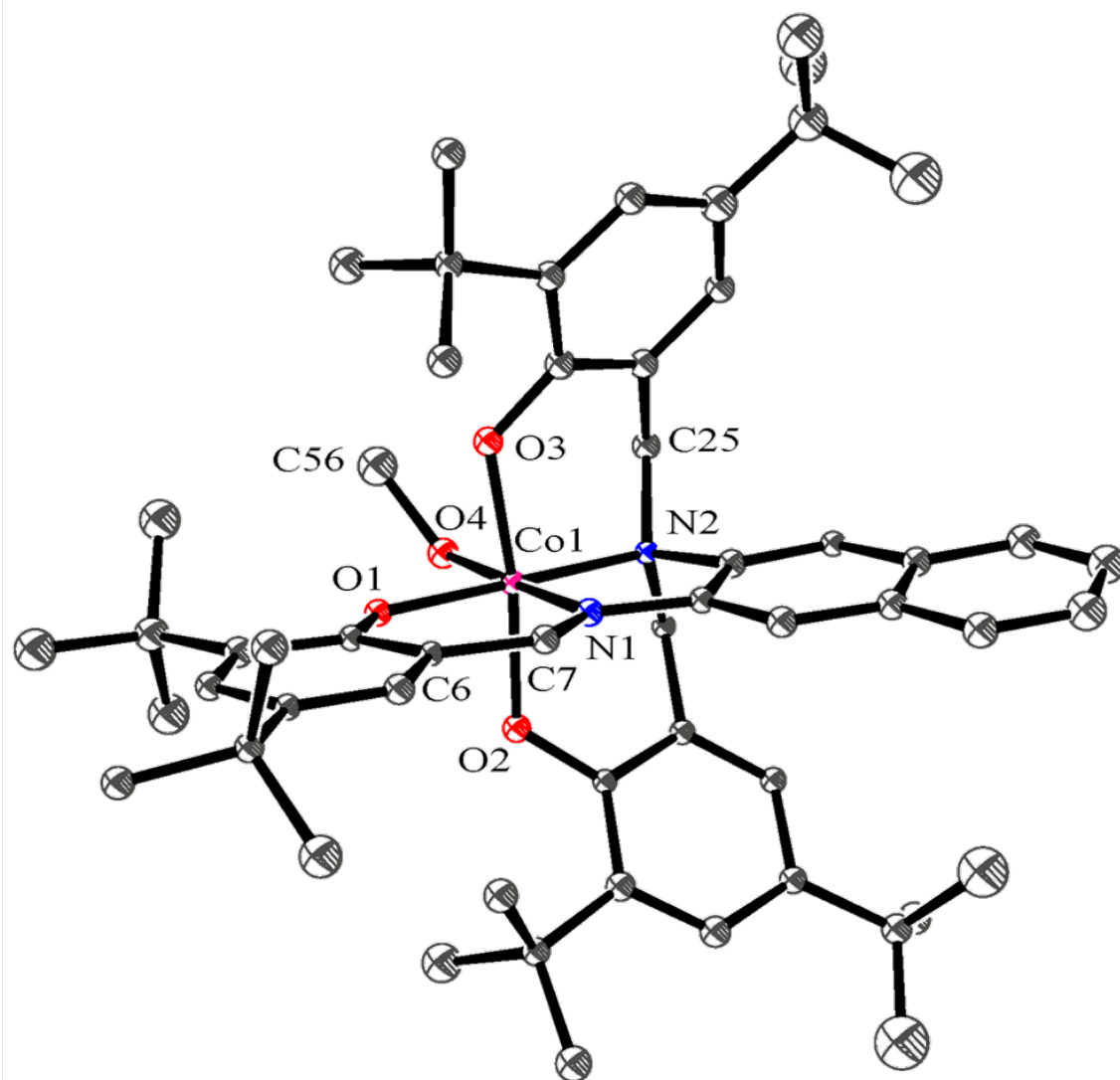
Figure 5.6. ORTEP diagram of **(2) [Co^{III}L^3(MeOH)]**.
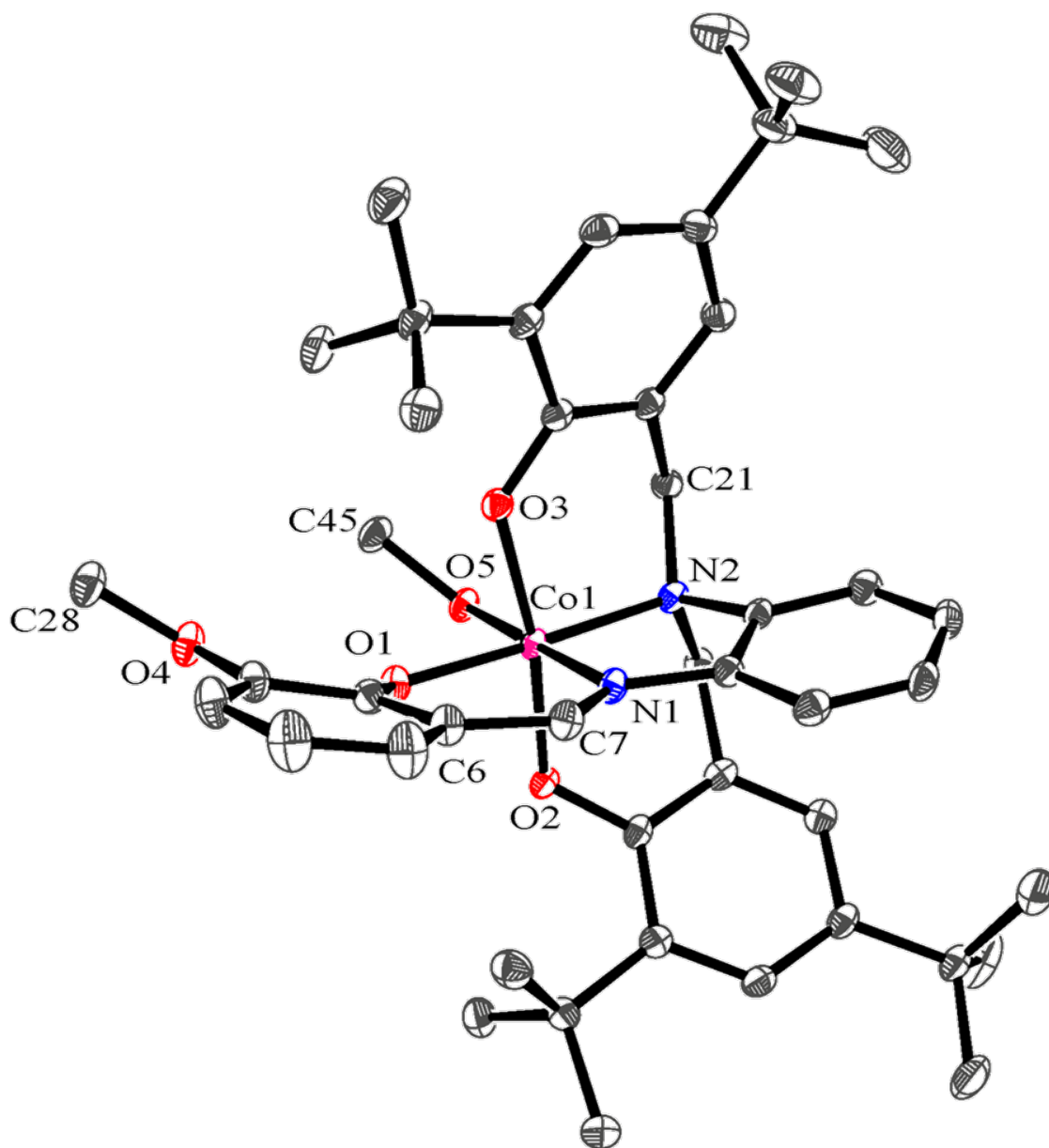
Figure 5.7. ORTEP diagram of **(3) [Co^{III}L⁴(MeOH)]**.
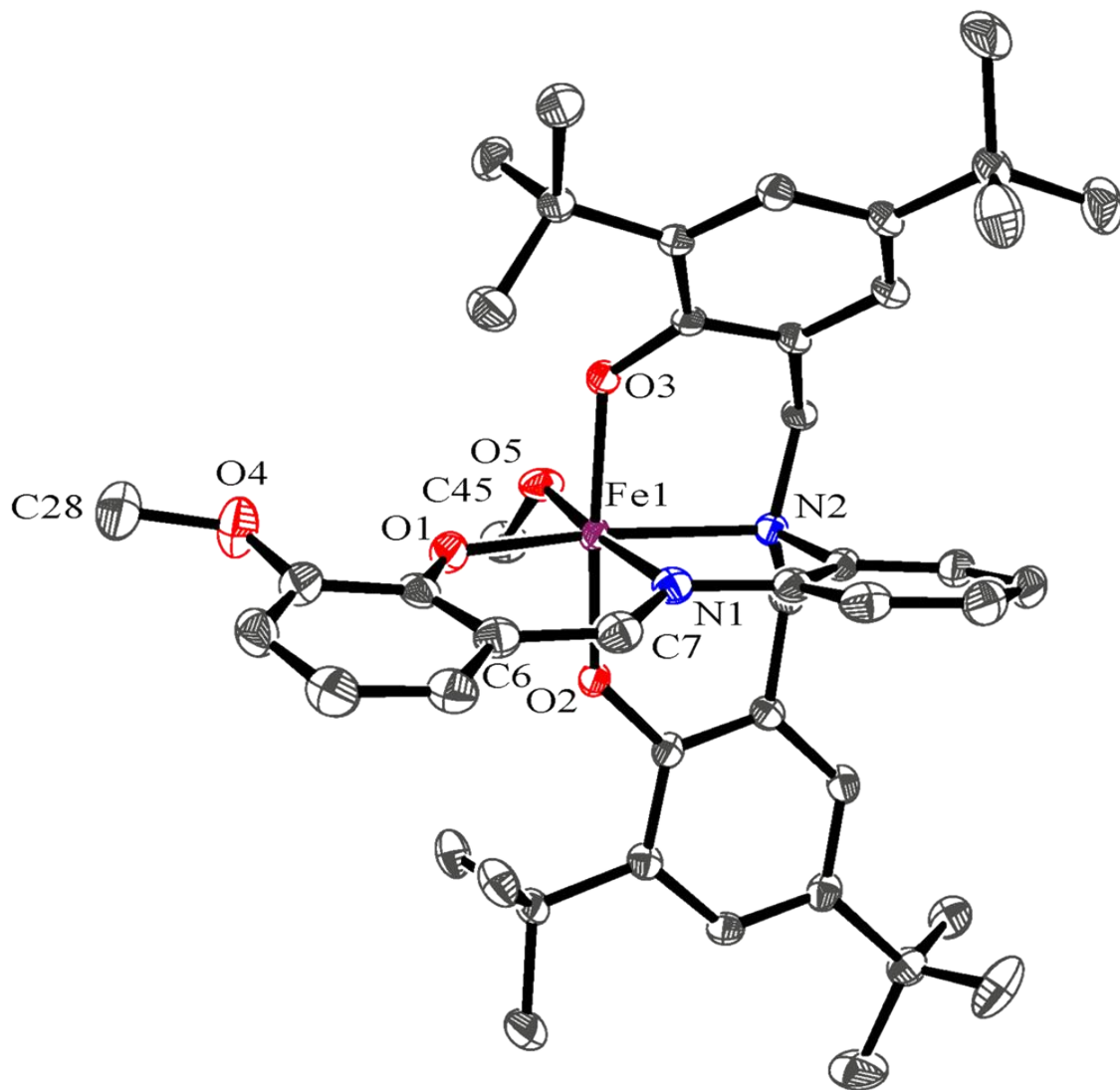
Figure 5.8. ORTEP diagram of **(4) [Fe^{III}L⁴(MeOH)]**.

Table 5.2. Selected bond lengths (Å) and angles.

(1) [Co^{III}L^1(MeOH)]	(2) [Co^{III}L^3(MeOH)]	(3) [CoL^4(MeOH)]	(4)[Fe^{III}L^4(MeOH)]
Co(1)-O(1) 1.883(2)	Co(1)-O(1) 1.888(1)	Co(1)-O(1) 1.8741(15)	Fe(1)-O(1) 1.971(2)
Co(1)-O(2) 1.932(2)	Co(1)-O(2) 1.950(1)	Co(1)-O(2) 1.9181(15)	Fe(1)-O(2) 1.9181(18)
Co(1)-O(3) 1.905(0)	Co(1)-O(3) 1.892(1)	Co(1)-O(3) 1.9057(15)	Fe(1)-O(3) 1.9317(18)
Co(1)-O(4) 1.994(1)	Co(1)-O(4) 2.010(1)	Co(1)-O(5) 1.9833(15)	Fe(1)-O(5) 2.0507(19)
Co(1)-N(1) 1.864(7)	Co(1)-N(1) 1.868(2)	Co(1)-N(1) 1.8799(18)	Fe(1)-N(1) 2.144(2)
Co(1)-N(2) 1.980(6)	Co(1)-N(2) 1.974(2)	Co(1)-N(2) 1.9722(18)	Fe(1)-N(2) 2.240(2)
N(2)-C(14) 1.5025(19)	N(2)-C(17) 1.471(3)	N(2)-C(14) 1.516(3)	N(2)-C(14) 1.491(3)
N(1)-C(7) 1.309(2)	N(1)-C(7) 1.302(2)	C(7)-N(1) 1.305(3)	C(7)-N(1) 1.295(4)
N(1)-C(8) 1.421(4)	N(1)-C(8) 1.428(2)	N(1)-C(8) 1.409(3)	N(1)-C(8) 1.419(4)
N(2)-C(13) 1.468(2)	N(2)-C(18) 1.511(2)	N(2)-C(21) 1.493(3)	N(2)-C(21) 1.507(3)
O(1)-Co(1)-O(3) 86.35(4)	O(1)-Co(1)-O(3) 86.32(6)	O(1)-Co(1)-O(5) 86.96(7)	O(1)-Fe(1)-O(5) 98.96(8)
O(2)-Co(1)-O(1) 86.19(5)	O(2)-Co(1)-O(1) 86.28(6)	O(1)-Co(1)-O(2) 87.73(7)	O(2)-Fe(1)-O(1) 93.51(8)
O(4)-Co(1)-O(3) 89.08(5)	O(4)-Co(1)-O(3) 88.34(6)	O(3)-Co(1)-O(2) 170.36(7)	O(2)-Fe(1)-O(3) 169.32(8)
O(2)-Co(1)-O(4) 82.13(5)	O(2)-Co(1)-O(4) 88.15(6)	O(2)-Co(1)-O(5) 84.83(6)	O(2)-Fe(1)-O(5) 88.02(8)
O(1)-Co(1)-O(4) 86.55(5)	O(1)-Co(1)-O(4) 87.36(6)	O(3)-Co(1)-O(5) 90.28(7)	O(3)-Fe(1)-O(5) 83.49(8)
N(1)-Co(1)-O(1) 95.29(5)	N(1)-Co(1)-O(1) 95.91(7)	N(1)-Co(1)-O(2) 93.25(7)	O(2)-Fe(1)-N(1) 95.37(8)
N(2)-Co(1)-O(4) 91.72(5)	N(2)-Co(1)-O(4) 89.85(6)	N(1)-Co(1)-O(5) 176.36(7)	O(5)-Fe(1)-N(1) 173.51(9)
N(1)-Co(1)-O(3) 93.65(5)	N(1)-Co(1)-O(3) 92.44(7)	O(2)-Co(1)-N(2) 93.68(7)	O(2)-Fe(1)-N(2) 86.76(8)
N(1)-Co(1)-N(2) 86.43(5)	N(1)-Co(1)-N(2) 86.88(7)	N(1)-Co(1)-N(2) 85.98(8)	N(1)-Fe(1)-N(2) 77.24(8)
O(3)-Co(1)-N(2) 93.52(5)	O(3)-Co(1)-N(2) 94.02(6)	O(1)-Co(1)-N(2) 177.45(7)	O(1)-Fe(1)-N(2) 87.74(8)
O(2)-Co(1)-N(1) 95.35(5)	O(2)-Co(1)-N(1) 91.47(7)	O(3)-Co(1)-N(2) 94.71(7)	O(3)-Fe(1)-N(2) 164.71(8)
O(2)-Co(1)-N(2) 93.68(5)	O(2)-Co(1)-N(2) 93.22(6)	N(2)-Co(1)-O(5) 91.05(7)	O(5)-Fe(1)-N(2) 96.32(8)

For the following discussion we will be using the nomenclature from **Scheme 5.1**, namely, when we refer to phenolato A and A', we are referring to chemically identical phenolato moieties appended through the tertiary nitrogen -N2. Phenolate B refers to the phenolato moiety connected to nitrogen -N1 through the Schiff base moiety.
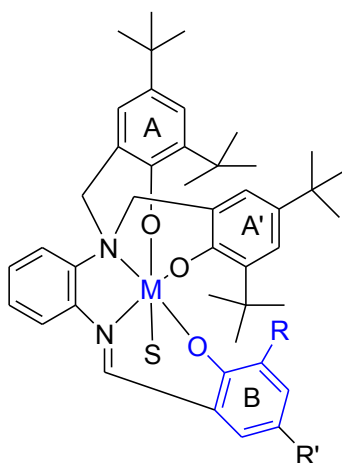
Scheme 5.1. Phenolate identification.

Compound **(4)** is different from the compounds previously mentioned. It has a coordination number of six, instead of five as for our previously reported system with a similar ligand. **Figure 5.8** shows the ORTEP diagram obtained from XRD data. It shows a six-coordinated iron complex with a methanol solvent molecule, and a N_2O_3-type pentadentate ligand. The bond lengths are consistent with a analogous high-spin iron(III) metal center, from our previous work.[1] The immediate environment around the iron center can be considered pseudo-octahedral, with a basal plane consisting of a central iron with N1, N2, O1, and O5 (angles between vary from 88° to 98°) and the two axial positions are occupied by O3 and O2. The Fe-O(phenolate) bond lengths are similar to our previous work, with the Fe-O1 bond length slightly longer by about 0.04 Å,

compared to Fe-O3 and Fe-O2 which correspond to the phenolates A and A'. The Fe-O5 (methanol) bond length is the longest at 2.05 Å, consistent with the fact that the methanol is protonated, therefore making O5 a poorer $\sigma-$ donor to the iron center. The Fe-N1(Schiff) bond is shorter by about 0.1 Å when compared to Fe-N2, also consistent with our previous work. It is noteworthy that all bond lengths to the iron center are all slightly longer than for the five coordinate iron systems, the most notable elongation of the Fe-O(phenolate) bonds which are all about 5-10% longer, the effect is less on the nitrogen donors. The phenylene ring, with phenolate B, has a dihedral angle of 0.02°, making those rings essentially planar to each other, allowing for $\pi-$delocalization.

For the remaining three compounds, namely **(1)**, **(2),** and **(3)** they all have a structure consistent with low-spin cobalt(III) ions with their respective complex in a six-coordinate environment of three phenolato oxygen atoms, two amine nitrogen atoms, and a molecule of methanol solvent at the sixth position, very similar to **(4)**.

The ORTEP diagram for **(1)** is shown in **Figure 5.5,** it can be considered pseudo-octahedral, where the twelve angles related to the Co(III) center to the adjacent donor atoms range from $82.13(5)^{\circ}$ to $93.68(5)^{\circ}$ as compared to 90° required for a perfect octahedron. The longest cobalt(III) bond is between Co-O(4) at 1.994 Å , similar to **(4)** for a protonated methanol. The shortest bonded atom to Co(III) is between Co-N(1) 1.864 Å, which is the Schiff base nitrogen (C=N, N(1)-C(7)) 1.309 Å). The phenolates attached to the N(2) are *trans* to one another (O3 and O2), where the Co-O(2) is 1.932 Å. The bond length between Co-O(3) is slightly shorter at 1.905Å. The dihedral angle between

the Schiff base phenolate B and the phenylene moiety (C(8)-N(1)-C(7)-C(6)) is 1.4^o which indicates extensive π–conjugation.

5.9. Redox properties.

It is widely established[1, 3] that phenolate moieties can undergo oxidation to phenoxyl radicals and most of the redox properties are attributed to ligand centered processes. The cyclic voltammograms (CV) of **(1), (2)**, **(3)**, and **(4),** were measured in dichloromethane using $TBAPF_6$ and $TBACIO_4$ (TBA = tetrabutylammonium) electrolytes. We evaluate the redox potentials of the ligand centered processes to assess the intra-ligand oxidation sequence and the prowess to withstand extensive redox cycling.

The cathodic waves observed near -0.65 V *vs.* Fc^+/Fc and are similar for complexes (**1**), (**2**), and (**3**) (**Table 5.3** and **Figures 5.9**, **5.10**, **5.11**, and **5.12**) are assigned to Co(III)/Co(II) couples based on literature values[8] for the related salophen type complexes. This is expected considering that the three complexes have low-spin cobalt centers have similar ligand environments with N_2O_3 pentadentate donors along with a solvent molecule, though the processes appear to be quasi-reversible.

At first glance the anodic side of the voltammograms are similar to their gallium and iron counterparts we have previously published,[1b] which can support generation of up to three phenoxyl radicals. For (**4**), it appears that the complex behaves in a very similar fashion as the related compounds previously reported in Chapter 4 and we will therefore not go into further details for (**4**).

We observe three anodic waves for (**1**), (**2**), and (**3**) all centered at $\approx$ 0.20 V (ΔE = 0.13 V), 0.60 V (ΔE = 0.15 V), and 1.0 V (ΔE = 0.16 V). The amplitudes of these waves

suggest that they are successive one-electron oxidations of all three phenolates. Bistability between reduced and oxidized forms must be achieved to withstand extensive redox-cycling. Thirty CV cycles for (**1**), (**2**), (**3**), and (**4**) resulted in minimal decomposition at the surface of the electrode, as indicated by a nearly perfect superimposition of the waves for cycling through both the first ligand-centered oxidation and the metal centered reduction.

In general, most processes appear to be reversible/quasi reversible, with values of ΔE ranging from ~ 0.12 to 0.23 V, when compared to the standard Fc/Fc^+ couple ($\Delta E = 0.12$ V). All the anodic oxidation waves reported here are believed to be associated with phenoxyl-radical formation.

Table 5.3. Cyclic Voltammetry data for (**1**), (**2**), (**3**), and (**4**).[a]

Compound	Process (vs Fc+/Fc)			
	a) (E1/2)V (ΔE V)	b)	c)	d)
$[Co^{III}(L^1)MeOH]$ (**1**)	-0.65V (ΔE 0.16V)	0.23V (ΔE 0.14V)	0.63V (ΔE 0.16V)	1.0V (ΔE 0.15V)
$[Co^{III}(L^3)MeOH]$ (**2**)	-0.67V (ΔE 0.12V)	0.17V (ΔE 0.12V)	0.57V (ΔE 0.11V)	0.92V (ΔE 0.14V)
$[Co^{III}(L^4)MeOH]$ (**3**)	-0.63V (ΔE 0.13V)	0.21V (ΔE 0.12V)	0.65V (ΔE 0.14V)	0.98V (ΔE 0.20V)
$[Fe^{III}(L^4)MeOH]$ (**4**)	-1.32V (ΔE 0.18V)	0.61V (ΔE 0.25V)	NA	NA

[a]All in DCM, $1x10^{-3}$M, (**4**) uses 0.1M TBAClO$_4$ as electrolyte and (**1**), (**2**) and (**3**) use 0.1M TBAPF$_6$.
(Fc+/Fc E½=0.47V ΔE=0.12V)
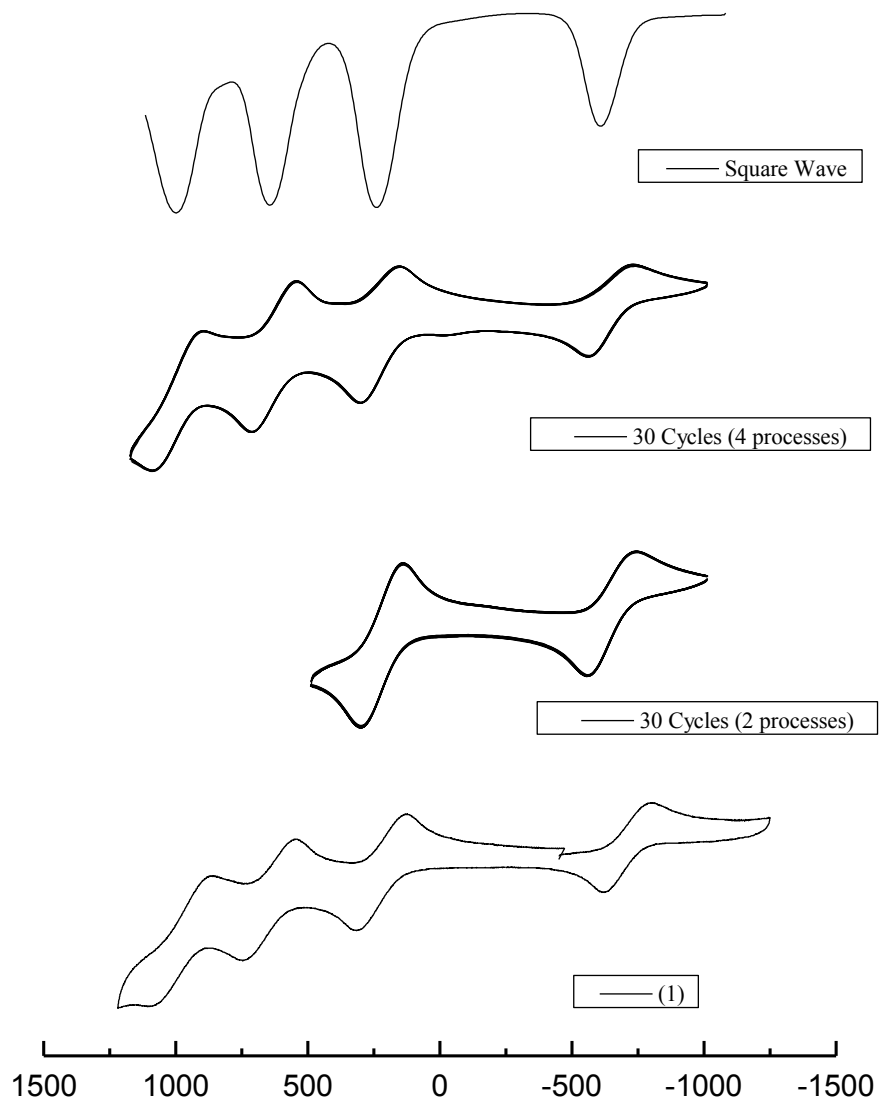
Figure 5.9. Cyclic Voltammograms of (**1**) in CH$_2$Cl$_2$.
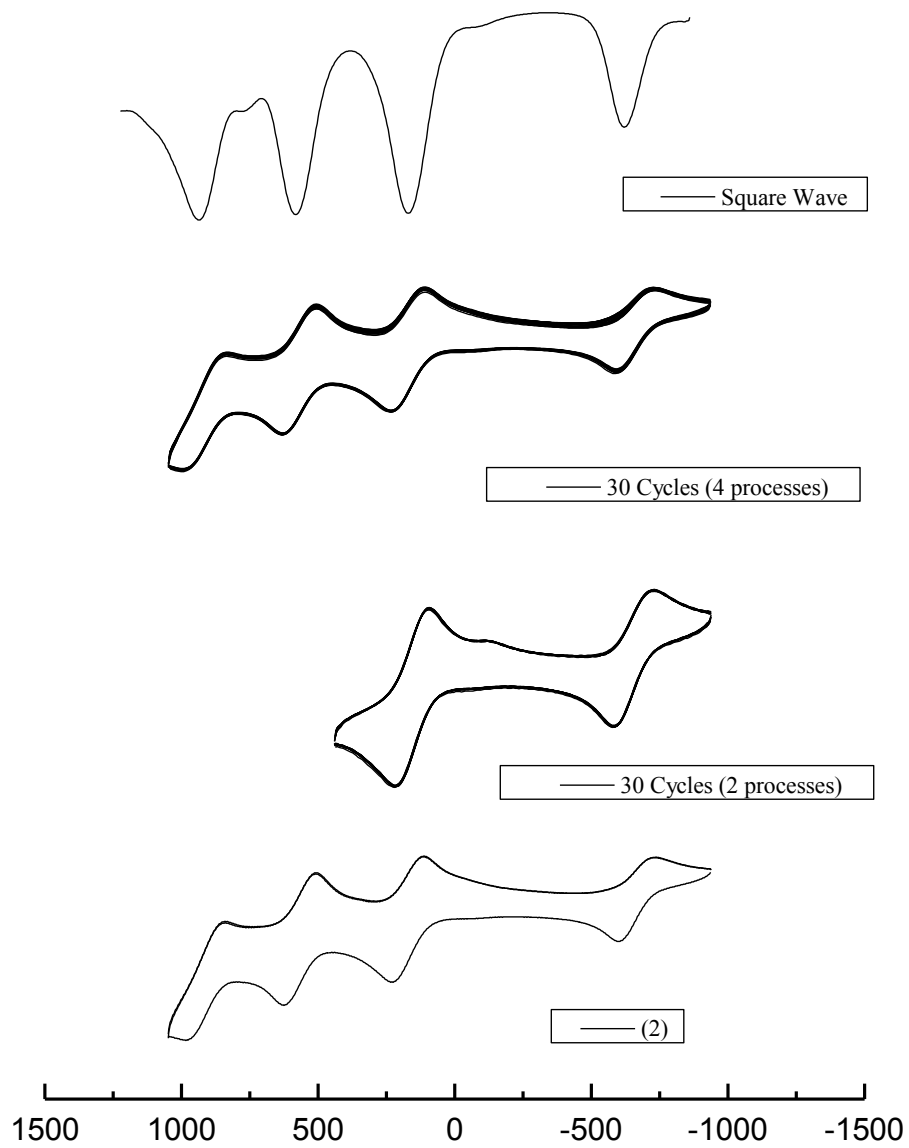
Figure 5.10. Cyclic Voltammograms of (**2**) in CH$_2$Cl$_2$.

Square Wave

30 Cycles (4 processes)

30 Cycles (2 processes)

(3)

1500   1000   500   0   -500   -1000   -1500
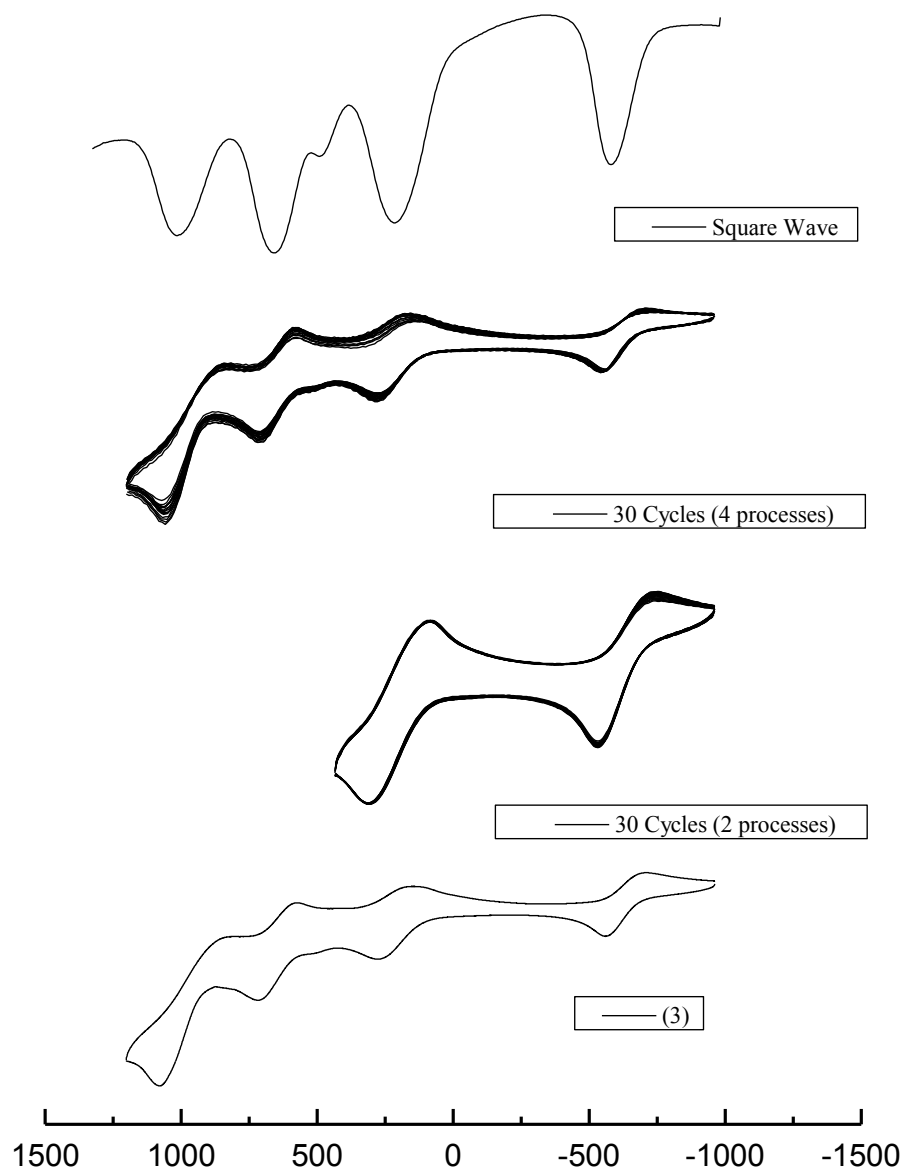
Figure 5.11. Cyclic Voltammograms of (**3**) in CH$_2$Cl$_2$.
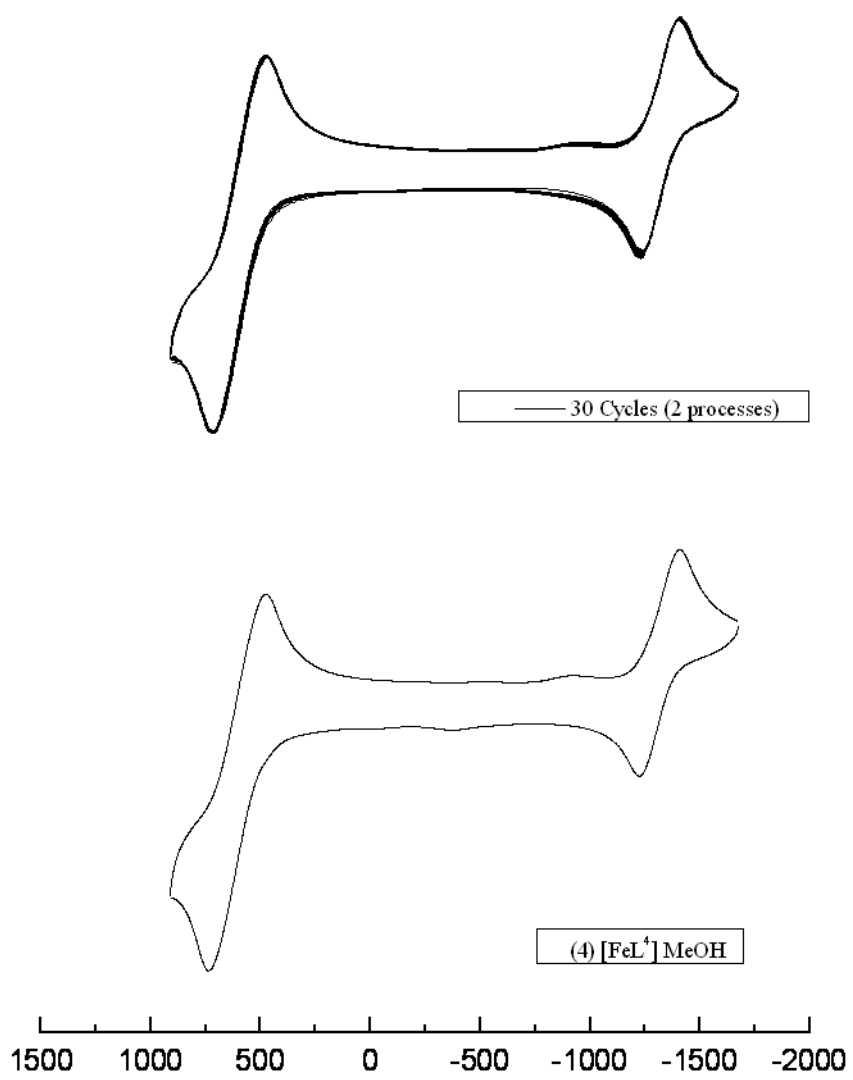
Figure 5.12: Cyclic Voltammograms of (**4**) in CH_2Cl_2

5.10. Electronic spectroscopy.

The visible absorption spectra of cobalt(III) phenolato-type complexes are theoretically expected to consist of singlet-to-singlet transitions (**Figure 5.13**). Although the exact details of the transitions, complicated by the various combination of the three phenolato π- orbital types (i.e. in-plane and out-of-plane), makes it hard to deconvolute into their proper formal assignments. Most of the low-energy bands around $\approx$ 750 ($\approx$ 1000 L $\cdot$ Mol$^{-1}\cdot$ cm^{-1}) nm are attributed to ligand metal-to-charge-transfer p$\pi_{\text{phenolate (out-of-plane)}}$ $\rightarrow$ d$\sigma^*_{\text{cobalt(III)}}$ transitions. Whereas the higher energy more intense bands around $\approx$ 500nm($\approx$ 9000 L $\cdot$ Mol$^{-1}\cdot$ cm^{-1}) are attributed to p$\pi_{\text{phenolate (in- plane)}}$ $\rightarrow$ d$\sigma^*_{\text{cobalt(III)}}$ transitions. Compound **(4)** shows the typical (Fe$_{\text{d}\sigma^*}\leftarrow$O$_{\text{p}\pi}$) LMCT bands reported in Chapter 4.
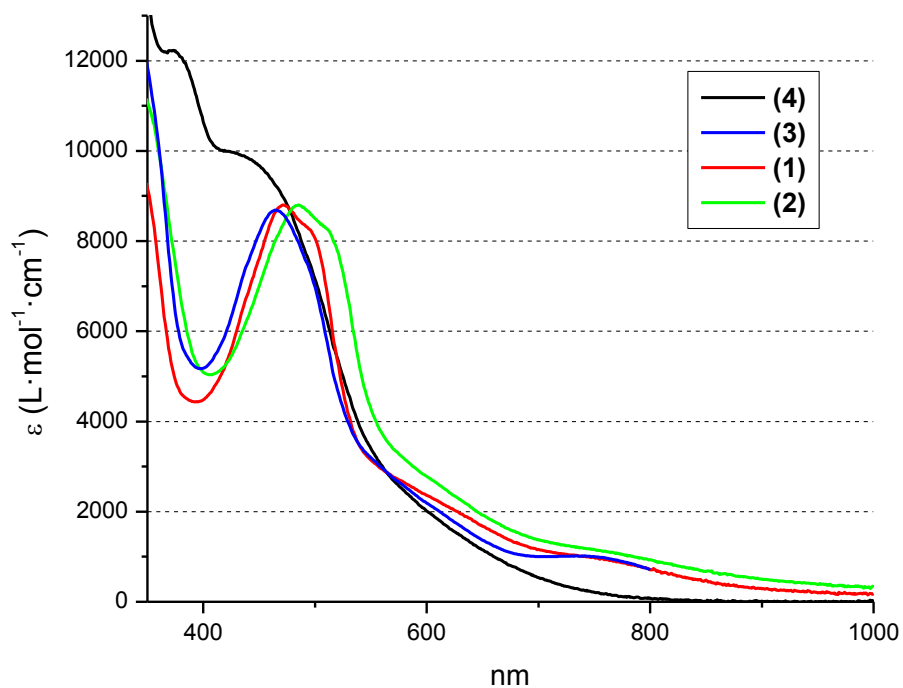
Figure 5.13. UV-vis spectra of **(1), (2), (3)**, and **(4)** in dichloromethane (1x10^{-4}M).

5.10. Electronic structure discussion.

We were interested in the comparison of the structural and electronic properties between (i) the six-coordinate iron complex vs. our previously reported five-coordinate complex (Chapter 4) and (ii) the redox reaction undergone by complexes (**1**), (**2**), and (**4**) to study the electronic structure and loci of oxidations. We used models comparable to (**1**), (**2**), and (**4**) namely (**1'**), (**2'**), and (**4'**) (shown in F**igure 5.14**, below). The six *tertiary*-butyl groups appended to the phenolate rings were replaced by hydrogen atoms (-H) to make the calculations more practical in the same manner as Chapter 4. All geometries are in good agreement with the experimentally deduced structures. All the discussions will refer to the nomenclature introduced earlier. All calculations in this chapter were done using the B3PW91/6-31G(d) level of theory[5] and included solvent effects (dichloromethane) using the IEF-PCM polarizable continuum model.[6]

S = CH$_3$OH
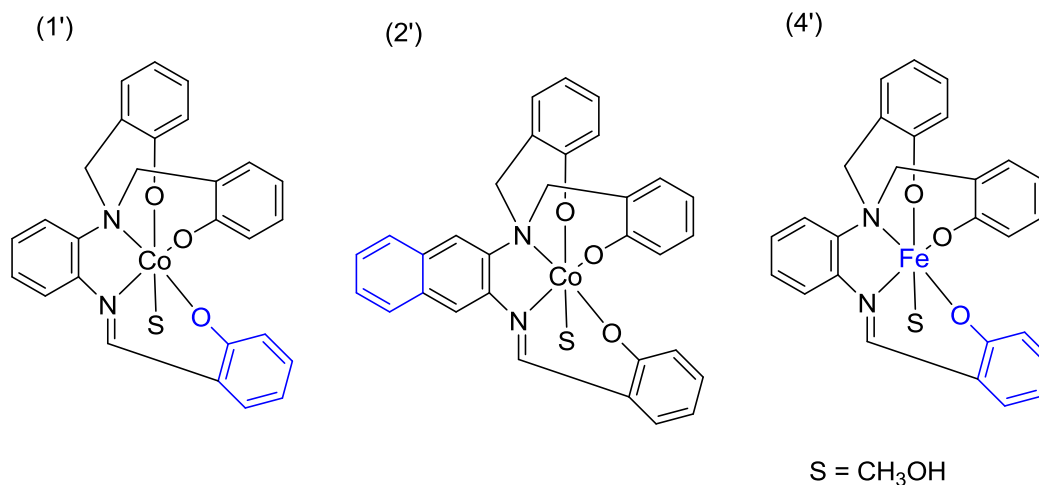
Figure 5.14. Models used for the electronic structure calculations.

5**.11. Calculated electronic behavior**

The identification of the sequential order in which the phenolate rings get oxidized into phenoxyl radicals is of pivotal interest to this work. The cyclic voltammetry data discussed earlier, showed considerable similarity between all the cobalt(III) complexes (**1**), (**2**), and (**3**)**.** All three complexes exhibited three independent, well define, reversible, 1e⁻ oxidative processes and a 1e⁻ reductive process. For the low-spin cobalt(III) processes we expect that any phenoxyl-radical generated will *not* magnetically couple to the cobalt(III) metal center, since there are no unpaired electrons from the cobalt(III) center to pair with. We investigated the following series of calculations $(1')\rightarrow(1')^+\rightarrow(1')^{2+}\rightarrow(1')^{3+}$ and $(2')\rightarrow(2')^+\rightarrow(2')^{2+}\rightarrow(2')^{3+}$ to get a better understanding of the redox properties, and to explore the differences, if any, between the complexes.

The Parent Compounds Molecular Orbitals Ladders.

Here we discuss the differences between (**1'**) and (**2'**) parent compounds and the orbitals descriptions. Both have low-spin cobalt(III) metal centers with Mulliken charges of ~1.05, consistent with a low-spin cobalt(III) ion. The MO ladder is shown in **Figure 5.15** below, and orbital contributions in **Figure 5.16, 5.17, 5.18, 5.19**, and **Tables 5.4** and **5.5**.
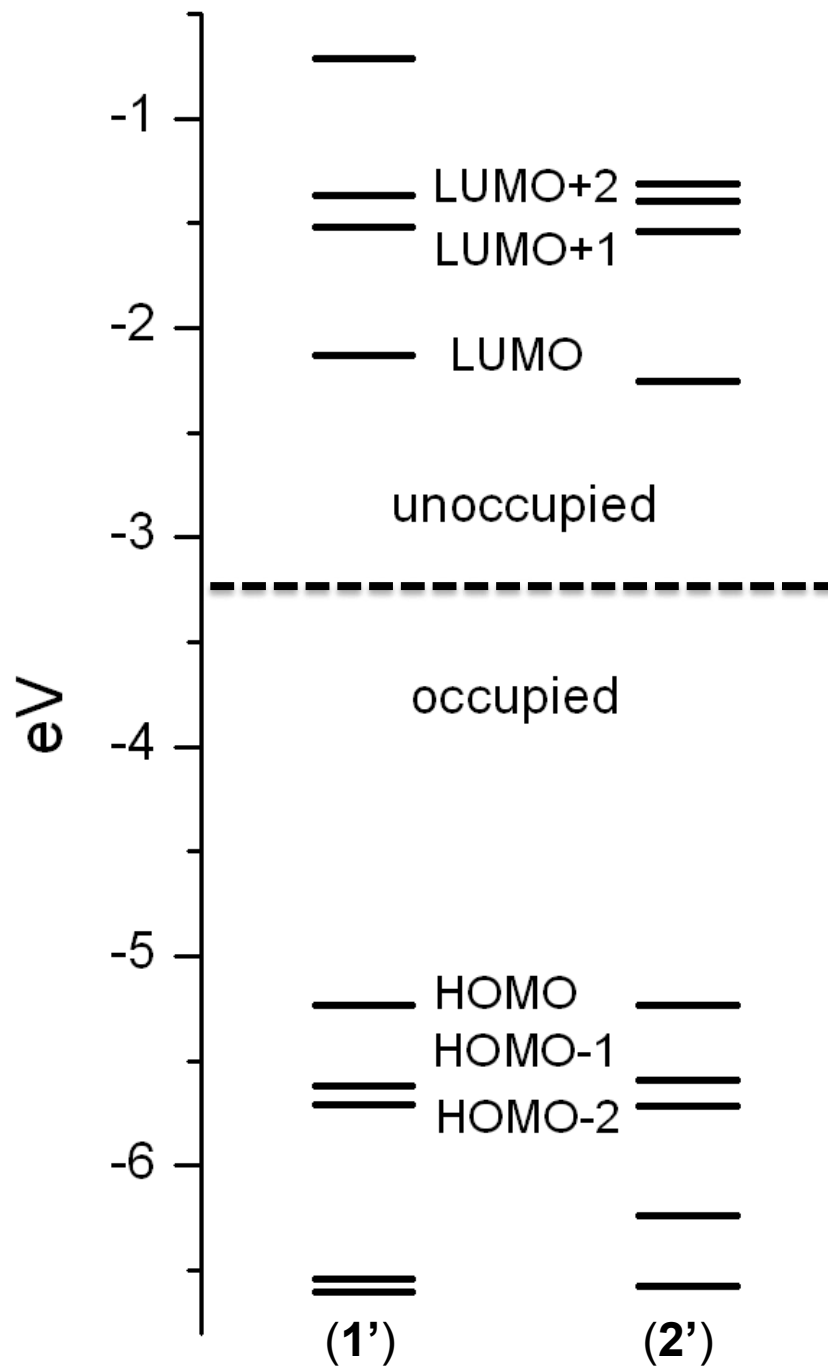
Figure 5.15. Comparitive by side MO ladder for (**1'**) and (**2'**) DFT models.

Table 5.4. Orbital Composition and Energy for (1').

Orbital	Energy (a.u)	Energy (eV)	% Co	% Phenol A	% Phenol A'	% Phenol B	%CH3OH	% Phenylene
LUMO+3	-0.03	-0.7	0.3	1.5	3.1	1.3	0.0	93.8
LUMO+2	-0.05	-1.4	64.4	10.2	8.7	7.8	0.0	8.9
LUMO+1	-0.06	-1.5	65.7	4.2	3.4	4.6	6.0	16.1
LUMO	-0.08	-2.1	3.4	0.2	0.3	35.2	0.1	60.8
HOMO	-0.19	-5.2	5.7	14.1	76.8	0.7	0.4	2.3
HOMO-1	-0.21	-5.6	7.1	0.9	0.8	73.7	0.0	17.5
HOMO-2	-0.21	-5.7	0.0	77.8	15.8	0.2	0.0	5.1
HOMO-3	-0.24	-6.5	8.4	6.3	5.0	48.8	0.0	31.5
HOMO-4	-0.24	-6.6	0.1	15.8	77.9	0.3	0.0	5.9

Table 5.5. Orbital Composition and Energy for (2').

Orbital	Energy (a.u)	Energy (eV)	% Co	% Phenol A	% Phenol A'	% Phenol B	%CH3OH	% Naphtalene
LUMO+3	-0.05	-1.3	13.3	1.1	1.9	11.2	0.2	72.3
LUMO+2	-0.05	-1.4	54.1	10.4	8.5	6.5	0.3	20.2
LUMO+1	-0.06	-1.5	63.2	3.2	3	3.8	1.2	25.6
LUMO	-0.08	-2.3	2.9	0.3	0.3	29.3	0.1	67.1
HOMO	-0.19	-5.2	0	13.9	77.5	0.4	0.4	7.8
HOMO-1	-0.21	-5.6	6.8	1	0.6	66.9	0	24.7
HOMO-2	-0.21	-5.7	3.4	78	15.4	0.2	1.1	1.9
HOMO-3	-0.23	-6.2	1.1	0.2	3.1	23.3	0	72.3
HOMO-4	-0.24	-6.6	4.7	15.5	46.5	15.1	0	18.2
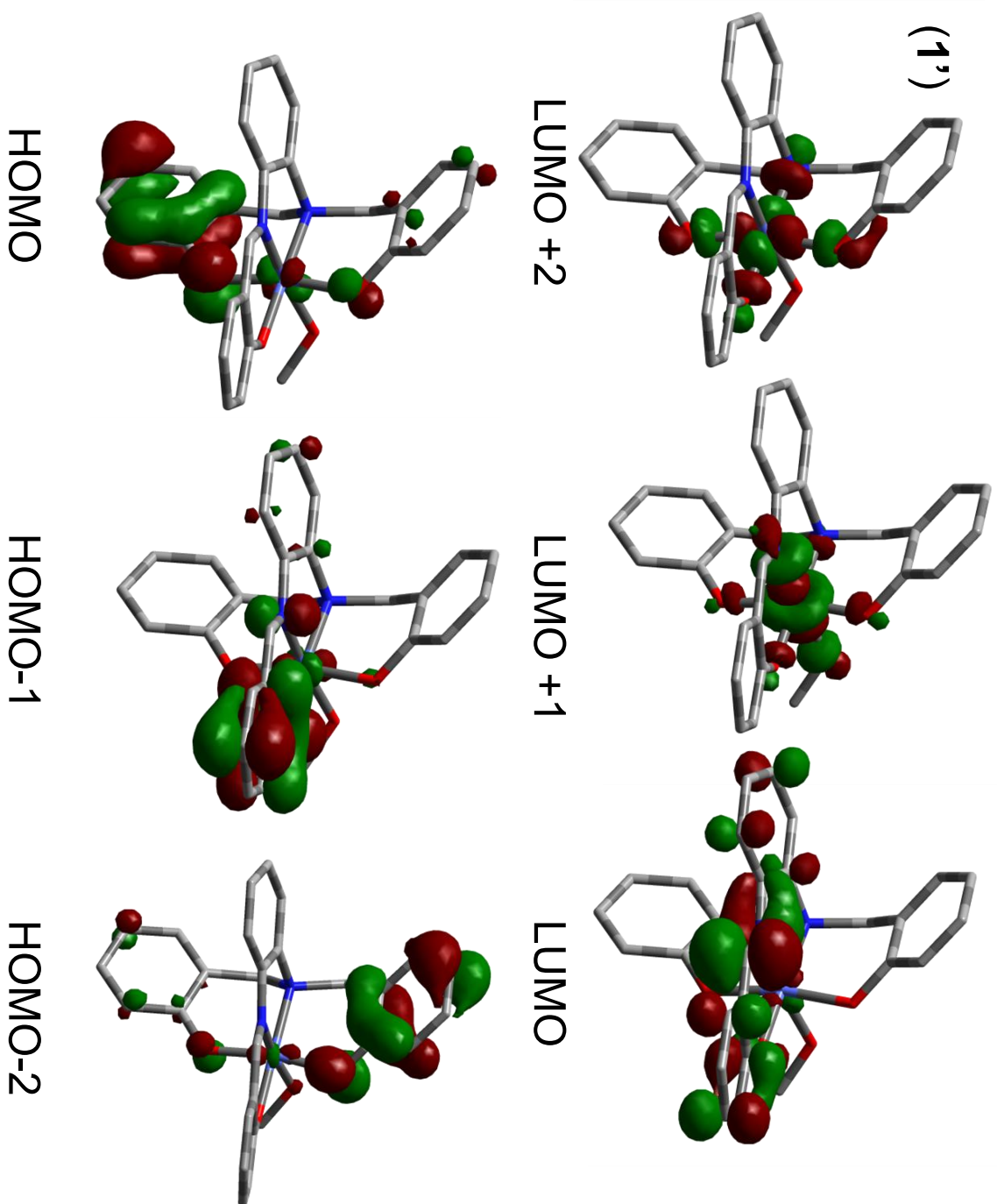
Figure 5.16. MO orbital plots of (**1'**) (Hydrogen omitted for Clarity)
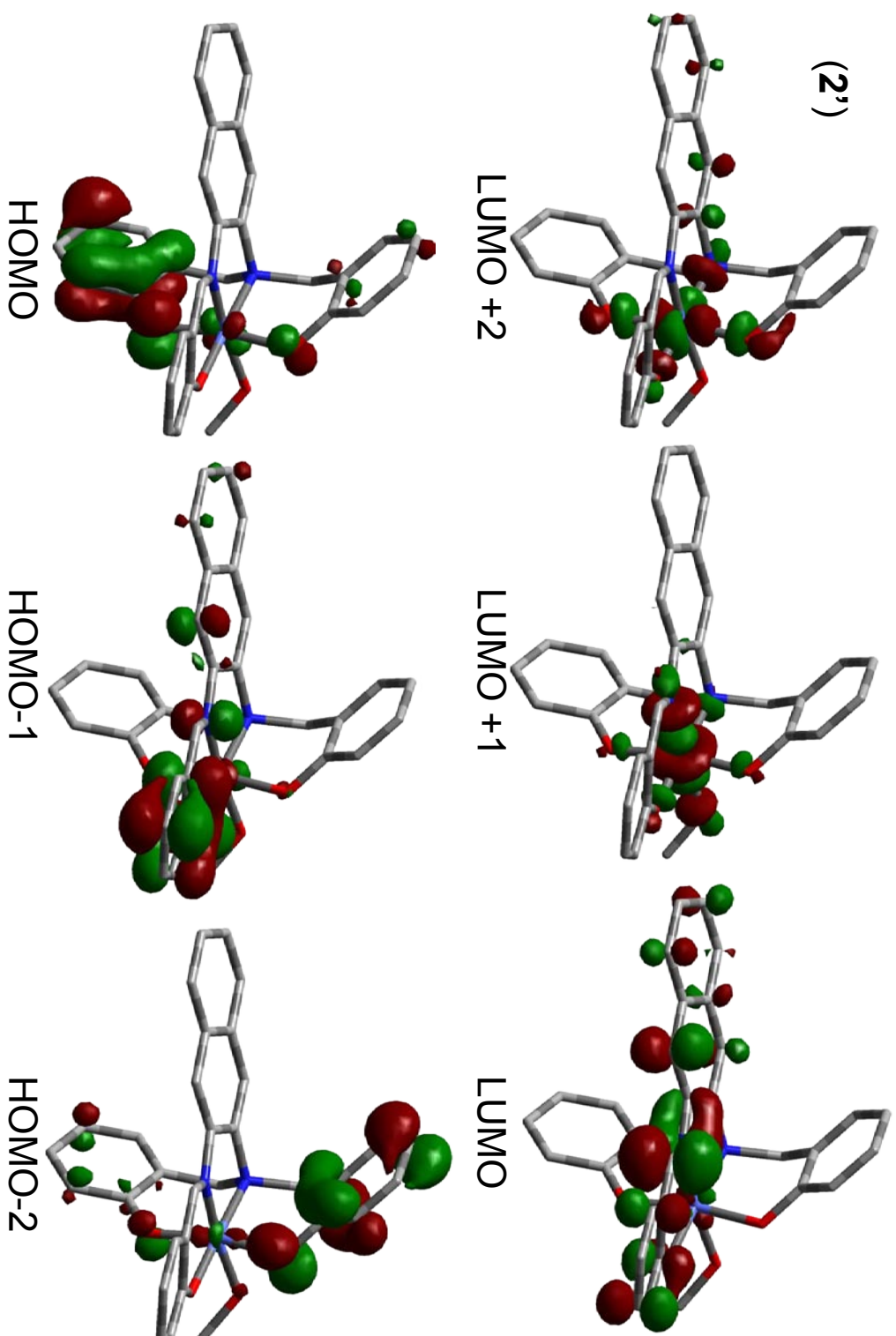
Figure 5.17. MO orbital plots of (2') (Hydrogen omitted for Clarity)

	HOMO-4	HOMO-3	HOMO-2	HOMO-1	HOMO	LUMO	LUMO+1	LUMO+2	LUMO+3
% Co	0.1	8.4	0	7.1	5.7	3.4	65.7	64.4	0.3
% Phenol A	15.8	6.3	77.8	0.9	14.1	0.2	4.2	10.2	1.5
% Phenol A'	77.9	5	15.8	0.8	76.8	0.3	3.4	8.7	3.1
% Phenol B	0.3	48.8	0.2	73.7	0.7	35.2	4.6	7.8	1.3
%CH3OH	0	0	1.1	0	0.4	0.1	6	0	0
% Phenylene	5.9	31.5	5.1	17.5	2.3	60.8	16.1	8.9	93.8
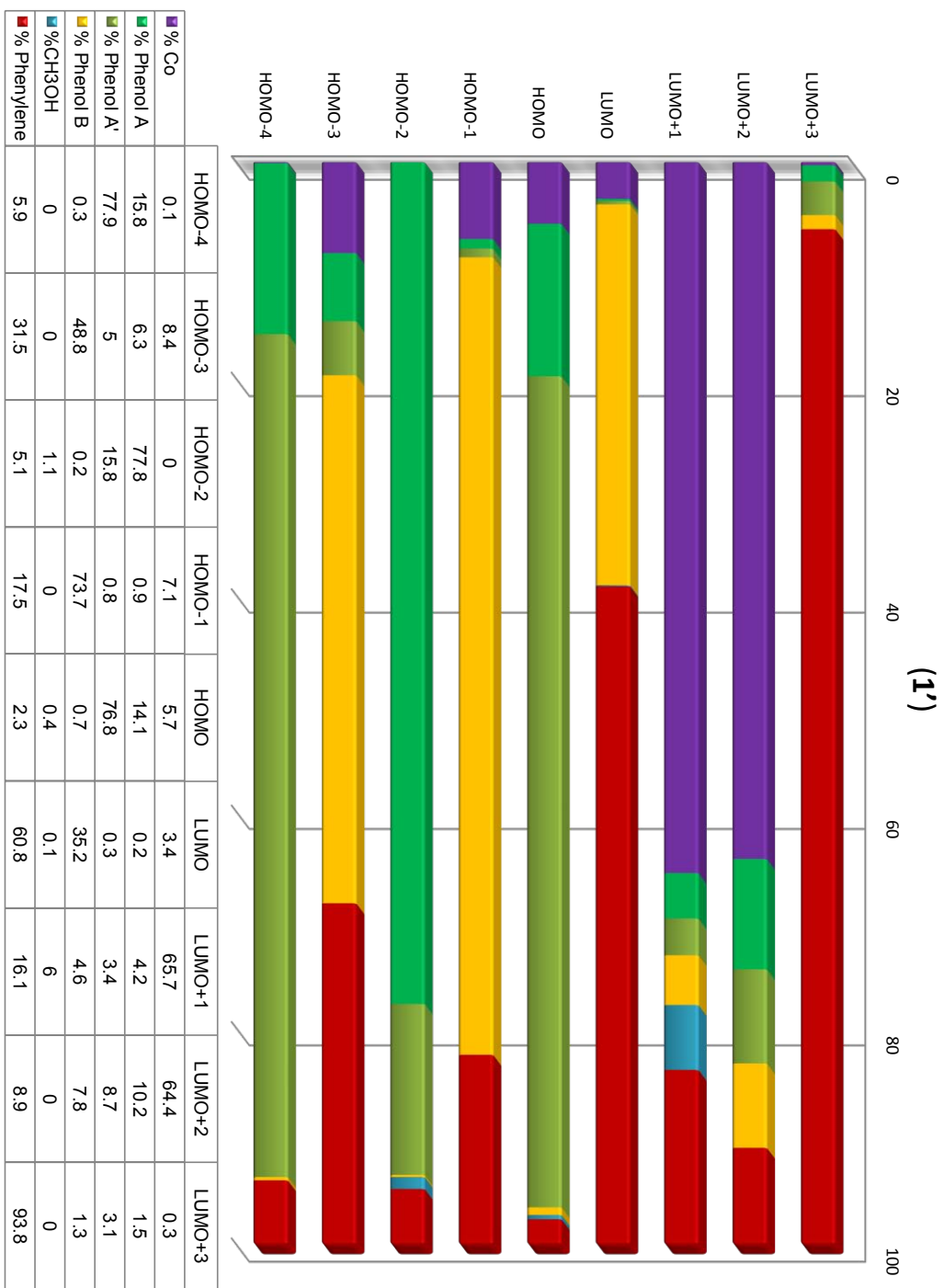
Figure 5.18. Graphical MO contribution for (**1'**).

	HOMO-4	HOMO-3	HOMO-2	HOMO-1	HOMO	LUMO	LUMO+1	LUMO+2	LUMO+3
% Co	4.7	1.1	3.4	6.8	0	2.9	63.2	54.1	13.3
% Phenol A	15.5	0.2	78	1	13.9	0.3	3.2	10.4	1.1
% Phenol A'	46.5	3.1	15.4	0.6	77.5	0.3	3	8.5	1.9
% Phenol B	15.1	23.3	0.2	66.9	0.4	29.3	3.8	6.5	11.2
%CH3OH	0	0	1.1	0	0.4	0.1	1.2	0.3	0.2
% Naphtalene	18.2	72.3	1.9	24.7	7.8	67.1	25.6	20.2	72.3
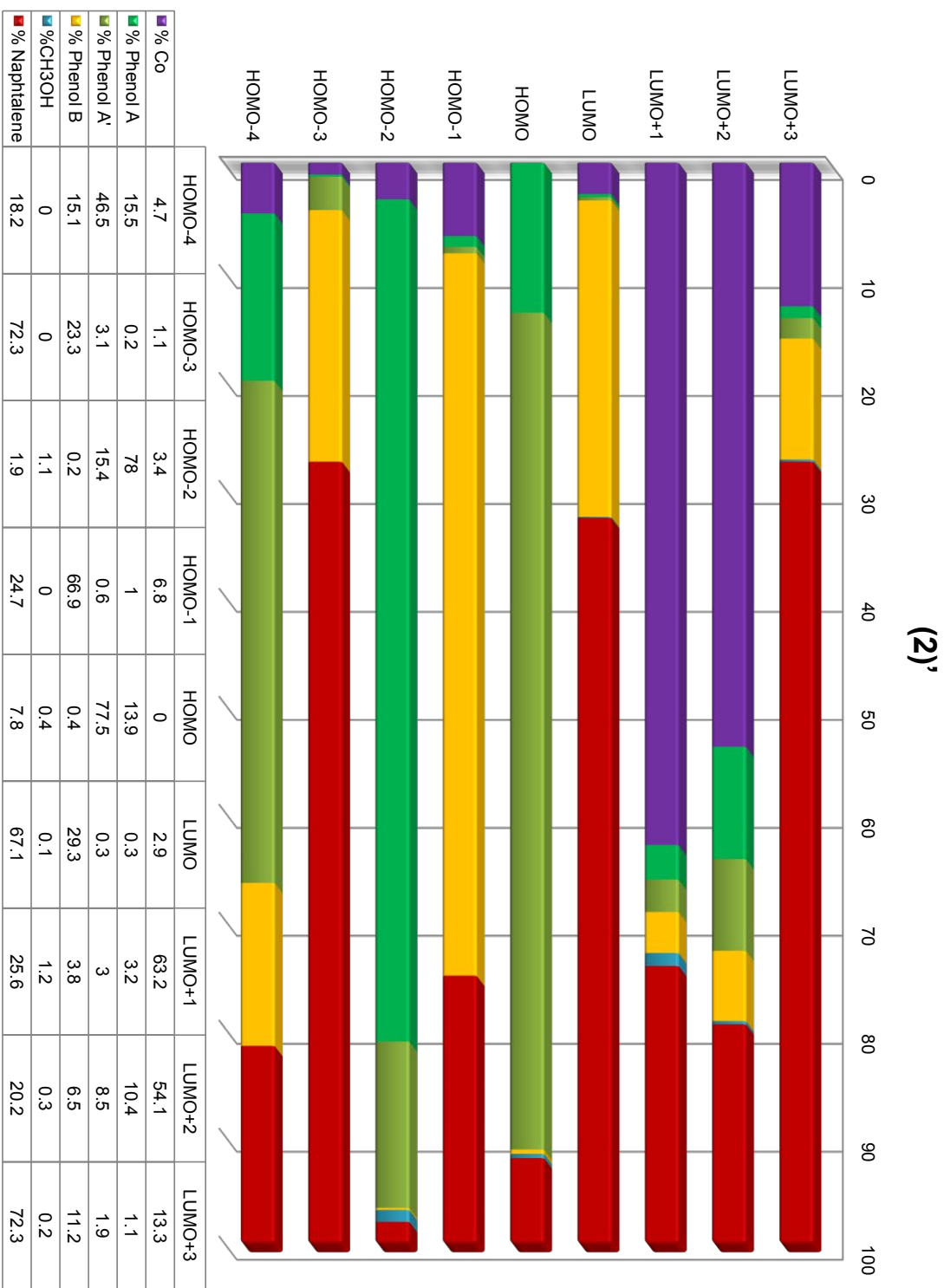
Figure 5.19. Graphical MO contribution for (**2'**).

5.12. Orbital contribution discussion

Frontier orbitals are well-known to be responsible for much of the reactivity of metal complexes[1, 9] and they can be useful to predict and help differentiates in behaviors in complex molecules. For compounds (**1'**) and (**2'**) we expect that the occupied orbitals will relate to the oxidative redox chemistry, namely HOMO, HOMO-1, and HOMO-2, and similarly we expect the first unoccupied orbital to relate to the reductive processes. The energies of orbitals are very similar for (1') and (2') as indicated in **Figure 5.15**, where all the occupied and some of unoccupied orbitals are very similar and comparable in energy. The HOMOs have essentially the same energy, whereas the LUMOs for (**2'**) is 0.2 eV lower then for (**1'**) resulting in a HOMO-LUMO gap of 3.1 eV for (**1'**) and the slightly smaller 2.9 eV for (**2'**), consistent with electrochemical gap, for which we observe a smaller gap for (**2**).

For (**1'**) (**Table 5.4** and **Figure 5.18**) the HOMO is 77% based on phenol A', the HOMO-1 is 74% on phenol B, and HOMO-2 is 78% on phenol A. For (**2'**) (**Table 5.5** and **Figure 5.19**) the HOMO is 78% on A', HOMO-1 is 67% on B and HOMO-2 is 78% on A. The LUMO for (**1'**) is 61% based on the phenylene bridge moiety, and similarly the LUMO of (**2'**) is 68% on the naphthalene bridge. It is noteworthy that the usually expected LUMO would be composed of the remaining two empty e_g* type orbital of the low-spin cobalt(III) ion, but in both (**1'**) and (**2'**) those cobalt(III) d orbitals are LUMO+1 and LUMO+2, and we found that it seemingly was not basis set dependant (B3PW91 with SDD on cobalt, aug-cc-pVQZ on C,O and 6-311++g(d,p) on H. Thus we attempt to

assign the reductive electrochemical waves observed as an aromatic diamine type radical formation[10].

5.13. Redox calculations

We have modeled the following compounds $(1')\rightarrow(1')^{+}\rightarrow(1')^{2+}\rightarrow(1')^{3+}$ and $(2')\rightarrow(2')^{+}\rightarrow(2')^{2+}\rightarrow(2')^{3+}$ to gain an understanding of the redox properties. We also have modeled $(4')\rightarrow(4')^{+}$ using a similar spin-coupled radical metal as discussed in Chapter 4. The results are shown in **Table 5.7** and **Figure 5.20**.

Table 5.7. Mulliken charge and Mulliken spin analysis.[a]

	Mulliken Spins	Mulliken Charge	Co-O	C(ring)-O
(1') (S = 0)				
Co (III)	--	1.05		
Ring A	--	-0.43	1.89	1.33
Ring A'	--	-0.45	1.88	1.32
Ring B (C=N)	--	-0.28	1.87	1.29
(1'')+ (S = 1/2)				
Co (III)	0.04	1.08		
Ring A	0.10	-0.29	1.85	1.33
Ring A'	0.88	0.16	1.89	1.28
Ring B	0.00	-0.22	1.86	1.30
(1')2+ (S = 2/2)				
Co (III)	0.04	1.11		
Ring A	1.01	0.33	1.88	1.28
Ring A'	0.99	0.31	1.88	1.28
Ring B	0.01	-0.15	1.85	1.30
(1')3+ (S = 3/2)				
Co (III)	0.03	1.15		
Ring A	1.01	0.37	1.88	1.28
Ring A'	1.01	0.36	1.87	1.28
Ring B	0.93	0.43	1.88	1.27

(2') (S =0 /2)				
Co (III)	--	1.05		
Ring A	--	-0.43	1.89	1.33
Ring A'	--	-0.45	1.88	1.32
Ring B	--	-0.28	1.87	1.29
(2')$^+$ (S = 1/2)				
Co (III)	0.04	1.09		
Ring A	0.08	-0.30	1.85	1.33
Ring A'	0.90	0.18	1.90	1.28
Ring B	0.0	-0.22	1.86	1.30
(2')$^{2+}$ (S = 2/2)				
Co (III)	0.05	1.12		
Ring A	0.06	-0.26	1.84	1.34
Ring A'	0.96	0.24	1.90	1.28
Ring B	0.78	0.29	1.88	1.27
(2')$^{3+}$ (S = 3/2)				
Co (III)	0.03	1.15		
Ring A	1.01	0.37	1.88	1.28
Ring A'	1.01	0.36	1.87	1.28
Ring B	0.76	0.33	1.88	1.27
(4') (S = 5/2)				
Fe (III)	4.26	1.44		
Ring A	0.22	-0.47	1.88	1.32
Ring A'	0.15	-0.51	1.95	1.33
Ring B	0.17	-0.36	1.93	1.30
(4')$^{+1}$ (S = 4/2)				
Fe (III)	4.20	1.47		
Ring A	0.31	-0.36	1.84	1.33
Ring A'	-0.92	0.16	2.10	1.27
Ring B	0.18	-0.29	1.89	1.31

[a] B3PW91/6-31G(d) IEF-PCM (dichloromethane).

(1'), S = 0

(1')⁺, S = 1/2

(1')²⁺, S = 2/2

(1')³⁺, S = 3/2

(2'), S = 0

(2')⁺, S = 1/2

(2')²⁺, S = 2/2

(2')³⁺, S = 3/2

-1e⁻
+1e⁻
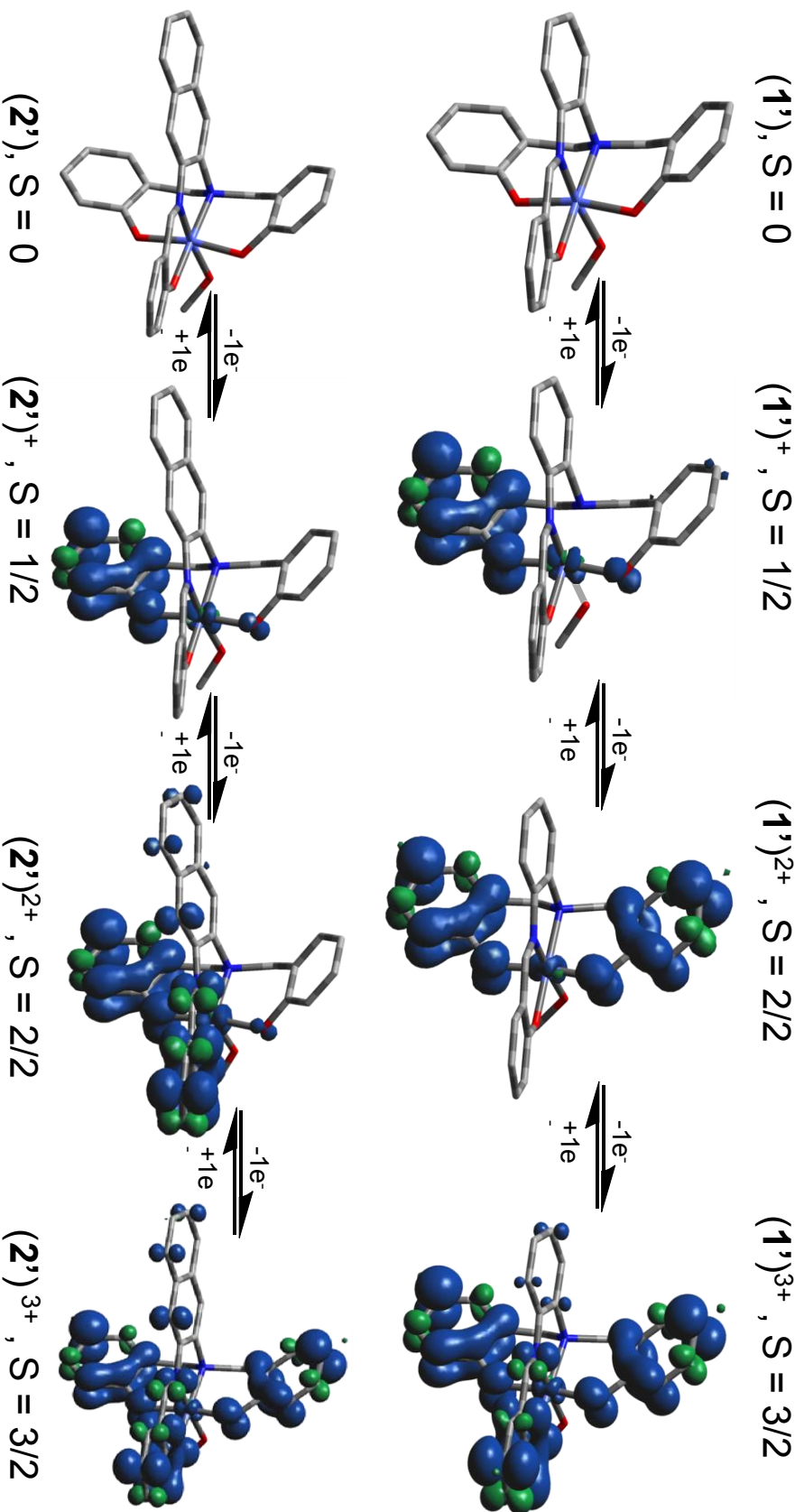
Figure 5.20. Spin Density plots for (**1'**)→(**1'**)⁺→(**1'**)²⁺→(**1'**)³⁺ and (top) and (**2'**)→(**2'**)⁺→(**2'**)²⁺→(**2'**)³⁺ bottom).
(α spin density in blue, β in green)

We observe that for the (**1'**) series of oxidations that the ligand is oxidized, and not the metal centers, as is clearly indicated by the Mulliken spin densities (≈ 0) and the constant Mulliken charge (≈ 1.10) across all four oxidation states. The spin density plots (**Figure 5.20** top) clearly show that the first oxidation (**1'$^+$**) is located on phenolate ring A, (**1'**)$^{2+}$ is on A' and (**1'**)$^{3+}$ is on B. Whereas, for the (**2'**) series, (**Figure 5.20** bottom) (**2'**)$^+$ is located on phenolate ring A, (**2'**)$^{2+}$ is on B, and (**1'**)$^{3+}$ is on A'. The oxidation of (**2'**) is consistent with the frontier orbital description. However the (**1'**) series deviates slightly from the frontier orbital model, where we would expect the second oxidation of phenolate B rather than A'. This might not be too unusual, since the geometry is re-optimized in our calculation affecting the potential for the next oxidation, thereby deviating slightly from the frontier orbital picture of the parent compound. Investigation of this issue is beyond the scope of the present study. For the six-coordinate (**4'**) iron (III) system we observe a very similar pattern to the one presented in Chapter 4, for which (**4'**)$^+$ shows -β spin density phenoxyl radical on phenolate A' (see **Figure 5.21**).

(4'), S = 5/2   (4')$^{+1}$, S = 4/2

−1e⁻
+1e⁻
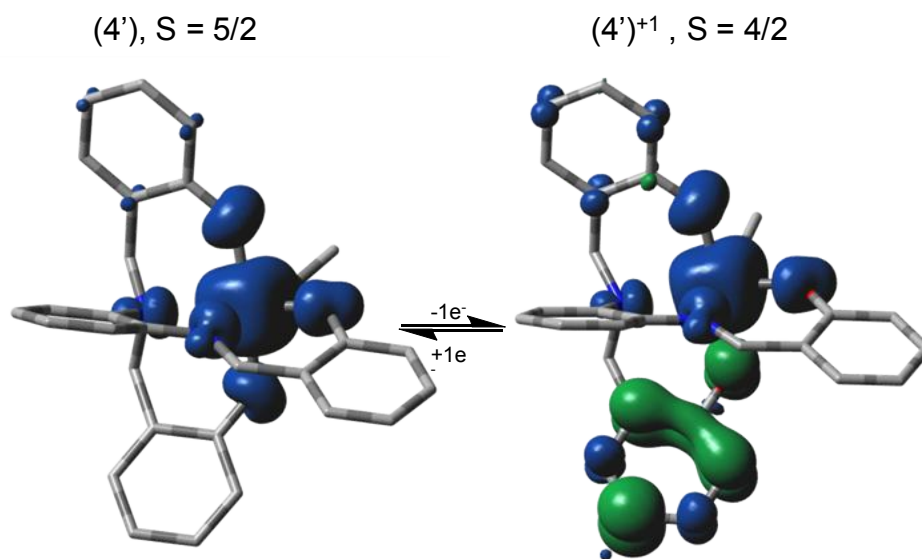
Figure 5.21. Spin density plot for (**4'**) (left) and (**4'**)$^{+}$ (right) (α spin density in blue, β in green)

5.14. Conclusion

We synthesized and characterized a series of four metal complexes, all of them six coordinate with an N_2O_3 type pentadentate ligand. The sixth position was occupied by a solvent molecule of methanol. Cyclic voltammetry data indicates that there are three accessible oxidations associated with the formation of the phenoxyl radicals, and one reduction, associated with an aromatic diamine-type radical formation, whereas the Co(III)/Co(II) reductions were irreversible and not observed in the cyclic voltammetry solvent window. Compound (**4**) exhibited what appears to be two closely packed successive 1e⁻ oxidative process and a 1e⁻ process associated with the Fe(II)/Fe(III) couple. Computational studies have helped to elucidate the location of these oxidations for (**1**) and (**2**) and the inferred electrochemical reactions are shown in **Figure 5.22**. The redox behavior of compound (**3**) has been shown to be comparable to (**1**).
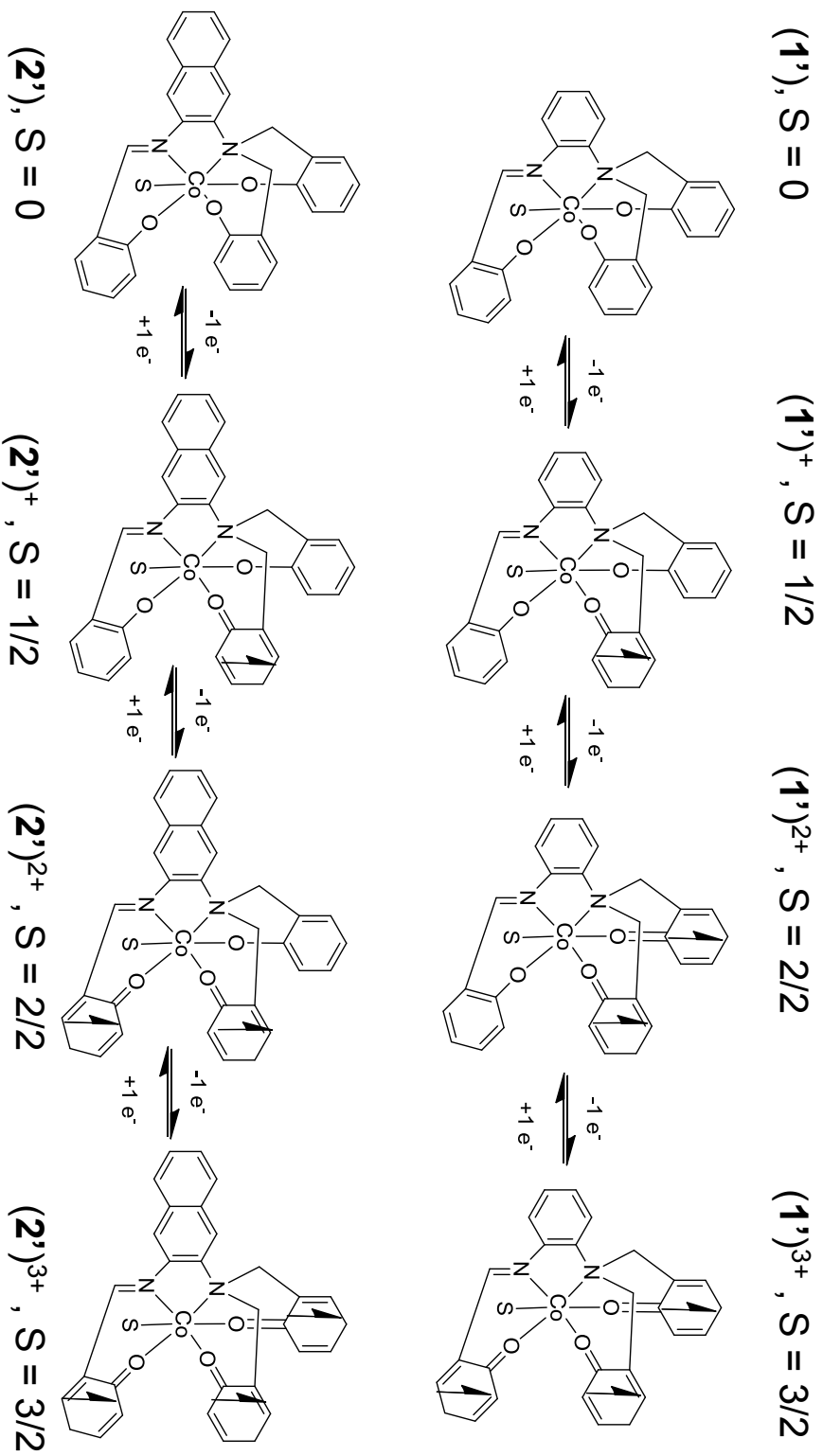
Figure 5.22. Electrochemical reactions for (**1'**) (top) and (**2'**)(bottom).

5.15. References

1.   (a) Lanznaster, M.; Heeg, M. J.; Yee, G. T.; McGarvey, B. R.; Verani, C. N., Design of Molecular Scaffolds Based on Unusual Geometries for Magnetic Modulation of Spin-Diverse Complexes with Selective Redox Response. *Inorg. Chem.* **2007,** *46* (1), 72-78; (b) Lanznaster, M.; Hratchian, H. P.; Heeg, M. J.; Hryhorczuk, L. M.; McGarvey, B. R.; Schlegel, H. B.; Verani, C. N., Structural and Electronic Behavior of Unprecedented Five-Coordinate Iron(III) and Gallium(III) Complexes with a New Phenol-Rich Electroactive Ligand. *Inorg. Chem.* **2006,** *45* (3), 955-957.

2.   Gagne, R. R.; Koval, C. A.; Lisensky, G. C., Ferrocene as an internal standard for electrochemical measurements. *Inorg. Chem.* **1980,** *19* (9), 2854-2855.

3.   Imbert, C.; Hratchian, H. P.; Lanznaster, M.; Heeg, M. J.; Hryhorczuk, L. M.; McGarvey, B. R.; Schlegel, H. B.; Verani, C. N., Influence of Ligand Rigidity and Ring Substitution on the Structural and Electronic Behavior of Trivalent Iron and Gallium Complexes with Asymmetric Tridentate Ligands. *Inorg. Chem.* **2005,** *44* (21), 7414-7422.

4.   Frisch, M. J.; Trucks, G. W.; Schlegel, H. B.; Scuseria, G. E.; Robb, M. A.; Cheeseman, J. R.; Scalmani, G.; Barone, V.; Mennucci, B.; Petersson, G. A.; Nakatsuji, H.; Caricato, M.; Li, X.; Hratchian, H. P.; Izmaylov, A. F.; Bloino, J.; Zheng, G.; Sonnenberg, J. L.; Hada, M.; Ehara, M.; Toyota, K.; Fukuda, R.; Hasegawa, J.; Ishida, M.; Nakajima, T.; Honda, Y.; Kitao, O.; Nakai, H.; Vreven, T.; Montgomery, J. A.; Peralta, J. E.; Ogliaro, F.; Bearpark, M.; Heyd, J.; Brothers, J. E.; Kudin, K. N.; Staroverov, V. N.; Kobayashi, R.; Normand, J.; Raghavachari, K.; Rendell, A.; Burant, J.

C.; Iyengar, S. S.; Tomasi, J.; Cossi, M.; Rega, N.; Millam, J. M.; Klene, M.; Knox, J. E.; Cross, J. B.; Bakken, V.; Adamo, C.; Jaramillo, J.; Gomperts, R.; Stratmann, R. E.; Yazyev, O.; Austin, A. J.; Cammi, R.; Pomelli, C.; Ochterski, J. W.; Martin, R. L.; Morokuma, K.; Zakrzewski, V. G.; Voth, G. A.; Salvador, P.; Dannenberg, J. J.; Dapprich, S.; Parandekar, P. V.; Mayhall, N. J.; Daniels, A. D.; Farkas, O.; Foresman, J. B.; Ortiz, J. V.; Cioslowski, J.; Fox, D. J., *Gaussian G09* Wallingford CT, 2009.

5.   (a) Krishnan, R.; Binkley, J. S.; Seeger, R.; Pople, J. A., Self-consistent molecular orbital methods. XX. A basis set for correlated wave functions. *J. Chem. Phys.* **1980,** *72* (1), 650-654; (b) Perdew, J. P., Density-functional approximation for the correlation energy of the inhomogeneous electron gas. *Phys. Rev. B* **1986,** *33*, 8822; (c) Becke, A. D., Density-functional exchange-energy approximation with correct asymptotic behavior. *Phys. Rev. A: Gen. Phys.* **1988,** *38* (6), 3098-100; (d) Becke, A. D., Density-functional thermochemistry. III. The role of exact exchange. *J. Chem. Phys.* **1993,** *98* (7), 5648-52.

6.   (a) Miertus, S.; Scrocco, E.; Tomasi, J., Electrostatic interaction of a solute with a continuum - a direct utilization of abinitio molecular potentials for the prevision of solvent effects. *Chem. Phys.* **1981,** *55* (1), 117-129; (b) Miertus, S.; Tomasi, J., Approximate evaluations of the electrostatic free-energy and internal energy changes in solution processes. *Chem. Phys.* **1982,** *65* (2), 239-245; (c) Cossi, M.; Rega, N.; Scalmani, G.; Barone, V., Energies, structures, and electronic properties of molecules in solution with the C-PCM solvation model. *J. Comput. Chem.* **2003,** *24* (6), 669-681; (d) Tomasi, J.; Mennucci, B.; Cammi, R., Quantum Mechanical Continuum Solvation Models. *Chem. Rev.* **2005,** *105* (8), 2999-3094.

7.   Blaudeau, J.-P.; McGrath, M. P.; Curtiss, L. A.; Radom, L., Extension of Gaussian-2 (G2) theory to molecules containing third-row atoms K and Ca. *J. Chem. Phys.* **1997,** *107* (13), 5016-5021.

8.   (a) Eichhorn, E.; Rieker, A.; Speiser, B.; Stahl, H., Electrochemistry of Oxygenation Catalysts. 3.1 Thermodynamic Characterization of Electron Transfer and Solvent Exchange Reactions of Co(salen)/[Co(salen)]+ in DMF, Pyridine, and Their Mixtures. *Inorg. Chem.* **1997,** *36* (15), 3307-3317; (b) Rohrbach, D. F.; Heineman, W. R.; Deutsch, E., Thin-layer spectroelectrochemical studies of cobalt and copper Schiff base complexes. *Inorg. Chem.* **1979,** *18* (9), 2536-2542.

9.   (a) Allard, M. M.; Odongo, O. S.; Lee, M. M.; Chen, Y.-J.; Endicott, J. F.; Schlegel, H. B., Effects of Electronic Mixing in Ruthenium(II) Complexes with Two Equivalent Acceptor Ligands. Spectroscopic, Electrochemical, and Computational Studies. *Inorg. Chem.* **2010,** *49* (15), 6840-6852; (b) Hindo, S. S.; Shakya, R.; Rannulu, N. S.; Allard, M. M.; Heeg, M. J.; Rodgers, M. T.; da Rocha, S. R. P.; Verani, C. N., Synthesis, Redox, and Amphiphilic Properties of Responsive Salycilaldimine-Copper(II) Soft Materials. *Inorg. Chem.* **2008,** *47* (8), 3119-3127; (c) Shakya, R.; Hindo, S. S.; Wu, L.; Allard, M. M.; Heeg, M. J.; Hratchian, H. P.; McGarvey, B. R.; da Rocha, S. R. P.; Verani, C. N., Archetypical Modeling and Amphiphilic Behavior of Cobalt(II)-Containing Soft-Materials with Asymmetric Tridentate Ligands. *Inorg. Chem.* **2007,** *46* (23), 9808-9818; (d) Pierpont, C. G.; Lange, C. W., The Chemistry of Transition Metal Complexes Containing Catechol and Semiquinone Ligands. In *Prog. Inorg. Chem.*, Kenneth, D. K., Ed. 2007; pp 331-442; (e) Solomon, E. I.; Decker, A.; Lehnert, N., Non-

heme iron enzymes: Contrasts to heme catalysis. *Proc. Natl. Acad. Sci. U. S. A.* **2003,** *100* (7), 3589-3594.

10.   (a) da Cunha, C. J.; Dodsworth, E. S.; Monteiro, M. A.; Lever, A. B. P., Bis(2,2'-bipyridine)(1,2-diimino-9,10-anthraquinone)ruthenium(II) Derivatives: A ZINDO Analysis of a Redox Series Involving Coupled Proton and Electron Transfers. *Inorg. Chem.* **1999,** *38* (23), 5399-5409; (b) Kalinina, D.; Dares, C.; Kaluarachchi, H.; Potvin, P. G.; Lever, A. B. P., Spectroscopic, Electrochemical, and Computational Aspects of the Charge Distribution in Ru(acac)2(R-o-benzoquinonediimine) Complexes. *Inorg. Chem.* **2008,** *47* (21), 10110-10126; (c) Metcalfe, R. A.; Lever, A. B. P., Tetraammineruthenium(II) and -ruthenium(III) Complexes of o-Benzoquinone Diimine and Their Redox Series. *Inorg. Chem.* **1997,** *36* (21), 4762-4771; (d) Rusanova, J.; Rusanov, E.; Gorelsky, S. I.; Christendat, D.; Popescu, R.; Farah, A. A.; Beaulac, R.; Reber, C.; Lever, A. B. P., The Very Covalent Diammino(o-benzoquinonediimine) Dichlororuthenium(II). An Example of Very Strong π-Back-Donation. *Inorg. Chem.* **2006,** *45* (16), 6246-6262.

APPENDIX A

Supplementary for Electronic and Redox Behavior of Low-Symmetry Iron(III)

Complexes with [N$_2$O$_3$] Electroactive Ligands (Chapter 4)

A.4.1. Simulation of EPR Spectra.

In figure S1 are given labels for the features found in all of the spectra that will be discussed. All spectra contain A, B, C, and D while the free radical is found only after oxidation or electrolysis. The main change seems to be in the position of B. It was found impossible to get a satisfactory simulation mostly due to the fact that there are five different parameters to adjust. A good assignment of these five parameters would require a high field spectrometer with variable frequencies.
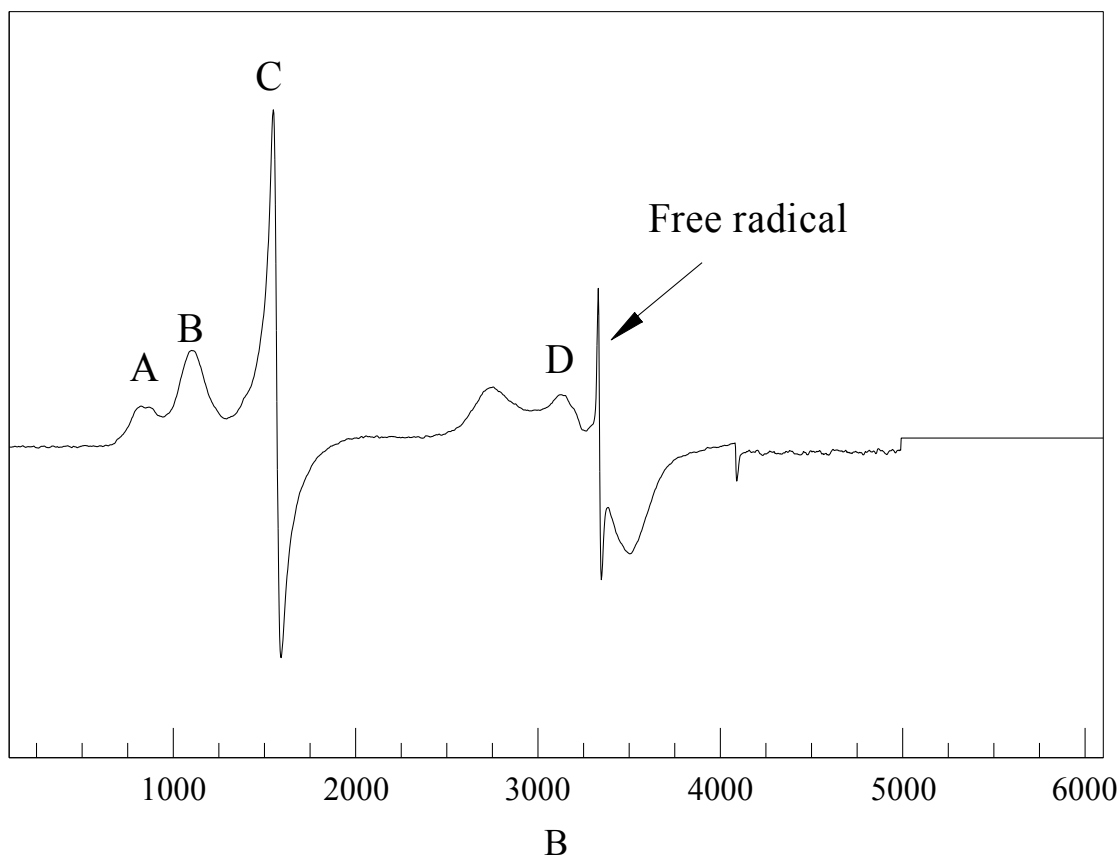
Figure A.4.1. EPR spectra of (**2**)$^+$ in dichloromethane.

In simulating the spectra it was assumed that the spin Hamiltonian for S = 5/2 to be

$$H = \beta_e \hat{S} \cdot g \cdot B + D\{\hat{S}_z^2 - \tfrac{1}{3}S(S+1)\} + E\{\hat{S}_x^2 - \hat{S}_y^2\} + B_4^0 \hat{O}_4^0 + B_4^2 \hat{O}_4^2 + B_4^4 \hat{O}_4^4 \qquad (1)$$

The $\hat{O}_4^m$ spin operators are given in several references. The g value is taken as 2.0023 in Equation (1) but this still leaves five adjustable parameters; D, E, B_4^0, B_4^2 and B_4^4. By convention, $|E|$ has values between zero and $|D|/3$. For $|D|$ values greater than 5000 gauss the A, B, C portion of the spectrum is generally seen in different forms. When $|E| = |D|/3$ the C peak is predominate as can be seen in **Figure A.4.2** below.
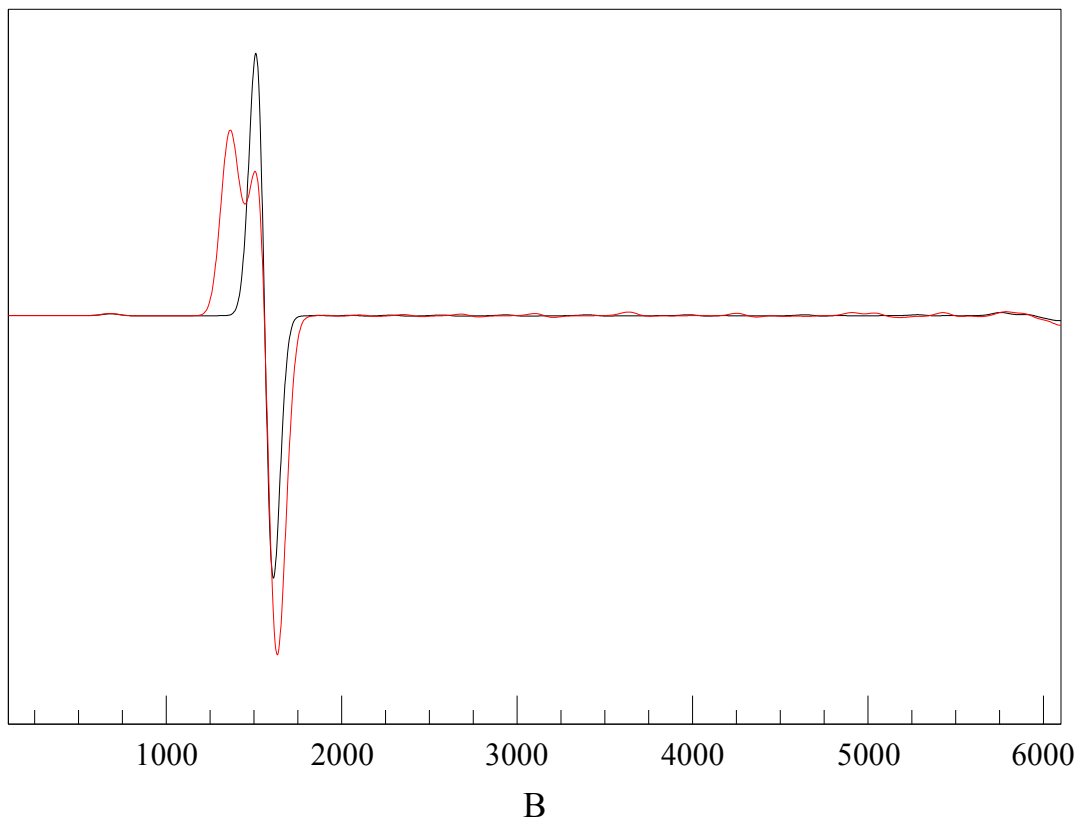
Figure A.4.2. Compound (**2**) (black) was simulated with $D = 6000$ gauss, E = 2000 gauss and B_4^0, B_4^2, $B_4^4 = 0$. red was simulated with $D = 6000$ gauss, $E = 2000$ gauss and $B_4^0 = 12$ gauss, $B_4^2 = 0$, $B_4^4 = 6$ gauss.

When E is less than $D/3$, the C peak splits into three parts but changing the B_4^m parameters can change the appearance as can be seen in red in the Figure (2). The apparent B feature is not in the field region seen in the experimental spectra. Please note that a weak A feature can be seen also. I can find no set of parameters that give the D part of the experimental spectrum when E is close to $D/3$. If we take smaller values of E we can get all four features (A, B, C, D) but the fit is bad. Particularly the A feature becomes too intense. This can be seen below in **Figure A.4.3.**
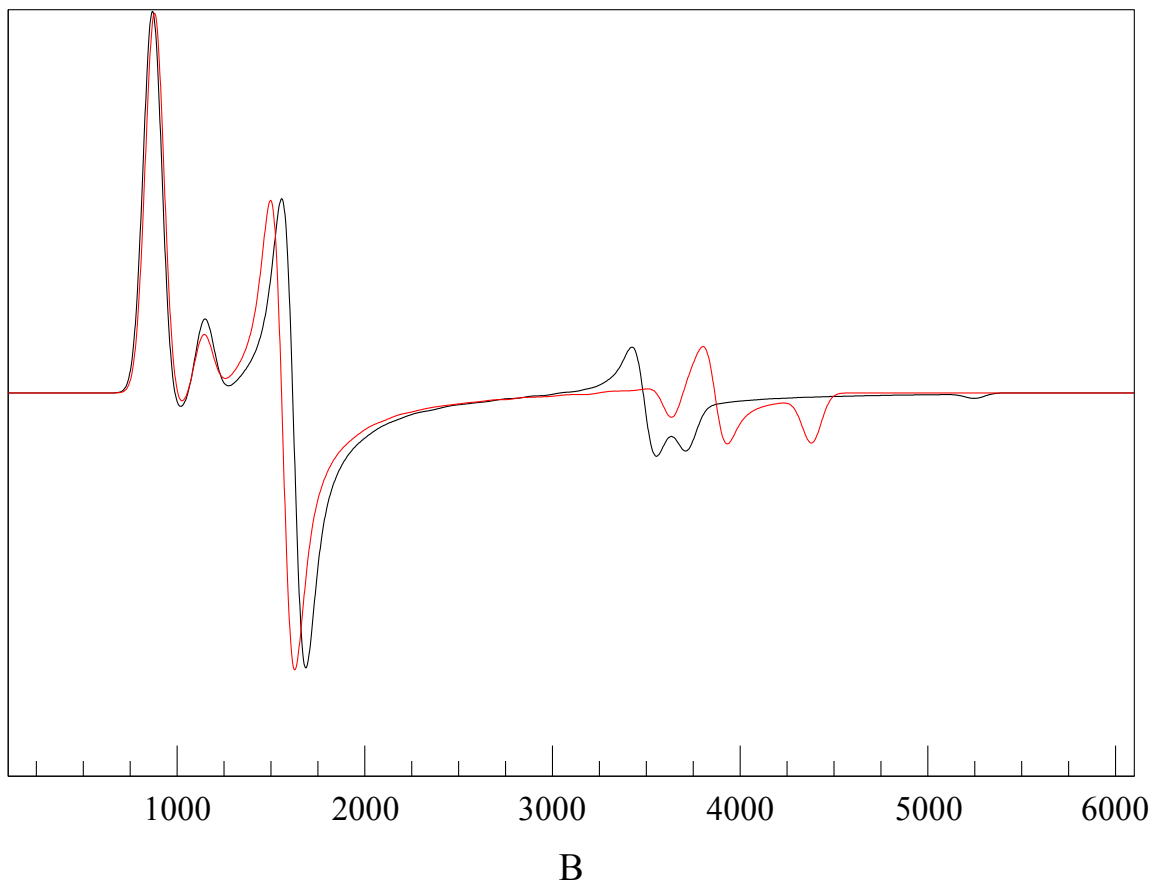
Figure A.4.3. Compound (**2**) (black) was simulated with $D = 5500$ gauss, $E = 230$ gauss and $B_4^0 = 10$ gauss, $B_4^2 = -10$ gauss, $B_4^4 = 5$ gauss. Red was simulated with $D = 15,000$ gauss, $E = 1000$ gauss and $B_4^0 = 10$ gauss, $B_4^2 = -10$ gauss, $B_4^4 = 5$ gauss.

This summarized the problems encountered for simulating these EPR spectra. There may be a mixture of different compounds in sample, but the only way to do this analysis is to go to a high magnetic field system that can detect the higher field portion of the spectrum and determining the affect of changing the frequency of the spectrometer on these transitions.

A.4.5. MASS SIMULATION
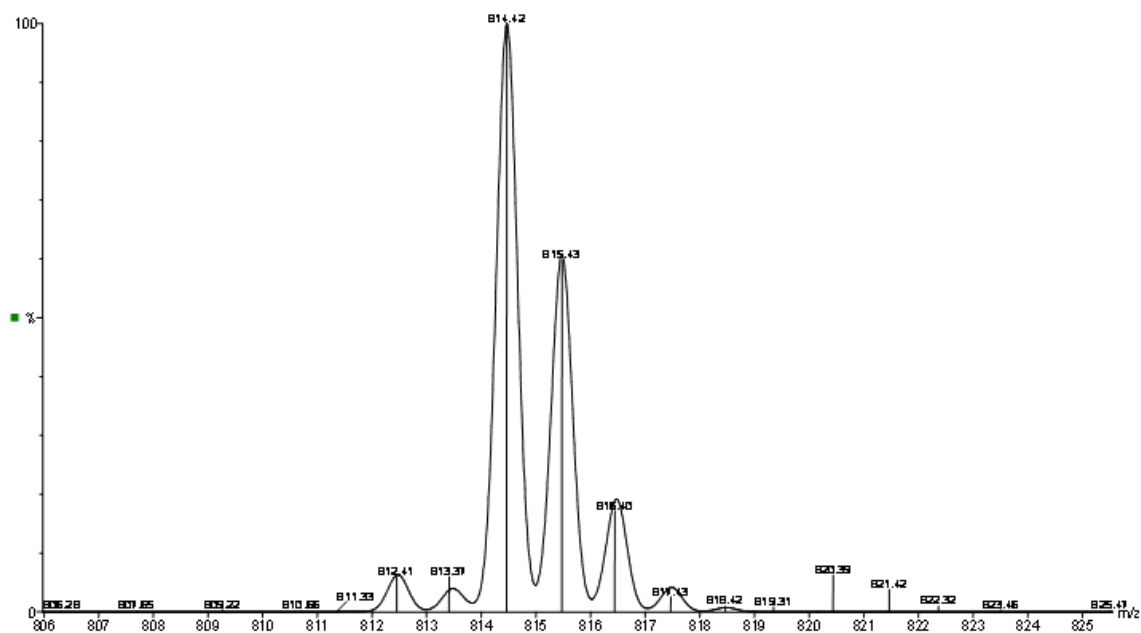
Figure A.4.4.Mass Spectrometry simulation with spectra for **(1)** [$C_{57}H_{71}N_4O_3Fe$] = M/z = 814.4, Cone 20.
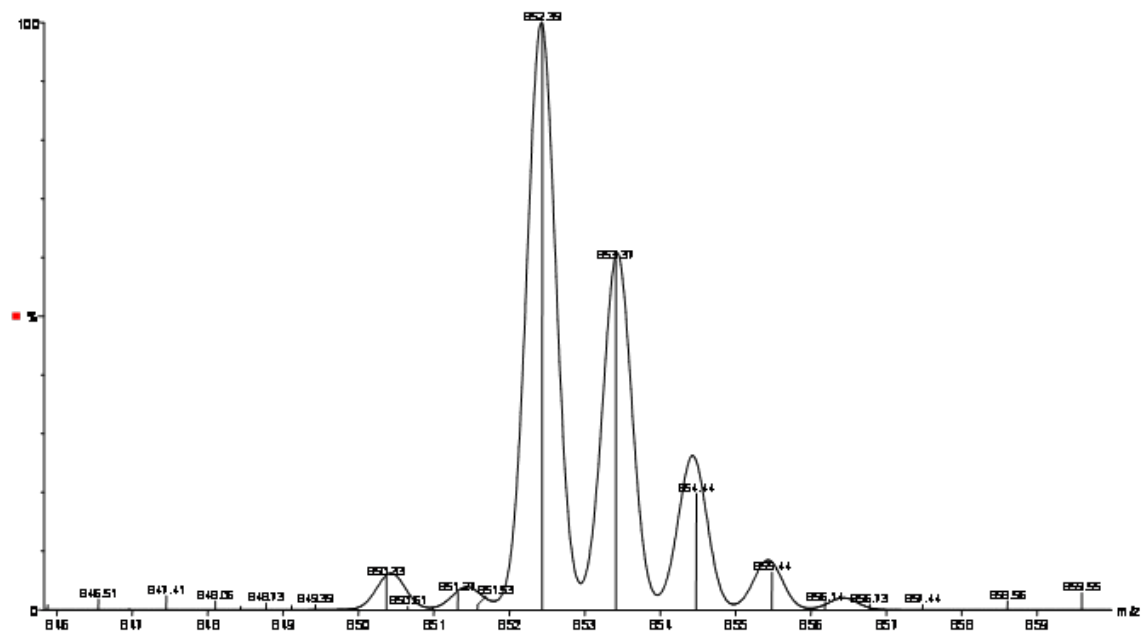
Figure A.4.5. Mass Spectrometry simulation with spectra for **(1)** [$C_{57}H_{71}N_4O_3Fe$] + K = M/z = 852.4, Cone 20.

Table A.4.3. Mulliken charge and spin analysis for Gas Phase **(1')**, **(1')⁺**, **(2')**, **(2')⁺** and **(2')²⁺**

	Mulliken Spins	Mulliken Charge	Fe-O	C(ring)-O
(1') (S = 5/2)				
Fe (III)	4.18	1.24		
Ring A	0.25	-0.37	1.84	1.34
Ring A'	0.24	-0.38	1.86	1.33
Ring B	0.17	-0.24	1.92	1.30
(1')⁺ (S = 4/2)				
Fe (III)	4.14	1.38		
Ring A	-0.17	-0.08	1.86	1.32
Ring A'	-0.40	0.02	1.90	1.30
Ring B	0.24	-0.13	1.87	1.31
(2') (S = 5/2)				
Fe (III)	4.17	1.30		
Ring A	0.23	-0.39	1.86	1.33
Ring A'	0.23	-0.40	1.86	1.33
Ring B (CH₃)	0.24	-0.40	1.87	1.33
(2')⁺ (S = 4/2)				
Fe (III)	4.06	1.19		
Ring A	0.26	-0.25	1.82	1.34
Ring A'	0.20	-0.20	1.84	1.33
Ring B	-0.69	0.13	1.95	1.28
(2')²⁺ (S = 3/2)				
(DCM)				
Fe (III)	4.12	1.39		
Ring A	-0.90	0.27	1.96	1.28
Ring A'	0.45	-0.19	1.82	1.34
Ring B	-0.49	0.27	1.97	1.28

A.4.6. CARTESIAN COORDINATES

(1') (DCM): E = -2640.019060 a.u.

H	1.10416600	6.27678300	0.44848900
C	1.12278600	5.27869900	0.01783700
C	0.21894500	4.31995000	0.47046400
C	2.05043300	4.96450600	-0.98040800
C	1.99370400	-2.00408900	3.01026900
H	3.35110600	-3.47641700	3.78719900
O	0.61476400	-0.32456900	2.05266000
C	3.18571400	-2.72491300	3.01920400
C	1.75786500	-1.02493800	2.02861600
H	2.46224600	1.29153100	0.54416700
C	0.22433500	3.02169100	-0.07184300
O	-0.66122200	2.11373300	0.35295200
C	4.16398400	-2.48629100	2.04951500
C	2.74507600	-0.77810800	1.04503400
C	2.06108000	3.67710100	-1.51965500
O	-2.24567700	0.03114800	1.48125500
C	3.93187700	-1.51783300	1.07148100
C	2.53701500	0.32283700	0.03941700
C	1.15808000	2.70084000	-1.08585000
C	-4.59885700	0.12322400	1.61235200
H	3.40103300	0.39079200	-0.63385700
H	2.77717500	3.42283900	-2.29844000
H	4.69105300	-1.32152500	0.31710700
H	-6.73575600	0.15444300	1.59525700
C	-3.40539000	-0.19564100	0.91875700
C	-5.83834200	-0.11029300	1.04180700
N	1.27297800	0.18881200	-0.75563800
C	1.12250500	1.33776200	-1.72473500
H	1.91262600	1.26036500	-2.48297400
H	0.16458800	1.17458100	-2.23223900
C	-3.52368900	-0.79164300	-0.38251900
N	-1.13298100	-1.04893200	-0.80318900
C	1.16769000	-1.06333000	-1.49048100
C	-5.95787400	-0.68553900	-0.24048100
H	3.21110500	-1.15446400	-2.16822200
C	-2.38776500	-1.23249900	-1.12773100
C	2.23823600	-1.63350800	-2.18083100
C	-4.81175000	-1.02331000	-0.93097500
C	-0.09823600	-1.67781800	-1.53285100
H	-2.60775700	-1.77942300	-2.04774200
H	-4.88065600	-1.47965900	-1.91583800
C	-0.25645600	-2.88770000	-2.22621100
C	2.06750800	-2.82363200	-2.88866000
H	-1.20971100	-3.40529000	-2.20407900

C	0.82039700	-3.45155000	-2.90520300
H	0.68823400	-4.39160700	-3.43234100
H	2.90996900	-3.26350300	-3.41343400
Fe	-0.50546600	0.27757800	0.69547200
H	-0.50645100	4.55240700	1.24495300
H	2.75726300	5.71031600	-1.33195900
H	-4.50804300	0.56352700	2.60051700
H	-6.93701300	-0.86424400	-0.67282700
H	5.09388400	-3.04734900	2.05294500
H	1.22690800	-2.17666000	3.75996300

(1') [+] **(DCM):** E= -2639.818265 a.u.

H	-1.72886200	6.29356400	-0.41661000
C	-1.62778500	5.28537500	-0.02933600
C	-0.75461800	4.39949100	-0.61075700
C	-2.40447900	4.87645400	1.07814000
C	-1.68294300	-2.29328100	-2.93864600
H	-2.92421900	-3.87494100	-3.69070200
O	-0.44764900	-0.49177200	-2.01581300
C	-2.83530800	-3.07250400	-2.96362000
C	-1.55627600	-1.24850000	-2.00683400
H	-2.47437400	1.10882600	-0.67432100
C	-0.62867600	3.05872400	-0.09383300
O	0.18493800	2.25618100	-0.66563700
C	-3.87446200	-2.82711800	-2.05916200
C	-2.60153500	-0.99453200	-1.08654800
C	-2.29622900	3.57085900	1.60070000
O	2.29061900	0.46416800	-1.29041800
C	-3.74727800	-1.79586300	-1.12855200
C	-2.49957900	0.15962500	-0.12721700
C	-1.42566600	2.65023700	1.05099100
C	4.64060600	0.61497900	-1.41365700
H	-3.38490500	0.19643500	0.51758900
H	-2.90564700	3.29258800	2.45513500
H	-4.55433700	-1.60209300	-0.42639900
H	6.77774900	0.67863500	-1.39146200
C	3.46391300	0.15815300	-0.78159800
C	5.88711100	0.31074200	-0.88935800
N	-1.25195000	0.13780400	0.71854500
C	-1.23625500	1.29263000	1.67927200
H	-2.01118500	1.14235200	2.43955700
H	-0.26910800	1.25930600	2.19593900
C	3.58996100	-0.63995800	0.40129200
N	1.20242300	-1.02335200	0.77256300
C	-1.09324500	-1.10676000	1.47251100
C	6.01946100	-0.46464100	0.27982700

H	-3.12514200	-1.22917700	2.18617600
C	2.46431300	-1.18770700	1.08637800
C	-2.14382800	-1.69136200	2.18053900
C	4.88261800	-0.93146000	0.90869900
C	0.18401400	-1.69391000	1.49289900
H	2.69860600	-1.79853200	1.95987700
H	4.96318100	-1.53771900	1.80759000
C	0.37340500	-2.90416600	2.17726400
C	-1.94011600	-2.87846900	2.88281100
H	1.33456100	-3.40540100	2.14363700
C	-0.68302700	-3.48703800	2.87089000
H	-0.52616400	-4.42599800	3.39248400
H	-2.76437700	-3.33205800	3.42369900
Fe	0.51976700	0.29976600	-0.67323400
H	4.53820200	1.21203200	-2.31407100
H	-0.14295100	4.66163900	-1.46724000
H	-3.09821000	5.57443100	1.53519900
H	7.00268300	-0.69406100	0.67683500
H	-0.86750700	-2.46754600	-3.63386700
H	-4.77312100	-3.43598900	-2.07634800

(1') $^{2+}$ (DCM): E= -2639.562428 a.u.

H	-1.65641800	6.32527700	-0.53117500
C	-1.57638300	5.32038000	-0.13150500
C	-0.70386600	4.41606000	-0.68502100
C	-2.38067500	4.93269400	0.96405800
C	-1.66485700	-2.49098700	-2.86962100
H	-2.97982500	-3.99113300	-3.64209500
O	-0.39059100	-0.77426200	-1.92219300
C	-2.85425200	-3.17234800	-2.94229200
C	-1.51101400	-1.40041800	-1.93803400
H	-2.48460700	1.08153700	-0.74483600
C	-0.61005100	3.07931500	-0.14800500
O	0.19616200	2.25482600	-0.70268700
C	-3.92138500	-2.80069300	-2.09330200
C	-2.61121300	-1.02836200	-1.06279400
C	-2.30039400	3.62818200	1.50730200
O	2.25803300	0.40393300	-1.28368700
C	-3.78714700	-1.73956500	-1.16715400
C	-2.49829800	0.16386200	-0.14645100
C	-1.43063500	2.69367400	0.98770800
C	4.60623400	0.51016100	-1.49633600
H	-3.38999600	0.22560900	0.48550900
H	-2.92922400	3.37184300	2.35417500
H	-4.63336000	-1.48434100	-0.53718400
H	6.74588500	0.54140400	-1.53044500

C	3.45055100	0.11458500	-0.79747800
C	5.86394200	0.22236400	-0.98290400
N	-1.25914900	0.16646300	0.69880900
C	-1.25938400	1.34520000	1.64006300
H	-2.04661200	1.20368200	2.38775400
H	-0.30078700	1.31324100	2.17108700
C	3.59036500	-0.60624900	0.43183900
N	1.20546400	-0.95350100	0.84712600
C	-1.10670200	-1.06264900	1.48652000
C	6.01443800	-0.47284700	0.23204900
H	-3.16111800	-1.21075500	2.14122100
C	2.47074900	-1.11242900	1.15756300
C	-2.16988100	-1.65004700	2.17353500
C	4.88960800	-0.88285200	0.92476700
C	0.18255100	-1.62029100	1.56377100
H	2.70857800	-1.69260300	2.04950100
H	4.98943000	-1.43028700	1.85813900
C	0.37599600	-2.80741900	2.28592400
C	-1.96210700	-2.81454800	2.91214200
H	1.34757000	-3.28861900	2.29885100
C	-0.69156000	-3.39404600	2.95925300
H	-0.53224100	-4.31382900	3.51262800
H	-2.79324700	-3.27222500	3.43819200
Fe	0.53409900	0.31703200	-0.62581000
H	4.48623300	1.04726300	-2.43111400
H	-0.07258100	4.65831000	-1.53295000
H	-3.07407800	5.64401500	1.40020700
H	7.00468500	-0.68899100	0.61810100
H	-0.81313100	-2.73541100	-3.49480400
H	-4.86252500	-3.33788100	-2.14629700

(2') (DCM): E = -2680.461138 a.u.

H	0.76410600	4.17069400	-3.61805000
C	0.31366700	3.41140800	-2.98615800
H	-1.64663700	4.31682100	-2.98743200
H	2.13030300	2.28987300	-2.81428600
C	-1.03483900	3.49209700	-2.63484600
C	1.08611300	2.34900000	-2.52592200
H	2.35706200	-0.14166100	-3.08367000
H	0.76769000	-0.92813900	-2.91518500
C	1.68259700	-0.65306300	-2.38707800
C	-1.60033600	2.50526500	-1.83307600
C	0.52796800	1.36103300	-1.70387700
H	-1.52939600	-0.92263100	-2.20984400
H	-2.65147200	2.56737900	-1.57293500
H	2.16784300	-1.55543600	-2.01516500

H	-2.96083400	0.09022300	-2.01337400
C	-0.82840100	1.43650400	-1.35974700
H	3.09233100	1.43675600	-1.14555900
N	1.32904200	0.22846700	-1.23495100
C	-2.23386500	-0.52583800	-1.46915900
H	5.24065800	0.74519200	-0.81421300
H	-4.87140900	-1.16285400	-1.59288500
C	2.56632500	0.71461700	-0.51281300
N	-1.42107100	0.37090400	-0.56206800
C	4.91115600	-0.16958700	-0.32544000
C	-2.94973000	-1.64694200	-0.76421700
C	-4.31903900	-1.85551300	-0.96115000
C	3.54121900	-0.36883000	-0.11925100
H	2.20107200	1.26001700	0.36425300
C	5.85673400	-1.10825500	0.08877700
H	-3.18863700	1.34153800	0.16208400
O	-0.91575200	-2.36679500	0.27103500
C	-2.22330300	-2.53746600	0.06137600
Fe	0.21858200	-0.87293900	0.36855400
C	-4.97954900	-2.93468200	-0.37248300
C	3.10337100	-1.56348700	0.50419700
C	-2.27702400	0.88317600	0.56493900
O	1.80978100	-1.82033900	0.68448000
C	5.42147200	-2.28275000	0.71098200
H	-3.05557500	3.38745100	1.28821800
C	4.06342000	-2.51192200	0.91124600
H	-2.59750200	-0.00642500	1.11704200
H	6.14382300	-3.02747300	1.03617600
C	-2.89518000	-3.62243100	0.65558000
C	-4.25688800	-3.81719900	0.43700100
C	-1.57168600	1.84695700	1.47881500
C	-2.12573100	3.09707900	1.77302000
H	-4.75834500	-4.66086900	0.90470900
O	0.20757400	0.27772900	1.85171400
C	-0.36227600	1.46162600	2.10428500
C	-1.51785400	3.96676400	2.67966100
C	0.24756400	2.34292500	3.01731600
C	-0.32618400	3.58000700	3.30056400
H	0.16011100	4.24570800	4.00935900
H	6.91487200	-0.92839100	-0.07669100
H	3.71164300	-3.42449900	1.38412300
H	1.17148500	2.02992500	3.49537100
H	-1.96631500	4.93184400	2.89638200
H	-2.32462500	-4.29937300	1.28508800
H	-6.04232600	-3.08258300	-0.53987300

(2')⁺ (DCM): E = -2680.261785 a.u.

H	-4.90988100	-4.46491800	1.01611100
C	-4.41954900	-3.61410300	0.55075100
C	-3.02907600	-3.52591100	0.57577100
C	-5.18232300	-2.61559700	-0.06238700
C	0.69002000	2.12815000	2.98995900
H	0.85333700	3.97002400	4.08274300
O	0.36401600	0.15361900	1.71098400
C	0.25054200	3.38820400	3.39075400
C	-0.07865200	1.36404100	2.09698000
H	-2.53770200	0.14583000	1.26036200
C	-2.38289200	-2.43199200	-0.02098900
O	-1.04228800	-2.34816500	-0.00640300
C	-0.95597900	3.90252800	2.90771600
C	-1.30187200	1.87317400	1.60830400
C	-4.53978700	-1.52644100	-0.65378000
O	1.75170100	-2.02515200	0.43064300
C	-1.71904100	3.14274700	2.01967900
C	-2.16773100	1.02369400	0.71974700
C	-3.14511000	-1.42256400	-0.65003900
C	3.94809500	-2.71751800	0.84379100
H	-3.05182600	1.58929500	0.40450600
H	-5.12694500	-0.74717700	-1.13412100
H	-2.66064700	3.53589500	1.64374900
H	6.01491200	-3.20934900	1.09471600
C	2.99503800	-1.74720500	0.35837100
C	5.29586300	-2.48096300	0.73563700
N	-1.46165800	0.47851200	-0.49841300
C	-2.44682600	-0.29282000	-1.35956700
H	-3.18784700	0.41277000	-1.75160100
H	-1.87093800	-0.66675200	-2.21344800
C	3.46879500	-0.50664100	-0.23467500
N	1.26188700	0.17594900	-1.33575400
C	-0.83409100	1.51905600	-1.30986700
C	5.74601900	-1.27938000	0.14471300
H	-2.59154100	2.76450500	-1.39891300
C	2.52858900	0.60161600	-0.64527700
C	-1.56186100	2.64344900	-1.71773400
C	4.83264000	-0.31606700	-0.33372500
C	0.49298800	1.36688500	-1.73501500
H	3.08544700	1.28746200	-1.29011400
H	5.21714700	0.59661600	-0.77902600
C	1.06505000	2.33525300	-2.56981700
C	-0.98220900	3.60923000	-2.53449700
H	2.08483200	2.22146500	-2.92202400
C	0.33564900	3.45259700	-2.96541100

H	0.79619000	4.19444000	-3.60994600
H	-1.56093000	4.47605700	-2.83739000
Fe	0.09459500	-0.90829300	0.22774800
H	3.54946700	-3.62846900	1.27689700
H	-2.42399400	-4.29212700	1.05119500
H	-6.26587800	-2.68218100	-0.07725100
H	6.81055100	-1.08989200	0.05375900
H	1.62357900	1.71393100	3.35898600
H	-1.29905400	4.88510400	3.21688300
H	2.22585100	1.16767200	0.24195300
C	1.55256000	-0.66569000	-2.53989100
H	2.23043600	-0.14920700	-3.22720800
H	2.00419200	-1.60833700	-2.22851600
H	0.61363300	-0.87708900	-3.05336200

(2')$^{2+}$ (DCM): E = -2680.041694 a.u.

C	3.74702500	-4.34555000	-0.45401700
H	4.14580100	-5.26456000	-0.86923600
C	2.47945800	-3.92674700	-0.77368700
C	4.54066800	-3.56548500	0.41735700
C	1.96206500	-2.69917900	-0.22130100
H	1.83528300	-4.48058500	-1.44768400
C	4.04945800	-2.36279900	0.97434900
H	5.54471100	-3.89201500	0.66734100
O	0.78347700	-2.32576100	-0.55739500
C	2.77778100	-1.91295600	0.68899400
H	4.68393700	-1.79735100	1.64983800
Fe	-0.26209500	-0.66537400	-0.45457600
C	2.21232500	-0.71185700	1.40474200
O	-0.35192000	0.78529500	-1.55624500
O	-1.94233600	-1.57545600	-0.92033400
N	1.45230200	0.26386500	0.54518000
N	-1.31280900	0.22330100	1.24612600
H	3.02643000	-0.18034900	1.90895400
H	1.52512100	-1.05229400	2.18752800
C	0.45536900	1.79807500	-1.90227300
C	-3.17495900	-1.34465000	-0.66933800
C	2.35809900	0.77785800	-0.55282400
C	0.91190700	1.32460300	1.40248100
C	-2.59132900	0.78821500	0.67958000
C	-0.44628300	1.30141500	1.75478000
C	-1.60545900	-0.75304100	2.34494400
C	-0.03925000	2.79547100	-2.76093500
C	1.77510100	1.87892700	-1.39816300
C	-4.16875600	-2.23326200	-1.22207300

C	-3.58216300	-0.23549700	0.17825100
H	2.59256600	-0.09568800	-1.17435400
H	3.30729600	1.10681100	-0.11662700
C	1.74430200	2.32439100	1.91385300
H	-3.09508900	1.39220600	1.43771600
H	-2.30213100	1.45757800	-0.13642600
C	-0.94470000	2.27270800	2.62934100
H	-2.21058000	-0.28081700	3.12541400
H	-2.14392800	-1.61231100	1.94224500
H	-0.66801800	-1.09255900	2.78435400
C	0.77235600	3.86449100	-3.12353900
H	-1.05578800	2.70454800	-3.13008100
C	2.56548700	2.96986200	-1.76861400
C	-5.49804800	-2.04194600	-0.93956500
H	-3.81687200	-3.04643400	-1.84730900
C	-4.92629800	-0.08980800	0.44830500
H	2.79581700	2.34407000	1.64958100
C	1.23454300	3.30235000	2.76362700
H	-1.98425200	2.25507200	2.93737900
C	-0.11186600	3.27326200	3.12491700
H	0.38764000	4.62910200	-3.79169100
C	2.07788000	3.95590600	-2.62852300
H	3.58001700	3.04307200	-1.38575000
H	-6.25061700	-2.70769200	-1.34749400
C	-5.88466500	-0.97230700	-0.10081300
H	-5.26434800	0.72154000	1.08538200
H	1.89032500	4.07790800	3.14532900
H	-0.51749500	4.02404100	3.79510700
H	2.71221100	4.79120500	-2.90741300
H	-6.93407300	-0.82224600	0.13036900

(1') (gas): E= -2640.003642 a.u.

H	1.18793900	6.25602500	0.45425300
C	1.19000100	5.25976800	0.01882800
C	0.27809200	4.31197700	0.47446300
C	2.10605400	4.94027300	-0.98816900
C	1.98467900	-2.01940500	2.99553200
H	3.33884100	-3.49118800	3.77577300
O	0.61001000	-0.34657900	2.02547400
C	3.17587200	-2.73920400	3.00759600
C	1.75325100	-1.04069600	2.01312000
H	2.46192300	1.27873900	0.53860000
C	0.26387400	3.01661400	-0.07332000
O	-0.62367400	2.11598400	0.35266400

C	4.15842500	-2.50128700	2.04240600
C	2.74540700	-0.79268100	1.03526900
C	2.09707800	3.65659500	-1.53344400
O	-2.26252900	0.06250500	1.47472000
C	3.93138500	-1.53225800	1.06535900
C	2.53824400	0.31051100	0.03320100
C	1.18576900	2.69025000	-1.09627600
C	-4.61144400	0.16111800	1.60884700
H	3.40479400	0.38086000	-0.63934300
H	2.80419900	3.39774000	-2.31958100
H	4.69431600	-1.33474900	0.31427800
H	-6.74569200	0.19952100	1.58866200
C	-3.41529000	-0.16259200	0.91635800
C	-5.84765700	-0.06955600	1.03773000
N	1.27598200	0.18052500	-0.76332100
C	1.12784700	1.32766300	-1.73239400
H	1.90934300	1.24020000	-2.50059200
H	0.16234100	1.17377000	-2.22913400
C	-3.53699200	-0.76409000	-0.38503800
N	-1.14524800	-1.03599300	-0.79427100
C	1.15510100	-1.07330700	-1.48613900
C	-5.97003700	-0.64813700	-0.24536200
H	3.19648700	-1.19537200	-2.15501500
C	-2.40259200	-1.20879600	-1.12225400
C	2.21817100	-1.66363000	-2.17054300
C	-4.82727600	-0.99102100	-0.93363400
C	-0.11756900	-1.67639700	-1.52028000
H	-2.62092700	-1.75131400	-2.04705800
H	-4.89803100	-1.44876500	-1.91844500
C	-0.28526700	-2.89141300	-2.20292200
C	2.03699000	-2.85758500	-2.86817600
H	-1.24213400	-3.40241800	-2.16888300
C	0.78419500	-3.47238000	-2.87842300
H	0.64280200	-4.41744500	-3.39479900
H	2.87563800	-3.31253400	-3.38670500
Fe	-0.51505200	0.29168000	0.71046900
H	-0.43903400	4.54560600	1.25547200
H	2.81896000	5.67963400	-1.34113500
H	-4.51425300	0.60417800	2.59464200
H	-6.95037900	-0.82311000	-0.67689200
H	5.08796400	-3.06301200	2.04994600
H	1.21278700	-2.18903600	3.74002600

(1')$^+$ (gas): E=-2639.732565

H	-1.22984000	6.33539100	-0.50121500
C	-1.22087900	5.33924300	-0.06980500

C	-0.33767100	4.38890400	-0.54284100
C	-2.11202700	5.02008900	0.97309700
C	-1.84018500	-2.05339800	-2.91518800
H	-3.11380900	-3.60941400	-3.65559500
O	-0.61964100	-0.24163500	-2.00288600
C	-2.98937600	-2.82421500	-2.91609800
C	-1.68662700	-1.01648800	-1.96137100
H	-2.48126000	1.29780600	-0.53447400
C	-0.32601500	3.07941500	0.02177300
O	0.52560700	2.19985200	-0.42060800
C	-3.99887300	-2.59429700	-1.96350800
C	-2.70487900	-0.78760500	-0.98533700
C	-2.11175800	3.73642100	1.53736700
O	2.23492000	0.17848500	-1.40377300
C	-3.84660000	-1.58537100	-1.00751700
C	-2.53495500	0.33697400	-0.00687700
C	-1.23736700	2.75541000	1.08431100
C	4.58032100	0.15130900	-1.65183600
H	-3.40427500	0.39486400	0.66016100
H	-2.80071400	3.50786600	2.34634100
H	-4.63211700	-1.41670800	-0.27551000
H	6.71458700	0.06257500	-1.71605200
C	3.40916400	-0.15174700	-0.92448700
C	5.82422800	-0.18742500	-1.14583700
N	-1.26957900	0.24195200	0.79507100
C	-1.15974600	1.40421300	1.74302400
H	-1.94476400	1.32089900	2.50585500
H	-0.19727700	1.28884900	2.25690600
C	3.53462200	-0.83932100	0.32950000
N	1.13651000	-1.02385200	0.79411000
C	-1.14895000	-1.00592600	1.54689500
C	5.95952900	-0.85095000	0.09311500
H	-3.16716300	-1.04874500	2.30432000
C	2.40146500	-1.25912000	1.07728400
C	-2.20423600	-1.54849600	2.28118700
C	4.82867300	-1.17383000	0.81246100
C	0.10630900	-1.64218600	1.54396000
H	2.61686900	-1.84124300	1.97574000
H	4.91373700	-1.69625300	1.76225800
C	0.26058900	-2.85764400	2.22978800
C	-2.03273500	-2.73893400	2.98729300
H	1.19779600	-3.40098800	2.17194000
C	-0.80090300	-3.39584900	2.95152700
H	-0.66945500	-4.33812300	3.47422500
H	-2.86133000	-3.15778200	3.54933200
Fe	0.52639400	0.31435800	-0.65081700

H	4.47269400	0.65958200	-2.60404600
H	0.36434800	4.60065600	-1.34243200
H	-2.80448100	5.76964900	1.34288200
H	6.94389900	-1.10808400	0.46933000
H	-1.04816200	-2.20165900	-3.64177600
H	-4.89664200	-3.20428200	-1.96630400

(2')(gas): E = -2680.443578

H	-0.57376	3.5716	5.25539
C	-0.13278	2.97814	4.45992
H	1.81071	3.90767	4.59985
H	-1.93815	1.88397	4.08887
C	1.20123	3.16406	4.09471
C	-0.90253	2.02697	3.79748
H	-2.18575	-0.53588	3.77028
H	-0.59879	-1.26174	3.41047
C	-1.51443	-0.86545	2.96694
C	1.7561	2.38563	3.08401
C	-0.35694	1.25505	2.76342
H	1.6203	-1.05509	2.76797
H	2.79772	2.52294	2.81476
H	-2.00639	-1.65085	2.39376
H	3.08392	-0.06395	2.78419
C	0.98839	1.4259	2.41112
H	-2.87967	1.52344	2.22871
N	-1.1612	0.2595	2.05764
C	2.34504	-0.54105	2.12591
H	-5.0094	0.90726	1.96392
H	4.97245	-1.09211	2.00839
C	-2.3944	0.9091	1.46287
N	1.56857	0.54517	1.41334
C	-4.76094	0.12119	1.25694
C	3.03455	-1.51784	1.21477
C	4.41789	-1.70266	1.30207
C	-3.41719	-0.04547	0.90495
H	-2.02216	1.59594	0.69316
C	-5.76225	-0.6804	0.71243
H	3.34716	1.63626	0.93603
O	0.93456	-2.05835	0.27053
C	2.25781	-2.27549	0.31379
Fe	-0.08518	-0.48745	0.22404
C	5.07237	-2.64845	0.51458
C	-3.02978	-1.05485	-0.00209
C	2.45297	1.25118	0.42676
O	-1.73615	-1.21664	-0.28221

C	-5.35231	-1.66966	-0.19976
H	3.14702	3.85405	0.31241
C	-4.0278	-1.8943	-0.58034
H	2.79989	0.47019	-0.2566
H	-6.11819	-2.30262	-0.63124
C	2.88897	-3.26362	-0.49479
C	4.27333	-3.40372	-0.36246
C	1.77812	2.3519	-0.34265
C	2.29492	3.64535	-0.33115
H	4.76754	-4.1466	-0.97665
O	0.17943	0.78154	-1.12336
C	0.67224	2.02861	-1.16273
C	1.75803	4.65731	-1.1338
C	0.1289	3.01594	-2.02737
C	0.69013	4.30022	-1.96865
H	0.27353	5.06103	-2.61353
H	-6.79131	-0.55	0.97499
H	-3.77179	-2.66472	-1.27733
H	-0.67528	2.78943	-2.69587
H	2.14363	5.65517	-1.1116
H	2.32821	-3.87176	-1.17348
H	6.1309	-2.7928	0.57439

(2')⁺ (gas): E= -2680.64525526

H	-4.92435600	-4.33332600	1.10081200
C	-4.43410600	-3.48932600	0.62375200
C	-3.04684900	-3.43721700	0.58084200
C	-5.20085300	-2.46469100	0.06220100
C	0.86820600	1.98401600	2.98520400
H	1.09978200	3.76890100	4.15344000
O	0.45757100	0.08142100	1.63200400
C	0.46630000	3.23019800	3.45403500
C	0.05579500	1.27765000	2.08883100
H	-2.44140500	0.12600200	1.31566100
C	-2.40944400	-2.35102700	-0.04048900
O	-1.08102300	-2.29481200	-0.11282700
C	-0.74304500	3.78582000	3.03573800
C	-1.17231100	1.82620500	1.66705400
C	-4.56829200	-1.38047900	-0.54847200
O	1.63877000	-2.10012600	0.16120700
C	-1.55115300	3.08089000	2.14612300
C	-2.08320500	1.02044700	0.79052300
C	-3.17837200	-1.31267000	-0.61326900
C	3.79011300	-2.75614200	0.80254200
H	-2.97811300	1.60283900	0.53605500

H	-5.16533300	-0.58446700	-0.98867900
H	-2.50147000	3.50573400	1.82919500
H	5.83009100	-3.24842400	1.22274000
C	2.88643000	-1.80160600	0.23305600
C	5.14454400	-2.51841800	0.80341800
N	-1.44163100	0.51524600	-0.47004300
C	-2.46798600	-0.19655600	-1.31932700
H	-3.19473100	0.54332900	-1.67819900
H	-1.92762100	-0.57230600	-2.19710100
C	3.39867500	-0.56682700	-0.30799500
N	1.20685600	0.16549300	-1.41136200
C	-0.82543600	1.56543400	-1.26395000
C	5.64131400	-1.32398000	0.25037900
H	-2.52744600	2.88403900	-1.20316500
C	2.49944900	0.55253500	-0.76912800
C	-1.52628500	2.72874100	-1.59282400
C	4.76869600	-0.36885400	-0.29578300
C	0.46511800	1.37608700	-1.76834900
H	3.07294800	1.18189600	-1.46060300
H	5.18261000	0.54953900	-0.70546000
C	1.02446700	2.33728500	-2.61531000
C	-0.95686500	3.69125900	-2.41720800
H	2.01658100	2.18929300	-3.03189300
C	0.31997300	3.49096500	-2.93815900
H	0.76825400	4.23097800	-3.59413500
H	-1.51280000	4.59208100	-2.65892800
Fe	0.09480500	-0.90962500	0.14942800
H	3.35972700	-3.66926100	1.20131700
H	-2.43396300	-4.22336400	1.01086000
H	-6.28495000	-2.50775400	0.10183100
H	6.71030400	-1.13289100	0.24581400
H	1.80036800	1.53162600	3.31094900
H	-1.05730300	4.75819600	3.40240600
H	2.23844600	1.18090000	0.09107400
C	1.42228300	-0.68945800	-2.60715700
H	2.09233900	-0.20360700	-3.32655500
H	1.85008300	-1.64570300	-2.30250600
H	0.46094900	-0.87271100	-3.09095000

A.4.7. Related compounds structure and synthesis
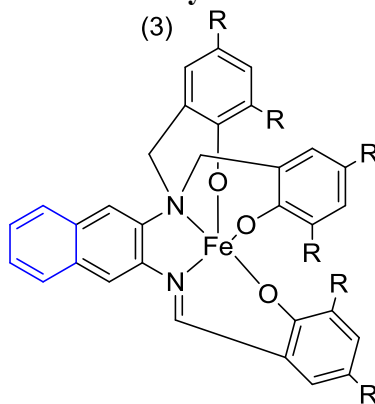
Figure A.4.6. Compound (3)

[FeL³] (3): $H_3L^{3'}$ (0.20 g, 0.25 mmol) $FeCl_3$ (0.032 g, 0.20 mmol) $NaOCH_3$ (0.040 g, 0.74 mmol) Yield = 0.179 g (82.6%). ESI (m/z$^+$) (in MeOH) = 864.7 for $[C_{55}H_{71}N_2O_3Fe + H^+]^+$. Anal. Calcd for $[C_{55}H_{71}N_2O_3Fe]$: C, 75.04; H, 8.44; N, 3.13%. Found: C, 75.06; H, 8.44; N, 3.13%. IR data (KBr, cm^{-1}): 2953(s) (C-H, alkane), 1602(s), (C=N); 1581(s), (C=C, aryl); 1252(s), (C-N); 1201(s), (C-O); 873(b), (C-H, phen).

[FeL³] (3) $[Fe(C_{55}H_{71}N_2O_3)]$ appeared as dark rods. A total of 92,860 reflections were recorded, of which 24,321 were unique. The asymmetric unit contains two independent iron complexes without counterions or solvents. One of *tert*-butyl groups was disordered over 3 positions and kept isotropic. Hydrogen positions were placed in observed and calculated positions for **1** and **3** and were calculated for **2**.

Table A.4.4. Crystal Data[a][1]

	[FeL^3] (3)
Formula	C$_{55}$H$_{71}$FeN$_2$O$_3$
M	863.99
Space group	P(-1)
a / Å	15.8704(5)
b/ Å	16.2473(4)
c/ Å	21.0057(6)
α/ °	84.049(1)
β/ °	71.559(1)
γ/ °	75.613(1)
V/ Å^3	4975.2(2)
Z	4
T/ K	100(2)
λ/ Å	0.71073
D_{calc}/ g cm^{-3}	1.153
μ/ mm^{-1}	0.346
$R(F)$ (%)	4.93
$Rw(F)$ (%)	10.08

[a] $R(F) = \sum\|F_o| - |F_c\| / \sum|F_o|$ for I > $2\sigma(I)$; $Rw(F) = [\sum w(F_o{}^2 - F_c{}^2)^2 / \sum w(F_o{}^2)^2]^{1/2}$ for I > $2\sigma(I)$.

Table A.4.5. Selected Bond Lengths(Å) and Angles for (3).

(3) [FeL^3]	
Fe-O1	1. 9107 (14)
Fe-O2	1. 8611 (14)
Fe-O3	1. 8664 (14)
Fe-N1	2.0746(17)
Fe-N2	2.2591(16)
N1-C7	1.309(3)
N2-C25	1.503(3)
N2-C18	1.493 (3)
O1-Fe-O2	102.56(6)
O1-Fe-O3	96.73(6)
O2-Fe-O3	115.66(6)
O1-Fe-N2	163.06(6)
O3-Fe-N2	88.77(6)
O2-Fe-N2	89.30(6)
O1-Fe-N1	86.81(6)
O3-Fe-N1	119.95(7)
O2-Fe-N1	121. 88 (7)
N2-Fe-N1	76.60(6)
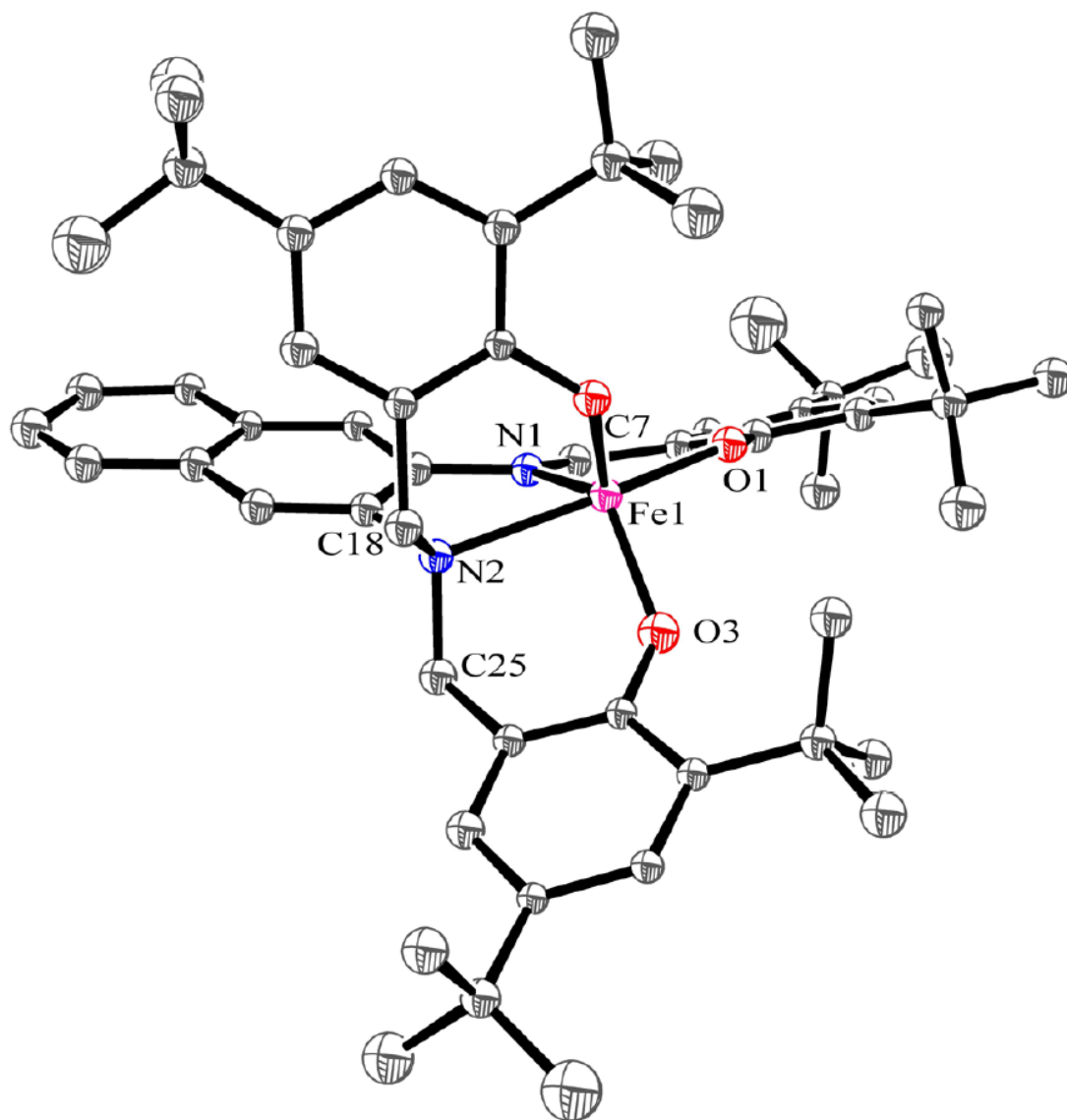
Figure A.4.7: ORTEP **(3) [FeL^3]**, Fe-O ≈ 1.88 Å, Fe-N1= 2.07Å, Fe-N2= 2.26Å, C7-N1= 1.309(3)Å.

Table A.4.6. Cyclic voltammetry values for **) [FeL^3]**.

Compound	Electrolyte	Process (vs. Fc+/Fc)			
		a) E1/2 (red.)	b) (1st Ox.)	c) (2nd Ox.)	c) (3 Ox.)
[Fe^{III}(L^{ox3})] **(3)**	TBAPF$_6$	-1.47V (ΔE 0.18V)	0.54V (ΔE 0.12V)	0.67V (ΔE 0.12V)	NA
[Fe^{III}(L^{ox3})] **(3)**	TBAClO$_4$	-1.41V (ΔE 0.14V)	0.56V (ΔE 0.18V)	NA	NA
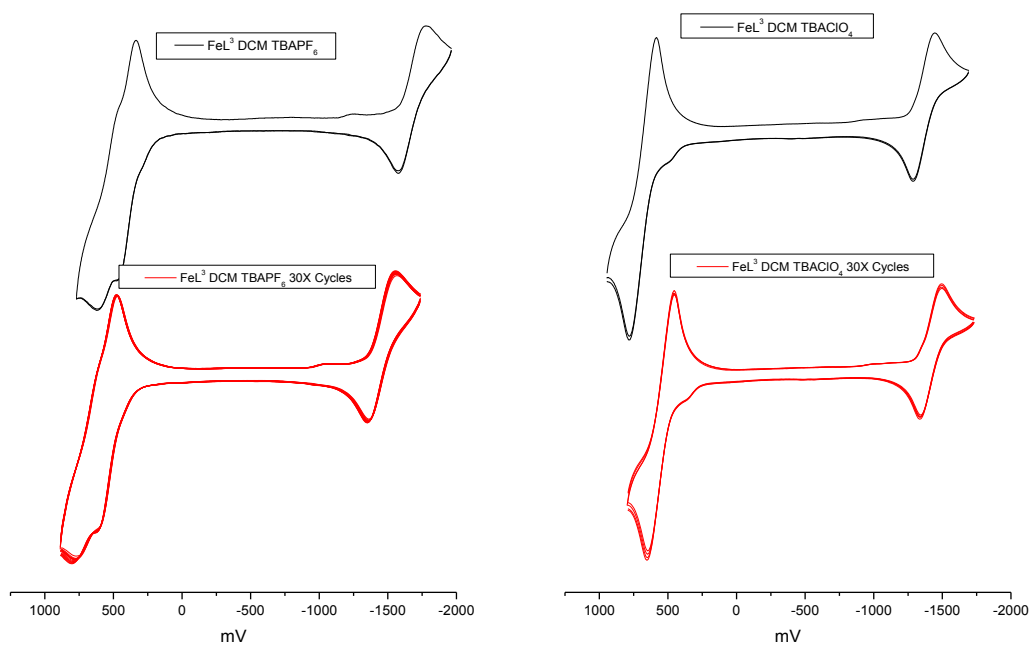
Figure A.4.8. Cyclic Voltamettry for [FeL^3].
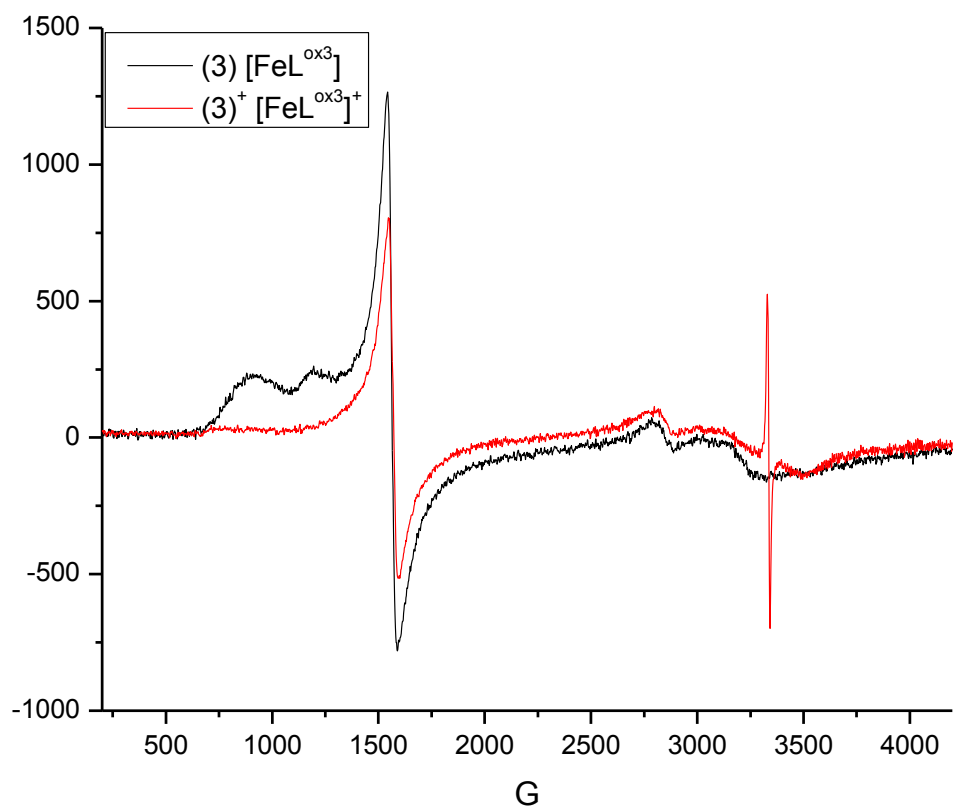
Figure A.4.9. EPR for (3) (Dichloromethane solution)
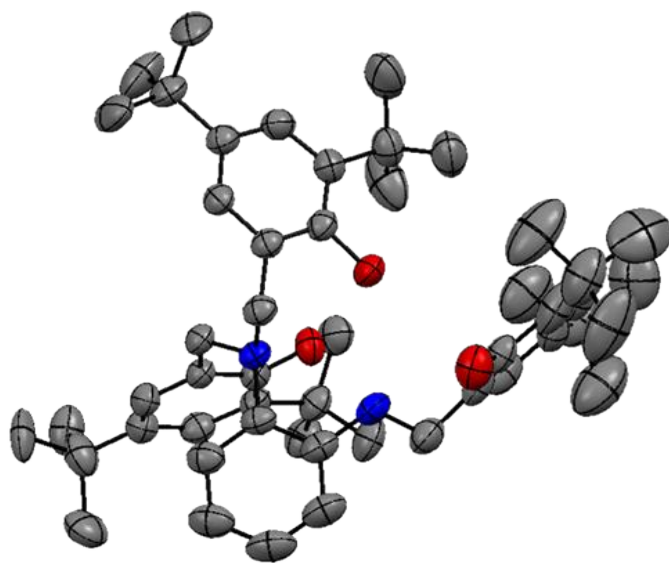
Figure A.4.10. ORTEP of H_3L^1.
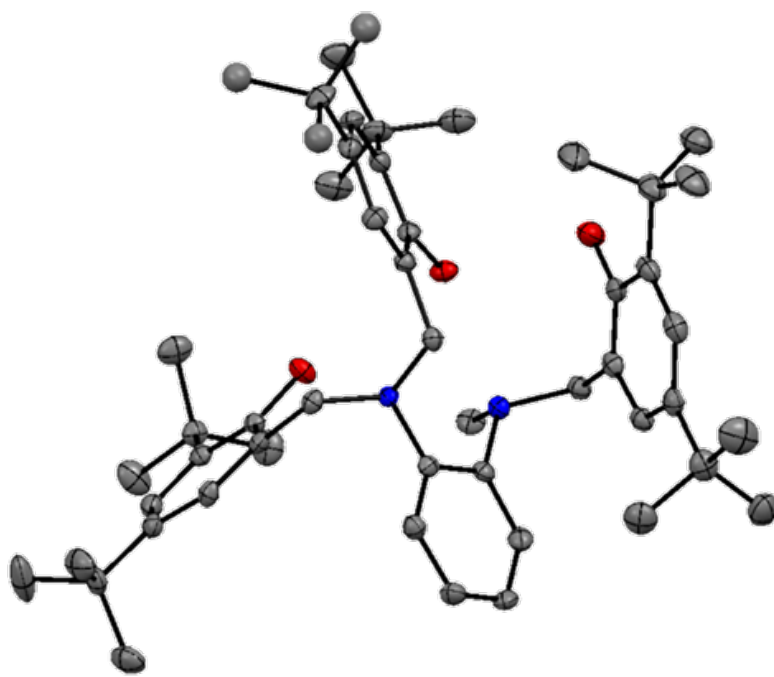
Figure A.4.11. ORTEP of H_3L^2.

Spin unrestricted density functional theory (DFT) calculations were carried out with the B3LYP[3-5] functional and the 6-31G(d)[6-15] basis set in the development version of Gaussian[16]. Solvation in dichloromethane was modeled with the integral equation formalism polarizable continuum model (IEF-PCM)[17-19]. Geometries were fully optimized without symmetry constraints, and stationary points were verified via frequency analysis. Vertical electronic excitation energies and intensities were calculated by time-dependent density functional theory (TD-DFT).[20,21] Molecular orbitals were plotted with GaussView.[22]

(1)   Hess, C. R.; Weyhermüller, T.; Bill, E.; Wieghardt, K. *Inorganic Chemistry* **2010**, *49*, 5686-5700.
(2)   Imbert, C.; Hratchian, H. P.; Lanznaster, M.; Heeg, M. J.; Hryhorczuk, L. M.; McGarvey, B. R.; Schlegel, H. B.; Verani, C. N. *Inorganic Chemistry* **2005**, *44*, 7414-7422.
(3)   Becke, A. D. *The Journal of Chemical Physics* **1993**, *98*, 5648-5652.
(4)   Lee, C.; Yang, W.; Parr, R. G. *Physical Review B* **1988**, *37*, 785.
(5)   Miehlich, B.; Savin, A.; Stoll, H.; Preuss, H. *Chemical Physics Letters* **1989**, *157*, 200-206.
(6)   Binning Jr., R. C.; Curtiss, L. A. *J. Comp. Chem.* **1990**, *11*, 1206-1216.
(7)   Blaudeau, J.-P.; McGrath, M. P.; Curtiss, L. A.; Radom, L. *Journal of Chemical Physics* **1997**, *107*, 5016-5021.
(8)   Ditchfield, R.; Hehre, W. J.; Pople, J. A. *Journal of Chemical Physics* **1971**, *54*, 724.
(9)   Francl, M. M.; Pietro, W. J.; Hehre, W. J.; Binkley, J. S.; DeFrees, D. J.; Pople, J. A.; Gordon, M. S. *Journal of Chemical Physics* **1982**, *77*, 3654-3665.
(10)   Gordon, M. S. *Chemical Physics Letters* **1980**, *76*, 163-168.
(11)   Hariharan, P. C.; Pople, J. A. *Theoretical Chemistry Accounts* **1973**, *28*, 213-222.
(12)   Hariharan, P. C.; Pople, J. A. *Mol. Phys.* **1974**, *27*, 209-214.
(13)   Hehre, W. J.; Ditchfield, R.; Pople, J. A. *Journal of Chemical Physics* **1972**, *56*, 2257.
(14)   Rassolov, V. A.; Pople, J. A.; Ratner, M. A.; Windus, T. L. *Journal of Chemical Physics* **1998**, *109*, 1223-1229.
(15)   Rassolov, V. A.; Ratner, M. A.; Pople, J. A.; Redfern, P. C.; Curtiss, L. A. *J. Comp. Chem.* **2001**, *22*, 976-984.
(16)   Frisch, M. J.; Trucks, G. W.; Schlegel, H. B.; Scuseria, G. E.; Robb, M. A.; Cheeseman, J. R.; Scalmani, G.; Barone, V.; Mennucci, B.; Petersson, G. A.; Nakatsuji, H.; Caricato, M.; Li, X.; Hratchian, H. P.; Izmaylov, A. F.; Bloino, J.; Zheng, G.; Sonnenberg, J. L.; Hada, M.; Ehara, M.; Toyota, K.; Fukuda, R.; Hasegawa, J.; Ishida, M.; Nakajima, T.; Honda, Y.; Kitao, O.; Nakai, H.; Vreven, T.; Montgomery, J. A., Jr.; Peralta, J. E.; Ogliaro, F.; Bearpark, M.; Heyd, J. J.; Brothers, E.; Kudin, K. N.; Staroverov, V.; Kobayashi, R.; Normand, J.; Raghavachari, K.; Rendell, A.; Burant, J. C.; Iyengar, S. S.; Tomasi, J.; Cossi, M.; Rega, N.; Millam, J. M.; Klene, M.; Knox, J. E.; Cross, J. B.; Bakken, V.; Adamo, C.; Jaramillo, J.; Gomperts, R.; Stratmann, R. E.; Yazyev, O.; Austin, A. J.; Cammi, R.; Pomelli, C.; Ochterski, J. W.; Martin, R. L.; Morokuma, K.; Zakrzewski, V. G.; Voth, G. A.; Salvador, P.; Dannenberg, J. J.; Dapprich, S.; Parandekar, P. V.; Mayhall, N. J.; Daniels, A. D.; Farkas, O.; Foresman, J. B.; Ortiz, J. V.; Cioslowski, J.; Fox, D. J.; Revision H.04 ed.; Gaussian, Inc.: Wallingford, CT, 2009.
(17)   Miertus, S.; Scrocco, E.; Tomasi, J. *Chem. Phys.* **1981**, *55*, 117-129.
(18)   Miertus, S.; Tomasi, J. *Chem. Phys.* **1982**, *65*, 239-245.
(19)   Tomasi, J.; Mennucci, B.; Cammi, R. *Chemical Reviews* **2005**, *105*, 2999-3094.
(20)   Vlcek , A., Jr; Zális, S. *Coord. Chem. Rev.* **2007**, *251* 258.
(21)   Grimme, S. In *Reviews in Computational Chemistry*; Kenny B. Lipkowitz, R. L. T. R. C., Ed., 2004; pp 153.
(22)   Gaussian Inc.
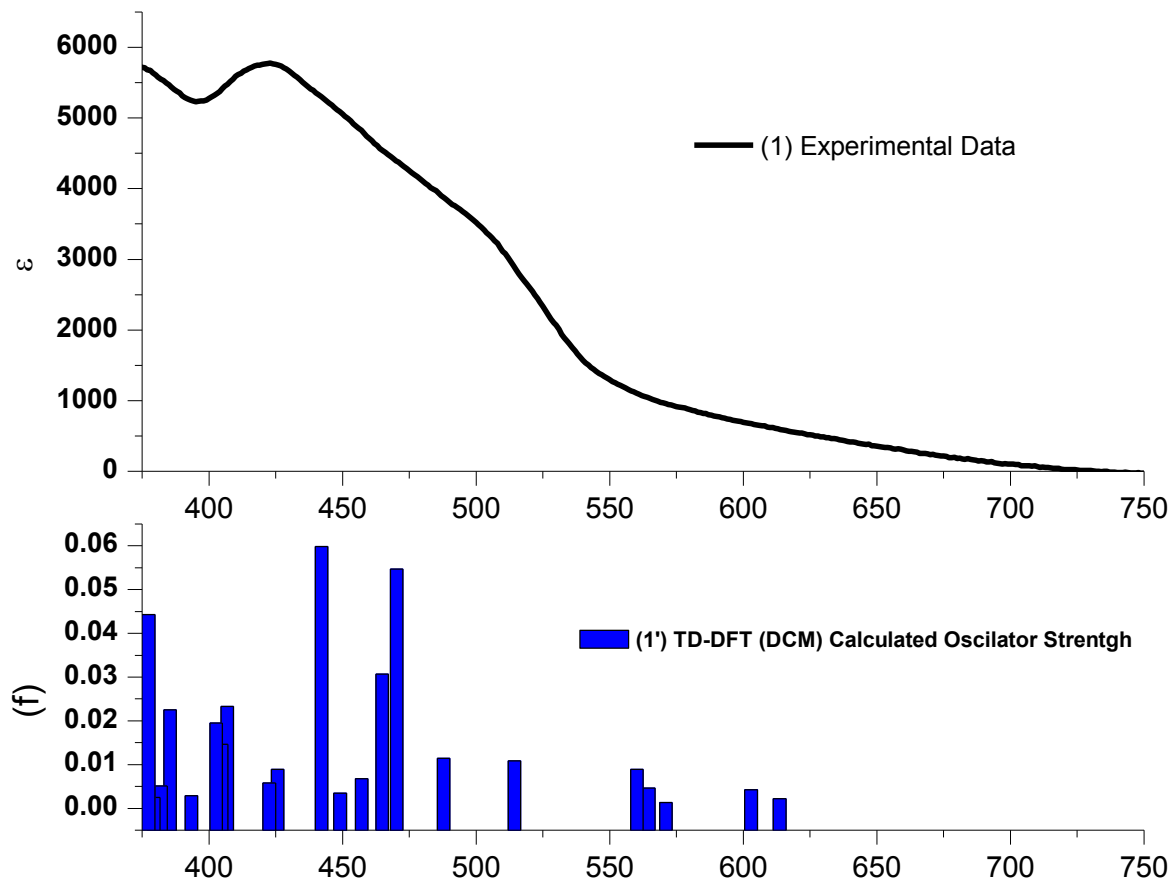
Figure A.Z. Experimental versus TD-DFT Absorption spectra **(1)** in dichloromethane. (B3LYP/6-31G(d) IEF-PCM)
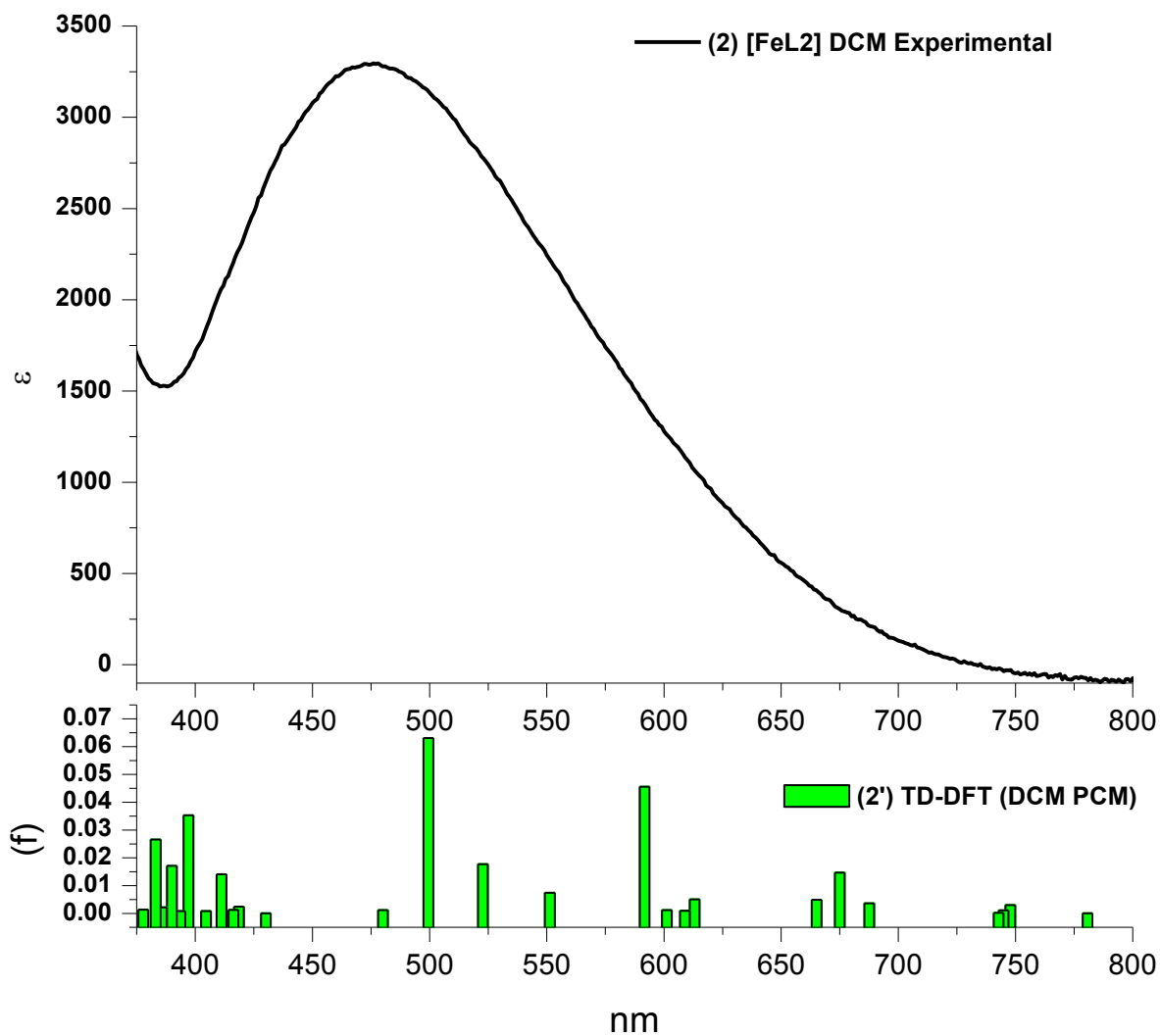
Figure A.Z. Experimental versus TD-DFT Absorption spectra **(2)** in dichloromethane. (B3LYP/6-31G(d) IEF-PCM)
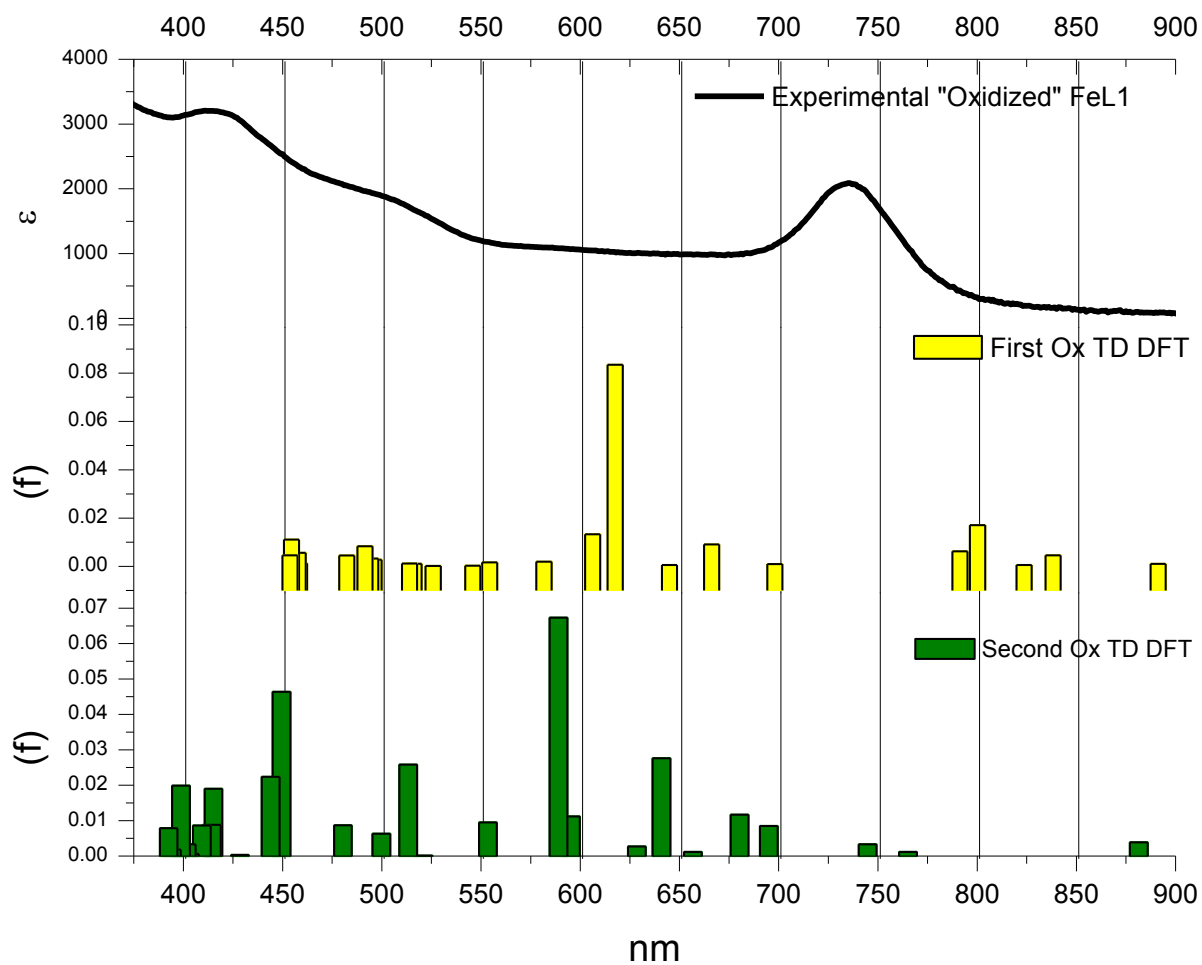
Figure A.Z. Absorption spectra **(1)**[+] (black) in dichloromethane compared to experimental versus TD-DFT for **(1')**[+] (yellow) and **(1')**[2+] (green). (B3LYP/6-31G(d) IEF-PCM)

Figure A.Z. Absorption spectra **(2)**[+] (black) in dichloromethane compared to experimental versus TD-DFT for **(2')**[+] (orange) and **(2')**[2+] (purple). (B3LYP/6-31G(d) IEF-PCM)

Table A.4.X. TD-DFT calculated Oscillator strength and assignments for **(1')**.
(B3LYP/6-31G(d) IEF-PCM)

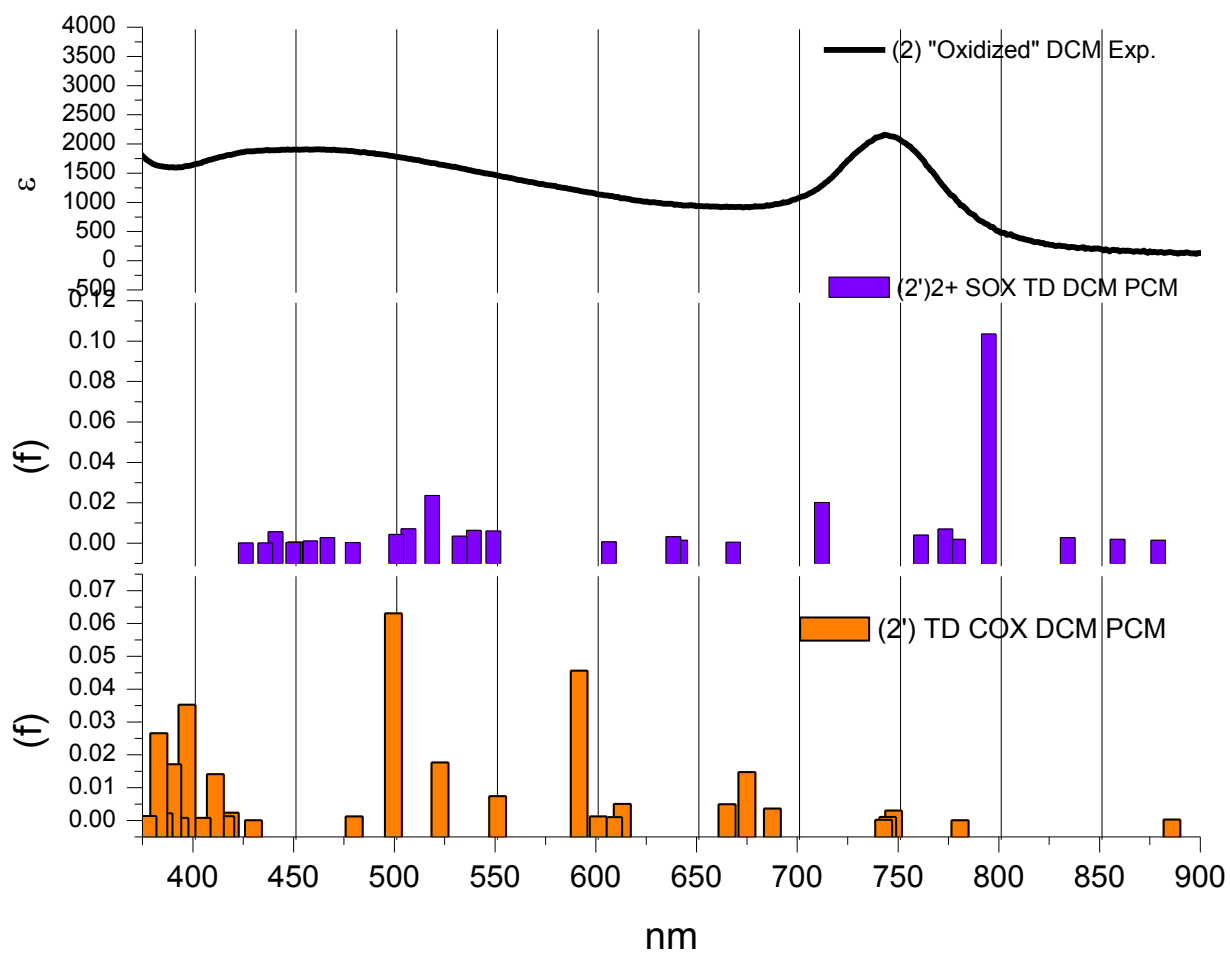| #	nm	1000 cm-1	(f)	Assignment
1	613.6	16.3	0.0022	121->122B(.898) 119->122B(.253) 120->122B(-.202) 124->127A(.169)
2	602.9	16.6	0.0042	120->122B(.847) 121->123B(.272) 121->122B(.252) 119->122B(-.196)
3	571.1	17.5	0.0013	121->123B(.71) 119->122B(-.379) 120->123B(.368) 120->122B(-.321)
4	564.6	17.7	0.0046	120->123B(.702) 121->123B(-.559) 119->123B(-.273) 119->122B(-.239)
5	560.2	17.9	0.0089	119->122B(.71) 120->123B(.418) 121->123B(.278) 121->122B(-.236)
6	514.3	19.4	0.0108	119->123B(.885) 120->123B(.388)
7	487.9	20.5	0.0114	124->127A(.576) 119->122B(-.372) 121->124B(.354) 126->127A(-.29)
8	470.3	21.3	0.0547	121->124B(.818) 121->125B(.321) 119->124B(-.26) 121->126B(-.197)
9	464.9	21.5	0.0307	120->124B(.635) 121->125B(-.51) 121->126B(-.271) 119->124B(-.243)
10	457.1	21.9	0.0068	120->125B(.627) 120->126B(.436) 120->124B(-.298) 121->125B(-.264)
11	449.1	22.3	0.0035	118->122B(.568) 120->125B(-.362) 123->127A(-.354) 117->122B(-.224)
12	442.2	22.6	0.0598	121->125B(.523) 120->124B(.434) 121->126B(.313) 120->125B(.308)
13	425.7	23.5	0.0089	119->124B(.728) 126->127A(.548) 120->124B(.25) 121->124B(.175)
14	422.6	23.7	0.0058	126->127A(.742) 119->124B(-.426) 124->127A(.297) 119->125B(-.283)
15	406.8	24.6	0.0233	125->127A(.611) 119->125B(.507) 119->126B(.266) 120->125B(.228)
16	404.8	24.7	0.0146	121->126B(.676) 119->125B(.318) 118->122B(.243) 125->127A(-.24)
17	402.7	24.8	0.0195	125->127A(.712) 124->127A(-.344) 121->126B(.304) 121->125B(-.224)
18	393.5	25.4	0.0029	120->126B(.686) 119->125B(.347) 120->127B(.309) 120->125B(-.25)
19	385.5	25.9	0.0225	115->122B(.448) 114->122B(.432) 118->122B(.345) 123->127A(.258)
20	382.1	26.2	0.0051	118->123B(.853) 117->123B(-.259) 119->125B(.191)
21	379.4	26.4	0.0025	117->122B(.828) 118->122B(.404) 114->122B(-.178) 119->126B(.176)
22	377.4	26.5	0.0443	119->126B(.712) 124->127A(-.284) 117->122B(-.259) 120->126B(.243)
23	371.9	26.9	0.0235	114->122B(.568) 117->122B(.353) 118->122B(-.322) 123->127A(-.291)
24	360.3	27.8	0.0017	116->122B(.751) 117->123B(-.361) 121->127B(.282) 114->123B(.248)
25	360.1	27.8	0.006	121->127B(.571) 116->122B(-.491) 114->123B(.387) 115->123B(.248)
26	359.5	27.8	0.002	117->123B(.849) 116->122B(.345) 118->123B(.312) 121->127B(.161)
27	355.5	28.1	0.028	121->127B(.486) 122->127A(-.354) 114->123B(-.301) 121->127A(-.293)
28	352.7	28.4	0.0281	114->123B(.428) 122->127A(-.36) 115->123B(.322) 121->127A(-.315)
29	350	28.6	0.0083	120->127B(.767) 121->127B(.277) 120->126B(-.238) 119->127B(-.234)
30	344.1	29.1	0.0042	119->127B(.365) 122->127A(-.336) 121->127A(-.318) 116->127A(-.285)

Table A.4.X. TD-DFT calculated Oscillator strength and assignments for (1')⁺.
(B3LYP/6-31G(d) IEF-PCM)

#	nm	1000 cm-1	(f)	Assignment
1	2630.4	3.8	0.0126	125->126A(.997)
2	1913.2	5.2	0.0081	124->126A(.994)
3	994.8	10.1	0.0019	121->126A(.914) 123->126A(.25) 116->126A(.22)
4	952.6	10.5	0.0004	123->126A(.958) 121->126A(-.249)
5	881.4	11.3	0.0039	122->126A(.975) 117->126A(.175)
6	765.1	13.1	0.0012	121->122B(.918) 120->122B(.249) 121->124B(.171)
7	744.8	13.4	0.0033	117->126A(.8) 120->126A(-.489) 119->126A(.22) 122->126A(-.198)
8	695	14.4	0.0085	121->123B(.912) 120->122B(.312)
9	680.3	14.7	0.0117	120->122B(.886) 121->123B(-.313) 121->122B(-.25)
10	656.8	15.2	0.0012	120->126A(.749) 119->126A(.42) 117->126A(.342) 116->126A(.223)
11	640.9	15.6	0.0276	120->123B(.824) 121->124B(.361) 116->126A(-.239) 120->124B(.185)
12	628.5	15.9	0.0027	116->126A(.674) 118->126A(-.349) 120->123B(.338) 120->126A(-.269)
13	595.3	16.8	0.0112	119->126A(.811) 117->126A(-.389) 120->126A(-.287) 118->126A(-.236)
14	589	17	0.0673	121->124B(.828) 120->123B(-.336) 121->125B(-.202)
15	553.5	18.1	0.0095	120->124B(.894) 121->125B(-.318) 120->123B(-.19)
16	521	19.2	0.0001	118->126A(.853) 116->126A(.401) 119->126A(.265)
17	513.3	19.5	0.0258	121->125B(.776) 120->125B(.361) 120->124B(.317) 119->122B(-.19)
18	499.8	20	0.0063	119->122B(.565) 124->127A(-.446) 125->127A(-.405) 120->126B(-.287)
19	480.4	20.8	0.0087	119->122B(.591) 120->125B(.497) 124->127A(.37) 125->127A(.286)
20	449.5	22.2	0.0464	120->125B(.642) 119->123B(-.506) 121->125B(-.25) 119->122B(-.237)
21	444	22.5	0.0224	119->123B(.808) 119->122B(-.314) 120->125B(.299) 121->126B(.172)
22	428.5	23.3	0.0003	118->122B(.982)
23	415.2	24.1	0.019	115->126A(.639) 119->124B(.372) 114->126A(-.338) 121->127B(.296)
24	414.4	24.1	0.0088	119->124B(.697) 115->126A(-.407) 121->127B(.26) 114->126A(.235)
25	409.3	24.4	0.0086	121->127B(.614) 121->126B(-.508) 119->124B(-.464)
26	403.3	24.8	0.0006	118->123B(.962)
27	401.7	24.9	0.0033	123->127A(.528) 119->126B(-.417) 119->124B(-.34) 117->122B(.242)
28	398.8	25.1	0.0199	125->127A(.713) 120->126B(-.481) 124->127A(-.284) 120->127B(.251)
29	394.2	25.4	0.0018	117->122B(.755) 118->124B(-.339) 120->127B(.25) 124->127A(.235)
30	392.6	25.5	0.0079	118->124B(.835) 120->127B(.275) 124->127A(.251) 120->126B(-.228)

Table A.4.X. TD-DFT calculated Oscillator strength and assignments for **(1')**[2+].
(B3LYP/6-31G(d) IEF-PCM)

#	nm	1000 cm-1	(f)	Assignment
1	1953	5.1	0.0057	124->125A(.989)
2	1591.5	6.3	0.0023	124->126A(.993)
3	1069.1	9.4	0.0115	121->122B(.947) 121->123B(.208)
4	1047.6	9.5	0.0008	123->125A(.982)
5	929.6	10.8	0.0038	121->123B(.866) 121->124B(-.421)
6	919.5	10.9	0.0001	123->126A(.983)
7	891.2	11.2	0.001	122->125A(.914) 121->125A(-.243) 117->125A(.164)
8	838.3	11.9	0.0046	122->126A(.592) 121->125A(-.419) 118->125A(-.34) 119->125A(.316)
9	823.6	12.1	0.0005	122->126A(.578) 121->126A(-.413) 119->125A(-.41) 118->126A(-.264)
10	800.2	12.5	0.017	121->124B(.867) 121->123B(.379) 121->125B(-.171)
11	791.3	12.6	0.0062	119->126A(.606) 119->125A(.413) 118->126A(.348) 118->125A(.329)
12	698.1	14.3	0.0009	121->125A(.768) 118->125A(-.372) 119->126A(-.293) 121->126A(-.224)
13	666.2	15	0.0091	121->125B(.795) 120->122B(.531)
14	644.9	15.5	0.0005	121->126A(.802) 122->126A(.416) 119->125A(-.172) 121->125A(.165)
15	617.6	16.2	0.0835	120->122B(.761) 121->125B(-.455) 117->125A(-.183)
16	606.2	16.5	0.0133	117->125A(.57) 116->125A(.407) 116->126A(-.321) 120->125A(.263)
17	581.7	17.2	0.0019	120->125A(.445) 116->125A(-.438) 117->126A(.413) 120->126A(.321)
18	554.4	18	0.0016	120->125A(.665) 120->126A(-.364) 119->125A(-.318) 117->125A(-.293)
19	545.9	18.3	0.0003	120->123B(.979)
20	525.9	19	0.0002	120->124B(.98)
21	516.2	19.4	0.0011	120->126A(.792) 116->125A(.28) 117->126A(-.256) 120->125A(.245)
22	514	19.5	0.0012	118->125A(.672) 119->126A(-.486) 119->125A(.421) 118->126A(-.243)
23	496.1	20.2	0.0027	118->122B(.781) 118->126A(-.41) 119->126A(.232) 117->122B(.186)
24	494.4	20.2	0.0032	118->126A(.68) 118->122B(.448) 119->126A(-.3) 119->125A(-.287)
25	491.5	20.3	0.0083	119->122B(.854) 124->127A(-.272) 117->122B(.214) 121->126B(.189)
26	482.3	20.7	0.0045	124->127A(.655) 121->126B(-.48) 119->122B(.296) 120->125B(.249)
27	458.5	21.8	0.0013	117->122B(.729) 121->126B(.33) 120->125B(.292) 113->122B(-.252)
28	457.9	21.8	0.0056	120->125B(.777) 117->122B(-.43) 121->126B(.259) 118->122B(.161)
29	454.5	22	0.0111	117->125A(.537) 116->126A(.508) 120->125B(.326) 121->127B(-.304)
30	453.7	22	0.0046	121->127B(.55) 117->125A(.347) 121->126B(.334) 116->126A(.291)

Table A.4.X. TD-DFT calculated Oscillator strength and assignments for **(2')**.
(B3LYP/6-31G(d) IEF-PCM)

#	nm	1000 cm-1	(f)	Assignment
1	2751.6	3.6	0.0004	130->131A(.91) 129->131A(.41)
2	2353.9	4.2	0.0052	129->131A(.908) 130->131A(-.41)
3	942.3	10.6	0.0071	126->131A(.878) 123->131A(-.304) 120->131A(.255)
4	885.9	11.3	0.0003	128->131A(.98)
5	780.7	12.8	0.0001	127->131A(.989)
6	747.8	13.4	0.003	121->131A(.784) 123->131A(.368) 125->131A(-.359) 126->127B(-.226)
7	744.9	13.4	0.0011	126->127B(.909) 125->127B(.29) 121->131A(.196)
8	742.8	13.5	0.0002	125->127B(.761) 126->128B(-.55) 126->127B(-.21) 126->129B(.192)
9	687.6	14.5	0.0036	126->128B(.696) 125->127B(.482) 125->128B(-.427) 126->127B(-.219)
10	675	14.8	0.0147	125->128B(.821) 126->128B(.396) 125->127B(.213)
11	665.1	15	0.0049	123->131A(.544) 121->131A(-.498) 126->131A(.38) 125->131A(-.358)
12	613.1	16.3	0.0051	126->129B(.908) 125->129B(-.286)
13	608.9	16.4	0.001	124->131A(.684) 125->131A(.619) 123->131A(.321)
14	601.2	16.6	0.0012	124->131A(.698) 125->131A(-.544) 123->131A(-.421)
15	591.7	16.9	0.0456	125->129B(.836) 126->130B(-.381) 126->129B(.276)
16	551.3	18.1	0.0074	122->131A(.97)
17	522.7	19.1	0.0177	125->130B(.919) 126->130B(.302) 125->129B(.165)
18	499.5	20	0.0631	126->130B(.809) 125->130B(-.304) 125->129B(.3) 119->127B(-.172)
19	480.1	20.8	0.0012	120->131A(.811) 123->131A(.381) 117->131A(.207) 119->131A(-.171)
20	430.1	23.3	0.0001	124->127B(.995)
21	418.6	23.9	0.0024	126->131B(.969)
22	416.3	24	0.0013	124->128B(.985)
23	411.2	24.3	0.0141	125->131B(.946)
24	404.6	24.7	0.0008	123->127B(.984)
25	397.1	25.2	0.0353	122->127B(.773) 119->127B(.456) 119->128B(-.266)
26	393.6	25.4	0.0008	123->128B(.887) 124->129B(.389)
27	390	25.6	0.0171	119->128B(.618) 122->128B(.487) 122->127B(.426) 117->128B(-.233)
28	385.7	25.9	0.0022	124->129B(.896) 123->128B(-.406)
29	383.1	26.1	0.0266	119->131A(.755) 119->127B(-.4) 116->131A(-.26) 122->128B(-.21)
30	377.8	26.5	0.0014	119->127B(.607) 119->131A(.552) 122->127B(-.321) 122->128B(.223)

Table A.4.X. TD-DFT calculated Oscillator strength and assignments for **(2')**[+].
(B3LYP/6-31G(d) IEF-PCM)

#	nm	1000 cm-1	(f)	Assignment
1	2751.6	3.6	0.0004	130->131A(.91) 129->131A(.41)
2	2353.9	4.2	0.0052	129->131A(.908) 130->131A(-.41)
3	942.3	10.6	0.0071	126->131A(.878) 123->131A(-.304) 120->131A(.255)
4	885.9	11.3	0.0003	128->131A(.98)
5	780.7	12.8	0.0001	127->131A(.989)
6	747.8	13.4	0.003	121->131A(.784) 123->131A(.368) 125->131A(-.359) 126->127B(-.226)
7	744.9	13.4	0.0011	126->127B(.909) 125->127B(.29) 121->131A(.196)
8	742.8	13.5	0.0002	125->127B(.761) 126->128B(-.55) 126->127B(-.21) 126->129B(.192)
9	687.6	14.5	0.0036	126->128B(.696) 125->127B(.482) 125->128B(-.427) 126->127B(-.219)
10	675	14.8	0.0147	125->128B(.821) 126->128B(.396) 125->127B(.213)
11	665.1	15	0.0049	123->131A(.544) 121->131A(-.498) 126->131A(.38) 125->131A(-.358)
12	613.1	16.3	0.0051	126->129B(.908) 125->129B(-.286)
13	608.9	16.4	0.001	124->131A(.684) 125->131A(.619) 123->131A(.321)
14	601.2	16.6	0.0012	124->131A(.698) 125->131A(-.544) 123->131A(-.421)
15	591.7	16.9	0.0456	125->129B(.836) 126->130B(-.381) 126->129B(.276)
16	551.3	18.1	0.0074	122->131A(.97)
17	522.7	19.1	0.0177	125->130B(.919) 126->130B(.302) 125->129B(.165)
18	499.5	20	0.0631	126->130B(.809) 125->130B(-.304) 125->129B(.3) 119->127B(-.172)
19	480.1	20.8	0.0012	120->131A(.811) 123->131A(.381) 117->131A(.207) 119->131A(-.171)
20	430.1	23.3	0.0001	124->127B(.995)
21	418.6	23.9	0.0024	126->131B(.969)
22	416.3	24	0.0013	124->128B(.985)
23	411.2	24.3	0.0141	125->131B(.946)
24	404.6	24.7	0.0008	123->127B(.984)
25	397.1	25.2	0.0353	122->127B(.773) 119->127B(.456) 119->128B(-.266)
26	393.6	25.4	0.0008	123->128B(.887) 124->129B(.389)
27	390	25.6	0.0171	119->128B(.618) 122->128B(.487) 122->127B(.426) 117->128B(-.233)
28	385.7	25.9	0.0022	124->129B(.896) 123->128B(-.406)
29	383.1	26.1	0.0266	119->131A(.755) 119->127B(-.4) 116->131A(-.26) 122->128B(-.21)
30	377.8	26.5	0.0014	119->127B(.607) 119->131A(.552) 122->127B(-.321) 122->128B(.223)

Table A.4.X. TD-DFT calculated Oscillator strength and assignments for
$(2')^{2+}$.(B3LYP/6-31G(d) IEF-PCM)

#	nm	1000 cm-1	(f)	Assignment
1	1776.5	5.6	0.0019	129->130A(.996)
2	1536.4	6.5	0.0004	129->131A(.998)
3	1132.7	8.8	0.0005	126->128B(.96)
4	1045.8	9.6	0.0099	126->129B(.834) 126->127B(.512)
5	879.1	11.4	0.0015	127->130A(.714) 128->130A(.448) 125->130A(-.389) 121->130A(.222)
6	858.9	11.6	0.0019	128->130A(.734) 125->130A(.368) 123->130A(-.323) 127->130A(-.303)
7	834.2	12	0.0028	127->131A(.673) 125->131A(-.432) 126->131A(.327) 124->131A(.269)
8	795	12.6	0.1035	126->127B(.686) 126->129B(-.428) 126->130B(-.303) 123->130A(-.284)
9	779.8	12.8	0.0019	124->131A(.627) 128->131A(-.492) 127->131A(-.261) 123->130A(-.25)
10	773.5	12.9	0.007	123->130A(.481) 124->131A(.459) 128->130A(.395) 128->131A(.324)
11	761.4	13.1	0.004	128->131A(.798) 123->130A(-.394) 124->131A(.204) 125->130A(.19)
12	712.2	14	0.0202	126->130B(.915) 126->127B(.267) 126->129B(-.171)
13	668.2	15	0.0005	126->130A(.951)
14	641.9	15.6	0.0015	126->131A(.749) 127->131A(-.392) 127->130A(-.251) 125->130A(-.232)
15	638.5	15.7	0.0033	125->130A(.608) 127->130A(.44) 123->130A(.414) 126->131A(.297)
16	606.5	16.5	0.0007	125->131A(.76) 127->131A(.46) 126->131A(.36)
17	549.2	18.2	0.006	122->131A(.673) 122->130A(.442) 125->131A(-.379) 124->131A(-.209)
18	539.4	18.5	0.0064	121->130A(.599) 122->130A(.464) 125->130A(.355) 122->131A(-.323)
19	532.4	18.8	0.0035	125->127B(.99)
20	518.8	19.3	0.0236	124->130A(.531) 121->130A(.498) 122->130A(-.474) 122->131A(.266)
21	507	19.7	0.0071	126->131B(.964)
22	501	20	0.0044	124->130A(.736) 122->130A(.528) 124->131A(-.252) 122->131A(-.206)
23	479.4	20.9	0.0004	123->131A(.915) 123->130A(.26) 120->131A(.21)
24	466.8	21.4	0.0028	124->127B(.933) 118->127B(-.208) 123->127B(.171)
25	458.3	21.8	0.0011	125->128B(.969)
26	450.8	22.2	0.0006	120->131A(.595) 124->128B(.464) 122->131A(-.315) 121->131A(.302)
27	449.8	22.2	0.0004	123->127B(.91) 124->127B(-.226) 118->127B(-.168)
28	441	22.7	0.0057	124->128B(.842) 120->131A(-.36) 121->131A(-.206)
29	436	22.9	0.0001	125->129B(.974)
30	426.3	23.5	0.0001	122->127B(.785) 121->127B(.526) 123->128B(-.215)

118B 120B 122B 124B 126B
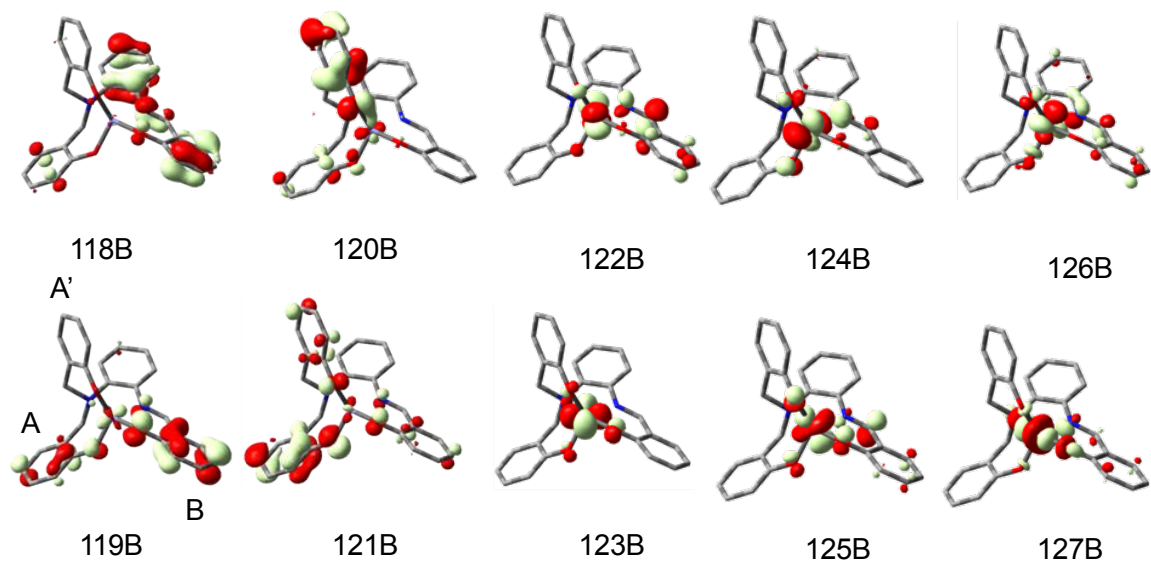
A'

A

B

119B 121B 123B 125B 127B

Figure A.4.Z. Canonical Orbitals for (**1'**). (B3LYP/6-31G(d) IEF-PCM)

APPENDIX B

Supplementary for Redox chemistry of selected 6 coordinates cobalt and Iron complexes using pentadentate-N_2O_3 electro-active.

(relates to Chapter 5)

Cartersian Coordinates:

(1') [CoL^1] E = Co-2874.091259 a.u.

H	-2.05374000	1.97790500	4.38105400
H	-0.16963500	0.56241000	3.70348400
H	3.58634800	-0.94596300	3.22969000
C	-1.89584800	1.77113300	3.32647900
C	-0.82239900	0.97675300	2.94259900
H	-3.61352500	2.90622400	2.67839300
H	1.54822600	-0.01179100	2.78768600
C	3.63177100	-1.43173500	2.25689300
C	-2.77387700	2.28927500	2.37284300
C	4.69424700	-2.24667400	1.93953100
C	1.48993100	-0.38932200	1.76709700
C	-0.61124500	0.70133500	1.58452100
H	-4.40706400	-3.99811300	1.38493000
C	2.57193800	-1.20362700	1.34185700
H	3.45178200	4.70772300	0.05181300
C	-2.58276200	1.99691100	1.02545600
N	0.44696400	-0.06320000	1.05605900
C	4.71475000	-2.87171600	0.67434400
C	-4.01997400	-3.14079700	0.83779600
H	5.54654500	-3.52181600	0.41207700
C	-4.89040800	-2.13306800	0.41285000
C	2.55229200	4.17797400	-0.25470300
C	1.33596600	4.86071000	-0.33577400
C	-1.51161800	1.19806200	0.63822900
H	-3.27608000	2.38427900	0.28524500
C	-2.65712500	-3.05820100	0.57851200
C	2.62739600	2.82039700	-0.55267000
C	2.59699100	-1.82758700	0.05053000
C	-4.36636300	-1.04402400	-0.28076500
C	0.19317400	4.16625000	-0.73133100
H	-0.76040300	4.68632500	-0.80683100
H	-5.02893200	-0.24811200	-0.61819000
C	3.70165100	-2.67534800	-0.24015800
C	1.47920700	2.11239100	-0.95385200
C	-2.11531400	-1.96500600	-0.13325200
C	0.25580500	2.81001900	-1.05175500
C	-3.00345700	-0.95315500	-0.56826900
N	-1.25643000	0.83308400	-0.75363100
Co	0.26117000	-0.45201300	-0.75970100
O	1.55664900	0.82603500	-1.27764000
O	1.67679300	-1.67687000	-0.84512300

```
O          -0.82215300   -1.94648600   -0.40037400
C          -0.92650000    2.05549100   -1.56756300
H          -1.81231200    2.70079500   -1.59684000
C          -2.45992200    0.18236400   -1.37560100
H          -3.23436600    0.94490700   -1.52344300
H          -0.74879900    1.68750300   -2.58455800
H          -2.12927600   -0.14057300   -2.36811600
O           0.13167900   -0.66939300   -2.73099800
H           0.95677100   -0.19234100   -2.94740300
H           0.95958000   -2.56561700   -3.00259700
C           0.12035400   -1.96508800   -3.35641500
H          -0.81849100   -2.43768400   -3.07365700
H           0.16314600   -1.83081100   -4.44042700
H          -1.97692900   -3.83868300    0.91080800
H          -5.95454000   -2.19147800    0.62396300
H           5.49932000   -2.41185600    2.64876700
H           3.72256700   -3.15811000   -1.21307900
H           3.57014800    2.28324000   -0.48616000
H           1.27860700    5.91821700   -0.09318700
```

(**1'**)$^+$ [CoL^1]$^+$ E = -2873.900202 a.u.
```
H          -1.95900100    2.13277000    4.35438600
H          -0.12696500    0.64206600    3.69120100
H           3.65502300   -0.89193100    3.16646100
C          -1.81463400    1.90267400    3.30305600
C          -0.77070500    1.06625300    2.92829200
H          -3.49586800    3.08577200    2.64592800
H           1.60051700    0.05356100    2.75574500
C           3.65157300   -1.42303600    2.21721600
C          -2.68062300    2.43498700    2.34586700
C           4.68144100   -2.27564800    1.89528900
C           1.51113700   -0.36462300    1.75380500
C          -0.57696100    0.76363400    1.57387800
H          -4.56640000   -3.86457900    1.42917100
C           2.56217600   -1.21487600    1.33109100
H           3.65046100    4.50602700   -0.02238700
C          -2.50963100    2.11564800    1.00208800
N           0.45430200   -0.04353600    1.05677000
C           4.63916700   -2.95819500    0.66107100
C          -4.13018700   -3.03257100    0.88544700
H           5.44671700   -3.63706700    0.39771900
C          -4.95570600   -1.99183000    0.41638600
C           2.72699300    4.01756900   -0.32320600
C           1.54910100    4.76330200   -0.43640200
C          -1.46798800    1.27351500    0.62463400
H          -3.19391600    2.51868100    0.26182800
C          -2.77540300   -2.98812700    0.65711500
C           2.72846200    2.65203300   -0.58141200
C           2.52606400   -1.89937500    0.07333700
C          -4.41162600   -0.90459400   -0.28671200
C           0.36955100    4.12897000   -0.82270600
H          -0.54966900    4.70229400   -0.92158200
H          -5.07028900   -0.11889300   -0.64585300
C           3.59551300   -2.78230400   -0.22409400
C           1.54198900    2.00736700   -0.97524500
C          -2.20111500   -1.88393700   -0.05555300
```

```
C          0.35774100    2.76364600   -1.10614100
C         -3.05491500   -0.82866700   -0.53719000
N         -1.23423400    0.87124200   -0.76577600
Co         0.23782600   -0.47597700   -0.74786400
O          1.55942400    0.70907600   -1.26912300
O          1.56297000   -1.77832900   -0.78968000
O         -0.93569100   -1.88591100   -0.26482200
C         -0.85842600    2.06109500   -1.61165900
H         -1.71344500    2.74483200   -1.64798700
C         -2.46500100    0.26770400   -1.36615300
H         -3.21310000    1.05201700   -1.52369600
H         -0.70291200    1.66597400   -2.62214700
H         -2.17323700   -0.10277300   -2.35488100
O          0.06210900   -0.76615800   -2.70032600
H          0.88828600   -0.32854200   -2.98280600
H          0.79438700   -2.71340500   -2.89549800
C         -0.00834500   -2.08616800   -3.28432500
H         -0.97769300   -2.50044900   -3.01183800
H          0.05967800   -1.98609500   -4.36952000
H         -2.10374400   -3.76544100    1.00691300
H         -6.02517000   -2.02716400    0.59894100
H          5.51119300   -2.42640000    2.57832900
H          3.56858000   -3.30930100   -1.17310800
H          3.63524300    2.06088200   -0.49024800
H          1.55120800    5.82851600   -0.22474700
```

$(\mathbf{1'})^{2+}$ $[CoL^1]^{2+}$ E = -2873.676782

```
H         -2.02068600    1.70084500    4.57025700
H         -0.20009700    0.26483600    3.79758800
H          3.34895100   -1.64180900    3.26680900
C         -1.86641900    1.57029600    3.50367800
C         -0.82852500    0.75872800    3.06505300
H         -3.52057400    2.83959800    2.94421500
H          1.40546800   -0.50057700    2.87228000
C          3.43252600   -1.94941700    2.22743600
C         -2.71085600    2.20843800    2.59287100
C          4.47268500   -2.74997500    1.82136600
C          1.38868000   -0.70514500    1.80360000
C         -0.61952600    0.58218200    1.68995600
H         -4.32561600   -4.24864800    0.83635600
C          2.44367600   -1.50502100    1.30793300
H          3.59126100    4.87885100   -0.00819500
C         -2.52133200    2.02426400    1.22738300
N          0.40722600   -0.18940800    1.10826300
C          4.54799900   -3.13655100    0.46623100
C         -3.93174300   -3.32125600    0.43391700
H          5.36634900   -3.77144400    0.13644600
C         -4.80696000   -2.25649400    0.13748300
C          2.68911300    4.32530100   -0.24646800
C          1.45217700    4.99844500   -0.32293200
C         -1.48378300    1.20812000    0.78641400
H         -3.18753600    2.51259200    0.52273300
C         -2.58437800   -3.17517000    0.21733200
C          2.74215200    2.97164600   -0.46597900
```

C	2.52805900	-1.89507200	-0.06623100
C	-4.32165900	-1.04014600	-0.38778200
C	0.26315800	4.30577700	-0.64173500
H	-0.66596000	4.86102100	-0.72831900
H	-5.02515000	-0.24695900	-0.62241400
C	3.60594900	-2.72599900	-0.45489300
C	1.53336400	2.24605800	-0.75306900
C	-2.07145700	-1.93625800	-0.30414000
C	0.27840700	2.94879900	-0.86648700
C	-2.97679600	-0.85791400	-0.61903400
N	-1.23535600	0.94917600	-0.63773400
Co	0.28208900	-0.33630900	-0.75306100
O	1.61806000	0.97902400	-0.91163000
O	1.66403900	-1.54130900	-0.97515000
O	-0.80925000	-1.84620300	-0.48961800
C	-0.92115800	2.21492800	-1.37566300
H	-1.79526300	2.87156400	-1.34112600
C	-2.45126500	0.36877500	-1.29587200
H	-3.23620300	1.13062600	-1.33153400
H	-0.76708500	1.93376900	-2.42340200
H	-2.17246300	0.15102000	-2.33257800
O	0.16695400	-0.37843100	-2.72578400
H	1.02397200	-0.02865700	-3.02762400
H	0.65596300	-2.38266900	-3.08408500
C	-0.05312700	-1.63088300	-3.43126900
H	-1.07525900	-1.94007700	-3.22309400
H	0.06307300	-1.43886400	-4.49890100
H	-1.86990800	-3.96102300	0.43881900
H	-5.87215900	-2.36984200	0.31149000
H	5.22392700	-3.08348200	2.52955300
H	3.66803200	-3.02629600	-1.49614200
H	3.66570600	2.40605600	-0.40219700
H	1.40956900	6.06816300	-0.14512600

(1')$^{3+}$ [CoL^1]$^{3+}$ E = -2873.431989 a.u.

H	-2.10089900	1.65787200	4.57054900
H	-0.25828600	0.23498000	3.81702800
H	3.36972100	-1.61935200	3.27419600
C	-1.92153300	1.53998800	3.50706800
C	-0.87144100	0.74084100	3.08002300
H	-3.56789300	2.80635000	2.92482000
H	1.41054000	-0.43487700	2.90228200
C	3.41808200	-1.91716500	2.23145600
C	-2.74925700	2.18196400	2.58269300
C	4.46171300	-2.75569100	1.80339300
C	1.38113000	-0.65365300	1.83743100
C	-0.64150200	0.58711700	1.70532100
H	-4.28341600	-4.30986300	0.75594100
C	2.44769400	-1.47225900	1.34292200
H	3.57755700	4.90637200	-0.02619700
C	-2.54206300	2.01192500	1.21580500
N	0.40329200	-0.16795400	1.13369300
C	4.54675300	-3.17583400	0.45814100
C	-3.89692600	-3.37154800	0.37263900
H	5.35828400	-3.82553000	0.14791600
C	-4.78203200	-2.30932000	0.09272900

C	2.67686400	4.34787500	-0.25762200
C	1.43710700	5.01734000	-0.33655600
C	-1.49495200	1.20680000	0.78603400
H	-3.20410600	2.50307300	0.51014200
C	-2.55075300	-3.20789900	0.16615200
C	2.73379900	2.99306400	-0.46537000
C	2.53349400	-1.89247200	-0.04641000
C	-4.30812600	-1.07612600	-0.41093900
C	0.24683400	4.31914500	-0.64904300
H	-0.68261500	4.87284200	-0.73953400
H	-5.02071200	-0.28879900	-0.63635900
C	3.60758200	-2.76218100	-0.45340200
C	1.52515200	2.26599600	-0.74652700
C	-2.05279000	-1.95188500	-0.32808400
C	0.26844000	2.96236000	-0.86549500
C	-2.96602500	-0.87874600	-0.63518400
N	-1.23288600	0.94636900	-0.63604200
Co	0.27241200	-0.31489800	-0.73939800
O	1.60814500	0.99508700	-0.89937000
O	1.69886800	-1.52997600	-0.92911300
O	-0.78682500	-1.83793800	-0.49119800
C	-0.92370600	2.21813800	-1.37547100
H	-1.80560300	2.86256400	-1.33837400
C	-2.44607900	0.35420100	-1.30299800
H	-3.23152000	1.11421500	-1.33817600
H	-0.77294300	1.93897200	-2.42371200
H	-2.15858700	0.14232300	-2.33810800
O	0.15027400	-0.37355400	-2.69131500
H	0.90270700	0.12681400	-3.05534300
H	0.93286200	-2.25345700	-3.20337200
C	0.06747700	-1.63061200	-3.42860000
H	-0.85170000	-2.12327200	-3.12360300
H	0.02383600	-1.38292400	-4.48949500
H	-1.82873100	-3.98937300	0.37793000
H	-5.84657400	-2.43667700	0.26006000
H	5.20568600	-3.08482500	2.52099500
H	3.63970000	-3.06069800	-1.49558800
H	3.65946000	2.43135300	-0.39960400
H	1.39194000	6.08814000	-0.16689100

(2') [CoL^3] E = -3027.630490 a.u.

H	-2.48154400	0.58059100	-2.53615600
H	-0.16577000	-0.19017700	-3.31123100
O	-1.90583200	1.33865400	-2.31500500
H	1.50751200	-0.71776000	-3.06719700
C	0.52088900	-0.65349800	-2.59360500
H	0.33244700	1.97316400	-2.66646900
H	1.75409800	-3.08785000	-2.90999100
C	0.04306500	-2.00979700	-2.18629000
C	0.77465000	-3.16968900	-2.44162600
O	-1.93781800	-0.99266300	-1.34143400
C	0.25872300	-4.42476500	-2.11993000
C	-1.22474200	-2.09001400	-1.57087600
H	2.01226700	1.44013200	-2.57598500
C	-1.00387800	-4.50959500	-1.52745300

```
C           -1.73796900   -3.36020200   -1.24955100
C            1.11112600    1.62626600   -1.97932800
H           -1.41843400   -5.48253600   -1.27217300
N            0.60762400    0.31447100   -1.44397400
Co          -1.18552900    0.58799200   -0.62224900
O           -2.89640000    0.87851200    0.08483700
H            3.30150400   -0.17448300   -1.55298000
O           -0.76194900    2.28109300    0.07634700
C            1.40233400    2.62754800   -0.90653700
H            3.36531700    3.09675600   -1.63367200
C           -4.77512800    0.45998200    1.41094600
C           -3.39709200    0.27312200    1.11153000
C            1.49515500   -0.20356000   -0.40366100
C            2.61257300    3.32298200   -0.87960200
C            0.41086300    2.88792000    0.06801700
C            2.83898500   -0.39556400   -0.59505800
H           -6.42379000   -0.00189800    2.68125300
N           -0.50575600   -0.29513200    0.87599200
C           -5.36534000   -0.16392000    2.48965200
H            5.50216300   -0.87631000   -0.67158100
C            0.88716800   -0.49691900    0.84260100
C            0.68357000    3.87432700    1.04150300
C            2.86578900    4.30127000    0.07999300
C           -2.64443000   -0.57275100    1.99243100
C            3.65723300   -0.87006900    0.45965600
C           -1.24966700   -0.77742400    1.83272100
C            1.88602900    4.57076400    1.03972300
C            5.05096500   -1.07597200    0.29746100
C           -4.62600300   -1.00738700    3.34639800
H            2.06476400    5.32744200    1.80108500
C            1.66816200   -0.92735800    1.89838800
C           -3.28685000   -1.19663500    3.09304000
H           -0.76531300   -1.39508100    2.58899900
C            3.05717600   -1.13092500    1.73215300
C            5.81999700   -1.52021500    1.34799900
H            6.88691300   -1.67606200    1.21370100
H            1.23746100   -1.10146200    2.87967500
H           -2.69108800   -1.83294800    3.74457100
C            3.88030000   -1.58333000    2.79790700
C            5.22865200   -1.77487100    2.60882800
H            3.42541300   -1.77879500    3.76599300
H            5.84784300   -2.12369800    3.43088200
C           -2.65816200    2.56527800   -2.34211100
H           -1.96231200    3.36097400   -2.08308600
H           -3.04474000    2.71611400   -3.35338600
H           -3.46901000    2.53006600   -1.61325200
H            0.83356200   -5.32322400   -2.32674300
H           -2.71845600   -3.42017400   -0.78403900
H           -5.34944000    1.10695000    0.75401100
H           -5.10563700   -1.49133700    4.19148700
H           -0.07914300    4.07834300    1.78901900
H            3.81075600    4.83733800    0.08398100
```

(**2'**)$^+$ [CoL^3]$^+$ E = a.u. -3027.439069
```
H           -2.41434100    0.85908500   -2.50640300
H           -0.17622600   -0.02824400   -3.31555000
```

O	-1.83592500	1.57963200	-2.18788000
H	1.47000200	-0.64506400	-3.10016200
C	0.48992200	-0.55193500	-2.62018100
H	0.41415300	2.08449500	-2.58148600
H	1.58738400	-3.04322100	-3.03730100
C	-0.05292500	-1.89405700	-2.25659600
C	0.60924200	-3.08288900	-2.56247500
O	-1.96960900	-0.80430100	-1.35184300
C	0.01935500	-4.31424600	-2.28152500
C	-1.31597000	-1.93236100	-1.63063500
H	2.06646200	1.47639500	-2.52636000
C	-1.24210900	-4.35235400	-1.67919800
C	-1.90570800	-3.17629900	-1.34804500
C	1.17607900	1.66292300	-1.91711900
H	-1.70776600	-5.30957300	-1.45813700
N	0.62663900	0.36034300	-1.42660300
Co	-1.15342100	0.66099300	-0.56781700
O	-2.80440800	1.02043500	0.20512700
H	3.31657000	-0.18309800	-1.55392200
O	-0.56454800	2.24701700	0.28891100
C	1.51394200	2.62198000	-0.81927200
H	3.42495700	3.17702700	-1.60505500
C	-4.73118700	0.53111500	1.43462000
C	-3.36300200	0.30756200	1.13733000
C	1.50201300	-0.23731400	-0.41279600
C	2.69045900	3.34595900	-0.82248500
C	0.55400500	2.86795000	0.22778700
C	2.84259100	-0.44654400	-0.61248200
H	-6.42420900	-0.00062800	2.61649500
N	-0.50733100	-0.36244100	0.85544600
C	-5.37179700	-0.19142000	2.42066500
H	5.49326300	-0.97985700	-0.70870600
C	0.88043600	-0.59502300	0.81006500
C	0.83493100	3.85774800	1.22860200
C	2.94876700	4.30936000	0.16737500
C	-2.66830900	-0.67569100	1.91329800
C	3.64313900	-1.00390300	0.41476100
C	-1.28157800	-0.91556900	1.74998600
C	2.01478300	4.56056600	1.19217600
C	5.03256000	-1.22924600	0.24391600
C	-4.69253700	-1.17163000	3.17435700
H	2.23206700	5.30590500	1.95065900
C	1.64488600	-1.10795200	1.84016200
C	-3.35997300	-1.39873500	2.91992900
H	-0.82539900	-1.62499800	2.43957000
C	3.03005800	-1.33183800	1.66584100
C	5.78460900	-1.75698900	1.26748400
H	6.84806600	-1.92925500	1.12791200
H	1.20312600	-1.33286100	2.80619000
H	-2.80987000	-2.14066300	3.49447800
C	3.83640000	-1.86893100	2.70423300
C	5.18096200	-2.07783400	2.50714800
H	3.37274300	-2.11618100	3.65580900
H	5.78803300	-2.49283300	3.30686300
C	-2.58624500	2.81370100	-2.13524100
H	-1.88665100	3.59789600	-1.85009100

H	-2.98267300	3.01704000	-3.13221100
H	-3.38823600	2.73636300	-1.40061000
H	0.53775100	-5.23600400	-2.52889000
H	-2.88179000	-3.19340800	-0.87161900
H	-5.25954800	1.28298500	0.85611500
H	-5.21327900	-1.73133700	3.94467100
H	0.09053700	4.01458200	2.00257500
H	3.88120600	4.86442900	0.13968700

(**2'**)$^{2+}$ [CoL^3]$^{2+}$ E = -3027.216603 a.u.

H	-2.36554200	0.91677800	-2.52086100
H	-0.17275700	0.01678000	-3.31792600
O	-1.81262200	1.62178600	-2.12894000
H	1.47243900	-0.59877700	-3.10168900
C	0.48986700	-0.51666400	-2.62743700
H	0.40734400	2.12171000	-2.55859100
H	1.59417100	-3.00872000	-3.05922600
C	-0.05007700	-1.86296800	-2.27794500
C	0.61583000	-3.04921600	-2.58566000
O	-1.96303800	-0.77332300	-1.36927300
C	0.02511300	-4.28082600	-2.30722200
C	-1.31036500	-1.90847500	-1.65211800
H	2.05913500	1.51821200	-2.50462400
C	-1.23538900	-4.32321600	-1.70460000
C	-1.90041300	-3.14886400	-1.36714300
C	1.16911500	1.70010700	-1.89509100
H	-1.69994600	-5.28153100	-1.48783500
N	0.62494100	0.38578400	-1.41806300
Co	-1.13263300	0.65957200	-0.55721700
O	-2.80198100	0.99477900	0.24161900
H	3.32919500	-0.12024400	-1.53543100
O	-0.55089700	2.22535500	0.34386900
C	1.50255400	2.65378200	-0.79072500
H	3.39214100	3.25614100	-1.59220100
C	-4.74109600	0.55355100	1.44408400
C	-3.36259700	0.29045200	1.13607600
C	1.50548000	-0.22148100	-0.41434000
C	2.66216000	3.40020900	-0.80092400
C	0.55121500	2.87251800	0.27249400
C	2.84643500	-0.41318300	-0.60797700
H	-6.43919600	-0.00050800	2.60633100
N	-0.49748400	-0.41086900	0.84216700
C	-5.39306300	-0.19217100	2.39025700
H	5.50132000	-0.91845200	-0.69202800
C	0.88229100	-0.63248800	0.79186800
C	0.82144100	3.85904300	1.28170600
C	2.91034700	4.36272100	0.19653500
C	-2.66374900	-0.75180200	1.87686000
C	3.64354300	-0.99941500	0.41106000
C	-1.27087800	-0.99728300	1.71440100
C	1.98389300	4.58701700	1.23598600
C	5.03060800	-1.20471200	0.24439000
C	-4.71280600	-1.21929800	3.09231400
H	2.19522400	5.33122200	1.99681600
C	1.64201100	-1.18340000	1.81603800

```
C           -3.36926000   -1.48050600    2.84079300
H           -0.82944100   -1.73249600    2.38314500
C            3.02574800   -1.38021400    1.64727400
C            5.77908500   -1.76368000    1.26045300
H            6.84489600   -1.91914100    1.12206100
H            1.19233700   -1.44547400    2.76870300
H           -2.85610100   -2.25445000    3.40387000
C            3.82596100   -1.94577400    2.67688300
C            5.17429100   -2.13473300    2.48298500
H            3.35591300   -2.23030000    3.61409100
H            5.78078400   -2.57108000    3.27074000
C           -2.56763100    2.85764200   -2.07024800
H           -1.89537600    3.62394300   -1.68952900
H           -2.88000400    3.10661000   -3.08591700
H           -3.42967700    2.74708400   -1.41175200
H            0.54390200   -5.20132800   -2.55726800
H           -2.87723600   -3.16886300   -0.89266200
H           -5.23553400    1.34141300    0.88607500
H           -5.24170700   -1.80057000    3.84023800
H            0.08284900    3.99253600    2.06535600
H            3.83007500    4.93783300    0.16190300
```

(2')$^{3+}$ [CoL^3]$^{3+}$ E = -3026.974198 a.u.

```
H           -2.48170600   -0.47232000   -2.64195900
H            0.03785200   -0.91589200   -3.20347000
O           -1.94271100    0.32600800   -2.49424100
H            1.74428500   -1.13130000   -2.82293600
C            0.74031700   -1.12942900   -2.39085000
H            0.21130500    1.32282300   -3.02691900
H            2.16890300   -3.45579100   -2.58649300
C            0.44701100   -2.46819900   -1.79352600
C            1.23975100   -3.56439000   -2.03556900
O           -1.55932600   -1.67748800   -0.78197700
C            0.84401100   -4.85094400   -1.60078600
C           -0.78715700   -2.65861900   -1.07344100
H            1.93002600    1.11470800   -2.71399000
C           -0.37858900   -5.04901700   -0.92479200
C           -1.19382200   -3.97682400   -0.66540300
C            0.96032100    1.25970400   -2.23003700
H           -0.66482700   -6.04619500   -0.60761100
N            0.63427900    0.02515200   -1.43333500
Co          -1.18713700    0.15927000   -0.69976100
O           -2.96157700    0.30778500   -0.10804900
H            3.36978900   -0.17534000   -1.44743000
O           -1.10305600    2.00535600   -0.39073900
C            0.98149800    2.51994000   -1.42510500
H            2.84234200    3.24682500   -2.18652600
C           -4.82339200    0.25702000    1.27778600
C           -3.40755600    0.14442800    1.07108500
C            1.55844600   -0.12857700   -0.30122900
C            1.98419800    3.45175800   -1.55381100
C           -0.14413600    2.83332900   -0.58047600
C            2.91566300   -0.20797300   -0.46138900
H           -6.42480100    0.15545500    2.67856300
```

N	-0.42974300	-0.10446700	1.00471500
C	-5.35328800	0.07431100	2.52733800
H	5.61720900	-0.38687400	-0.44625600
C	0.96675900	-0.17708200	0.98772000
C	-0.22599600	4.11284600	0.07179500
C	1.90291500	4.69605100	-0.88733300
C	-2.54734100	-0.14922500	2.20826600
C	3.76619700	-0.32791400	0.66906600
C	-1.13440400	-0.24202100	2.09848700
C	0.79088600	5.02080100	-0.08249500
C	5.16808300	-0.40784000	0.54228400
C	-4.51361800	-0.22298800	3.63169400
H	0.74654100	5.98375200	0.41494800
C	1.78353600	-0.27929200	2.11215700
C	-3.13654100	-0.32852500	3.46676400
H	-0.60409100	-0.44904800	3.02428600
C	3.17974000	-0.35590300	1.97729400
C	5.96368200	-0.50915700	1.66868800
H	7.04239000	-0.56963400	1.56124800
H	1.36844100	-0.28796600	3.11388300
H	-2.50766700	-0.54956900	4.32368200
C	4.02615400	-0.45725500	3.11592100
C	5.39085300	-0.53294800	2.95959100
H	3.58037000	-0.47563800	4.10613000
H	6.03396000	-0.61086000	3.83049200
C	-2.74359700	1.47825800	-2.89046500
H	-2.07830500	2.33796900	-2.90412200
H	-3.12090500	1.28474900	-3.89481300
H	-3.55945800	1.62851700	-2.18359200
H	1.49076900	-5.69857300	-1.80306800
H	-2.13603000	-4.07484200	-0.13678400
H	-5.43959900	0.48216600	0.41425200
H	-4.94917900	-0.36513500	4.61490200
H	-1.09570600	4.31094500	0.68915100
H	2.70891900	5.41277400	-1.00700400

(**4'**) [FeL^4] E = -2755.074746 a.u.

H	5.17713800	-3.18178300	1.75496400
C	4.65581600	-2.44719000	1.14511300
H	-5.81140200	-1.54748500	2.71292600
C	5.33408300	-1.31893300	0.67803400
H	-3.93338700	0.04742700	2.97979500
C	3.31294200	-2.64103600	0.83978000
C	-4.90706600	-1.65807400	2.12251700
C	-3.86033200	-0.77089300	2.26595300
H	1.72513000	2.77433400	4.18964700
H	-1.82653500	0.76254400	2.56327200
C	4.64642300	-0.38865200	-0.10010300
H	-0.02620600	1.14157600	3.62183900
H	5.16507600	0.49349100	-0.47202700
C	1.63225200	2.42222500	3.16611100
H	-5.59573200	-3.42302400	1.08113000
C	-4.77986800	-2.71382000	1.20107500
C	2.61303000	-1.70624600	0.05327700
C	0.63340600	1.51172300	2.84291300

C	-2.67368600	-0.89326300	1.50385600
C	-1.62681800	0.04847900	1.75932200
H	3.30574600	3.57431800	2.43726700
C	2.52188300	2.86529800	2.18724900
C	3.30078700	-0.56737400	-0.42523100
C	0.49985800	1.03966900	1.52846100
O	1.33430100	-1.90195000	-0.23155200
C	-3.63316800	-2.86851900	0.44403900
N	-0.49120900	0.12484500	1.12653900
C	-2.54978900	-1.96408600	0.55843200
C	2.41686400	2.37634700	0.88800400
C	1.42293900	1.45783600	0.55349300
H	3.12030700	2.70966000	0.13060500
O	-1.47991100	-2.14703500	-0.16408100
C	2.58683600	0.39054800	-1.33007800
H	3.25207900	1.22758300	-1.58472800
H	0.91537900	-3.36805500	-2.60802400
N	1.29594700	0.91883600	-0.78734100
H	2.32257400	-0.10081200	-2.27549200
C	0.06560700	-2.93671200	-3.13606600
H	0.21748400	-3.02341400	-4.21598100
O	0.01661600	-1.55495800	-2.75778600
C	0.79300400	1.94949200	-1.74954300
H	1.51846100	2.77361600	-1.80226300
H	-0.85036700	-3.45660400	-2.84022700
O	-1.42734000	0.27142400	-1.65806400
H	-0.75080800	-1.11149800	-3.15888600
H	0.78588000	1.45492700	-2.72936800
C	-0.57282700	2.47707400	-1.43842200
C	-0.81020700	3.83412900	-1.21772300
C	-1.65287300	1.56464400	-1.45567000
C	-2.10536700	4.31602900	-1.02857800
H	0.03299500	4.52294300	-1.20533800
C	-2.95737200	2.05944700	-1.27323900
C	-3.17513700	3.41847900	-1.06311800
H	-4.19143700	3.78031000	-0.92145000
Fe	-0.15698500	-0.85394200	-0.70607600
H	-2.27783100	5.37551000	-0.86007900
H	-3.78638500	1.35669300	-1.29570700
H	-3.53450500	-3.68617900	-0.26440700
H	2.77577200	-3.51441100	1.20054800
H	6.38236000	-1.16450300	0.91828100

$(\mathbf{4'})^+ [FeL^4]^+ E = -2754.877858$ a.u.

H	5.25602600	-3.07733900	1.76598800
C	4.71090700	-2.35757300	1.16061200
H	-5.80470800	-1.83381300	2.62225900
C	5.35692100	-1.21703300	0.67807900
H	-3.96598600	-0.21510100	2.99199000
C	3.36857800	-2.57964600	0.87543800
C	-4.90406000	-1.87778200	2.01817900
C	-3.87941900	-0.97647300	2.21969300
H	1.58883200	2.71757800	4.23952500
H	-1.88470800	0.59757800	2.58509200
C	4.64425600	-0.30128300	-0.09416500

H	-0.12460200	1.06328700	3.63277200
H	5.14308800	0.58750600	-0.47505200
C	1.51412800	2.37806400	3.21064400
H	-5.56199100	-3.57734900	0.85670600
C	-4.76194600	-2.85989700	1.02133700
C	2.64875100	-1.65862300	0.09617400
C	0.53577100	1.45426600	2.86526400
C	-2.69731300	-1.01689000	1.44129600
C	-1.67322700	-0.06715400	1.74407000
H	3.17477400	3.57059100	2.51862300
C	2.40718100	2.85165500	2.24898000
C	3.29806200	-0.50754800	-0.40044300
C	0.42716200	0.99821600	1.54334600
O	1.36229800	-1.88113700	-0.16469400
C	-3.61923500	-2.93209700	0.24431800
N	-0.54301100	0.07399600	1.10829700
C	-2.56088200	-2.01532500	0.42412200
C	2.32790900	2.38056600	0.94176400
C	1.35359900	1.44959000	0.58713500
H	3.03561900	2.73677700	0.19917400
O	-1.48795000	-2.11783000	-0.31881900
C	2.56144400	0.43203300	-1.30740600
H	3.20241100	1.28980900	-1.54715000
H	1.44812200	-2.96708900	-2.60410800
N	1.24738300	0.92519300	-0.76820300
H	2.31795300	-0.05666000	-2.25878200
C	0.57073300	-2.70778100	-3.19361400
H	0.83394800	-2.65023300	-4.25231700
O	0.14111800	-1.40962700	-2.73559000
C	0.75568600	1.97300700	-1.71449300
H	1.47724500	2.79884000	-1.75072900
H	-0.21603100	-3.44972300	-3.03459300
O	-1.52567500	0.35056500	-1.61963800
H	-0.62459200	-1.11714200	-3.25563900
H	0.73500700	1.51041500	-2.70853900
C	-0.60412200	2.50989400	-1.38967400
C	-0.84438100	3.84606600	-1.15728200
C	-1.72327100	1.59137600	-1.41015600
C	-2.15866800	4.31436600	-0.95478900
H	-0.01904600	4.55223000	-1.14050800
C	-3.05658300	2.09213600	-1.20584800
C	-3.25936000	3.43357200	-0.98650600
H	-4.26168200	3.82020200	-0.83161800
Fe	-0.09930500	-0.89093900	-0.68790800
H	-2.32302700	5.37213700	-0.77401200
H	-3.87320900	1.37770700	-1.22778500
H	-3.50789800	-3.69329400	-0.52209800
H	2.85088800	-3.45972200	1.24633600
H	6.40484900	-1.04109000	0.90286700

Appendix C

The Trivalent Cobalt Case

R. Shakya, C. Imbert, H. P. Hratchian, M. Lanznaster, M. J. Heeg, B. R. McGarvey,

M. Allard, H. B. Schlegel, C. N. Verani

"Structural, spectroscopic, and electrochemical behavior of trans-phenolato cobalt(III) complexes of asymmetric NN'O ligands as archetypes for metallomesogens."

My contribution to this work consisted of the electronic structure calculations in joint collaboration with Dr. Hrant Hratchian from Professor Schlegel laboratory.

Structural, spectroscopic, and electrochemical behavior of *trans*-phenolato cobalt(III) complexes of asymmetric NN′O ligands as archetypes for metallomesogens

Rajendra Shakya,[a] Camille Imbert,[a] Hrant P. Hratchian,[a] Mauricio Lanznaster,[a] Mary Jane Heeg,[a] Bruce R. McGarvey,[b] Marco Allard,[a] H. Bernhard Schlegel[a] and Claudio N. Verani*[a]

In order to understand and predict structural, redox, magnetic, and optical properties of more complex and potentially mesogenic electroactive compounds such as $[Co^{III}(L^{t\text{-}BuLC})_2]ClO_4$ (**1**), five archetypical complexes of general formula $[Co^{III}(L^{RA})_2]ClO_4$, where $R =$ H (**2**), *tert*-butyl (**3**), methoxy (**4**), nitro (**5**), and chloro (**6**), were obtained and studied by means of several spectrometric, spectroscopic, and electrochemical methods. The complexes **2**, **4**, and **6** were characterized by single-crystal X-ray diffraction, and show the metal center in an approximate D_{2h} symmetry. Experimental results support the fact that the electron donating or withdrawing nature of the phenolate-appended substituents changes dramatically the redox and spectroscopic properties of these compounds. The $3d^6$ electronic configuration of the metal ion dominates the overall geometry adopted by these compounds with the phenolate rings occupying *trans* positions to one another. Formation of phenoxyl radicals has been observed for **1**, **3**, and **6**, but irreversible ligand oxidation takes place upon bulk electrolysis. These data were compared to detailed B3LYP/6-31G (d)-level computational calculations and have been used to account for the results observed. A comparison between compound **1** and archetype **3**, validates the approach of using archetypical models to study metal-containing soft materials.

Introduction

Interest in metal-containing soft materials has increased due to applications towards molecular electronics[1] and magnetic films.[2] These materials are usually composed of an organic fragment attached to a ligand capable of coordinating metals. Rigid ligands such as terpy (2,6-di(pyridin-2-yl)pyridine) and R_2bzimpy (2,6-bis[N′-R-benzimidazol-2-yl]pyridine, R = H, Me) have been used to append different groups, thus forming building blocks for molecular transistors,[3] polymers,[4] liquid crystals,[5] and plastics.[6] More flexible alkylpyridyl ligands have been used for sensing purposes,[7–9] whereas asymmetric tridentate ligands remain largely unexplored. The design of soft materials based on these ligands leads to unique physical properties associated with dissimilar donor sets and metallation is expected to allow for some control over the final behavior of these materials.[10] Our group is interested in soft materials with electroactive and metallomesogenic properties as alternatives to phase-dependent spin-crossover switching.[1] The ground state switching mechanism in such metallomesogens is supposedly phase-independent, thus broadening the potential for molecular electronic applications. Ongoing research in our laboratories focuses on asymmetric ligands with pyridine and phenol pendant-arms, and we have developed a new ligand $HL^{t\text{-}BuLC}$ along with its first cobalt complex $[Co^{III}(L^{t\text{-}BuLC})_2]ClO_4$ (**1**). Compound **1** was thoroughly

[a]Department of Chemistry, Wayne State University, 5101 Cass Ave., Detroit, MI 48202, USA. E-mail: cnverani@chem.wayne.edu
[b]Department of Chemistry and Biochemistry, University of Windsor-401 Sunset Ave., Windsor, ON N9B 1P4, Canada

The cation of the metallomesogen $[Co^{III}(L^{t\text{-}BuLC})_2]ClO_4$ (**1**):

The Archetypical Ligands:

The Complexes (**2**) – (**6**):

$[Co^{III}(L^A)_2]ClO_4$ (**2**); R and R′ = H
$[Co^{III}(L^{tBu2A})_2]ClO_4$ (**3**); R and R′ = *tert*-butyl
$[Co^{III}(L^{OMeA})_2]ClO_4$ (**4**); R = methoxy, R′ = H
$[Co^{III}(L^{NO2A})_2]ClO_4$ (**5**); R = H and R′ = nitro
$[Co^{III}(L^{Cl2A})_2]ClO_4$ (**6**); R and R′ = chloro

Scheme 1

characterized and exhibited a complex electrochemical behavior, but attempts to obtain crystallographic information failed. In order to model and predict the behavior of this class of metal-containing soft material, we have followed the widely accepted bioinorganic approach of using model complexes to mimic structural and electronic properties of active centers in enzymes.[11] In this bioinspired approach, we investigated a series of discrete archetypical complexes $[Co^{III}(L^{RA})_2]ClO_4$ that retain key attributes of **1** (Scheme 1), by means of mass spectrometry, vibrational, electronic, and EPR spectroscopy, and electrochemical methods. The results obtained from these archetypes will allow us to infer important characteristics of **1** leading to a better understanding of its behavior, as well as a more rational approach to the synthesis and expected properties of similar materials. Complexes **2**, **4**, and **6**

Fig. 1 Synthesis of the ligand HL$^{t\text{-}BuLC}$. (i) Nitrile reduction by LiAlH$_4$ in THF; (ii) Schiff-base condensation with 2-pydinecarboxyaldehyde in MeOH followed by (iii) reduction with NaBH$_4$.

were studied by X-ray crystallography, and experimental trends are analyzed *via* computational calculations. Comparisons between compound **1** and the archetype **3** are included.

Results and discussion

Syntheses and characterizations

The ligand HL$^{t\text{-}BuLC}$ was synthesized by treatment of *para*-(heptyloxy)benzenaniline with 2-pyridinecarboxaldehyde followed by reduction and treatment with 2,4-di-*tert*-butyl-6-(chloromethyl)phenol as indicated in Fig. 1. The archetypical ligands were obtained by Schiff-base condensation of appropriately substituted salicylaldehydes and aminomethyl-pyridine in MeOH followed by reduction with NaBH$_4$ yielding HL^A, HL^{tBu2A} and HL^{Cl2A} with *ortho*- and *para* *tert*-butyl and chloro groups respectively, HL^{OMeA} with an *ortho*-methoxy group, and HL^{NO2A} with a *para*-nitro group. The ligands were characterized by ^{1}H-NMR, ESI mass spectrometry, and IR spectroscopy, with overall yields of 80–85%.

Compound **1** was obtained as a waxy material upon treatment of the ligand HL$^{t\text{-}Bu2LC}$ with hexahydrated cobalt(II) perchlorate in MeOH using triethylamine as base and was characterized by IR and UV-visible spectroscopy, and mass analysis. Attempts to obtain the elemental analysis of **1** failed. Nonetheless, the presence of vibrational modes associated with the ligand, mainly those related to C–H stretching of the tertiary butyl and heptyl groups along with perchlorate counterions, clearly indicates complex formation. Additionally, the ESI mass analysis of **1** shows a prominent peak cluster at $m/z = 1270$ indicating the formation of the cationic species [Co^{III}(L$^{t\text{-}BuLC}$)$_2$]$^+$. No evidence of multimetallic species was found and the nature of the metal ion is confirmed by the simulation of the isotopic distribution of the above mentioned cluster (Fig. 2).

The peak pattern for **1** is in excellent agreement with the pattern observed for archetype **3** and consistent with other compounds discussed here. These data support a complex formed with a 2 : 1 ligand : metal ratio. The study of the potential metallomesogenic properties of **1**$^+$ is under development with different counterions to avoid the risks involved with perchlorate chemistry. The results shall appear in a separate account. Complexes **2–6** were synthesized in a similar way and all complexes show good elemental analyses and well defined $m/z = $ [M^{III}(L)$_2$]$^+$ peaks in MeOH, as observed by ESI mass spectrometry in the positive mode. Peak simulation showed good agreement between position and isotopic distributions.[12] The analyses suggest that these complexes retain

their structure both in solution and as a solid, as expected for hexacoordinate complexes of an inert 3d^6 ion. All complexes present a perchlorate counterion found at 1116–1088 cm^{-1} in the IR spectrum.

Molecular structures

The molecular structures of archetypes **2**, **4**, and **6** were determined by X-ray diffraction of monocrystals grown from MeOH. Fig. 3 displays the ORTEP diagrams of the complex cations and Table 1 shows selected bond lengths and angles. All three structures are composed of pseudo-octahedral cations with the Co(III) ion surrounded by two facially-coordinated and deprotonated ligands (L^{RA})$^-$ with R $=$ H, MeO, and Cl for **2**, **4**, and **6** respectively. Complex **2** presents a single discrete cationic species in its unit cell, whereas **4** exhibits two cations (indicated as #1 and #2) and three cations are observed for **6** (indicated as #1, #2, and #3). In each of these cations the tridentate ligands adopt a *sym-fac* coordination,[13] and the cobalt ions are in an exact or pseudo centrosymmetric environment described in a Bailar, Miessler, and Tarr notation[14] as [Co⟨N$_{am1}$N$_{am2}$⟩⟨N$_{py1}$N$_{py2}$⟩⟨O$_{phen1}$O$_{phen2}$⟩]. The equivalent donor sets in both ligands are *trans* to each other and the distances and angles are in good agreement with the values expected for coordination of the N$_{am}$, N$_{py}$, and O$_{phen}$ donor sets with a low-spin cobalt(III) ion with *trans*-phenolate geometry.[15] The Co–O$_{phenolate}$ distances range from 1.988 to 1.920 Å, with **6**
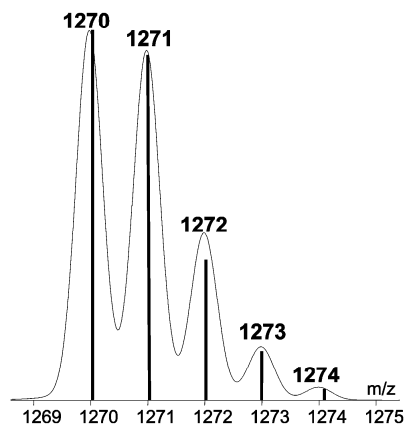
Fig. 2 Isotopic distribution for **1**. Bar cluster: experimental. Continuous spectrum: simulated cluster.

(a) [Co^{III}(L^A)$_2$]$^+$

(b) [Co^{III}(L^{OMeA})$_2$]$^+$

(c) [Co^{III}(L^{Cl2A})$_2$]$^+$
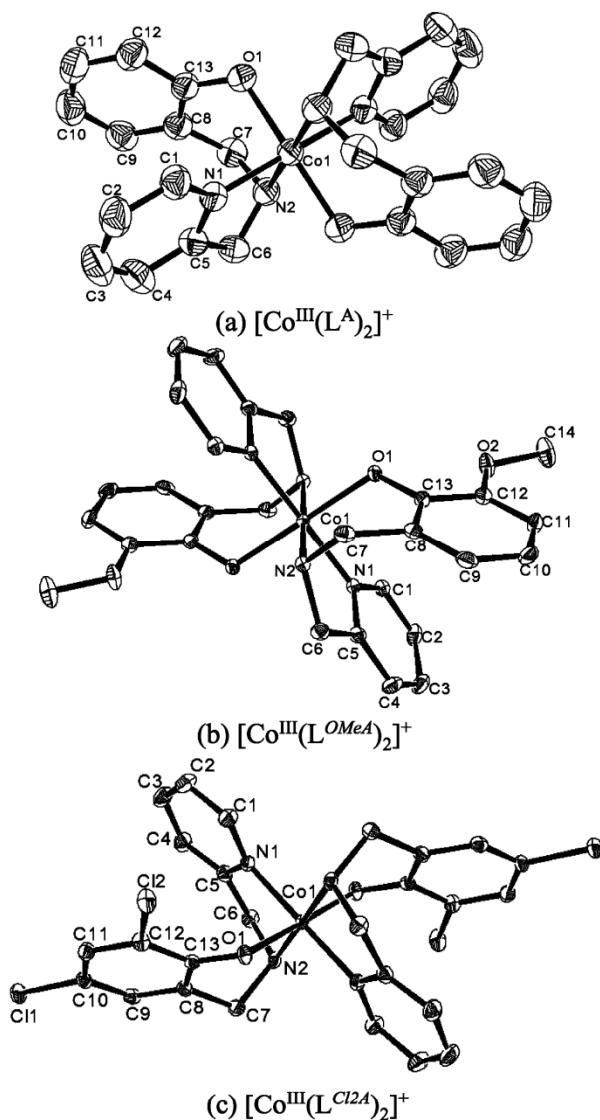
Fig. 3 ORTEP representations at 50% probability for the cations of complexes (a) **2**, (b) **4**, and (c) **6**. Counterions, solvents, and hydrogen atoms excluded for clarity.

grouping at the low end of this range, thus consistent with the presence of two electron-withdrawing chloro substituents on each phenolate ring. The Co–N$_{amine}$ and Co–N$_{pyridine}$ distances show less variation and range from 1.946 to 1.964 Å. Ordered perchlorate anions are also present and show Cl–O bonds ranging from 1.412 to 1.428 Å. In contrast to the described *sym-fac* coordination for these ligands with the cobalt(III) ion, we have recently reported on the *unsym-fac* coordination mode for iron(III) complexes[16] with the ligands (L^A)$^-$ and (L^{t-Bu2A})$^-$. The iron(III) complexes are described as [Fe⟨N$_{am1}$O$_{phen2}$⟩⟨N$_{am2}$O$_{phen1}$⟩⟨N$_{py1}$N$_{py2}$,⟩], thus displaying a *cis*-arrangement of the phenolate rings, with the Fe(III) center in an approximate C_{2v} symmetry. For structures **2**, **4**, and **6** the cobalt(III) center adopts an approximate D_{2h} symmetry in which the orbitals

d$_{x^2-y^2}$ and d$_{z^2}$ transform as a$_g$, whereas d$_{xy}$, d$_{xz}$ and d$_{yz}$ transform respectively as b$_{1g}$, b$_{2g}$, and b$_{3g}$. In order to further understand the *cis/trans* geometric preferences observed in these complexes computational calculations were performed and analyzed (*vide infra*).

UV-visible spectroscopy

The spectra of the archetypical ligands and of compound **1** were taken in CH$_2$Cl$_2$, and the spectra of archetypes **2–6** were taken in 1 : 1 mixtures of CH$_2$Cl$_2$–CH$_3$OH to assure homogeneity of all solutions. The apparent lower extinction coefficients observed for **1** when compared to **2–6** are due to the higher molecular mass of the former species. Table 2 summarizes the results and Fig. 4 shows spectra of the complexes. Intense $\pi \rightarrow \pi^*$ intraligand bands were observed in the UV region for **1–6**, whereas p$\pi_{phenolate}$ $\rightarrow$ d$\sigma^*_{cobalt(III)}$ charge transfer bands were found between 430 and 470 nm for all complexes, thus in good agreement with values reported in the literature.[14] Comparison between unsubstituted and *tert*-butyl-substituted species shows this LMCT band shifting from 431 nm in **2** to 470 nm in **3**. Therefore, the latter archetypical complex models the behavior of compound **1**, were this transition is observed at 466 nm. Similar trends were observed for previously reported iron compounds with comparable ligands.[15] Complex **5** presents a broad p$\pi_{phenolate}$ $\rightarrow$ p$_{NO2}$ intraligand charge transfer band at 377 nm that superimposes the p$\pi_{phenolate}$ $\rightarrow$ d$\sigma^*_{cobalt(III)}$ transition preventing further discussion. This band has been observed for the protonated and non-metallated ligand at 323 nm. The presence of several independent cations observed in the crystal structures of **4** and **6** do not pose a problem to the UV-visible studies because the cations are expected to assume similar and averaged bond lengths and angles when in solution. The low spin character of these species was confirmed by EPR spectroscopy and the six electrons of a cobalt(III) center in a D_{2h} symmetry will be described by a [b$_{1g}^2$, b$_{2g}^2$, b$_{3g}^2$, a$_g^0$, a$_g^0$] configuration. Dominant σ-bonding interactions will arise because d–d transitions are low in intensity and occupation of the b$_{1g}$, b$_{2g}$, and b$_{3g}$ orbitals precludes the presence of strong π-bonds, as supported by the relatively long Co–O bonds observed for **2**, **4**, and **6**. Compound **1** and archetypes **2–6** also exhibit a transition between 560 and 670 nm. This band
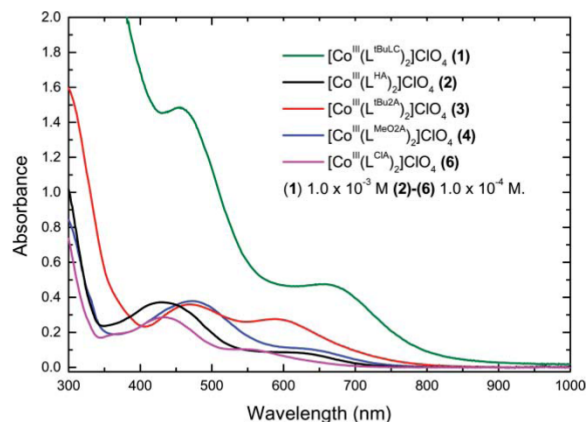
Fig. 4 UV-visible spectra of complexes **1–6** in CH$_2$Cl$_2$.

Table 1 Selected bond distances (Å) and angles (°) for **2**, **4**(#1), and **6**(#1)

	[Co^{III}(L^A)$_2$]ClO$_4$ (**2**)		[Co^{III}(L^{OMeA})$_2$]ClO$_4$·H$_2$O (**4**) Cation #1		[Co^{III}(L^{Cl2A})$_2$]ClO$_4$ (**6**) Cation #1	
Co1–O1	1.9158(12)		Co1–O1	1.9204(15)	Co1–O1	1.8986(13)
Co1–N2	1.9624(15)		Co1–N2	1.9590(18)	Co1–N2	1.9573(16)
Co1–N1	1.9563(15)		Co1–N1	1.9484(18)	Co1–N1	1.9611(16)
O1–C13	1.338(2)		C13–O1	1.347(2)	C13–O1	1.321(2)
C7–C8	1.493(3)		C7–C8	1.500(3)	C7–C8	1.506(3)
C7–N2	1.495(3)		C7–N2	1.492(3)	C7–N2	1.497(3)
N2–C6	1.477(3)		N2–C6	1.485(3)	N2–C6	1.490(3)
C5–C6	1.491(3)		C5–C6	1.493(3)	C5–C6	1.495(3)
Bite angles:						
O1–Co1–N2	94.28(6)		O1–Co1–N2	94.48(7)	O1–Co1–N2	94.68(6)
N2–Co1–N1	82.84(7)		N1–Co1–N2	84.70(8)	N1–Co1–N2	84.65(7)
Average distances:						
C–C in Py	1.375(9)		C–C in Py	1.383(3)	C–C in Py	1.383(4)
C–N in Py	1.343(3)		C–N in Py	1.350(4)	C–N in Py	1.350(4)
C–C in Ph	1.389(12)		C–C in Ph	1.395(13)	C–C in Ph	1.393(13)
					C–Cl	1.742(4)

Table 2 UV-visible and electrochemical parameters for ligands and complexes

	λ/nm (ε/L mol^{-1} cm^{-1})[a]	$E_{1/2}{}^1$/V (ΔE/V)[b]	$E_{1/2}{}^2$/V (ΔE/V)	$E_{1/2}{}^3$/V (ΔE/V)
HL^A	262 (4500); 268 (4350); 278 (3150); 332 (190)	Irreversible behavior		
HL^{t-BuA}	262 (3750); 268 (3550); 282 (2990)	—	0.33 (0.19)	0.84 (0.39)
HL^{OMeA}	262 (3930); 281 (2650)	Not measured		
HL^{NO2A}	262(5040); 323 (11 100)	Not measured		
HL^{Cl2A}	262 (3680); 293 (2980)	Not measured		
[Co(L^{t-BuLC})$_2$]ClO$_4$ (**1**)	466 (1463); 672 (495)	−0.83(0.26)	0.38 (0.14)	
[Co(L^A)$_2$]ClO$_4$ (**2**)	261sh (11 240); 282 (10 680); 431 (2770); 623 (910)	−0.91(0.30)	—	—
[Co(L^{t-BuA})$_2$]ClO$_4$ (**3**)	251sh (19 110); 289 (16 250); 470 (3590); 589 (2080)	−0.90(0.38)	0.43 (0.10)	0.78 (0.10)
[Co(L^{MeOA})$_2$]ClO$_4$ (**4**)	292 (9140); 471 (3790); 637 (1023)	−0.88(0.13)	—	—
[Co(L^{NO2A})$_2$]ClO$_4$ (**5**)	228 (18 650); 369 (15 780); 607 (402)	−0.55(0.13)	—	—
[Co(L^{Cl2A})$_2$]ClO$_4$ (**6**)	258 (12 450); 286sh (9618); 431 (2850); 564 (966)	−0.67(0.20)	0.87 (0.09)	1.29 (0.14)

[a] Spectra measured in CH$_2$Cl$_2$ for ligands and **1**. Spectra in CH$_2$Cl$_2$–MeOH (1 : 1) for **2–6**. [b] All CVs measured in CH$_2$Cl$_2$, with TBAPF$_6$ as the supporting electrolyte. Scan rate of 100 mV s^{-1} at RT using a three electrode system (glassy carbon, Ag/AgCl, Pt wire). Potentials referenced *vs* the ferrocenium/ferrocene couple.

has been attributed to the d–d transition $^1A_{1g} \rightarrow {}^1T_{2g}$,[14] but some caution is necessary since none of the compounds studied here or in the cited reference belong to a genuine O_h point group. Even considering that the $^1T_{2g}$ term splits into $^1A_1 + {}^1B_1 + {}^1B_2$,[17] this band is too intense for a pure d–d transition.

Electrochemistry and EPR spectroscopy

Compound **1** and archetypes **2–6** had their electrochemistry measured in CH$_2$Cl$_2$, and the data are shown in Table 2. Compound **1** is characterized by a complex electrochemical behavior that involves a quasi-reversible reduction at −0.83 V *vs* Fc$^+$/Fc attributed to the Co(III)/Co(II) pair and several irreversible follow-up oxidations attributed to the ligand. If the oxidation stops immediately after the first oxidative process, reversibility is attained. Since this process presents *ca* twice the peak current of the metal-centered process, it might be associated to a 2e$^-$-process,[18] but further investigation is needed in order to firmly establish the number of electrons transferred. The Co(III)/Co(II) reduction is observed between −0.55 and −0.90 V *vs* Fc$^+$/Fc for archetypes **2** to **6**, spanning a 0.36 V window. It follows the expected trend that electron-donating substituents will increase electronic density around the metal center decreasing the redox potentials, whereas electron withdrawing groups will increase these potentials.[19] It has

been suggested[20] that such a large window indicates occupation of a d$_{x^2-y^2}$ orbital of the metal upon reduction. It reflects the occupation of an a$_g$ molecular orbital with d$_{x^2-y^2}$ character in these D_{2h} species. Calculations support this trend and will be detailed later in this paper. Interestingly, only **3** and **6** with respectively appended *tert*-butyl and chloro groups show reversible or quasi-reversible ligand-centered processes as seen in Fig. 5. Compound **3** shows processes at 0.43 and 0.78 V, while **6** exhibits much more
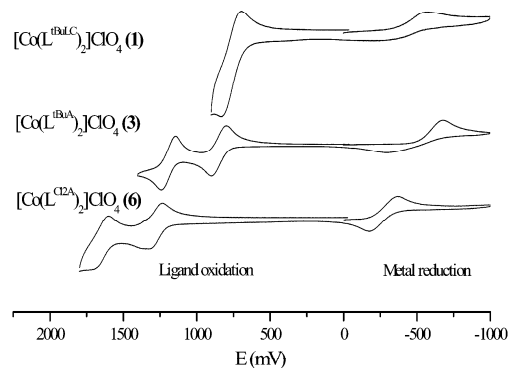
Fig. 5 Cyclic voltammograms of **1**, **3**, and **6** in CH$_2$Cl$_2$.

positive values. Such processes fall within the range expected for the conversion of coordinated phenolates into phenoxyl species.[21] The archetype **3** was able to model the behavior of compound **1** in regard to potentials and quasi-reversibility of the metal-centered reductive process. The behavior of the oxidative processes is more complex, because **3** presents two independent waves while **1** displays a multielectron process. Nonetheless, the archetypical compound **3** gave pertinent information about the oxidative potentials. At this point, it is not clear why the appended liquid crystalline group in **1** causes such changes.

Electrolyses at controlled potentials in CH_2Cl_2 solutions were carried out for **3** and **6** to confirm the nature of these processes. Aliquots were isolated under anaerobic conditions before and after the electrolysis and EPR spectra were measured at 120 K. Complexes **3** and **6** present silent spectra before the electrolysis, thus supporting the expected low-spin configuration for the $3d^6$ ions. Upon electrolysis of the first and second oxidative processes (at 1.05 V and 1.40 V respectively) an initial EPR signal is observed at 3300 G with $g = 2.004$ for **3**, as expected for a phenoxyl radical. However, a broader signal with a 35 G line-width is also present overtaking the previous signal toward the end of the electrolyses (Fig. 6). This signal is suggested to arise from a free radical on a nitrogen atom; such radicals have a nitrogen hyperfine interaction of ca 15 G which gives a three line pattern about 30 G. A similar behavior was observed for **6**. Post-electrolysis voltammetry reinforces the decomposition of **3** and no further analyses were taken.
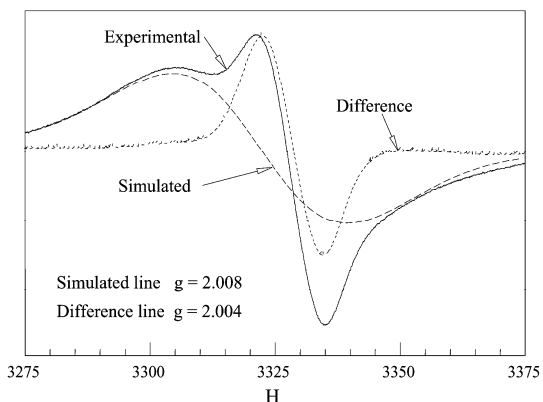
Fig. 6 EPR of the product from the oxidative electrolysis of **3** at 1.40 V.

Electronic structure calculations and analysis

We have recently reported on iron(III) and gallium(III)[16] complexes with similar imine and amine ligands and we have shown that tertiary-butyl groups play a pivotal role in the stabilization of phenoxyl radicals. In the same account we have shown that the phenolate rings adopt a *cis*-configuration in Fe(III) and Ga(III) complexes. Here, we were interested in assessing the energetics related to the preferential *trans* coordination of the phenolate arms in the Co(III) compounds described in this work, as well as in performing an electronic structure analysis to obtain a clear description of the molecular orbitals in compounds **2–6**. Calculations were carried out using the GAUSSIAN suite of electronic structure programs.[22] The B3LYP/6-31G(d) level of theory[23] was employed throughout these and the previously

published calculations. Standard methods[24] were used to fully minimize structures without symmetry constraints and located stationary points were characterized by analytic vibrational frequencies. Reported energies include the zero-point vibrational correction. Preliminary calculations on the full structures of **2–6** yielded similar results to $[Co^{III}(L^A)_2]^+$. Therefore, we consider $[Co^{III}(L^A)_2]^+$ a suitable model for this set of complexes and restrict our discusion in this section to this model structure as a representative case for **2–6**. The cation $[Co^{III}(L^A)_2]^+$ can adopt two configurations; one given by $[\langle N_{am1}N_{am2}\rangle\langle N_{py1}N_{py2}\rangle\langle O_{phen1}O_{phen2}\rangle]$ referred to as "*trans-phenolates*," and another given by $[\langle N_{am1}O_{phen2}\rangle\langle O_{phen1}N_{am2}\rangle\langle N_{py1}N_{py2}\rangle]$ called "*cis-phenolates*." The structures of **2**, **4**, and **6** present a "*trans-phenolates*" configuration. Relative energies for *cis*- and *trans*-phenolates $[Co(L^A)_2]^+$ are shown together with minimized structures in Fig. 7. Calculated energies show that the *trans*-configuration is favored by *ca* 4 kcal mol^{-1}, and in spite of a relatively small energy difference, the results are in good agreement with the trends observed experimentally.
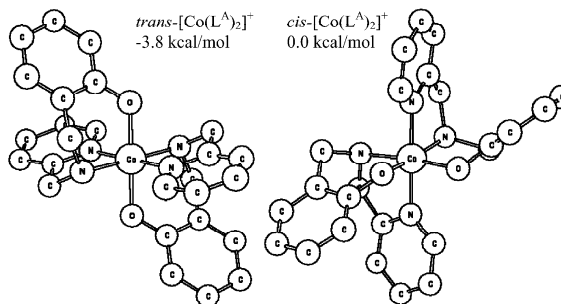
Fig. 7 B3LYP/6-31G(d) minimized geometries and energies for *trans*- and *cis*-$[Co(L^A)_2]^+$. H atoms have been omitted for clarity.

A qualitative molecular orbital description of these compounds has been drawn using the partitioning scheme of Whangbo, Schlegel, and Wolfe,[25] and includes Mulliken molecular orbital percent compositions in terms of fragment orbitals. Two fragments have been defined: (i) the cobalt(III) center and (ii) the ligands. Results for the *trans*- and *cis*-configurations are summarized in Table 3. The *trans*-configuration of $[Co(L^A)_2]^+$ belongs to the pseudo point group D_{2h}, and symmetry assignments are based on the transformations of ligand and metal orbital symmetry adapted linear combinations (SALCs) in this group. The *cis*-configuration suggests a D_{2v} point group, but the orientation of the two pyridine rings perpendicular to each other lowers the symmetry and therefore orbital labels are excluded. Molecular orbital diagrams are given in Fig. 8 projected onto the WSW fragment orbital basis.

The HOMO and HOMO − 1 molecular orbitals for these configurations are nearly degenerate and their energies remain unchanged for both *trans*- and *cis*-configurations. Additionally, the molecular orbital diagrams show that for most occupied orbitals, energies are independent of the metal center, *i.e.*, the HOMO, HOMO − 1, HOMO − 2, and HOMO − 3 energies for $[Co(L^A)_2]^+$ show a small metal contribution and are characterized as non-bonding phenolate SALCs. The HOMO and HOMO − 1 molecular orbitals are nearly identical in energy, and it becomes clear that the observed ligand configuration is not dictated by their stabilization or destabilization. The highest occupied molecular

Table 3 Molecular orbital energies and compositions for $[Co(L^A)_2]^+$ with "*trans-phenolates*" and "*cis-phenolates*" configurations[a]

	Energy[b]		Symmetry[c]		% Metal[d]		% Ligand	
	trans	*cis*	*trans*	*cis*	*trans*	*cis*	*trans*	*cis*
LUMO + 1	−4.48	−4.39	b$_{1u}$	—	0.5	33.5	99.5	66.5
LUMO	−4.61	−4.51	a$_g$	—	67.9	32.4	32.1	67.6
HOMO	−7.86	−7.87	b$_{3g}$	—	8.2	5.6	91.8	94.4
HOMO − 1	−7.89	−7.88	b$_{2u}$	—	0.7	4.7	99.3	95.3
HOMO − 2	−8.96	−8.95	—	—	0.1	0.1	99.9	99.9
HOMO − 3	−8.97	−8.96	—	—	0.2	0.4	99.8	99.6
HOMO − 4	−9.62	−9.14	b$_{2g}$	—	33.6	27.7	66.4	72.3
HOMO − 5	−9.68	−9.54	b$_{2u}$	—	3.3	10.8	96.7	89.2

[a] The "*trans-phenolates*" configuration for $[Co(L^A)_2]^+$ is described by $[Co\langle N_{am1}N_{am2}\rangle\langle N_{py1}N_{py2}\rangle\langle O_{phen1}O_{phen2}\rangle]$, whereas the "*cis-phenolates*" configuration is $[Co\langle N_{am1}O_{phen2}\rangle\langle O_{phen1}N_{am2}\rangle\langle N_{py1}N_{py2}\rangle]$. The N_{py1}–Co–N_{py2} axis has been placed along the z-direction; the y-axis bisects the O_{phen1}–Co–O_{phen2} angle; the x-axis bisects the N_{am1}–Co–N_{am2} angle. [b] Energy given in eV. [c] Pseudo symmetry labels have been assigned according to the D_{2h} group. For non-bonding orbitals, pseudo symmetry labels are given only where ligand orbitals mimic symmetry adapted linear combinations. [d] "% Metal" and "% Ligand" correspond to the character of the molecular orbitals.
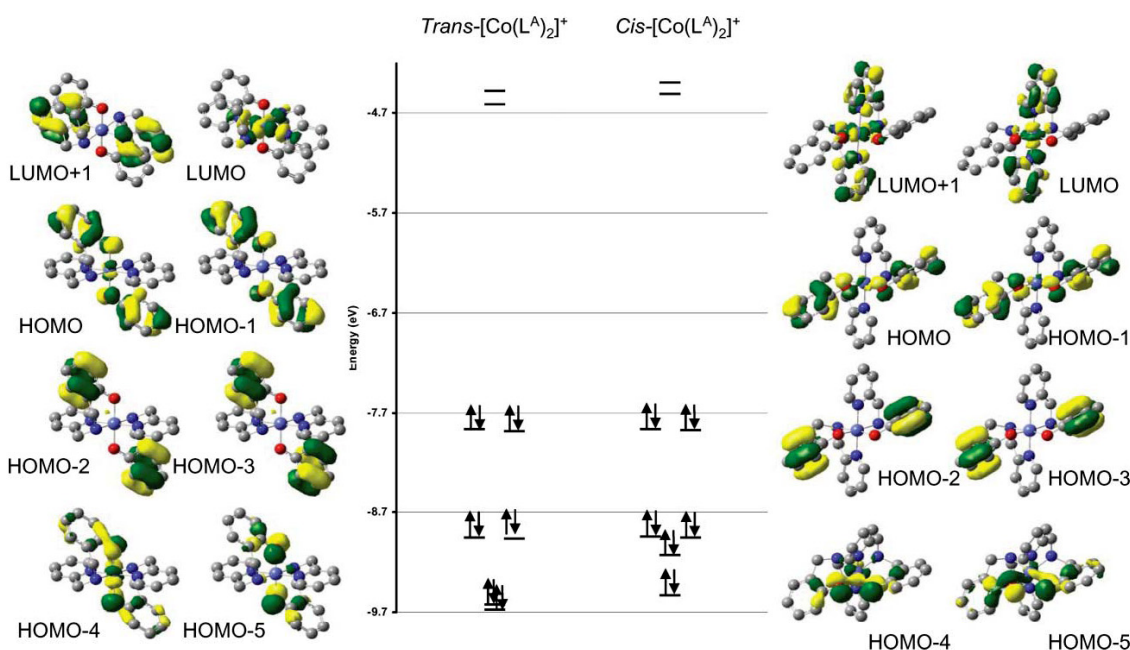
Fig. 8 (a) Molecular orbital energy level diagram for *trans*- and *cis*-$[Co(L^A)_2]^+$ and renderings of selected MOs projected onto the WSW fragment orbital basis.

orbital displaying significant metal character in both *cis*- and *trans*-phenolate structures is HOMO − 4. In the *trans*-phenolate structure this molecular orbital results from a four electron interaction between the occupied Co-centered d$_{xz}$ orbital and occupied phenolate SALC that is commonly characterized as the in-plane O orbital. The HOMO − 4 of the *cis*-phenolate isomer is less stable by roughly 0.5 eV. This molecular orbital is derived from a two electron interaction between the unoccupied Co-centered d$_{x^2-y^2}$ orbital and the same in-plane O centered phenolate SALC. The LUMO entails 67.9% of metallic character, is labeled a$_g$ and relates to an unoccupied d$_{x^2-y^2}$ AO, thus reinforcing the notion that in the reductive process given by Co(III) (3d$^6_{l.s.}$) + e$^-$ → Co(II) (3d^7), an electron is promoted to the LUMO. It justifies the considerable changes in potential for complexes with different groups attached to the phenolate ring.

Conclusions

In order to understand and predict the properties of more complex soft materials with potential metallomesogenic properties such as compound **1**, we have investigated the behavior of five cobalt(III) complexes **2–6**. These complexes were excellent archetypes in delivering fundamental information on structural, UV-visible and redox behavior of compound **1**. Archetype **3** mimicked accurately the peak position for the p$\pi_{phenolate}$ → d$\sigma^*_{cobalt(III)}$ charge transfer band and metal and ligand-centered redox potentials. Based on spectroscopic and spectrometric methods, as well as by the results of our calculations and by inference from structural data for the archetypes **2**, **4**, and **6**, compound **1** should exhibit two ligands coordinated in a *trans*-configuration $[Co\langle N_{am1}N_{am2}\rangle\langle N_{py1}N_{py2}\rangle\langle O_{phen1}O_{phen2}\rangle]$, with similar bond lengths

and angles. If aiming at redox-driven switchable materials, design should be limited to systems in which *tert*-butyl and chloro groups are appended to the phenolate rings. These are the only species showing generation of phenoxyl radicals. Future work will focus on the mesogenic properties of **1** and in the development of Fe(III)-containing soft materials. Comparisons between $d^5_{high\text{-}spin}$ and $d^6_{low\text{-}spin}$ systems will be possible, as well as the understanding of the influence of *cis* and *trans* coordination of the phenolates to the metal centers. We are also investigating the cobalt archetypes of bromo- and iodo-substituted ligands that show absence of perchlorate counterions in the IR spectrum. It suggests cobalt(II) stabilization and further NMR and EPR studies are underway.

Experimental

Materials and methods

Reagents were used as received. CH_2Cl_2 was used from an Innovative Technologies solvent purification system, and MeOH was distilled over CaH_2. IR spectra were measured on a Tensor 27 FTIR-Spectrophotometer. ^1HNMR spectra were taken using Varian 300 and 400 mHz instruments. ESI(positive) spectra were measured in a triple quadrupole Micromass QuattroLC mass spectrometer with ESCi source. Elemental analyses were performed by Midwest Microlab, Indianapolis-IN, USA. UV-visible spectroscopy were performed on a Cary 50 spectrometer in the range 250 to 1000 nm. The samples were mortar-ground and heat-dried under vacuum overnight to eliminate solvent molecules. CV experiments were performed using a BAS 50 W voltammetric analyzer. A standard three-electrode-cell was employed with a glassy-carbon working electrode, a Pt-wire auxiliary electrode, and an Ag/AgCl reference electrode under an inert atmosphere at RT. All potentials are given *vs* Fc^+/Fc.[26] First derivative X-band EPR spectra were performed with a Bruker ESP 300 spectrometer at 120 K using liquid nitrogen as the coolant.

X-Ray structural determinations for 2, 4, and 6

All data were determined using either a Bruker P4/CCD or a Bruker X8 APEX-II kappa geometry diffractometer with Mo radiation and a graphite monochromator. Frame data were indexed and integrated with the manufacturer's software[27] and models were refined with SHELX-97.[27] Table 4 shows collection data for the three structures.

$[Co^{III}(L^A)_2]ClO_4$ (**2**) crystallized as irregular dark fragments. A sample $0.6 \times 0.4 \times 0.4$ mm was used for data collection at 295 K. 2450 frames were collected, yielding 8898 reflections, of which 2953 were independent. Hydrogen positions were observed and refined, including the amine proton. The cobalt atom occupies a crystallographic inversion center. The perchlorate anion is on a 2-fold axis. Diffraction data for $[Co^{III}(L^{OMeA})_2]ClO_4 \cdot H_2O$ (**4**) were collected at 100 K on a crystal $0.15 \times 0.04 \times 0.02$ mm. A sphere of data was measured at 20 s per frame and $0.3°$ between frames. 4471 frames were collected, yielding 79107 reflections, of which 7444 were independent. The hydrogen atoms were placed in observed positions and refined. The asymmetric unit contains two half-complexes, one perchlorate anion and one uncoordinated molecule of water. Both Co(III) atoms occupy inversion centers. Diffraction data for $[Co^{III}(L^{Cl2A})_2]ClO_4$ (**6**) were measured on a red irregular sample $0.18 \times 0.16 \times 0.15$ mm at 100 K. Frames were collected as a series of sweeps with the detector at 40 mm and $0.3°$ between each frame. 3334 frames were collected at 10 s per frame, yielding 117026 reflections, with 14459 of them independent. Hydrogen positions were observed or calculated. The asymmetric unit consists of 2 half-complexes, one full complex and 2 perchlorate anions. Co1 and Co2 occupy inversion centers.

CCDC reference numbers 285941, 285942 and 286103.

For crystallographic data in CIF or other electronic format see DOI: 10.1039/b514190g

Syntheses

Preparation of the ligand HL^{tBuLC}. A 30 mL MeOH solution of *para*-(heptyloxy) benzenaniline (0.3 g: 1.0 mmol) was treated with 2-pyridinecarboxyaldehyde (0.11 g: 1.0 mmol) at 50 °C for 2 h, yielding a pale yellow solution. $NaBH_4$ (0.56 g: 1.5 mmol) was than added at 0 °C in small portions. The solution was stirred at room temperature for 2 h, the solvent was evaporated, and the amine formed was extracted with dichloromethane, dried over $MgSO_4$ and isolated. The amine so obtained was dissolved in 30 mL

Table 4 Crystal data[a]

	$[Co^{III}(L^A)_2]ClO_4$ (**2**)	$[Co^{III}(L^{OMeA})_2]ClO_4 \cdot H_2O$ (**4**)	$[Co^{III}(L^{Cl2A})_2]ClO_4$ (**6**)
Formula	$C_{26}H_{26}ClCoN_4O_6$	$C_{28}H_{32}Co_1Cl_1N_4O_9$	$C_{26}H_{22}Co_1Cl_5N_4O_6$
M	584.89	662.96	722.66
Space group	$C2/c$	$P2_1/n$	$P2_1/n$
$a/Å$	20.2884(15)	11.8170(8)	11.1872(6)
$b/Å$	8.4867(7)	14.8833(9)	22.7813(13)
$c/Å$	15.4068(12)	17.2517(12)	22.1940(13)
$β/°$	109.344(2)	108.448(3)	98.922(2)
$V/Å^3$	2503.0(3)	2878.2(3)	5587.9(5)
Z	4	4	8
T/K	295(2)	100(2)	100(2)
$λ/Å$	0.71073	0.71073	0.71073
$D_{calc}/g\,cm^{-3}$	1.552	1.530	1.718
$μ/mm^{-1}$	0.843	0.751	1.143
$R(F)$ (%)	3.05	3.93	3.34
$Rw(F)$ (%)	7.45	8.12	7.90

[a] $R(F) = \sum \|F_o| - |F_c\|/\sum |F_o|$ for $I > 2\sigma(I)$; $Rw(F) = [\sum w(F_o^2 - F_c^2)^2/\sum w(F_o^2)^2]^{1/2}$ for $I > 2\sigma(I)$.

CH$_2$Cl$_2$, and then refluxed in the presence of 2,4-di-*tert*-butyl-6-(chloromethyl)phenol (0.26 g: 1.0 mmol) and excess of Et$_3$N overnight. The reaction mixture was washed with 10% NaHCO$_3$, the organic layer was isolated and dried over MgSO$_4$ and then roto-evaporated to yield the ligand HL$^{t\text{-}BuLC}$. IR data (KBr, cm^{-1}): 3456 (O–H); 2953–2859 (s) (C–H), 1608 (s), 1526 (s), 1474 (s) (C=N$_{py}$, C=C aromatic). ^{1}H-NMR data [400 MHz, CDCl$_3$, 300 K] δ (ppm): 0.90 [t, 3H (CH$_3$)]; 1.22–1.46 (overlapped m, 26H (CH$_2$) and s, ^{t}Bu (CH$_3$)]; 1.82 [m, 2H (OCH$_2$CH$_2$)]; 3.72 (s, 2H (Ph–CH$_2$–N–)]; 3.78 [s, 2H (N–CH$_2$–Ar)]; 3.9 [t, 2H (Ar–O–CH$_2$–)]; 4.0 [s, 2H (Py–CH$_2$–N–)]; 6.8 [s, 1H (aryl)]; 6.94 [d, 2H (aryl)]; 6.96 [d, 2H (aryl)]; 7.16 [d, 2H (aryl)] 7.48 [d, 2 H (aryl)]; 7.51 [d, 2 H (aryl)] 7.2–7.8 [m, 3H (pyridine)]; 8.57 [d, 1 H (pyridine)]. MS data (ESI$^+$ in MeOH): m/z = 607 [HL$^{t\text{-}BuLC}$ + H]$^+$.

Preparation of the ligands HL^A, HL$^{t\text{-}BuA}$, HL^{OMeA}, HL^{NO2A}, and HL^{Cl2A}. The ligands HL^A and HL$^{t\text{-}BuA}$ were obtained according to literature procedures.[29,30] The ligands HL^{OMeA}, HL^{NO2A}, and HL^{Cl2A} were synthesized according to a general procedure in which 2-aminomethyl-pyridine (1.08 g: 10.0 mmol) and the appropriate aldehyde (10.0 mmol) were condensed in 20 mL of MeOH at 40 °C. After 2 h, NaBH4 (0.5 g: 15 mmol) was added at 0 °C. The solvent was roto-evaporated and the crude product was dissolved in 100 mL of 5% aqueous NaHCO$_3$. Extraction with 4 × 25 mL of dichloromethane took place, and the combined extracts were dried over MgSO$_4$. The solutions were concentrated and allowed to stand for several days at 0 °C giving microcrystalline solids. The characterizations follow.

HL^{OMeA} (2-methoxy-6-{[(pyridin-2-ylmethyl)-amino]-methyl}-phenol}). 2-Hydroxy-3-methoxy-benzaldehyde (1.52 g: 10 mmol) was used. Yield = 2.0 g (82%); mp = oil. IR data (KBr, cm^{-1}): 3304 (O–H); 1591 (s), 1571 (m), 1464(s) (C=N$_{py}$, C=C aromatic); 1274 (s) (C–O). ^{1}H-NMR data [400 MHz, CDCl$_3$, 300 K] δ (ppm): 3.85, 3.92 [2 × s, 2 ×1 H (CH$_2$)]; 4.04 [3 × s, 3 × 1 H (CH$_3$)]; 6.6 [d,1 H (aryl)]; 6.7 [t,1 H (aryl)]; 7.1 [d, 1 H (aryl)]; 7.2–7.6 [m, 3 H (py)]; 8.57 [d, 1 H (py)]. EI data: m/z: 244 [HL^{OMeA}]; 152 [HL^{OMeA} – (PyCH$_2$–)]; 137 [HL^{OMeA} – (PyCH$_2$NH–)]; 107 [(PyCH$_2$NH–)].

HL^{NO2A} (4-nitro-2-{[(pyridin-2-ylmethyl)-amino]-methyl}-phenol}). 2-Hydroxy-5-nitro-benzaldehyde (1.67 g: 10 mmol) was used. Yield = 2.2 g (84%); mp (uncorrected) = 151–153 °C; IR data (KBr, cm^{-1}): 3305 (O–H); 1595 (s), 1570 (m), 1477(s)(C=Npy, C=C ar); 1280 (s) (C–O). ^{1}H-NMR data [400 MHz, CDCl$_3$, 300 K] δ (ppm): 3.94, 4.06 [2 × s, 2 × 1 H (CH$_2$)]; 6.9 [d, 1 H (aryl)]; 7.2–7.7 [m, 3 H (Py)]; 7.9 [s,1 H (aryl)]; 8.1 [d, 1 H (aryl)] 8.59 [d, 1 H (Py)]. EI data m/z: 259 [HL^{NO2A}]; 107 [(PyCH$_2$NH–)].

HL^{Cl2A} (2,4-dichloro-6-{[(pyridin-2-ylmethyl)-amino]-methyl}-phenol}). 3,5-Dichloro-2-hydroxy-benzaldehyde (1.91 g: 10 mmol) was used. Yield = 2.4 g (85%); mp (uncorrected) = 110–112 °C. IR data (KBr, cm^{-1}): 3427 (O–H); 1596 (m), 1573(m), 1439 (s) (C=N$_{py}$, C=C$_{ar}$); 1294 (s) (C–O). ^{1}H-NMR data [400 MHz, CDCl$_3$, 300 K] δ (ppm): 3.91, 3.97 [2 × s, 2 × 1 H (CH$_2$)]; 6.8 [s,1 H (aryl)]; 7.1 [s, 1 H (aryl)], 7.2–7.6 [m, 3 H (Py)]; 8.59 [d, 1 H (Py)]. MS data (ESI$^+$ in MeOH): m/z = 283.0 [HL^{Cl2A} + H]$^+$.

Preparation of the compound [Co(L$^{t\text{-}BuLC}$)$_2$]ClO$_4$ (1). A 25 mL MeOH solution of HL$^{t\text{-}BuLC}$ (0.31 g: 0.5 mmol) and Et$_3$N (0.14 mL: 1.0 mmol) was treated with a 2 mL MeOH solution of Co(ClO$_4$)$_2$·6H$_2$O (0.10 g: 0.25 mmol). The resulting brown solution was stirred at room temperature and filtered to discard any unreacted solids after 2 h. Slow solvent evaporation yielded

a brown waxy precipitate that was frit-filtered and washed with water and cold methanol and dried under vacuum. The complex was characterized by IR and UV-visible spectroscopy, and mass spectrometry. Yield 70%. IR data (KBr, cm^{-1}) 2950 (C–H stretches from alkyl chain); 1096 (Cl–O from ClO$_4^-$), 1608 (C=N stretch form the pyridine ring); MS data (ESI$^+$ in MeOH): m/z = 1270 [Co^{III}(L$^{t\text{-}BuLC}$)$_2$]$^+$.

CAUTION! Although no difficulties were experienced, complexes **1–6** were isolated as their perchlorate salts, and therefore they should be handled as potentially explosive compounds.

Preparation of the archetypes 2–6. Due to similar procedures, a general synthetic route is described for these syntheses. A solid sample of Co(ClO$_4$)$_2$·6H$_2$O (0.37 g: 1.0 mmol) was added to a 30 mL MeOH solution containing 2.0 mmol of the appropriate ligand and Et$_3$N (0.28 mL: 2.0 mmol). After homogenization the resulting solution is stirred at room temperature for 1 h, when it is filtered to isolate any solid material. After 24 h dark brown microcrystalline precipitates were frit filtered and washed with cold water and diethyl ether, and recrystallized in MeOH by slow evaporation at ambient conditions.

[Co^{III}(L^A)$_2$]ClO$_4$ (2). Yield 79%. Elemental anal. calcd for C$_{26}$H$_{26}$N$_4$Cl$_1$O$_6$Co$_1$: C, 53.39, H, 4.48, N 9.58%. Found: C, 53.41, H, 4.53, N, 9.49%. IR data (KBr, cm^{-1}): 1092 (Cl–O from ClO$_4^-$), 1595 (C=N from pyridine). MS data (ESI$^+$ in MeOH): m/z = 485 [Co^{III}(L^A)$_2$]$^+$.

[Co^{III}(L$^{t\text{-}BuA}$)$_2$]ClO$_4$·CH$_3$OH (3). Yield 78%. Elemental anal. calcd for C$_{43}$H$_{62}$N$_4$Cl$_1$O$_7$Co$_1$: C, 61.38, H, 7.43, N 6.66%. Found: C, 61.48, H, 7.38, N 6.77%. IR data (KBr, cm^{-1}): 1108 (Cl–O from ClO$_4^-$), 2867–2952 (C–H stretches from *tert*-butyl groups), 3438 (O–H stretch, broad). MS data (ESI$^+$ in MeOH): m/z = 709 [Co^{III}(L$^{t\text{-}BuA}$)$_2$]$^+$.

[Co^{III}(L^{OMeA})$_2$]ClO$_4$·H$_2$O (4). Yield 75%. Elemental anal. calcd for C$_{28}$H$_{32}$N$_4$Cl$_1$O$_9$Co$_1$: C, 50.73, H, 4.87, N 8.45%. Found: C, 50.69, H, 4.90, N 8.21%. IR data (KBr, cm^{-1}) 1104 (Cl–O from ClO$_4^-$), 1244 (s) (C–O from methoxy groups). MS data (ESI$^+$ in MeOH): m/z = 545 [Fe^{III}(L^{OMeA})$_2$]$^+$.

[Co^{III}(L^{NO2A})$_2$]ClO$_4$ (5). Yield 73%. Elemental anal. calcd for C$_{26}$H$_{24}$N$_6$Cl$_1$O$_{10}$Co$_1$: C, 46.27, H, 3.58, N 12.45%. Found: C, 46.30, H, 3.54, N 12.31%. IR data (KBr, cm^{-1}) 1092 (Cl–O from ClO$_4^-$), 1476(s) (N=O stretch from nitro groups). MS data (ESI$^+$ in MeOH): m/z = 575 [Co^{III}(L^{NO2A})$_2$]$^+$.

[Co^{III}(L^{Cl2A})$_2$]ClO$_4$·CH$_3$OH (6). Yield 72%. Elemental anal. calcd for C$_{27}$H$_{26}$N$_4$O$_7$Cl$_5$Co$_1$ C, 42.97, H, 3.47, N 7.42%. Found: C, 42.91, H, 3.38, N, 7.57%. IR data (KBr, cm^{-1}) 1102 (Cl–O from ClO$_4^-$). MS data (ESI$^+$ in MeOH): m/z (100%) = 621 [Co^{III}(L^{Cl2A})$_2$]$^+$.

Acknowledgements

References and notes

1 T. Fujigaya, D.-L. Jiang and T. Aida, *J. Am. Chem. Soc.*, 2003, **125**, 14690.

2 D. R. Talham, *Chem. Rev.*, 2004, **104**, 5479.

3 J. Park, A. N. Pasupathy, J. I. Goldsmith, C. Chang, Y. Yaish, J. R. Petta, M. Rinkoski, J. P. Sethna, H. D. Abruna, P. L. McEuen and D. C. Ralph, *Nature*, 2002, **417**, 722.

4 J. Hjelm, R. W. Handel, A. Hagfeldt, E. C. Constable, C. E. Housecroft and R. J. Forster, *Inorg. Chem.*, 2005, **44**, 1073.

5 S. Hayami, K. Danjobara, Y. Shigeyoshi, Y. Ogawa, Y. Maeda and Y. Inorg, *Chem. Commun.*, 2005, **08**, 506.

6 (*a*) S. J. Rowan and J. B. Beck, *Faraday Discuss.*, 2005, **128**, 43; (*b*) J. B. Beck and S. J. Rowan, *J. Am. Chem. Soc.*, 2003, **125**, 13922.

7 D. Mandon, A. Nopper, T. Litrol and S. Goetz, *Inorg. Chem.*, 2001, **40**, 4803.

8 T. Storr, Y. Sugai, C. A. Barta, Y. Mikata, M. J. Adam, S. Yano and C. Orvig, *Inorg. Chem.*, 2005, **44**, 2698.

9 (*a*) S. I. Kirin, P. Dübon, T. Weyhermu lller, E. Bill and N. Metzler-Nolte, *Inorg. Chem.*, 2005, **44**, 5405; (*b*) S. I. Kirin, C. M. Happel, S. Hrubanova, T. Weyhermüller, C. Klein and N. Metzler-Nolte, *Dalton Trans.*, 2004, 1201.

10 (*a*) J. Garcia-Tojal, B. Donnadieu, J. P. Costes, J. L. Serra, L. Lezama and T. Rojo, *Inorg. Chim. Acta*, 2002, **333**, 132; (*b*) M. Scarpellini, A. Neves, A. J. Bortoluzzi, I. Vencato, V. Drago, W. A. Ortiz and C. Zucco, *J. Chem. Soc., Dalton Trans.*, 2001, 2616; (*c*) L. Casella, M. Gullotti, A. Pintar, L. Messori, A. Rockenbauer and M. Gyor, *Inorg. Chem.*, 1987, **26**, 1031; (*d*) R. C. Burrows and J. C. Bailar, Jr., *J. Am. Chem. Soc.*, 1966, **88**, 4150.

11 See: *Chem. Rev.*, 2004, 104 for an overview of the biomimetic approach. Contributions on pages 419, 903, and 1077 are recommended.

12 Archetype **3** shows the same pattern with $m/z = 709, 710, 711$, and 712. A cluster of three peaks is seen for archetypes **2** (485, 486,487), **4** (545, 546, 547), and **5** (575, 576, 577), whereas **6** displays eight peaks (621–628) due to the isotopic contribution of the chloro groups.

13 D. L. Kepert, *Inorganic Stereochemistry*, Springer-Verlag, New York, 1982, p. 114.

14 The notation $\langle A_1 B_2 \rangle$ indicates that A is *trans* to B, with A and B corresponding to the pyridine (N_{py}), amine (N_{am}), or phenolato (O_{phen}) groups. Subscripts 1 and 2 designate respectively the first and the second ligand. This concise notation saves space and was adapted by G. Miessler and D. Tarr, in *Inorganic Chemistry*, Pearson-Prentice Hall, pages 311–315, 2004 from the original work by John Bailar, Jr in *J. Chem. Educ.* 1957, **34**, 334 and 623. The link to Prof. Bailar's work has been explained by Prof. Miessler in a personal communication.

15 M. S. Shongwe, S. K. M. Al-Hatmi, H. M. Marques, R. Smith, R. Nukada and M. Mikuriya, *J. Chem. Soc., Dalton Trans.*, 2002, 4064 and references therein.

16 C. Imbert, H. P. Hratchian, M. Lanznaster, M. J. Heeg, L. Hryhorczuk, B. R. McGarvey, H. B. Schlegel and C. N. Verani, *Inorg. Chem.*, 2005, **44**, 7414.

17 A. Chakravorty and B. Behera, *Inorg. Chem.*, 1967, **06**, 1812.

18 P. Chaudhuri, C. N. Verani, E. Bill, E. Bothe, T. Weyhermueller and K. Wieghardt, *J. Am. Chem. Soc.*, 2001, **123**, 2213.

19 (*a*) A. Pui, I. Berdan, I. Morgenstern-Badarau, A. Gref and M. Perree-Fauvet, *Inorg. Chim. Acta*, 2001, **320**, 167; (*b*) H. P. Fritz and L. W. G. Vitè, *Z. Anorg. Allg. Chem.*, 1972, **392**, 271.

20 A. M. Tait, F. V. Lovecchio and D. H. Busch, *Inorg. Chem.*, 1977, **16**, 2206.

21 (*a*) F. Thomas, G. Gellon, I. Gautier-Luneau, E. Saint-Aman and J. L. Pierre, *Angew. Chem., Int. Ed.*, 2002, **41**, 3047; (*b*) Y. Shimazaki, S. Huth, A. Odani and O. Yamauchi, *Angew. Chem., Int. Ed.*, 2000, **39**, 1666; (*c*) A. Philibert, F. Thomas, C. Philouze, S. Hamman, E. Saint-Aman and J. L. Pierre, *Chem. Eur. J.*, 2003, **09**, 3803; (*d*) S. Itoh, S. Takayama, R. Arakawa, A. Furuta, M. Komatsu, A. Ishida, S. Takamuku and S. Fukuzumi, *Inorg. Chem.*, 1997, **36**, 1407; (*e*) B. A. Jazdzewski and W. B. Tolman, *Coord. Chem. Rev.*, 2000, **200–202**, 633; (*f*) J. Hockertz, S. Steenken, K. Wieghardt and P. Hildebrandt, *J. Am. Chem. Soc.*, 1993, **115**, 11222.

22 M. J. Frisch, G. W. Trucks, H. B. Schlegel, G. E. Scuseria, M. A. Robb, J. R. Cheeseman, J. A. Montgomery, T. Vreven, K. N. Kudin, J. C. Burant, J. M. Millam, S. S. Iyengar, J. Tomasi, V. Barone, B. Mennucci, M. Cossi, G. Scalmani, N. Rega, G. A. Petersson, H. Nakatsuji, M. Hada, M. Ehara, K. Toyota, R. Fukuda, J. Hasegawa, M. Ishida, T. Nakajima, Y. Honda, O. Kitao, H. Nakai, M. Klene, X. Li, J. E. Knox, H. P. Hratchian, J. B. Cross, V. Bakken, C. Adamo, J. Jaramillo, R. Gomperts, R. E. Stratmann, O. Yazyev, A. J. Austin, R. Cammi, C. Pomelli, J. W. Ochterski, P. Y. Ayala, K. Morokuma, G. A. Voth, P. Salvador, J. J. Dannenberg, V. G. Zakrzewski,S. Dapprich, A. D. Daniels, M. C. Strain, O. Farkas, D. K. Malick, A. D. Rabuck, K. Raghavachari, J. B. Foresman, J. V. Ortiz, Q. Cui, A. G. Baboul, S. Clifford, J. Cioslowski, B. B. Stefanov, G. Liu, A. Liashenko, P. Piskorz, I. Komaromi, R. L. Martin, D. J. Fox, T. Keith, M. A. Al-Laham, C. Y. Peng, A. Nanayakkara, M. Challacombe, P. M. W. Gill , B. Johnson, W. Chen, M. W. Wong, C. Gonzalez and J. A. Pople, *03, GAUSSIAN*, Gaussian Inc., C. T. Wallingford, 2003.

23 (*a*) A. D. Becke, *Phys. Rev. A*, 1988, **38**, 3098; (*b*) A. D. Becke, *J. Chem. Phys.*, 1993, **98**, 5648; (*c*) C. T. Lee, W. T. Yang and R. G. Parr, *Phys. Rev. B*, 1988, **37**, 785; (*d*) P. J. Stephens, F. J. Devlin, C. F. Chabalowski and M. J. Frisch, *J. Phys. Chem.*, 1994, **98**, 11623; (*e*) R. Ditchfield, W. R. Hehre and J. A. Pople, *J. Chem. Phys.*, 1971, **54**, 724; (*f*) M. S. Gordon, *Chem. Phys. Lett.*, 1980, **76**, 163; (*g*) P. C. Hariharan and J. A. Pople, *Theor. Chim. Acta*, 1973, **28**, 213; (*h*) P. C. Hariharan and J. A. Pople, *Mol. Phys.*, 1974, **27**, 209; (*i*) W. J. Hehre, R. Ditchfield and J. A. Pople, *J. Chem. Phys.*, 1972, **56**, 2257.

24 (*a*) H. B. Schlegel, *J. Comput. Chem.*, 1982, **3**, 214; (*b*) H. P. Hratchian and H. B. Schlegel, in *Theory and Applications of Computational Chemistry: The First 40 Years*, ed. C. E. Dykstra, K. S. Kim, G. Frenking and G. E. Scuseria, 2005, pp. 195–259.

25 M.-H. Whangbo, H. B. Schlegel and S. Wolfe, *J. Am. Chem. Soc.*, 1977, **99**, 1296.

26 R. Gagne, C. Koval and G. Licenski, *Inorg. Chem.*, 1980, **19**, 2854.

27 (*a*) *APEX-II and SMART*, Bruker AXS Inc., Madison, WI., USA, 2004; (*b*) *SHELX-97, Programs for Crystal Structure Analysis (Release 97-2)*, G. M. Sheldrick, Institüt für Anorganische Chemie der Universität, D-3400 Göttingen, Germany.

28 G. Sheldrick, *SHELX-97*, University of Göttingen, Germany, 1997 and 2003.

29 (*a*) A. Horn, I. Vencato, A. J. Bortoluzzi, R. Hoerner, R. A. Silva, F. Nome, B. Spoganicz, V. Drago, H. Terenzi, M. C. B. de Oliveira, R. Werner, W. Haase and A. Neves, *Inorg. Chim. Acta*, 2005, **358**, 339; (*b*) A. Johansson, M. Abrahamsson, A. Magnuson, P. Huang, J. Maartensson, S. Styring, L. Hammarstroem, L. Sun and B. Aakermark, *Inorg. Chem.*, 2003, **42**, 7502; (*c*) S. Menage, G. Gellon, J.-L. Pierre, D. Zurita and E. Saint-Aman, *Bull. Soc. Chim. Fr.*, 1997, **134**, 785; (*d*) R. Viswanathan, M. Palaniandavar, T. Balasubramanian and P. T. Muthiah, *J. Chem. Soc., Dalton Trans.*, 1996, 2519; (*e*) R. Uma, R. Viswanathan, M. Palaniandavar and M. Lakshminarayanan, *J. Chem. Soc., Dalton Trans.*, 1994, 1219; (*f*) A. Neves, M. A. de Brito, I. Vencato, V. Drago, K. Griesar, W. Haase and Y. P. Mascarenhas, *Inorg. Chim. Acta*, 1993, **214**, 05.

30 (*a*) J. M. Mitchell and N. S. Finney, *J. Am. Chem. Soc.*, 2001, **123**, 862; (*b*) Y.-L. Wong, Y. Yan, E. S. Chan, Q. Yang, T. C. Mak and D. K. Ng, *J. Chem. Soc., Dalton Trans.*, 1998, 3057.

Appendix D

The Divalent Cobalt case

R. Shakya, S. S. Hindo, L. Wu, M. M. Allard, M. J. Heeg, H. P. Hratchian, B. R. McGarvey, S. R. P. da Rocha, C. N. Verani,

"Archetypical Modeling and Amphiphilic Behavior of Cobalt(II)-Containing Soft-Materials with Asymmetric Tridentate Ligands"

My contribution to this work consisted of the electronic structure calculations in joint collaboration with Dr. Hrant Hratchian from Professor Schlegel's laboratory.

Archetypical Modeling and Amphiphilic Behavior of Cobalt(II)-Containing Soft-Materials with Asymmetric Tridentate Ligands

Rajendra Shakya,[†] Sarmad Sahiel Hindo,[†] Libo Wu,[‡] Marco M. Allard,[†] Mary Jane Heeg,[†] Hrant P. Hratchian,[§] Bruce R. McGarvey,[||] Sandro R. P. da Rocha,[‡] and Cláudio N. Verani*,[†]

Department of Chemistry, Wayne State University, Detroit, Michigan 48202, Department of Chemical Engineering, Wayne State University, Detroit, Michigan 48202, Department of Chemistry, Indiana University, Bloomington, Indiana 47405, and Department of Chemistry and Biochemistry, University of Windsor, Windsor, ON N9B 1P4, Canada

Received June 16, 2007

The stabilization of a bivalent oxidation state in cobalt complexes of phenolate-based asymmetric tridentate ligands with iodo and bromo substituents is studied. The complexes $[Co^{II}(L^{IA})_2]\cdot2CH_3OH$ (**1**) and $[Co^{II}(L^{BrA})_2]\cdot CH_3OH$ (**2**) were characterized by means of several spectroscopic and spectrometric techniques. The molecular structure of **1** was determined by diffractometric analysis and reveals the cobalt(II) ion in a distorted-octahedral geometry. The centrosymmetric metal ion adopts a local D_{2h} symmetry and is surrounded by facially coordinated ligands. Equivalent donor sets in both ligands are trans to each other, and DFT calculations suggest that the fac–trans configuration is favored by a small margin when compared to the fac–cis isomers. Both DFT calculations and EPR spectroscopy agree with a high-spin $S = {}^3/_2$ electronic configuration given by $[a_g{}^1, b_{1g}{}^1, a_g{}^1, b_{2g}{}^2, b_{3g}{}^2]$. This oxidation state was indirectly observed by the lack of a $p\pi_{phenolate} \rightarrow d\sigma^*_{cobalt(III)}$ charge-transfer band, which is found between 430 and 470 nm for similar cobalt(III) species. On the basis of the geometrical preferences and the oxidation state of archetypical **1** and **2**, two metallosurfactants $[Co^{II}(L^{I-ODA})_2]$ (**3**) and $[Co^{II}(L^{I-NOBA})_2]\cdot CH_2Cl_2$ (**4**) were obtained. The redox chemistry of **1–4** is marked by metal- and ligand-centered activity with several follow up processes and film formation on the electrode. Both metallosurfactants exhibit amphiphilic properties and organization, as shown by compression isotherms and Brewster angle microscopy but exhibit dissimilar collapse mechanisms; whereas **3** collapses at constant pressure, **4** exhibits a constant-area collapse. Langmuir–Blodgett films are readily obtained and were characterized by equilibrium contact angle and atomic force microscopy.

Introduction

The incorporation of transition metals to soft matter is receiving increasing interest due to potential uses toward responsive materials.[1–4] These materials are composed of a functional fragment attached to a ligand capable of coordinating metals, and their self-assembling properties facilitate the preparation of highly ordered extended structures and films. Macrocycles,[5,6] functionalized terpyridines,[7] and other symmetrical alkylpyridyl moieties with equivalent donors have been used as building blocks for cobalt(II) dendrimer-based transistors,[8] responsive ruthenium and osmium polymers,[9] multistimuli lanthanide-based plastics,[10] and metal–peptide bioconjugates.[11–13]

(1) Talham, D. R. *Chem. Rev.* **2004**, *104*, 5479.
(2) Griffiths, P. C.; Fallis, I. A.; Chuenpratoom, T.; Watanesk, R. *Adv. Colloid Interface Sci.* **2006**, *122*, 107.
(3) Domonguez-Gutierrez, D.; Surtchev, M.; Eiser, E.; Elsevier, C. J. *Nano Lett.* **2006**, *6*, 145.
(4) (a) Blasini, D. R.; Flores-Torres, S.; Smilgies, D.–M.; Abruña, H. D. *Langmuir* **2006**, *22*, 2082. (b) Storrier, G. D.; Takada, K.; Abruña, H. D. *Langmuir* **1999**, *15*, 872.
(5) Bowers, J.; Danks, M. J.; Bruce, D. W. *Langmuir* **2003**, *19*, 292.
(6) Fujigaya, T.; Jiang, D.-L.; Aida, T. *J. Am. Chem. Soc.* **2003**, *125*, 14690.
(7) Schubert, U. S.; Hofmeyer, H.; Newkome, G. R. *Modern Terpyridine Chemistry*; Wiley-VCH: Weinheim, Germany, 2006.
(8) Park, J.; Pasupathy, A. N.; Goldsmith, J. I.; Chang, C.; Yaish, Y.; Petta, J. R.; Rinkoski, M.; Sethna, J. P.; Abruna, H. D.; McEuen, P. L.; Ralph, D. C. *Nature* **2002**, *417*, 722.
(9) Hjelm, J.; Handel, R. W.; Hagfeldt, A.; Constable, E. C.; Housecroft, C. E.; Forster, R. J. *Inorg. Chem.* **2005**, *44*, 1073.

Scheme 1

Archetypical Complexes:
(R = I- or Br-, X = H)

$[Co^{II}(L^{IA})_2] \cdot 2MeOH$ (1)
$[Co^{II}(L^{BrA})_2] \cdot MeOH$ (2)

Amphiphilic Complexes:
(R = I-, X = ODA or NOBA)

$[Co^{II}(L^{I-ODA})_2]$ (3)
$[Co^{II}(L^{I-NOBA})_2] \cdot CH_2Cl_2$ (4)

ODA :

NOBA :
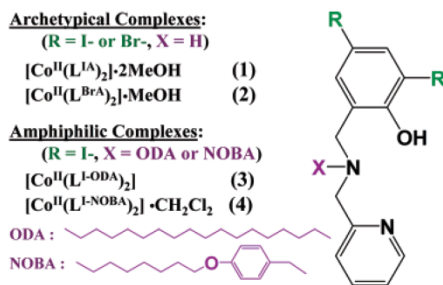
Moving toward asymmetric chelators with dissimilar donor sets[14] enables us to impart unique optical, magnetic, and redox responses leading to a broader role for metal-containing soft materials (McSM) as smart materials. Scrupulous selection of responsive donor sets and a thorough understanding of the coordination modes are pivotal for the accountability and reproducibility of these systems and may lead to improved activity. However, because the use of asymmetries increases the complexity of the approach, the design of systems based on asymmetric tridentate ligands remains largely unexplored. We are interested in redox-responsive asymmetric McSMs in which one of the donors is a phenol moiety. Phenols can be deprotonated, forming negatively charged phenolates that have the ability to form phenoxyl radicals upon oxidation. Coupling between the radical and the metal center leads to ground state switching and, therefore, to magnetic response. Phenolates also support optical responsiveness, depending on the presence or absence of ligand-to-metal charge-transfer bands related to the nature and oxidation state of the metal.

Our group has demonstrated that the mesogenic compound $[Co^{III}(L^{tBuLC})_2]ClO_4$ can generate phenoxyl radicals and that a series of $[Co^{III}(L^{RA})_2]ClO_4$ complexes with asymmetric tridentate ligands containing *tert*-butyl, methoxy, nitro, and chloro groups occupying the fourth- and sixth- positions of a phenolate ring can model successfully its coordination sphere.[15] Excellent consistency between the geometric, optical, and redox trends of the soft material and its archetypes was achieved. In this series, chloro-substituted phenolates are capable of stabilizing the quasi-reversible formation of phenoxyl radicals, so that we decided to study

other halogen-substituted counterparts. Interestingly, we have observed that the iodo and bromo-substituted phenolate groups of the tridentate ligands HL^{BrA} and HL^{IA} are capable of stabilizing bivalent cobalt ions, thus forming the compounds $[Co^{II}(L^{BrA})_2]$ (1) and $[Co^{II}(L^{IA})_2]$ (2). We envisioned the development of McSMs based on such ligands, and in this article, we present the chemistry of 1 and 2 and their analogous metallosurfactants $[Co^{II} (L^{I-ODA})_2]$ (3) and $[Co^{II} (L^{I-NOBA})_2] \cdot CH_2Cl_2$ (4), in which octadecyl (OD) and nonyloxybenzyl (NOB) are functionalities incorporated to the secondary amine (A) of the archetypical ligands (Scheme 1). These metallosurfactants have potential as precursors for ordered responsive Langmuir–Blodgett films.

Experimental Section

Materials and Methods. All of the reagents were used as received from commercial sources. Methanol was dried using calcium hydride, and dichloromethane was doubly purified using alumina columns in an Innovative Technologies solvent purification system. Infrared spectra were measured from 4000 to 400 cm^{-1} as KBr pellets on a Bruker Tensor 27 FTIR spectrophotometer. ^{1}H NMR spectra were measured using a Varian 400 MHz instrument. ESI (positive) spectra were measured in a Micromass Quattro LC triple quadrupole mass spectrometer, and experimental assignments were simulated for peak position and isotopic distribution. Elemental analyses were performed by Midwest Microlab: Indianapolis, Indiana. Visible spectroscopy from 1.0×10^{-4} dichoromethane solutions were performed using a Cary 50 spectrometer in the range of 250 to 1100 nm. Cyclic voltammetry experiments were performed using a BAS 50W potentiometer. A standard three-electrode-cell was employed with a glassy-carbon working electrode, a platinum-wire auxiliary electrode, and a Ag/AgCl reference electrode under an inert atmosphere at room temperature. Potentials are plotted versus Ag/AgCl and presented versus Fc$^+$/Fc.[16] First derivative X-Band EPR spectra of 1.0×10^{-3} M acetone solutions of 1 and 2 were performed with a Bruker ESP 300 spectrometer, using liquid helium as the coolant.

X-ray Structural Determination for 1. Crystals appeared as amber triangular rods, and a sample approximately $0.2 \times 0.15 \times 0.15$ mm^3 was used for data collection. Diffraction data were measured on a Bruker X8 APEX-II kappa geometry diffractometer with Mo radiation and a graphite monochromator. Frames were collected at 100 K as a series of sweeps with the detector at 40 mm and 0.3 degrees between each frame and were recorded for 5 s. A total of 3007 frames were collected yielding 28 555 reflections, of which 5898 were independent. *APEX-II* and *SHELX-97* software[17,18] were used in the collection and refinement of the models. Hydrogen positions were placed in observed positions. The cobalt atom occupies a crystallographic inversion center. The asymmetric unit consists of one-half of the cobalt complex and one methanol solvate.

Electronic Structure Calculations. The B3LYP/6-31G(d) level of theory[19] was employed throughout, and all of the calculations were done using the *Gaussian* series of programs.[20] Geometries were fully minimized, without symmetry constraints, using standard methods.[21] Located stationary points were characterized by computing analytic vibrational frequencies. Reported energies include zero-

(10) (a) Rowan, S. J.; Beck, J. B. *Faraday Discuss.* **2005**, *128*, 43; (b) Beck, J. B.; Rowan, S. J. *J. Am. Chem. Soc.* **2003**, *125*, 13922.
(11) Mandon, D.; Nopper, A.; Litrol, T.; Goetz, S. *Inorg. Chem.* **2001**, *40*, 4803.
(12) Storr, T.; Sugai, Y.; Barta, C. A.; Mikata, Y.; Adam, M. J.; Yano, S.; Orvig, C. *Inorg. Chem.* **2005**, *44*, 2698.
(13) (a) Kirin, S. I.; Dübon, P.; Weyhermüller, T.; Bill, E.; Metzler-Nolte, N. *Inorg. Chem.* **2005**, *44*, 5405; (b) Kirin, S. I.; Happel, C. M.; Hrubanova, S.; Weyhermüller, T.; Klein, C.; Metzler-Nolte, N. *Dalton Trans.* **2004**, 1201.
(14) (a) García-Tojal, J.; Donnadieu, B.; Costes, J. P.; Serra, J. L.; Lezama, L.; Rojo, T. *Inorg. Chim. Acta* **2002**, *333*, 132. (b) Scarpellini, M.; Neves, A.; Bortoluzzi, A. J.; Vencato, I. Drago, V.; Ortiz, W. A.; Zucco, C. *J. C. S. Dalton Trans.* **2001**, 2616. (c) Casella, L.; Gullotti, M.; Pintar, A.; Messori, L.; Rockenbauer, A.; Gyor, M. *Inorg. Chem.* **1987**, *26*, 1031. (d) Burrows, R. C.; Bailar, J. C., Jr. *J. Am. Chem. Soc.* **1966**, *88*, 4150.
(15) Shakya, R.; Imbert, C.; Hratchian, H. P.; Lanznaster, M.; Heeg, M. J.; McGarvey, B. R.; Allard, M.; Schlegel, H. B.; Verani, C. N. *Dalton Trans.* **2006**, 2517.

(16) Gagne, R.; Koval, C.; Licenski, G. *Inorg. Chem.* **1980**, *19*, 2854.
(17) *APEX II*; Bruker AXS Inc.: Madison WI, USA.
(18) Sheldrick, G., *SHELX-97*, University of Göttingen: Göttingen, Germany, 1997.

point correction. Cartesian coordinates of all of the optimized structures are provided in the Supporting Information.

Compression Isotherms and LB Films. Langmuir isotherms were measured in an automated KSV 200 minitrough at 23 ± 0.5 °C. In all of the experiments, Ultrapure water (Barnstead NANO pure) was used with a resistivity of 17.5−18 M$\Omega\cdot$cm^{-1}. Any impurities from the surface of freshly poured aqueous subphase were removed by vacuum, after the compression of the barriers. Spreading solutions of a known concentration (1.0 mg·mL^{-1}) were prepared in spectra grade chloroform, and a known quantity (typically 30 μL) was then spread on the clean aqueous subphase. The system was allowed to equilibrate for ca. 20 min before monolayer compression. The Π versus A compression isotherms were obtained at a compression rate of 10 mm·min^{-1}. The pressure was measured using the Wilhelmy plate method (paper plates 12 × 8 mm^2). At least three independent measurements were carried out per sample with excellent reproducibility attained. The films were transferred onto 40 × 20 × 0.08 mm^3 mica substrates (Ted Pella, Inc) at different target pressures.

Brewster Angle Microscopy. A KSV-Optrel BAM 300 with a HeNe laser (10mW, 632.8 nm) and a CCD detector was used in all of the micrographs. The compression rate was 5 mm/min, the field of view was 800 × 600 microns, and the lateral resolution was about 1 μm.

Contact Angle Measurements. The static contact angle of the substrates was determined to examine the quality of the deposited layers. The contact angle was determined on a KSV CAM 2000 goniometer equipped with a CCD camera. All of the data were collected at room temperature.

Atomic Force Microscopy. The surface topography of the LB films on fused silica substrates was examined using a Molecular Image Corp PicoSPM LE atomic force microscope using the tapping mode operation. A BS-Multi 75 silicon cantilever was used.

Synthesis of the Ligands. The archetypical ligands HL^{IA} and HL^{BrA} were synthesized as described in the literature.[15,22] The ligands HL^{I-ODA} and HL^{I-NOBA} were synthesized as follows:

The Organic Precursor 2,4-Di-iodo-6-(chloromethyl)phenol, I−CMP. 3,5 diiodosalicylaldehyde (1.87 g, 5.0 mmol) in 70 mL MeOH solution was reduced with NaBH$_4$ (0.29 g, 8.0 mmol) at 0 °C. After stirring the solution at the room temperature for 2 h, the solvent was removed and the crude product was dissolved in water. Diluted HCl (1M) was added dropwise, precipitating the solid 3,5 diiodobenzyl alcohol at pH ∼5.0. The alcohol is extracted with dichloromethane and dried over Na$_2$SO$_4$. Thionyl chloride (0.50 g, 5.0 mmol) is added to a solution of the alcohol (1.12 g, 3.0 mmol) in 80 mL dichloromethane. After 2 h at room temperature, the solvent was removed and the crude product was isolated as a brownish powder. Yield 92%. IR (KBr, cm^{-1}) 1451(s) (C=C$_{ar}$); 1264 (s) (C−O); ^{1}H− NMR [400 MHz, CDCl$_3$, 300K] δ/ppm = 4.60, [2x s 2x 1H (CH$_2$)]; 7.60 [s,1 H (aryl)]; 7.90 [s, 1 H (aryl)] ESI pos. in MeOH m/z = 493.8 for [HL−H$^+$]$^+$.

The Ligand 2,4-Diiodo-6-((octadecyl(pyridin-2-ylmethyl)amino)methyl)phenol, HL^{I-ODA}. Pyridine carboxyaldehyde (1.07 g, 10 mmol) was treated with octadecyl-1-amine (2.69 g, 10 mmol) in methanol at 50 °C for 1 h, yielding a yellow solution. NaBH$_4$ (0.55 g, 15 mmol) was added slowly at 0 °C. The resulting solution was stirred for 2 h at room temperature, when the solvent was removed and the crude product was extracted with 3 × 50 mL dichloromethane. The combined extracts were dried over MgSO$_4$, and the product was isolated by evaporation of the solvent. The resulting amine (1.8 g, 5 mmol) and Et$_3$N (1.4 mL, 10 mmol) were refluxed for 24 h in 50 mL dichloromethane in the presence of 2,4-di-iodo-6-(chloromethyl)phenol (1.97 g, 5 mmol). After completion, the product was washed with 4 × 30 mL of 5% NaHCO$_3$, and the organic layer was dried over MgSO$_4$. Upon solvent evaporation, an oil-like product was obtained and later recrystallized in acetone to give an off-white powder. Yield: 75%. IR (KBr, cm^{-1}) 2850(s) 2914(s) (alkyl− CH−); 1593(m), 1541(m) ,1452(s) (C=N$_{py}$, C=C$_{ar}$);1275 (s) (C−O) ^{1}H− NMR [400 MHz, CDCl$_3$, 300 K] δ/ppm = 0.858 [3× 1 H (CH$_3$)]; 1.219 [m, 30H (alkyl chain CH$_2$)]; 1.64 [t, 2 H (−NCH$_2$CH$_2$−)]; 2.63 [m 2H (−NCH$_2$−)]; 3.90 [4H(−NCH$_2$Py and −NCH$_2$Ph−]; 7.20 [s, 1H (aryl)]; 7.30 [s, 1H (aryl)] 7.20−7.90 [m, 3H (py)]; 8.61 [d, 1H (py)] ESI pos. in MeOH: m/z = 719.0 for [HL^{I-ODA} + H$^+$]$^+$.

Synthesis of the Ligand 2,4-Diiodo-6-(((4-(nonyloxy)benzyl)-(pyridin-2-ylmethyl)amino)methyl)phenol, HL^{I-NOBA}. 2-aminomethylpyridine (1.08 g; 10 mmol) was added to the solution of 4-(nonyloxy)benzaldehyde (2.48 g, 10 mmol) in methanol at 50 °C. The yellow solution obtained was stirred for 1 h and then reduced with NaBH$_4$ (0.55 g, 15 mmol) at 0 °C. After 2 h under stirring at room temperature, the solvent was removed and the crude product was added to a 100 mL of 5% aqueous NaHCO$_3$ and extracted with dichloromethane. The combined extracts were dried over MgSO$_4$, and the oil-like product was isolated and vacuum-dried. To a 50 mL dichloromethane solution containing 1.02 g (3 mmol) of the amine and 0.8 mL (6 mmol) of Et$_3$N was added 1.18 g (3 mmol) of 2,4-di-iodo-6-(chloromethyl)phenol, and the solution was refluxed for 24 h. Upon completion, the product was washed with 5% NaHCO$_3$, and the organic layer was dried in MgSO$_4$, giving an oily product, which was vacuum-dried and characterized by IR, NMR, and Mass analysis. IR (KBr, cm^{-1}) 2855(s), 2933(s) (alkyl- CH-); 1611(m), 1511(m), 1443(s) (C=Npy, C=Car); 1289(s) (C−O) ^{1}H NMR [400 MHz, CDCl$_3$, 300 K] δ/ppm = 0.87 [3 × 1H (CH$_3$)]; 1.27−1.42 [m, 12H (alkyl chain CH$_2$)]; 1.75 [m, 2H (−PhO−CH$_2$CH$_2$−)]; 3.62 [s 2H (−OPhCH$_2$N−)]; 3.71 [s, 2H (−NCH$_2$Ph−]; 3.787[s, 2H (−NCH$_2$Py−]; 3.91 [t, 2H (−PhOCH2−]; 6.83−7.18 [m, 4H (Ph)]; 7.20−7.90 [m, 3H (py)]; 8.61 [d, 1H (py)] ESI pos. in MeOH: m/z = 699.41 for [HL^{I-NOBA} + H$^+$]$^+$.

Synthesis of the Complexes. The archetypical complexes **1** and **2** and the metallosurfactants **3** and **4** were synthesized under aerobic conditions using the general procedure described below:

(19) (a) Becke, A. D. *Phys. Rev. A* **1988**, *38*, 3098. (b) Becke, A. D. *J. Chem. Phys.* **1993**, *98*, 5648. (c) Lee, T.; Yang, W. T.; Parr, R. G. *Phys. Rev. B* **1988**, *37*, 785. (d) Ditchfield, R.; Hehre, W. R.; Pople, J. A. *J. Chem. Phys.* **1971**, *54*, 724. (e) Gordon, M. S. *Chem. Phys. Lett.* **1980**, *76*, 163. (f) Hariharan, P. C.; Pople, J. A. *Theor. Chim. Acta.* **1973**, *28*, 213. (g) Hariharan, P. C.; Pople, J. A. *Mol. Phys.* **1974**, *27*, 209. (h) Hehre, W. R.; Ditchfield, R.; Pople, J. A. *J. Chem. Phys.* **1972**, *56*, 225.
(20) Frisch, M. J.; Trucks, G. W.; Schlegel, H. B.; Scuseria, G. E.; Robb, M. A.; Cheeseman, J. R.; Montgomery, J. A., Jr.; Vreven, T.; Kudin, K. N.; Burant, J. C.; Millam, J. M.; Iyengar, S. S.; Tomasi, J.; Barone, V.; Mennucci, B.; Cossi, M.; Scalmani, G.; Rega, N.; Petersson, G. A.; Nakatsuji, H.; Hada, M.; Ehara, M.; Toyota, K.; Fukuda, R.; Hasegawa, J.; Ishida, M.; Nakajima, T.; Honda, Y.; Kitao, O.; Nakai, H.; Klene, M.; Li, X.; Knox, J. E.; Hratchian, H. P.; Cross, J. B.; Bakken, V.; Adamo, C.; Jaramillo, J.; Gomperts, R.; Stratmann, R. E.; Yazyev, O.; Austin, A. J.; Cammi, R.; Pomelli, C.; Ochterski, J. W.; Ayala, P. Y.; Morokuma, K.; Voth, G. A.; Salvador, P.; Dannenberg, J. J.; Zakrzewski, V. G.; Dapprich, S.; Daniels, A. D.; Strain, M. C.; Farkas, O.; Malick, D. K.; Rabuck, A. D.; Raghavachari, K.; Foresman, J. B.; Ortiz, J. V.; Cui, Q.; Baboul, A. G.; Clifford, S.; Cioslowski, J.; Stefanov, B. B.; Liu, G.; Liashenko, A.; Piskorz, P.; Komaromi, I.; Martin, R. L.; Fox, D. J.; Keith, T.; Al-Laham, M. A.; Peng, C. Y.; Nanayakkara, A.; Challacombe, M.; Gill, P. M. W.; Johnson, B.; Chen, W.; Wong, M. W.; Gonzalez, C.; Pople, J. A. *Gaussian 03*, revision C.02; Gaussian, Inc.: Wallingford, CT, 2004.
(21) Schlegel, H. B. *J. Comp. Chem.* **1982**, *03*, 214.
(22) Shakya, R.; Peng, F.; Liu, J.; Heeg, M. J.; Verani, C. N. *Inorg. Chem.* **2006**, *45*, 6263.

Scheme 2
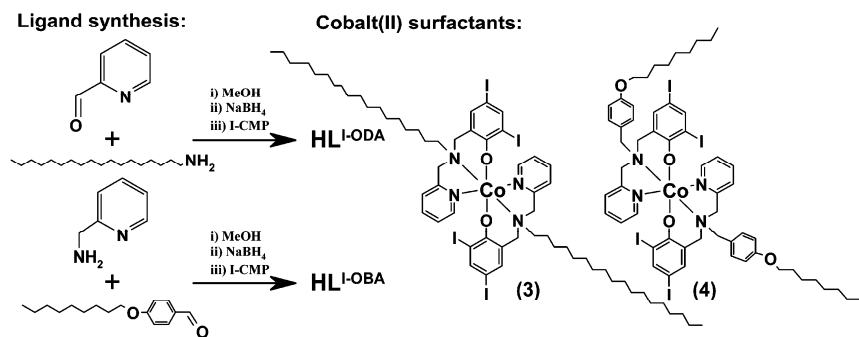
A solid sample of $[Co(H_2O)_6](ClO_4)_2$ (0.37 g, 1.0 mmol) was added to a 30 mL MeOH solution containing 2.0 mmol of the appropriate ligand and Et_3N (0.28 mL; 2.0 mmol). The solution was stirred at room temperature for 1 h. A yellowish-brown muddy product was vacuum filtered and washed with cold methanol and ether. The product was recrystallized using a 1:1 solvent mixture of methanol and dichloromethane.

$[Co^{II}(L^{IA})_2]\cdot 2CH_3OH$ (1). Yield = 81% Anal. Calcd for $C_{28}H_{30}N_4Co_1I_4O_4$: C, 31.93; H, 2.87; N, 5.32. Found: C, 32.81, H, 2.63, N 5.32. IR (KBr, cm^{-1}) 1603(m), 1561(s), 1448(s) (C=Npy, C=CAr); 1328(m) (C−O); ESI Pos. in MeOH: m/z (100%) = 989.6 for $[Co^{II}(L^{IA})_2 + H^+]^+$.

$[Co^{II}(I^{,BrA})_2]\cdot CH_3OH$ (2). Yield = 79% Anal. Calcd for $C_{27}H_{26}N_4Co_1Br_4O_3$: C, 38.93, H, 3.15, N 6.73. Found: C, 39.43, H, 3.09, N 6.65. IR (KBr, cm^{-1}) 1603(m), 1572(s), 1454(m) (C=Npy, C=CAr); 1328(m) (C−O); ESI Pos. in MeOH: m/z (100%) = 798.8 for $[Co^{II}(L^{BrA})_2+H^+]^+$.

$[Co^{II}(L^{I-ODA})_2]$ (3). Yield = 76% Anal. Calcd for $C_{62}H_{94}N_4$-$Co_1I_4O_2$: C, 49.84, H, 6.34, N 3.75. Found: C, 49.79, H, 6.29, N 3.67. IR (KBr, cm^{-1}) 2852(s), 2923(s) (alkyl− CH−); 1605(m), 1562(s), 1447(s) (C=Npy, C=CAr); 1329(m) (C−O); ESI Pos. in MeOH: m/z (100%) = 1493.8 for $[Co^{II}(L^{I-ODA})_2+H^+]^+$.

$[Co^{II}(L^{I-NOBA})_2]\cdot CH_2Cl_2$ (4). Yield = 79% Anal. Calcd for $C_{59}H_{72}N_4Co_1I_4Cl_2O_4$: C, 46.05; H, 4.72; N, 3.64. Found: C, 45.89, H, 4.74, N 3.67. IR (KBr, cm^{-1}) 2853(s), 2922(s) (alkyl− CH−); 1607(m), 1561(s), 1446(s) (C=Npy, C=CAr); 1326(m) (C−O); ESI Pos. in MeOH: m/z (100%) = 1454.7 for $[Co^{II}(L^{I-NOBA})_2+H^+]^+$.

Results and Discussion

Synthesis and Characterization of the Archetypes 1 and 2. The archetypical ligands HL^{BrA} and HL^{IA} were synthesized as reported in our previous work.[15,23] Aiming at the synthesis of cobalt(III) complexes with the bromo- and iodo-substituted ligands HL^{BrA} and HL^{IA} under aerobic conditions, a pale-yellowish-brown precipitate formed immediately after the addition of $[Co^{II}(H_2O)_6](ClO_4)_2$ in methanol. After stirring the mixture at room temperature for 1 h, the precipitate was frit-filtered, vacuum-dried, and characterized by IR spectroscopy, ESI spectrometry, and elemental analysis. The IR spectra of **1** and **2** show the usual bands expected for the ligands with minor shifting indicative of metal coordination but lack the expected peaks for the perchlorate counterion at ca. 1097 cm^{-1}. The ESI mass analysis evidence $[M+H]^+$

peak clusters for **1** and **2** with the proper mass and isotopic distribution. Because the ^{59}Co ion presents 100% abundance, the isotopic distribution is attributed to the presence of carbon, nitrogen, and oxygen atoms. Elemental analysis also provided compelling evidence for **1** and **2** to contain bivalent cobalt ions. The UV−visible spectra of **1** and **2** differ significantly from those of trivalent cobalt in similar environments[15] in which the characteristic phenolate-to-cobalt(III) charge transfer is missing. Final evidence about the oxidation state of the metal center came via the X-ray diffraction analysis of the iodo-substituted **1**, in which the absence of counterions is confirmed. EPR spectroscopy, expected to be silent in low-spin $3d^6$ cobalt(III) species, also yielded a signal for cobalt(II). The stabilization of these cobalt(II) complexes is related, at least partially, to the low solubility of the complexes in methanol. A full discussion of this data is offered later in this article.

Synthesis and Characterization of the Metallosurfactants 3 and 4. To explore the stabilization of bivalent cobalt and to aim at the development of amphiphilic materials based on these archetypes, we synthesized the new ligands HL^{I-ODA} and HL^{I-NOBA}. The ligands incorporate, respectively, amphiphilic octadecyl and nonyloxybenzyl moieties attached to the secondary amine of HL^{IA}. Initial attempts to synthesize HL^{I-ODA} and HL^{I-NOBA} using picolyl chloride, as described in similar procedures,[24] yielded less-than-satisfactory results. In an attempt to improve the ligand synthesis, the new precursor I−CMP (2,4-di-iodo-6-(chloromethyl)phenol) was obtained. Treatment of 2-hydroxy-3,5-diiodobenzaldehyde with NaBH$_4$ gave the corresponding alcohol that was treated with thionyl chloride, yielding the desired precursor. The new ligands HL^{I-ODA} and HL^{I-NOBA} were synthesized by the treatment of the appropriate aldehyde with the amine counterpart, followed by the reduction and nucleophillic substitution with I−CMP, as shown in the left-hand side of Scheme 2. The ligands were thoroughly characterized by NMR, IR spectroscopy, and ESI mass spectrometry. The cobalt-containing surfactants **3** and **4** are shown in the right-hand side of Scheme 2 and were synthesized by reacting a methanol solution of the corresponding ligand with $[Co^{II}$-$(H_2O)_6](ClO_4)_2$ in a 2:1 ligand-to-metal molar ratio at 40 °C for 1 h. In both cases, a yellowish muddy precipitate was

(23) Imbert, C.; Hratchian, H. P.; Lanznaster, M.; Heeg, M. J.; Hryhorczuk, L. M.; McGarvey, B. R.; Schlegel, H. B.; Verani, C. N. *Inorg. Chem.* **2005**, *44*, 7414−7422.

(24) Neves, A.; Romanowski, S. M.; Vencato, I.; Mangrich, A. S. *J. Chem. Soc., Dalton Trans.* **1998**, 617.
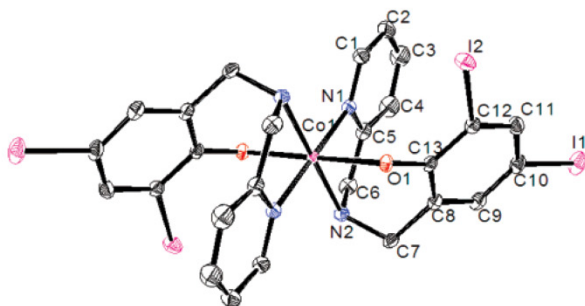
Figure 1. ORTEP representation at 50% probability for **1**. Hydrogen atoms excluded for clarity. Selected bond lengths (Å): Co1−O1 = 2.0746(11), Co1−N2 = 2.1558(14), Co1−N1 = 2.1220(14), C13−O1 = 1.3156(19), C7−C8 = 1.500(2), C7−N2 = 1.490(2), N2−C6 = 1.473(2), C5−C6 = 1.508(3). Bite angles (°): O1−Co1−N2 = 89.48(5), N1−Co1−N2 = 79.59-(5). Average distances (Å): C−C in Py = 1.383(3), C−N in Py = 1.340-(2), C−C in Ph = 1.400(2), C−I = 2.0992(16)

Table 1

formula	$C_{28}H_{30}N_4O_4I_4Co$
fw	1053.09
space group	$P2(1)/c$
a (Å)	12.5495(5)
b (Å)	11.1716(4)
c (Å)	12.3229(4)
β (deg)	97.435(1)
V (Å^3)	1713.1(1)
Z	2
T (K)	100(2)
λ (Å)	0.71073
density$_{calcd}$ (g cm^{-3})	2.042
μ (mm^{-1})	4.142
R(F)^a (%)	2.03
Rw(F) (%)	4.66

^{a} R(F) = $\Sigma||F_o| - |F_c||/\Sigma|F_o|$; Rw(F) = $[\Sigma w(F_o^2 - F_c^2)^2/\Sigma w(F_o^2)^2]^{1/2}$ for $I > 2\theta(I)$.

isolated by frit filtration, washed with excess cold methanol, and vacuum-dried for several days, yielding amorphous powders after recrystallization in methanol/dichloromethane. The IR features for **3** and **4** resemble those in the corresponding ligands, with minor shifts indicative of metal coordination and absent perchlorate peaks. The ESI mass analyses of the complexes show masses and isotopic distributions in good agreement with the [M+H$^+$]$^+$ ion. Similar to archetypes **1** and **2**, the UV−visible spectra show the absence of the ligand-to-metal charge-transfer band that is characteristic of cobalt(III) complexes that contain phenolates.

Molecular Structure of Archetype 1. The molecular structure of **1** was determined by X-ray crystallography with single crystals obtained from slow evaporation of a 1:1 solvent mixture of methanol and dichloromethane. The ORTEP diagram for **1** is depicted in Figure 1 with selected bond lengths and angles provided in Table 2. Analogous to the previously reported cobalt(III) complexes,[15] the structure of this complex is composed of a pseudo-octahedral metal center surrounded by two tridentate (L^{IA})$^-$ ligands adopting a sym-fac coordination.[25] The cobalt ions are in a centrosymmetric environment described in a Bailar, Miessler, and Tarr

(25) Kepert, D. L. *Inorganic Stereochemistry*, Springer-Verlag: New York 1982, p 114.

Table 2. Comparison of Molecular Orbital Energies and Compositions for $[Co(L^A)_2]^+$ with Trans-Phenolates and Cis-Phenolates Configurations^a

	Energy		Symmetry		% Metal		% Ligand	
	trans	cis	trans	cis	trans	cis	trans	cis
LUMO+1	−0.98	−0.93			0.9	1.0	99.1	99.0
LUMO	−1.06	−0.95			0.6	2.8	99.4	97.2
HOMO	−4.11	−4.25	a$_g$		19.7	9.1	80.3	90.9
HOMO −1	−4.52	−4.41	b$_{2u}$		1.1	10.3	98.9	89.7
HOMO −2	−4.82	−5.14	b$_{1g}$		21.4	28.4	78.6	71.6
HOMO −3	−5.39	−5.42	a$_g$		47.7	19.8	52.3	80.2
HOMO −4	−5.85	−5.82			0.3	25.2	99.7	74.8
HOMO −5	−5.85	−5.85			0.1	0.0	99.9	100.0
HOMO −6	−5.99	−5.88	b$_{2u}$		3.6	9.2	96.4	90.8
HOMO −7	−6.26	−6.37	b$_{3g}$		74.0	25.5	26.0	74.5

^{a} The trans-phenolates configuration for $[Co(L^A)_2]^+$ is described by $[Co\langle N_{am1}N_{am2}\rangle\langle N_{py1}N_{py2}\rangle\langle O_{phen1}O_{phen2}\rangle]$, whereas the cis-phenolates configuration is $[Co\langle N_{am1}O_{phen2}\rangle\langle O_{phen1}N_{am2}\rangle\langle N_{py1}N_{py2}\rangle]$. The N_{py1}−Co−N_{py2} axis has been placed along the z direction; the y axis bisects the O_{phen1}−Co−O_{phen2} angle; the x axis bisects the N_{am1}−Co−N_{am2} angle. Energy is given in eV. Pseudo symmetry labels have been assigned according to the D_{2h} group. For nonbonding orbitals, pseudo-symmetry labels are given only where ligand orbitals mimic symmetry-adapted linear combinations. % Metal and % Ligand correspond to the character of the molecular orbitals.

notation[26] as $[Co\langle N_{am1}N_{am2}\rangle\langle N_{py1}N_{py2}\rangle\langle O_{phen1}O_{phen2}\rangle]$, meaning that the equivalent donor sets in both ligands are trans to each other. The cobalt(II) center adopts an approximate D_{2h} symmetry, with its nearest neighbors and a Co^{II}−O$_{phenolate}$ distance of 2.07 Å that is comparable to others found in the literature;[27] however, being longer than those for the previously reported Co^{III}−O$_{phenolate}$.[15] Although some caution is necessary with pseudo-octahedral systems, the increment in the bond length can be explained as a consequence of Jahn−Teller distortion in a high-spin cobalt(II) 3d^7 system with S = $^3/_2$. The average Co−N$_{amine}$ (2.16 Å) and the average Co−N$_{pyridyl}$ bond length (2.12 Å) are also in good agreement with previously reported values,[13b,28] and are similarly longer that the equivalent value of 1.95−1.96 Å in trivalent complexes. Assuming this "trans-phenolates" geometry as the preferential one, as will be shown by the DFT calculations, a correlation between the structure of archetype **1** and amphiphiles **3** and **4** can be drawn.

EPR Spectroscopy of Archetypes 1 and 2. The EPR spectra of **1** and **2** have been measured to assess the oxidation state, geometry, and electronic configuration of the archetypes. In a pseudo-octahedral D_{2h} symmetry, the d$_{x^2-y^2}$ and d$_{z^2}$ orbitals transform as a$_g$, whereas d$_{xy}$, d$_{xz}$, and d$_{yz}$ transform respectively as b$_{1g}$, b$_{2g}$, and b$_{3g}$. The b$_{xg}$ set has closely related energies and is separated from the a$_g$ set by a large energy gap. A low-spin electronic configuration given by

(26) The notation $\langle A_1B_2\rangle$ indicates that A is trans to B, with A and B corresponding to the pyridine (Npy), amine (Nam), or phenolato (Ophen) groups. Subscripts 1 and 2 designate respectively the first and the second ligand. This concise notation saves space and was adapted by G. Miessler and D. Tarr in *Inorganic Chemistry*, Pearson-Prentice Hall, 2004, pp 311−315, from the original work by John Bailar, Jr., in *J. Chem. Ed.* 1957, **34**, 334 and 623. The link to Prof. Bailar's work has been explained by Prof. Miessler in a personal communication.
(27) Higgs, T. C.; Carrano, C. J. *Inorg. Chem.* **1997**, *36*, 291.
(28) (a) Mohamadou, A.; Jubert, C.; Barbier, J. *Inorg. Chim. Acta* **2006**, *359*, 273, (b) Comba, P.; Kerscher, M.; Merz, M.; Müller, V.; Pritzkow, H.; Remenyi, R.; Schiek, W.; Xiong, Y. *Chem.−Eur. J.* **2002**, *8*, 5750, (c) Makowska-Grzyska, M. M.; Szajna, E.; Shipley, C.; Arif, A. M.; Mitchell, M. H.; Halfen, J. A.; Berreau, L. M. *Inorg. Chem.* **2003**, *42*, 7472.
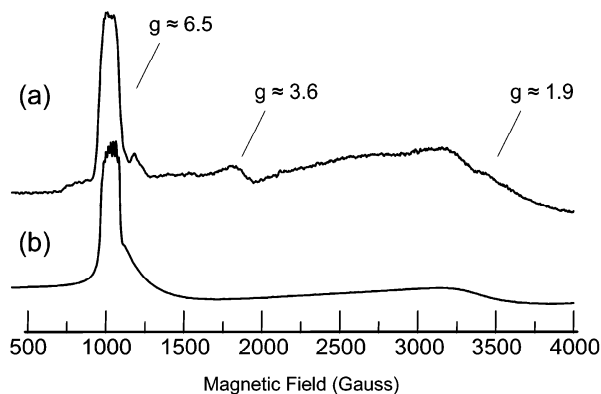
Figure 2. (a) Frozen liquid spectrum of **1** in methanol/dichloromethane at 4.1 K. (b) Simulation of the spectra observed for **1** and **2**.

$[a_g{}^0,a_g{}^0,b_{1g}{}^2,b_{2g}{}^2,b_{3g}{}^2]$ is expected for a cobalt(III) ion and is thus associated with a lack of signal typical of diamagnetic species. Therefore, the fact that we can observe a signal at ca. 4 K per se is indicative of the presence of cobalt(II) ions. This is in excellent agreement with the lack of a counterion observed independently by IR spectroscopy and X-ray crystallography. The spin Hamiltonian that represents transitions in the lowest Kramer's doublet for $S = {}^3/_2$ in a near-octahedral $3d^7$ configuration is given by $H = \beta_e[g_xH_xS_x+g_yH_yS_y+g_zH_zS_z] + A_xS_xI_x + A_yS_yI_y + A_zS_zI_z$,[29] where S is taken to be $S = {}^1/_2$. EPR measurements are only possible at liquid helium temperatures for cobalt (II) as a result of short spin−lattice relaxation times. The spectra become broader as the temperature is increased, and at liquid nitrogen temperatures ($\sim$77 K) the signal disappears.

Both **1** and **2** exhibit essentially identical features with distinct signal-to-noise ratios. The frozen-liquid spectrum of **1** in methanol/dichloromethane at 4.1 K is shown in part a of Figure 2 as the first derivative of the absorption spectrum. The most-prominent feature in the spectra is a peaklike signal at ca. 1000 G, which is a turning point for a broad line with a principal g value of 6.5 and two other signals with much-smaller g values. The narrow shape of the peak is due to a small hyperfine interaction for the isotope ^{59}Co ($I = {}^7/_2$) for this principal direction (attributed to z). To illustrate the origin of this peak, we show in part b of Figure 2 a simulation for $g_z = 6.5$ and $A_z = 16$ G, with the other principal directions having identical values of $g_{x,y} = 1.9$ and $A_{x,y} = 100$ G. At the base of the $g = 6.5$ peak, there appears to be another peaklike feature with $g = 6.9$ and a resolved hyperfine interaction of about 60 G. A turning point is also seen at $g = 3.58$, and another intense broad turning point is seen at $g = \sim1.9$. It suggests that two different cobalt(II) species are present in solution, and because of the labile nature of the ion, these are most likely different conformers formed in solution. Similar behavior has been reported for other divalent cobalt species.[30,31]

In near-octahedral fields, the orbital motion in the $^4T_1$ ground state of cobalt(II) is not quenched, resulting in a large spin−orbit interaction, which produces a Kramer's doublet ground state. This Kramer's doublet is always fitted to an $S = {}^1/_2$ spin Hamiltonian. The EPR signal of a high-spin cobalt-(II) ion in a nondistorted-octahedral environment exhibits a single $g \approx 4.34$. If distortion of this octahedral field occurs, three different g values ranging from 6.9 to 2.0 are observed. In tetrahedral and cubic fields, the g value is near 2.3. For low-spin cobalt(II) ions resulting from strong crystal fields with large distortions, g values will be slightly different than 2.0. On the basis of this discussion, the EPR results indicate **1** and **2** as being high-spin in nature and located in a pseudo-octahedral environment.

Electronic Structure Calculations. In a recent article, we investigated iron(III) and gallium(III) complexes of asymmetric NN′O ligands,[23] concluding that facial coordination of the ligands is favored, along with a cis distribution of the phenolates. In an account on trivalent cobalt complexes,[15] we have shown that phenolate rings adopt a trans configuration in a D_{2h} local symmetry, favored by at least 4.0 kcal/mol. Here, we are interested in assessing the D_{2h} facial, all-trans geometry observed experimentally for **1**, to infer whether it is reasonable to expect **3** and **4** to have a similar local D_{2h} trans ligand configuration. A comparison between bivalent and trivalent cobalt is also included. The same level of theory was employed throughout the calculations in this and in the aforementioned accounts, thus allowing direct comparisons.

Complex **1** has a $3d^7_{high\,spin}$ cobalt(II) center and iodo substituents in the second and fourth positions of the phenolate moiety of the ligand. To make the calculations more affordable, these groups are replaced by hydrogen atoms, and the resulting model is called $\mathbf{1^H}$. Considering this a suitable model, the energetics of the cobalt(II) complexes with cis and trans phenolates, described respectively as $[\langle N_{am1}N_{am2}\rangle\langle N_{py1}O_{phen2}\rangle\langle O_{phen1}N_{py2}\rangle]$ and $[\langle N_{am1}N_{am2}\rangle\langle N_{py1}N_{py2}\rangle\langle O_{phen1}O_{phen2}\rangle]$, were compared. The optimized geometry of the trans isomer of $\mathbf{1^H}$ is in good agreement with the crystal structure of **1** and is depicted in the top left-hand side of Figure 3.

The calculations favor the trans configuration of $\mathbf{1^H}$ by 2.3 kcal·mol^{-1}. This energy difference between isomers is similar to the 3.8 kcal·mol^{-1} isomer difference observed for the equivalent cobalt(III) model complexes.[15] Despite the small energy difference, our computational results do agree with the experimentally observed preference for the trans isomer. Similar to the cobalt(II) case,[15] the energy preference can be understood by considering the energies of the frontier molecular orbitals (Table 2). The MOs of $\mathbf{1^H}$ reveal some metal character in the HOMO, HOMO-2, and HOMO-3 orbitals for the trans structure, as shown in the right-hand side of Figure 3 and in Table 2, indicating that these are the d-based orbitals in a pseudo-octahedral D_{2h} symmetry related to the high-spin electronic configuration $[a_g{}^1,b_{1g}{}^1,a_g{}^1,b_{3g}{}^2,b_{2g}{}^2]$

(29) McGarvey, B. R. *Transition Metal Chemistry*; Carlin, R. L., Ed.; Marcel Dekker, Inc.: New York, 1966, vol. 03, p 175.

(30) Scarpellini, M.; Wu, A. J.; Kampf, J. W.; Pecoraro, V. L. *Inorg Chem.* **2005**, *44*, 5001.

(31) Tubbs, K. J.; Szajna, E.; Bennett, B.; Halfen, J. A.; Watkins, R. W.; Arif, A. M.; Berreau, L. M. *Dalton* **2004**, 2398.
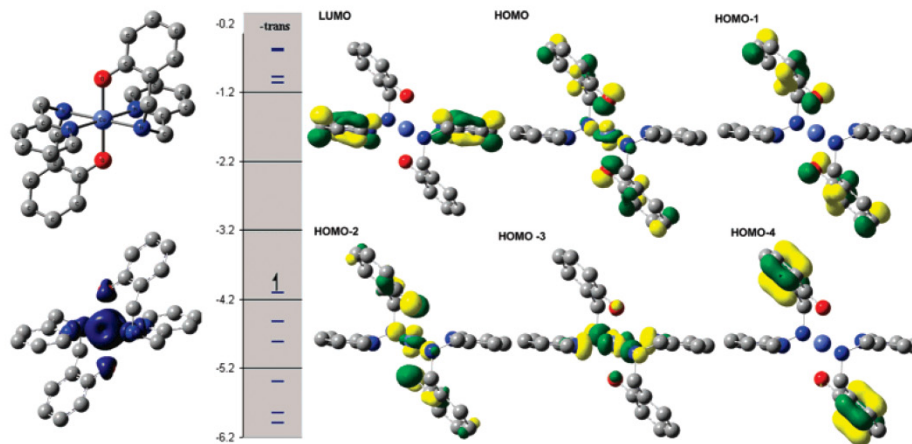
Figure 3. Left: Minimized structure exhibiting the favored trans-phenolates configuration for $\mathbf{1^H}$ (top) and the equivalent spin-density plot (bottom). Center: Orbital energy ladder for the model $\mathbf{1^H}$. Right: Selected frontier MOs for the trans $\mathbf{1^H}$ showing prevalent metal or ligand character.

with an $S = {}^3/_2$ ground state. These correspond to the singly occupied orbitals, and the $b_{1g}{}^1$ MO lies slightly higher in energy than the $a_g{}^1$ orbital. Both HOMO and HOMO-2 orbitals show considerable phenolate character via the contribution of the 2p orbitals in the oxygen centers, whereas the HOMO-3 orbital entails sigma interactions within the xz plane, thus consistent with the four nitrogen donors combining with a $d_{z^2-x^2}$ orbital. This $d_{z^2-x^2}$ component is part of the linear combination for the d_{z^2} orbital, more appropriately described as $d2_{z^2-x^2-y^2}$ (combination of $d_{z^2-x^2}$ and $d_{z^2-y^2}$), thus transforming as a_g in a D_{2h} group. These results are consistent with our expectations described in the EPR section above. Whereas the highest-occupied MOs displaying metal character have similar energies for both the cis and trans isomers, the second-highest-occupied MO for the trans structure is 0.4 eV more stable than the corresponding cis MO. This trend continues to the third- and fourth-highest-occupied MOs, with the trans isomer MOs being more stable by 0.3 and 0.8 eV. We also note that the relative stability of the trans isomer, relative to the cis geometry, may increase if we had not replaced the iodo groups in $\mathbf{1}$ with hydrogen atoms. Indeed, preliminary results from a study in our labs related to similar complexes suggest that replacement of the hydrogen atoms by chlorides in the phenolate moiety leads to an increase in the stabilization of the favored isomer by ca. 7.0 kcal·mol^{-1}.[32] Although the presence of different conformers cannot be ruled out, as discussed in the EPR section, it seems reasonable from these results to predict that the prevalent trans geometry is also found in the metallosurfactants $\mathbf{3}$ and $\mathbf{4}$.

Figure 3 also shows the spin-density plot for $\mathbf{1^H}$, and it is clear that the majority of the excess spin density is localized on the metal center, with a small degree of excess spin on the immediate six neighbors of the coordination sphere. Specifically, the cobalt center has a net Mulliken spin population of 2.74, consistent with an oxidation state assignment of a bivalent cobalt ion.
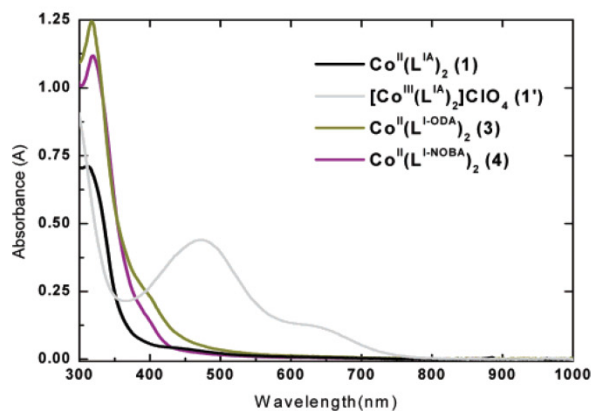
Figure 4. UV−vis spectra of 1.0×10^{-4} M dichloromethane solutions for $\mathbf{1}$, $\mathbf{1'}$, $\mathbf{3}$, and $\mathbf{4}$ at room temperature. Assignments λ (nm)/ϵ (Lmol^{-1}cm^{-1}) are as follows: For $\mathbf{1}$ (black trace): 264/21085; 312/7122. For $\mathbf{2}$ (not shown): 262/24 777; 316/8814. For $\mathbf{3}$ (dark-yellow trace): 257/31 981; 317/12 324. For $\mathbf{4}$ (purple trace): 264/31 981; 321/11 149. For $\mathbf{1'}$: 282/10 202; 474/4389; 631/1320.

Electronic Spectroscopy of 1−4. The UV−vis spectra of $\mathbf{1-4}$ were taken in 1.0×10^{-4} M dichloromethane solutions. The spectra of selected complexes are shown in Figure 4. The main feature observed for $\mathbf{1-4}$ is the presence of intense $\pi \rightarrow \pi^*$ intraligand bands between 312 and 321 nm. The most-remarkable indication of the bivalent nature of these species is the lack of the $p\pi_{phenolate} \rightarrow d\sigma^*_{cobalt(III)}$ charge-transfer band found at 474 nm for the iodo-substituted cobalt(III) $\mathbf{1'}$ and is systematically found between 430 and 470 nm for the previously reported cobalt(III) complexes with similar ligands.[15] This observation is in agreement with the expected spectrum of d^7 high-spin cobalt(II) systems.[33] The absence of the LMCT band for the bivalent species when compared to equivalent trivalent species is reflected by a considerable decrease in the color of the complexes and suggests that optical responsiveness can be attained either by means of electrochemical or chemical stimuli.

(32) Allard, M.; Verani, C. N., unpublished results. These results are part of an upcoming article on the chemistry of iron-containing amphiphiles.

(33) Lever, A. B. P. *Inorganic Electronic Spectroscopy*; Elsevier Science: New York, 1984; pp 203−245.
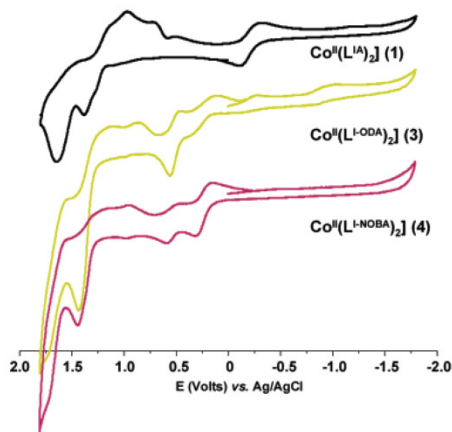
Figure 5. CVs of **1** (black trace), **3** (dark-yellow trace), and **4** (violet trace) as 1.0×10^{-4} M dichloromethane solutions with 0.1 mol L^{-1} TBAPF$_6$ at room temperature. Scan rate at 100 mV·s^{-1} using a three-electrode system (W = carbon, ref = Ag/AgCl, Aux. = platinum wire). Ferrocene was used as an internal standard ($E_{1/2} = 0.40$ V).

Redox Properties of 1−4. Cyclic voltammograms of **1−4** were measured in dichloromethane using TBAPF$_6$ as a supporting electrolyte to evaluate the response of the compounds toward redox stimuli in the time scale of the voltammetric experiments. The cyclic voltammograms of **1**, **3**, and **4** are shown in Figure 5, and the potentials are given in Table 3. Unexpectedly, an intricate redox behavior is observed for each of these complexes, much different from that observed for the equivalent cobalt(III) chloro-substituted analogue [Co^{III}(L^{Cl2A})$_2$] published previously.[15] Analogue [Co^{III}(L^{Cl2A})$_2$] has shown a reversible behavior with potentials for the cobalt(III)/cobalt(II) couple observed at −0.67 versus Fc$^+$/Fc, whereas quasi-reversible ligand-centered processes were observed at 0.87 and 1.29 versus Fc$^+$/Fc. It is evident from the shape of the voltammograms for **1**, **3**, and **4**, as well as by the amplitude of the different processes, that multiple reductions and oxidations take place at the surface of the electrode. The behavior of **1** resembles accurately that for **2** (not shown).

Ligand-centered oxidations around 1.5 and 1.75 V (vs Ag/AgCl) can be observed in all of the species, falling within the expected range observed for the chloro-substituted analogue and related to the oxidation of phenolates to phenoxyl radicals. Nonetheless, each of these processes give rise to multiple ligand-based reductions tentatively attributed to the phenoxyl-to-phenolate process in the species derived from the parent complexes. Three reductions for **1** and **2** and two for **3** and **4** are observed even when cycling of the potential happens immediately after the formation of the first phenoxyl radical. It suggests that a single oxidation suffices to trigger follow-up reactions, probably polymeric in nature and associated to the activation of the iodo groups. The metal-centered processes in **1** and **2** are found to be quasi-reversible and within comparable potentials to that of the chloro analogue [Co^{III}(L^{Cl2A})$_2$]. The scenario changes considerably for **3** and **4**, where once again multiple processes indicative of catalytic decomposition take place. This behavior is consistent within several scan rates at 50, 100,

and 500 mV·sec^{-1} in dichloromethane. Finally, the use of successive scanning (∼15 cycles) in dichloromethane at 100 mV·sec^{-1} reveals film formation at the surface of the electrode, as characterized by an increase of the peak current after each scan.[9] One can conclude that the replacement of either *tert*-butyl or chloro groups by iodo substitutents in the phenol ring fails in leading to improved redox responses based on metal or ligand activities. Although this fact limits the use of these amphiphiles as responsive materials considerably, the presence of iodo-substituted phenols might be key in the development of conductive polymerized films and will be further explored in our lab.

Amphiphilic Properties, Brewster Angle Microscopy, and Langmuir Film Formation of HL$^{I−ODA}$, HL$^{I−NOBA}$, 3, and 4. The logic behind the synthesis of the ligands HL$^{I−ODA}$ and HL$^{I−NOBA}$ consists of attaching simple organic fragments of nonpolar nature to the amine nitrogen of the archetypical **1**. These organic fragments are expected to confer amphiphilic properties to the newly synthesized systems in which the octadecyl and nonyl-oxo-benzene fragments, respectively present in HL$^{I−ODA}$ and HL$^{I−NOBA}$, act as hydrophobic counterparts of a polar head group. Inclusion of a metal ion such as cobalt(II) is expected to modify the amphiphilicity of the system as a result of changes in the molecular dipole moment and the coordination to two of the amphiphilinc ligands to one metal center, forming new species. The amphiphilic properties of both ligands, **3** and **4**, are displayed in Figure 6 as compression isotherms plotting surface pressure (Π, mN·m^{-1}) versus area per molecule (A, Å^2). These isotherms give information about the 2D behavior of the resulting Langmuir film at the air/water interface, the collapse pressure (π_c), and the area at the collapse of the monolayer (A_c). The surfactant is initially dissolved in an immiscible organic solvent and subsequently spread on the water surface. As the barriers of the trough are compressed, the tension (γ) of the air−water interface in the presence of the amphiphilic species decreases as compared to that of the bare air−water interface ($\gamma_0 = 72$ mN·m^{-1} at 23 °C), resulting in an increase in Π ($= \gamma_0 - \gamma$). The isotherms for HL$^{I−ODA}$, HL$^{I−NOBA}$, **3**, and **4** reveal that all of the species are interfacially active. Each isotherm was repeated at least three times, and excellent reproducibility was attained.

The individual molecules of the protonated ligands start interacting with each other at the air/water interface at ca. 45 Å^2·molecule^{-1} for both ligands, forming an expanded phase.[34] No phase transitions were observed, and collapse pressures of ca. 20 mN·m^{-1} were recorded. Areas at collapse of 41 and 35 Å^2·molecule^{-1} for HL$^{I−ODA}$ and HL$^{I−NOBA}$ respectively can be determined by extrapolating the Π versus A curve at its steepest slope before the collapse, where it intercepts the x axis.[1] The A_c values determined for the

---

(34) For monolayers, it is common to use the terms gaseous (G), expanded (E), and condensed (C) to describe the phases. In G-phases, the molecules of the monolayer are far apart from each other so that minimal force is exerted on one another. In E-phases, interactions among the molecules are semi-randomic, resembling interactions in a liquid. C-phases resemble interactions in a solid. For an excellent introductory text on the subject, see Petty, M. C. "Langmuir−Blodgett Films".

Table 3

compounds	reductions[a] (V vs F_c^+/F_c)	oxidations[b] (V vs F_c^+/F_c)
(**1**)	$-0.74, +1.01, +0.67, +0.50, +0.23$	$-0.58, +0.79, +0.91, +1.17$
(**2**)	$-0.81, +1.15, +0.71, +0.55, +0.27$	$-0.68, +0.80, +0.89, +1.17$
(**3**)	$-0.72, +1.10, +0.74, +0.66, +0.41, +0.02, -0.32$	$-0.60, -0.11, +0.11, +0.98, +1.27$
(**4**)	$-0.25, +1.15, +0.83, +0.74, +0.52, +0.07$	$-0.11, +0.17, +0.55, +1.02. +1.31$

[a] The potential given is the cathodic peak potential E_{pc} versus F_c^+/F_c. [b] The potential given is the anodic peak potential E_{pa} versus F_c^+/F_c.
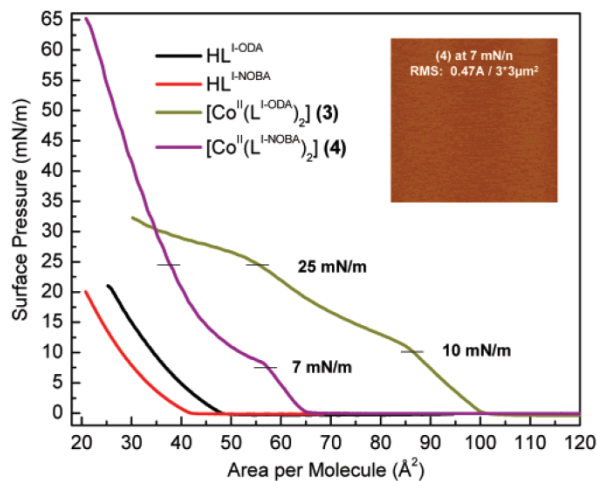
Figure 6. Compression isotherms at the air/water interface for HL^{I-ODA} (black), HL^{I-NOBA} (red), (**3**) (dark yellow), and (**4**) (violet). Inset: Tapping mode AFM (topography) of **4** at 7 mN·m^{-1}. Pressures by which LB films were deposited are indicated at 7, 10, and 25 mN·m^{-1}.

ligands are much larger than the $20-22$ Å^2·molecule^{-1} observed for heptadecanoic acid[35] but closer to the area occupied by bulkier species like eruric and dimyristolphosphatidic acid (38 and 51 Å^2·molecule^{-1}).[36]

Drastic changes are observed in the amphiphilic properties when the ligands are compared to the cobalt complexes. The individual molecules of **3** start interacting at the air/water interface at ca. 100 Å^2·molecule^{-1}, whereas the molecules of **4** interact at a much lower area of ca. 65 Å^2·molecule^{-1}. We start the discussion with the isotherm of **4**, which exhibits a phase transition at about 8 mN·m^{-1}, forming a condensed phase that collapses with a sudden drop in pressure after 65 mN·m^{-1} with an average area of 48 Å^2·molecule^{-1}. The collapse shows the signature of a constant-area collapse.[37] An increase of ca. $10-15$ Å^2·molecule^{-1} in the A_c value is observed when **4** is compared to HL^{I-NOBA}. Considering some rearrangements of the hydrophobic chains, this increase is in agreement with simple molecular mechanics calculations that suggest **4** to be only ca. 18 Å longer than the nonmetallated ligand. Additionally, it has been observed independently by us[38] and others[39] that an increase of about 10 Å^2·molecule^{-1} can be expected upon complexation of

Scheme 3
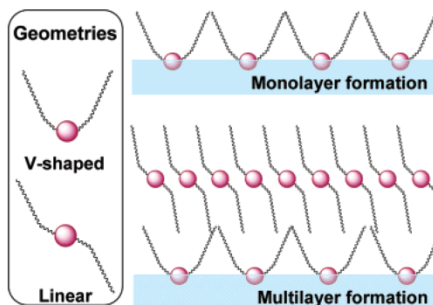
bivalent ions. **3** displays an intricate profile that includes two inflections, at about 13 and 24 mN·m^{-1}, followed by expansions of the areas occupied per molecule. Contrary to the clear collapse observed for **4**, the moving barriers of the trough come to touch each other without a noticeable drop in pressure. This behavior differs from the expected constant-area collapse of a monolayer and led us to consider the isotherm for **3** as representative of the growth of a collapsing monolayer. Understanding that the kinetics of monolayer collapse has been best described as confused,[40] recent work[36,41] may be helpful in this discussion. In monolayers of divalent metal (manganese, cobalt, cadmium, and lead) complexes of stearic acid formed in situ, the nature of the metal ion determines whether collapse happens at constant area or pressure.[42] The formation of a plateau is the signature of a constant-pressure collapse, and all of the monolayers follow the Ries mechanism[43] of folding, bending, and breaking into multilayers. Similar to these metal-containing fatty acids, **3** and **4** exhibit a head group connected to two tail groups, and, therefore, two arrangements are possible: a v-shaped geometry that allows for monolayer formation due to its amphiphilic nature, and a linear geometry (Scheme 3). The latter is unstable at the air/water interface but can form domains or layers on top of hydrophobic interfaces such as the monolayer resulting from the v-shaped geometry.

Hence, we suggest that in the case of **3**, where octadecyl chains are attached directly to the tertiary nitrogen of the head group, unrestricted movement may allow for both the v-shaped and the linear geometries (depicted in Schemes 2 and 3). This leads to constant-pressure collapse followed by the formation of multilayers. On the other hand, the presence of the alkoxy groups in **4** leads to a less-flexible molecule,

(35) Goncalves da Silva, A. M. P. S.; Armitage, D. A.; Linford, R. G. *J. Colloid Interface Sci.* **1993**, *156*, 433.
(36) Petty, M. C. *Langmuir−Blodgett Films*; Cambridge University Press: New York, 1996; pp 65−93.
(37) Kundu, S.; Datta, A.; Hazra, S. *Phys. Rev.* **2006**, *E 73*, 051608
(38) Driscoll, J.; Jayathilake, H.; Wu, L.; Bordenyuk, A.; Heeg, M. J.; Verani, C. N.; Benderskii, A.; da Rocha, S. R. P. submitted to *Langmuir*.
(39) Kraus, S.; Mandler, D. *Langmuir* **2006**, *22*, 7462.

(40) Ybert. C.; Lu, W.; Moeller, G.; Knobler, C. M. *J. Phys.: Condens. Matter* **2002**, *14*, 4753.
(41) Vaknin, D.; Bu, W.; Satija, S. K.; Travesset, A. *Langmuir* **2007**, *23*, 1888.
(42) Kundu, S.; Datta, A.; Hazra, S. *Langmuir* **2005**, *21*, 5894.
(43) Ries, H. E., Jr. *Nature* **1979**, *281*, 287.

and the v-shaped geometry is favored. An approximation of this geometry is also depicted in Schemes 2 and 3, where the two hydrophobic nonyl chains are symmetrically repelled outward and the head group is in contact with the water surface. When comparing the behavior of **3** and **4** with that of the stearic acid complexes with divalent ions, a major difference is evident: In the latter case, both the ligand (protonated stearic acid) and the metal charges remain unchanged, with a M/L stoichiometry assumed constant as 1:2. As a result, the nature of the metal ion determines the surfactant geometry, and the collapse profile, as v-shaped for the smaller manganese(II) and cobalt(II) (constant pressure) or linear for the bulkier cadmium(II) and lead(II) ions (constant area). In this study, the ion is kept constant for **3** and **4**, but the nature of the ligand changes considerably. The same cobalt(II) ion seems to collapse at constant pressure for **3** and constant area for **4**, implying that the nature of the ligand is also instrumental in defining the mechanism of collapse.

The Brewster or polarization angle can be detected when the intensity of the vertical component of reflected polarized light passes through a minimum while moving between two media of dissimilar refractive index. Because agglomerates, domains, and monolayers differ in refractive index from the surrounding area, visualization of bidimensional structures in films becomes possible. Brewster angle microscopy (BAM) was used in the films of **3** and **4** in an attempt to investigate these two possible collapse mechanisms. Figure 7 shows a series of BAM micrographs for both complexes.

Careful analysis of the micrographs for **3** reveals that condensed domains of elongated shape are present before compression. At around 10 mN·m^{-1}, hence before the first inflection, a smooth film is observed and was interpreted as the formation of a monolayer. At around 23 mN·m^{-1}, thus close to the second inflection, condensed domains are observed again, and we interpret that as an indication that the monolayer has collapsed after the first inflection. Because no drop in pressure was observed, it confirms the constant pressure mechanism. Domains of elongated shape are observed immediately after the second inflection (∼28 mN·m^{-1}), indicating further folding of the multilayer. It is noteworthy that a recent article on the patterns in domains of Langmuir monolayers shows comparable isotherm and micrographs for *N*-hexadecanoyl L-alanine on a zinc(II)-containing subphase.[44] Although the BAM data succeeds in diagnosing the presence of a collapsed multilayer, the study of the linear versus v-conformation molecular shapes cannot be attained by this technique. Similarly, the micrographs of **4** are in good agreement with the proposed constant-area collapse. Only minor aggregates were observed before compression, and a uniform monolayer was observed at 7 mN·m^{-1}. Between 8−10 mN·m^{-1}, coinciding with the inflection seen on the isotherm, a somewhat uneven and rough pattern can be observed. It was first considered as an indication of collapse, but as the compression moves to higher surface pressures (25 mN·m^{-1}), a homogeneous film

(44) Hoffmann, F.; Stine, K. J.; Hühnerfuss *J. Phys. Chem. B* **2005**, *109*, 240.
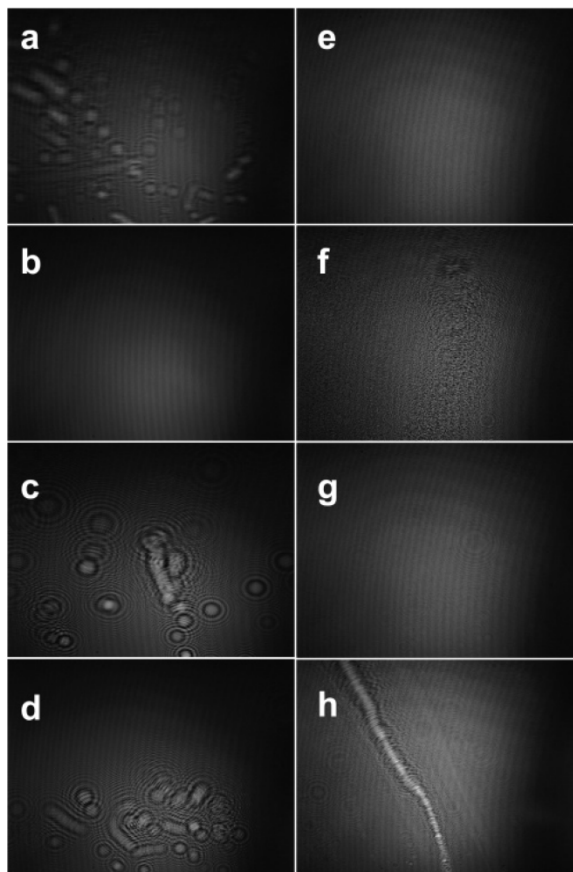
Figure 7. BAM micrographs for amphiphiles **3** (left) and **4** (right): (a) **3** before compression; (b) **3** at Π = 10 mN·m^{-1}; (c) **3** at Π = 23 mN·m^{-1}; (d) **3** at Π = 28 mN·m^{-1}; (e) **4** at Π = 7 mN·m^{-1}; (f) **4** at Π ≈ 8−10 mN·m^{-1} (g) **4** at Π = 25 mN·m^{-1}; (h) **4** at Π = 65 mN·m^{-1}.

is observed. Therefore, we interpret the rough surface seen around 8−10 mN·m^{-1} as a mesophase that leads to some sort of reorganization of the monolayer. Collapse of the monolayer is clearly observed at ca. 65 mN·m^{-1}.

One can conclude that the coordination of bivalent cobalt to the deprotonated form of HL$^{I−ODA}$ yielded **3**, which suggests the octadecyl fragment might be too long and flexible to support high collapse pressures and, consequently, highly packed Langmuir monolayers. The same reaction with the deprotonated form of HL$^{I−NOBA}$ yielded **4**, a system of well-characterized structure that shows amphiphilic properties, good organization, and collapse pressure.

Equilibrium Contact Angles and Atomic Force Microscopy for the Langmuir−Blodgett Films of 3 and 4. Langmuir monolayers of **3** and **4** are readily transferred onto mica substrates. In an attempt to assess the nature of the films, we carried on depositions at 10 and 25 mN·m^{-1} for **3** and at 7 and 25 mN·m^{-1} for **4**, as indicated in Figure 6. Characterization of these films was performed via equilibrium contact angle (θ) and atomic force microscopy. The measurement of θ at which a liquid/air interface meets the solid surface is used as a quantitative measure of the wetting of a solid by a liquid[45] and helps determine whether a

monolayer has been transferred to a substrate by comparing the pre- and post-deposition angle formed by a drop of water on a given substrate. Whereas hydrophilic surfaces such as mica yield an effective $\theta \approx 0°$, highly hydrophobic surfaces present angles between 70 and 90°. The higher the θ value, the more hodrophobic the surface. Average values of 80 and 90° were observed for the films of **3** at 10 and 25 mN·m^{-1} respectively, whereas 91° was observed for **4** at 7 and 25 mN·m^{-1}. In all of the cases, there is a sharp contrast between the θ value of the hydrophilic mica substrate and that of the hydrophobic LB films, suggesting that the polar head is in contact with the mica surface, whereas the hydrophobic chains point outward. It is interesting that the two films obtained for **4** present equivalent hydrophobicity, whereas those for **3** indicate an increase in hydrophobicity in moving from 10 to 25 mN·m^{-1}. On the basis of the isotherm profiles, the BAM micrographs, and the differences in contact angles, it seems that a single monolayer is transferred for both LB films of **4**, whereas for **3** a monolayer is transferred only at 10 mN·m^{-1}. Tapping mode AFM data was obtained for all of the LB films and revealed smooth surfaces. The inset in Figure 6 exemplifies the topography of the LB film for **4** at 7 mN·m^{-1}. Unfortunately, several attempts to determine the thickness of the films by scratching their surface with the tip of the cantilever proved to be unsuccessful at this point.

Summary and Conclusions

We have observed that the iodo and bromo substituents in the phenolate group of asymmetric NN'O ligands stabilize cobalt(II) ions and yield the compounds [Co^{II}(L^{IA})$_2$] (**1**) [Co^{II}(L^{BrA})$_2$] (**2**). This was the starting point for the development of amphiphilic species based on the incorporation of OD and NOB functionalities to similar head groups. The cobalt(II) metallosurfactants [Co^{II}(L^{I-ODA})$_2$] (**3**) and [Co^{II}(L^{I-NOBA})$_2$]·CH$_2$Cl$_2$ (**4**) were isolated and studied. A crystal structure was obtained for **1** and showed a centrosymmetric pseudo-octahedral metal center surrounded by two facially coordinated ligands. The equivalent donor sets in both ligands are trans to each other, and the metal adopts a local D_{2h} symmetry that is favored by at least 2.3 kcal·mol^{-1} when compared to cis-coordinated isomers in a simplified model with nonsubstituted phenolate groups. Because this experimentally determined trans-phenolates geometry is the preferencial one, a correlation between the coordination sphere in archetype **1** and in amphiphiles **3** and **4** is proposed. The results for DFT calculations and EPR spectroscopy are in excellent agreement, indicating a high-spin $S = \frac{3}{2}$ electronic configuration given by $[a_g^1, b_{1g}^1, a_g^1, b_{2g}^2, b_{3g}^2]$ and located in pseudo-octahedral environments. This oxidation state was indirectly observed by the lack of counterion vibrations in the infrared spectrum and by the lack of a p$\pi_{phenolate} \rightarrow$ d$\sigma^*_{cobalt(III)}$ charge-transfer band found between 430 and 470 nm for similar cobalt(III) species. The absence of the LMCT band observed for all of the species suggests that optical responsiveness can be attained by switching from cobalt-(III) to cobalt(II), either via electrochemical or chemical stimuli. The electrochemistry of **1**−**4** is marked by metal-centered and ligand-centered activity. Regrettably, these oxidations and reductions lead to chemical side reactions and film formation, limiting the use of the amphiphiles as redox responsive materials. Both nonmetallated ligands and metallosurfactants are interfacially active. The McSMs **3** and **4** present different collapse mechanisms, leading to the formation of mono or multilayers that depend on the nature of the ligand and the pressure by which Langmuir monolayers are deposited on mica. Surfactant **3** may adopt a v-shaped or a linear geometry, leading to a constant-pressure collapse mechanism that fosters the formation of multilayers. In the case of the more-rigid **4**, the v-shaped geometry is preferred, favoring a constant-area collapse and the formation of monolayers. Collapses and mono/multilayer formations were identified by Brewster angle microscopy. Deposition onto mica substrates yielded Langmuir−Blodgett films, as characterized by equilibrium contact angle and atomic force microscopy.

Therefore, one can onclude that the nature of the substituents in the phenol ring allows for the stabilization of a divalent cation but compromises the reversibility of the phenoxyl radical formed upon ligand oxidation. We have also shown that metallosurfactant **4** is prone to form ordered monolayers due to the presence of polar and more-rigid benzyloxy groups and shorter alkyl chains. The polar group might improve the submersion of the head group, whereas the short tails may prevent excessive disorder triggered by a linear geometry of the amphiphile. Current efforts involve the study of the influence of different transition-metal ions such as manganese, iron, nickel, copper, and zinc in the behavior of these amphiphiles. A thorough analysis of the Langmuir and LB films is also planned.

(45) de Gennes, P. G. *Rev. Mod. Phys.* **1985**, *57*, 827 − 863.

Appendix E

The Cu$_4$-carboxylato Cluster

Rajendra Shakya, Sarmad Sahiel Hindo, Libo Wu, Suolong Ni, Marco M. Allard, Mary Jane Heeg,

Sandro R. P. da Rocha, Gordon T. Yee, Hrant P. Hratchian, Cláudio N. Verani.

"Amphiphilic and Magnetic Properties of a New Class of Cluster-Bearing [L$_2$Cu$_4$(μ_4-O)(μ_2-carboxylato)$_4$] Soft Materials"

My contribution to this work consisted of assisting Dr. Hrant Hratchian with the electronic structure calculations as a joint collaboration.

Amphiphilic and Magnetic Properties of a New Class of Cluster-Bearing [L₂Cu₄(μ₄-O)(μ₂-carboxylato)₄] Soft Materials

Rajendra Shakya,[a] Sarmad Sahiel Hindo,[a] Libo Wu,[c] Suolong Ni,[d] Marco Allard,[a] Mary Jane Heeg,[a] Sandro R. P. da Rocha,[c] Gordon T. Yee,[d] Hrant P. Hratchian,*[b] and Cláudio N. Verani*[a]

Dedicated to Professor David Rorabacher on the occasion of his retirement after 50 years of service

Abstract: A general approach toward amphiphilic systems bearing multimetallic clusters and their ability to form Langmuir–Blodgett films is presented. The synthetic strategy to stabilize these clusters involves the use of a ligand (HL) containing an N_2O-donor set and long octadecanoic chains to obtain the carboxylate-supported [L₂Cu₄(μ₄-O)(μ₂-OAc)₄]·EtOH (**1**) and [L₂Cu₄(μ₄-O)(μ₂-OBz)₄] (**2**) in which OAc⁻ and OBz⁻ represent acetate (**1**) and benzoate (**2**) co-ligands. These species were thoroughly characterized and had their structures solved by X-ray crystallography. We observed that the μ-oxo Cu₄ cluster is antiferromagnetically coupled and used broken-symmetry density functional theory (DFT) calculations to describe the main superexchange pathways of the tetracopper core. We also describe the amphiphilic properties of the ligand and the cluster-containing systems by means of area versus pressure isotherms and show that these cluster-bearing species can be transferred onto solid substrates yielding homogeneous Langmuir–Blodgett films, as characterized by atomic force microscopy and contact angle measurements.

Keywords: amphiphiles · cluster compounds · copper · density functional calculations · Langmuir–Blodgett films · magnetic properties

Introduction

One of the main challenges of modern coordination chemistry is to find ways of translating the considerable amount of information learned from small molecules into useful systems that foster the development of new materials. A main step in this process is the need for small molecules to be organized in highly ordered assemblies and, usually, the need for transfer onto surfaces. The rich chemistry of transition-metal complexes is profuse in systems with well-understood, controllable, and tunable properties, and the incorporation of these motifs into soft materials—thus allowing for interface and surface organization—is highly desirable. Recent advances in the field of metal-containing soft materials point to successful applications toward molecular electronics,[1–4] responsive thin films,[5,6] and hierarchical materials.[7] Other emerging applications focus on metallopolymers[8–10] and dendrimers[11,12] or metallosurfactants[13–15] and mesogens[16–19] taking advantage of the geometric, redox, and magnetic properties of transition-metal centers to build up organized supramolecular architectures based on organic scaffolds. The inclusion of three-dimensional metal clusters

[a] R. Shakya, S. S. Hindo, M. Allard, Dr. M. J. Heeg, Prof. C. N. Verani
Department of Chemistry, Wayne State University
Detroit, MI 48202 (USA)
Fax: (+1)313-577-2554
E-mail: cnverani@chem.wayne.edu

[b] Dr. H. P. Hratchian
Department of Chemistry
Indiana University
Bloomington, IN 47405 (USA)
Fax: (+1)812-855-8300
E-mail: hhratchi@indiana.edu

[c] L. Wu, Prof. S. R. P. da Rocha
Department of Chemical Engineering
Wayne State University
Detroit, MI 48202 (USA)

[d] S. Ni, Prof. G. T. Yee
Department of Chemistry
Virginia Polytechnic Institute and State University
Blacksburg, VA 424061 (USA)

in soft materials is particularly relevant for molecular electronics for which several oxidation and ground states can become useful for efforts toward information storage. Nonetheless, except for iron–sulfur core dendrimers,[12,20] the approach remains largely unexplored due to intrinsic synthetic challenges. We have shown[16] that this constraint can be overcome by the use of pre-assembled carboxylate-based dimers that interact with properly designed ligands conferring specific properties to the final assembly. Since formation of carboxylate-supported clusters[21,22] has been reported for several first-row metal ions, this methodology constitutes an important starting point. Our interest for transition metals and surface chemistry[23–25] led us to embark on an effort to develop amphiphilic cluster-containing materials capable of film formation. In this article, we present a synthetic strategy for obtaining the Cu_4-cluster-bearing complexes $[L_2Cu_4(\mu_4\text{-}O)(\mu_2\text{-}OAc)_4]\cdot EtOH$ (**1**) and $[L_2Cu_4(\mu_4\text{-}O)(\mu_2\text{-}OBz)_4]$ (**2**) with the new N_2O-terdentate ligand HL (Scheme 1) and μ_2-bridging acetate (μ_2-OAc), benzoate (μ_2-

The ligand HL:

The amphiphilic complexes:

$[L_2Cu_4(\mu_4\text{-}O)(\mu_2\text{-}OAc)_4]\cdot EtOH$ **(1)**   OAc = H_3C

$[L_2Cu_4(\mu_4\text{-}O)(\mu_2\text{-}OBz)_4]$ **(2)**   OBz =
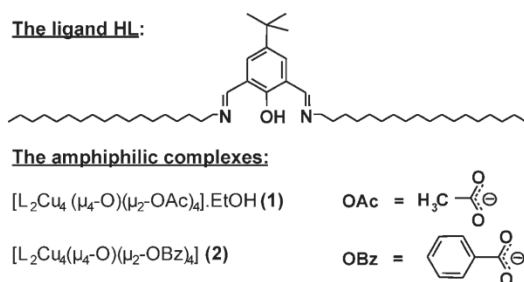
Scheme 1.

OBz), and μ_4-oxo groups as co-ligands. Both complexes have been exhaustively characterized by spectroscopic and spectrometric techniques and had their structures solved by X-ray crystallography. Since the magnetic properties of multicopper species depends heavily on the cluster geometry,[26] we also investigated the magnetic properties of these complexes both experimentally and by means of molecular calculations. Trying to ascertain the contributions of different magnetic pathways, we present for the first time density functional theory (DFT) calculations on the whole tetracopper core using broken-symmetry approaches. Finally, we describe the amphiphilic properties of the ligand and the cluster-containing systems as pressure versus area isotherms and show that these cluster-bearing species can be transferred onto solid substrates yielding homogeneous Langmuir–Blodgett films characterized by atomic force microscopy and contact angle measurements. The implications of these results toward the design of magnetic and responsive films that incorporate clusters are also offered.

Results and Discussion

Synthesis and characterization: The ligand was synthesized by treatment of the precursor 5-*tert*-butyl-2-hydroxyisophtaldehyde and 1-octadecylamine and was analyzed by ${}^1H$ NMR and IR spectroscopy as well as ESI mass spectrometry.[16] Complexes **1** and **2** were synthesized by treatment of a solution of the ligand in ethanol with distinct copper salts, and, in both cases, a tetrametallic μ_4-oxo, μ_2-carboxylato bridged core was identified. Copper(II) acetate in a 1:2 ligand-to-metal molar ratio was used to obtain **1**, with the acetate groups acting as μ_2-bridging co-ligands. Few examples of structurally characterized acetato-bridged cores have been reported[27] and the acetate-supported structure is considerably less usual than the equivalent chloro-bridged core.[28–30] When copper perchlorate is added simultaneously with sodium benzoate, complex **2** is obtained with μ_2-bridging benzoate groups replacing the acetate groups observed for **1**. The use of benzoates as co-ligands was intended to validate this synthetic path as a general approach for carboxylate-supported cluster formation. The IR spectra of both **1** and **2** show sharp peaks at about 2920–2850 cm^{-1} corresponding to C−H stretches of the alkyl chains and *tert*-butyl groups. Coordination of the imine nitrogen atoms to the copper is evidenced by a shift of the C=N peak in the ligand to about 1630 cm^{-1} in the complexes. Finally, a sharp peak of medium intensity at 527 cm^{-1} relates to the Cu−O vibration of the μ_4-oxo Cu_4 core.[27,31,32] The microanalyses were in good agreement with the described structures. Further evidence for the stability of the Cu_4 core is given by ESI mass spectrometry (ESI-MS) data taken in methanol, with peaks related to $[M-(OAc)]^+$ for **1** and $[M-(OBz)]^+$ for **2**. These peaks show the expected isotopic distribution associated with copper ions coordinated to N- and O-donors, as shown in Figure 1. The optical behavior of **1** and **2** was studied in dichloromethane. The spectra of both complexes exhibited strong absorption bands at around 380 and 672 nm ($\varepsilon \approx 18000$ and 300 $M^{-1}cm^{-1}$, respectively). The higher energy band is assigned to a $p\pi_{phenolate}\rightarrow d\pi^*_{copper}$ charge-transfer band, whereas the lower energy band is attributed to a d–d transition of the metal,[30,33–35] probably $b_{3g}\rightarrow b_{1g}$ in nature, reflecting an idealized local symmetry C_{4v} expected for each of the square pyramidal copper(II) ions. A weak shoulder at about 800 nm can represent a deviation from this idealized C_{4v} environment either due to the presence of distinct donor sets or due to a square-planar character. The spectrum of **2** in different concentrations is displayed in Figure S1 (Supporting Information) as an illustrative example.

Description of the structures: The crystal structures of both complexes **1** and **2** have been solved and show considerable similarity. The structure of **1** was published elsewhere,[16] and Figure 2 displays the ORTEP diagram for **2** with selected bond lengths and angles. Compound **2** is composed of discrete neutral molecules consisting of two deprotonated ligands (L$^-$), each delivering a set of three donor atoms N_2O
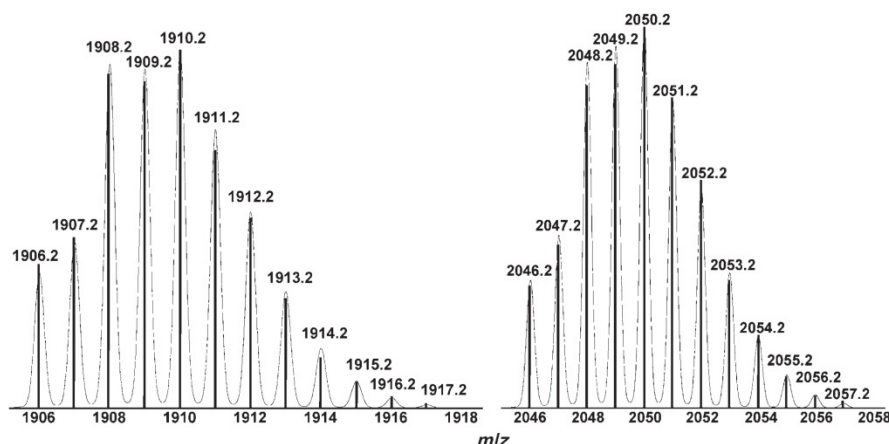
Figure 1. Experimental (bars) and simulated (continuum) ESIMS data for the isotopic cluster referring to $[1-OAc]^+$ (left) and $[2-OBz]^+$ (right)
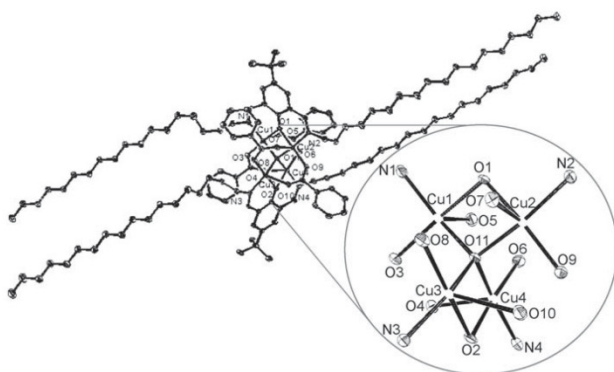
Figure 2. ORTEP at the 50% level representation of the neutral molecule **2**. Copper distances: Cu1−O11: 1.9159, Cu1−O5: 2.3774, N2−Cu2:1.9784, Cu2−O9: 1.9373, Cu1−O3: 1.9498, Cu1−N1: 1.983, Cu1−O1: 2.0004, Cu1−Cu2: 3.0064, Cu1−Cu3: 3.2525, Cu1−Cu4: 3.1935, Cu2−Cu3: 3.1723, Cu2−Cu4: 3.1908, Cu3−Cu4: 2.9975, Cu2−O(11): 1.9134, Cu2−O1: 1.9864, Cu2−O7: 2.2574, Cu3−O11: 1.9379, Cu3−O8: 1.9452, Cu3−N3: 1.9829, Cu3−O2: 1.9859, Cu3−O10: 2.3507, Cu4−O11: 1.9173, Cu4−O6: 1.9383, Cu4−N4: 1.989, Cu4−O2: 1.9922, Cu4−O4: 2.2678 Å; average distances: C−C in Ph:1.411, C−C in Ph:1.403, C−C in C18H37 chains: 1.527, C−C in OBz: 1.387 Å; selected angles: N2−Cu2−O7 :89.63, N4−Cu4−O11 :164.46, Cu1−O1−Cu2:97.89, Cu3−O2−Cu4:97.79, Cu3−O11−Cu1:115.12, Cu3−O11−Cu4:102.06, Cu1−O11−Cu4:112.84, Cu3−O11−Cu2:110.91, Cu1−O11−Cu2:103.46, Cu4−O1−Cu2: 112.81°.

to a cluster of four copper(II) centers μ_4-bridged by a distorted tetrahedral oxygen atom (O11).[27,29,36] Two benzoate groups link Cu1 and Cu4 and another two link Cu2 and Cu3, with each benzoate showing alternating short (1.94 Å) and long (2.35 Å) Cu−O bonds. The four Cu−N$_{imine}$ bonds are consistently found at 1.98 Å, fostering a five-coordinate geometry. A square-pyramidal geometry can be inferred from τ values[37] ranging from 0.011 to 0.103. Interestingly, the halogeno-bridged counterparts tend to have a more pronounced trigonal-bipyramidal character.[30]

The main differences between **1** and **2** relate to the substitution of the μ_2-bridging acetato by benzoato ligands, with

an apparent distortion of the organic scaffold of the latter resulting from the presence of the bulky benzoate rings. However, keeping in mind that both structures are comparable in quality ($R_1 = 0.0531$ and 0.0497 for **1** and **2**, respectively), we observe similarities between both cores: All Cu−O$_{phen}$ bonds are found between 1.98 and 1.99 Å, the Cu−O$_{oxo}$ bonds range only from 1.98 to 2.00 Å, and changes in angles are also minimal (Figures S2 and S3 in the Supporting Information), with the most pronounced difference being a mere 2° in the intradimer Cu-O-Cu values.

Magnetic susceptibility: Temperature-dependent magnetization data was collected from 300 to 1.8 K in order to evaluate the nature and magnitude of the magnetic coupling superexchange pathways in **1** and **2**, as well as the potential influence of the long octadecyl chains. Figure 3 shows the χ
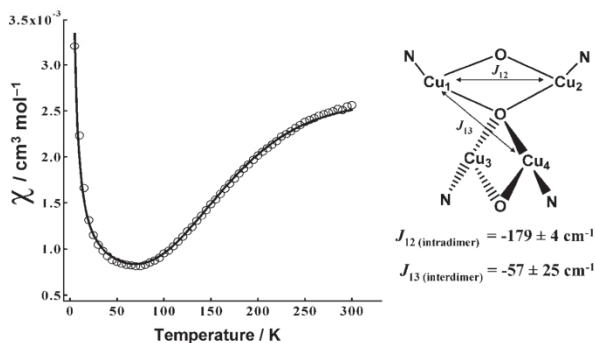
Figure 3. Magnetic susceptibility for **2**: Inset: Coupling scheme.

versus T magnetization plot for **2**, while data for **1** is shown in Figure S4 (in the Supporting Information). Both compounds exhibit a dominant antiferromagnetic behavior, and we have fit the data to the simplified model suggested by Haase, Krebs, et al.,[29] under which the tetranuclear copper

core is treated as a dimer of Cu_2O_2 dimers. The approach is depicted on the right hand side of Figure 3 along with the magnetic data with the dimer indicated in blue. Four possible superexchange pathways must be considered: The Cu-O_{phen}-Cu and Cu-O_{oxo}-Cu intradimer interactions and the interdimer Cu-O_{oxo}-Cu and Cu-OAc-Cu interactions. Since each μ_2-bridging benzoate ligand shows a short and a long $Cu-O$ bond, the potential coupling through these groups is considered to be irrelevant. The spin Hamiltonian for **1** and **2** is described by Equation (1), and the magnetic susceptibility data [Eq. (2)] were fit by non-linear least-squares methods, corrected for a typographical error previously published.[29] The inclusion of the second term accounts for the magnetic susceptibility from monomeric Cu^{II} impurities at a mole fraction given by x_p. The third term is the temperature-independent paramagnetism (TIP). All other constants in Equation (2) have their usual meanings and values.

$$H = -2[J_{12}(S_1 \cdot S_2 + S_3 \cdot S_4) + \\ J_{13}(S_1 \cdot S_3 + S_1 \cdot S_4 + S_2 \cdot S_3 + S_2 \cdot S_4)] \tag{1}$$

This expression considers two main magnetic interactions given by J_{12} and J_{13}. The former describes the intradimer coupling constant, whereas the latter takes into account the interdimer coupling through the μ_4-oxo bridge, as indicated above. In using Equation (2), we have chosen to fix the g value at 2.19, a reasonable value for the Cu^{II} ion. It leaves four adjustable parameters, and, for **1**, the best fit of the data yields $J_{12} = -212 \pm 5$ cm^{-1}, $J_{13} = -98 \pm 28$ cm^{-1}, $x_p = (2.34 \pm 0.05)\%$, TIP $= 0.00098 \pm 0.00001$ cm^3 mol^{-1}, and $R = 0.0795$, in which $R = \Sigma[(\chi_{calcd} - \chi_{exptl})/\chi_{exptl}]^2$.

The fit to the data is well within acceptable limits. As reported previously,[29] the uncertainty in the value for J_{13} is substantial, because of the lack of data at temperatures above 300 K. At this point, we are not able to collect data at high temperatures. Similarly, for **2**, the fit yields $J_{12} = -179 \pm 4$ cm^{-1}, $J_{13} = -57 \pm 25$ cm^{-1}, $x_p = (3.05 \pm 0.06)\%$ and TIP $= 0.00061 \pm 0.00002$ cm^3 mol^{-1}, which are consistent with the values found for the acetate analogue **1**. The fit is slightly better with $R = 0.0362$. Comparison of the data for **1** and **2** shows that the relatively greater magnitude of J_{12} compared to J_{13} is in agreement with previously published data, as shown by selected examples[27,29,30,32] in Table T1 (in the Supporting Information). A difference of about 30 cm^{-1} in the coupling constants points to stronger coupling in **1** than in **2**. As mentioned in the previous section, close examination of the two molecular structures reveals minimal differences that should lead to similar superexchange pathways and do not justify the observed coupling values. These differences in J_{12} and J_{13} between the two compounds might be an arti-

fact resulting from the lack of data at high temperatures. On the other hand, a previous article[16] on the mesomorphic properties of **1** showed that vicinal imine bonds, about 3.40 Å apart, appear to contribute to columnar formation. These interactions are suggestive of some degree of π-stacking and are absent in **2**. One can suggest that this imine overlap can reinforce some long-order coupling phenomenon. Having collected the experimental data concerning the magnetic susceptibility of the complexes, we turned to density functional theory calculations to provide an accurate molecular orbital description of the superexchange pathways that facilitate the observed spin–spin couplings.

Electronic structure calculations and analysis: Calculations on Cu_4 clusters are limited to a few examples of cubane-like structures[38] and—to the best of our knowledge—are nonexistent for μ_4-oxo-bridged scaffolds. To make our DFT calculations more tractable, we employed a structural model for **1** and **2**, shown in Figure 4. This model preserves the
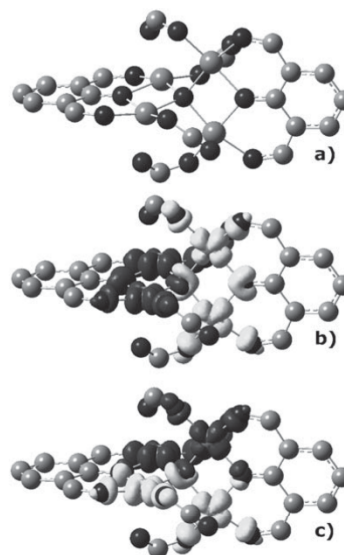
Figure 4. a) 3D rendering of the computational model, b) spin density plot for the broken-symmetry interdimer coupled state, and c) equivalent spin density plot for the intradimer state. Mulliken spin densities (electrons) for the interdimer coupled state: Cu1 = 0.74, Cu2 = 0.74, Cu3 = −0.74, Cu4 = −0.74, O = 0.00, O_{phen12} = 0.09, O_{phen34} = −0.09. Mulliken spin densities (electrons) for the intradimer coupled state: Cu_1 = −0.72, Cu_2 = 0.72, Cu_3 = −0.72, Cu_4 = 0.72, O = 0.00, O_{phen12} = 0.00, O_{phen34} = 0.00.

central Cu_4O core, the N_2O_{phen} ligand framework connecting the metal centers by two Cu_2 units; the bridging formate groups (COO$^-$) replace the original acetate and benzoate groups. The optimized structure belongs to the D_2 point

$$\chi_m = (1 - x_p)\frac{Ng^2\beta^2}{kT}\frac{10\exp(2J_{12}/kT) + 2\exp(-2J_{12}/kT) + 4\exp(-2J_{13}/kT)}{5\exp(2J_{12}/kT) + 3\exp(-2J_{12}/kT) + \exp(-4J_{12}/kT) + 6\exp(-2J_{13}/kT) + \exp(-4J_{13}/kT)} + x_p\frac{Ng^2\beta^2}{3kT}S(S+1) + TIP \tag{2}$$

group and the bond lengths and angles are in good agreement with the crystallographic data for **2**. Exceptions are the Cu−O$_{formate}$ bonds and intradimer Cu-(μ_4-O)-Cu angles, which, in the DFT optimized structure, are 0.06–0.18 Å and ~10° smaller than the corresponding parameters in the crystal structure of **2**. The shorter distances are attributed to the weak nature of the bonding interaction that may be overestimated with the level of theory employed here (see the Experimental Section below for details), whereas the smaller angles are attributed to the absence of the long alkyl chains that may distort the angles between the two Cu$_2$ dimers in **2**. Superexchange pathways were studied by converging broken-symmetry open-shell singlet states corresponding to the expected spin configurations. Two states corresponding to the inter- and intradimer coupled configurations have been considered. It is worth noting that the benzoate groups do not engage in the spin couplings and that two possible and equivalent intradimer states are present. We arbitrarily chose the intradimer state in which copper centers bridged by the same two formate groups have parallel spins. Before evaluating the results relevant for superexchange pathways, the electronic structure that is predicted from qualitative molecular orbital theory must be considered given that two Cu centers have one unpaired α electron each, while the other two Cu centers have one unpaired β electron each, the symmetry of the open-shell singlet wavefunctions of the D_2 model structure is C_2 for both the inter- and intradimer coupling cases. Since the local coordination sphere at each metal atom is square pyramidal, the unpaired electron at each site occupies the d$_{x^2-y^2}$ orbital. Figures 4b and c include the spin density difference plots for the calculated broken-symmetry states; the Mulliken spin densities support the characterization of these as correct broken-symmetry open-shell singlet states. Furthermore, calculation of the spatial overlap of α and β densities shows that 2.0 α and 2.0 β electrons are unpaired.

From the spin densities, we noticed that the μ_4-O bridge is involved with both spin-coupling pathways. Indeed, the central oxygen atom is the communication source for opposing copper spin centers in the interdimer state, and it plays a key role in the superexchange pathway in the intradimer state. Because the spin densities have C_2 symmetry, the magnetic molecular orbitals are delocalized across all four metal atoms. From a practical point of view, the symmetry of our broken-symmetry states makes it difficult to identify, simply from inspection, the magnetic molecular orbitals that are responsible for the computed spin density differences as well as the experimentally observed magnetism. Instead, we have evaluated the spatial overlap of all α molecular orbitals with the β density and vice versa. Figures 5a and b show molecular orbitals with less than 0.90 e$^-$ overlap with the opposite spin density. In the interdimer case (Figure 5a), the HOMO and HOMO−5 are the important contributors to the spin coupling with 0.36 and 0.51 e$^-$ opposite spin overlaps, respectively. For the intradimer case (Figure 5b), the HOMO, HOMO−1, HOMO−2, and HOMO−4 are important contributors to the spin coupling with 0.56, 0.76, 0.80, and
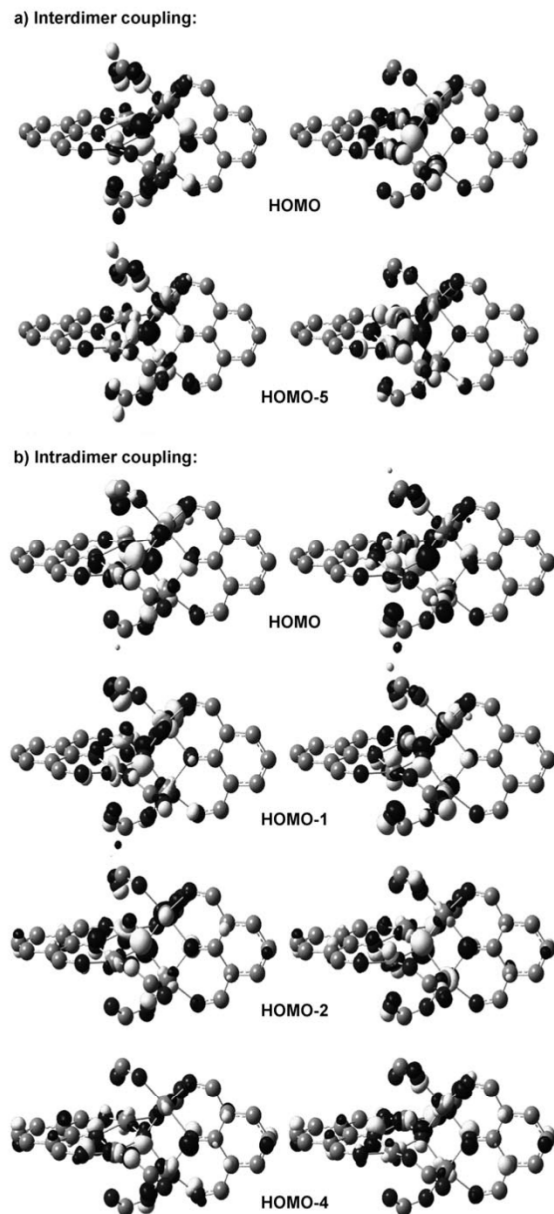
Figure 5. Selected molecular orbital renderings from the broken-symmetry coupled states: a) inter- and b) intradimer. α orbitals are shown on the left; β orbitals are shown on the right.

0.63 e$^-$ opposite spin overlaps, respectively. Mulliken percent character values (over selected atomic centers) for these orbitals are given in Table 1. As might be expected, the α/β molecular orbital pairs are symmetric in their relative compositions. For example, the interdimer coupled state α-HOMO is comprised of d$_{x^2-y^2}$ on two Cu centers, d$_{z^2}$ on the two other Cu centers, and a p orbital on the central μ_4-O. The β-HOMO is comprised of the same p orbital on the central μ_4-O and Cu d$_{x^2-y^2}$ and d$_{z^2}$ orbitals on the metal

Table 1. Mulliken percent character values for selected HOMO frontier orbitals for the inter- and intradimer-coupled broken-symmetry states.

MO		% Population						
		Cu1	Cu2	Cu3	Cu4	O	$O_{phen-1,2}$	$O_{phen-3,4}$
interdimer								
HOMO	α	10.4	10.4	6.9	6.9	19.7	6.8	0.6
	β	6.9	6.9	10.4	10.4	19.7	0.6	6.8
HOMO−5	α	13.8	13.8	7.6	7.6	14.2	1.5	0.1
	β	7.6	7.6	13.8	13.8	14.2	0.1	1.5
intradimer								
HOMO	α	10.5	8.8	10.5	8.8	14.9	3.2	3.2
	β	8.8	10.5	8.8	10.5	14.9	3.2	3.2
HOMO−1	α	12.4	7.8	12.4	7.8	10.4	1.9	1.9
	β	7.8	12.4	7.8	12.4	10.4	1.9	1.9
HOMO−2	α	10.5	5.9	10.5	5.9	12.3	4.7	4.7
	β	5.9	10.5	5.9	10.5	12.3	4.7	4.7
HOMO−4	α	9.3	4.1	9.3	4.1	4.8	6.5	6.5
	β	4.1	9.3	4.1	9.3	4.8	6.5	6.5

pairs opposite the α-HOMO. The relative compositions quantify this symmetry. In the interdimer coupled state, the Cu1 and Cu2 orbitals make up 10.4% of the α-HOMO, and the Cu3 and Cu4 orbitals make up 6.9% of α-HOMO. For the β-HOMO, 6.9% of the orbital character comes from the Cu1 and Cu2 orbitals, and 10.4% comes from the Cu3 and Cu4 orbitals. Again, this symmetry results from a description of the total complex as a dimer of dimers. All of the magnetic molecular orbitals can be described as symmetric or antisymmetric combinations of Cu_2 dimer fragment orbitals interacting through the central μ_4-O bridge. The μ_4-O orbitals hybridize to σ-bonds with the dominant Cu_2 dimer orbitals. In most cases, the μ_4-O bridge also forms a σ-bond with the other Cu_2 dimer. However, the character of the interactions between the μ_4-O and this Cu_2 dimer in the interdimer HOMO and the intradimer HOMO−1 and HOMO−2 are best described as nonbonding. Interestingly, d_{z^2} orbitals on the minor Cu_2 dimer in the interdimer HOMO and intradimer HOMO−2 have hybridized with other d orbitals to tip slightly off their local z axes. As a result, the interactions with the μ_4-O in these two molecular orbitals do have some π-bonding character, albeit quite small.

In the interdimer coupled state, the calculations show that the μ_4-O is the sole center facilitating spin coupling, while in the intradimer coupled state the phenolate-O atoms act together with the μ_4-O to couple Cu spins. Although phenolate-O atoms engage in the intradimer superexchange pathway, the μ_4-O atom is the largest individual contributor to three of the magnetic molecular orbitals. The exception is the intradimer HOMO−4, in which all three O atoms are nearly equal participants. The spatial overlap between α and β spin orbitals is greatest for the intradimer coupled state. Because the α/β spatial overlap is related to the coupling strength, this indicates that the intradimer coupling should be stronger than for the interdimer case. This is further supported by the DFT energy difference between these states, which favors the intradimer state by more than 100 cm^{-1}. These results qualitatively agree with our magnetization

data discussed above. Further DFT studies of specific structure–superexchange correlations are ongoing and will be reported in future work.

Amphiphilic properties and Langmuir–Blodgett film formation: The amphiphilic properties of the ligand HL and the complexes **1** and **2** are displayed as surface pressure (Π in mN m^{-1}) versus area per molecule (A in Å^2) in Figure 6.
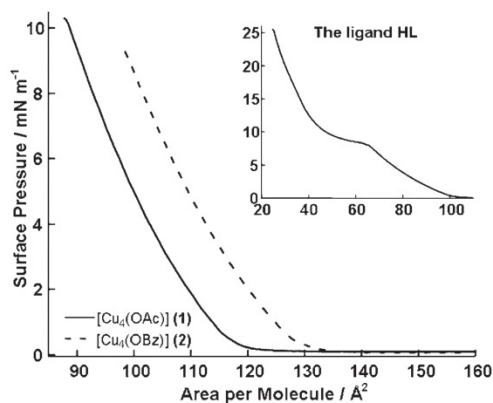
Figure 6. Surface pressure versus area per molecule isotherms at the air–water interface for the ligand HL, **1**, and **2**.

These isotherms give information about the two-dimensional behavior of the resulting amphiphilic film, the limiting area per molecule (A_{lim}), the collapse pressure (Π_c), and the area at the collapse of the monolayer (A_c). The film remaining after solvent evaporation has the thickness of a single molecule and is referred to as a monolayer. As the barriers of the trough are compressed, the tension (γ) of the air–water interface in the presence of the ligand or complexes decreases relative to that of the bare air–water interface (γ_0), resulting in an increase in Π ($=\gamma_0-\gamma$). The isotherms for the ligand, and complexes **1** and **2** were obtained and revealed amphiphilic behavior for all species. One of the main concerns for cluster-containing amphiphilic molecules is that they should keep their composition at the air–water interface without disassembling into smaller species. In order to ensure consistency, each isotherm was repeated at least three times; excellent reproducibility was attained for both HL and the complexes **1** and **2**. Overnight experiments in which the monolayers were left resting at the interface for extended periods of time gave consistent areas per molecule. Similarly, ESI-MS data of aged solutions of **1** and **2** in dichloromethane reproduced the behavior observed for fresh samples reinforcing the notion that the tetracopper clusters are stable. The molecules of the protonated ligand start interacting with each other at the air–water interface at about 100 Å^2 molecule^{-1} forming an expanded phase that is followed by a phase transition at about 65 Å^2 molecule^{-1}. This transition may be due to rearrangement of the alkyl chains that favor an alignment needed for a condensed phase. The

monolayer of the ligand exhibits a moderate collapse pressure at 25 mN m^{-1}. The critical area $A_c = 47$ Å^{2}molecule^{-1} can be determined by extrapolating the Π versus A curve at its steepest slop before the collapse to zero pressure at which it intercepts the x axis.[5] The A_c value determined for the ligand is much larger than the 20 Å^{2}molecule^{-1} observed for heptadecanoic acid,[39] but closer to the area occupied by more voluminous species like *cis*-13-docosenoic acid (eruric acid, $C_8H_{17}CH=CHC_{11}H_{22}COOH$, 38 Å^{2}molecule^{-1}) and dimyristolphosphatidic acid (51 Å^{2}molecule^{-1}).[40] The presence of bulky tertiary butyl groups is likely to play a role in the packing of the ligand. Ongoing research in our labs focuses on methyl- and halogeno-substituted ligands.

The individual molecules for both **1** and **2** start interacting at the air–water interface at about 127 and 137 Å^{2}molecule^{-1}, respectively, but **1** shows a more condensed monolayer than **2** throughout. The molecules of **1** in the monolayer can be compressed to an average area of about 110 Å^2 collapsing at a pressure of 10.25 mN m^{-1}. Molecules of **2** in the monolayer can be compressed to 121 Å^{2}molecule^{-1} collapsing at 9.4 mN m^{-1}. When **1** is compared to the ligand, an increase of about 63 Å^{2}molecule^{-1} in the A_c value is observed. It is known that a maximum increase of about 10 Å^{2}molecule^{-1} is observed upon complexation of the Cu^{II} ion.[41] Thus, the magnitude of the increase observed from HL to **1** reinforces the presence of a cluster. Similarly, the behavior observed for **2** reflects the presence of a bulkier core associated with the four benzoate groups, which prevents the molecules from coming in closer proximity. It is useful to compare these areas with other bulky species, such as substituted fullerenes.[42] In the case of 1-*tert*-butyl-9-hydrofullerene-60, the observed limiting areas of about 20 Å^{2}molecule^{-1} clearly indicate the presence of multilayers and the fact that up to six molecules can tumble over each other. In this regard, the large areas observed for **1** and **2** reinforce the notion of monolayer formation. The relatively low collapse pressures can be tentatively attributed to the presence of four hydrophobic alkyl chains, each with its origin about 90° from one another, that envelope the Cu$_4$-cluster decreasing the hydrophilic character of the core (Scheme 2).

Cu^{II}
N$_2$O ligand
Alkyl chain
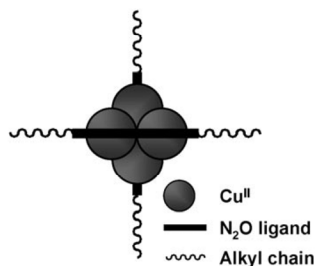
Scheme 2.

It is established that incorporation of salts increases the ionic strength of the subphase, influencing the properties of

the monolayers and, in general, improving the order of charged fatty acid surfactants and metallosurfactants.[43] In the particular case of fatty acids, the order enhancement comes through coordination of the acetate head groups with the metal cations; however, more recently, it has been observed that changes in the A_c value may be related to charge.[44] This dependence seems related to the design of the metallosurfactant. To assess the effect of metal salts on the amphiphilic behavior of **1** and **2**, sodium chloride was added to the water subphase. A minor increase in collapse pressures to about 11 mN m^{-1} was observed and associated with a considerable increase in area per molecule. In the presence of the electrolyte, compound **1** expands its structure considerably, occupying an area of 175 Å^{2}molecule^{-1}, whereas **2** shows a rather moderate expansion to 150 Å^{2}molecule^{-1}. Since the complexes are neutral, the expansions observed are attributed to strong ion–dipole interactions and by ion-induced dipole interactions associated with minor structural rearrangements. The less shielded neutral core of acetate-containing **1** is more susceptible to such repulsions, while the benzoate groups around **2** may insulate the Cu$_4$ core more effectively.

The monolayers of **1** and **2** in pure water are readily transferred onto mica substrates with deposition ratios close to unity and forming homogeneous Langmuir–Blodgett films. Monolayers of **1** and **2** were deposited at 8 mN m^{-1} and are shown in Figure S5 (see the Supporting Information). Equilibrium contact angle (θ) measurements of 84 and 85° were observed for the monolayers of **1** and **2**, respectively, in clear contrast with the $\theta = 0°$ for the hydrophilic mica substrate. Several attempts to scratch the surface of the transferred film were unsuccessful, suggesting that the monolayers are strongly attached to the mica substrate.

Conclusions

In this paper we presented data regarding μ_4-oxo tetracupric cores supported by four μ_2-carboxylate groups and two amphiphilic and deprotonated L$^-$ ligands that contain an N$_2$O-donor set and long C_{18}-alkyl chains. Carboxylate sources are acetates for **1** and benzoates for **2**, and together these species validate a new general approach to synthesize μ_4-oxo-bridged metal clusters. These cluster-bearing species act as metallosurfactants showing moderate collapse pressures and allowing for Langmuir film formation at the air–water interface with subsequent transfer onto a solid substrate. The resulting Langmuir–Blodgett films showed remarkable homogeneity and were characterized by atomic force microscopy and contact angle measurements. The magnetic properties of these complexes were studied both experimentally and theoretically and show that antiferromagnetic interactions dominate the coupling scheme and that the superexchange mechanisms rely heavily on the Cu-oxo-Cu pathway. Ongoing research in our labs involves the full characterization of these films, as well as the systematic use of alternative side chains varying in length and nature, and the formation

of [Cu_4-bridge-Cu_4-bridge] extended systems by the replacement of one or more acetate co-ligands by terephtalic acid, aiming at extended magnetic materials with amphiphilic properties.

Experimental Section

Materials and methods: Reagents and solvents were used as received from commercial sources and ethanol was distilled over CaH_2. IR spectra were measured as KBr pellets on a Tensor 27 FTIR-Spectrophotometer. ^{1}H NMR spectra were measured using a Varian 400 MHz instrument. Mass spectrometry in ESI(positive) mode was measured in a Micromass QuattroLC triple quadrupole mass spectrometer. Experimental assignments were simulated based on peak position and isotopic distributions. Elemental analyses were performed by Midwest Microlab, Indianapolis, IN. UV/Vis spectra of 1.0×10^{-4} M solutions of the samples in dichloromethane were performed in a Cary 50 spectrometer. Magnetic measurements as a function of temperature were performed from 1.8 to 300 K for **1** and **2** on a 5 or 7 T Quantum Design MPMS SQUID magnetometer. Diamagnetic corrections were attained with Pascal's constants, and the diamagnetic susceptibility of the sample holder was also taken into account.

X-ray structural determination for 2: Diffraction data were measured on a Bruker X8 APEX-II kappa geometry diffractometer with Mo radiation and a graphite monochromator at 100 K. Frames were collected as a series of sweeps with the detector at 40 mm and 0.3° between each frame. Frames were recorded for 5 s. Crystals of **2** [$C_{124}H_{194}N_4O_{11}Cu$] grew as green plates, and the sample used for data collection was approximately $0.32 \times 0.23 \times 0.14$ mm³. A total of 3190 frames were collected yielding 107490 reflections, with 29020 of which being independent. Hydrogen positions were placed in calculated positions. No solvent or ions were present in the crystal. Thermal parameters increase along the length of the pendant chains. The asymmetric unit contains one neutral molecule. Complex **2**: Formula, $C_{126}H_{194}N_4O_{11}Cu_4$; M_r; 2170.99 amu; space group $P\bar{1}$; cell constants $a = 13.0185(5)$, $b = 19.9429(8)$, $c = 24.3042(9)$ Å, $\alpha = 98.926(2)$, $\beta = 101.618(2)$, $\gamma = 100.642(2)°$; $V = 5951.9(4)$ Å³; $Z = 2$; $T = 100(2)$ K; $\lambda = 0.71073$ Å; $\rho_{calcd} = 1.211$ g cm⁻³; $\mu = 0.763$ mm⁻¹; $R(F) = 4.97\%$; $Rw(F) = 13.16\%$.

Electronic structure calculations: Becke's three-parameter hybrid exchange functional was used with the nonlocal correlation functional of Perdew and Wang for all DFT calculations.[45] The Pople style 3-21G basis set was used on C and H atoms, while the 6-31G(d) basis set was used on N, O, and Cu centers. The model system geometry was optimized by standard methods.[46] The geometry was found on the high-spin, $M_s = 5$, potential-energy surface. Calculations were carried out with the GAUSSIAN suite of electronic structure programs.[47] For all broken-symmetry calculations, the UB3PW91/6-31G(d) model chemistry was used, and stabilities[48] of all wave functions were verified.

Surface pressure versus area isotherms and Langmuir–Blodgett films: Monolayer experiments were carried out by using an automated KSV minitrough at 23.0 ± 0.5 °C. Ultrapure water (Barnstead NANOpure) with a resistivity of 17.5–18 MΩ cm⁻¹ was used in all experiments. Impurities present at the surface of the freshly poured aqueous subphase were removed by vacuum after the compression of the barriers without surfactant. Spreading solutions were prepared in spectra grade chloroform. A freshly prepared surfactant solution (30 μL) with a known concentration (1.0 mg mL⁻¹) was then spread on the clean aqueous subphase. The system was allowed to equilibrate for about 15 min before monolayer compression. The Π versus A isotherms were obtained at a compression rate of 5 mm min⁻¹. The Wilhelmy plate method (paper plates 20 mm × 10 mm) was used to measure the surface pressure. The selected graph represents the results of at least three independent measurements with excellent reproducibility. Monolayers (single layer per substrate) were transferred onto $40 \times 20 \times 0.08$ mm³ mica substrates (Ted Pella, Inc) at different target pressures.

Atomic force microscopy and contact angle measurements: The surface topography of freshly prepared Langmuir–Blodgett (LB) films on mica substrates was examined by using a PicoSPM LE (Molecular Image Corp) AFM under tapping mode operation with a BS-Multi 75 (Budgetsensors, Inc) silicon cantilever. The static contact angle of the modified substrates was determined in order to follow the quality of the film. Contact angles were determined on a goniometer (KSV CAM 200) equipped with a CCD camera. All data were collected at room temperature.

Syntheses: The syntheses of the ligand and **1** were reported previously.[16]

[$L_2Cu_4(\mu_4$-O)(μ_2-OBz)$_4$] (2): A solution of HL (0.35 g, 0.5 mmol) in ethanol (40 mL) was treated with a solid sample of Cu(ClO$_4$)$_2$·6H$_2$O (0.37 g, 1.0 mmol) followed by addition of sodium benzoate (0.29 g, 2.0 mmol). The resulting green solution was gently heated for 1 h, cooled to room temperature, and filtered. Crystals suitable for X-ray analysis were obtained after slow evaporation of the solvent. Yield = 78%; m.p. = 78–81 °C; IR (KBr): $\tilde{v} = 1629$ ($v_{C=N}$), 2852–2922 cm⁻¹ (v_{C-H} from alkyl chain and *tert*-butyl); ESI⁺ in MeOH: m/z: 2550.5 [M–OBz]⁺; elemental analysis calcd (%) for $C_{124}H_{194}Cu_4N_4O_{11}$: C 68.60, H 9.01, N 2.58; found: C 68.31, H 9.09, N 2.52.

[1] a) R. A. Wassel, C. B. Gorman, *Angew. Chem.* **2004**, *116*, 5230; *Angew. Chem. Int. Ed.* **2004**, *43*, 5120; b) C. Joachim, J. K. Gimzewski, A. Aviram, *Nature* **2000**, *408*, 541.

[2] P. J. Low, *Dalton Trans.* **2005**, 2821.

[3] J. Park, A. N. Pasupathy, J. I. Goldsmith, C. Chang, Y. Yaish, J. R. Petta, M. Rinkoski, J. P. Sethna, H. D. Abruña, P. L. McEuen, D. C. Ralph, *Nature* **2002**, *417*, 722.

[4] S. Flores-Torres, G. R. Hutchison, L. J. Soltzberg, H. D. Abruña, *J. Am. Chem. Soc.* **2006**, *128*, 1513.

[5] D. R. Talham, *Chem. Rev.* **2004**, *104*, 5479.

[6] a) A. Pasc-Banu, C. Sugisaki, T. Gharsa, J.-D. Marty, I. Gascon, M. Krämer, G. Pozzi, B. Desbat, S. Quici, I. Rico-Lattes, C. Mingotaud, *Chem. Eur. J.* **2005**, *11*, 6032; b) M. Clemente-León, E. Coronado, C. J. Gómez-García, C. Mingotaud, S. Ravaine, G. Romualdo-Torres, P. Delhaès, *Chem. Eur. J.* **2005**, *11*, 3979; c) D. Y. Takamoto, E. Aydil, J. A. Zasadzinski, A. T. Ivanova, D. K. Schwartz, T. Yang, P. S. Cremer, *Science* **2001**, *293*, 1292.

[7] Y. Bodenthin, U. Pietsch, H. Mohwald, D. G. Kurth, *J. Am. Chem. Soc.* **2005**, *127*, 3110.

[8] S. J. Rowan, J. B. Beck, *J. Am. Chem. Soc.* **2003**, *125*, 13922.

[9] J. L. Bender, P. S. Corbin, C. L. Fraser, D. H. Metcalf, F. S. Richardson, E. L. Thomas, A. M. Urbas, *J. Am. Chem. Soc.* **2002**, *124*, 8526.

[10] I. Manners, *Science* **2001**, *294*, 1664.

[11] D. R. Blasini, S. Flores-Torres, D.-M. Smilgies, H. D. Abruña, *Langmuir* **2006**, *22*, 2082.

[12] T. L. Chasse, R. Sachdeva, Q. Li, Z. Li, R. J. Petrie, C. B. Gorman, *J. Am. Chem. Soc.* **2003**, *125*, 8250.

[13] S. Kraus, D. Mandler, *Langmuir* **2006**, *22*, 7462.

[14] P. C. Griffiths, I. A. Fallis, D. J. Willock, A. Paul, C. L. Barrie, P. M. Griffiths, G. M. Williams, S. M. King, R. K. Heenan, R. Görgl, *Chem. Eur. J.* **2004**, *10*, 2022; King, R. K. Heenan, R. Görgl, *Chem. Eur. J.* **2004**, *10*, 2022.

[15] J. Bowers, K. E. Amos, D. W. Bruce, R. K. Heenan, *Langmuir* **2005**, *21*, 5696.

[16] R. Shakya, P. H. Keyes, M. J. Heeg, A. Moussawel, P. A. Heiney, C. N. Verani, *Inorg. Chem.* **2006**, *45*, 7587.

[17] E. Terazzi, S. Suarez, S. Torelli, H. Nozary, D. Imbert, O. Mamula, J.-P. Rivera, E. Guillet, J.-M. Bénech, G. Bernardinelli, R. Scopelliti, B. Donnio, D. Guillon, J.-C. Bünzli, C. Piguet, *Adv. Funct. Mater.* **2006**, *16*, 157.

[18] a) K. Binnemans, *Chem. Rev.* **2005**, *105*, 4148; b) K. Binnemans, K. Lodewyckx, B. Donnio, D. Guillon, *Chem. Eur. J.* **2002**, *08*, 1101.

[19] a) J. L. Serrano, T. Sierra, *Coord. Chem. Rev.* **2003**, *242*, 73; b) J. L. Serrano, T. Sierra, *Chem. Eur. J.* **2000**, *06*, 759.

[20] T. L. Chasse, C. B. Gorman, *Langmuir* **2004**, *20*, 8792.

[21] a) L. M. C. Beltran, J. R. Long, *Acc. Chem. Res.* **2005**, *38*, 325; b) M. Eddaoudi, D. Moler, H. Li, B. Chen, T. M. Reineke, M. O'Keeffe, O. M. Yaghi, *Acc. Chem. Res.* **2001**, *34*, 319.

[22] A. J. Tasiopoulos, A. Vinslava, W. Wernsdorfer, K. A. Abboud, G. Christou, *Angew. Chem.* **2004**, *116*, 2169; *Angew. Chem. Int. Ed.* **2004**, *43*, 2117.

[23] R. Shakya, C. Imbert, H. P. Hratchian, M. Lanznaster, M. J. Heeg, B. R. McGarvey, M. A. Allard, H. B. Schlegel, C. N. Verani, *Dalton Trans.* **2006**, 2517.

[24] C. Imbert, H. P. Hratchian, M. Lanznaster, M. J. Heeg, L. Hryhorczuk, B. R. McGarvey, H. B. Schlegel, C. N. Verani, *Inorg. Chem.* **2005**, *44*, 7414.

[25] a) M. Lanznaster, H. P. Hratchian, M. J. Heeg, L. Hryhorczuk, B. R. McGarvey, H. B. Schlegel, C. N. Verani, *Inorg. Chem.* **2006**, *45*, 955; b) M. Lanznaster, M. J. Heeg, G. T. Yee, B. R. McGarvey, C. N. Verani, *Inorg. Chem.* **2007**, *46*, 72.

[26] a) A. Mukherjee, R. Raghunathan, M. K. Saha, M. Nethaji, S. Ramasesha, A. R. Chakravarty, *Chem. Eur. J.* **2005**, *11*, 3087; b) F. Bramsen, A. D. Bond, C. J. McKenzie, R. G. Hazell, B. Moubaraki, K. S. Murray, *Chem. Eur. J.* **2005**, *11*, 3087; c) G. Aromí, J. Ribas, P. Gamez, O. Roubeau, H. Kooijman, A. L. Spek, S. Teat, E. MacLean, H. Stoeckli-Evans, J. Reedijk, *Chem. Eur. J.* **2004**, *10*, 6476.

[27] L. Chen, S. Breeze, R. Rousseau, S. Wang, L. Thompson, *Inorg. Chem.* **1995**, *34*, 454.

[28] W. E. Hatfield, J. A. Barnes, G. W. Inman, Jr., *Inorg. Chem.* **1971**, *10*, 1725.

[29] S. Teipel, K. Griesar, W. Haase, B. Krebs, *Inorg. Chem.* **1994**, *33*, 456.

[30] J. Reim, K. Griesar, W. Haase, B. Krebs, *J. Chem. Soc. Dalton Trans.* **1995**, 2649.

[31] M. Bera, W. Wong, G. Aromi, J. Ribas, D. Ray, *Inorg. Chem.* **2004**, *43*, 4787.

[32] S. Mukharjee, Th. Weyhermuller, E. Bothe, K. Weighard, P. Chaudhuri, *Eur. J. Inorg. Chem.* **2003**, 863.

[33] J. Reim, W. Werner, W. Haase, B. Krebs, *Chem. Eur. J.* **1998**, *4*, 289.

[34] M. Mikuria, K. Minowa, R. Nukada, *Bull. Chem. Soc. Jpn.* **2002**, *75*, 2595.

[35] V. McKee, S. Tandon, *J. Chem. Soc. Dalton Trans.* **1991**, 221.

[36] S. Breeze, S. Wang, L. Chen, *J. Chem. Soc. Dalton Trans.* **1996**, 1341.

[37] A. W. Addison, T. N. Rao, J. Reedjik, J. van Rijn, G. C. Verschoor *J. Chem. Soc. Dalton Trans.* **1984**, 1349. The τ value is a structural index that systematizes five-coordination geometries and is defined by $\tau=[\beta-\alpha/60°]$ with $\alpha=\beta=180°$ for a square pyramid ($\tau=0$, C_{4v}) and $\alpha-\beta<180°$ for a trigonal bipyramid ($\tau-1$, D_{3h}). The individual τ values of 0.011, 0.041, 0.103, and 0.076 were found, respectively, for Cu1, Cu2, Cu3, and Cu4.

[38] E. Ruiz, *Struct. Bonding* **2004**, *113*, 71, and references [82] and [83] therein.

[39] A. M. P. S. Goncalves da Silva, D. A. Armitage, R. G. Linford, *J. Colloid Interface Sci.* **1993**, *156*, 433.

[40] M. C. Petty, *Langmuir-Blodgett Films*, Cambridge University Press, Cambridge, **1996**, pp. 65–93.

[41] S. Kraus, D. Mandler, *Langmuir* **2006**, *22*, 7462.

[42] G. Williams, A. Soi, A. Hirsch, M. R. Bryce, M. C. Petty, *Thin Solid Films* **1993**, *230*, 73.

[43] a) S. Di Bella, S. Sortino, S. Conoci, S. Petralia, S. Casilli, L. Valli, *Inorg. Chem.* **2004**, *43*, 5368; b) M. C. Petty, *Langmuir–Blodgett Films*, Cambridge University Press, Cambridge, **1996**, pp. 32–37, and references therein.

[44] a) K. Wang, M. Haga, M. D. Hossain, H. Shindo, K. Hasebe, H. Monjushiro, *Langmuir* **2002**, *18*, 3528; b) M. Haga, N. Kato, H. Monjushiro, K. Wang, M. D. Hossain, *Supramol. Sci.* **1998**, *5*, 337.

[45] a) A. D. Becke, *J. Chem. Phys.* **1993**, *98*, 5648–5652; b) J. P. Perdew, Y. Wang, *Phys. Rev. B* **1992**, *45*, 13244.

[46] H. P. Hratchian, H. B. Schlegel in *Theory and Applications of Computational Chemistry: The First Forty Years* (Eds.: C. E. Dykstra, G. Frenking, K. S. Kim, G. E. Scuseria), Elsevier, Amsterdam, **2005**, p. 195.

[47] Gaussian 03 (Revision B.05), M. J. Frisch, G. W. Trucks, H. B. Schlegel, G. E. Scuseria, M. A. Robb, J. R. Cheeseman, J. A. Montgomery Jr., T. Vreven, K. N. Kudin, J. C. Burant, J. M. Millam, S. S. Iyengar, J. Tomasi, V. Barone, B. Mennucci, M. Cossi, G. Scalmani, N. Rega, G. A. Petersson, H. Nakatsuji, M. Hada, M. Ehara, K. Toyota, R. Fukuda, J. Hasegawa, M. Ishida, T. Nakajima, Y. Honda, O. Kitao, H. Nakai, M. Klene, X. Li, J. E. Knox, H. P. Hratchian, J. B. Cross, C. Adamo, J. Jaramillo, R. Gomperts, R. E. Stratmann, O. Yazyev, A. J. Austin, R. Cammi, C. Pomelli, J. W. Ochterski, P. Y. Ayala, K. Morokuma, G. A. Voth, P. Salvador, J. J. Dannenberg, V. G. Zakrzewski, S. Dapprich, A. D. Daniels, M. C. Strain, O. Farkas, D. K. Malick, A. D. Rabuck, K. Raghavachari, J. B. Foresman, J. V. Ortiz, Q. Cui, A. G. Baboul, S. Clifford, J. Cioslowski, B. B. Stefanov, G. Liu, A. Liashenko, P. Piskorz, I. Komaromi, R. L. Martin, D. J. Fox, T. Keith, M. A. Al-Laham, C. Y. Peng, A. Nanayakkara, M. Challacombe, P. M. W. Gill, B. Johnson, W. Chen, M. W. Wong, C. Gonzalez, J. A. Pople, Gaussian, Inc., Pittsburgh, PA, **2004**.

[48] R. Seeger, J. A. Pople, *J. Chem. Phys.* **1977**, *66*, 3045.

Appendix F

The Divalent Copper Surfactant

Jeffery A. Driscoll, <u>Marco M. Allard</u>, L. Wu, Mary J. Heeg, S. R P da Rocha, Cláudio N. Verani

My contribution to this work consisted of the electronic structure calculations in joint collaboration with Prof. Schlegel's laboratory, and performing cyclic voltammetry experiments.

Interfacial Behavior and Film Patterning of Redox-Active Cationic Copper(II)-Containing Surfactants

Jeffery A. Driscoll,[a] Marco M. Allard,[a] Libo Wu,[b] Mary Jane Heeg,[a] Sandro R. P. da Rocha,*[b] and Cláudio N. Verani*[a]

Dedicated to Professor Ken Karlin for his contribution to copper–pyridine chemistry

Abstract: Herein, we describe the synthesis and characterization of a novel series of single-tail amphiphiles L^{PyC_n} (Py = pyridine, $C_n = C_{18}$, C_{16}, C_{14}, C_{10}) and their copper(II)-containing complexes, which are of relevance for patterned films. The *N*-(pyridine-2-ylmethyl)alkyl-1-amine ligands and their complexes $[Cu^{II}Cl_2(L^{PyC_{18}})]$ (**1**), $[Cu^{II}Cl_2(L^{PyC_{16}})]$ (**2**), $[Cu^{II}Cl_2(L^{PyC_{14}})]$ (**3**), $[Cu^{II}Br_2(L^{PyC_{18}})]$ (**4**), $[Cu^{II}Br_2(L^{PyC_{16}})]$ (**5**), and $[Cu^{II}Br_2(L^{PyC_{10}})]$ (**6**) were synthesized, isolated, and characterized by means of mass spectrometry, IR and NMR spectroscopies, and elemental analysis. Complexes **1**, **2**, **3**, and **6** had their molecular structure solved by X-ray diffraction methods, which showed that the local geometry around the metal center is distorted square planar. With the aim of using these species as precursors for redox-responsive films, an assessment of their electrochemical properties involved cyclic voltammetry in different solvents, with different supporting electrolytes and scan rates. Density functional theory calculations of relevant species in bulk and at interfaces were used to evaluate their electronic structure and dipole moments. The morphology and order of the resulting films at the air/water interface were studied by isothermal compression and Brewster angle microscopy. Biphasic patterned Langmuir films were observed for all complexes except **3** and **6**, and dependence on the chain length and the nature of the halogen coligand determine the characteristics of the isotherms and their intricate topology. Complexes **3** and **6**, which have shorter chain lengths, failed to exhibit organization. These results exemplify the first comprehensive study of the behavior of single-tail metallosurfactants, which are likely to lead to high-end technological applications based on their patterned films.

Keywords: Brewster angle microscopy · copper · Langmuir films · metallosurfactants · redox chemistry

Introduction

Interest in structured and patterned films has increased as a result of their potential for molecular electronics,[1] biosensing,[2] and other high-end technological applications.[3] Similarly, an effort is being made toward understanding the cooperativity between transition-metal ions and amphiphilic organic scaffolds. This interaction leads to redox,[4] optical,[5,6] and magnetic[7] behavior and distinctive order, and has been explored thus far in thixotropic,[8] mesogenic,[9] and micellar[10] design.

Although self-assembly remains the chief approach for film formation,[11–13] isothermal compression[14] allows for greater control over the final morphology.[15,16] This characteristic is fundamental for device nanofabrication, but only in the recent past has the design of amphiphilic precursors departed from lipids to encompass alkylamines,[17] polymers and copolymers,[18] and dendrimers[19] within its subjects. This departure coincides with the availability of surface-dedicated techniques, such as Brewster angle microscopy[20,21] (BAM) and fluorescence microscopy[22] that allow for real-time evaluation of the film compression at the air/water interface.

[a] Dr. J. A. Driscoll, M. M. Allard, Dr. M. J. Heeg, Prof. C. N. Verani
Department of Chemistry
Wayne State University
Detroit Michigan, 48202 (USA)
Fax: (+1)313-577-8822
E-mail: cnverani@chem.wayne.edu

[b] L. Wu, Prof. S. R. P. da Rocha
Department of Chemical Engineering
Wayne State University
Detroit Michigan, 48201 (USA)
Fax: (+1)313-577-3810
E-mail: sdr@eng.wayne.edu

Supporting information for this article is available on the WWW under http://dx.doi.org/10.1002/chem.200801215.

The above reasons strongly indicate that understanding how metallosurfactants can drive complex interfacial phenomena, such as morphological changes, domain formation, and collapse mechanisms, with the aim of device development, would constitute a major accomplishment. Nonetheless, with few isolated and characterized precursors,[5,10,23,24] the details of these phenomena are still to be realized.

In recent years, our groups have spearheaded systematic research in this area by focusing on a comprehensive approach that encompasses synthesis,[25] modeling,[26] and surface behavior. We have demonstrated the feasibility of Langmuir–Blodgett (LB) films with magnetic copper(II) clusters,[27] the redox-state control and dependence of a collapse mechanism on cobalt(II) films,[28] and the factor that determines the delicate equilibrium between redox activity and amphiphilicity in copper/phenoxyl species.[29]

Herein, we present an in-depth investigation of the properties of novel single-tail cationic copper(II)-containing surfactants with the ligands $L^{PyC_{18}}$, $L^{PyC_{16}}$, $L^{PyC_{14}}$, and $L^{PyC_{10}}$, in which Py = pyridine and C_n indicates the alkyl chain length.

$C_{18}H_{37}$ ($L^{PyC_{18}}$)	X = Cl :	[Cu^{II}Cl$_2$($L^{PyC_{18}}$)]	**1**
$C_{16}H_{33}$ ($L^{PyC_{16}}$)		[Cu^{II}Cl$_2$($L^{PyC_{16}}$)]	**2**
$C_{14}H_{29}$ ($L^{PyC_{14}}$)		[Cu^{II}Cl$_2$($L^{PyC_{14}}$)]	**3**
$C_{10}H_{21}$ ($L^{PyC_{10}}$)	X = Br :	[Cu^{II}Br$_2$($L^{PyC_{18}}$)]	**4**
		[Cu^{II}Br$_2$($L^{PyC_{16}}$)]	**5**
		[Cu^{II}Br$_2$($L^{PyC_{10}}$)]	**6**
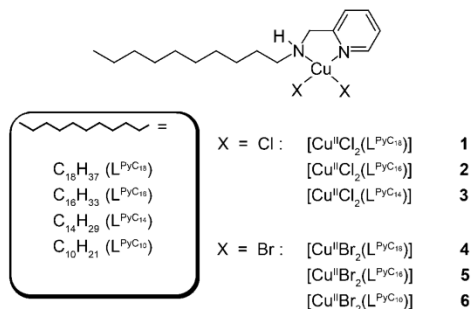
We describe the synthesis and characterization of these new materials along with the molecular structures for **1**, **2**, **3**, and **6**. Examination of their redox properties by using cyclic voltammetry methods relevant for responsive films is presented, along with the behavior at the air/water interface, which was studied by meticulous use of BAM. An assessment of the results supported by density functional theory (DFT) calculations is also included. These findings are expected to have a positive impact on the development of responsive metal-containing LB films in the near future.

Results and Discussion

Synthesis: Treatment of 2-pyridinecarboxyaldehyde with the appropriate alkylamine in methanol gives a Schiff base, which is reduced in the presence of sodium borohydride to give the chelating alkylpyridin-2-ylmethylamine ligands $L^{PyC_{18}}$, $L^{PyC_{16}}$, $L^{PyC_{14}}$, and $L^{PyC_{10}}$ with overall yields of 78–84%. These species were fully characterized by ^{1}H NMR spectroscopy, ESIMS, and IR spectroscopy. The ^{1}H NMR spectroscopic data showed the corresponding protons expected

from the combined C–H groups from the pyridine and the alkyl chains, as reported in the Experimental Section. The IR spectroscopic data showed peaks at $\tilde{v} = 1484$–1426 cm^{-1} that were assigned to the stretching vibration of the aromatic C=N$_{Py}$ and C=C bonds, peaks in the $\tilde{v} = 2920$–2850 cm^{-1} range associated with typical alkyl vibrations, and peaks at $\tilde{v} = 3306$ cm^{-1} that are indicative of the amine nature of the ligand. The ESIMS signals in the positive mode showed peaks with m/z 361.3, 333.3, 305.3, and 249.3 for $[L^{PyC_n}+H^+]$ for $n = 18$, 16, 14, and 10, respectively. Signal simulation showed excellent agreement with position and isotopic distributions.

Complexes **1**–**6** were all synthesized in a similar manner by treating the appropriate ligand with copper(II) chloride (**1**–**3**) or copper(II) bromide (**4**–**6**), and were isolated as microcrystalline materials and fully characterized. The IR spectra display peaks associated with the ligand, with small shifts indicative of metal coordination. Cu–halogen bonds were not within the detection range.[30] The ESIMS analysis of **1**–**3** in methanol shows peak clusters at m/z 458.2, 430.2, and 402.2 associated with the $[Cu^{II}Cl(L^{PyC_n})]^+$ fragment, whereas **4**–**6** show equivalent peaks for the $[Cu^{II}Br(L^{PyC_n})]^+$ fragment at m/z 504.2, 476.2, and 392.3. Each of these cluster peaks display unique profiles related to the presence of isotopic distributions that contain copper (69.2% ^{63}Cu and 30.8% ^{65}Cu), chlorides (75.8% ^{35}Cl and 24.2% ^{37}Cl), and bromides (50.7% ^{79}Br and 40.6% ^{81}Br). Selected examples of such profiles can be seen in Figure 1. All elemental analyses are in excellent agreement with the expected calculated values. Based on the data above, it can be inferred that complexes **1** to **6** are formed by a single ligand coordinated to the copper center and to anionic (Cl$^-$ or Br$^-$) ligands.
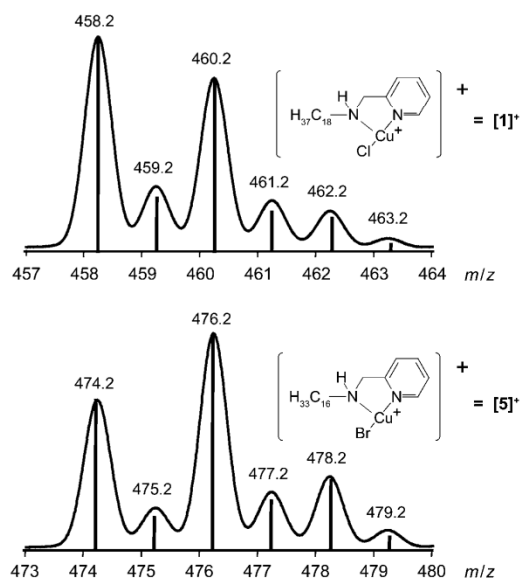
Figure 1. The $[M-X]^+$ ESIMS peak clusters for **1**$^+$ (X = Cl$^-$) and **5**$^+$ (X = Br$^-$). The relative abundance axes are omitted for clarity.

Molecular structures: The molecular structures of **1**, **2**, **3**, and **6** were determined by X-ray crystallography of single crystals obtained from slow evaporation of distinct 1:1 solvent mixtures. Except for the length of the alkyl chain, the chloro-containing complexes **1**, **2**, and **3** display similar general features, including bond lengths and angles. Several attempts to obtain X-ray quality crystals for bromo-containing complexes **4** and **5** failed, but successful molecular structure information was obtained for the analogue complex **6**, which has a $L^{PyC_{10}}$ ligand. Based on complementary techniques, this complex is expected to serve as an accurate model for the geometry adopted by **4** and **5**. The ORTEP diagrams for compounds **1** and **6** are depicted in Figure 2, with selected
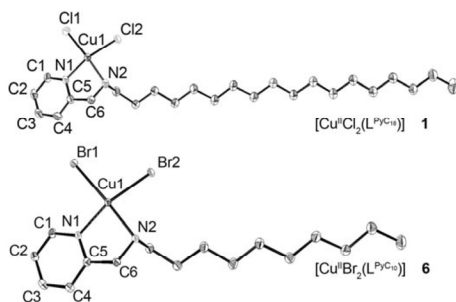
Figure 2. ORTEP diagrams for **1** and **6** with ellipses drawn at the 50% probability level. Selected bond lengths [Å] and angles [°] for **1**: Cu1–N1 = 2.0134(19), Cu1–N2 = 2.028(2), Cu1–Cl1 = 2.2470(6), Cu1–Cl2 = 2.2878(6), C6–N2 = 1.470(3) Å; N1-Cu-N2 = 80.96(8), N1-Cu-Cl1 = 95.69(6), N2-Cu-Cl1 = 176.61(6), N1-Cu-Cl2 = 160.21, N2-Cu-Cl2 = 89.81(6), Cl1-Cu1-Cl2 = 93.54(3)°. Selected bond lengths [Å] and angles [°] for **6**: Cu1–N1 = 2.0142(15), Cu1–N2 = 2.0361(15), Cu1–Br1 = 2.3926(3), Cu1–Br2 = 2.4285(3) Å; N1-Cu-N2 = 81.19(6), N1-Cu-Br1 = 95.89(4), N2-Cu1-Br1 = 176.95(4), N1-Cu1-Br2 = 159.26(5), N2-Cu1-Br2 = 90.05(4), Br1-Cu1-Br2 = 92.996(10)°. See the Supporting Information for details of **2** and **3**.

bond lengths and angles provided. Figures S1 and S2 in the Supporting Information present data for **3** and **4**. Species **1**, **2**, and **3** crystallize in the triclinic space group $P\bar{1}$ and consist of discrete and neutral molecules with a CuN_2Cl_2 coordination sphere. The Cu–N_{Py} bond lengths for these species vary between 2.007 and 2.013 Å, whereas the Cu–N_{amine} bond lengths are 2.028 to 2.032 Å. Two *cis*-oriented chloro ligands complete the coordination sphere around the metal ion. The bond length of one of the chloro ligands is slightly shorter at about 2.25 Å, whereas the other Cu–Cl length is about 2.29 Å. The bite angles of the amine and pyridine nitrogen atoms from the L^{PyC_n} ligand coordinated to copper are about 81° and the Cl-Cu-Cl angles exceed 90°, whereas the N-Cu-Cl angles exceed 160°. This reinforces the notion of a distorted square planar environment that is favored for bivalent copper ions because considerable deviation occurs from the 90° expected in a perfect square planar geometry.[31,32]

Complex **6** also presents a triclinic $P\bar{1}$ space group and has a local CuN_2Br_2 coordination sphere with slightly longer Cu–N bonds due to the presence of bulkier bromo ligands.

One of the Cu–Br bonds is comparable to the Cu–Cl bonds described above, whereas the other one is longer with a length of 2.43 Å. These bond lengths are in good agreement with reported values.[33,34]

All of the above species are loosely associated in the solid state as $[Cu^{II}(L^{PyC_n})X_2]_2$ (X = Cl^-, Br^-) dimers through long Cu···X′ bonds (2.75 and 2.93 Å for Cl′ and Br′, respectively; see Figure S1 in the Supporting Information). This weakly bound dimer readily dissociates in solution, as evidenced by EPR spectroscopy and ESIMS measurements at low cone voltage. The hydrocarbon chains in all of the above species present an average C–C bond length of 1.52 Å, whereas the average C–C ring bond length is 1.48 Å.

Redox properties of the precursors: To develop responsive films, a thorough understanding of the redox properties of the precursors is needed. Several compounds were scanned in acetonitrile to assess the redox potentials of the copper ion. It was observed that the length of the alkyl chains has a negligible effect on the potentials, thus suggesting an absence of ligand-inductive effects or decreasing rates of interfacial electron transfer.[35] Compounds **1** and **5** were selected and studied in a range of solvents with distinct polarities and with different supporting electrolytes. The results allow us to present an accurate picture regarding their redox potentials, reversibility, and cyclability. The two supporting electrolytes used were tetrabutylamonium hexafluorophosphate (TBAPF$_6$) and perchlorate (TBAClO$_4$), which were chosen with the aim of observing how they favor electrochemical reversibility.[36] The solvents were dichloromethane, acetonitrile, and dimethylformamide. Several scan rates were probed and the best reversibility was attained at 150 mVs^{-1}. Table 1 summarizes the results, with all potentials reported versus the Fc$^+$/Fc couple. No formation of metallic copper was observed.

The 3d^9 copper(II) ion has a flexible coordination sphere that favors square planar, square pyramidal, or trigonal bipyramidal geometries, whereas the reduced copper(I) counterpart, which has a 3d^{10} configuration, prefers a tetrahedral geometry.[37] Because of this geometrical reorganization during the redox process, an irreversible behavior is expect-

Table 1. Cyclic voltammetry data for **1** and **5**.[a]

Compound	Solvent	Electrolyte	$E_{1/2}$ (ΔE_p) [V]	$|I_{pc}/I_{pa}|$
$[Cu^{II}Cl_2(L^{PyC_{18}})]$ (**1**)	DCM	TBAPF$_6$	−0.70 (0.24)	1.2
	DCM	TBAClO$_4$	−0.74 (0.23)	1.9
	ACN	TBAPF$_6$	−0.48 (0.16)	1.3
	ACN	TBAClO$_4$	−0.54 (0.29)	2.5
$[Cu^{II}Br_2(L^{PyC_{16}})]$ (**5**)	DCM	TBAPF$_6$	−0.73 (0.17)	1.6
	DCM	TBAClO$_4$	−0.75 (0.20)	1.2
	ACN	TBAPF$_6$	−0.51 (0.13)	1.5
	ACN	TBAClO$_4$	−0.52 (0.15)	1.4
	DMF	TBAPF$_6$	−0.55 (0.20)	2.4
	DMF	TBAClO$_4$	−0.55 (0.24)	2.1

[a] Room temperature measurements. Potentials are referenced versus the Fc$^+$/Fc couple (Fc = ferrocene). Individual $\Delta E_{Fc^+/Fc}$ values range from 0.09 to 0.11 V.

ed. Therefore, it is somewhat surprising that both **1** and **5** display quasi-reversible behavior at low potentials.

As can be seen in Figure 3, compound **1** shows limited reversibility. In dichloromethane (data not shown), peak separations (ΔE_p) greater than 0.20 V suggest near irreversible
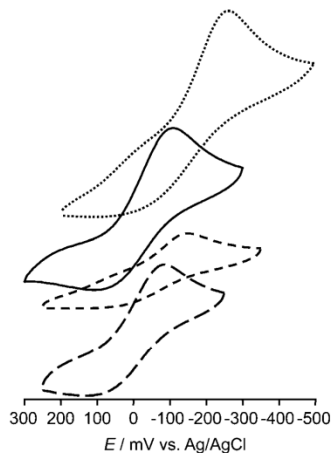
Figure 3. Selected cyclic voltammograms for 1.0×10^{-3} M solutions of **1** and **5** in acetonitrile with different supporting electrolytes. ·····: **1** with TBAClO$_4$, ——: **5** with TBAClO$_4$, -----: **1** with TBAPF$_6$, ---: **5** with TBAPF$_6$.

behavior. In acetonitrile, when TBAClO$_4$ is present the value of ΔE_p is about 0.30 V and $|I_{pc}/I_{pa}| > 2.0$, which indicates an irreversible process. Changing the supporting electrolyte to TBAPF$_6$ decreases ΔE_p to half the previous value, which suggests quasi-reversible behavior that is also supported by an $|I_{pc}/I_{pa}|$ value that approaches unity. The coordinating nature of dimethylformamide was thought to help stabilize the redox processes observed for **5**. However, an irreversible behavior was observed with values of $\Delta E_p \approx 0.20$ V and $|I_{pc}/I_{pa}|$ values greater than 2.0.

Acetonitrile seems to foster similar $E_{1/2}$ values independent of the supporting electrolyte, and ΔE_p values of ≈ 0.20 V and $|I_{pc}/I_{pa}| \approx 1.5$ also attest for the quasi-reversible nature of the Cu^{II}/Cu^I couple. The opposite was observed when noncoordinating dichloromethane was used. The nature of the electrolyte leads to smaller peak separations associated with larger $|I_{pc}/I_{pa}|$ values.

In an attempt to generalize these observations, the following conclusions can be drawn: 1) The presence of halides leads to quasi-reversible redox processes, 2) the redox processes of chloro-containing **1** are less reversible than bromo-containing **5**, 3) the use of TBAPF$_6$ as the electrolyte favors smaller ΔE values within quasi-reversible ranges, and 4) acetonitrile supports better reversibility, followed by dichloromethane and then dimethylformamide.

It is suggested that this observed quasi-reversibility is related to the unique coordination spheres of **1** and **5**, which have both halogen and pyridine donors. Chlorocopper(II) systems [Cu^{II}Cl$_4$]$^{-2}$, [Cu^{II}Cl$_3$(S)]$^-$, and [Cu^{II}Cl$_2$(S)$_2$]^0 (S = sol-

vent) are expected to be square planar, but tend to be tetrahedral in solvents with high dielectric constants and high donor number, such as acetonitrile.[37,38] Similarly, the presence of PF$_6^-$ counterions leads to distorted planar geometry in environments with similar denticity and structure as those of L^{PyC16} and L^{PyC18}.[39] Therefore, **1** and **5** deviate considerably from the expected square planar geometry, both as solids (see the structural data) and in solution. Consequently, the 3d$^9 \rightleftharpoons$ 3d^{10} reorganization becomes energetically affordable and gives the observed quasi-reversible processes.

Amphiphilic properties and film patterning: To evaluate the amphiphilic behavior of **1–6**, the resulting Langmuir monolayers were studied by surface pressure versus area (Π vs. A) isotherms and BAM. Compression isotherms give information about the 2D behavior of the resulting Langmuir film at the air/water interface, the presence of mesophasic changes, the collapse pressure (π_c), and the average area per molecule at the collapse of the monolayer at collapse (A_c). The surfactant is initially dissolved in an immiscible organic solvent, such as chloroform, and subsequently spread on the water surface. As the barriers of the trough are compressed, the tension (γ) of the air/water interface in the presence of the amphiphilic species decreases as compared with that of the bare air/water interface ($\gamma_0 = 72$ mN m^{-1} at 23 °C), resulting in an increase in Π ($= \gamma_0 - \gamma$). Figure 4 shows the results for ligand L^{PyC18} and its chloro (**1**) and bromo (**4**) copper-containing analogues (top), and L^{PyC16} and its derivatives **2** and **5** (Figure 4, bottom). It is worth noting that L^{PyC14}, L^{PyC10}, **3**, and **6** were unable to form organized films at the air/water interface. Based on their erratic behavior under compression, it can be concluded that these species dissolve in the subphase. Further studies involving light scattering are
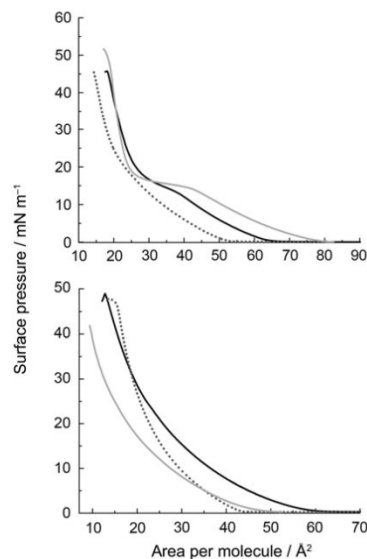
Figure 4. Pressure versus area isotherms of a) ligand L^{PyC18} (——) and its copper complexes **1** (——) and **4** (·····), and b) ligand L^{PyC16} (——) and its copper complexes **2** (——) and **5** (·····).

currently under development to determine the appropriate mechanisms. The compression isotherms of ligands $L^{PyC_{18}}$ and $L^{PyC_{16}}$ are discussed below and reveal intrinsic differences. Ligand $L^{PyC_{18}}$ exhibited a typical uneventful compression at low pressures with average areas per molecule reaching 70–80 $Å^2$, which reflects a lack of organization. As the pressure increased, the ligand underwent a phase transition at 13–17 mN m^{-1} analogously described as a gas-to-liquid transformation. This can be attributed to an increased repulsion between the individual molecules on the surface. A steeper slope was observed after this transition. The average area per molecule at collapse (A_c) was obtained by extrapolating the steepest part of the curve down to zero pressure.[3, 14] The pyridine head-group of the ligand seems to have interfered little with the packing of the monolayer, and the observed area of 23–25 $Å^2$ molecule^{-1} is comparable to the packing reported for a carboxylic acid with an equivalent number of carbon atoms.[40] The formal film collapse happened at 45–50 mN m^{-1}. Unlike $L^{PyC_{18}}$, ligand $L^{PyC_{16}}$ does not display any phase transitions and collapses at around 40 mN m^{-1} with similar average areas per molecule. It is clear that the average areas at collapse should be similar, and that the plateaulike phase transition for the former ligand must be related to the presence of longer alkyl chains and their organization on the surface. Events related to this behavior might be associated with the configuration and the presence of different degrees of defects in the chains. Complex **1** reinforces this notion by displaying a similar overall behavior with a comparable plateau from 12–18 mN m^{-1} and an average area of 30–31 $Å^2$. A more expanded isotherm is expected after the addition of a bulky and charged copper cation. Interestingly, if the chloro ligands in **1** are replaced by bromo ligands in **4**, this phase transition disappears almost completely and smaller average areas of 25–27 $Å^2$ are observed. Intuitively, it would seem that bromo-substituted **4** should have a greater area per molecule than its chloro-substituted counterpart **1**. However, the polarizability of the bromides might allow for improved solubility into the subphase, which would lead to higher organization of the aliphatic chains. In spite of the expected dynamic equilibrium at the interface, the relative geometry of the polar metal-containing head group should also be considered; assuming the higher mass and polarizability of the bromo ligands, a more pronounced tetrahedral character could be favored in solution, whereas the chloro-containing **1** would be less distorted. The inclusion of metals to $L^{PyC_{16}}$ gives **2** and **5**, but similarly to the ligand, neither species exhibits obvious phase transitions in their isotherms. Overall, the C_{16} species start organizing at lower area per molecule values and collapse at slightly lower pressures than their C_{18} counterparts, which thus reflects the influence of the chain length. In contrast to **1** and **4**, species **2** and **5** display similar A_c values of 26–28 $Å^2$ at collapse, with **5** showing a steeper slope. The reported collapse pressures for **1**, **2**, **4**, and **5** are significantly greater than those observed for other metal–surfactant complexes. However, the A_c increase is less noticeable than that of a phenanthroline-based surfactant upon copper inser-

tion,[41] but is significantly smaller than that of a bipyridyl-rhenium(I) surfactant[5b] with the same hydrocarbon chain length. Comparison with another recently published cuproamphiphile,[29] in which the surfactant head group is a *tert*-butyl-substituted phenolate, also suggests that the pyridine-based systems give higher collapse values and more organized films. Differences in the ligand head groups, the oxidation states of the ions, and their electronic structures explain the significant variation in A_c between the 3d copper(II) and the 5d rhenium(I) surfactants.

BAM studies: BAM uses polarized light passing through media with dissimilar refractive indexes and is the most powerful method available to identify structures such as agglomerates and domains in films at the air/water interface.[42] The compression of films has been investigated for $L^{PyC_{18}}$, **1**, and **2**, and also $L^{PyC_{16}}$, **4**, and **5** to assess the dynamics of phase change and domain formation and to gain insight in the behavior observed during the isothermal compression experiments discussed above. Selected images for $L^{PyC_{18}}$, **1**, and **2** are shown in Figure 5. Beginning with ligand $L^{PyC_{18}}$
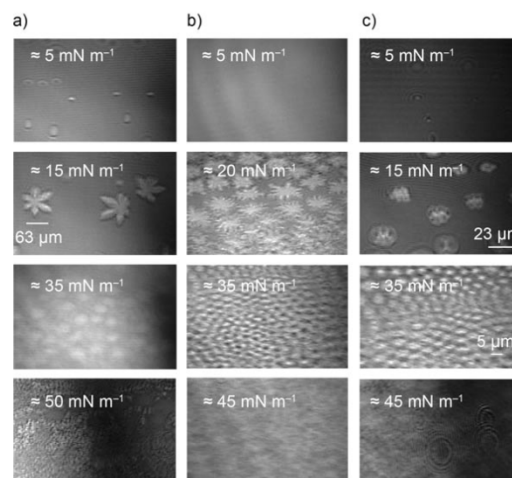
Figure 5. Selected BAM micrographs of a) ligand $L^{PyC_{18}}$, b) **1**, and c) **4**.

(Figure 5a), compression at 5 mN m^{-1} showed a homogeneous surface with sporadic Newton circles,[43] which were attributed to multilayer granule formation from ejection of matter due to localized oscillations. As the lateral compression continued, the pressure increases prompted the ligand to undergo a 2D liquid–gas phase transition (13–15 mN m^{-1}). At this point, nucleation led to a condensed leaflike domain formation. These domains resemble side-branching morphologies that have been observed for other secondary amines, such as dioctadecylamine.[44] As compression was continued beyond the plateau, the number of domains quickly increased, whereas an overall decrease in size from ≈63 to 25 μm was observed. Around 35–40 mN m^{-1}, the interspatial distance decreased to the point that a homo-

geneous film was formed and continued through collapse at $50\,mN\,m^{-1}$. The BAM micrographs for chloro-containing **1** are shown in Figure 5b and start with a homogeneous monolayer that subexists up to 8–$9\,mN\,m^{-1}$, at which point domain formation begins and coincides with the region that precedes the plateau observed in the isotherm of the compound. From this plateau onward, the emerging domains adopt five- to seven-fold branched star-shaped morphology and continue to develop throughout compression. The domains decrease in size at higher surface pressures, and display more ordered spherical morphologies until the surface reaches relative homogeneity prior to collapse at $45\,mN\,m^{-1}$. Interestingly, the film of bromo-containing **4** (Figure 5c) shows the formation of a homogeneous film up to 9–$12\,mN\,m^{-1}$ with sporadic Newton rings. In good agreement with the lack of a plateau in its isotherm, no formation of branched star-shaped domains was observed. Only small and sparse spherical domains were observed at 15–$20\,mN\,m^{-1}$, and at higher surface pressures ($35\,mN\,m^{-1}$ and upwards) these domains decreased in size and led to homogeneity. At higher surface pressures, similar film topologies were observed for **4** and **1**. The higher the compression becomes, the smaller the interspatial distance between the resulting domains, which leads to comparable collapse pressures and morphologies. It has been suggested by Vollhardt and Wiedemann[45] that the growth of these structures is due to domain crowding from supersaturation on the surface of the surrounding phase. Additionally, we hypothesize that a dynamic equilibrium exists between the dihalogenated species $[Cu^{II}(L^{PyC_n})X_2]$ and their monohalogenated and solvated analogues $[Cu^{II}X(H_2O)(L^{PyC_n})]^+$ and $[Cu^{II}(H_2O)_2(L^{PyC_n})]^{2+}$ at the air/water interface. Each of these species should display distinct dipole moments that increase molecular motion. Formation of domains would, therefore, be a mechanism to stabilize the film by decreasing mobility.

During lateral compression of the ligand $L^{PyC_{16}}$, no clear plateau comparable to that of $L^{PyC_{18}}$ was observed. A well-organized monolayer was detected up to $8\,mN\,m^{-1}$, with few Newton circles appearing slightly above $9\,mN\,m^{-1}$. Nucleation and domain formation started to appear at $16\,mN\,m^{-1}$. At $21\,mN\,m^{-1}$, round flowerlike domains (see Figure S3 in the Supporting Information) were formed and combined without reverting back to the initial homogeneous film exhibited early in the experiments. These domains do not resemble the side-branched leaflike domains observed for $L^{PyC_{18}}$, and seem to have a tip-splitting morphology.[44] This suggests that the shorter alkyl chain length of the ligand dictates the resulting pattern of the condensed phase. It would be interesting to compare different lengths of alkyl chains, but it has been observed that chains shorter than hexadecane (C_{16}) are dissolved in the subphase under the current experimental conditions. Similarly to $L^{PyC_{16}}$, the isotherm of **2** does not display an apparent plateau, and a homogeneous film without domain formation was observed up to $24\,mN\,m^{-1}$. The addition of a metal to the ligand and the presence of halogeno coligands permitted the monolayer to withstand nearly three times the surface pressure of the non-

metalated species. At $25\,mN\,m^{-1}$, oscillations associated with possible film buckling appeared. Nonhomogeneous spherical domains began to form and continued through collapse at around $50\,mN\,m^{-1}$. Compound **5** showed similar isotherms as the ligand and chlorinated species. Nonetheless, a homogeneous film was observed and domains were not detected throughout the lateral compression stage up to the collapse point. As previously suggested, the aliphatic chains must exhibit high interaction energies to provide ordered liquid-condensed-phase monolayers.[46] Furthermore, a delicate balance between the selection of the coligands and the length of the alkyl chains seems to exist, and appears pivotal to the control of domain formation in Langmuir films of these metallosurfactants. In these experiments, surface pressure was the only variable. Domain morphology can also be influenced by factors such as distinct compression rates, time and temperature changes, and subphase modification.[17,44,47,48] Ongoing work in our labs focuses on these factors. Similarly, to assess the relationship between domain formation and degree of disorder, a detailed study based on atomic-force microscopy and sum frequency generation vibrational spectroscopy is currently underway.

Electronic structure calculations: A series of electronic structure calculations were carried out on simplified models to evaluate our explanations about the electrochemical and amphiphilic behavior of the copper precursors **1–6**. Figure 6a shows the models we used, which consist of aminomethylpyridine head groups with shorter ethyl chains. These simplified ligands are coordinated to copper and chloro groups as in $[Cu^{II}Cl_2(L^{PyC_n})]$ to mimic compounds **1–3**, and bromo groups as in $[Cu^{II}Br_2(L^{PyC_n})]$ to mimic **4–6**. A model in which one chloro group is replaced by water, described as $[Cu^{II}Cl(H_2O)L]^+$, was considered; this is the most likely species to be in equilibrium with $[Cu^{II}Cl_2L]$ at the air/water interface. Another model, $[Cu^{II}(H_2O)_2L]^{2+}$, was included for comparison purposes, in spite of the fact that its concentration is not expected to be significant because the stabilization of the $2+$ charge would be energetically demanding when chloride ions are present. In general terms, it can be seen that all species exhibit a SOMO with distinctive metal character. This orbital is best described as the $d_{x^2-y^2}$ orbital, which interacts in a σ fashion with the p-type orbitals of the halogen and nitrogen donors, as shown in Figure 6b. In idealized N_4 square planar environments, this would correspond to the antibonding b_{1g} molecular orbital.[49] However, compounds **1–6** have $NN'Cl_2$ and $NN'Br_2$ coordination environments, and therefore, much lower symmetry. Considering equivalency between the amine and pyridine nitrogen atoms would lead to N_2Cl_2 and N_2Br_2 environments of approximate C_2 symmetry. In that case, the SOMOs should be labeled as a. Because more elaborate calculations would be required to ascertain the answer to this question, the discussion will be restricted to the relative energies of the highest occupied molecular orbital (HOMO, which herein coincides with the SOMO) and the lowest unoccupied molecular orbital (LUMO). The influence of the different monodentate li-
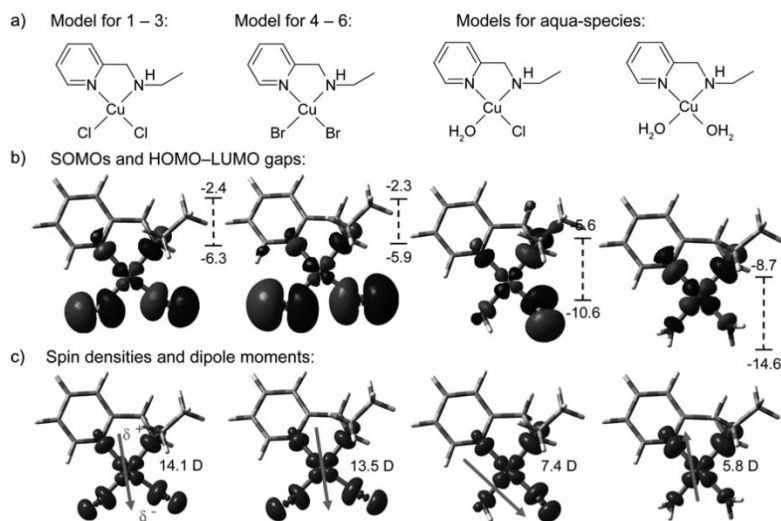
Figure 6. a) Simplified models of the surfactants, b) Singly occupied molecular orbitals (SOMOs) for these models, and c) spin-density plots.

$d_{x^2-y^2}$ character, as proposed previously. Equally interestingly, the analysis of the dipole moments may allow for the discussion of the observed behavior in Langmuir films. Models for the nonmetalated ligand show a dipole moment of 2.09 D, whereas $[Cu^{II}Cl_2L]$ and $[Cu^{II}Br_2L]$ show higher but similar dipole moments of 13–14 D. The value observed for the ligand is comparable to that of pyridine alone (2.30 D),[50] and upon metalation the chloro species displays a slightly higher value than the bromo species. This is consistent with the electronegativity trend for the halogen atoms. A considerable difference is seen when $[Cu^{II}Cl_2L]$ is compared to $[Cu^{II}Cl(H_2O)L]^+$, in which the replacement of a chloro group results in a dramatic decrease in the original dipole moment value to about half. This decrease is also followed by a change in the direction of the vector. In the event that $[Cu^{II}(H_2O)_2L]^{2+}$ would form in appreciable concentrations, an inversion of the dipole takes place. A picture of the dynamic character of the films can be drawn, when considering these species, and the equivalent bromo-substituted ones, at the air/water interface. Because the $[Cu^{II}Cl_2L]\rightleftharpoons[Cu^{II}Cl(H_2O)L]^+$ and, to a lesser extent, the $[Cu^{II}Cl(H_2O)L]^+\rightleftharpoons[Cu^{II}(H_2O)_2L]^{2+}$ equilibria are supposed to occur quickly, the dipole moment of these species will be changing constantly. The change is followed by molecular rearrangements at the air/water interface, which can trigger aggregation and domain formation as the surface pressure changes.

gands (Cl⁻, Br⁻, and H₂O) on the energy of the HOMO and the HOMO–LUMO gap is dramatic. Following an arbitrary scale, as shown in Table 2, the $[Cu^{II}Cl_2L]$ and $[Cu^{II}Br_2L]$ species display comparable gaps of 3.6 to 3.9 eV, whereas $[Cu^{II}Cl(H_2O)L]^+$ and $[Cu^{II}(H_2O)_2L]^{2+}$ show more pronounced values of 5.0 to 5.9 eV due to the presence of positive charges.

Table 2. Electronic structure parameters.

Compound	HOMO [eV]	LUMO [eV]	Electron affinity [eV]	Dipole moment [D]
$[Cu^{II}Cl_2L]$	−6.3	−2.4	1.2	14.1
$[Cu^{II}Br_2L]$	−5.9	−2.3	1.3	13.5
$[Cu^{II}Cl(H_2O)L]^+$	−10.6	−5.6	5.0	7.4
$[Cu^{II}(H_2O)_2L]^{+2}$	−14.6	−8.7	9.1	5.8

It is assumed that the $Cu^{II}\rightarrow Cu^I$ reduction processes will depend mainly upon the relative energies of the SOMO orbitals of the bivalent $3d^9$ metal complex. Therefore, for the formation of a $3d^{10}$ Cu^I species by the addition of one electron, the vertical electron affinity is the best parameter for comparison. The affinity for $[Cu^{II}Cl_2L]$ and $[Cu^{II}Br_2L]$ was calculated and found to be 1.2 and 1.3 eV, respectively, which leads to the conclusion that $[Cu^{II}Br_2L]$ should have a more energetically favorable reduction. As such, this is in excellent agreement with the observed electrochemical data, in which compound 5 displays slightly more affordable reductions than 1. Therefore, it is expected that $[Cu^{II}Cl(H_2O)L]^+$ would display more positive potentials. As can be observed in Figure 6c the spin-density plots and the orientation of the dipole moments are provided. The spin density reinforces the notion that the unpaired electron of each model does correlate to the SOMO, and that this shows a

Conclusion

Herein we have synthesized and characterized a series of novel surfactants and metallosurfactants. New pyridine-based ligands L^{PyC_n} ($C_n = C_{18}$, C_{16}, C_{14}, C_{10}) were treated with halogeno-copper(II) salts to give compounds 1–6, described as $[Cu^{II}(L^{PyC_n})X_2]$. Compounds 1, 2, 3, and 6 had their molecular structure solved by X-ray diffraction methods, which showed that the local geometry around the metal center is distorted square planar. The electrochemical behavior of these species revealed that the unique coordination sphere, which contains halogen atoms and pyridines, leads to quasi-reversible—rather than the expected irreversible—redox processes. This property is enhanced in bromo-substituted species in acetonitrile if TBAPF₆ is used as the supporting electrolyte. These results were partially supported by DFT-based vertical electron affinity calculations that suggest a more energetically favorable reduction for bromo-substitut-

ed models. Isothermal compression revealed that longer chain lengths, such as $-C_{18}H_{37}$ in $L^{PyC_{18}}$ and **1**, lead to the formation of a plateau that corresponds to a biphasic film. On the other hand, chain lengths like $-C_{16}H_{33}$ in $L^{PyC_{16}}$, **2**, and **5** do not display such obvious mesophasic change. The effect of the chain length seems to be overcome by the nature of the anionic coligand because the larger bromo complex in **4** lacked the expected plateau. This was attributed to a higher subphase solubility compared to that of the chlorinated complexes. Furthermore, variation of the chain length in absence of the metal ion dictates the morphological characteristics on the condensed domains. The metalated complexes provide more homogeneous monolayer formation at significantly higher pressures compared with the ligands alone. Finally, chain lengths shorter than $C_{16}H_{33}$ (as seen in **3** and **6**) typically failed to exhibit any organization at the air/water interface under the current experimental settings. Although the lack of a larger body of work prevents us from attempting generalizations for metallosurfactants in general, these results exemplify the first detailed study on the behavior of single-tail copper surfactants at the air/water interface and as solid films. The analysis of calculated dipole moments was used to rationalize the behavior observed in Langmuir films, in which models of the ligands showed dipole moments comparable to that of pyridine. The metal-containing complexes displayed considerably higher dipole moments that indicated the efficacy of metalation as a tool for surfactant design. The equilibrium between dihalogenated complexes and monohalogenated/solvated complexes results in dynamic changes in the dipole moment, which leads to the biphasic topologies observed experimentally. On the basis of these observations, we can conclude that the behavior of metallosurfactants is unique and can be modulated further, thereby leading to a general strategy for morphological control. Thus, it can be envisioned that customized film patterning can and will be useful for the design of LB-based devices that take advantage of the intrinsic properties of metal centers. Ongoing research in our labs is focused on the development of a broader selection of metallosurfactants, such as iron and cobalt analogues, and on the alteration of deposition conditions, such as temperature and compression rate. The inclusion of different ions is aimed at redox reversibility and spin-crossover properties, whereas the changing deposition methods focus on the control of the patterning phenomenon.

Experimental Section

Materials and methods: All the reagents were obtained from commercial sources and were used without further purification. Dichloromethane was purified by using an I.T. solvent purification system. ^{1}H NMR spectra were recorded by using a Varian 400 MHz instrument. IR spectra were measured from $\tilde{v} = 4000$ to $400\ cm^{-1}$ by using KBr pellets on a Tensor 27 FTIR-spectrophotometer. ESIMS were measured on a Micromass QuattroLC triple quadrupole mass spectrometer equipped with an electrospray/APCI source, Waters Alliance 2695 LC autosampler, and photodiode array UV detector. Experimental assignments were simulated

based on signal position and isotopic distributions. Elemental analyses were performed by Midwest Microlab, Indianapolis, Indiana. Cyclic voltammetry experiments were performed by using a BAS 50W voltammetric analyzer. A standard three-electrode cell was employed with a glassy carbon working electrode, a Pt wire auxiliary electrode, and an Ag/AgCl reference electrode under an inert atmosphere at RT. Potentials are presented versus $Fc^{+}/Fc^{[51]}$ as the internal standard. Dry dichloromethane, acetonitrile, and dimethylformamide were used as the solvents. The concentration of the analytes was 1.0×10^{-3} M and the concentration of the supporting electrolytes TBAPF$_6$ and TBAClO$_4$ was 0.1 M. Experiments were run at scan rates of 50, 100, 150, 200, and 300 mV s^{-1}.

X-ray structural determination for 1, 2, 3, and 6: Diffraction data for complex **1** were collected on a Bruker P4/CCD diffractometer equipped with Mo$_{K\alpha}$ radiation and a graphite monochromator at 213 K. Data were measured at 10 s frame^{-1} with 0.3° between frames. Diffraction data for the remaining three structures (**2**, **3**, and **6**) were measured on a Bruker APEX-II kappa geometry diffractometer with Mo$_{K\alpha}$ radiation and a graphite monochromator at 100 K. Frames were collected with the detector at 40 mm, 0.3° between each frame, and 5–10 s frame^{-1}. All frame data were indexed and integrated by using the manufacturer's SMART, SAINT, and SADABS software.$^{[52]}$ The models were refined by using Sheldrick's SHELX-97 software.$^{[53]}$ A summary of the crystal structure parameters is shown below. These four complexes crystallize as dimers through an inversion center, with long axial Cu···X interactions and N−H···X hydrogen bonds.

Complex 1: Formula = $C_{48}H_{88}N_4Cl_4Cu_2$; $M_r = 990.10$; space group = $P\bar{1}$; $a = 7.5068(8)$, $b = 9.7426(12)$, $c = 19.250(2)$ Å; $\alpha = 90.194(2)$, $\beta = 98.838(2)$, $\lambda = 109.470(2)°$; $V = 1309.4(3)$ Å^3; $Z = 1$; $T = 213(2)$ K; $\lambda = 0.71073$ Å; $\rho_{calcd} = 1.256$ g cm^{-3}; $\mu = 1.051$ mm^{-1}; $R(F) = 3.64\%$; $wR(F) = 8.63\%$.

Complex 2: Formula = $C_{44}H_{80}N_4Cl_4Cu_2$; $M_r = 934.00$; space group = $P\bar{1}$; $a = 7.4943(10)$, $b = 9.7419(12)$, $c = 17.533(2)$ Å; $\alpha = 98.810(6)$, $\beta = 94.108(7)$, $\lambda = 108.915(6)°$; $V = 1186.5(3)$ Å^3; $Z = 1$; $T = 100(2)$ K; $\lambda = 0.71073$ Å; $\rho_{calcd} = 1.307$ g cm^{-3}; $\mu = 1.155$ mm^{-1}; $R(F) = 2.91\%$; $wR(F) = 7.22\%$.

Complex 3: Formula = $C_{40}H_{72}N_4Cl_4Cu_2$; $M_r = 877.90$; space group = $P\bar{1}$; $a = 7.5668(4)$, $b = 9.6649(5)$, $c = 16.0276(8)$ Å; $\alpha = 84.406(2)$, $\beta = 85.506(2)$, $\lambda = 70.545(2)°$; $V = 1098.63(10)$ Å^3; $Z = 1$; $T = 100(2)$ K; $\lambda = 0.71073$ Å; $\rho_{calcd} = 1.327$ g cm^{-3}; $\mu = 1.243$ mm^{-1}; $R(F) = 3.14\%$; $wR(F) = 6.87\%$.

Complex 6: Formula = $C_{32}H_{56}N_4Br_4Cu_2$; $M_r = 943.53$; space group = $P\bar{1}$; $a = 7.4601(3)$, $b = 10.0349(4)$, $c = 14.1949(7)$ Å; $\alpha = 100.620(2)$, $\beta = 96.781(2)$, $\lambda = 109.911(2)°$; $V = 963.03(7)$ Å^3; $Z = 1$; $T = 100(2)$ K; $\lambda = 0.71073$ Å; $\rho_{calcd} = 1.627$ g cm^{-3}; $\mu = 5.279$ mm^{-1}; $R(F) = 2.33\%$; $wR(F) = 5.12\%$.

Compression isotherms: The Π versus A isotherms were examined by using an automated KSF Minitrough at (22.8 ± 0.5) °C. Ultra-pure water with a resistivity of 17.5–18 MΩ cm^{-1} was obtained from a Barnstead NANOpure system and used in all experiments. Impurities present at the surface of the freshly poured aqueous subphase were removed by vacuum after compression of the barriers. Spreading solutions were prepared in spectroscopy-grade chloroform. A known quantity (typically 25 μL) of freshly prepared surfactant solution with a known concentration (1 mg mL^{-1}) was then spread on the clean aqueous subphase. The system was allowed to equilibrate for approximately 10 min before monolayer compression. The Π versus A isotherms were obtained at a compression rate of 10 mm min^{-1}. The Wilhelmy plate method (paper plates, 40 mm diameter) was used to measure the pressure.$^{[54]}$ At least three independent measurements were carried out per sample, with excellent reproducibility attained.

BAM studies: A KSV-Optrel BAM 300 equipped with a HeNe laser (10 mW, 632.8 nm) and a CCD detector was used for all micrographs. The compression rate was 10 mm min^{-1}, the field of view was 800×600 microns, and the lateral resolution was about 2–4 μm.

Electronic structure calculations: The B3LYP/6–311G(d) level of theory$^{[55]}$ was employed throughout to allow for the handling of negatively charged species. All calculations were done by using the Gaussian series of programs.$^{[56]}$ Geometries were fully minimized without symmetry constraints by using standard methods.$^{[57]}$ Located stationary points

were characterized by computing analytic vibrational frequencies. Reported energies include zero-point correction. Cartesian coordinates of all optimized structures are provided as supporting material.

Synthesis of the surfactants $L^{PyC_{18}}$, $L^{PyC_{16}}$, $L^{PyC_{14}}$, $L^{PyC_{10}}$: 2-Pyridinecarboxyaldehyde (1.07 g, 10 mmol) was treated with 1 equivalent of the appropriate alkylamine (1-octadecylamine, 1-hexadecylamine, 1-tetradecylamine, 1-decylamine) in methanol (50 mL). The resulting compounds were gently heated at reflux to give the equivalent imines, which were reduced in the presence of NaBH₄. The resulting compounds were obtained as off-white and waxy solids after being washed with CH_2Cl_2 and 5% NaHCO₃, then dried over Na_2SO_4 and recrystallized in acetone (yields = 78–84%). ¹H NMR (400 MHz, CDCl₃, 300 K): $\delta = 0.85$ (1×t, 3×1 H; CH₃), 1.20–1.50 (m, 32 H, 28 H, 24 H, 16 H, respectively; CH₂), 2.62 (1×t, 2H; CH₂NH), 3.89 (s, 2×1 H; Py–CH₂–NH), 7.14–7.61 (m, 3×1 H; pyridine), 8.49 ppm (d, 1 H; pyridine); IR (KBr): $\tilde{v} = 3306$ (s) (N–H$_{amine}$), 2920–2850 (C H$_{alkyl}$), 1426–1484 cm⁻¹ (s) (C=C$_{Py}$); ESIMS (MeOH): m/z: 361.3 [$L^{PyC_{18}}$+H⁺]; 333.3 [$L^{PyC_{16}}$+H⁺]; 305.3 [$L^{PyC_{14}}$+H⁺]; 249.3 [$L^{PyC_{10}}$+H⁺].

Synthesis of copper-containing surfactant complexes 1–3: Complexes **1–3** were all synthesized in a similar manner, in which the appropriate ligand (1.0 mmol) was treated with $CuCl_2 \cdot 2 H_2O$ (0.183 g, 1 mmol; 1:1 ratio) in methanol (50 mL). The solution was kept under mild reflux, and gave a blue solution. Upon cooling, the complex was recrystallized from EtOH/CHCl₃ to give X-ray quality crystals that were used for structure determination.

[Cu^{II}Cl₂(L$^{PyC_{18}}$)] (1): Yield 84%; m.p. 206–208°C; IR (KBr): $\tilde{v} = 2924$(s), 2849(s) (alkyl–CH–); 1380 (C=N$_{Ar}$, Ar=aromatic); 1606(s), 1573(m), 1468(s) (C=N$_{Py}$, C=C); ESIMS (MeOH): m/z: 458.2 (100) [Cu^{II}Cl-(L$^{PyC_{18}}$)]⁺; elemental analysis calcd (%) for $C_{24}H_{44}Cl_2CuN_2$: C 58.23, H 8.79, N 5.61; found: C 57.65, H 8.72, N 5.63.

[Cu^{II}Cl₂(L$^{PyC_{16}}$)] (2): Yield 88%; m.p. 203–205°C; IR (KBr): $\tilde{v} = 2852$ (s), 2925 (s) (alkyl CH); 1610 (s), 1560 (m), 1472 (m) (C=N$_{Py}$, CH=CH); 1133 cm⁻¹ (s) (R⁻–NH–R); ESIMS (MeOH): m/z (%): 430.2 (100) [Cu^{II}Cl(L$^{PyC_{16}}$)]⁺; elemental analysis calcd (%) for $C_{22}H_{40}Cl_2CuN_2$: C 56.58, H 8.63, N 6.00; found: C 56.48, H 8.35, N 5.82.

[Cu^{II}Cl₂(L$^{PyC_{14}}$)] (3): Yield 78%; m.p. 204–205°C; IR (KBr): $\tilde{v} = 2854$ (s), 2925 (s) (alkyl CH); 1608 (s), 1564 (m), 1471 (m) (C=N$_{Py}$, CH=CH); 1130 cm⁻¹ (s) (R⁻–NH–R); ESIMS (MeOH): m/z (%): 402.2 (100) [Cu^{II}Cl(L$^{PyC_{14}}$)]⁺; elemental analysis calcd (%) for $C_{20}H_{36}Cl_2CuN_2$: C 54.72, H 8.27, N 6.38; found: C 54.26, H 7.90, N 6.33.

Synthesis of copper-containing surfactant complexes 4–6: Complexes **4–6** were synthesized in a manner similar to that of **1–3**, except that $CuCl_2 \cdot 2H_2O$ was replaced by the salt CuBr₂ (1 mmol), and the resulting solution was green instead of blue. Upon recrystallization from iPrOH/CHCl₃, X-ray quality crystals of **6** were isolated.

[Cu^{II}Br₂(L$^{PyC_{18}}$)] (4): Yield 87%; m.p. 172–174°C; IR (KBr): $\tilde{v} = 2850$ (s), 2920 (s) (alkyl CH); 1370 (C=N$_{arom}$); 1159 (s) (R⁻–NH–R); 1607 (s), 1573 (m), 1471 cm⁻¹ (m) (C=N$_{Py}$, C=C); ESIMS (MeOH): m/z (%): 504.2 (100) [Cu^{II}Br(L$^{PyC_{18}}$)]⁺; elemental analysis calcd (%) for $C_{24}H_{44}Br_2CuN_2$: C 49.28, H 7.75, N 4.79; found: C 49.31, H 7.60, N 4.79.

[Cu^{II}Br₂(L$^{PyC_{16}}$)] (5): Yield 83%; m.p. 170–172°C; IR (KBr): 2850 (s), 2922 (s) (alkyl CH₂); 1610 (s), 1569 (m), 1470 (m) (C=N$_{Py}$, C=C); 1150 cm⁻¹ (s) (R⁻–NH–R); ESIMS (MeOH): m/z (%): 476.2 (100) [Cu^{II}Br(L$^{PyC_{16}}$)]⁺; elemental analysis calcd (%) for $C_{20}H_{36}Br_2CuN_2$: C 47.53, H 7.25, N 5.04; found: C 47.48, H 7.18, N 5.03.

[Cu^{II}Br₂(L$^{PyC_{10}}$)] (6): Yield 76%; m.p. 142–143°C; IR (KBr): $\tilde{v} = 2834$ (s), 2931 (s) (alkyl CH); 1605 (s), 1568 (m), 1477 (m) (C=N$_{Py}$, CH=CH); 1127 cm⁻¹ (s) (R⁻–NH–R); ESIMS (MeOH): m/z (%): 392.3 (100) [Cu^{II}Br(L$^{PyC_{10}}$)]⁺; elemental analysis calcd (%) for $C_{16}H_{28}Cl_2CuN_2$: C 40.73, H 5.98, N 5.94; found: C 41.02, H 5.80, N 4.56.

Acknowledgements

[1] a) R. A. Wassel, C. B. Gorman, *Angew. Chem.* **2004**, *116*, 5230; *Angew. Chem. Int. Ed.* **2004**, *43*, 5120; b) A. Dei, D. Gatteschi, C. Sangregorio, L. Sorace, *Acc. Chem. Res.* **2004**, *37*, 827; c) C. Joachim, J. K. Gimzewski, A. Aviram, *Nature* **2000**, *408*, 541.

[2] T. Govindaraju, P. J. Bertics, R. T. Raines, N. L. Abbott, *J. Am. Chem. Soc.* **2007**, *129*, 11223.

[3] D. R. Talham, *Chem. Rev.* **2004**, *104*, 5479.

[4] J. Park, A. N. Pasupathy, J. I. Goldsmith, C. Chang, Y. Yaish, J. R. Petta, M. Rinkoski, J. P. Sethna, H. D. Abruna, P. L. McEuen, D. C. Ralph, *Nature* **2002**, *417*, 722.

[5] a) J. Zhang, B. W.-K. Chu, N. Zhu, V. W.-W. Yam, *Organometallics* **2007**, *26*, 5423; b) V. W.-W. Yam, B. Li, Y. Yang, B. W.-K. Chu, K. M.-C. Wong, K.-K. Cheung, *Eur. J. Inorg. Chem.* **2003**, 4035; c) B. W.-K. Chu, V. W.-W. Yam, *Inorg. Chem.* **2001**, *40*, 3324.

[6] L. Boubekeur-Lecaque, B. J. Coe, K. Clays, S. Foerier, T. Verbiest, I. Asselberghs, *J. Am. Chem. Soc.* **2008**, *130*, 3286.

[7] K. Binnemans, Y. G. Galyametdinov, R. Van Deun, D. W. Bruce, S. R. Collinson, A. P. Polishchuk, I. Bikchantaev, W. Haase, A. V. Prosvirin, L. Tinchurina, I. Litvinov, A. Gubajdullin, A. Rakhmatullin, K. Uytterhoeven, L. Van Meervelt, *J. Am. Chem. Soc.* **2000**, *122*, 4335.

[8] J. B. Beck, S. J. Rowan, *J. Am. Chem. Soc.* **2003**, *125*, 13922.

[9] K. Binnemans, K. Lodewyckx, B. Donnio, D. Guillon, *Chem. Eur. J.* **2002**, *8*, 1101.

[10] a) P. C. Griffiths, I. A. Fallis, T. Chuenpratoom, R. Watanesk, *Adv. Colloid Interface Sci.* **2006**, *122*, 107; b) P. C. Griffiths, I. A. Fallis, D. J. Willock, A. Paul, C. L. Barrie, P. M. Griffiths, G. M. Williams, S. M. King, R. K. Heenan, R. Goergl, *Chem. Eur. J.* **2004**, *10*, 2022.

[11] I. Yildiz, J. Mukherjee, M. Tomasulo, F. M. Raymo, *Adv. Func. Mater.* **2007**, *17*, 814.

[12] a) J. W. Ciszek, Z. K. Keane, L. Cheng, M. P. Stewart, L. H. Yu, D. Natelson, J. M. Tour, *J. Am. Chem. Soc.* **2006**, *128*, 3179; b) J. M. Tour, *Acc. Chem. Res.* **2000**, *33*, 791.

[13] L. Kosbar, C. Srinivasan, A. Afzali, T. Graham, M. Copel, L. Krusin-Elbaum, *Langmuir* **2006**, *22*, 7631.

[14] For examples, see: a) M. C. Petty, *Langmuir–Blodgett Films: An Introduction*, Cambridge University Press, NY (USA), **1996**; b) R. H. Tredgold, *Order in Thin Organic Films*, Cambridge University Press, NY (USA), **1994**.

[15] X. Chen, S. Lenhert, M. Hirtz, N. Lu, H. Fuchs, L. Chi, *Acc. Chem. Res.* **2007**, *40*, 393.

[16] N. Nandi, D. Vollhardt, *Acc. Chem. Res.* **2007**, *40*, 351.

[17] A. Flores, P. Ize, S. Ramos, R. Castillo, *J. Chem. Phys.* **2003**, *119*, 5644.

[18] a) T. J. Joncheray, K. M. Denoncourt, C. Mathieu, M. A. R. Meier, U. S. Schubert, R. S. Duran, *Langmuir* **2006**, *22*, 9264; b) S. Peleshanko, J. Jeong, R. Gunawidjaja, V. V. Tsukruk, *Macromolecules* **2004**, *37*, 6511.

[19] I. Bury, B. Donnio, J.-L. Gallani, D. Guillon, *Langmuir* **2007**, *23*, 619.

[20] D. Hoenig, D. Moebius, *J. Phys. Chem.* **1991**, *95*, 4590.

[21] S. Hénon, J. Meunier, *Rev. Sci. Instrum.* **1991**, *62*, 936.

[22] C. M. Knobler, *Advances in Chemical Physics, Vol. 77*, (Eds.: I. Prigogine, S. A. Rice), Wiley, NY (USA), **1990**, p. 397.

[23] For examples, see: a) F. W. Vergeer, X. Chen, F. Lafolet, L. De Cola, H. Fuchs, L. Chi, *Adv. Funct. Mater.* **2006**, *16*, 625; b) P. Lehmann, C. Symietz, G. Brezesinski, H. Kra, D. G. Kurth, *Langmuir* **2005**, *21*, 5901; c) S. Di Bella, S. Sortino, S. Conoci, S. Petralia, S. Casilli, L. Valli, *Inorg. Chem.* **2004**, *43*, 5368; d) K. Wang, M.-A. Haga, M. D. Hossain, H. Shindo, K. Hasebe, H. Monjushiro, *Langmuir* **2002**, *18*, 3528.

[24] For earlier work on isolated and characterized metallosurfactants, see: D. A. Jaeger, M. F. Peacock, D. S. Bohle, *Langmuir* **2003**, *19*, 4859, and references [3] and [4] therein.

[25] R. Shakya, C. Imbert, H. P. Hratchian, M. Lanznaster, M. J. Heeg, B. R. McGarvey, M. Allard, H. B. Schlegel, C. N. Verani, *Dalton Trans.* **2006**, 2517.

[26] C. Imbert, H. P. Hratchian, M. Lanznaster, M. J. Heeg, L. M. Hryhorczuk, B. R. McGarvey, H. B. Schlegel, C. N. Verani, *Inorg. Chem.* **2005**, *44*, 7414.

[27] R. Shakya, S. S. Hindo, L. Wu, S. Ni, M. Allard, M. J. Heeg, S. R. P. da Rocha, G. T. Yee, H. P. Hratchian, C. N. Verani, *Chem. Eur. J.* **2007**, *13*, 9948.

[28] R. Shakya, S. S. Hindo, L. Wu, M. M. Allard, M. J. Heeg, H. P. Hratchian, B. R. McGarvey, S. R. P. da Rocha, C. N. Verani, *Inorg. Chem.* **2007**, *46*, 9808.

[29] S. S. Hindo, R. Shakya, N. S. Rannulu, M. M. Allard, M. J. Heeg, M. T. Rodgers, S. R. P. da Rocha, C. N. Verani, *Inorg. Chem.* **2008**, *47*, 3119.

[30] K. Nakamoto, *Infrared and Raman Spectra of Inorganic and Coordination Compounds*, 5th ed., Wiley, NY (USA), **1997**.

[31] M. Lanznaster, M. J. Heeg, G. T. Yee, B. R. McGarvey, C. N. Verani, *Inorg. Chem.* **2007**, *46*, 72.

[32] N. M. Villeneuve, R. R. Schroeder, L. A. Ochrymowycz, D. B. Rorabacher, *Inorg. Chem.* **1997**, *36*, 4475.

[33] R. Karmakar, C. R. Choudhury, D. L. Hughes, G. P. A. Yap, M. S. El Fallah, C. Desplanches, J.-P. Sutter, S. Mitra, *Inorg. Chim. Acta* **2006**, *359*, 1184.

[34] H. Nagao, N. Komeda, M. Mukaida, M. Suzuki, K. Tanaka, *Inorg. Chem.* **1996**, *35*, 6809.

[35] K. W. Pollak, J. W. Leon, J. M. J. Frechet, M. Maskus, H. D. Abruna, *Chem. Mater.* **1998**, *10*, 30.

[36] F. Barriere, W. E. Geiger, *J. Am. Chem. Soc.* **2006**, *128*, 3980.

[37] D. B. Rorabacher, *Chem. Rev.* **2004**, *104*, 651.

[38] M. Elleb, J. Meullemeestre, M. J. Schwing-Weill, F. Vierling, *Inorg. Chem.* **1980**, *19*, 2699.

[39] J. Foley, S. Tyagi, B. J. Hathaway, *J. Chem. Soc. Dalton Trans.* **1984**, 1.

[40] J. B. Peng, G. T. Barnes, I. R. Gentle, *Adv. Colloid Interface Sci.* **2001**, *91*, 163.

[41] S. Kraus, D. Mandler, *Langmuir* **2006**, *22*, 7462.

[42] A. Gericke, A. V. Michailov, H. Huehnerfuss, *Vib. Spectrosc.* **1993**, *4*, 335.

[43] J. Galvan-Miyoshi, S. Ramos, J. Ruiz-Garcia, R. Castillo, *J. Chem. Phys.* **2001**, *115*, 8178.

[44] A. Flores, E. Corvera-Poire, C. Garza, R. Castillo, *J. Phys. Chem. B* **2006**, *110*, 4824.

[45] G. Weidemann, D. Vollhardt, *Thin Solid Films* **1995**, *264*, 94.

[46] G. Gabrielli, G. Caminati, M. Puggelli, *Adv. Colloid Interface Sci.* **2000**, *87*, 75.

[47] U. Gehlert, D. Vollhardt, *Langmuir* **1997**, *13*, 277.

[48] A. Gopal, K. Y. C. Lee, *J. Phys. Chem. B* **2001**, *105*, 10348.

[49] T. Albright, J. K. Burdett, M.-H. Whangbo, *Orbital Interactions in Chemistry*, Wiley, NY (USA), **1985**.

[50] a) Reference [14a], p. 72; b) D. Möbius, *Ber. Bunsenges. Phys. Chem.* **1978**, *82*, 848.

[51] R. R. Gagne, C. A. Koval, G. C. Lisensky, *Inorg. Chem.* **1980**, *19*, 2854.

[52] *APEX II, SMART, SAINT*, and *SADABS*, Bruker AXS, Madison WI, USA, **2004**.

[53] G. Sheldrick, *Acta Cryst* **2008**, A64, 112.

[54] A. Gopal, V. A. Belyi, H. Diamant, T. A. Witten, K. Y. C. Lee, *Los Alamos Natl. Lab., Prepr. Arch., Condens. Matter* **2004**, arXiv:cond-mat/0409147.

[55] a) A. D. Becke, *Phys. Rev. A* **1988**, *38*, 3098; b) A. D. Becke, *J. Chem. Phys.* **1993**, *98*, 5648; c) T. Lee, W. T. Yang, R. G. Parr, *Phys. Rev.* **1988**, *B37*, 785; d) R. Ditchfield, W. R. Hehre, J. A. Pople, *J. Chem. Phys.* **1971**, *54*, 724; e) M. S. Gordon, *Chem. Phys. Lett.* **1980**, *76*, 163; f) P. C. Hariharan, J. A. Pople, *Theo. Chim. Acta* **1973**, *28*, 213; g) P. C. Hariharan, J. A. Pople, *Mol. Phys.* **1974**, *27*, 209; h) W. R. Hehre, R. Ditchfield, J. A. Pople, *J. Chem. Phys.* **1972**, *56*, 225.

[56] Gaussian 03, Revision D.01, M. J. Frisch, G. W. Trucks, H. B. Schlegel, G. E. Scuseria, M. A. Robb, J. R. Cheeseman, J. A. Montgomery, Jr., T. Vreven, K. N. Kudin, J. C. Burant, J. M. Millam, S. S. Iyengar, J. Tomasi, V. Barone, B. Mennucci, M. Cossi, G. Scalmani, N. Rega, G. A. Petersson, H. Nakatsuji, M. Hada, M. Ehara, K. Toyota, R. Fukuda, J. Hasegawa, M. Ishida, T. Nakajima, Y. Honda, O. Kitao, H. Nakai, M. Klene, X. Li, J. E. Knox, H. P. Hratchian, J. B. Cross, V. Bakken, C. Adamo, J. Jaramillo, R. Gomperts, R. E. Stratmann, O. Yazyev, A. J. Austin, R. Cammi, C. Pomelli, J. W. Ochterski, P. Y. Ayala, K. Morokuma, G. A. Voth, P. Salvador, J. J. Dannenberg, V. G. Zakrzewski, S. Dapprich, A. D. Daniels, M. C. Strain, O. Farkas, D. K. Malick, A. D. Rabuck, K. Raghavachari, J. B. Foresman, J. V. Ortiz, Q. Cui, A. G. Baboul, S. Clifford, J. Cioslowski, B. B. Stefanov, G. Liu, A. Liashenko, P. Piskorz, I. Komaromi, R. L. Martin, D. J. Fox, T. Keith, M. A. Al-Laham, C. Y. Peng, A. Nanayakkara, M. Challacombe, P. M. W. Gill, B. Johnson, W. Chen, M. W. Wong, C. Gonzalez, J. A. Pople, Gaussian, Inc., Wallingford CT, **2004**.

[57] H. B. Schlegel, *J. Comput. Chem.* **1982**, *3*, 214.

Appendix G

Cu Salycilaldimine Soft Material

Sarmad Sahiel Hindo, Rajendra Shakya, N. S. Rannulu, Marco M. Allard, Mary Jane Heeg, M. T. Rodgers, Sandro R. P. da Rocha and Claudio N. Verani

"Synthesis, Redox, and Amphiphilic Properties of Responsive Salycilaldimine-Copper(II) Soft Materials."

My contribution to this work consisted of the electronic structure calculations.

Synthesis, Redox, and Amphiphilic Properties of Responsive Salycilaldimine-Copper(II) Soft Materials

Sarmad Sahiel Hindo,[†] Rajendra Shakya,[†] N. S. Rannulu,[†] Marco M. Allard,[†] Mary Jane Heeg,[†] M. T. Rodgers,[†] Sandro R. P. da Rocha,[‡] and Claudio N. Verani*,[†]

Department of Chemistry and Department of Chemical Engineering, Wayne State University, Detroit, Michigan 48202

Hydrolysis of the asymmetric pyridine- and phenol-containing ligand HL[1] (2-hydroxy-4-6-di-*tert*-butylbenzyl-2-pyridylmethyl)imine) led to the use of bis-(3,5-di-*tert*-butyl-2-phenolato-benzaldehyde)copper(II), [$Cu^{II}(L^{SAL})_2$] (**1**) as a precursor for bis-(2,4-di-*tert*-butyl-6-octadecyliminomethyl-phenolato)copper(II), [$Cu^{II}(L^2)_2$] (**3**), bis-(2,4-di-*tert*-butyl-6-octadecyl aminomethyl-phenolato)copper(II), [$Cu^{II}(L^{2A})_2$] (**3′**), and bis-(2,4-di-*tert*-butyl-6-[(3,4,5-tris-dodecyloxy-phenylimino)-methyl]-phenolato)copper(II), [$Cu^{II}(L^3)_2$] (**4**). These complexes exhibit hydrophilic copper-containing head groups, hydrophobic alkyl and alkoxo tails, and present potential as precursors for redox-responsive Langmuir–Blodgett films. All systems were characterized by means of elemental, spectrometric, spectroscopic, and electrochemical techniques, and their amphiphilic properties were probed by means of compression isotherms and Brewster angle microscopy. Good redox activity was observed for **3** with two phenoxyl radical processes between 0.5 and 0.8 V vs Fc^+/Fc, but this complex lacks amphiphilic behavior. To attain good balance between redox response and amphiphilicity, increased core flexibility in **3′** and incorporation of alkoxy chains in **4** were attempted. Film formation with collapse at 14 mN·m^{-1} was observed for the alkoxy-derivative but redox-response was seriously compromised. Core flexibility improved Langmuir film formation with a higher formal collapse and showed excellent cyclability of the ligand-based processes.

Introduction

Metal-containing soft materials merge the intrinsic properties of transition metals with those of functional organic scaffolds to build up organized architectures.[1,2] The relevance of such materials to the growing field of molecular electronics[3] is increasing considerably because it has been demonstrated that self-assembled films of triple-decker porphyrin-lanthanide precursors can be used for information storage.[4] In spite of the large footprint, these systems use multiple oxidations for writing of information, whereas the subsequent reductions are used for reading of stored data.[5]

Consequently, impending relevance can be envisioned for organized stimulus-responsive Langmuir–Blodgett films composed of monometallic precursors that present multiple redox states and smaller footprints. The stabilization of organic radicals in such precursors will play a vital role in attaining

* To whom correspondence should be addressed. E-mail: cnverani@chem.wayne.edu. Phone: 313 577 1076. Fax: 313 577 8022.
† Department of Chemistry.
‡ Department of Chemical Engineering.
(1) (a) Bowers, J.; Amos, K. E.; Bruce, D. W.; Heenan, R. K. *Langmuir* **2005**, *21*, 5696. (b) Talham, D. R. *Chem. Rev.,* **2004**, *104*, 5479. (c) Griffiths, P. C.; Fallis, I. A.; Willock, D. J.; Paul, A.; Barrie, C. L.; Griffiths, P. M.; Williams, G. M.; King, S. M.; Heenan, R. K.; Görgl, R. *Chem.—Eur. J.* **2004**, *10*, 2022. (d) Rueff, J. M.; Masciocchi, N.; Rabu, P.; Sironi, A.; Skoulios, A. *Eur. J. Inorg. Chem.* **2001**, 2843.
(2) (a) Terazzi, E.; Suarez, S.; Torelli, S.; Nozary, H.; Imbert, D.; Mamula, O.; Rivera, J.-P.; Guillet, E.; Bénech, J.-M.; Bernardinelli, G.; Scopelliti, R.; Donnio, B.; Guillon, D.; Bünzli, J.-C.; Piguet, C. *Adv. Funct. Mater.* **2006**, *16*, 157. (b) Serrano, J. L.; Sierra, T. *Coord. Chem. Rev.* **2003**, *242*, 73. (c) Donnio, B. *Curr. Opin. Colloid Interface Sci.* **2002**, *07*, 371.
(3) (a) Low, P. J. *Dalton Trans.* **2005**, 2821. , and references therein. (b) Joachin, C.; Gimzewski, J. K.; Aviran, A. *Nature* **2000**, *408*, 541. (c) Dei, A.; Gatteschi, D.; Sangregorio, C.; Sorace, L. *Acc. Chem. Res.* **2004**, *37*, 827. (d) Kahn, O.; Martinez, C. J. *Science* **1998**, *279*, 44. (e) Verdaguer, M. *Science* **1996**, *272*, 698.
(4) Liu, Z.; Yasseri, A. A.; Lindsey, J. S.; Bocian, D. F. *Science* **2003**, *302*, 1543.
(5) (a) Padmaja, K; Youngblood, W. J.; Wei, L.; Bocian, D. F.; Lindsey, J. S. *Inorg. Chem.* **2006**, *45*, 5479. (b) Roth, K. M.; Dontha, N.; Dabke, R. B.; Gryko, D. T.; Clausen, C.; Lindsey, J. S.; Bocian, D. F.; Kuhr, W. G. *J. Vac. Sci. Technol.* **2000**, *18B*, 2359.
(6) (a) Lanznaster, M.; Hratchian, H. P.; Heeg, M. J.; Hryhorczuk, L. M.; McGarvey, B. R.; Schlegel, H. B.; Verani, C. N. *Inorg. Chem.* **2006**, *45*, 955. (b) Lanznaster, M.; Heeg, M. J.; Yee, G. T.; McGarvey, B. R.; Verani, C. N. *Inorg. Chem.* **2007**, *46*, 72.

redox states beyond those expected for the metallic ion. Ligands based on *tert*-butyl substituted phenolates[6,7] ensure the required phenolate/phenoxyl bistability[8] needed to render their complexes as viable prototypical molecular switches that enable multiple read/write cycles.

Copper(II) salicylaldehydes have been used as synthetic precursors in the self-assembly of catalysts,[9,10] in smectic mesogens to avoid bimetallic cores,[11] as well as in modified electrodes.[12] The seminal work of Nagel et al.,[13] entailing the condensation of hexadecylamine with 4-hydroxysalicy-laldehyde applied this concept to metallosurfactants while pointing to the importance of polar substituents attached to the headgroup to achieve organized monolayers. Therefore, the main challenge in the development of precursors based on *tert*-butyl substituted phenolates is the fact that while these groups can enhance the redox properties, their bulkiness and apolar nature may compromise the amphiphilic behavior of the resulting materials.

We have developed and studied iron(III)- and cobalt(II/III)-containing soft materials based on the asymmetric pyridine and phenol pendant-arms ligand HL^1, depicted in its deprotonated form in Scheme 1.[14] Owing to this interest, the synthesis and characterization of copper(II) complexes was attempted, but ligand hydrolysis yielded [Cu^{II}(L^{SAL})$_2$] (**1**) where L^{SAL-} is the deprotonated 2,4-*tert*-butylsalycilal-dehyde as the main product and [(L^{SAL})$_2$Cu^{II}$_2$(μ-OCH$_3$)$_2$] (**5**) as a minor component. Because free copper(II) ions mediate ligand hydrolysis,[15] **1** was used as a precursor for the formation of [Cu^{II}(L^1)$_2$] (**2**), as well as for the metallosur-factants [Cu^{II}(L^2)$_2$] (**3**) and [Cu^{II}(L^3)$_2$] (**4**). Complex **3** allows for in situ reduction yielding the equivalent and more flexible amine complex [Cu^{II}(L^{2A})$_2$] (**3'**). Species **3**, **3'**, and **4** are candidates as amphiphilic precursors for redox-responsive Langmuir–Blodgett films. This paper describes the delicate

(7) (a) Philibert, A.; Thomas, F.; Philouze, C.; Hamman, S.; Saint-Aman, E.; Pierre, J. L. *Chem.—Eur. J.* **2003**, *09*, 3803. (b) Thomas, F.; Gellon, G.; Gautier-Luneau, I.; Saint-Aman, E.; Pierre, J.-L. *Angew. Chem., Int. Ed.* **2002**, *41*, 3047. (c) Shimazaki, Y.; Huth, S.; Odani, A.; Yamauchi, O. *Angew. Chem., Int. Ed.* **2000**, *39*, 1666. (d) Jazdzewski, B. A.; Tolman, W. B. *Coord. Chem. Rev.* **2000**, *200*(202), 633. (f) Hockertz, J.; Steenken, S.; Wieghardt, K.; Hildebrandt, P. *J. Am. Chem. Soc.,* **1993**, *115*, 11222.
(8) (a) Marchivie, M.; Guionneau, P.; Howard, J.; Chastanet, G.; Letard, J.-F.; Goeta, A.; Chasseau, D. *J. Am. Chem. Soc.* **2002**, *124*, 194. (b) Pease, A. R.; Jeppesen, J. O.; Stoddart, J. F.; Luo, Y.; Collier, C. P.; Heath, J. R. *Acc. Chem. Res.* **2001**, *34*, 433. (c) Fabbrizzi, L.; Licchelli, M.; Pallavicini, P. *Acc. Chem. Res.* **1999**, *32*, 846.
(9) Murphy, E. F.; Schmid, L.; Bürgi, T.; Maciejewski, M.; Baiker, A. *Chem. Mater.* **2001**, *13*, 1296.
(10) Murphy, E. F.; Ferri, D.; Baiker, A. *Inorg. Chem.* **2003**, *42*, 2559.
(11) Paschke, R.; Liebsch, S.; Tschierske, C.; Oakley, M. A.; Sinn, E. *Inorg. Chem.* **2003**, *42*, 8230.
(12) Shervedani, R. K.; Mozaffari, S. A. *Anal. Chem.* **2006**, *78*, 4957.
(13) Nagel, J.; Oertel, U.; Friedel, P.; Komber, H.; Möbius, D. *Langmuir* **1997**, *13*, 4693.
(14) (a) Shakya, R.; Hindo, S. S.; Wu, L.; Allard, M.; Heeg, M. J.; Hratchian, H. P.; McGarvey, B. R.; da Rocha, S.; Verani, C. N. *Inorg. Chem.* **2007**, *46*, 9808. (b) Shakya, R.; Imbert, C.; Hratchian, H. P.; Lanznaster, M.; Heeg, M. J.; McGarvey, B. R.; Allard, M.; Schlegel, H. B.; Verani, C. N. *Dalton Trans.* **2006**, 2517. (c) Imbert, C.; Hratchian, H. P.; Lanznaster, M.; Heeg, M. J.; Hryhorczuk, L. M.; McGarvey, B. R.; Schlegel, H. B.; Verani, C. N. *Inorg. Chem.* **2005**, *44*, 7414.
(15) (a) Eichhorn, G. L.; Bailar, J. C., Jr. *J. Am. Chem. Soc.,* **1953**, *75*, 2905. (b) Eichhorn, G. L.; Marchand, N. D. *J. Am. Chem. Soc.,* **1956**, *78*, 2688.

Scheme 1. Complexes and Their *tert*-Butyl Substituted Ligands

The Complexes:

[Cu^{II}(L^{SAL})$_2$]	(**1**)	[Cu^{II}(L^{2A})$_2$]	(**3'**)
[Cu^{II}(L^1)$_2$]	(**2**)	[Cu^{II}(L^3)$_2$]	(**4**)
[Cu^{II}(L^2)$_2$]	(**3**)	[(L^{SAL})$_2$Cu^{II}$_2$(μOCH$_3$)$_2$]	(**5**)

The Ligands:

(L^1)$^-$ (L^2)$^-$ (L^{2A})$^-$ (L^3)$^-$
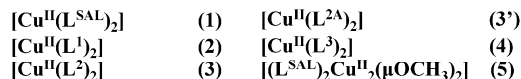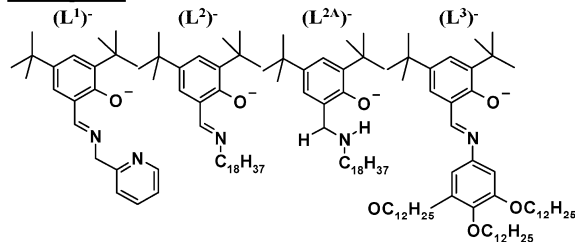
balance between redox and amphiphilic behavior observed in these species and offers a rationale for improving these properties, the advantages, and the limitations of this approach. These findings are expected to have a positive impact in the future design of responsive films.

Results and Discussion

Ligand Hydrolysis. Treatment of HL^1 with hydrated copper(II) perchlorate in methanol produced [Cu^{II}(L^1)$_2$] (**2**) in poor yields. The electrospray ionization (ESI) mass spectrum (positive ion mode) of the isolated compound presented *m/z* = 710 for [**2** + H$^+$]$^+$. However, the spectrum of the reaction mixture contained peaks at *m/z* = 530 and 655 suggesting the presence of additional products along with **2**. In wet methanol, the peak at *m/z* = 530 became dominant and was identified as related to the main hydrolysis product [Cu^{II}(L^{SAL})$_2$] (**1**) as [**1** + H$^+$]$^+$. Slow evaporation of the solvent yielded a few crystals of [(L^{SAL})$_2$Cu^{II}$_2$(μCH$_3$O)$_2$] (**5**) that presented *m/z* = 655 for [**5** + H$^+$]$^+$. Infrared spectros-copy of the isolated solids revealed strong peaks at 1619 and 1424 cm^{-1}, attributed to the stretching and bending modes of carbonyl groups, respectively. Precursor **1** was later obtained synthetically in gram amounts and yielded X-ray quality crystals.

X-ray Structures. Both **1** and **5** were analyzed by single crystal diffraction methods and their molecular structures are displayed in Figure 1. Complex **1** shows two deprotonated ligands coordinated to a copper(II) center in a square-planar environment where the O—Cu—O angles deviate slightly from the expected 90.0°. The ligands are positioned trans to one another, and the molecule adopts an approximate D_{2h} local symmetry. The bond lengths of the Cu—O$_4$ coordination sphere are in good agreement with similar species reported in the literature,[16] where the Cu—O$_{carbonyl}$ bonds are longer than the Cu—O$_{phenolate}$ bonds. The entire molecule minus the *tert*-butyl substituents is planar (mean deviation 0.02 Å). There are no close axial contacts nor ligands to Cu and no

(16) (a) Lin, Z.-D.; Zang, W. *Acta Crystallogr.* **2006**, *E62*, 1074. (b) Sun, Y.-X.; Gao, G.-Z. *Acta Crystallogr.* **2005**, *E61*, 354. (c) Ali, H. M.; Abdul Halim, S. N.; Ng, S. W. *Acta Crystallogr.* **2005**, *E61*, 1429. (d) Elmali, A.; Elerman, Y.; Svoboda, I.; Fuess, H. *Z. Kristallogr.* **1995**, *210*, 612.
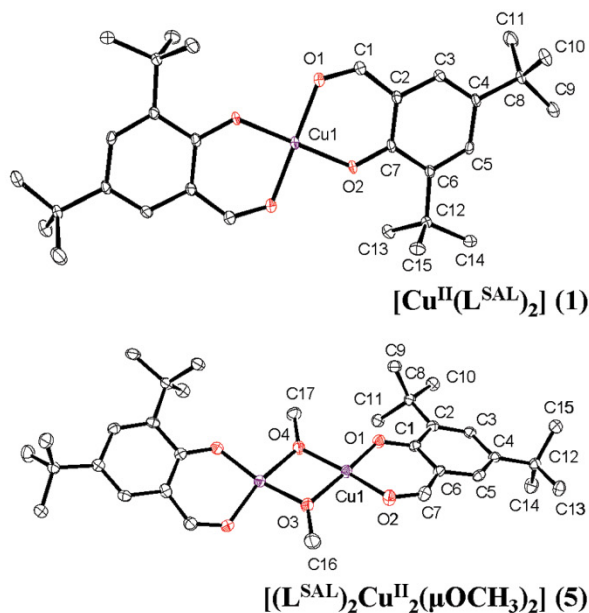
$[Cu^{II}(L^{SAL})_2]$ (1)

$[(L^{SAL})_2Cu^{II}_2(\mu OCH_3)_2]$ (5)

Figure 1. ORTEP diagrams for **1** and **5**. Selected bond lengths (Å) and angles (°) for **1**: Cu(1)−O(2) = 1.876; Cu(1)−O(1) = 1.952; C(1)−O(1) = 1.254; C(7)−O(2) = 1.305, O(2)−Cu(1)−O(2) = 180.00; O(1)−Cu(1)−O(1) = 180.00; O(2)−Cu(1)−O(1) = 92.83; O(2)−Cu(1)−O(1) = 87.17. For **5**: Cu(1)−Cu(1) = 2.996; Cu(1)−O(1) = 1.894; Cu(1)−O(3) = 1.895; Cu(1)−O(4) = 1.914; Cu(1)−O(2) = 1.933; C(1)−O(1) = 1.301; C(7)−O(2) = 1.253; Cu(1)−O(4)−Cu(1) = 103.02; O(3)−Cu(1)−O(4) = 76.25; O(1)−Cu(1)−O(3) = 167.51; O(4)−Cu(1)−O(2) = 166.41; O(1)−Cu(1)−O(4) = 96.80; O(1)−Cu(1)−O(2) = 94.40; O(3)−Cu(1)−O(2) = 94.03.

ring stacking nor counterions are present. The binuclear complex **5** shows two copper(II) ions doubly bridged by two deprotonated methoxide groups. Each copper center is also coordinated to a 3,5-di-*tert*-butyl-2-hydroxybenzaldehyde ligand in distorted square planar geometries. Interestingly, the molecule presents idealized C_{2v} symmetry with the two ligands positioned cis to one another, thus suggesting that dimer formation may precede hydrolysis. Bond lengths and angles are in good agreement with similar structures.[17] Because few crystals of this dimer were generated, no further investigations were carried out.

Syntheses. The formation of **1** as the main product of imine hydrolysis has driven a series of reactivity studies in which several amine-containing substrates were tested. When **1** was treated with 2-aminomethylpyridine, the initially targeted **2** was obtained, as indicated by the peak at m/z = 710 in the ESI mass spectrum corresponding to $[2 + H^+]^+$ with the proper isotopic distribution. When 2-aminomethylpyridine was replaced by 1-octadecylamine and 1,2,3-tris(dodecyloxy)-5-methylbenzene, the amphiphiles **3** and **4** were obtained as shown in Scheme 2. These species were isolated and carefully investigated by several spectroscopic methods. The most remarkable feature in the infrared spectrum of **1** is associated with the stretch of the carbonyl groups ($\nu_{C=O}$) at 1619 cm^{-1}. This peak disappears for **2**, **3**, and **4** and a new peak is observed around 1588 cm^{-1} for the

Scheme 2. Structures for **3**, **3′**, and **4** and Their ESI(Pos) Peak Clusters for $[M + H^+]^+$ [a]
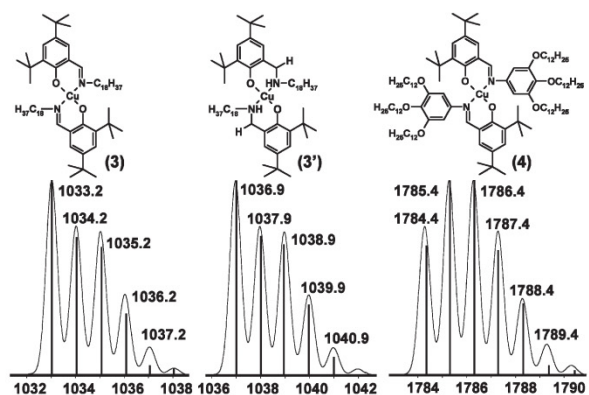
[a] The relative abundance axis of each complex is omitted for clarity.

C=N stretch of imine groups. The absence of strong peaks around 1090 cm^{-1} for all isolated complexes indicates lack of perchlorate counterions and supports the presence of two coordinated phenolates in a neutral molecule. To test the effect of a decreased framework rigidity, reduction of the imine −C=N− bonds was attempted by treating **3** and **4** with sodium borohydride and aiming at the equivalent but more flexible amine −HC−NH− counterparts. These attempts failed for **4** but worked well for the octadecylamine-substituted ligand in **3** converting it to **3′** in quantitave yields. The identity of the compound was confirmed by infrared spectroscopy and mass spectrometry: disappearance of the C=N stretch peak along with a corresponding 4 mass-unit increase, related to the addition of two hydrogen atoms per ligand, was observed. The elemental analyses of **3**, **3′**, and **4** are in excellent agreement with these formulations. block

Electronic Spectra. The electronic spectra of **1**, **3**, and **4** were measured in dichloromethane as a characterization tool for the new amphiphiles. Figure 2 displays intense bands observed in the ultraviolet and early visible range, whereas much less intense d−d bands (not shown) are observed between 600 and 1000 nm. The bands around 250–280 and 310–325 nm are attributed to intraligand $\sigma \rightarrow \pi^*$ and/or $\pi \rightarrow \pi^*$ transitions. The nature of the bands in the 380–420 nm range has been previously assigned to intraligand processes, metal-to-ligand, and ligand-to-metal charge transfers.[18–21] These bands are assigned as having a predominant ligand-to-metal charge transfer character. The presence of $N_{imine} \rightarrow Cu^{II}$ and $O_{phenolate} \rightarrow Cu^{II}$ charge transfers is suggested because of the presence of high extinction coefficients.

(17) Wrobleski, D. A; Rauchfuss, T. B.; Rheingold, A. L.; Lewis, K. A. *Inorg. Chem.* **1984**, *23*, 3124.

(18) (a) Rigamonti, L.; Demartin, F.; Forni, A.; Righetto, S.; Pasini, A. *Inorg. Chem.* **2006**, *45*, 10976. (b) Iglesias, A. L.; Aguirre, G.; Somanathan, R.; Parra-Hake, M. *Polyhedron* **2004**, *23*, 3051.
(19) (a) Kasumov, V. T.; Koeksal, F.; Sezer, A. *Polyhedron* **2005**, *24*, 1203. (b) Kuzniarska-Biernacka, I.; Kurzak, K.; Kurzak, B.; Jezierska, J. *J. Sol. Chem.* **2003**, *32*, 719. (c) Losada, J.; del Peso, I.; Beyer, L. *Inorg. Chim. Acta* **2001**, *321*, 107. (d) Kurzak, K.; Kuzniarska-Biernacka, I.; Kurzak, B.; Jezierska, J. *J. Sol. Chem.* **2001**, *30*, 709.
(20) (a) Bill, E.; Müller, J.; Weyhermüller, T.; Wieghardt, K. *Inorg. Chem.* **1999**, *38*, 5795. (b) Auerbach, U.; Eckert, U.; Wieghardt, K.; Nuber, B.; Weiss, J. *Inorg. Chem.* **1990**, *29*, 938.
(21) (a) Jazdzewski, B. A.; Holland, P. L.; Pink, M.; Young, V. G., Jr.; Spencer, D. J. E.; Tolman, W. B. *Inorg. Chem.* **2001**, *40*, 6097.
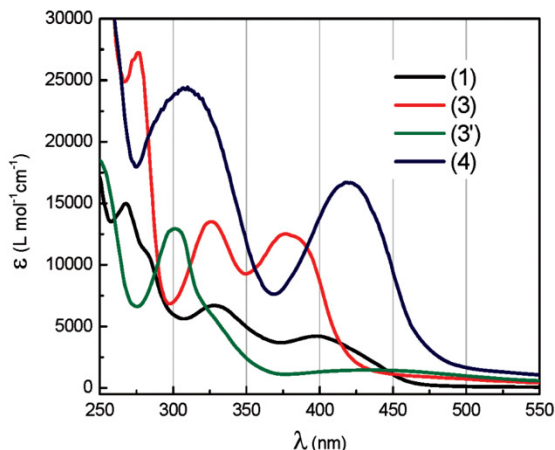
Figure 2. UV–visible spectra for **1**, **3**, **3′**, and **4** in 1.0×10^{-4} M dichloromethane solutions. λ_{max}, nm (ε, L·mol^{-1}·cm^{-1}) for **1**: 282 (15,600), 325 (9500), 403 (7700); for **3** 276 (27,200), 325 (13,300), 380 (12,500); for **3′** 229 (18,300), 301 (13,100), 330sh ($\sim$4000), 448 (1900); for **4** 250 ($\sim$39,000), 310 (24,500), 420 (16,700). The d−d bands are found at 692 (170) for **1**, 662 (260) for **3**, 680 (280) for **3′**, and 725 (350) for **4**.

The position of this band in **3** is in good agreement with other alkyl-substituted ligands in similar solvents,[22] but its intensity is considerably decreased in **3′** where the aldimine chromophore has been reduced. Also noteworthy is the fact that when comparing **1** and **3**, a hypsochromic (blue) shift of $\sim$20 nm is observed, but comparison between **1** and **4** reveals a $\sim$20 nm bathochromic (red) shift. Because all of these species have tertiary butyl groups attached to the second and fourth positions of the phenolate rings, the nature of the groups in the sixth position must be considered, namely carbaldehyde for **1**, octadecyliminomethyl for **3** and **3′**, and tris(dodecyloxy)phenyl-iminomethyl for **4**. Assuming some degree of distortion from square planar to tetrahedral[23] in **3** and **4**, the hypsochromic effect is attributed to the free motion of these alkyl groups that leads to distortions on the iminomethyl moiety diminishing the extent of the π-delocalization. The bulky nature of the phenyl groups in **4**, as well as the presence of the trialkoxy auxochromes, is suggested to stabilize π-delocalization.

Redox Properties. Cyclic voltammograms in dichloromethane solutions of **1**, **3**, **3′**, and **4** were measured to assess the redox potentials of ligand-centered processes. All potentials are reported at 100 mV·s^{-1} and versus the Fc$^+$/Fc couple, unless noted otherwise. A study was also performed to evaluate the reversibility of the phenolate/phenoxyl couples in **3** and **3′** by cycling 50 times through the wave associated with the first and second ligand-centered process. This cycling is intended to simulate switching mechanisms that will play a key role in responsive films. These results are shown in Figure 3. For all compounds the metal-centered reduction is observed between -1.60 and -1.80 V, whereas the oxidation appears around -0.90 and -1.20 V. All processes are irreversible with peak separations (ΔEp)
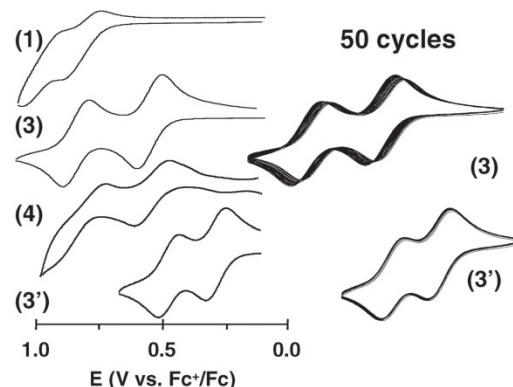
Figure 3. Cyclic voltammetry of 1.0×10^{-3} M CH$_2$Cl$_2$ solutions of **1**, **3**, **3′**, and **4**: First and second ligand-centered processes at 0.82 and 0.98 for **1**; 0.54 and 0.83 for **3**; 0.29 and 0.48 for **3′**; and 0.53 and 0.80 V vs Fc$^+$/Fc for **4**. The amplitude of the current for each compound is omitted for clarity.

reaching up to 0.50 V. This is not unexpected for the Cu(II)/Cu(I) couple because of the considerable geometrical reorganization and charge balance involved in the process. A preferred tetrahedral geometry for the reduced ion is anticipated, and the presence of two phenolate ligands confer a negatively charged core. Because the 3d^{10} configuration of Cu(I) increases lability, one of the phenolate ligands might have its bond weakened or broken to decrease the electronic density around the metal.[6b,24,25] If metal reduction is prevented, one can focus on the most important features associated with the ligand-based processes. Two reversible or quasi-reversible processes are expected in these systems and associated with the oxidation of the *tert*-butyl phenolate species into the corresponding phenoxyl radicals. The radical nature of these species was also observed by spectrophotometric experiments, where addition of (NH$_4$)$_2$[Ce^{IV}(NO$_3$)$_6$][26] to dichloromethane solutions of **3** and **3′** at room temperature yielded a new band respectively at 390 nm ($\varepsilon \sim 4500$ L·mol^{-1}·cm^{-1}) and 440 nm ($\varepsilon \sim 7000$ L·mol^{-1}·cm^{-1}) (Supporting Information Figure S1). The considerable difference in band position is in good agreement with previously reported values for copper-phenoxyl species conjugated to imine[27] and amine[28] groups and therefore similar to **3** and **3′**.

As can be seen in Figure 3, compound **1** shows limited reversibility with processes at 0.82 and 0.98 V vs Fc$^+$/Fc. The peak separation for the first process reaches 0.15 V and increases further to 0.16 V for the second process, rendering

(22) Aguilar-Martinez, M.; Saloma-Aguilar, R.; Macias-Ruvalcaba, N.; Cetina-Rosado, R.; Navarrete-Vazquez, A.; Gomez-Vidales, V.; Zentella-Dehesa, A.; Toscano, R. A.; Hernandez-Ortega, S.; Fernandez-G., J. M. *Dalton Trans.* **2001**, 2346.

(23) Elias, H.; Hasserodt-Taliaferro, C.; Hellriegel, L.; Schoenherr, W.; Wannowius, K. J. *Inorg. Chem.* **1985**, *24*, 3192.

(24) (a) Neves, A.; Rossi, L. M.; Bortoluzzi, A. J.; Szpoganicz, B.; Wiezbicki, C.; Schwingel, E.; Haase, W.; Ostrovsky, S. *Inorg. Chem.* **2002**, *41*, 1788. (b) Neves, A.; Verani, C. N.; de Brito, M. A.; Vencato, I.; Mangrich, A.; Oliva, G.; Souza, D. H. F.; Batista, A. *Inorg. Chim. Acta* **1999**, *290*, 207.

(25) Villeneuve, N. M.; Schroeder, R. R.; Ochrymowycz, L. A.; Rorabacher, D. B. *Inorg. Chem.* **1997**, *36*, 4475.

(26) Nair, V.; Deepthi, A. *Chem. Rev.* **2007**, *107*, 1862.

(27) (a) Parker, D.; Davies, E. S.; Wilson, C.; McMaster, J. *Inorg. Chim. Acta* **2007**, *360*, 203. (b) Benisvy, L.; Bill, E.; Blake, A. J.; Collison, D.; Davies, E. S.; Garner, C. D.; McArdle, G.; McInnes, E. J. L.; McMaster, J.; Ross, S. H. K.; Wilson, C. *Dalton Trans.* **2006**, 258.

(28) Halfen, J. A.; Jazdzewski, B. A.; Mahapatra, S.; Berreau, L. M.; Wilkinson, E. C.; Que, L., Jr.; Tolman, W. B. *J. Am. Chem. Soc.* **1997**, *119*, 8217.

them irreversible. The |Ipc/Ipa| peak ratio cannot be calculated accurately, but visual inspection suggests that the intensity of the anodic peak is greater than that of the cathodic peak indicating that |Ipc/Ipa| < 1. It implies that a smaller concentration of the phenolate species is present at the surface of the electrode in the time scale of the experiment because of either depletion or chemical transformation. Two well-shaped processes are observed for **3** at 0.53 and 0.83 V versus Fc^+/Fc. These seem to be quasi-reversible because ΔEp reaches 0.10 V at 100 mV·s^{-1}, slightly larger than those values observed experimentally for the Fc^+/Fc couple under identical conditions. The quasi-reversibility is supported by an increase in the peak separation at higher scan rates with |Ipc/Ipa| values ranging from 1.27 at 100 mV·s^{-1} to 1.48 at 300 mV·s^{-1} for the first redox process. The insertion of bulky groups intended to enhance the amphiphilic properties in **4** appears to compromise the redox reversibility of the compound. The first ligand-centered peak is comparable to that of **3**, but a peak separation ΔEp of 0.14 V (|Ipc/Ipa| = 1.65), thus comparable to that of **1**, renders it irreversible. This irreversibility is increased in the second process. It is possible that the presence of tris(dodecyloxy)phenyl substituents increases the distance between the redox-active core of the molecule and the electrode surface, decreasing the rate of interfacial electron transfer, as seen in dendrimeric porphyrins.[29] From the point of view of redox reversibility, **3′** can be considered the best system. The ligand-centered processes shift to more positive potentials, namely 0.29 and 0.48 V versus Fc^+/Fc with separation peaks ΔEp = 0.09 V and |Ipc/Ipa| = 1.21, thus well within the limits observed for the Fc^+/Fc couple.

The switch-like activity is fundamental for potential uses in information storage and appears to depend heavily on the geometry adopted by the central atom. Octahedral systems tend to show rather limited switch-like cyclability, whereas five-coordinate systems[6] display reversible processes at 0.63 and 0.81 V vs Fc^+/Fc with minor decay after 20–50 cycles. To the best of our knowledge, the cyclability of square planar copper-phenolate systems is not known. On the basis of the data presented above, **3** and **3′** display good reversibility in the ligand-centered processes. Experiments were attempted cycling fifty times the two waves in a switch-like process. In spite of the initial results with **3**, a shift of up to 0.17 V can be detected between the first and the fiftieth cycle (Supporting Information Figure S2). The observed shift suggests a small but constant decay that might limit the use of this compound in responsive films. An excellent result was achieved with **3′** in which no significant changes (0.04 V) were detected after 50 cycles, thus indicating that decomposition of the generated species in the time scale of the voltammetry experiment did not take place. These results suggest that cycling of the phenoxyl species is viable in a flexible four-coordinate geometry and in noncoordinating solvents. Pending characterization of the amphiphilic properties of these two compounds, formation and study of Langmuir–Blodgett films of **3** and **3′** will be pursued.

Scheme 3

Electronic Structure Calculations. A series of computational calculations were run to correlate the experimental data observed for the ligand-centered redox properties of complexes **1**, **3**, **3′**, and **4** with their electronic nature. The B3LYP/6–311+G(d) level of theory[30] was employed to handle negatively charged species using the GAUSSIAN suite.[31] Geometries were fully minimized, without symmetry constraints, using standard methods.[32] It is assumed that all phenolate → phenoxyl processes described above will depend solely or mainly upon the relative energies of the HOMO orbitals of the ligand, from where electrons are withdrawn in an oxidative process, and that the higher the energy of the orbital, the more energetically affordable is the oxidation. Therefore, the models are nonmetallated and simplified versions of the deprotonated phenolate ligands as shown in Scheme 3. Considering that **1** shows the more positive potential, the HOMO orbital of the equivalent model system should be the lowest in energy and will display the lowest comparative energy. The model for **3** (also related to **4**) yields a higher comparative energy and that of **3′** exhibits the highest energy—therefore the most affordable oxidation process—in excellent agreement with the observed experimental trends. For **1** and **3**, π-delocalization seems to play an important role. One can conclude that energetically favorable oxidations can be achieved by replacing the −C=O by −C=NR groups attached to the phenolate ring. Similarly,

(29) Pollak, K. W.; Leon, J. W.; Frechet, J. M. J.; Maskus, M.; Abruna, H. D. *Chem. Mater.* **1998**, *10*, 30.

(30) (a) Becke, A. D. *Phys. Rev. A* **1988**, *38*, 3098. (b) Becke, A. D. *J. Chem. Phys.* **1993**, *98*, 5648. (c) Lee, T.; Yang, W. T.; Parr, R. G. *Phys. Rev. B* **1988**, *37*, 785. (d) Ditchfield, R.; Hehre, W. R.; Pople, J. A. *J. Chem. Phys.* **1971**, *54*, 724. (e) Gordon, M. S. *Chem. Phys. Lett.* **1980**, *76*, 163. (f) Hariharan, P. C.; Pople, J. A. *Theo. Chim. Acta.* **1973**, *28*, 213. (g) Hariharan, P. C.; Pople, J. A. *Mol. Phys.* **1974**, *27*, 209. (h) Hehre, W. R.; Ditchfield, R.; Pople, J. A. *J. Chem. Phys.* **1972**, *56*, 225.

(31) Frisch, M. J.; Trucks, G. W.; Schlegel, H. B.; Scuseria, G. E.; Robb, M. A.; Cheeseman, J. R.; Montgomery, J. A.; Vreven, T.; Kudin, K. N.; Burant, J. C.; Millam, J. M.; Iyengar, S. S.; Tomasi, J.; Barone, V.; Mennucci, B.; Cossi, M.; Scalmani, G.; Rega, N.; Petersson, G. A.; Nakatsuji, H.; Hada, M.; Ehara, M.; Toyota, K.; Fukuda, R.; Hasegawa, J.; Ishida, M.; Nakajima, T.; Honda, Y.; Kitao, O.; Nakai, H.; Klene, M.; Li, X.; Knox, J. E.; Hratchian, H. P.; Cross, J. B.; Bakken, V.; Adamo, C.; Jaramillo, J.; Gomperts, R.; Stratmann, R. E.; Yazyev, O.; Austin, A. J.; Cammi, R.; Pomelli, C.; Ochterski, J. W.; Ayala, P. Y.; Morokuma, K.; Voth, G. A.; Salvador, P.; Dannenberg, J. J.; Zakrzewski, V. G.; Dapprich, S.; Daniels, A. D.; Strain, M. C.; Farkas, O.; Malick, D. K.; Rabuck, A. D.; Raghavachari, K.; Foresman, J. B.; Ortiz, J. V.; Cui, Q.; Baboul, A. G.; Clifford, S.; Cioslowski, J.; Stefanov, B. B.; Liu, G.; Liashenko, A.; Piskorz, P.; Komaromi, I.; Martin, R. L.; Fox, D. J.; Keith, T.; Al-Laham, M. A.; Peng, C. Y.; Nanayakkara, A.; Challacombe, M.; Gill, P. M. W.; Johnson, B.; Chen, W.; Wong, M. W.; Gonzalez, C.; Pople, J. A. *GAUSSIAN 03*; Gaussian, Inc.: Wallingford, CT, 2003.

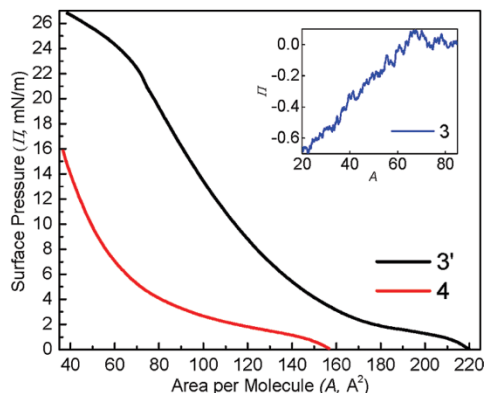(32) Schlegel, H. B. *J. Comput. Chem.* **1982**, *3*, 214.

Figure 4. Compression isotherms for **3'** (black trace) and **4** (red trace).

it can be suggested that the nature of the group R attached to the Schiff base will have some impact in the electronic delocalization. This was observed for protonated models in which R = $-CH_3$ or $-$aryl, but the minimization of the deprotonated **4** seemed dependent on the orientation of that additional aryl ring. Interestingly, **3'** presents a localized π-frame limited to the aromatic phenolate ring. It can be concluded that disruption of the delocalization fosters energetically affordable oxidations and should be used as a guideline in the design of future amphiphilic precursors.

Amphiphilic Properties. The synthesis of **3** and **4** targets the attachment of nonpolar amine-containing organic fragments to the *tert*-butyl-containing precursor **1** by Schiff base condensation. These organic fragments have played an important role in the redox properties of these compounds and are expected to confer amphiphilic properties acting as hydrophobic counterparts of the copper-containing headgroup. In-situ reduction of **3** yielded **3'**. The amphiphilic properties of **3**, **3'**, and **4** were studied by means of compression isotherms plotting surface pressure (Π, mN/m) versus area per molecule (A, Å^2) and Brewster angle microscopy (BAM). The compression isotherms give information about the 2D behavior of the resulting Langmuir film at the air/water interface. The compression isotherms indicate the presence of mono or multilayers, collapse pressures, and average areas per molecule. BAM uses polarized light passing through media with dissimilar refractive indexes and is the most powerful method to identify structures such as agglomerates and domains in films at the air/water interface.

Recent studies on the C$_{16}$-containing copper surfactants described by Nagel et al.[13] have shown that longer octadecyl (C$_{18}$) chains tend to lead to an increase of collapse pressures.[33] Similarly, it has been demonstrated that replacement of the hydroxy groups by methoxy groups[34] yields complex behavior at the air/water interface. Therefore, considering the presence of bulky *tert*-butyl groups on **3**, longer octadecyl chains were employed. Nonetheless, the isotherm of **3** was marked by an erratic profile (Figure 4, inset) that confirms lack of organization and suggests random molecular aggregation. Loss of matter to the subphase was supported by

areas as small as 15 Å$^2\cdot$molecule^{-1} and pressures have no clear physical meaning. The presence of *tert*-butyl groups attached to the headgroup of **3** is key to the observed redox behavior of the compound but precludes the formation of organized films. Moreover, careful analysis of the disposition of the salicylaldehyde groups in **1**, as revealed by X-ray diffraction, suggests that the octadecylamine chains in **3** (and **4**) will be oriented trans to each other in a rigid imine-like structure. Exploratory BAM at several surface pressures distinctively shows the presence of oval-shaped domains (Supporting Information Figure S3) that resemble vesicles[1c,35,36] along with concentric domains, generally referred to as Newton rings.[37] These rings are multilayer granules formed from the ejection of matter from the compressed monolayer when localized oscillations are present. Thus, in addition to the headgroups, the rigidity of the framework appears to prevent this molecule from exhibiting amphiphilic properties.

Amphiphilic activity depends on an optimal balance between the hydrophobic and hydrophilic properties of a given surfactant. As such, ways of improvement were considered in the design of surfactants based on *tert*-butylsalicyl-copper head groups. Two possible approaches were examined, involving a decrease of the framework rigidity or an increase in the number of alkyl chains present. Imine reduction provided the amine surfactant **3'** with a more flexible framework, whereas **4** was used to increase the number of alkyl, or more formally alkoxy, chains present. Reduced **3'** was initially dissolved in dichloromethane and subsequently spread on the water surface. As the barriers of the trough were compressed, the tension (γ) of the air–water interface in the presence of the amphiphilic species decreased as compared to that of the bare air–water interface ($\gamma_0 = 72$ mN$\cdot$m^{-1} at 23 °C), resulting in an increase in Π ($= \gamma_0 - \gamma$). Indeed, the isotherm (red trace) shown in Figure 4 exhibits considerable surface activity. Individual molecules begin interacting at very large areas of 220 Å^2, grow into a plateau-like region at low pressures, and increase consistently up to about 22 mN$\cdot$m^{-1}, when an inflection takes place. The isotherm of **4** is also shown in Figure 4 and reveals this species as interfacially active. No inflections indicative of phase transitions are observed, and a moderate pressure of 14 mN$\cdot$m^{-1} is reached.

Both approaches improve surface activity suggesting that a better equilibrium between hydrophilic and hydrophobic properties can be obtained in the design of redox-active surfactants. Interestingly, for both cases the compression barriers of the trough touch each other without the event of formal constant-area collapse characterized by a sudden decrease in the surface pressure.[38] We have suggested that metallosurfactants can exibit distinct collapse mechanisms,[14a]

(33) Pang, S.; Li, C.; Huang, J.; Liang, Y. *Colloids Surf.* **2001**, *A178*, 143.
(34) Hemakanthi, G.; Unni Nair, B.; Dhathathreyan, A. *Chem. Phys. Lett.* **2001**, *341*, 407.
(35) Dominguez-Gutierrez, D.; Surtchev, M.; Eiser, E.; Elsevier, C. J. *Nano Lett.* **2006**, *06*, 145.
(36) Svenson, S. *Curr. Opin. Colloid Interface Sci.* **2004**, *9*, 201.
(37) Galvan-Miyoshi, J.; Ramos, S.; Ruiz-Garcia, J.; Castillo, R. *J. Chem. Phys.* **2001**, *115*, 8178.
(38) (a) Vaknin, D.; Bu, W.; Satija, S. K.; Travesset, A. *Langmuir* **2007**, *23*, 1888. (b) Ybert, C.; Lu, W.; Moeller, G.; Knobler, C. M. *J. Phys.: Condens. Matter* **2002**, *14*, 4753.
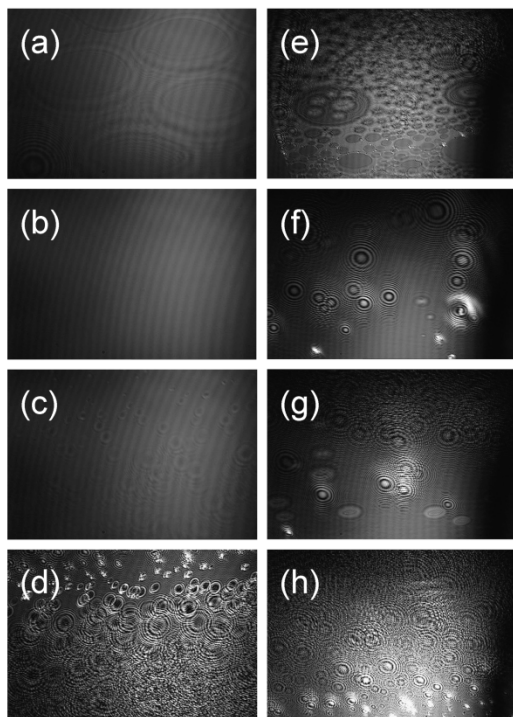
Figure 5. Brewster angle micrographs. For **3′**: (a) before compression, (b) below 2 mN·m⁻¹, (c) at 6 mN·m⁻¹, (d) at 21 mN·m⁻¹. For **4**: (e) before compression, (f) at 3 mN·m⁻¹, (g) at 5 mN·m⁻¹, and (h) at 14 mN·m⁻¹.

and this fact led to the consideration that, in spite of their shape, the isotherms describe the formation of multilayers. BAM was used to monitor the compression of **3′** and **4** in an attempt to investigate the nature of the resulting films. Figure 5 shows a series of selected micrographs gathered along the compression process for each of the amphiphiles.

Multiple domains are present before compression of **3′**. Before the first inflection in the isotherm, as well as at low surface pressures, an apparently homogeneous film is obtained. After this inflection the presence of Newton rings suggests instability of the film. At 20–21 mN·m⁻¹ the film ceases to behave as a monolayer. Before compression of **4**, a film composed of several bidimensional oval-shaped domains is present. At about 3 mN·m⁻¹ these domains seem to be replaced by a homogeneous monolayer, but the presence of several Newton rings suggest considerable instability. At 5 mN·m⁻¹, rings and oval-shaped domains similar to those observed for **3** are present. Comparison of the domains present at 3 and 5 mN·m⁻¹ suggest that only the former are flat, reinforcing the notion of a vesicular nature. Future dynamic light scattering experiments would be necessary to confirm this hypothesis. From 6 to 14 mN·m⁻¹, a considerable increase in the roughness of the surface and the appearance of multiple rings takes place; this is interpreted as indicative of multilayers. Similar to the octadecyl chains, **4** has a rigid structure with trans-oriented trialkoxy groups. However, the three oxidodecyl ($-OC_{12}H_{26}$) chains present per amine can rotate almost freely. Contrary to **3**, these chains can point outward from the air/water

interface, promoting a better equilibrium between the hydrophobic and hydrophilic portions of **4** and allowing for film formation. Because repulsion forces are also present, it is unlikely that all six chains can be aligned, accounting for the formation of multilayers.

Summary and Conclusions

In this Article we have used precursor **1** to develop a series of amphiphilic and redox-responsive complexes as candidates for the development of responsive films. We have demonstrated that the design of systems exhibiting a good balance between amphiphilicity and redox response is far from trivial. In **3** an apparent redox reversibility is obfuscated by a complete lack of amphiphilic behavior that prevents organization and ultimately the formation of films. The inclusion of three alkoxy groups per ligand in **4** appears to be key to the enhancement of the amphiphilic properties and to an improved response in the formation of relatively organized Langmuir films that show formal collapse at about 14 mN·m⁻¹. Nonetheless, the redox-response was seriously compromised by an increased separation between cathodic and anodic peaks in the first phenolate/phenoxyl process. This behavior is a signature for a quasi-reversible process that is unlikely to withstand switch-like activities and is related to the nature and the bulkiness of the group attached to the imine function. Finally, an increased flexibility of the core was attained for **3′** by an in situ reduction of the C═N groups present in **3**. Improved amphiphilicity and consequent Langmuir film formation with a higher formal collapse at 27 mN·m⁻¹ were observed. Moreover, excellent reversibility of the ligand-based processes and marginal decay upon switch-like cycling were also observed. The reversibility and cyclability seem to be associated with the disruption of the electronic delocalization between the phenolate and the C═N group and will be incorporated in the design of amphiphilic precursors for future responsive films.

On the basis of these results, it can be concluded that an increased flexibility of the core and electronic localization are fundamental to achieving a good balance between the desired redox and the amphiphilic properties. The replacement of the *tert*-butyl groups by other substituents that simultaneously foster phenolate/phenoxyl cycling and enhance the polarity of the headgroups—thus the amphiphilic behavior of the precursors—would be advantageous to the design of desired responsive Langmuir–Blodgett films. Recent advances[14b] suggest that chloro-groups might be able to deliver such properties. These results will pave the way to a new series of amine surfactants based on chloro-substituted phenolates coordinated to bivalent copper, nickel, and cadmium. The use of the latter cations should improve the thermodynamic stability of the resulting complexes leaving the ligand-centered redox activity unaltered. These topics are currently under development in our laboratories.

Experimental Section

Materials and Methods. All the reagents were obtained from commercial sources and were used without further purification. Dichloromethane was purified using an I.T. solvent purification

Table 1. Crystal Data for Complexes **1** and **5**[a]

complex	1	5
empirical formula	$C_{30}H_{42}Cu\,O_4$	$C_{32}H_{48}Cu_2\,O_6$
fw	530.18	655.78
temperature	100(2) K	100(2) K
wavelength	0.71073 Å	0.71073 Å
crystal system, space group	orthorhombic, $Pbca$	monoclinic, $C2/c$
unit cell dimensions	$a = 7.8735(5)$ Å	$a = 30.5691(9)$ Å
	$b = 16.6446(11)$ Å	$b = 9.5625(3)$ Å
	$c = 20.9754(15)$ Å	$c = 10.9862(3)$ Å
		$\beta = 90.632(3)$ deg
volume	2748.9(3) Å³	3211.26(16) Å³
Z, calculated density	4, 1.281 Mg/m³	4, 1.356 Mg/m³
absorption coefficient	0.827 mm⁻¹	1.364 mm⁻¹
final R indices [$I > 2\sigma(I)$]	R1 = 0.0428,	R1 = 0.0506,
	wR2 = 0.1079	wR2 = 0.1254
R indices (all data)	R1 = 0.0764,	R1 = 0.0729,
	wR2 = 0.1201	wR2 = 0.1301

$^a R(F) = \Sigma||F_o| - |F_c||/\Sigma|F_o|; \; wR(F) = [\Sigma w(F_o^2 - F_c^2)^2/\Sigma w(F_o^2)^2]^{1/2}$ for $I > 2\sigma(I)$.

system. IR spectra were measured from 4000 to 400 cm⁻¹ as KBr pellets on a Tensor 27 FTIR-spectrophotometer. ESI spectra were measured on a Micromass QuattroLC triple quadrupole mass spectrometer with an electrospray/APCI source and Walters Alliance 2695 LC, autosampler and photodiode array UV detector. Experimental assignments were simulated based on peak position and isotopic distributions. Elemental analyses were performed by Midwest Microlab, Indianapolis, Indiana. UV–visible spectra of 1.0 × 10⁻⁴ M dichloromethane solutions were recorded in the range 200 to 1000 nm on a Cary 50 spectrophotometer. Electrochemical experiments were performed in dichloromethane on a BAS 50W voltammetric analyzer. A standard three-electrode-cell was employed with a glassy-carbon working electrode, a Pt-wire auxiliary electrode, and an Ag/AgCl reference electrode under an inert atmosphere at room temperature. TBAPF₆ was used as the supporting electrolyte. The |Ipa/Ipc| values were obtained using available software within the BAS package. All potentials are given versus Fc⁺/Fc.[39]

X-ray Structural Determination for 1 and 5. Diffraction data were collected on a Bruker X8 APEX-II diffractometer equipped with Mo Kα radiation and a graphite monochromator at 100 K. Frames were collected at 10 s/frame (**1**) or 5 s/frame (**5**) and 0.3 degree between frames at a detector distance of 40 mm. The frame data were indexed and integrated with the manufacturer's SMART, SAINT, and SAD-ABS software.[40] Both structures were refined and reported using Sheldrick's SHELX-97 software.[41] Crystals of **1** formed as brown plates and yielded 16135 reflections, of which 3652 were independent. Hydrogen atoms in **1** were placed in observed positions, and the asymmetric unit contains one-half complex with the Cu atom occupying an inversion center in the lattice. Crystals of **5** appeared as pale green plates, and 27592 reflections were harvested of which 3985 were independent. Hydrogen positions in **5** were observed or calculated. The asymmetric unit in **5** consists of one-half dimeric complex with the bridging methoxy groups occupying a 2-fold axis. The hydrogen atoms on these methoxy groups are disordered in two sets of partial positions.

Table 1 lists the experimental parameters.

Compression Isotherms. The $\Pi - A$ isotherms were measured in an automated KSV 2000 minitrough at 23 ± 0.5 °C. Ultrapure water (Barnstead NANO pure) was used for all experiments with

a resistivity of 17.5–18 MΩ·cm⁻¹. Adventitious impurities at the surface of freshly poured aqueous subphases were removed by vacuum after barrier compression. Spreading of a known quantity (~30 μL) of 1.0 mg·mL⁻¹ chloroform solutions on the aqueous subphase was followed by about 20 min equilibrium time before monolayer compression. The isotherms were obtained at a compression rate of 5 mm·min⁻¹. The pressure was measured using the Wilhemy plate method (platinum plate, 40 mm perimeter). At least three independent measurements were carried out per sample with excellent reproducibility.

Brewster Angle Microscopy. A KSV-Optrel BAM 300 with a HeNe laser (10 mW, 632.8 nm) and a CCD detector was used in all micrographs. The compression rate was 5 mm/min, the field of view was 800 × 600 μm, and the lateral resolution was about 2 μm.

Syntheses. *Caution! Perchlorate salts are potentially explosive. Although the final products do not contain perchlorates, proper precautions should be taken for the synthesis.*

[Cu(L^SAL)₂] (1). Bis-(3,5-di-*tert*-butyl-2-phenolato-benzaldehyde)copper(II). To a stirring solution of 3,5-di-*tert*-butyl-2-hydroxy-benzaldehyde (0.515 g, 2.2 mmol) and 1.5 eq. triethylamine in 20 mL methanol was added a methanol solution (10 mL) of Cu(ClO₄)₂·6H₂O (0.375 g, 1 mmol), dropwise. After warming gently for 30 min, a brown microcrystalline solid was isolated by filtration. The precipitate was washed with 3 × 20 mL portions of cold methanol and 2 × 10 mL portions of cold ether and then dried under vacuum. The crude product was crystallized from 40 mL of methanol. After 24 h, a brown microcrystalline solid was isolated Yield = 95%. Anal. Calcd for [C₃₀H₄₂O₄Cu]: C, 67.96; H, 7.98. Found C, 67.77; H, 8.16%. IR (KBr, cm⁻¹) 1333 (v_{C-O}), 1619 ($v_{C=O}$), 2868–957 (v_{C-H} from *tert*-butyl groups). ESI pos. in MeOH: m/z = 530.1 for [**1** + H⁺]⁺.

[Cu^II(L²)₂] (3). Bis-(2,4-di-*tert*-butyl-6-octadecyliminomethyl-phenolato)copper(II). To a stirring solution of octadecylamine (0.270 g, 1.0 mmol) in 20 mL ethanol was added the precursor **1** (0.265 g, 0.5 mmol) in 10 mL methanol, dropwise. The solution was refluxed for 1 h. The solvent was removed to obtain an olive colored powder. The power was dissolved in dichloromethane:methanol mixture (1:1) and yielded a homogeneous powder that was dried under vacuum overnight. Yield = 72%. Anal. Calcd for [C₆₆H₁₁₆N₂O₂Cu]: C, 76.72; H, 11.32; N, 2.71. Found C, 76.32; H, 11.44; N, 2.77%. IR (KBr, cm⁻¹) 1590 ($v_{C=N}$), 2859–2961 (v_{C-H} from *tert*-butyl groups). ESI pos. in MeOH: m/z = 1033.2 for [**3** + H⁺]⁺.

[Cu^II(L^2A)₂] (3′). Bis-(2,4-di-*tert*-butyl-6-octadecylaminomethyl-phenolato)copper(II). To a stirring solution of **3** (0.270 g, 1.0 mmol) in 20 mL of a 1:1 methanol:dichloromethane mixture at 0 °C small portions of NaBH₄ (0.12 g, 3.0 mmol) were added. The solution was kept in an ice bath until gas evolution ceased. The solvent was removed, and the crude product was dissolved in dichloromethane and washed with 10 × 100 mL aliquots of a saturated aqueous solution of sodium chloride. The resulting solution was dried on NaSO₄, and the dichloromethane evaporated to yield a pale green powder.

Yield = 60%. Anal. Calcd for [C₆₆H₁₂₀N₂O₂Cu]: C, 76.43, H, 11.66, N, 2.70. Found C, 76.63, H, 10.95, N, 2.68%. IR (KBr, cm⁻¹) 2860–2963 (v_{C-H} from *tert*-butyl groups). ESI pos. in MeOH: m/z = 1036.9 for [**3′** + H⁺]⁺.

[Cu^II(L³)₂] (4). Bis-(2,4-di-*tert*-butyl-6-[(3,4,5-tris-dodecyloxy-phenylimino)-methyl]-phenolato)copper(II). Precursor **1** (0.265 g, 0.5 mmol) was added to a stirring 20 mL methanol solution of 3,4,5-tris-dodecyloxy-phenylamine[42](0.646 g, 1.0 mmol) dropwise. After a mild reflux of 2 h, two-thirds of the solvent was removed to precipitate a brown powder. The powder was isolated and washed

(39) Gagne, R.; Koval, C.; Licenski, G. *Inorg. Chem.* **1980**, *19*, 2854.
(40) *APEX II, SMART, SAINT and SADABS collection and processing programs are distributed by the manufacturer.*; Bruker AXS Inc.: Madison, WI, U.S.A.
(41) Sheldrick, G. *SHELX-97*; University of Gottingen: Germany, 1997.

with cold methanol and dried under vacuum. Yield = 61%. Anal. Calcd for [$C_{114}H_{196}N_2O_8Cu$]: C, 76.65; H, 11.06; N, 1.57. Found C, 76.38; H, 11.16; N, 1.71%. IR (KBr, cm^{-1}) 1588 ($v_{C=N}$), 2852–2956 (v_{C-H} from *tert*-butyl groups). ESI pos. in MeOH: *m/z* = 1784.9 for [**4** + H$^+$]$^+$.

Supporting Information Available: Three figures and a table with data for compounds **1**, **3**, and **3′** (PDF). This material is available free of charge via the Internet at http://pubs.acs.org.

IC702233N

(42) Percec, V.; Ahn, C.-H.; Bera, T. K.; Ungar, G.; Yeardley, D. J. P. *Chem.—Eur. J.* **1999**, *5*, 1070.

Appendix H

Nickel and Zinc Proteasome Inhibitors

Michael Frezza, Sarmad Sahiel Hindo, Dajena Tomco, Marco M. Allard, Qiuzhi Cindy Cui,

Mary Jane Heeg, Di Chen, Claudio N. Verani, Q. Ping Dou

"Comparative Activities of Nickel(II) and Zinc(II) Complexes of Asymmetric [NN'O] Ligands

as 26S Proteasome Inhibitors"

Inorganic Chemistry
Article

My contribution to this work consisted of the electronic structure calculations.

Comparative Activities of Nickel(II) and Zinc(II) Complexes of Asymmetric [NN′O] Ligands as 26S Proteasome Inhibitors

Michael Frezza,[†] Sarmad Sahiel Hindo,[‡] Dajena Tomco,[‡] Marco M. Allard,[‡] Qiuzhi Cindy Cui,[†] Mary Jane Heeg,[‡] Di Chen,[†] Q. Ping Dou,*[,†] and Cláudio N. Verani*[,‡]

[†]The Prevention Program, Barbara Ann Karmanos Cancer Institute, and Department of Pathology, School of Medicine, Wayne State University, Detroit, Michigan 48201, and [‡]Department of Chemistry, Wayne State University, 5101 Cass Ave. Detroit, Michigan 48202

In this study, we compare the proteasome inhibition capabilities of two anticancer candidates, $[Ni(L^{IA})_2]$ (**1**) and $[Zn(L^{IA})_2]$ (**2**), where L^{IA-} is the deprotonated form of the ligand 2,4-diiodo-6-(((2-pyridinylmethyl)amino)methyl) phenol. Species **1** contains nickel(II), a considerably inert ion that favors covalency, whereas **2** contains zinc(II), a labile transition metal ion that favors predominantly ionic bonds. We report on the synthesis and characterization of **1** and **2** using various spectroscopic, spectrometric, and structural methods. Furthermore, the pharmacological effects of **1** and **2**, along with those of the salts $NiCl_2$ and $ZnCl_2$, were evaluated in vitro and in cultured human cancer cells in terms of their proteasome-inhibitory and apoptotic cell-death-inducing capabilities. It is shown that neither $NiCl_2$ nor **1** have the ability to inhibit the proteasome activity at any sustained levels. However, $ZnCl_2$ and **2** showed superior inhibitory activity versus the chymotrypsin-like activity of both the 26S proteasome (IC_{50} = 5.7 and 4.4 μmol/L, respectively) and the purified 20S proteasome (IC_{50} = 16.6 and 11.7 μmol/L, respectively) under cell-free conditions. Additionally, inhibition of proteasomal activity in cultured prostate cancer cells by **2** was associated with higher levels of ubiquitinated proteins and apoptosis. Treatment with either the metal complex or the salt was relatively nontoxic toward human normal cells. These results strengthen the current working hypothesis that fast ligand dissociation is required to generate an $[ML^{IA}]^+$ pharmacophore, capable of interaction with the proteasome. This interaction, possibly via N-terminal threonine amino acids present in the active sites, renders the proteasome inactive. Our results present a compelling rationale for **2** along with its gallium(III) and copper(II) congeners to be further investigated as potential anticancer drugs that act as proteasome inhibitiors.

Introduction

The use of platinum-containing analogues has been a viable therapeutic strategy in a host of malignancies.[1–5] However, excessive toxicity has hampered their widespread use, leading to the investigation of other metal complexes and distinctive cellular apoptotic pathways.[6,7]

The 26S proteasome has gained substantial consideration as an anticancer target,[8–12] and proteasomal inhibition is a mechanism for tumor cell suppression currently being investigated in our groups. The main function of the ubiquitin−proteasome pathway is to degrade damaged or misfolded proteins.[13,14] Targeted proteins are tagged with a series of ubiquitin molecules which are then translocated to the 26S proteasome and subsequently degraded.[15,16] The enzymatic activity of the 26S proteasome is mediated by the 20S proteasome core that contains three pairs of catalytic

*To whom correspondence should be addressed. Phone: 313 576 8301. Fax: 313 576 8307. E-mail: doup@karmanos.org (Q.P.D.). Phone: 313 577 1076. Fax: 313 577 8022. E-mail: cnverani@chem.wayne.edu (C.N.V.).

(1) Guo, Z.; Sadler, P. J. *Angew. Chem., Int. Ed.* **1999**, *38*, 1512.
(2) Wong, E; Giandomenico, C. M. *Chem. Rev.* **1999**, *99*, 2451.
(3) Wang, D.; Lippard, S. J. *Nat. Rev. Drug Discovery* **2005**, *4*, 307.
(4) Choi, S.; Vastag, L.; Larrabee, Y. C.; Personick, M. L.; Schaberg, K. B.; Fowler, B. J.; Sandwick, R. K.; Rawji, G. *Inorg. Chem.* **2008**, *47*, 1352.
(5) Egger, A. E.; Hartinger, C. G.; Hamidane, H. B.; Tsybin, Y. O.; Keppler, B. K.; Dyson, P. J. *Inorg. Chem.* **2008**, *47*, 10626.
(6) Galanski, M; Arion, V. B.; Jakupec, M. A.; Keppler, B. K. *Curr. Pharm. Des.* **2003**, *9*, 2078.
(7) Ronconi, L.; Giovagnini, L.; Marzano, C.; Bettìo, F.; Graziani, R.; Pilloni, G.; Fregona, D. *Inorg. Chem.* **2005**, *44*, 1867.
(8) Giovagnini, L.; Sitran, S.; Montopoli, M.; Caparrotta, L.; Corsini, M.; Rosani, C.; Zanello, P.; Dou, Q. P.; Fregona, D. *Inorg. Chem.* **2008**, *47*, 6336.

(9) Cvek, B.; Milacic, V.; Taraba, J.; Dou, Q. P. *J. Med. Chem.* **2008**, *51*, 6256.
(10) Adsule, S.; Barve, V.; Chen, D.; Ahmed, F.; Dou, Q. P.; Padhye, S.; Sarkar, F. H. *J. Med. Chem.* **2006**, *49*, 7242.
(11) Beenen, M. A.; An, C.; Ellman, J. A. *J. Am. Chem. Soc.* **2008**, *130*, 6910.
(12) Paramore, A.; Frantz, S. *Nat. Rev. Drug Discovery* **2003**, *2*, 611.
(13) Peters, J. M.; Franke, W. W.; Kleinschmidt, J. A. *J. Biol. Chem.* **1994**, *269*, 7709.
(14) Goldberg, A. L. *Science* **1995**, *268*, 522.
(15) Dou, Q. P.; Li, B. *Drug Res. Update* **1999**, *2*, 215.
(16) Hochstrasser, M. *Cur. Opin. Cell Biol.* **1995**, *7*, 215.

sites responsible for its chymotrypsin-, trypsin-, and caspase-like activities.[17,18]

The validation of the proteasome as a target for cancer therapy came with the FDA approval of bortezomib for the treatment of multiple myeloma.[19,20] Studies have shown that bortezomib exerts its antitumor effects by binding and deactivating an N-terminal threonine of the chymotrypsin-like active center. Furthermore, other proteasome inhibitors, such as peptide derivatives with aldehydes, sulfones, and epoxyketones,[21] have been shown to be effective in the inactivation of the 26S proteasome by similar mechanisms. Such inhibition has been a valuable approach toward cancer therapy, because it has been shown that human cancer cells are more sensitive to proteasome inhibition than normal cells.[22,23]

We have demonstrated that 2:1 complexes $[M(L^{IA})_2]$, with $[NN'O]$ ligands and gallium(III) or copper(II), can promote proteasome inhibition in prostate cancer[24,25] and cisplatin-resistant neuroblastoma cells.[26] The mechanisms of inhibition are not entirely clear and could involve the deactivation of either the 19S terminal caps or the 20S core. Nonetheless, molecular modeling with similar complexes suggests that such species cannot dock into the proteasome satisfactorily, indicating that new bonds between the inhibitor and the 20S core must be established. Experimental results with equivalent copper(II) species suggest that a 1:1 pharmacophore $[M(L^{IA})]^+$ (or an aqua equivalent) is needed to allow coordination with the terminal threonine or other coordinating residues.[24,25] Thus, an equilibrium $[M(L^{IA})_2] \leftrightarrow [M(L^{IA})]^+ + L^{IA-}$ for 2:1 species seems necessary. Therefore, we aim at furthering these studies by designing similar $[M(L^{IA})_2]$ complexes using divalent nickel(II) and zinc(II) metals. Differences due to electronic configurations of the metals lead to species with characteristic behavior for ligand dissociation, as depicted in Scheme 1. Nickel(II) has a $3d^8$ configuration, which leads to nonzero ligand-field stabilization energies (LFSE) and, consequently, should foster slow ligand dissociation, whereas zinc(II) with a $3d^{10}$ configuration has zero LFSE, thus fostering rapid ligand dissociation.[27-29] Slow ligand dissociation would therefore

Scheme 1. Suggested Equilibrium of $[M(L^{IA})_2] \leftrightarrow [M(L^{IA})]^+ + L^{IA-}$ to Generate the $[M(L^{IA})]^+$ Pharmacophore
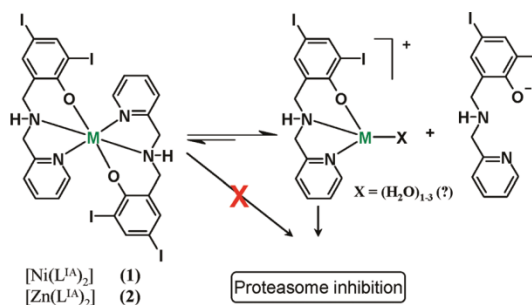
$[Ni(L^{IA})_2]$ (1)
$[Zn(L^{IA})_2]$ (2)

give rise to poor inhibition because no deactivation of the proteasomal active core takes place.

In this paper, we report on the synthesis and characterization of $[Ni(L^{IA})_2]$ (1) and $[Zn(L^{IA})_2]$ (2) using various spectroscopic, spectrometric, and structural methods. After careful characterization, these species were evaluated as proteasome inhibitors to the purified 20S proteasome and 26S proteasome in whole-cell extracts, as well as in intact prostate cancer and leukemia cells. The results follow.

Results and Discussion

Ligand Design. Our groups are interested in the development of discrete complexes of well-established stoichiometry, formed between asymmetric $[NN'O]$ ligands and transition metal ions for anticancer therapy. Such ligands are an evolution from terbutylated analogues used as biomimetic models for galactose−oxidase.[30] The presence of electron-donating and -withdrawing phenol substituents (i.e., H, ^tBu, Cl, Br, and I) in such complexes has shown a distinctive influence on the apoptosis of cisplatin-resistant neuroblastoma and prostate cancer cell lines.[25,26] We are mostly engaged with the phenol-based ligand 2,4-diiodo-6-(((2-pyridinylmethyl)amino)methyl)phenol, synthesized by treatment of 2-hydroxy-3,5-diiodobenzaldehyde with 2-amino-methylpyridine followed by reduction with sodium borohydride.[26] Upon deprotonation, this ligand leads to 2:1 ligand-to-metal $[M(L^{IA})_2]$ species with divalent ions, hence, eliminating the required charge balance by counterions. Moreover, a secondary amine in this ligand allows for the design of species with appended moieties to enhance water solubility[31,32] (currently at 4.5×10^{-5} mol/L for the

(17) Seemuller, E; Lupas, A.; Stock, D.; Lowe, J.; Huber, R.; Baumeister, W. *Science* **1995**, *268*, 579.

(18) Voges, D.; Zwickl, P.; Baumeister, W. *Annu. Rev. Biochem.* **1999**, *68*, 1015.

(19) Dou, Q. P.; Goldfarb, R. H. *IDrugs* **2002**, *5*, 828.

(20) Kane, R. C.; Farrell, A. T.; Sridhara, R.; Pazdur, R. *Clin. Cancer Res.* **2006**, *12*, 2955.

(21) (a) Borissenko, L.; Groll, M. *Chem. Rev.* **2007**, *107*, 687. (b) Kisselev, A. F.; Goldberg, A. L. *Chem. Biol.* **2001**, *08*, 739. (c) McCormack, T. A.; Cruikshank, A. A.; Grenier, L.; Melandri, F. D.; Nunes, S. L.; Plamondon, L.; Stein, R. L.; Dick, L. R. *Biochemistry* **1998**, *37*, 7792.

(22) Adams, J.; Palombella, V. J.; Sausville, E. A.; Johnson, J.; Destree, A.; Lazarus, D. D.; Maas, J.; Pien, C. S.; Prakash, S.; Elliott, P. J. *Cancer Res.* **1999**, *59*, 2615.

(23) An, B.; Goldfarb, R. H.; Siman, R.; Dou, Q. P. *Cell Death Differ.* **1998**, *5*, 1062.

(24) Hindo, S. S.; Frezza, M.; Tomco, D.; Heeg, M. J.; Hryhorczuk, L.; McGarvey, B. R.; Dou, Q. P.; Verani, C. N. *Eur. J. Med. Chem.* **2009**, accepted.

(25) Chen, D.; Frezza, M.; Shakya, R.; Cui, Q. C.; Milacic, V.; Verani, C. N.; Dou, Q. P. *Cancer Res.* **2007**, *67*, 9258.

(26) Shakya, R.; Peng, F.; Liu, J.; Heeg, M. J.; Verani, C. N. *Inorg. Chem.* **2006**, *45*, 6263.

(27) See, for example: (a) Miessler, G. L.; Tarr, D. A. *Inorganic Chemistry*, 3rd ed.; Pearson-Prentice Hall: Upper Saddle River, NJ, 2004; Chapter 12, pp 412−453. (b) Basolo, F.; Pearson, R. G. Mechanisms of Inorganic Reactions; 2nd ed.; John Wiley & Sons: New York, 1967; Chapter 3, pp.124−246.

(28) Sekaly, A. L. R.; Murimboh, J.; Hassan, N. M.; Mandal, R.; Ben Younes, M. E.; Chakrabarti, C. L.; Back, M. H. *Environ. Sci. Technol.* **2003**, *37*, 68.

(29) (a) Johnson, D. A.; Nelson, P. G. *Inorg. Chem.* **1995**, *34*, 5666. (b) Johnson, D. A.; Nelson, P. G. *Inorg. Chem.* **1995**, *34*, 3253.

(30) (a) Michel, F.; Thomas, F.; Hamman, S.; Philouze, C.; Saint-Aman, E.; Pierre, J.-L. *Eur. J. Inorg. Chem.* **2006**, *1-18*, 3684. (b) Shimazaki, Y.; Huth, S.; Odani, A.; Yamauchi, O. *Angew. Chem., Int. Ed.* **2000**, *39*, 1666. (c) Itoh, S.; Taki, M.; Takayama, S.; Nagatomo, S.; Kitagawa, T.; Sakurada, N.; Arakawa, R.; Fukuzumi, S. *Angew. Chem., Int. Ed.* **1999**, *38*, 2774. (d) Neves, A.; Verani, C. N.; de Brito, M. A.; Vencato, I.; Mangrich, A.; Oliva, G.; Souza, D. D. H. F.; Batista, A. A. *Inorg. Chim. Acta* **1999**, *290*, 207. (e) Vaidyanathan, M.; Viswanathan, R.; Palaniandavar, M.; Balasubramanian, T.; Prabhaharan, P.; Muthiah, T. P. *Inorg. Chem.* **1998**, *37*, 6418. (f) Zurita, D.; Gautier-Luneau, I.; Ménage, S.; Pierre, J.-L.; Saint-Aman, E. *J. Biol. Inorg. Chem.* **1997**, *2*, 46.

(31) (a) Storr, T.; Sugai, Y.; Barta, C. A.; Mikata, Y.; Adam, M. J.; Yano, S.; Orvig, C. *Inorg. Chem.* **2005**, *44*, 2698. (b) Melchior, M.; Rettig, S. J.; Liboiron, B. D.; Thompson, K. H.; Yuen, V. G.; McNeill, J. H.; Orvig, C. *Inorg. Chem.* **2001**, *40*, 4686. (c) Clevette, D. J.; Nelson, W. O.; Nordin, A.; Orvig, C.; Sjoberg, S. *Inorg. Chem.* **1989**, *28*, 2079.

(32) Lord, S. J.; Epstein, N. A.; Paddock, R. L.; Vogels, C. M.; Hennigar, T. L.; Zaworotko, M. J.; Taylor, N. J.; Driedzic, W. R.; Broderick, T. L.; Westcott, S. A. *Can. J. Chem.* **1999**, *77*, 1249.
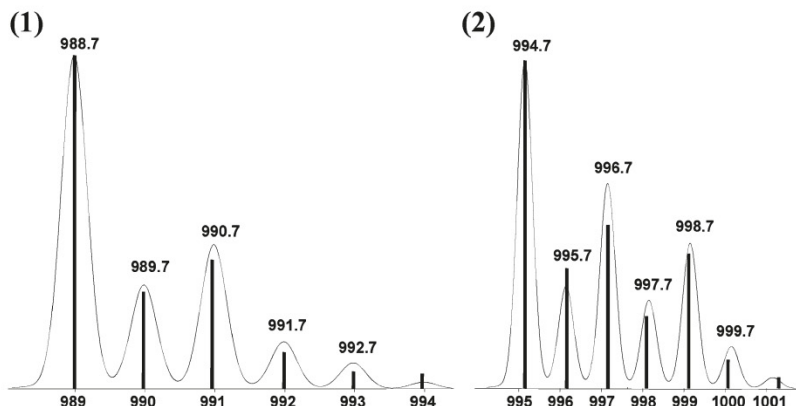
Figure 1. ESI(pos) peak clusters for $[1+(H^+)]^+$ and $[2+(H^+)]^+$ in methanol. The relative abundance axis of each complex is omitted for clarity.

equivalent gallium complex[26]) or lipophilicity.[33−36] Such changes can address concerns with future oral administration as therapeutics.

Syntheses, Spectrometric, and Spectroscopic Evaluation. Complexes $[Ni(L^{IA})_2]$ (1) and $[Zn(L^{IA})_2]$ (2) were synthesized by treatment of HL^{IA} with the proper acetate salts in methanol and were isolated in good yields (~80%). Triethylamine was used as a base to ensure ligand deprotonation. Spectrometric evaluation of 1 and 2 in methanol using electrospray ionization mass spectrometry (ESIMS) in the positive mode led to identification with a good isotopic distribution for the main peaks, $m/z = 988.7$ and 994.7, respectively, for $[1+(H^+)]^+$ and $[2+(H^+)]^+$ (Figure 1). The 1:1 ligand-to-metal species were also detected via ESIMS. Since such species only become prominent at higher cone voltages, they were considered a direct result of the fragmentation of 1 and 2. Infrared spectra confirmed the presence of the ligand and revealed the absence of peaks at ca. 1560 and 1450 cm^{-1} associated with potential acetate counterions. This gives further evidence that the 2:1 ligand-to-metal species are the favored products. Furthermore, elemental analyses were in excellent agreement with those expected for 1 and 2.

The ^{1}H NMR spectrum of the ligand shows the expected signals for protons at the pyridine and phenol rings between 7.0 and 9.0 ppm.[26] Distinctive signals for methylene groups vicinal to the pyridine and phenol rings appear respectively as singlet peaks at 3.94 and 3.91 ppm. At room temperature, the ^{1}H NMR spectrum of the zinc complex 1 is comparable to that of the ligand with further splitting of the peaks between 7 and 9 ppm, suggestive of two ligands with dissimilar conformations. Equally distinctive is the observation that the methylene signals become broadened and split into six ill-defined bands, indicating that the complex

is not rigid[37] and that at least six of the eight methylene protons are nonequivalent. By lowering the temperature to ca. −60 °C, these signals coalesce into three peaks. The amine proton, originally at 3.49 ppm in the ligand, splits into two broad peaks at 1.77 and 1.18 pm and appears at 2.20 ppm at low temperatures. The nickel species yielded broad and ill-defined ^{1}H NMR results, in agreement with the paramagnetic nature of a 3d^8 high-spin species. A detailed investigation of the ligand dynamics[38] of 1 and its gallium-containing counterpart[26] using VT-NMR properties is under development.

Molecular Structural Characterization. Good crystals for X-ray diffractometric analyses were isolated for 1 and 2 in chloroform and dichloromethane, respectively, and their molecular structures were determined. The ORTEP renditions for 1 and 2 are shown in Figure 2, and selected bond lengths and angles are displayed in Table 1. Complex 1 crystallizes in a monoclinic space group $P2_1/n$ composed of a nickel(II) ion coordinated to two deprotonated $(L^{IA})^-$ ligands, with each of them containing an $[N_{py}N_{am}O_{phen}]$ set of donors. Both ligands are facially coordinated with the two pyridine rings (Ni−$N_{py} \approx 2.09$ Å), the two amine groups (Ni−$N_{am} \approx 2.09$ Å), and the two phenolate rings (Ni−$O_{phen} \approx 2.04$ Å), arranged trans to one another to yield a pseudo-octahedral geometry. Crystals of 2 appeared as colorless needles and crystallize in an orthorhombic $P2_12_12_1$ space group, also showing a similar facial coordination of the $(L^{IA})^-$ ligands in a pseudo-octahedral geometry. However, whereas 1 exhibits a symmetrical all-trans environment described as $[Ni < N_{am1}N_{am2} > < N_{py1}N_{py2} > < O_{(phO-)1}O_{(phO-)2} >]$[39] in a bent arrangement,[36] 2 is described as having an all-cis $[Zn < N_{am1}O_{(phO-)2} > < N_{py1}N_{am2} > < O_{(phO-)1}N_{py2} >]$. As observed by the ^{1}H NMR spectrum with distinctive signals for methylene groups, the two ligands present dissimilar conformations.

We have demonstrated the role played by structural and electronic effects in a series of 3d$^{5−10}$ $[M(L)_2]$ species with such asymmetric NN′O ligands. Although ligand rigidity enforces *meridional* coordination in similar imine

(33) (a) Kirin, S. I.; Dübon, P.; Weyhermüller, T.; Bill, E.; Metzler-Nolte, N. *Inorg. Chem.* **2005**, *44*, 5405. (b) Kirin, S. I.; Happel, C. M.; Hrubanova, S.; Weyhermüller, T.; Klein, C.; Metzler-Nolte, N. *Dalton Trans.* **2004**, 1201.

(34) Shakya, R.; Imbert, C.; Hratchian, H. P.; Lanznaster, M.; Heeg, M. J.; McGarvey, B. R.; Allard, M.; Schlegel, H. B.; Verani, C. N. *Dalton Trans.* **2006**, 2517.

(35) Shakya, R.; Hindo, S. S.; Wu, L.; Allard, M. M.; Heeg, M. J.; Hratchian, H. P.; McGarvey, B. R.; Da Rocha, S. R. P.; Verani, C. N. *Inorg. Chem.* **2007**, *46*, 9808.

(36) Lesh, F. D.; Hindo, S. S.; Heeg, M. J.; Allard, M. M.; Jain, P.; Peng, B.; Hryhorczuk, L.; Verani, C. N. *Eur. J. Inorg. Chem.* **2009**, 345.

(37) Mugesh, G.; Singh, H. B.; Butcher, R. J. *Eur. J. Inorg. Chem.* **2001**, 669.

(38) Coggin, D. K.; Gonzalez, J. A.; Kook, A. M.; Stanbury, D. M.; Wilson, L. J. *Inorg. Chem.* **1991**, *30*, 1115.

(39) The notation $< A_1B_2 >$ indicates that A is trans to B, with A and B corresponding to the pyridine (Npy), amine (Nam), or phenolate (OphO−) donors. Subscripts 1 and 2 designate the first or the second ligand.
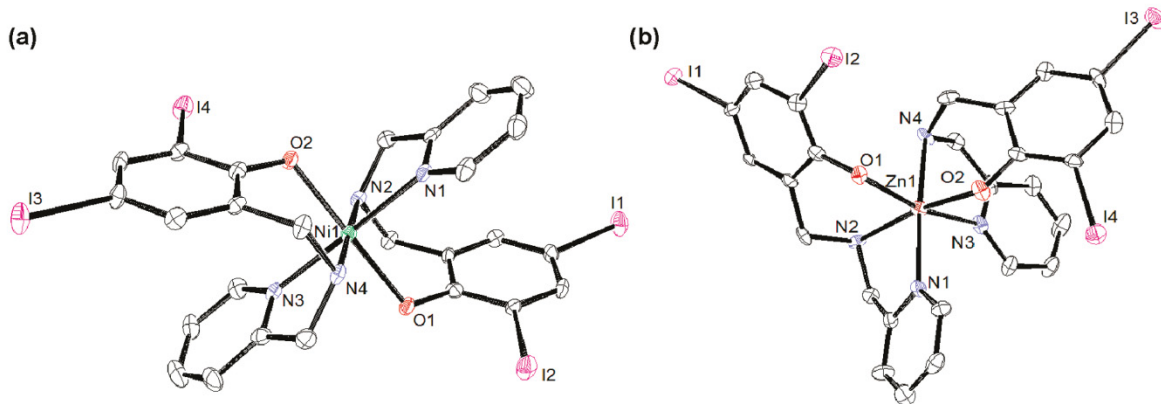
Figure 2. ORTEP diagrams at 50% probability level for **1** (a) and **2** (b).

Table 1. Selected Bond Lengths (Å) and Angles (deg) for **1** and **2**

1	2
Ni(1)−O(2) = 2.036(2)	Zn(1)−O(2) = 2.025(6)
Ni(1)−O(1) = 2.057(2)	Zn(1)−O(1) = 2.111(5)
Ni(1)−N(2) = 2.088(3)	Zn(1)−N(1) = 2.149(6)
Ni(1)−N(3) = 2.090(3)	Zn(1)−N(4) = 2.179(6)
Ni(1)−N(4) = 2.096(3)	Zn(1)−N(2) = 2.181(7)
Ni(1)−N(1) = 2.098(3)	Zn(1)−N(3) = 2.259(7)
O(2)−Ni(1)−O(1) = 179.52(10)	O(2)−Zn(1)−O(1) = 92.0(2)
O(2)−Ni(1)−N(2) = 87.86(10)	O(2)−Zn(1)−N(1) = 90.0(2)
O(1)−Ni(1)−N(2) = 91.99(10)	O(1)−Zn(1)−N(1) = 99.6(2)
O(2)−Ni(1)−N(3) = 89.60(10)	O(2)−Zn(1)−N(4) = 92.4(2)
O(1)−Ni(1)−N(3) = 90.87(10)	O(1)−Zn(1)−N(4) = 88.7(2)
N(2)−Ni(1)−N(3) = 99.14(11)	N(1)−Zn(1)−N(4) = 171.3(3)
O(2)−Ni(1)−N(4) = 92.66(10)	O(2)−Zn(1)−N(2) = 168.9(2)
O(1)−Ni(1)−N(4) = 87.49(10)	O(1)−Zn(1)−N(2) = 89.2(2)
N(2)−Ni(1)−N(4) = 179.47(11)	N(1)−Zn(1)−N(2) = 79.0(2)
N(3)−Ni(1)−N(4) = 80.76(11)	N(4)−Zn(1)−N(2) = 98.6(2)
O(2)−Ni(1)−N(1) = 88.86(10)	O(2)−Zn(1)−N(3) = 87.9(2)
O(1)−Ni(1)−N(1) = 90.66(10)	O(1)−Zn(1)−N(3) = 166.7(2)
N(2)−Ni(1)−N(1) = 81.01(11)	N(1)−Zn(1)−N(3) = 93.7(2)
N(3)−Ni(1)−N(1) = 178.45(11)	N(4)−Zn(1)−N(3) = 78.1(3)
N(4)−Ni(1)−N(1) = 99.10(12)	N(2)−Zn(1)−N(3) = 93.5(2)

ligands, electronic configuration leads to a *facial* coordination mode in flexible amines. The metal centers also dictate the preferential cis or trans orientation of equivalent phenolates and other donor sets in vicinal ligands, with $3d^5_{high-spin}$ ions[40] displaying a cis arrangement and $3d^6_{low-spin}$ and $3d^7_{high-spin}$ ions[36,37] supporting a trans orientation. Species **1** reinforces[38] the notion of an all-trans mode for $3d^8$ configurations, whereas **2** seems to fall within other $3d^{10}$ configurations[26,41−43] lacking a clear preference. Another remark is that, while most of the $O_{phenolate}$ bond lengths for **1** and **2** are comparable at 2.02−2.05 Å, one of the $Zn−O_{phenolate}$ bonds for **2** is elongated, reaching ca. 2.11 Å. This longer bond length is comparable to values found in the literature.[44] This is

(40) Imbert, C.; Hratchian, H. P.; Lanznaster, M.; Heeg, M. J.; Hryhorczuk, L. M.; McGarvey, B. R.; Schlegel, H. B.; Verani, C. N. *Inorg. Chem.* **2005**, *44*, 7414.

(41) Lanznaster, M.; Neves, A.; Vencato, I.; Bortoluzzi, A. J.; Gallardo, H.; Machado, S. P.; Assumpcao, A. M. C. *J. Braz. Chem. Soc.* **2006**, *17*, 289.

(42) Neves, A.; Vencato, I.; Verani, C. N. *J. Braz. Chem. Soc.* **1997**, *8*, 265.

(43) dos Anjos, A.; Bortoluzzi, A. J.; Szpoganicz, B.; Caro, M. S. B.; Friedermann, G. R.; Mangrich, A. S.; Neves, A. *Inorg. Chim. Acta* **2005**, *358*, 3106.

(44) Cotton, F. A.; Daniels, L. M.; Murillo, C. A.; Quesada, J. F. *Inorg. Chem.* **1993**, *32*, 4861.

attributed to the $3d^{10}$ electronic configuration of the zinc (II) ion, which favors electrostatic interactions.

Electronic Structure Calculations. A series of electronic structure calculations were carried out for the nickel-containing **1** and zinc-containing **2**, as well as on isomers with alternative geometries and binding modes, aiming at evaluating bond nature, delocalization, and energy differences between isomers. These results allowed for gaining insight on how the electronic structure of these species may foster the formation of the expected pharmacophores $[ML^{1A}]^+$. The optimized geometries for the electronic structures of **1** and **2** are in good agreement with the crystallographic data presented above.

Nickel Species. A recent study by Thomas et al.[45] on similar nickel complexes supports a favorable trans facial coordination of the ligands over the *meridional* mode by approximately 5.0 kcal/mol using a comparable level of theory. Therefore, we restricted our studies to two different all-trans *facial* isomers, namely, the structurally characterized **1** and a hypothetical **1′**. Isomer **1** displays both phenolate rings in parallel planes, whereas these same rings are perpendicular to one another in **1′** (Figure 3A). The energy difference between the two structures is 3.7 kcal/mol, clearly favoring **1** as the lowest energy state. Interestingly, we recently compared similar isomers with unsubstituted phenolate rings,[38] and the energy difference was a mere 1.1 kcal/mol. It can be suggested that the iodine substituents play a significant role in favoring **1** instead of **1′**. Furthermore, both isomers display triplet ground states with $S = 1$, consistent with a $3d^8$ high-spin configuration where two unpaired electrons populate the $d_{x^2−y^2}$ (SOMO) and d_{z^2} (SOMO−1) orbitals (Figure 3B).

Because divalent zinc is a $3d^{10}$ ion, it lacks LFSE, and the coordination mode is most likely the result of ligand sterics. For **2**, we observed a new facial all-cis [Zn < $N_{am1}O_{(phO−)2} >$ < $N_{py1}N_{am2} >$ < $O_{(phO−)1}N_{py2} >$] coordination mode for a doubly deprotonated species, well in contrast with the all-trans counterpart obtained by Neves et al.[43] with a nonsubstituted ligand. Thus, two different facial isomers were explored for the zinc complex, as shown in Figure 4A: the structurally characterized **2** and a hypothetical **2′** that matched the geometry

(45) Rotthaus, O.; Labet, V.; Philouze, C.; Jarjayes, O.; Thomas, F. *Eur. J. Inorg. Chem.* **2008**, 4215.

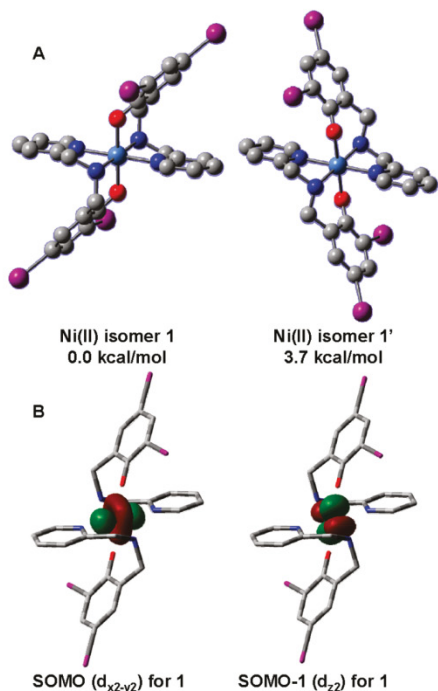**Figure 3.** (A) Depiction of the two facial [Ni(L^{IA})$_2$] isomers **1** and **1'**. (B) Selected MOs for unpaired electrons.
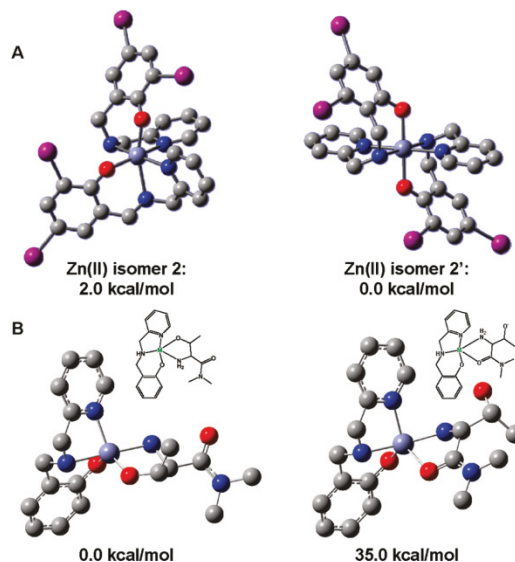

Figure 4. (a) Depiction of the two facial [Zn(L^{IA})$_2$] isomers **2** and **2'**. (b) Possible interaction between the fragment [Zn(L^{IA})]$^+$ and threonine.

adopted for the nickel-containing **1**. Interestingly, the calculations favor **2'** by a small margin of less than 2.0 kcal/mol, thus, in disagreement with the observed structure. Therefore, in the absence of a LFSE, the bonding is mainly ionic in nature, and other factors such as solvation, crystal packing, or intermolecular force effects must control the final geometry.

In order to address partial atomic charges, natural bond order (NBO) analysis was performed with both **1** and **2**; the results are shown in Table 2. It is clear from these charge distributions that the interaction between the Ni(II) center in **1** and the ligand is more delocalized, that is, covalent, than the interaction between the Zn(II) center and the ligand in **2**. This can be seen by lower charges on the metal: 1.3 for **1** versus 1.6 for **2**. The values for other atoms in **2** are consistently larger in magnitude, reinforcing the notion of more localized, that is, ionic, bonds. These values indicate that there is less stabilization of the positive divalent metal charge onto the ligands for **2** over **1**. This difference is significant, since both complexes are discrete neutral species with an overall zero charge. Thus, it is possible to conclude that an ionic nature would favor ligand dissociation in the biologic milieu for **2**, and the equilibrium suggested in Scheme 1 should be facilitated.

Finally, initial theoretical treatment of the possible binding modes between the fragment [Zn(L^{IA})]$^+$ and a deprotonated threonine residue were also performed. A simplified [Zn(L)]$^+$ fragment with an unsubstituted ligand was used, and in order to model the terminal nature of the threonine residue, a dimethylated amide residue was incorporated, as shown in Figure 4B. Two coordination modes were probed: the first considered

Table 2. NBO Partial Atomic Charges

	Ni (**1**)	Zn (**2**)
M	1.3	1.6
O1	−0.87	−0.90
O2	−0.87	−0.92
N1	−0.56	−0.64
N2	−0.75	−0.77
N3	−0.56	−0.61
N4	−0.75	−0.80

binding between the zinc center at the [Zn(L)]$^+$ fragment with the terminal (and deprotonated) hydroxyl group and the secondary amine group, whereas the second focused on the binding through the secondary amine and the carbonyl group of the amide residue. The first binding mode is approximately 35 kcal/mol more stable, and although this proposition is merely speculative at this point, it suggests that terminal hydroxo/amine coordination to zinc would be favored.

Induction of Cell Death and Inhibition of Cell Proliferation. The cytotoxic effects of NiCl$_2$, ZnCl$_2$, **1**, and **2** were tested in human leukemia Jurkat T cells treated at different concentrations for 18 h. After each treatment, a trypan blue exclusion assay was performed to assess cell death (Figure 5A). Cells treated with **2** exhibited a dose-dependent activity reaching 48%, 70%, 95%, and 100% cell death at 7.5, 10, 15, and 20 μmol/L, respectively. This turned to be the single viable species, since the metal salts and **1** had marginal cell-death induction, smaller than ∼10% compared with DMSO-treated cells, at as high as 20 μmol/L.

To substantiate this effect further, we evaluated whether **2** can suppress cell proliferation of human prostate cancer cells. C4-2B human prostate cancer cells were treated with NiCl$_2$, ZnCl$_2$, **1**, **2**, and the DMSO control at different concentrations for 18 h, followed by measurement of cell proliferation by MTT assay (Figure 5B). It was observed that cells treated with **2** suppressed cell
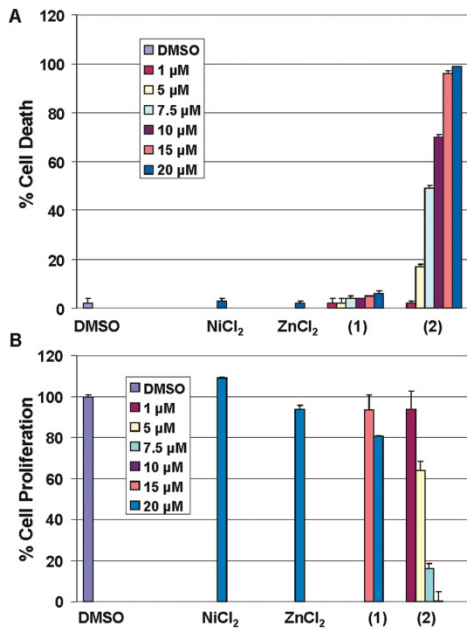
Figure 5. Cell death (A) and cell growth inhibition (B) on human leukemia and prostate cancer cells by $NiCl_2$, $ZnCl_2$, **1**, and **2**.
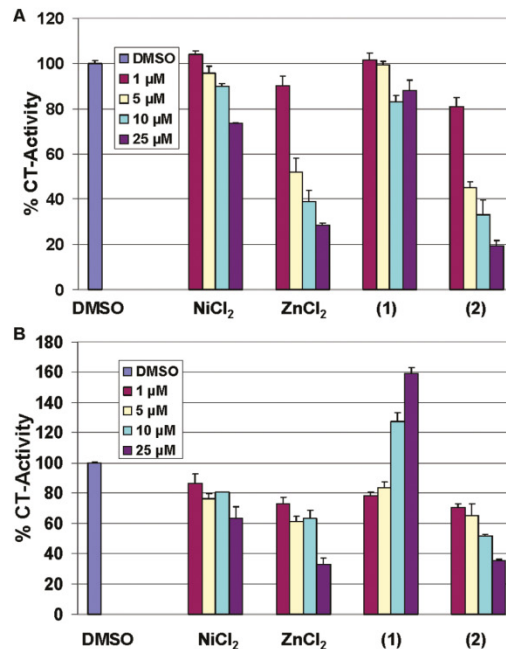

Figure 6. *In vitro* proteasome-inhibitory activity of $NiCl_2$, $ZnCl_2$, **1**, and **2**. (A) Inhibition of CT-like activity of 26S proteasome in C4-2B cell extract. (B) Inhibition of the CT-like activity of purified 20S proteasome.

proliferation in a dose-dependent manner (IC_{50} = ∼6 μmol/L), reaching 100% inhibition at 10 μmol/L. Furthermore, cells treated with **2** at 5 and 7.5 μmol/L decreased cell proliferation by ∼35% and ∼85%, respectively. Consistently, C4-2B cells treated with the metal salts or **1** showed little or no inhibitory effect, even at the highest concentration tested of 20 μmol/L.

In Vitro **Proteasome Inhibition.** To test the proteasome inhibitory capacity of these species, a comparison of the inhibitory activity of $NiCl_2$, $ZnCl_2$, **1**, and **2** to the 26S proteasomal activity was performed under cell-free conditions. An extract of C4-2B prostate cancer cells (Figure 6A) was used, and the results indicate that both the $ZnCl_2$ salt and **2** have the potential to inhibit the chymotrypsin-like activity of the 26S proteasome with IC_{50} values of 5.7 and 4.4 μmol/L, respectively. This result is consistent with our previous finding that zinc dithiocarbamate complexes can target and inhibit the proteasome.[46] However, extracts treated with **1** at as high as 25 μmol/L showed only ∼20% inhibition on the 26S proteasome, suggesting that intrinsic distinctive mechanisms of inhibition must be present for **1** and **2**. Consistent with this finding is the fact that $NiCl_2$ at 25 μmol/L could only inhibit the proteasomal activity by ∼25%.

To provide direct evidence for distinct mechanisms, we incubated a purified rabbit 20S proteasome with $NiCl_2$, $ZnCl_2$, **1**, and **2** at various concentrations, followed by measurement of the chymotrypsin-like activity (Figure 6B). We found that this activity was significantly inhibited with the salt $ZnCl_2$ and **2** with similar potencies (IC_{50} = 16.6 and 11.7 μmol/L, respectively). Although $NiCl_2$ showed modest inhibitory activity, **1** was rather inactive. Overall, our data remain consistent with the fact that the zinc ion,

both as a chloride salt and a complex with the $(L^{IA})^-$ ligand, is able to target and inhibit the proteasome under cell-free conditions.

Proteasome Inhibition and Apoptosis Induction in Intact Cancer Cells. To confirm the ability of **2** to inhibit the proteasomal activity in intact tumor cells, C4-2B human prostate cancer cells were first treated with different concentrations (5, 10, and 25 μmol/L) of $NiCl_2$, $ZnCl_2$, **1**, and **2** for 18 h, followed by measurement of proteasome inhibition. The values for proteasomal chymotrypsin-like activity are given as a percentage in Table 3. The C4-2B cells treated with **2** showed a dose-dependent inhibition of the proteasomal activity of 31% inhibition at 10 μmol/L and an 86% inhibition at 25 μmol/L. Consistently, levels of ubiquitinated proteins were increased in a dose-dependent manner in C4-2B cells (Figure S1, Supporting Information). In comparison, cells treated with either $NiCl_2$, $ZnCl_2$, or **1** showed negligible proteasome inhibitory effect.

It has been shown that proteasome inhibition can lead to decreased levels of androgen receptor (AR) expression.[47,48] Therefore, a decrease in such expression should be observed assuming proteasome activity inhibition by **2**. Consistently, this is the only species that down-regulated significantly AR, and 25 μmol/L treatment completely abrogated AR expression levels (Figure S1, Supporting Information). These results remain consistent with the ability of **2** to inhibit the proteasome activity.

It has been shown that inhibition of the proteasomal chymotrypsin-like activity selectively in transformed cells

(46) Milacic, V.; Chen, D.; Giovagnini, L.; Diez, A.; Fregona, D.; Dou, Q. P. *Toxicol. App. Pharm.* **2008**, *231*, 24.

(47) Lin, H. K.; Altuwaijri, S.; Lin, W. J.; Kan, P. Y.; Collins, L. L.; Chang, C. *J. Biol. Chem.* **2002**, *277*, 36570.

(48) Yang, H. J.; Murthy, S.; Sarkar, F. H.; Sheng, S.; Reddy, G. P. V.; Dou, Q. P. *J. Cell. Physiol.* **2008**, *217*, 569.

Table 3. Percentile of CT-Activity after Treatment with $NiCl_2$, $ZnCl_2$, **1**, and **2**

	dose, μM	C4-2B, %	SD^a (+/−)	PC3%	SD^a (+/−)	MCF 10A %	SD (+/−)
DMSO		100	0.81	100	1.56	100	3.00
$NiCl_2$	25	92	1.41	99	0.10	98	1.83
$ZnCl_2$	25	99	0.90	127	0.45	116	1.56
	5	84	0.87	101	0.01		
$[Ni(L^{IA})_2]$ (**1**)	10	83	0.96	81	1.59		
	25	80	2.27	92	0.85	89	1.96
	5	111	1.02	114	2.63	118	0.55
$[Zn(L^{IA})_2]$ (**2**)	10	69	0.14	17	1.38	97	1.48
	25	14	0.68	10	1.13	83	1.59

^{a} Standard deviation.

could result in the induction of apoptosis.[23] To investigate whether proteasome inhibition and androgen receptor down-regulation are associated with apoptotic cell death, apoptotic-specific poly-ADP-ribose polymerase (PARP) disappearance and morphological changes were measured in the same experiment (Figure 7, Figure S1, Supporting Information). The results show that only cells treated with 25 μmol/L of **2** were able to completely abrogate full-length PARP, whereas cells treated with either $NiCl_2$, $ZnCl_2$, or **1** at the highest concentration tested had little visible effects. Consistently, morphological changes (detached, shrunken, and apoptotic blebbing) were observed in cells treated with 25 μmol/L of **2** and to a significant but lesser extent at 10 μmol/L (Figure 7). Much fewer aberrant morphological changes were detected in the cells treated with metal salt or **1** at the highest concentration tested (Figure 7). These results show that the induction of apoptosis in C4-2B cells by **2** is associated with inhibition of the proteasomal chymotrypsin-like activity.

Upon demonstrating the ability of **2** to inhibit the proteasomal chymotrypsin-like activity in AR-dependent C4-2B prostate cancer cells, we then tested the effect of **2** on AR-independent PC-3 human prostate cancer cells. PC-3 cells were treated with 5, 10, and 25 μmol/L of **1** or **2** and their metal salt for 18 h, followed by measurement of the proteasome activity, accumulated levels of ubiquitinated proteins, and apoptosis induction. The percentage
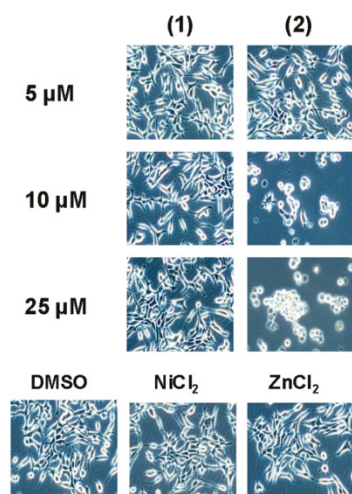
of proteasomal chymotrypsin-like activity is designated in Table 3 with DMSO as a control. We found that **2** could inhibit the proteasomal activity and induce apoptotic cell death in PC-3 prostate cancer cells, whereas **1**, $NiCl_2$, and $ZnCl_2$ showed little or no effect (Table 3, Figure S2).

Kinetics of Proteasome Inhibition and Apoptosis Induction. To study the kinetic effect of proteasome inhibition, C4-2B prostate cancer cells were treated with 15 μmol/L of **2** over different time points (2−18 h), and their cell lysates were used to measure the proteasomal-chymotrypsin-like activity (Figure 8A). The proteasomal chymotrypsin-like activity was inhibited by 18%, 42%, 57%, and 63% respectively at 2, 4, 8, and 18 h. This result was consistent with the time-dependent increase in levels of accumulated ubiquitinated proteins. Furthermore, lower levels of AR were detected in cells treated with **2** at all time points, and complete abrogation of AR expression is detected in cells after 18 h of treatment. Importantly, apoptosis-specific PARP down-regulation was detected at later time points, with complete PARP disappearance at 18 h (Figure S3, Supporting Information). Apoptosis induction at later time points is also typified with the appearance of aberrant morphological changes (detached, shrunken, and apoptotic blebbing; Figure 8B). These results clearly demonstrate that induction of the apoptosis occurs after proteasome inhibition. Thus, proteasome inhibition appears to be required for apoptosis induction.

Tumor Cell Selectivity. The ability to distinguish normal from malignant cells is of paramount importance for

Figure 7. Cellular morphological effects of $NiCl_2$, $ZnCl_2$, **1**, and **2** on C4-2B prostate cancer cells.
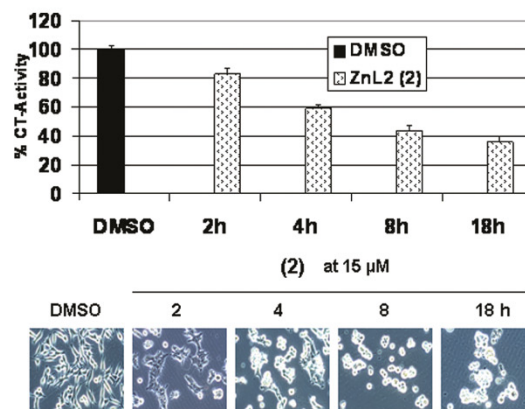
Figure 8. Kinetic effect of proteasome inhibition and apoptosis induction by **2** in C4-2B prostate cancer cells.

developing clinically relevant anticancer drugs. To determine whether inhibition of prostate cancer cellular proteasome activity achieved by **2** is selective toward malignant cells but not normal cells, we used normal-immortalized human breast cell line MCF-10A. The MCF-10A cells were treated with different concentrations of **2** as high 25 μmol/L for 18 h, followed by measurement of proteasomal chymotrypsin-like activity and apoptosis. We found that when these nontransformed cells were treated with **2**, only 17% proteasome inhibition was detected at the highest concentrations tested (Table 3). Other treatments also had little effect on MCF-10A cells (Table 3). To determine whether the inability of **2** to inhibit the proteasome activity at sustainable levels is associated with the lack of apoptosis induction in these normal immortalized breast cells, apoptosis-associated morphological changes were then assessed in the same experiment. These normal, immortalized MCF-10A cells showed only little such cell-death-related detachment after treatment with **2** up to 18 h at the highest concentration tested (Figure S4, Supporting Information). Furthermore, the species NiCl$_2$, ZnCl$_2$, and **1** had little or no cytotoxic effect on normal cells. Our data suggest that **2** could inhibit the proteasome activity and induce apoptosis selectively in human cancer cells but not in normal immortalized cells, validating **2** as a promising proteasome inhibitor.

Summary and Conclusions

In this paper, we report on two new coordination complexes as potential anticancer candidates, namely, [Ni(L^{IA})$_2$] (**1**) and [Zn(L^{IA})$_2$] (**2**). Both species were characterized by several spectroscopic, spectrometric, and structural methods and display a well-established 2:1 ligand-to-metal stoichiometry. DFT calculations considering different isomers of **1** and **2** were performed and show good agreement with the nickel species but fail to predict the appropriate geometry for the zinc-containing species. Furthermore, initial studies considering coordination of a 1:1 [Zn(L)]$^+$ fragment with threonine suggest a favorable coordination through the terminal hydroxyl group of the amino acid.

The effects of NiCl$_2$, ZnCl$_2$, **1**, and **2** were tested toward a purified rabbit 20S proteasome and 26S proteasome in cell extracts (in which cell membranes have been disrupted) of leukemia and human prostate cancer cell lines. The results indicate that only **2** and ZnCl$_2$ have a direct inhibitory effect on the proteasome to any significant level. Furthermore, when NiCl$_2$, ZnCl$_2$, **1**, and **2** were tested on the 26S proteasome of cultured intact leukemia and human prostate cancer cells, it was evidently shown that only **2** exhibited potent antiproliferative and cell-death-inducing activity. Similarly, only **2** induced higher levels of ubiquitinated proteins, which were associated with decreased levels of proteasomal chymotrypsin-like activity. In addition, the decrease of proteasomal chymotrypsin-like activity observed for **2** is tightly associated with tumor cell apoptosis, as seen by the morphological changes and the apparent disappearance of the full-length PARP fragment. Species **2** also showed remarkably low cytotoxicity toward normal human breast cells.

This sharp contrast in proteasome activity inhibition between **1** and **2** is suggested to be related to the nature of the metal ion and its degree of reactivity when combined with

NN′O-containing ligands. As observed in similar complexes from our group,[24] considerable proteasome inhibition can be attained through 1:1 ligand-to-metal species that is believed to be the pharmacophore in all of these species. Therefore, an equilibrium [M(L^{IA})$_2$] ↔ [M(L^{IA})]$^+$ + L^{IA-} seems necessary to facilitate the formation of the pharmacophore with available coordination sites capable of interaction with the 20S proteasome, likely to be via the N-terminal threonine residue. It is observed from the molecular structures and DFT calculations available that covalent interactions prevail in **1**, while **2** is ionic in nature. We, therefore, propose that this intrinsic difference defines the facility of pharmacophore formation and determines the activity of these species. The lack of activity observed for ZnCl$_2$ in intact cells reinforces the notion offered for the equivalent copper counterparts[24] that the ligand (L^{IA})$^-$ serves as a shuttle vector to cross the cellular membrane. Taken together, we suggest that the presence of the fragment [Zn(L^{IA})]$^+$ is required for proteasome inhibition. At this point, it is not clear whether the ligand dissociation [Zn(L^{IA})$_2$] ↔ [Zn(L^{IA})]$^+$ + L^{IA-} is intra- or extracellular, and, if intracellular, before or after reaching the 26S proteasome. Furthermore, it is likely that water molecules will coordinate to the zinc ion, forming [Zn(L^{IA})-(H$_2$O)$_n$]$^+$ hydrated species. The investigation of these issues is a current goal of our groups and will be properly developed in the future. Nonetheless, the data observed thus far provide a compelling rationale for the clinical development of **2** as a potential anticancer drug.

Experimental Section

Materials and Methods. All reagents were obtained from commercial sources and were used as received. Methanol was distilled over CaH$_2$. IR spectra were measured from 4000 to 400 cm^{-1} as KBr pellets on a Tensor 27 FTIR spectrophotometer. ESI spectra in the positive mode were measured in methanol on a Micromass Quattro LC triple quadrupole mass spectrometer with an electrospray/APCI source and a Walters Alliance 2695 LC autosampler and photodiode array UV detector. Experimental assignments were simulated on the basis of peak location and isotopic distributions. The ^{1}H NMR spectra were measured in CDCl$_3$ on a Varian Unity-300 instrument. Elemental analyses were performed by Midwest Microlab, Indianapolis, Indiana. Trypan blue exclusion dye was purchased from Sigma Aldrich (St. Louis, MO). The peptide substrate Suc-LLVY-AMC (for the proteasomal chymotrypsin-like activity) was purchased from Calbiochem, Inc. (San Diego, CA). RPMI 1640, penicillin, and streptomycin were purchased from Invitrogen (Carlsbad, CA). Fetal bovine serum was purchased from Aleken Biologicals (Nash, TX). Antibodies against ubiquitin, actin, and secondary antibodies were purchased from Santa Cruz Biotechnology (Santa Cruz, CA). Mouse monoclonal antibody against human PARP was purchased from BIOMOL International LP (Plymouth Meeting, PA).

X-Ray Structural Determination for [Ni(L^{IA})$_2$] (1) and [Zn(L^{IA})$_2$] (2). Diffraction data were measured on a Bruker X8 APEX-II κ geometry diffractometer with Mo radiation and a graphite monochromator. Frames were recorded for 10 s at 100 K with the detector at 40 mm and 0.3° between each frame. APEX-II[49] and SHELX[50] software were used in the collection and refinement of the models (Table 4).

Crystals of [Ni(L^{IA})$_2$] (**1**) were colorless plates. A total of 86 456 reflections were counted, which averaged to 10 883

(49) APEX II collection and processing programs are distributed by the manufacturer: *APEX II*; Bruker AXS Inc.: Madison WI, 2005.
(50) Sheldrick, G. M. *Acta Crystallogr.* **2008**, *A64*, 112–122.

Table 4. Crystal Data and Structure Refinements for [Ni(L^{IA})$_2$] (**1**) and [Zn(L^{IA})$_2$] (**2**)

formula	C$_{29}$H$_{25}$C$_{19}$I$_4$N$_4$O$_2$Ni	C$_{29}$H$_{30}$C$_{16}$I$_4$N$_4$O$_3$Zn
fw	1346.89	1268.24
space group	$P2_1/n$	$P2_12_12_1$
a (Å)	18.4231(5)	13.2593(4)
b (Å)	10.1797(3)	15.4882(5)
c (Å)	22.1493(6)	19.6143(6)
β (deg)	92.8120(10)	
V (Å^3)	4148.9(2)	4028.0(2)
Z	4	4
temp (K)	100(2)	100(2)
λ (Å)	0.71073	0.71073
density, calcd (Mg cm^{-3})	2.156	2.091
μ (mm^{-1})	4.057	4.109
R(F) (%)^a	3.63	6.33
Rw(F) (%)^a	5.91	13.18

^{a} $R(F) = \sum ||F_o| - |F_c||/\sum|F_o|$; $Rw(F) = [\sum w(F_o^2 - F_c^2)^2/\sum w(F_o^2)^2]^{1/2}$ for $I > 2\sigma(I)$.

independent data. Hydrogen atoms were placed at calculated positions except for those on nitrogen which were observed. The complex crystallized with 3 equiv of chloroform. All atoms occupy general positions.

Crystals of [Zn(L^{IA})$_2$] (**2**) appeared as colorless needles. A total of 77 377 reflections were measured, yielding 14 112 unique data. Hydrogen atoms were placed in calculated positions. The complex crystallized with 3 equiv of methylene chloride and 1 equiv of water. All atoms occupy general positions.

Electronic Structure Calculation Methods. The B3LYP level of theory[51] with the SDD[52] basis sets was employed throughout because of the presence of iodine atoms, and all of the calculations were done using the Gaussian[53] series of programs. Geometries were fully minimized, without symmetry constraints, using standard methods.[54] Located stationary points were characterized by computing analytic vibrational frequencies. Reported energies include zero-point correction. Cartesian coordinates of all of the optimized structures are provided in the Supporting Information.

Syntheses. The iodo-substituted ligand HL^{IA} was synthesized by the treatment of 2-hydroxy-3,5-diiodobenzaldehyde with 2-aminomethylpyridine in methanol followed by reduction with sodium borohydride, as previously published.[26]

(51) (a) Becke, A. D. *J. Chem. Phys.* **1993**, *98*, 5648. (b) Becke, A. D. *Phys. Rev. A* **1988**, *38*, 3098. (c) Lee, T.; Yang, W. T.; Parr, R. G. *Phys. Rev. B* **1988**, *37*, 785. (d) Gordon, M. S. *Chem. Phys. Lett.* **1980**, *76*, 163. (e) Hariharan, P. C.; Pople, J. A. *Mol. Phys.* **1974**, *27*, 209. (f) Hariharan, P. C.; Pople, J. A. *Theor. Chim. Acta* **1973**, *28*, 213. (g) Hehre, W. R.; Ditchfield, R.; Pople, J. A. *J. Chem. Phys.* **1972**, *56*, 225. (h) Ditchfield, R.; Hehre, W. R.; Pople, J. A. *J. Chem. Phys.* **1971**, *54*, 724.

(52) Dolg, M.; Wedig, U.; Stoll, H.; Preuss, H. *J. Chem. Phys.* **1987**, *86*, 866.

(53) Frisch, M. J.; Trucks, G. W.; Schlegel, H. B.; Scuseria, G. E.; Robb, M. A.; Cheeseman, J. R.; Montgomery, J. A.; Vreven, T.; Kudin, K. N.; Burant, J. C.; Millam, J. M.; Iyengar, S. S.; Tomasi, J.; Barone, V.; Mennucci, B.; Cossi, M.; Scalmani, G.; Rega, N.; Petersson, G. A.; Nakatsuji, H.; Hada, M.; Ehara, M.; Toyota, K.; Fukuda, R.; Hasegawa, J.; Ishida, M.; Nakajima, T.; Honda, Y.; Kitao, O.; Nakai, H.; Klene, M.; Li, X.; Knox, J. E.; Hratchian, H. P.; Cross, J. B.; Bakken, V.; Adamo, C.; Jaramillo, J.; Gomperts, R.; Stratmann, R. E.; Yazyev, O.; Austin, A. J.; Cammi, R.; Pomelli, C.; Ochterski, J. W.; Ayala, P. Y.; Morokuma, K.; Voth, G. A.; Salvador, P.; Dannenberg, J. J.; Zakrzewski, V. G.; Dapprich, S.; Daniels, A. D.; Strain, M. C.; Farkas, O.; Malick, D. K.; Rabuck, A. D.; Raghavachari, K.; Foresman, J. B.; Ortiz, J. V.; Cui, Q.; Baboul, A. G.; Clifford, S.; Cioslowski, J.; Stefanov, B. B.; Liu, G.; Liashenko, A.; Piskorz, P.; Komaromi, I.; Martin, R. L.; Fox, D. J.; Keith, T.; Al-Laham, M. A.; Peng, C. Y.; Nanayakkara, A.; Challacombe, M.; Gill, P. M. W.; Johnson, B.; Chen, W.; Wong, M. W.; Gonzalez, C.; Pople, J. A. *GAUSSIAN 03*; Gaussian, Inc.: Wallingford, CT, 2003.

(54) Schlegel, H. B. *J. Comput. Chem.* **1982**, *3*, 214.

[Ni(L^{IA})$_2$] (1). A 15 mL methanol solution of HL^I (0.49 g, 1.1 mmol) was added dropwise to a 15 mL of a methanol solution of Ni(OAc)$_2$·2H$_2$O (0.25 g, 1.2 mmol) at 45 °C. After 45 min, a purple precipitate was obtained, isolated by frit filtration, and washed with cold methanol and ether. The solid was recrystallized in chloroform. Yield = 0.95 g (88%). Elem anal. calcd for **1**, C$_{26}$H$_{22}$NiI$_4$N$_4$O$_2$: C, 31.58; H, 2.24; N, 5.67. Found: C, 31.47; H, 2.30; N, 5.56. IR (KBr, cm^{-1}): 3068 ν(N−H), 1606, 1593 (C=N from pyridine), 1486 (C−O from phenyl). ESI pos. in MeOH: m/z = 988.9 for [NiL$_2$ + H$^+$]$^+$.

[Zn(L^{IA})$_2$] (2). A 15 mL methanol solution containing HL^I (0.51 g, 1.1 mmol) was added dropwise to a 15 mL methanol solution of Zn(OAc)$_2$·2H$_2$O (0.26 g, 1.2 mmol) at 45 °C. A white precipitate was obtained after 1 h, isolated by frit filtration, and washed with cold methanol and ether. The solid was recrystallized in dichloromethane. Yield = 0.85 g (77%). Elem anal. calcd for **2**, C$_{26}$H$_{22}$ZnI$_4$N$_4$O$_2$: C, 31.37; H, 2.23; N, 5.63. Found: C, 31.27; H, 2.38; N, 5.58. IR (KBr, cm^{-1}): 3290 (N−H), 1608 (C=N from pyridine), 3079 ν(N−H). ESI pos. in MeOH: m/z = 994.9 for [ZnL$_2$ + H$^+$]$^+$.

Cell Cultures and Whole-Cell Extract Preparation. Human prostate cancer cells, C4-2B and PC-3, and human leukemia Jurkat T cells were grown in RPMI-1640 supplemented with 10% fetal bovine serum and maintained at 37 °C and 5% CO$_2$. MCF-10A (normal, derived from benign human breast tissue) was obtained and cultured as previously described.[55] A whole-cell extract was prepared as previously described.

Cell Proliferation Assay. Cells were seeded in quadruplicate in a 96-well plate and grown until 70−80% confluence was reached, followed by treatment with the indicated agents for 18 h. After that, the 3-(4,5-dimethylthiazol-2-yl)-2,5-diphenyltetrazolium bromide (MTT) assay was done as described previously.

Trypan Blue Assay. Jurkat T cells were treated with NiCl$_2$, ZnCl$_2$, **1**, and **2** for 18 h at the indicated concentrations followed by the measurement of cell death. The trypan blue dye exclusion assay was performed by mixing 100 μL of a cell suspension with 50 μL of 0.4% trypan blue dye before injecting it into a hemocytometer and counting. The number of cells that absorbed the dye and those that excluded the dye were counted, from which the percentage of nonviable cells to total cells was calculated.

Proteasomal Activity in Whole-Cell Extract or Purified 20S Proteasome. C4-2B whole-cell extract (8 μg) or a purified 20S rabbit proteasome (35 ng) was incubated with 10 μmol/L of the CT-substrate, Suc-LLVY-AMC, in 100 μL of the assay buffer [50 mmol/L Tris-HCl (pH 7.5)] in the presence of NiCl$_2$, ZnCl$_2$, **1**, and **2** at various concentrations or solvent DMSO as a control. After 2 h of incubation at 37 °C, the production of hydrolyzed AMC groups was measured using a Wallac Victor3 multilabel counter with an excitation filter of 365 nm and an emission filter of 460 nm.

Proteasome CT-Like Activity in Cells. Proteins extracted from cells after each treatment were incubated for 2 h at 37 °C in 100 μL of the assay buffer (50 mmol/L Tris-HCL, pH 7.5) with 10 μmol/L of the fluorogenic substrate Suc-LLVY-AMC, as described previously.

Western Blot Analysis. Cell extracts were separated by SDS-PAGE and transferred to a nitrocellulose membrane. A western blot analysis was performed using specific antibodies to PARP, ubiquitin, or AR, followed by visualization using the HyGLO reagent (Denville Scientific, Metuchin, NJ).

Cellular Morphology Analysis. A Zeiss Axiovert 25 microscope was used for all microscopic imaging with phase contrast for cellular morphology. Magnification was ×100.

(55) Daniel, K. G.; Chen, D.; Orlu, S.; Cui, Q. C.; Miller, F. R.; Dou, Q. P. *Breast Cancer Res.* **2005**, *7*, R897.

Supporting Information Available: This material is available free of charge via the Internet at http://pubs.acs.org.

Appendix I

Copper, Nickel and Zinc Amphiphiles

Frank D. Lesh, Sarmad Sahiel Hindo, Mary Jane Heeg, Marco M. Allard, Prateek Jain, Bo Peng,

Lew Hryhorczuk, Cláudio N. Verani

"On the Effect of Coordination and Protonation Preferences in the Amphiphilic Behavior of

Metallosurfactants with Asymmetric Headgroups"

My contribution to this work consisted of the electronic structure calculations.

On the Effect of Coordination and Protonation Preferences in the Amphiphilic Behavior of Metallosurfactants with Asymmetric Headgroups

Frank D. Lesh,[a] Sarmad Sahiel Hindo,[a] Mary Jane Heeg,[a] Marco M. Allard,[a] Prateek Jain,[a] Bo Peng,[a] Lew Hryhorczuk,[a] and Cláudio N. Verani*[a]

The metallosurfactants $[Ni^{II}(L^{tBuODA})(OAc)]$ (**1**), $[Ni^{II}(L^{tBuODA})_2]$ (**2**), $[Cu^{II}(HL^{tBuODA})(L^{tBuODA})]ClO_4 \cdot CH_3OH$ (**3**), and $[Zn^{II}(HL^{tBuODA})_2](ClO_4)_2$ (**4**) {where HL^{tBuODA} = 2,4-di-*tert*-butyl-6-[(octadecyl(pyridin-2-ylmethyl)amino)methyl]phenol} were synthesized and characterized in an attempt to establish how coordination modes and protonation preferences relate to amphiphilic behavior. The archetypical compounds $[Ni^{II}(L^{tBuI})(OAc)] \cdot CH_3OH$ (**5**), $[Ni^{II}(L^A)_2] \cdot CH_3OH \cdot H_2O$ (**6**), $[Ni^{II}(L^{tBuA})_2] \cdot 2CH_3OH$ (**7**), $[Cu^{II}(HL^{tBuA})(L^{tBuA})]ClO_4$ (**8**), and $[Zn^{II}(HL^{tBuA})(L^{tBuA})]ClO_4$ (**9**) were synthesized to model the stoichiometric, coordination, and protonation chemistry in the waxy metallosurfactants **1–4**. Detailed data analysis and comparison between **1–4** and **5–9** involved mass spectrometric and spectroscopic methods along with crystallographic determination of **5** ($P2_1/c$), **6** ($P\bar{1}$), **7** ($P2_1/c$), **8'** (the analogue of **8** with tetraphenylborate counterions, $P2_1/c$), and **9** ($P\bar{1}$). DFT calculations were used to identify the frontier orbitals, polarizability, and dipole moments. Species **1–4** had their compression isotherms measured and monitored by means of Brewster angle microscopy. The nickel-containing **1** is square planar, while **2** has a neutral octahedral core with two deprotonated ligands. The five-coordinate copper-containing **3** has a monocationic core associated with one protonated ligand, whereas the dicationic zinc-containing **4** has a four-coordinate core with protonated ligands. It was observed that Langmuir films of **1** display approximately half of the average molecular area observed for **2–4** and that the flexibility and coordination number of the cores foster distinctive collapse mechanisms. Therefore, careful choice of the metal ion leads to control of surfactant-to-metal ratio, selection of coordination modes and structural properties, and the understanding of the protonation preferences of the ligands. This information will play an important role in the development of metal-containing responsive films.
(© Wiley-VCH Verlag GmbH & Co. KGaA, 69451 Weinheim, Germany, 2009)

Introduction

Molecular architectures displaying cooperativity among transition metals and amphiphilic organic scaffolds combine unique geometric, electronic, redox, and magnetic behavior[1–4] with distinctive ordering morphologies. The approach has been used with impressive results in the design of soft materials with tixotropic,[5] mesogenic,[6] ionophoric,[7] luminescent,[8] and micellar[9] properties. This fact points out to the potential role of discrete metallosurfactant materials in the emerging field of responsive thin films.[10,11,12] However, metallosurfactants (i.e. surfactants containing transition-metal ions) are usually assembled at the air/water interface without isolation of the precursors. As a consequence, lack of precise control in (i) the surfactant-to-metal ratio, (ii) the coordination modes and the final structure of the material, and (iii) protonation preferences limit reproducibility leading to adventitious defects. Therefore having well defined, isolated, and characterized

precursors is of paramount importance. Nevertheless, the small body of work available on the isolation and air/water interface behavior of metallosurfactant precursors still poses a major drawback to the approach.[13,14]

At the forefront of this area, our group has focused on synthetic, modeling, and surface protocols involving the incorporation of magnetic μ-oxo-Cu_4 clusters in Langmuir–Blodgett films,[15,16] the observation of distinctive collapse mechanisms on cobalt(II) films,[17] and the design of redox-active copper-containing amphiphiles.[18,19] In a series of studies with iron(III),[20] cobalt(II/III),[21] and gallium-(III)[22] we have demonstrated that structural and electronic effects can determine the preferential geometry of redox-active asymmetric NN′O ligands in $[ML_2]$ metallosurfactants. Structural rigidity of the ligand takes precedence to the electronic configuration of the metal ion and favors *meridional* coordination when asymmetric amines and imines are compared. On the other hand, electronic configuration is a determining factor when flexible amines are involved; a *facial* coordination mode is preferred, and the metal dictates the preferential *cis* or *trans* orientation of equivalent phenolates and other donor sets in vicinal ligands. Consequently, $3d^5$ high-spin configuration leads to *cis*-arrangement while $3d^6$ low-spin and $3d^7$ high-spin ions support

[a] Department of Chemistry, Wayne State University,
  5101 Cass Ave., Detroit, MI 48202, USA
  Fax: +1-313-577-8822
  E-mail: cnverani@chem.wayne.edu
  Supporting information for this article is available on the WWW under http://www.eurjic.org or from the author.

trans-orientation. Gallium(III), with $3d^{10}$ configuration, does not seem to exhibit a clear preference. These observations are serving as guidelines to the design of metal-containing amphiphiles for redox-responsive Langmuir–Blodgett films.

In this article we describe the synthesis and amphiphilic behavior of nickel(II), copper(II), and zinc(II) complexes with an asymmetric NN'O ligand. Due to the $3d^{8-10}$ electronic configurations found in these bivalent metal ions, stoichiometric preferences, coordination modes, and ligand protonation status can lead to distinct $[M^{II}(HL)X]^{2+}$, $[M^{II}(L)X]^+$, $[M^{II}(L)_2]^0$, $[M^{II}(HL)(L)]^+$, and $[M^{II}(HL)_2]^{2+}$ products (Scheme 1). Because of the waxy texture of most of the resulting metallosurfactants, archetypical modeling (i.e. the investigation of a series of discrete complexes that retain key structural and electronic attributes) was used to assess the nature of these products. A careful comparison between the stoichiometric and protonation status and the amphiphilic behavior is offered.
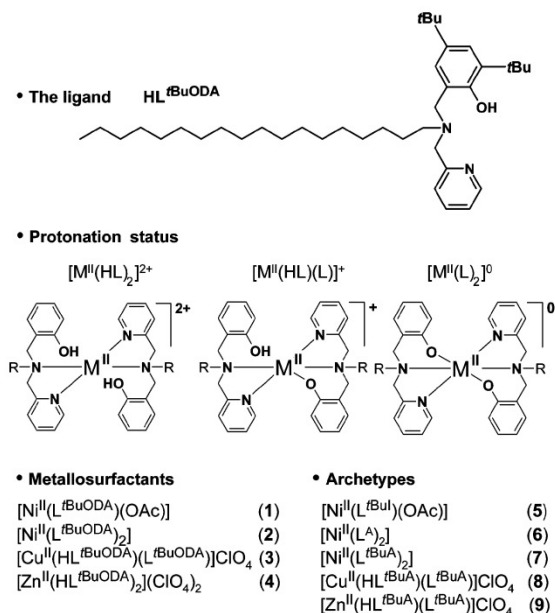
Scheme 1. The ligand HL^{tBuODA}, possible protonation status for metallosurfactants and archetypes studied.

Results and Discussion

The Ligands

Condensation of 1-octadecylamine with 2-pyridinecarboxaldehyde in methanol with subsequent reduction in the presence of sodium borohydride gave the amine precursor that was treated with 2,4-di-*tert*-butyl-6-(chloromethyl)phenol to generate the ligand HL^{tBuODA}. Similarly, the archetypical ligands were synthesized with 80–85% yields following literature procedures[17,20,21] and characterized by means of ESI mass spectrometry, ^{1}H NMR, and infrared spectroscopy.

The Metallosurfactants

Treatment of the ligand HL^{tBuODA} with several metal salts yielded products with textures varying from waxy to solid. Compound $[Ni^{II}(L^{tBuODA})(OAc)]$ (**1**) was isolated upon complexation in methanol of HL^{tBuODA} with nickel-(II) acetate tetrahydrate in a 1:1 ligand-to-metal ratio. Similarly, treatment of the ligand with hexahydrated perchlorate salts of nickel(II), copper(II), or zinc(II) in a 2:1 ratio yielded $[Ni^{II}(L^{tBuODA})_2]$ (**2**), $[Cu^{II}(HL^{tBuODA})(L^{tBuODA})]$-ClO$_4$·CH$_3$OH (**3**), and $[Zn^{II}(HL^{tBuODA})_2](ClO_4)_2$ (**4**), respectively. Triethylamine was used as a base to assist phenol deprotonation in all cases. The waxy constitution of compounds **1** and **2** precluded elemental analysis as a tool for characterization. The ESI mass analysis of **1** indicates the presence of peak clusters at $m/z = 635.4$ and $m/z = 695.4$ corresponding respectively to $[Ni(L^{tBuODA})]^+$ and $[Ni-(L^{tBuODA})(OAc) + H]^+$. The former peak is favored at higher cone voltages, whereas the latter is more abundant at lower cone voltages. Similarly, **2** shows a peak cluster at $m/z = 1214.0$ providing evidence for species such as $[Ni(L^{tBuODA})_2 + H]^+$ or $[Ni(HL^{tBuODA})(L^{tBuODA})]^+$. The use of triethylamine in the synthetic procedure, as well as the absence of infrared peaks at 1090 cm^{-1} for perchlorate counterions, supports that the ligands are fully deprotonated and that the singly charged peak observed is formed in situ. The ESI mass analysis of **3** suggests the formation of the cationic species $[Cu^{II}(HL^{tBuODA})(L^{tBuODA})]^+$ with a peak cluster at $m/z = 1219.0$. Likewise, **4** shows a peak cluster at $m/z = 1220.0$ implying the formation of the species $[Zn^{II}(HL^{tBuODA})(L^{tBuODA})]^+$. Additional interpretation of the fragmentation patterns suggests the existence of the species $[Zn^{II}(HL^{tBuODA})_2]^{2+}$, as confirmed by a prominent peak cluster at $m/z = 641.5$ for the species $[Zn^{II}-(HL^{tBuODA})_2 + CH_3OH]^{2+}$. This dicationic species is par-
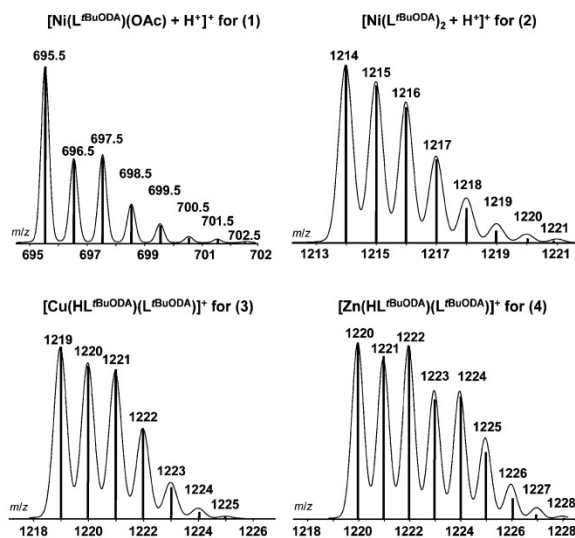
Figure 1. ESI(pos) peak clusters with experimental (bars) and simulated (continuum) isotopic distributions for **1**–**4**. The relative abundance axis of each complex is omitted for clarity.

ticularly visible at low cone voltages. The peak clusters of interest were simulated and agree well in their patterns, positions, and isotopic distributions, and substantiate the behavior of the metal ions. These spectrometric profiles are shown in Figure 1. Infrared analysis further suggests metal coordination by the sharp doublet of the C=N bonds in pyridine rings between 1590–1570 cm^{-1}. These peaks are shown broadened and shifted in the spectra of the compounds, along with the presence of characteristic C–H stretching contribution of the alkyl chain and tertiary butyl groups from the ligand. Additionally, **1** shows an antisymmetric stretch at 1574 cm^{-1} for its coordinated acetate. While the neutral compound **2** lacks a perchlorate peak, **3** and **4** display strong Cl–O stretchings at ca. 1105 cm^{-1}, indicative of the presence of perchlorate counterions. Because precipitates were isolated for **3** and **4**, elemental analyses were carried out and are in good agreement with these formulations.

The Archetypes

Archetypical modeling was used in order to correlate the amphiphilic behavior observed for **1–4** with detailed structural information. A series of discrete complexes was studied in which the long alkyl chain is replaced by a hydrogen atom, whereas other key features like the chelating headgroup are left unchanged. These species were synthesized using perchlorate salts analogously to the metallosurfactants above, and are described as [Ni^{II}(L^{tBuI})(OAc)]·CH$_3$OH (**5**), [Ni^{II}(L^A)$_2$]·CH$_3$OH·H$_2$O (**6**), [Ni^{II}(L^{tBuA})$_2$]·2CH$_3$OH (**7**), [Cu^{II}(HL^{tBuA})(L^{tBuA})]ClO$_4$ (**8**), and [Zn^{II}(HL^{tBuA})(L^{tBuA})]ClO$_4$ (**9**). The archetypical ligands HL^{tBuI}, HL^A, and HL^{tBuA} are depicted in Scheme 2. Species **7** has been recently studied by Thomas et al.,[23] along with a series of related [Ni^{II}(NN'O)$_2$] complexes, but no X-ray structure was available. Elemental analyses of the compounds **5–9** are in excellent agreement with theoretical percentages, and the ESI(pos) mass spectra exhibit distinct *m/z* = [M^{II}(L)$_2$]$^+$ and [M^{II}(HL)(L)]$^+$ peaks in methanol. Peak cluster simulation of these archetypes parallel those obtained for the metallosurfactants **1–4**, reinforcing the notion

Figure 2. ORTEP diagrams at 50% probability for **5**, **6**, **7**, **8'**, and **9**. Solvents, counterions, and hydrogen atoms are excluded for clarity.
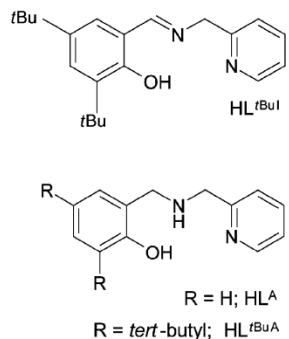
Scheme 2. The ligands HL^{tBuI}, HL^A, and HL^{tBuA} used in the archetypes.

that the expected ligand-to-metal ratios were achieved. The neutrality of the nickel(II) complexes, as well as the presence of protonated ligands, is once again confirmed by the

respective absence or presence of a peak associated with the perchlorate counterion at around 1100–1090 cm^{-1} in their IR spectra.

Molecular Structures and Coordination Modes

Discrete mononuclear crystals of archetypes **5**–**9** were structurally resolved by X-ray diffraction. The ORTEP diagrams are displayed in Figure 2, and selected bond lengths and angles summarized in Table 1.

The Nickel Archetypes 5, 6, and 7: The coordination environment for the nickel(II) metal center in complex **5** approximates a square-planar geometry with the deprotonated ligand (L^{tBuI})$^-$ meridionally coordinated through an NN'O donor set of N$_{imine}$ and N$_{pyridine}$, and O$_{phenolate}$ atoms, along with a deprotonated terminally coordinated acetate group occupying the fourth position. Both *trans* angles are smaller than 180°, thus confirming a distorted square-planar geometry. The bond angles and lengths at the metal center agree with literature values of mono-substituted imine complexes with similarly organized donor frameworks. For example, the Ni–O$_{phenolate}$, Ni–O$_{acetate}$, and Ni–N$_{imine}$ bonds herein are 1.82, 1.88 and 1.84 Å, respectively, closely resembling the values found for the complex [Ni(L)(OAc)], where L is the deprotonated form of the 6-[(E)-({[(2S)-1-benzylpyrrolidin-2-yl]methyl}imino)-methyl]-2-*tert*-butyl-4-methylphenol.[24] Finally, it is noteworthy that the ligand (L^{tBuI})$^-$ in **5** is definitely an imine, as evidenced by the short bond length between C7–N1 (1.30 Å). Even though the ligand (L^{tBuODA})$^-$ in **1** is more flexible than that in **5** and could possibly adopt a facial conformation in a tetrahedral coordination sphere, the preferential coordination modes of a low-spin 3d^8 ion like nickel(II) should favor a square-planar geometry. Therefore, **5** provides an acceptable model for the coordination environment for the surfactant **1**.

Complexes **6** and **7** are intended to act as archetypical models for species **2**, which displays two fully deprotonated ligands (L^{tBuODA})$^-$ and neutral character. In fact the results observed for both archetypes with ligands (L^A)$^-$ for **6** and (L^{tBuA})$^-$ for **7** give consistent information about the coordination modes of NN'O ligands around nickel(II). The coordination geometries resemble those observed for cobalt(III/II) complexes recently reported by this group.[17,21] These structures are arranged pseudo-octahedrally in an approximate D_{2h} local symmetry about the nickel(II) center, coordinated by two deprotonated, facially coordinated ligands. Hence, **6** and **7** are described in BMT[25] notation as [Ni <N$_{am1}$N$_{am2}$> <N$_{py1}$N$_{py2}$> <O$_{phen1}$O$_{phen2}$>]. The Ni–N$_{amine}$ bond lengths consistently measure 2.11 Å, while the Ni–O$_{phenolate}$ bond lengths are 2.09 Å and the Ni–N$_{pyridine}$ bond lengths are 2.08 and 2.10 Å. The six-coordinate geometry and absorption spectra (vide infra) indicate the presence of a high spin 3d^8 ion.[23,26] On the basis of the structures of these two archetypes, an accurate picture of the coordination modes present in **2** can be drawn.

The Copper Archetype 8': By means of counterion exchange, single crystals of the complex [Cu^{II}(HL^{tBuA})-(L^{tBuA})]B(Ph)$_4$ (**8'**) were obtained from the perchlorate parent species **8** to gather comparative information about the coordination modes and geometrical parameters of the copper-containing surfactant **3**. It contains a discrete [Cu^{II}(HL^{tBuODA})(L^{tBuODA})]$^+$ cation in which a single ligand is deprotonated, whereas another one remains protonated. Therefore, the coordination sphere around the copper(II) center in **8'**, and consequently in **8** and **3** as well, approximates a distorted N$_2$N$_2$'O square-pyramidal geometry (τ = 0.34)[27] in which the protonated O$_{phenol}$ assumes a remote position (viz. Cu1···O2 > 3.80A). The angles between adjacent corner atoms of the basal plane (O1–Cu1–N2 93.0°, O1–Cu1–N4 91.2°, N1–Cu1–N4 92.4°, and N2–Cu1–N1 81.0°) are consistent with pseudo-square pyramidal interplane angles approximating 90°, where the atoms O1, N4, N1, and N2 are situated on the vertices of the plane, while the pyridine nitrogen, N3, is apically coordinated to the copper center (2.27 Å). The *trans* amine nitrogen to opposing amine nitrogen bond angle is 152.4° and the *trans* phenolate oxygen to pyridine nitrogen bond angle is 173.0°, leaving the bond angles comprising the apical pyridine ni-

Table 1. Selected bond lengths [Å] and angles [°] for **5**, **6**, **7**, **8'**, and **9**.

5	6	7	8'	9
Ni1–O1 1.8215(9)	Ni1–O1 2.0916(17)	Ni1–O1 2.0869(13)	Cu1–O1 1.9501(15)	Zn1–O1 1.960(3)
Ni1–N1 1.8416(10)	Ni1–N1 2.0829(18)	Ni1–N1 2.1039(16)	Cu1–N2 1.9938(18)	Zn1–N3 2.074(4)
Ni1–N2 1.8863(10)	Ni1–N2 2.1119(19)	Ni1–N2 2.1117(17)	Cu1–N4 2.0419(19)	Zn1–N2 2.141(4)
Ni1–O2 1.8840(8)			Cu1–N1 2.0609(19)	Zn1–N1 2.147(4)
			Cu1–N3 2.2708 (19)	Zn1–N4 2.175(4)
Bite angles	Bite angles	Bite angles	Bite angles	Bite angles
O1–Ni1–N1 94.87(4)	O1–Ni1–N2 89.60(7)	O1–Ni1–N2 89.66(6)	O1–Cu1–N2 93.01(7)	O1–Zn1–N2 94.10(13)
N1–Ni1–N2 85.72(4)	N1–Ni1–N2 79.86(7)	N1–Ni1–N2 80.12(6)	N2–Cu1–N1 81.02(7)	N2–Zn1–N1 78.96(15)
			N4–Cu1–N3 79.21(7)	N3–Zn1–N4 80.44(14)
Average distances	Average distances	Average distances	Average distance	Average distances
Py C–C 1.3856(18)	Py C–C 1.3835(3)	Py C–C 1.371(3)	Py C–C 1.381(3)	Py C–C 1.374(8)
Py C–N 1.3534(15)	Py C–N 1.3395(3)	Py C–N 1.347(2)	Py C–N 1.345(3)	Py C–N 1.346(6)
Ph C–C 1.4081(16)	Py C–C 1.3933(4)	Ph C–C 1.3975(3)	Ph C–C 1.398(3)	Ph C–C 1.396(7)

trogen (O1–Cu1–N3 98.3°, N2–Cu1–N3 126.9°, N4–Cu1–N3 79.2°, and N1–Cu1–N3 88.2°) to reveal the degree of structural distortion. The increased copper to apical pyridine nitrogen bond length (2.27 Å) grants further evidence concerning the structure: the phenol group is neither bonded nor contributing structurally to the rigidity of the system. The other pyridine is situated *cis* to this apical pyridine with a Cu–N distance of 2.06 Å. Also occupying *cis* positions are the $O_{phenolate}$ atom (Cu1–O1 1.95 Å) and the N_{amine} atom (Cu1–N2 2.0 Å) of the deprotonated ligand. In addition, the N_{amine} of the protonated ligand is positioned *trans* (Cu1–N4 2.04 Å) to its opposing N_{amine} of the deprotonated ligand. These bond lengths are in good agreement with reported values.[28,29]

The Zinc Archetype 9: Analogous to the copper(II) center in the archetypical systems **8** and **8′**, the zinc(II) metal center in complex **9** bears ligand coordination through an $N_2N_2'O$ donor set consisting of two tertiary amine and pyridine nitrogen atoms, and a single deprotonated phenolate oxygen atom. Similarly, the second phenol oxygen atom is protonated and lies 3.42 Å from the metal center. Calculation of the relative amount of trigonality reveals that the structural coordination geometry is more characteristic of trigonal bipyramidal geometry with a τ value of 0.79. The pseudo-trigonal bipyramidal geometry of the complex demonstrates facial ligand coordination organized in an approximate C_{2v} local symmetry, where the phenolate oxygen atom (Zn1–O1 1.96 Å) and pyridine nitrogen atoms (Zn1–N1 2.15, Zn1–N3 2.07 Å) are positioned on the vertices of the equatorial plane, and the *trans* tertiary amine nitrogen atoms are apically coordinated to the zinc center (Zn1–N2 2.14, Zn1–N4 2.17 Å). The angles at the zinc ion center around the equatorial plane are consistent with pseudo-trigonal bipyramidal inter-plane angles approximating the ideal 120° (O1–Zn1–N1 128.41°, N1–Zn1–N3 114.29°, N3–Zn1–O1 117.24°), while the N2–Zn1–N4 axial bond angle

is 175.98°, deviating slightly from 180° linearity. The range for the pyridine nitrogen to amine nitrogen axial-to-equatorial bond angles containing the zinc ion center, N_{ax}–Zn–N_{eq}, is 80–100°, and the amine nitrogen to phenolate oxygen axial-to-equatorial bond angle range at the zinc ion center, N_{ax}–Zn–O_{eq}, is 89–94°. For purpose of contrast, it is interesting to consider the distinguishing features that exist between zinc complexes with local pseudo-trigonal bipyramidal geometries. For instance the cation [Zn(TMPA)(OBz)]$^+$,[30] where TMPA is tris[(2-pyridyl)-methyl]amine and OBz is a benzoate ligand, is functionally comparable to **9**. The TMPA-based complex exhibits a slightly elongated Zn^{II} to axial N_{amine} bond length (2.26 Å) along with shorter Zn–$N_{pyridine}$ distances, when compared to **9**. The axial Zn–$O_{benzoate}$ bond (1.95 Å), on the other hand, is nearly equivalent to the equatorial Zn–$O_{phenolate}$ bond (1.96 Å) in **9**. Equally relevant is the precise crystallographic work described by Neves et al.[31–33] on zinc-phenolate ligands. It has been postulated that both the nature of the phenol ring substituent and the geometry adopted around the metal play a crucial role in the length of the Zn–$O_{phenolate}$ bond. Unsubstituted ligands yield the longest bonds (2.15 Å), whereas bromo- and *tert*-butyl-substituted phenolates yield comparable bonds reaching 1.90 to 1.96 Å, respectively. This is in good agreement with the value observed for **9**. It is noteworthy that while most ligands yield [ZnL$_2$] species, *tert*-butyl-substituted ligands are prone to form partially protonated [Zn(HL)(L)]$^+$ species. This has been observed even when zinc acetate, which fosters phenol deprotonation, is used. Unfortunately, **9** does not seem to be a valid archetypical model for **4**. The archetype possesses a single protonated ligand, whereas elemental analysis and mass spectrometry support the presence of two protonated ligands in the surfactant. This is also consistent with an unusual collapse mechanism pattern observed in the Langmuir films of **4**.

Table 2. UV/vis parameters for ligands and complexes.

Compounds [a] Ligands	λ [nm] (ε) [L mol^{-1} cm^{-1}][b]
HL^{tBuODA}	263 (7290), 268 (7200), 280 (5600)
HL^{tBuA}	262 (3750), 268 (3550), 282 (2990)
Nickel species	
[Ni^{II}(L^{tBuODA})(OAc)] (**1**)	288 (6180), 422 (860), 604 {11} [c]; 965 {8}
[Ni^{II}(L^{tBuI})(OAc)]·CH$_3$OH (**5**)	261(6250), 348 sh (4030), 425, (915), 510 {10}
[Ni^{II}(L^{tBuODA})$_2$] (**2**)	264 (9350), 620 {31}, 965 {12}
[Ni^{II}(L^4)$_2$]·2CH$_3$OH (**6**)	304 (8250), 605 {14}, 952 {5}
[Ni^{II}(L^{tBuA})$_2$]·2CH$_3$OH (**7**)	306 (9220), 610 {18}, 960 {8}
Copper species[d]	
[Cu^{II}(HL^{tBuODA})(L^{tBuODA})]ClO$_4$·CH$_3$OH (**3**)	247 (18200), 287 (9340), 328 sh (4900), 498 (1060), 651 (660)
[Cu^{II}(HL^{tBuA})(L^{tBuA})]ClO$_4$ (**8**)	241 (20900), 289 (9800), 474 (1140), 640 (490)
Zinc species	
[Zn^{II}(HL^{tBuODA})$_2$](ClO$_4$)$_2$ (**4**)	263 (9540), 269 (8300), 290 (6340)
[Zn^{II}(HL^{tBuA})(L^{tBuA})]ClO$_4$ (**9**)	240 (12530), 289 (4600)

[a] Spectra measured in dichloromethane/methanol (1:1), unless otherwise noted. [b] Values for equivalent peaks within a similar group are sorted in columns. [c] All solutions are 1.0×10^{-4} M, except for values indicated in curly brackets where 1.0×10^{-2} M solutions were used. [d] Spectra measured in dichloromethane.

Electronic Spectroscopy

The electronic spectra of the ligands HL^{tBuODA} and HL^{tBuA}, surfactant complexes 1–4, and archetypes 5–9 were measured either in dichloromethane or in 1:1 solutions of dichloromethane/methanol. The results are summarized in Table 2 and selected spectra for the copper species 3 and 8 are shown in Figure 3. The ligands HL^{tBuODA} and HL^{tBuA} show expected similarities in the ultraviolet region, assigned to intense intraligand $\sigma \rightarrow \pi^*$ and $\pi \rightarrow \pi^*$ bands.
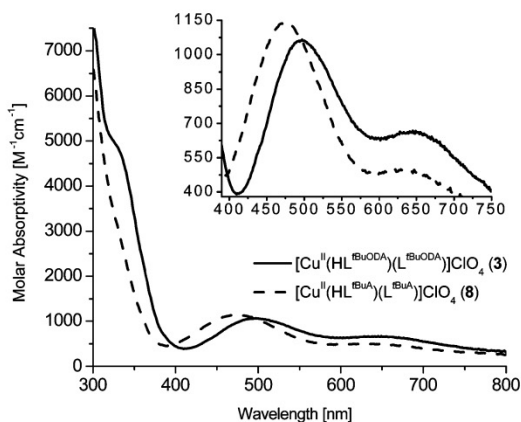
Figure 3. UV/vis spectra of complexes 3 and 8 in dichloromethane, 1.0×10^{-4} M. Inset: 3 and 8 at 1.0×10^{-2} M.

Electronic information is also limited for 4 and 9 as a consequence of the intrinsic nature of the $3d^{10}$ zinc(II) ion. The interpretation of the spectra is restricted to the observation of comparable profile contours for the intraligand $\pi \rightarrow \pi^*$ bands in both species. Assessment of the differences in coordination geometry revealed by mass spectrometry and elemental analysis was not possible. The square-planar $3d^8$ low-spin ($S = 0$) nickel(II) complex 1 reveals its nature with a medium-intensity band at 422 nm, attributed to a $^1A_{1g} \rightarrow {}^1A_{2g}$ spin-allowed d–d transition. [34] The archetype 5 displays a similar, albeit slightly more intense, band at 425 nm, along with a ill-defined shoulder at 348 nm. These features are less intense but comparable with those of low-spin $[Ni^{II}(salen)]$,[26] and attributed respectively to charge transfer and π–π^* transitions. The nickel-centered d–d transitions are also comparable at 510 nm. The pseudo-octahedral nickel(II) species 2, 6, and 7 do not display this band and are characterized by less intense signals around 605–620 nm, ($\varepsilon \approx 20$–30) and 950–965 nm ($\varepsilon \approx 5$–15), respectively attributed to $^3A_{2g} \rightarrow {}^3T_{1g}(P)$ and $^3A_{2g} \rightarrow {}^3T_{2g}$ spin-allowed d–d transitions.[35] This is in good agreement with the observation that lower wavelength absorption bands are associated with low-spin square planar electronic configurations, while higher wavelength bands are found for high-spin octahedral configurations.[36] The positions of the observed absorptions in 1, 2, 5–7 indicate that in solution, 1 and 5 remain low-spin and 2, 6, and 7 remain high-spin. The high-spin ($S = 1$) nature of these species can be inferred by the presence of broad and ill-defined H^1 NMR peaks, but EPR detection is precluded due to the presence of an integer spin associated to the approximate $[e_g^2 t_{2g}^4]$ configuration (in an idealized O_h symmetry) for the Ni^{II} ion. Very recently Thomas et al.[23] have isolated a series of nickel compounds related to the archetypes 6, and 7 confirming the high-spin nature of pseudo-octahedral $[Ni^{II}(NN'O)_2]$ systems. The most noticeable parallel between the nickel(II) surfactant 2 and the archetypes 6 and 7 is the similarity in shape and wavelength ranges for the two overlaid spectral curves. This validates further the use of archetypical complexes in providing direct insight to the coordination mode and local geometry of the metal center in architectures of higher complexity.

The agreement between the copper-containing surfactant 3 and archetype 8 is excellent. A broad band transition present at 498 and 474 nm, respectively in 3 and 8, is attributed to a well characterized[37–39] phenolate $\rightarrow$ copper(II) charge-transfer transition. A lower intensity band centered at 640–650 nm is likely to have overlapping charge transfer and d–d band nature. The only evident deviation is the presence of a shoulder at 328 nm in the spectrum of 3 and absent in 8. This shoulder is ascribed to a $N(\pi) \rightarrow Cu^{II}$ charge transfer observed for square-pyramidal copper(II) species.[40] It is possible to hypothesize that the alkyl group attached to the N_{amine} atom in 3 impinges a certain degree of distortion to the coordination environment around copper, thus causing bathochromic shifts. Indeed, all the charge-transfer bands in 3 seem to be red-shifted by about 10–20 nm. Therefore, the shoulder at 328 nm in 3 would be overlapped by more intense intraligand bands in 8. Similar shifts have been observed by our group in phenolate-containing copper amphiples with distinct apolar chains.[18]

Electronic Structure Calculations

A series of electronic structure calculations were carried out on archetypical nickel-containing 6, copper-containing 8, and zinc-containing 9, as well as on model 3′ (a model for the copper metallosurfactant 3 comprising of shortened alkyl chains). Attempts to model 4 were made considering multiple different geometrical arrangements, but lack of convergence towards a satisfactory minimum preclude discussion at this time. Single point energy calculations on 6 were carried out with nuclear coordinates obtained directly from the crystallographic structure (see Figure 2 above). The optimized geometries for structures of 8 and 9 are in good agreement with the crystallographic data presented above. Structural and electronic properties were evaluated to gain insight on the binding modes of the amphiphilic complexes. A recent study on 7[23] supports the favorable *trans* facial coordination of the ligands over the meridional mode by ca. 5.0 kcal mol^{-1} using a comparable level of theory. Similar values were obtained for 6 suggesting that the $3d^8$ ion favors *trans,fac* coordination.

This is similar to the results observed for $3d^7$ ions, and in clear opposition to the preferred *cis,fac* observed for $3d^5$ ions. As shown in Figure 4, the spin density plot for the nickel archetype 6 is consistent with two unpaired electrons being arranged in the $d_{x^2-y^2}$ and d_{z^2} orbitals and resulting

in an $S = 1$ ground state. This triplet state is expected for six-coordinate high-spin bivalent nickel ($3d^8$) complexes. The molecular orbital plots of the singly occupied orbitals, namely the SOMO ($d_{x^2-y^2}$) and SOMO-1(d_{z^2}) orbitals are also available. The dipole moment for **6** is small in magnitude, reaching 0.10 Debye. This is not unexpected if the high symmetry of the all-*trans* binding mode of the ligands is taken into account, as it becomes clear by inspection of the spin density plot.
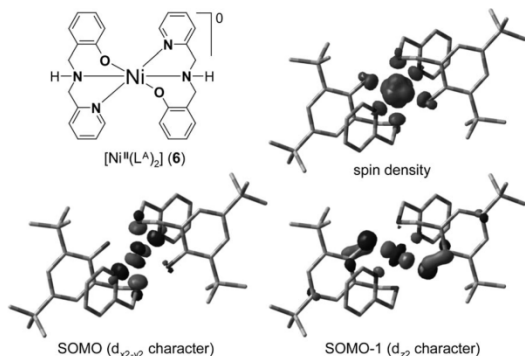
Figure 4. Selected MOs and spin density plot for the archetype **6**.

The copper archetype **8** displays the SOMO consistent with a $d_{x^2-y^2}$ orbital in good agreement with the expected behavior of a bivalent copper ($3d^9$) ion in a five coordinate complex (Figure 5). Comparison between **8** and the model **3′** shows similar geometrical arrangement and comparable bond lengths and angles. An almost identical hydrogen-bonding mode between the phenolate-phenol oxygen atoms is also present. One noticeable difference is the presence of a longer Cu–N$_{amine}$ bond length for **3′** (ca. 0.03 Å) as compared to that of **8**. This lengthening must be associated with the change from a secondary amine in **8** to a tertiary amine in **3′**, and corroborates with the observations from the UV/vis spectra. The model **3′** also displays a SOMO consistent with a $d_{x^2-y^2}$ orbital. The spin density plots reinforce this notion. Both **3′** and **8** have comparable dipole moments of 13.9 and 13.7 Debye, respectively. Overall, the archetypical **8** can be considered in excellent agreement with model **3′**, and therefore, with metallosurfactant **3**.

Owing to their $3d^{10}$ configuration, the zinc complexes exhibit an $S = 0$ spin state. Consequently, **9** has no spin density plot and its frontier bonding orbitals are predominantly ligand-based (see Figure S1, Supporting Information). This increase in ionic character can be reinforced by comparing the Mulliken charges in archetypes **8** and **9**. An increase is observed in the Mulliken charge from 0.84 for the copper center in **8** to 0.94 for the zinc center in **9**. Similarly, the copper-bound phenolate-oxygen shows a charge of –0.77, compared to –0.80 in the zinc-bound phenolate-oxygen. The increasing charge separation in **9** corroborates with a decreased covalent character. The dipole moment of **9** is on the same order of magnitude as for **3′** and **8**, though slightly larger at 14.5 Debye.
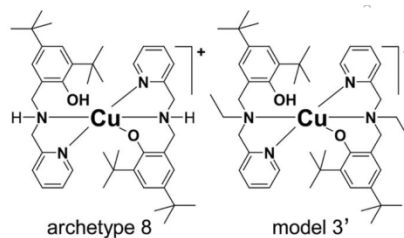
Figure 5. Selected molecular orbitals and spin-density plot for the optimized structures of the archetype **8** and model **3′**.

Amphiphilic Properties

The amphiphilic properties of species **1**–**4** were studied by way of compression isotherms[41] plotting surface pressure (Π, mN m^{-1}) vs. average area per molecule [A (Å)^2] and Brewster angle microscopy. Compression isotherms are performed in a minitrough with movable barriers and allow for two-dimensional activities that transpire at the air/water interface, which result in the formation of Langmuir films. The assessment of mono- or multilayers, collapse pressures (π_c), limiting areas per molecule (A_{lim}), and the area at the collapse of the monolayer (A_c) become evident. When the barriers of a minitrough are compressed, the tension (γ) of the amphiphile-containing air/water interface decreases as compared to that of the air/water interface only ($\gamma_0 = 72$ mN m^{-1} at 23 °C), following in an increase in Π (= $\gamma_0 - \gamma$). When conducting compression isotherms in concert with Brewster angle microscopy, polarized light passes throughout media with different refractive indexes at the air/water interface revealing agglomerates and domains, as well homogeneity in films.

Species **1**–**4** resemble structurally a series of *tert*-butyl-substituted phenolate-containing amphiphiles published recently by our group.[18] The main difference is the presence

of a methylpyridine arm attached to the N_{amine} atom. Similarly, the ligand HL^{tBuODA} used in this article is related to the ligand HL^{IODA} with iodo groups occupying the 2nd and 4th position of the phenolate ring. This ligand stabilizes bivalent cobalt ions in the $[Co^{II}(L^{IODA})_2]$ species.[17] A detailed comparison among these species will be provided. The isotherms for **1–4** are shown in Figure 6 and present moderate collapse pressures. For **1**, with a single alkyl chain and a higher dipole moment, the individual molecules start interacting at the air/water interface at around 85 Å^2 molecule^{-1}, whereas the molecules of **2**, **3**, and **4** interact at much higher areas of 185, 230, and 195 Å^2 molecule^{-1}, respectively. Hence, species **2–4** are characterized by large average areas per molecule reflecting the *trans* arrangement of the alkyl chains. At least partially, the high areas observed for **3** and **4** are also related to the presence of a cationic core. However, no clear pattern can be observed correlating an increase in average areas with increasing core charge, since the monocationic **3** displays higher areas than the dicationic **4**. In spite of the distinctive average areas, **1**, **3**, and **4** present similar profiles with an inflection point around 10–14 mN m^{-1} followed by a less steep compression pattern. Interestingly, species **4** shows a much more accentuated decline, resembling the profile of a system with constant-pressure collapse,[42] while **2** shows the opposite behavior, displaying a more steep isotherm after the inflection point at 18 mN m^{-1}. This led to the suspicion that in spite of a continuous compression profile and lack of traditional collapse, the inflection point in these systems may coincide with folding, bending, and breaking into multilayers proposed by the Ries mechanism.[43,44] Brewster angle microscopy was used to evaluate the homogeneity of the films and corroborates with the idea that agglomerates similar to those expected in multilayers exist after the inflection points. The results are shown in Figure 7, where it can be seen that for **1–4** flat domains coexist before compression at low surface pressures. Upon compression, seemingly homogeneous films are observed up to pressures that precede the inflection points, when the appearance of multiple ring-shaped events predominates. These rings are multilayer granules formed from the ejection of matter from the compressed monolayer when localized oscillations are present and account for the thermodynamic instability of the film.[45]

In an attempt to correlate structural and amphiphilic properties of **1–4**, as well as to compare with other similar metalloamphiphiles the following conclusions can be drawn: It is evident that **2–4** have roughly twice the area per molecule than **1**, this is due to the fact that **2–4** have two HL^{tBuODA} ligands coordinated to the metal center, while **1** contains a single ligand. The areas observed for **2–4** are comparable to other *tert*-butyl-substituted phenolate-containing amphiphiles.[18] Replacement of these substituents by more polar groups, as well as the design of surfactants with a single alkyl chain as in **1**, seems to be necessary to achieve ordered films with higher collapse pressures. The nickel(II) complex **2** has a neutral octahedral core with two deprotonated $(L^{tBuODA})^-$ ligands, while copper-containing **3** has a five-coordinate monocationic core associated with
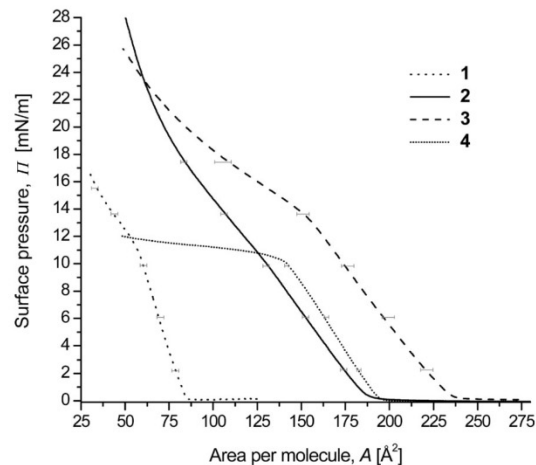
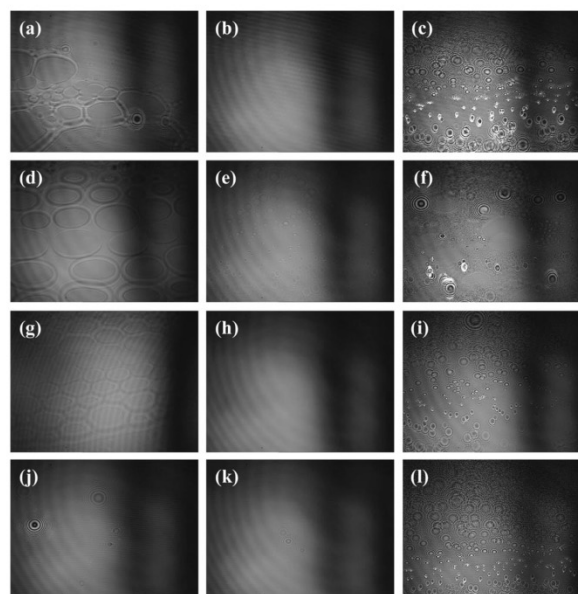Figure 6. Langmuir–Blodgett isotherms of the metallosurfactants.

Figure 7. Selected Brewster angle micrographs. For **1**: (a) before compression, (b) between 1–10 mN m^{-1}, (c) after 11 mN m^{-1}. For **2**: (d) before compression, (e) between 3–10 mN m^{-1}, (f) after 11 mN m^{-1}. For **3**: (g) before compression, (h) between 2–12 mN m^{-1}, (i) after 13 mN m^{-1}. For **4**: (j) before compression, (k) between 1–10 mN m^{-1}, and (l) after 11 mN m^{-1}.

one protonated HL^{tBuODA} ligand, and zinc-containing **4** has a dicationic four-coordinate core with both HL^{tBuODA} ligands protonated. It seems that in moving from rigid octahedral cores as in **2** to more flexible cores in **3** and **4**, a tendency toward constant-pressure collapse can be observed. This is in excellent agreement with the behavior observed for cobalt amphiphiles,[18] in which increased core-flexibility also led to a constant-pressure collapse mechanism. Finally, it is not clear why **2** and **4** display similar average areas per molecule, while **3** shows higher areas.

Summary and Conclusions

In this article we have synthesized and characterized the metallosurfactants [Ni^{II}(L^{tBuODA})(OAc)] (**1**) [Ni^{II}-(L^{tBuODA})$_2$] (**2**), [Cu^{II}(HL^{tBuODA})(L^{tBuODA})]ClO$_4$·CH$_3$OH (**3**), and [Zn^{II}(HL^{tBuODA})$_2$](ClO$_4$)$_2$ (**4**). Due to the waxy texture of some of the metallosurfactants and due to the inability of getting crystal structures for **1**–**4**, archetypical modeling was used to assess the nature of these products. For this reason, species [Ni^{II}(L^{tBuI})(OAc)]·CH$_3$OH (**5**), [Ni^{II}(L^{A})$_2$]·CH$_3$OH·H$_2$O (**6**), [Ni^{II}(L^{tBuA})$_2$]·2CH$_3$OH (**7**), [Cu^{II}(HL^{tBuA})(L^{tBuA})]ClO$_4$ (**8**), and [Zn^{II}(HL^{tBuA})(L^{tBuA})]-ClO$_4$ (**9**) were synthesized. Careful analysis of **5**–**9** allowed us to evaluate the relationship between stoichiometric, coordination, and protonation preferences in metallosurfactants **1**–**4**, and therefore, draw structure/amphiphilic function relationships.

The nickel(II) complex **1** is square planar, whereas **2** has a neutral octahedral core with two deprotonated (L^{tBuODA})$^-$ ligands. Copper-containing **3** has a five-coordinate monocationic core associated with one protonated HL^{tBuODA} ligand, whereas the zinc-containing **4** has a dicationic four-coordinate core with both HL^{tBuODA} ligands protonated. DFT calculations were used to identify the frontier orbitals, polarizability, and dipole moments. In an attempt to correlate structural and amphiphilic properties of **1**–**4**, as well as to compare with other similar metalloamphiphiles the following conclusions can be drawn: in Langmuir films of **1**, the average molecular area is approximately half of that needed for **2**–**4**. Nonetheless the areas observed for **2**–**4** are comparable to other *tert*-butyl-substituted phenolate-containing amphiphiles. The nature of the core, reflected by its flexibility and coordination number seems to foster distinctive collapse mechanisms. Flexible penta- and tetracoordinate cores show a tendency to support constant-pressure collapse mechanisms. This behavior was also observed for structurally related cobalt amphiphiles, but in that case, the coordination modes were kept constant while the ligand flexibility was variable. The results reported here suggest that (i) control of the surfactant-to-metal ratio, (ii) selection of the coordination modes and structural properties of the material, and (iii) understanding of the protonation preferences of the ligands can be achieved by careful choice of the metal ion. Awareness of this information will allow to push current limits in reproducibility of thin films of metallosurfactants and is expected to pave the way toward the development of metal-containing responsive films.

Experimental Section

Materials and Methods: Reagents and solvents were used as received from commercial sources. Methanol was distilled from CaH$_2$, and dichloromethane was doubly purified on alumina columns using an Innovative Technologies solvent purification system. Infrared spectra were measured from 4000 to 400 cm^{-1} with a Tensor 27 FTIR-Spectrophotometer as KBr pellets. ^{1}H NMR spectra were measured with Varian 300 and 400 MHz instruments. ESI(+) spectra were measured in a triple quadrupole Micromass Quat-

troLC mass spectrometer with ESCi source. Elemental analyses were performed by Midwest Microlab, Indianapolis, IN. UV/Vis spectroscopy from 1.0×10^{-2} to 1.0×10^{-4} M dimethylformamide, dichloromethane, or dichloromethane/methanol (1:1) solutions were performed using a Cary 50 spectrometer within the 250 to 1100 nm range.

Compression Isotherms: The compression isotherms were measured in an automated KSV 2000 minitrough at 23 ± 0.5 °C. Ultrapure water (Barnstead NANO pure) was used with a resistivity of 17.5–18 MΩcm^{-1} for all experiments. Surface impurities of the freshly poured aqueous subphases were removed by vacuum after barrier compression. Solutions of the complexes were prepared by dissolving 1.0 mg mL^{-1} in chloroform. A known quantity ($\approx$ 30 µL) of chloroform solutions was dispersed on the aqueous subphase, followed by ca. 20 min. equilibrium time before monolayer compression. The compression-isotherms were obtained at a compression rate of 5 mm min^{-1}. The surface pressure was measured using the Wilhelmy plate method (paper plates, 40 mm perimeter). A minimum of three independent measurements were carried out per sample with excellent reproducibility.

Brewster Angle Microscopy: A KSV-Optrel BAM 300 with a HeNe laser (10 mW, 632.8 nm) and a CCD detector were used in all micrographs. The compression rate was 5 mm min^{-1}, the field of view was 800×600 microns, and the lateral resolution was about 2 µm.

X-ray Structural Determinations: Diffraction data were measured using a Bruker P4/CCD or a Bruker X8 APEX-II kappa geometry diffractometer with Mo radiation and a graphite monochromator at 100 or 213 K. Frames were collected for 10 s and 0.2 or 0.3 ° between each frame. The frame data was indexed and integrated with the manufacturer's software.[46] SHELX-97 was used for refinement.[47] The collected crystal data for the five structures is shown in Table 3.

CCDC-703004 (for **5**), -703005 (for **6**), -703006 (for **7**), -703007 (for **8**), -703008 (for **9**) contain the supplementary crystallographic data for this paper. These data can be obtained free of charge from The Cambridge Crystallographic Data Centre via www.ccdc.cam.ac.uk/data_request/cif.

[Ni(C$_{23}$H$_{30}$N$_2$O$_3$)]·CH$_3$OH (5): Crystallized as red-amber rods, and a sample approximately $0.26 \times 0.20 \times 0.16$ mm^3 was used for data collection. 6513 frames were collected, yielding 101662 reflections, of which 8947 were independent. Hydrogen positions were placed in calculated or observed positions. The asymmetric unit consists of one neutral complex, with one equivalent of methanol solvate. [Ni(C$_{26}$H$_{26}$N$_4$O$_2$)]·(H$_2$O)·(CH$_3$OH) (**6**) crystallized as pale violet rods. A sample $0.28 \times 0.12 \times 0.15$ mm^3 was used for data collection. 1850 frames were collected, yielding 6605 reflections, of which 5292 were independent. Hydrogen positions were observed or calculated. The asymmetric unit contains two half coordination molecules, each with Ni occupying a crystallographic inversion center, and one equivalent each of solvents water and methanol.

[Ni(C$_{42}$H$_{58}$N$_4$O$_2$)]·2CH$_3$OH (**7**) crystallized as pale yellow-green rods and plates.

A sample $0.24 \times 0.18 \times 0.12$ mm^3 was used for data collection. 1850 frames were collected, yielding 53411 reflections, of which 7392 were independent. Hydrogen positions were observed and refined. The dataset exhibited a rotated 180 degree twin about the (100) reciprocal axis, and corrections were made by use of CELL-NOW, SAINT-7, and TWINABS.[46,47] The twin component refined to 41% of the total diffraction. Within the coordination complex, Ni occupies a crystallographic inversion center. The asymmetric unit

Table 3. Crystal data.

	5	6	7	8′	9
Formula	$C_{24}H_{34}NiN_2O_4$	$C_{27}H_{32}NiN_4O_4$	$C_{44}H_{66}NiN_4O_4$	$C_{67}H_{83}BCuN_4O_3$	$C_{42}H_{59}ClZnN_4O_6$
M	473.24	535.28	773.72	1066.72	816.75
Space group	$P2_1/c$	$P\bar{1}$	$P2_1/c$	$P2_1/c$	$P\bar{1}$
a [Å]	14.8325(6)	9.4001(6)	13.864(3)	10.7795(5)	11.439(3)
b [Å]	7.0996(3)	11.7678(8)	12.596(3)	27.7798(10)	13.745(5)
c [Å]	22.2614(9)	11.8448(8)	12.297(3)	20.1353(9)	15.891(5)
α [°]		100.501(1)			96.456(8)
β [°]	94.382(2)	90.400(1)	105.450(4)	97.053(2)	110.106(5)
γ [°]		101.558(2)			108.547(4)
V [Å^3]	2337.38(17)	1260.9(2)	2069.8(7)	5983.9(4)	2154.3(11)
Z	4	2	2	4	2
T [K]	100(2)	213(2)	213(2)	100(2)	213(2)
λ [Å]	0.71073	0.71073	0.71073	0.71073	0.71073
$D_{calcd.}$ [g cm^{-3}]	1.345	1.410	1.241	1.184	1.259
μ [mm^{-1}]	0.862	0.810	0.515	0.413	0.681
$R(F)$ (%)[a]	3.43	3.87	3.59	4.70	7.47
$Rw(F)$ (%)	8.87	10.09	7.61	10.38	19.88

[a] $R(F) = \Sigma||F_o| - |F_c|| / \Sigma|F_o|$ for $I > \sigma(I)$; $Rw(F) = [\Sigma w(F_o^2 - F_c^2)^2/\Sigma w(F_o^2)^2]^{1/2}$ for $I > 2\sigma(I)$.

contains one half complex and one molecule of methanol solvate. [Cu(C$_{42}$H$_{59}$N$_4$O$_2$)]·B(C$_6$H$_5$)$_4$·CH$_3$OH (8′) crystallized as square, purple plates. The sample mounted measured $0.24 \times 0.22 \times 0.03$ mm^3. 1397 frames were collected, yielding 51713 reflections, of which 14731 were unique. Hydrogen atoms were placed in observed or calculated positions. The asymmetric unit contains one cation, a tetraphenylborate anion and one equivalent of methanol solvent. [Zn(C$_{42}$H$_{59}$N$_4$O$_2$)](ClO$_4$) (9) presents as yellow plates. The sample used was $0.4 \times 0.2 \times 0.05$ mm^3. 1850 frames yielded 11230 reflections, of which 8803 were unique. Hydrogen atoms were placed in observed or calculated positions. Partially occupied positions were assigned for disorder in the *tert*-butyl groups C15–17 and C36–38. In addition, C36–38 and C36′-38′ were kept isotropic during refinement. Typical large thermal parameters were displayed by the perchlorato anion.

Computational Calculations: Electronic Structure Calculations Methods. The B3LYP/6-31G(d) level of theory[48] was employed throughout. All calculations were done using the GAUSSIAN series of programs.[49] Geometries were fully minimized unless otherwise indicated, without symmetry constraints, using standard methods.[50] Cartesian coordinates of all optimized structures are provided as supporting material.

Syntheses

Preparation of the Ligands HL^A, HL^{tBu2A}, HL^{tBu2I}, and HL^{tBu2ODA}: The ligands were synthesized according to the literature.[17,20,21] Basic procedures are explained for the syntheses of the nickel, copper, and zinc complexes.

Preparation of the Metallosurfactant [Ni^{II}(L^{tBuODA})(OAc)] (1): A 10 mL MeOH solution of Ni(OAc)$_2$·4H$_2$O (0.25 g, 1.0 mmol) was added dropwise to a 30 mL MeOH solution of HL^{tBuODA} (0.58 g, 1.0 mmol). The solution was stirred and gently refluxed for 2 h, and then filtered to eliminate unreacted solids. Slow solvent evaporation after concentration to one-third of its original volume yielded a waxy, dark green film layer. Yield 0.50 g, 72% for [C$_{41}$H$_{68}$N$_2$O$_3$Ni$_1$] (1214.6). IR data (KBr): ṽ = 2933–2857 (alkyl chain and *tert*-butyl C–H stretches), 1609 (C=N from pyridine), 1574 (antisym. acetate stretch), 1480 (C–O from phenyl) cm^{-1}. MS data (ESI$^+$ in MeOH): m/z = 695.4 [Ni(L^{tBuODA})(OAc) + H]$^+$.

Preparation of the Metallosurfactants [Ni^{II}(L^{tBuODA})$_2$] (2), [Cu^{II}(HL^{tBuODA})(L^{tBuODA})]ClO$_4$ (3), and [Zn^{II}(HL^{tBuODA})$_2$]-(ClO$_4$)$_2$ (4)

CAUTION! *Although no difficulties were experienced, species 3–4 and 8–9 were isolated as their perchlorate salts, and therefore they should be handled as potentially explosive.*

A 10 mL MeOH solution containing the salts Ni(ClO$_4$)$_2$·6H$_2$O (0.18 g, 0.5 mmol), Cu(ClO$_4$)$_2$·6H$_2$O (0.185 g, 0.5 mmol), or Zn(ClO$_4$)$_2$·6H$_2$O (0.186 g, 0.5 mmol) was added dropwise to a 30 mL MeOH solution containing HL^{tBuODA} (0.58 g, 1.0 mmol) and Et$_3$N (0.14 mL, 1.0 mmol). In each case the resulting solutions were stirred under mild reflux for 1–2 h and then filtered while warm. The solvent was removed by rotary evaporation and the crude products were dissolved in 50 mL dichloromethane and washed with 4×50 mL of saturated brine solution in a separation funnel. The dichloromethane phase was then dried with Na$_2$SO$_4$ and concentrated to one third of its origonal volume. Slow solvent evaporation yielded a brown thick oil for 2, a brownish green waxy solid for 3 and an off-white solid for 4.

2: Yield 0.42 g, 70% for [C$_{78}$H$_{130}$N$_4$O$_2$Ni$_1$] (1214.6). IR data (KBr): ṽ = 2958–2854 (alkyl chain and *tert*-butyl C–H stretches), 1610 (C=N from pyridine), 1467 (C–O from phenyl) cm^{-1}. MS data (ESI$^+$ in MeOH): m/z = 1214 [Ni(L^{tBuODA})$_2$ + H]$^+$. The consistency of the material precludes elemental analysis.

3: Yield 0.46 g, 68%. C$_{79}$H$_{135}$ClCuN$_4$O$_7$ (1351.9): calcd. C 70.18, H 10.02, N 4.14; found C 69.66, H 9.84, N 3.97. IR data (KBr): ṽ = 2922–2856 (alkyl chain and *tert*-butyl C–H stretches), 1611 (C=N from pyridine), 1467 (C–O from phenyl), 1104 (Cl–O from ClO$_4^-$) cm^{-1}. MS data (ESI$^+$ in MeOH): m/z = 1219.0 [Cu(HL^{tBuODA})-(L^{tBuODA})]$^+$.

4: Yield 0.50 g, 70%. C$_{78}$H$_{132}$Cl$_2$N$_4$O$_{10}$Zn (1422.2): calcd. C 65.87, H 9.36, N 3.94; found C 66.12, H 9.34, N 4.00. IR data (KBr): ṽ = 2923–2851 (alkyl chain and *tert*-butyl C–H stretches), 1608 (C=N from pyridine), 1472 (C–O from phenyl), 1116 (Cl–O from ClO$_4^-$) cm^{-1}. MS data (ESI$^+$ in MeOH): m/z = 1220.0 [Zn(HL^{tBuODA})-(L^{tBuODA})]$^+$ and 641.5 [($m/2$) + CH$_3$OH].

Preparation of the Archetype [Ni^{II}(L^{tBuI})(OAc)]·CH$_3$OH (5): The synthesis of this complex similarly follows that of 1. The crude red powder product obtained after roto-evaporation was recrystallized using a 1:1 dichloromethane/methanol solvent combination to give needle-like crystals. Yield 0.65 g, 77%. C$_{24}$H$_{34}$N$_2$NiO$_4$ (473.2): calcd. C 60.81, H 7.24, N 5.92; found C 59.92, H 7.26, N 6.18. IR data (KBr): ṽ = 1600 (C=N from pyridine), 1570 (antisym. acetate

stretch) cm^{-1}. 1487 (C–O from phenyl), 2957–2869 (C–H). MS data (ESI$^+$ in MeOH): m/z = 413.4 [Ni(L^{tBuI}) + CH$_3$OH]$^+$.

Preparation of the Archetypes [Ni^{II}(L^A)$_2$]·H$_2$O·CH$_3$OH (6), [Ni^{II}-(L^{tBuA})$_2$]·2CH$_3$OH (7), [Cu^{II}(HL^{tBuA})(L^{tBuA})]ClO$_4$ (8), [Zn^{II}-(HL^{tBuA})(L^{tBuA})]ClO$_4$ (9): A general synthetic approach was followed for the archetypical complexes. A 10 mL solution of Ni(ClO$_4$)$_2$·6H$_2$O (0.366 g, 1.0 mmol) for **6** and **7**, Cu(ClO$_4$)$_2$·6H$_2$O (0.370 g, 1 mmol) for **8**, or Zn(ClO$_4$)$_2$·6H$_2$O (0.372 g, 1 mmol) for **9** was added dropwise to a 30 mL MeOH solution containing 2.0 mmol of the appropriate ligand (HL^A for **6** and HL^{tBuODA} for **7**–**9**) and 2 equiv. of Et$_3$N (0.28 mL, 2.0 mmol). In each reaction, the resulting solution was stirred and warmed gently for 1 h. The metal complexes were recovered either by precipitation or by slow evaporation and were collected by filtration and washed with diethyl ether. Recrystallization in MeOH afforded suitable crystals for X-ray analysis for **6**, **7**, **8**, and **9** after slow solvent evaporation.

6: Yield 0.53 g, 79%. C$_{27}$H$_{32}$N$_4$NiO$_4$ (535.3): calcd. C 60.65, H 6.03, N 10.48; found C 60.23, H 6.17, N 10.21. IR data (KBr): ṽ = 3291 (N–H), 2924 (C–H stretches), 1606, 1593 (C=N from pyridine), 1486 (C–O from phenyl) cm^{-1}. MS data (ESI$^+$ in MeOH): m/z = 484.1 [Ni(L^A)$_2$ + H]$^+$.

7: Yield 0.59 g, 76%. C$_{44}$H$_{66}$N$_4$NiO$_4$ (773.7): calcd. C 68.35, H 8.61, N 7.25; found C 68.23, H 8.74, N 7.20. IR data (KBr): ṽ = 3322 (N–H), 2950 (C–H), 1607 (C=N from pyridine), 1469 (C–O from phenyl) cm^{-1}. MS data (ESI$^+$ in MeOH): m/z = 709.3 [Ni(L^{tBuA})$_2$ + H]$^+$.

8: Yield 0.68 g, 82%. C$_{42}$H$_{61}$ClCuN$_4$O$_7$ (832.9): calcd. C 60.56, H 7.38, N 6.73; found C 60.05, H 7.36, N 6.81. IR data (KBr): ṽ = 3439 (OH), 3259 (N–H), 2954 (C–H), 1603 (C=N from pyridine), 1443 (C–O from phenyl), 1120 (Cl–O from ClO$_4^-$) cm^{-1}. MS data (ESI$^+$ in MeOH): m/z = 714.4 [Cu(HL^{tBuA})(L^{tBuA})]$^+$. **Note:** X-ray quality crystals were generated through counterion exchange using a 3-fold excess of tetraphenylboron sodium salt in 50 mL methanol.

9: Yield 0.60 g, 73%. C$_{42}$H$_{59}$ClN$_4$O$_6$Zn (816.8): calcd. C 61.76, H 7.28, N 6.86; found C 61.84, H 7.32, N 6.90. IR data (KBr): ṽ = 3290 (N–H), 2957–2869 (C–H), 1608 (C=N from pyridine), 1474 (C–O from phenyl), 1097 (Cl–O from ClO$_4^-$) cm^{-1}. MS data (ESI$^+$ in MeOH): m/z = 715.2 [Zn^{II}(HL^{tBuA})(L^{tBuA})]$^+$.

Supporting Information (see also the footnote on the first page of this article): Selected MOs for compound **9**, Cartesian coordinates for DFT calculations.

[1] J. Park, A. N. Pasupathy, J. I. Goldsmith, C. Chang, Y. Yaish, J. R. Petta, M. Rinkoski, J. P. Sethna, H. D. Abruna, P. L. McEuen, D. C. Ralph, *Nature* **2002**, *417*, 722.

[2] a) J. Zhang, B. W.-K. Chu, N. Zhu, V. W.-W. Yam, *Organometallics* **2007**, *26*, 5423; b) V. W.-w. Yam, B. Li, Y. Yang, B. W.-k. Chu, K. M.-c. Wong, K.-k. Cheung, *Eur. J. Inorg. Chem.* **2003**, 4035; c) B. W.-K. Chu, V. W.-W. Yam, *Inorg. Chem.* **2001**, *40*, 3324.

[3] a) K. Binnemans, K. Lodewyckx, B. Donnio, D. Guillon, *Chem. Eur. J.* **2002**, *8*, 1101; b) K. Binnemans, Y. G. Galyametdinov, R. Van Deun, D. W. Bruce, S. R. Collinson, A. P. Polishchuk, I. Bikchantaev, W. Haase, A. V. Prosvirin, L. Tinchurina, I. Litvinov, A. Gubajdullin, A. Rakhmatullin, K. Uytterhoeven, L. Van Meervelt, *J. Am. Chem. Soc.* **2000**, *122*, 4335.

[4] a) J.-M. Rueff, N. Masciocchi, P. Rabu, A. Sironi, A. Skoulios, *Eur. J. Inorg. Chem.* **2001**, 2843; b) J.-M. Rueff, N. Masciocchi, P. Rabu, A. Sironi, A. Skoulios, *Chem. Eur. J.* **2002**, *08*, 1813.

[5] J. B. Beck, S. J. Rowan, *J. Am. Chem. Soc.* **2003**, *125*, 13922.

[6] S. Hayami, K. Danjobara, Y. Shigeyoshi, K. Inoue, Y. Ogawa, Y. Maeda, *Inorg. Chem. Commun.* **2005**, *8*, 506.

[7] I. K. Lednev, M. C. Petty, *Adv. Mater.* **1996**, *8*, 615.

[8] F. W. Vergeer, X. Chen, F. Lafolet, L. De Cola, H. Fuchs, L. Chi, *Adv. Funct. Mater.* **2006**, *16*, 625.

[9] P. C. Griffiths, I. A. Fallis, T. Chuenpratoom, R. Watanesk, *Adv. Colloid Interf. Sci.* **2006**, *122*, 107; P. C. Griffiths, I. A. Fallis, D. J. Willock, A. Paul, C. L. Barrie, P. M. Griffiths, G. M. Williams, S. M. King, R. K. Heenan, R. Goergl, *Chem. Eur. J.* **2004**, *10*, 2022.

[10] X. Chen, S. Lenhert, M. Hirtz, N. Lu, H. Fuchs, L. Chi, *Acc. Chem. Res.* **2007**, *40*, 393.

[11] L. Yang, H. Peng, K. Huang, J. T. Mague, H. Li, Y. Lu, *Adv. Funct. Mater.* **2008**, *18*, 1526.

[12] C. J. Brabec, N. S. Sariciftci, J. C. Hummelen, *Adv. Funct. Mater.* **2001**, *11*, 15.

[13] a) D. A. Jaeger, M. F. Peacock, D. S. Bohle, *Langmuir* **2003**, *19*, 4859; b) N. Arulsamy, D. S. Bohle, P. A. Goodson, D. A. Jaeger, V. B. Reddy, *Inorg. Chem.* **2001**, *40*, 836.

[14] a) H. J. Choi, M. P. Suh, *Inorg. Chem.* **2003**, *42*, 1151; b) M. F. Ryan, R. A. Metcalfe, A. B. P. Lever, M.-a. Haga, *J. Chem. Soc., Dalton Trans.* **2000**, 2357; c) K. Wang, M.-a. Haga, H. Monjushiro, M. Akiba, Y. Sasaki, *Inorg. Chem.* **2000**, *39*, 4022.

[15] R. Shakya, P. H. Keyes, M. J. Heeg, A. Moussawel, P. A. Heiney, C. N. Verani, *Inorg. Chem.* **2006**, *45*, 7587.

[16] R. Shakya, S. S. Hindo, L. Wu, S. Ni, M. Allard, M. J. Heeg, S. R. P. da Rocha, G. T. Yee, H. P. Hratchian, C. N. Verani, *Chem. Eur. J.* **2007**, *13*, 9948.

[17] R. Shakya, S. S. Hindo, L. Wu, M. M. Allard, M. J. Heeg, H. P. Hratchian, B. R. McGarvey, S. R. P. da Rocha, C. N. Verani, *Inorg. Chem.* **2007**, *46*, 9808.

[18] S. S. Hindo, R. Shakya, N. S. Rannulu, M. M. Allard, M. J. Heeg, M. T. Rodgers, S. R. P. da Rocha, C. N. Verani, *Inorg. Chem.* **2008**, *47*, 3119.

[19] J. A. Driscoll, M. M. Allard, L. Wu, M. J. Heeg, S. R. P. da Rocha, C. N. Verani, *Chem. Eur. J.* **2008**, accepted.

[20] C. Imbert, H. P. Hratchian, M. Lanznaster, M. J. Heeg, L. M. Hryhorczuk, B. R. McGarvey, H. B. Schlegel, C. N. Verani, *Inorg. Chem.* **2005**, *44*, 7414.

[21] R. Shakya, C. Imbert, H. P. Hratchian, M. Lanznaster, M. J. Heeg, B. R. McGarvey, M. Allard, H. B. Schlegel, C. N. Verani, *Dalton Trans.* **2006**, 2517.

[22] R. Shakya, F. Peng, J. Liu, M. J. Heeg, C. N. Verani, *Inorg. Chem.* **2006**, *45*, 6263.

[23] O. Rotthaus, V. Labet, C. Philouze, O. Jarjayes, F. Thomas, *Eur. J. Inorg. Chem.* **2008**, 4215.

[24] A. A. Khandar, S. A. Hosseini-Yazdi, S. A. Zarei, *Inorg. Chim. Acta* **2005**, *358*, 3211.

[25] BMT stems for Bailar, Missler and Tarr notation, where ⟨A1B2⟩ indicates that A is *trans* to B, with A and B corresponding to the pyridine (Npy) amine (Nam), or phenolato (Ophen) groups. Subscripts 1 and 2 designate respectively the first and the second ligand. This concise notation saves space and was adapted by G. Miessler and D. Tarr, in *Inorganic Chemistry*, Pearson-Prentice Hall, p. 311–315, **2004** from the original work by John Bailar, Jr, *J. Chem. Educ.* 1957, *34*, 334 and 623. The link to Prof. Bailar's work has been explained by Prof. Miessler in a personal communication to C.N.V.

[26] O. Rotthaus, F. Thomas, O. Jarjayes, C. Philouze, E. Saint-Aman, J.-L. Pierre, *Chem. Eur. J.* **2006**, *12*, 6953.

[27] A. W. Addison, T. N. Rao, J. Reedijk, J. Van Rijn, G. C. Verschoor, *J. Chem. Soc., Dalton Trans.* **1984**, 1349.

[28] A. Neves, C. N. Verani, M. A. de Brito, I. Vencato, A. Mangrich, G. Oliva, D. D. H. F. Souza, A. A. Batista, *Inorg. Chim. Acta* **1999**, *290*, 207.

[29] J. Kaizer, J. Pap, G. Speier, L. Parkanyi, L. Korecz, A. Rockenbauer, *J. Inorg. Biochem.* **2002**, *91*, 190.

[30] H. Adams, N. A. Bailey, D. E. Fenton, Q.-Y. He, *J. Chem. Soc., Dalton Trans.* **1997**, 1533.

[31] M. Lanznaster, A. Neves, I. Vencato, A. J. Bortoluzzi, H. Gallardo, S. P. Machado, A. M. C. Assumpcao, *J. Braz. Chem. Soc.* **2006**, *17*, 289.

[32] A. dos Anjos, A. J. Bortoluzzi, B. Szpoganicz, M. S. B. Caro, G. R. Friedermann, A. S. Mangrich, A. Neves, *Inorg. Chim. Acta* **2005**, *358*, 3106.

[33] A. Neves, I. Vencato, C. N. Verani, *J. Braz. Chem. Soc.* **1997**, *8*, 265.

[34] A. B. P. Lever, *Inorganic Electronic Spectroscopy*, 2nd ed., Elsevier Science, Amsterdam, **1984**.

[35] S. Mukhopadhyay, D. Mandal, D. Ghosh, I. Goldberg, M. Chaudhury, *Inorg. Chem.* **2003**, *42*, 8439.

[36] H. Ohtsu, K. Tanaka, *Inorg. Chem.* **2004**, *43*, 3024.

[37] a) R. Viswanathan, M. Palaniandavar, T. Balasubramanian, P. T. Muthiah, *J. Chem. Soc., Dalton Trans.* **1996**, 2519; b) U. Rajendran, R. Viswanathan, M. Palaniandavar, M. Lakshminarayanan, *J. Chem. Soc., Dalton Trans.* **1992**, 3563.

[38] a) E. Bill, J. Mueller, T. Weyhermueller, K. Wieghardt, *Inorg. Chem.* **1999**, *38*, 5795; b) U. Auerbach, U. Eckert, K. Wieghardt, B. Nuber, J. Weiss, *Inorg. Chem.* **1990**, *29*, 938.

[39] a) B. A. Jazdzewski, P. L. Holland, M. Pink, V. G. Young Jr., D. J. E. Spencer, W. B. Tolman, *Inorg. Chem.* **2001**, *40*, 6097; b) J. A. Halfen, B. A. Jazdzewski, S. Mahapatra, L. M. Berreau, E. C. Wilkinson, L. Que Jr., W. B. Tolman, *J. Am. Chem. Soc.* **1997**, *119*, 8217.

[40] a) S. Carvalho, R. Delgado, M. G. B. Drew, V. Felix, *Dalton Trans.* **2007**, 2431; b) C. A. VanOrman, K. V. Reddy, L. M. Sayre, F. L. Urbach, *Polyhedron* **2001**, *20*, 541; c) E. L. Hegg, S. H. Mortimore, C. L. Cheung, J. E. Huyett, D. R. Powell, J. N. Burstyn, *Inorg. Chem.* **1999**, *38*, 2961.

[41] M. C. Petty, *Langmuir–Blodgett Films*, Cambridge University Press, New York, **1996**, pp. 65.

[42] a) S. Kundu, A. Datta, S. Hazra, *Phys. Rev. E: Stat., Nonlinear, Soft Matter Phys.* **2006**, *73*, 051608/051601–051608/051607; b) S. Kundu, A. Datta, S. Hazra, *Langmuir* **2005**, *21*, 5894.

[43] C. Ybert, W. Lu, G. Moller, C. M. Knobler, *J. Phys.: Condens. Matter* **2002**, *14*, 4753.

[44] H. E. Ries Jr., *Nature* **1979**, *281*, 287.

[45] J. Galvan-Miyoshi, S. Ramos, J. Ruiz-Garcia, R. Castillo, *J. Chem. Phys.* **2001**, *115*, 8178.

[46] *APEX-II*, SMART, SAINT, SAINT-7, SADABS and TWIN-ABS collection and processing programs are distributed by the manufacturer. Bruker AXS, Inc., Madison WI, USA **2001**.

[47] a) H. Sheldrick, *SHELX-97 and CELL-NOW*, University of Göttingen, Germany, **1997**; b) G. M. Sheldrick, *Acta Crystallogr., Sect. A* **2008**, *64*, 112.

[48] a) R. Ditchfield, W. J. Hehre, J. A. Pople, *J. Chem. Phys.* **1971**, *54*, 724; b) W. J. Hehre, R. Ditchfield, J. A. Pople, *J. Chem. Phys.* **1972**, *56*, 2257; c) P. C. Hariharan, J. A. Pople, *Theor. Chim. Acta* **1973**, *28*, 213; d) P. C. Hariharan, J. A. Pople, *Mol. Phys.* **1974**, *27*, 209; e) M. S. Gordon, *Chem. Phys. Lett.* **1980**, *76*, 163; f) A. D. Becke, *Phys. Rev. A: Gen. Phys.* **1988**, *38*, 3098; g) C. Lee, W. Yang, R. G. Parr, *Phys. Rev. B: Condens. Matter* **1988**, *37*, 785; h) A. D. Becke, *J. Chem. Phys.* **1993**, *98*, 5648.

[49] M. J. Frisch, G. W. Trucks, H. B. Schlegel, G. E. Scuseria, M. A. Robb, J. R. Cheeseman, J. A. Montgomery, T. V. K. N. Kudin Jr., J. C. Burant, J. M. Millam, S. S. Iyengar, J. Tomasi, V. Barone, B. Mennucci, M. Cossi, G. Scalmani, N. Rega, G. A. Petersson, H. Nakatsuji, M. Hada, M. Ehara, K. Toyota, R. Fukuda, J. Hasegawa, M. Ishida, T. Nakajima, Y. Honda, O. Kitao, H. Nakai, M. Klene, X. Li, J. E. Knox, H. P. Hratchian, J. B. Cross, V. Bakken, C. Adamo, J. Jaramillo, R. Gomperts, R. E. Stratmann, O. Yazyev, P. Y. Ayala, K. Morokuma, G. A. Voth, P. Salvador, J. J. Dannenberg, V. G. Zakrzewski, S. Dapprich, A. D. Daniels, M. C. Strain, O. Farkas, D. K. Malick, A. D. Rabuck, K. Raghavachari, J. B. Foresman, J. V. Ortiz, Q. Cui, A. G. Baboul, S. Clifford, J. Cioslowski, B. B. Stefanov, G. Liu, A. Liashenko, P. Piskorz, I. Komaromi, R. L. Martin, D. J. Fox, T. Keith, M. A. Al-Laham, C. Y. Peng, A. Nanayakkara, M. Challacombe, P. M. W. Gill, B. Johnson, W. Chen, M. W. Wong, C. Gonzalez, J. A. Pople, *Gaussian 03, Revision D.01*, Gaussian, Inc., Wallingford CT, **2004**.

[50] H. B. Schlegel, *J. Comput. Chem.* **1982**, *3*, 214.

Appendix J

Iron Discoids

Frank D. Lesh, Rama Shanmugam, Marco M. Allard, Mauricio Lanznaster, Mary Jane Heeg, M. T. Rodgers, Jason M. Shearer, and Cláudio N. Verani

"A Modular Approach to Redox-Active Multimetallic Hydrophobes

of Discoid Topology"

My contribution to this work consisted of the electronic structure calculations.

A Modular Approach to Redox-Active Multimetallic Hydrophobes of Discoid Topology

Frank D. Lesh,[†] Rama Shanmugam,[†] Marco M. Allard,[†] Maurício Lanznaster,[†] Mary Jane Heeg,[†] M. T. Rodgers,[†] Jason M. Shearer,[‡] and Cláudio N. Verani*,[†]

[†]Department of Chemistry, Wayne State University, Detroit, Michigan 48202, and
[‡]Department of Chemistry, University of Nevada, Reno, Nevada 89557

A new modular $[Fe^{II}(Fe^{III}L^2)_3](PF_6)_2$ species with discoid (disk-like) topology exhibits redox and surfactant properties and points to a new approach for multimetallic Langmuir film precursors.

The combination of amphiphilic properties with controllable and tunable behavior of transition metal complexes leads to metal-containing surfactants that exhibit interfacial organization, along with variable geometric, charge, redox, optical, and magnetic properties.[1] Considerable progress has been made toward the understanding of this metal ion/amphiphile cooperativity in supramolecular assemblies.[2] Potential high-end uses of metallosurfactants include films for optoelectronics[3] and logic and memory operations[4] and micellar luminescence and electron transfer.[5] Our group is developing precursor metallosurfactants, aiming at the inclusion of ligand- and metal-centered redox activity while preserving the ability to organize into well-ordered films.[6] The current approach involves incorporation of selected metal ions into a phenolate-based headgroup of a designer amphiphile. The phenolate can then be oxidized into a phenoxyl radical. However, because the stabilization of radicals requires the incorporation of *tert*-butyl groups into the headgroup, it has been observed that improved redox properties lead to decreased amphiphilic character and vice versa. Therefore, the development of new topologies that can accommodate both properties becomes highly relevant. Recently, we reported
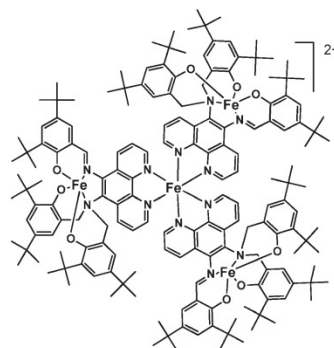
Figure 1. Modular discoid species $[Fe^{II}(Fe^{III}L^2)_3]^{2+}$.

on an $[Fe^{III}L^1]$ species $((L^1)^{3-}$ is a phenylene−diamine/triphenolate ligand) in which five-coordinate iron(III) centers seem to enhance the formation and reversibility of three consecutive phenolate/phenoxyl processes on the cyclic voltammetric time scale.[7] The related species $[Fe^{III}L^2]$, where $(L^2)^{3-}$ describes a similar phenanthrolinediamine/trisphenolate ligand, served as a module for $[Fe^{III}(L^2)Cu^{II}(Cl)_2(MeOH)]$. The redox responses in this bimetallic species are based on controlled oxidations and reductions of its fundamental components, i.e., the metal centers and the electroactive arms of the ligand.[10] Specific potentials trigger definite spin ground-state changes, as observed by EPR spectroscopy.

In this account, we describe the synthesis and characterization of the tetrametallic $[Fe^{II}(Fe^{III}L^2)_3](PF_6)_2$ (Figure 1), along with studies on its electrochemical and surfactant properties.

This discoid molecule (oblate spheroid with $x = y > z$) is a first example that reconciles the use of *tert*-butyl groups to promote redox activity and surfactancy by enhancement of

*To whom correspondence should be addressed. E-mail: cnverani@chem.wayne.edu.

(1) (a) Bodenthin, Y.; Pietsch, U.; Moehwald, H.; Kurth, D. G. *J. Am. Chem. Soc.* **2005**, *127*, 3110. (b) Talham, D. R. *Chem. Rev.* **2004**, *104*, 5479.

(2) (a) Hoogenboom, R.; Fournier, D.; Schubert, U. S. *Chem. Commun.* **2008**, 155–62. (b) Verani, C. *McGraw-Hill Yearb. Sci. Technol* **2010**, 142.

(3) (a) Zhang, J.; Chu, B. W.-K.; Chu, Z. N.; Yam, V. W.-W. *Organometallics* **2007**, *26*, 5423.

(4) (a) Wassel, R. A.; Gorman, C. B. *Angew. Chem., Int. Ed.* **2004**, *43*, 5120. (b) Low, P. J. *Dalton Trans* **2005**, 2821.

(5) (a) Guerrero-Martinez, A.; Vida, Y.; Dominguez-Gutierrez, D.; Albuquerque, R. Q.; De Cola, L. *Inorg. Chem.* **2008**, *47*, 9131. (b) Wang, K.; Haga, M.-a.; Monjushiro, H.; Akiba, M.; Sasaki, Y. *Inorg. Chem.* **2000**, *39* (18), 4022.

(6) (a) Hindo, S. S.; Shakya, R.; Rannulu, N. S.; Allard, M. M.; Heeg, M. J.; Rodgers, M. T.; da Rocha, S. R. P.; Verani, C. N. *Inorg. Chem.* **2008**, *47*, 3119. (b) Shakya, R.; Imbert, C.; Hratchian, H. P.; Lanznaster, M.; Heeg, M. J.; McGarvey, B. R.; Allard, M.; Schlegel, H. B.; Verani, C. N. *Dalton Trans.* **2006**, 2517.

(7) Lanznaster, M.; Hratchian, H. P.; Heeg, M. J.; Hryhorczuk, L. M.; McGarvey, B. R.; Schlegel, H. B.; Verani, C. N. *Inorg. Chem.* **2006**, *45*, 955.

(8) Lanznaster, M.; Heeg, M. J.; Yee, G. T.; McGarvey, B. R.; Verani, C. N. *Inorg. Chem.* **2007**, *46*, 72.

(9) Elemental analyses gave lower than expected carbon contents for $[Fe^{II}(Fe^{III}L^2)_3](PF_6)_2$. Best results were obtained for $[Fe^{II}(Fe^{III}L^2)_3](ClO_4)_2$ $(C_{171}H_{213}Cl_2Fe_4N_{12}O_{17}$, MW = 3002.88) with C (calcd/exptl), 68.40/ 68.63; H, 7.15/7.27; N, 5.60/5.68.

(10) Davis, M. I.; Orville, A. M.; Neese, F.; Zaleski, J. M.; Lipscomb, J. D.; Solomon, E. I. *J. Am. Chem. Soc.* **2002**, *124*, 602.

the species hydrophobic character. Thus, it supports the development of a modular approach to discoid multimetallic film precursors. Treatment of $[Fe^{III}L^2]$ with anhydrous $FeCl_2$ in a 3:1 ratio in methanol and under argon yielded the tetrametallic species $[Fe^{II}(Fe^{III}L^2)_3](PF_6)_2$ as a homogeneous microcrystalline solid. In spite of the apparent simplicity of the preparation, several attempts under aerobic conditions led to the formation of undesirable side products. This compound, as presently synthesized, was characterized by means of exact ESI mass spectrometry and elemental analysis.[9] Further characterization was obtained by comparative infrared, UV−visible, and XANES/EXAFS spectroscopies and electrochemical data between $[Fe^{II}(Fe^{III}L^2)_3](PF_6)_2$, the module $[Fe^{III}L^2]$, and the compound $[Fe^{II}(phen)_3](PF_6)_2$ (phen = 1,10-phenanthroline). The exact ESI-MS for the tetrametallic species (2802.3976 Da) in methanol exhibits peaks at $m/z = 1401.69970$ related to the bivalent cation $[Fe^{II}(Fe^{III}L^2)_3]^{+2}$ and 916.49504 associated with the module $[(Fe^{III}L^2)_3 + H^+]^+$. Comparison of the features present in the UV−visible spectra of $[Fe^{II}(Fe^{III}L^2)_3](PF_6)_2$, $[Fe^{III}L^2]$, and $[Fe^{II}(phen)_3](PF_6)_2$ in CH_2Cl_2 also permits one to ascertain the nature of the multimetallic species. The module $[Fe^{III}L^2]$ shows the expected intraligand $\pi \rightarrow \pi^*$ and N→Fe charge transfer bands at 281 and 333 nm (115 900 and 69 000 L $mol^{-1}cm^{-1}$), respectively. The phenolate-to-metal charge transfer bands[10] ($p\pi \rightarrow d\sigma^*$ and $p\pi \rightarrow d\pi^*$) appear at 411 and 463 nm (both at 27 500 L $mol^{-1}cm^{-1}$), thus unusually close to each other. This proximity is attributed to the five-coordination of the metal. The $[Fe^{II}(Fe^{III}L^2)_3](PF_6)_2$ species presents the analogous processes at 279 (249 700), 336 (96 000), and 486 nm (50 300 L $mol^{-1}cm^{-1}$), along with a new band at 525 nm (51 700 L $mol^{-1}cm^{-1}$). This new process is comparable to the metal-to-phenanthroline charge transfer present in $[Fe^{II}(phen)_3](PF_6)_2$ at 511 nm (9390 L $mol^{-1}cm^{-1}$), thus indicating the presence of all expected chromophores.[11] The IR spectrum of $[Fe^{II}(Fe^{III}L^2)_3](PF_6)_2$ presents peaks at 2870−2960 and 1605 cm^{-1} associated, respectively, with the *tert*-butyl and C=N groups in the module $[Fe^{III}L^2]$. Peaks associated with the counterion PF_6^- appear at 840 cm^{-1}. An equally prominent peak related to the out-of-plane deformation of the phenanthroline rings and enhanced through coordination is observed at 558 cm^{-1}. The XANES/EXAFS spectra of $[Fe^{II}(Fe^{III}L^2)_3](PF_6)_2$ and the module $[Fe^{III}L^2]$ are compared in Figure 2.

The edge position of $[Fe^{II}(Fe^{III}L^2)_3](PF_6)_2$ occurs at a slightly lower energy than that of $[Fe^{III}L^2]$ (7121.8(3) vs 7122.2(2) eV). A reduction from Fe(III) to Fe(II) should result in a lowering of the edge energy by ∼2−3 eV. This small shift in edge energy is, therefore, consistent with the presence of both trivalent and bivalent oxidation states, where the Fe(III) state is predominant. A pre-edge peak in the XANES of $[Fe^{II}(Fe^{III}L^2)_3](PF_6)_2$ occurs at 7113.0(1) eV, which corresponds to the parity-forbidden Fe(1s → 3d) transitions and has an area of 0.16(1) eV relative to the edge. These transitions gain intensity in noncentrosymmetric coordination environments through a dipole mechanism and are thus more intense in five- vs six-coordinate environments.[12] The Fe(1s → 3d) tran-

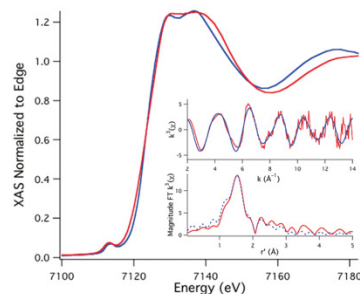**Figure 2.** XANES region of the Fe K-edge XAS for $[Fe^{II}(Fe^{III}L^2)_3]$-$(PF_6)_2$ (red) and $[Fe^{III}L^2]$ (blue). Inset: EXAFS region for $[Fe^{II}(Fe^{III}L^2)_3]$-$(PF_6)_2$. Data (red) and simulation (blue). Shell 1 (Fe−O): $n = 2$, $r = 1.839(6)$ Å, $\sigma^2 = 0.0048(13)$ Å^2. Shell 2 (Fe−N): $n = 3$, $r = 1.960(3)$ Å, $\sigma^2 = 0.0010(5)$ Å^2. Shell 3 (Fe−N): $n = 1$, $r = 2.104(13)$ Å, $\sigma^2 = 0.0030(2)$ Å^2. Shell 4 (Fe−C): $n = 4$, $r = 2.919(6)$ Å, $\sigma^2 = 0.0053(8)$ Å^2. $E° = 7128.7$ eV. $\varepsilon^2 = 0.63$.
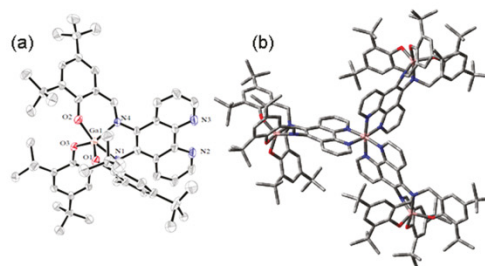

Figure 3. (a) ORTEP for $[GaL^2]$, Ga−O(3) = 1.828(3), Ga−O(1) = 828(3), Ga−O(2) = 1.899(3), Ga−N(4) = 1.975(4), Ga−N(1) = 2.266(4) Å. (b) MM-UFF model for $[Ga(GaL^2)_3]^{2+}$.

sition of $[Fe^{III}L^2]$ at 7113.2(1) eV has an area of 0.21(1) eV relative to the edge. Therefore, the average iron coordination environment is slightly more symmetric in $[Fe^{II}(Fe^{III}L^2)_3]$-$(PF_6)_2$ than in $[Fe^{III}L^2]$, suggesting that the multimetallic species contains both five- and six-coordinate iron centers. The EXAFS region of $[Fe^{II}(Fe^{III}L^2)_3](PF_6)_2$ was best modeled with iron surrounded by nitrogen and oxygen donors. Three shells are resolvable: one shell containing two short Fe−O scatterers at 1.84 Å, one shell containing three Fe−N or Fe−O scatterers at 1.96 Å, and one shell containing a single long Fe−N scatterer at 2.10 Å. This is consistent with the average iron environment predicted for $[Fe^{II}(Fe^{III}L^2)_3](PF_6)_2$.

In spite of several attempts, the determination of the molecular structure for $[Fe^{II}(Fe^{III}L^2)_3](PF_6)_2$ via X-ray diffraction was not possible. The structure of the module $[Fe^{III}L^2]$ was published recently,[8] but attempts to use it as a starting point for calculations has proven to be nontrivial due to the large number of unpaired electrons at the iron centers.

Therefore, we obtained a crystal structure for the analogous compound $[Ga^{III}L^2]$.[13] The ORTEP representation is shown in Figure 3a with selected bond lengths. The similar nature of the gallium and iron structures is inferred by their neutral character, the identity of the ligand showing a mono-substituted amine N4 with a single phenolate appended,

(11) All expected chromophores: Braterman, P. S.; Song, J.-I.; Peacock, R. D. *Inorg. Chem.* **1992**, *31*, 555.

(12) (a) Roe, A. L.; Schneider, D. J.; Mayer, R. J.; Pyrz, J. W.; Widom, J. L.; Que, L., Jr. *J. Am. Chem. Soc.* **1984**, *106*, 1676. (b) Westre, T. E.; Kennepohl, P.; DeWitt, J. G.; Hedman, B.; Hodgson, K. O.; Solomon, E. I. *J. Am. Chem. Soc.* **1997**, *119*, 6297.

(13) $[Ga^{III}L^2]$: $C_{63}H_{80}GaN_7O_3$, $M = 1053.06$ Bruker P4/CCD (Mo/graphite), $T = 208(2)$ K, triclinic, P(−1), $a = 13.5969(18)$, $b = 14.763(2)$, $c = 15.893(2)$Å, $\alpha = 113.395(4)$, $\beta = 92.907(4)$, $\gamma = 93.361(4)°$, $V = 2913.5(7)$ Å^3, $Z = 2$, $D_{calc} = 1.200$ Mg/m^3, abs. coeff = 0.522 mm^{-1}, 15 444 refls collected, 12 319 unique [R(int) = 0.042], $\theta = 2.04−28.31°$, R1 = 0.0754, wR2 = 0.1707, GOF $F^2 = 0.896$ [$I > 2\sigma(I)$].

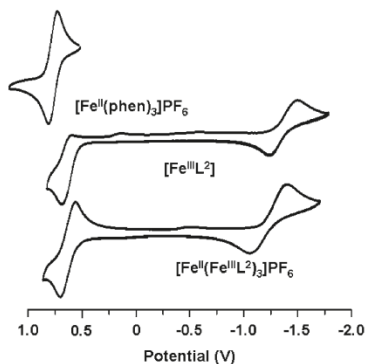**Figure 4.** CVs of $[Fe^{II}(phen)_3](PF_6)_2$ (top), $[Fe^{III}L^2]$ (middle), and $[Fe^{II}(Fe^{III}L^2)_3](PF_6)_2$ (bottom) in dichloromethane, $TBAPF_6$ vs Fc^+/Fc.

Figure 5. $[Fe^{II}(Fe^{III}L^2)_3](PF_6)_2$ at the air/water interface: (a) isothermal compression. Selected BAM images at (b) $10-40$ mN/m and (c) collapse.

whereas the vicinal amine N1 exhibits two of these groups. Furthermore, both species display a short bond length characteristic of a $C{=}N$ imine group and a metal center that is five-coordinated in a N_2O_3 environment. On the basis of these similarities, a model $[Ga^{III}(Ga^{III}L^2)_3]^{3+}$ was built and its geometry minimized using the molecular mechanics UFF force field[14] available in the Gaussian 03 software package.[15] This model describes one possible isomer, shown in Figure 3b, in which one module displays the singly appended phenolate pointing upward while the two other modules point downward. Although several isomers are possible,[16] the one displayed is more stable by *ca.* 20 kcal/mol when compared to three other calculated geometries. In all cases, the models provide evidence for the discoid nature of the multimetallic species. On the basis of the similar ionic radii of gallium(III) (0.76 Å) and iron$_{ls}$(II) (0.75 Å), as well as in the already established similarities between the complexes of both metals coordinated to these pentadentate ligands, an estimated geometric radius from the central metal to the periphery is calculated to lie between 9.0 and 11.0 Å. Examination of the positions occupied by the *tert*-butyl groups attached to each phenolate reveals that the majority of these groups point outward conferring an enhanced hydrophobic cushioning which prevents the charged and hydrophilic discoid core from sinking into water and leads to a differentiated topology. The redox responsivity of $[Fe^{II}(Fe^{III}L^2)_3](PF_6)_2$ was assessed by cyclic voltammetry (CV, vs Fc^+/Fc). Comparison with the $[Fe^{III}L^2]$ module and with $[Fe^{II}(phen)_3](PF_6)_2$ allowed for attributions to the origin of the observed processes (Figure 4).

The CVs for the multimetallic species and the module display a cathodic wave for the process ascribed to the Fe^{III}/Fe^{II} couple. This process is anodically shifted in the tetrametallic species to $E_{1/2} = -1.24$ V and is less reversible ($\Delta E_p = 0.33$ V; $|I_{pc}/I_{pa}| = 1.8$) than that of the module at $E_{1/2} = -1.37$ ($\Delta E_p = 0.25$ V; $|I_{pc}/I_{pa}| = 1.4$). The phenolate/phenoxyl oxidative process occurs for both $[Fe^{II}(Fe^{III}L^2)_3](PF_6)_2$ and $[Fe^{III}L^2]$ at *ca.* $E_{1/2} = 0.64$ V. Interestingly, an enhanced reversibility is observed in the multimetallic complex, as indicated by $|I_{pc}/I_{pa}| = 0.8$, compared to a value of 0.2 observed

for the module. This profile might be associated with—or at least influenced by—the Fe(II)−phenanthroline core, because the metal-centered process for the unsubstituted $[Fe^{II}(phen)_3](PF_6)_2$ appears at $E_{1/2} = 0.77$ V ($\Delta E_p = 0.08$ V; $|I_{pc}/I_{pa}| = 1.1$). To evaluate the efficacy of the discoid design to act in hydrophobic precursors for film formation, compression isotherms plotted as surface pressure (mN/m) vs average molecular area (Å^2) were recorded at the air/water interface in a Langmuir−Blodgett trough at 23 °C, as shown in Figure 5a. The quality of the films was monitored during compression using Brewster angle microscopy (BAM), Figure 5b. The molecules of $[Fe^{II}(Fe^{III}L^2)_3](PF_6)_2$ start to interact with each other at the subphase at *ca.* 320 Å^2/molecule. The BAM images display a highly homogeneous film from 10 to *ca.* 40 mN/m, when a decrease in the slope of the isotherm coincides with the formation of linearly oriented Newton rings,[17] suggestive of a formal constant pressure collapse mechanism.[18] The average limiting area per molecule is 280 Å^2/molecule, thus with a radius of *ca.* 9.5 Å, in excellent agreement with the estimated radius of the $[Ga^{III}(Ga^{III}L^2)_3]^{3+}$ model.

In summary, we have reported on the tetrametallic complex $[Fe^{II}(Fe^{III}L^2)_3](PF_6)_2$ of discoid topology. The presence of metallic centers and ligand moieties such as phenolates and coordinated phenanthrolines extends the redox capabilities of this species. Along with its hydrophobic character, this species is a strong candidate for the formation of redox-responsive monolayer films. To the best of our knowledge, this is the first example of a discoid tetrametallic species in which the presence of *tert*-butyl groups concomitantly enforces redox activity *and* surfactancy. This result points to a general strategy in which a modular approach can be used to develop redox-active homo- and heterometallic film precursors of discoid topology. The synthetic approach and film transfer onto solid substrates are under investigation in our laboratories.

(14) Rappé, A. K.; Casewit, C. J.; Colwell, K. S.; Goddard, W. A., III; Skiff, W. M. *J. Am. Chem. Soc.* **1992**, *114*, 10024.

(15) Frisch, M. J. *Gaussian 03*, revision D.01; Gaussian, Inc.: Wallingford, CT, 2004 (see Supporting Information for the full reference).

(16) Bergman, S. D.; Frantz, R.; Gut, D.; Kol, M.; Lacour, J. *Chem. Commun.* **2006**, 850.
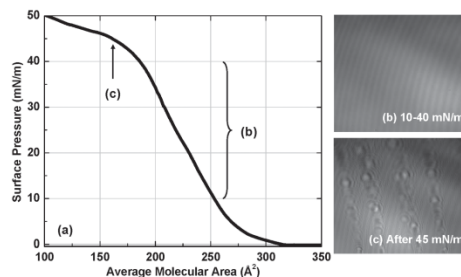
(17) Galvan-Miyoshi, J.; Ramos, S.; Ruiz-Garcia, J.; Castillo, R. *J. Chem. Phys.* **2001**, *115*, 8178.

(18) (a) Kundu, S.; Datta, A.; Hazra, S. *Langmuir* **2005**, *21*, 5894. (b) Kundu, S.; Datta, A.; Hazra, S. *Phys. Rev. E* **2006**, *73*, 051608.

ABSTRACT

**EXPERIMENTAL AND THEORETICAL ANALYSIS OF THE
ELECTRONIC BEHAVIOR IN FIVE-COORDINATE IRON(III) AND
SIX-COORDINATE COBALT(III) COMPLEXES WITH
ELECTROACTIVE PHENOL-RICH LIGANDS**

by

MARCO MATHIEU ALLARD

December 2010

Advisor: Dr. Cláudio N. Verani

Major: Chemistry (Inorganic)

Degree: Doctor of Philosophy

Three five-coordinate high-spin Iron(III) complexes containing pentadentate N_2O_3 ligands were synthesized and characterized, namely, **(1)** **[Fe^{III}(L^1)]** and **(2)** **[Fe^{III}(L^2)]**. Structural differences in ligand design, *N,N,N'*-tris(3,5-di-*tert*-butyl-2-hydroxybenzyl)benzene-1,2-diamine for **(1)** and *N,N,N'*-tris-(3,5-di-*tert*-butyl-2-hydroxybenzyl)-N'-methyl-benzene-1,2-diamine for **(2),** result in complexes that due to their forced geometry, asymmetry, and different electronic structures are able to foster phenoxyl radicals although show a sensitive dependence to both the solvent and the electrolyte system in the cyclic voltammetry. In the presence of TBAClO$_4$, **(1)** exhibits a two-electron oxidation, whereas in the presence of TBAPF$_6$**, (2)** exhibits three distinct phenolato/phenoxyl radical couples. Both **(1)** and **(2)** were redox-cycled 30 times without major decomposition at the surface of the electrode, indicating that the oxidized species are substitutionally inert. Three six coordinates low-spin cobalt(III) complexes were synthesized and their electrochemical reactions were investigated in details.

AUTOBIOGRAPHICAL STATEMENT

Marco Mathieu Allard

Department of Chemistry, Wayne State University, Detroit, MI 48202
Tel: (313) 577-9824   E-mail: mallard@chem.wayne.edu

Born November 2nd, 1980, Thetford Mines, Québec, Canada

EDUCATION
- 2003-present Ph. D. candidate (Inorganic Chemistry) under Cláudio N. Verani
  Wayne State University, Detroit, MI
- 1999-2003 B. S. Chemistry, ACS certified.
  Andrews University, Berrien Springs, MI
- 1995-1999 High School Diploma,
  Kingsway College, Oshawa, ON, Canada

HONORS AND AWARDS
- 2006 Research Assistantship funded by NSF
- 2006 Outstanding Teaching Assistant
- 2003 Outstanding Analytical Student Award, A.U.
- 2002-2003 Tait Family Endowed Scholarship, A.U.
- 2001-2002 Richard Minesinger Endowed Scholarship, A.U.
- 2000-2001 G. W. Mutch, R. M. Scorpio R. A. Wilkins Endowed Scholarship, A.U.
- 1998-1999 Leroy Albert Miller Scholarship for Scholastic Achievement, K.C.

CURRENT RESEARCH INTERESTS
- Synthesis and characterization of first row transition metal complexes which can stabilize phenoxyl radicals generation.
- Electronic structure studies of metal complexes, bonding and geometrical arrangements.
- Modular approach for synthesizing Macro-Molecules containing electro-active metals and ligands.
- Spectroscopy and electronic calculations for the elucidation of exited state structures and reactivity.

Training: Gaussian Suite Program, Electrochemistry, UV-VIS, IR, NMR, EPR, Mass Spectrometry, Schlenk technique, Glove Box.

RESEARCH EXPERIENCE
- 2003-present Graduate Studies.
- 2000 Undergraduate Summer Intern, Great Lakes Scientific, Stevensville, MI.
- 2001 Undergraduate Research, Andrews University
- 2002 Undergraduate Research, University of Notre-Dame

PROFESSIONAL AFFILIATION
- American Chemical Society (ACS)
- American Association for the Advancement of Science (AAAS)